Bosonic fields in strong-field gravity

by

Nils Peter Siemonsen

A thesis
presented to the University of Waterloo
in fulfillment of the
thesis requirement for the degree of
Doctor of Philosophy
in
Physics

Waterloo, Ontario, Canada, 2023

Examining Committee Membership

The following served on the Examining Committee for this thesis. The decision of the Examining Committee is by majority vote.

External Examiner:	Eugene Lim Professor, Dept. of Physics, King's College London
Supervisor(s):	William E. East Faculty, Perimeter Institute for Theoretical Physics
	Luis Lehner Faculty, Perimeter Institute for Theoretical Physics
Internal Member:	Avery Broderick Associate Professor, Dept. of Physics and Astronomy, University of Waterloo
Internal-External Member:	David Del Rey Fernández Assistant Professor, Dept. of Applied Mathematics, University of Waterloo
Other Member(s):	Huan Yang Assistant Professor, Dept. of Physics, University of Guelph

Author's Declaration

This thesis consists of material all of which I authored or co-authored: see **Statement of Contributions** included in the thesis. This is a true copy of the thesis, including any required final revisions, as accepted by my examiners.

I understand that my thesis may be made electronically available to the public.

Statement of Contributions

The chapters contain material and results produced in various collaborations:

Chapter 2 contains material from paper [339], co-authored with William E. East.
Chapter 3 contains material from paper [341], co-authored with William E. East.
Chapter 4 contains material from paper [340], co-authored with William E. East.
Chapter 5 contains material from paper [343], co-authored with Cristina Mondino, Daniel Egaña-Ugrinovic, Junwu Huang, Masha Baryakhtar, and William E. East.
Chapter 6 contains material from paper [342], co-authored with Taillte May and William E. East.

In addition, I have co-authored the three papers [55, 363, 209], which however, are not part of this thesis.

Abstract

In this thesis, we investigate bosonic fields in the strong-field and highly dynamical regime of general relativity focussing specifically on the black hole superradiance process of scalar and vector fields, as well as on the nonlinear dynamics of isolated and binary scalar boson stars. In the first part of this thesis, we lay the foundation to use boson stars as a particularly simple model to explore the dynamical behavior of inspiraling and merging ultra compact and black hole mimicking objects. To that end, we construct self-consistent initial data describing isolated and binary star configurations and subsequently utilizing numerical evolutions of the full Einstein-Klein-Gordon system of equations to explore this dynamical behavior. We investigate the linear stability properties of families of rotating stars in scalar theories with various types of self-interactions. Using numerical evolutions, we find that a linear instability present in rotating boson star solutions within linear scalar theories is quenched by nonlinear scalar interactions in a subset of stars. Furthermore, utilizing the conformal thin-sandwich formalism, we numerically construct generic binary boson star initial data satisfying the constraints of the Einstein equations. We adapt existing and introduce new methods, to initial data quality, as well as reduce residual orbital eccentricity. With these methods, we were able to generate self-consistent inspiral-merger-ringdown gravitational waveforms of eccentricity-reduced binary boson stars, for the first time. Lastly, scalar self-interactions may delay the merger time of identical inspiraling binary star configurations, or drive the system to an entirely different end state. In particular, we show explicitly that rotating boson stars can form during the merger of two non-spinning stars. In the second part of this thesis, we focus on how well-motivated ultralight scalar and vector bosons, extending the Standard Model of particle physics, can be probed through the observable signatures of the black hole superradiance process. Energy and angular momentum are extracted from a black hole via this mechanism, are deposited in an oscillating bosonic cloud, and finally dissipated through gravitational wave emission from the system. Here, we introduce the gravitational waveform model, `SuperRad`, modeling the cloud's oscillation frequency, growth and decay timescales, as well as the amplitude and phase evolution of the emitted gravitational radiation, for both scalar and vector boson clouds. This model combines state of the art analytical results with numerical computations to provide the most accurate predictions across the relevant parameter space. Moreover, we investigate the impact of a non-vanishing kinetic mixing between an ultralight vector boson forming a superradiant cloud and the Standard Model photon. Such mixing robustly results in the formation of a highly turbulent pair plasma within the bosonic cloud. We characterize the associated electromagnetic signatures and devise strategies to observe such signatures through multi-messenger observation campaigns.

Acknowledgements

I want to thank my advisor Will East for his guidance and advice throughout my years at Perimeter. I am thankful for his encouragements to think outside the box, to develop my own ideas, and to expand my horizon. I am particularly grateful for his support during tough times over the course of my PhD.

I am also grateful for my collaborators Masha Baryakhtar, Yilber Fabian Bautista, Daniel Egaña-Ugrinovic, Junwu Huang, Dana Jones, Taillte May, Cristina Mondino, and Lilli Sun. I would especially like to thank Junwu Huang for his advice and mentorship during the last year of my PhD.

I would like to thank the Strong Gravity Group for many lively discussions, throughout which I was able to take a step back, view problems from different angles, explore entirely new topics, revive long-forgotten knowledge, and grow as a researcher. Special thanks goes to Luis Lehner, Eric Poisson, Erik Schnetter, Daniel Siegel, and Huan Yang. I also want to thank Michael Müller for spending countless hours explaining plasma physics to me.

I am grateful to all those that made my time in Ontario joyful and unique. I thank Aman Agarwal, Yilber Fabian Bautista, Pablo Bosch, Ramiro Cayuso, Luciano Combi, Dhruv Desai, Guillaume Dideron, Anna Heffernan, Hanna Lynch, Taillte May, Soham Mukherjee, Michael Müller, and Mike Vasmer. In particular, I want to thank Soham Mukherjee and Hanna Lynch for all unforgettable canoe, skiing and bike trips.

Finally, I want to express my gratitude to Max Corman for her unconditional support. Her infectious excitement, her positivity and optimism, her passion for sports, plenty of nillix, and especially, her laugh that sparked it all, made this a very special time. Mmm...

Dedication

To my grandfather

Table of Contents

List of Figures

List of Tables

Chapter 1

Introduction

In an era of increasingly frequent and confident detections of gravitational wave events from compact binary mergers as well as precision electromagnetic observations—revolutionizing the way we observe the universe—now is an exciting time to leverage these observations and probe fundamental physics using astrophysical compact objects. These systems allow us to investigate and potentially detect deviations from the expected based on our currently accepted models of matter—the Standard Model of particle physics—and gravity—General Relativity. In this work, we focus on two classes of astrophysical objects, which enable, on the one hand, searches for new ultralight particles extending the Standard Model and, on the other hand, tests of the black hole paradigm.

1.1 The black hole paradigm

Gravitational wave and electromagnetic observations from isolated and binary ultra compact objects agree with the black hole hypothesis to a remarkable degree [6, 9, 12, 163, 165, 25]. This paradigm explains physics around these compact objects across several orders of magnitude in their masses $M_{\rm CO}$, from compact binary mergers and X-ray binaries, at small scales with $M_{\rm CO} \sim \mathcal{O}(10) M_\odot$, to active galactic nuclei, at large scales with $M_{\rm CO} \lesssim \mathcal{O}(10^{10}) M_\odot$. However, while these observations require ultra compact central engines, the defining feature of black holes—the event horizon—remains largely untested. Confronting the black hole hypothesis with observations requires an understanding of viable alternatives, i.e., ultra compact and black hole mimicking objects. These objects lack horizons, but exhibit general relativistic features like stable light rings, isolated ergoregions, and super-extremal spins, generally not present in black hole spacetimes within

General Relativity. A large class of these objects has been conceived within contexts ranging from bottom-up extensions to the Standard Model to top-down expectations based on low-energy limits of theories of quantum gravity [97] (further details with specific examples can be found in Sec. 2.1). The gravitational phenomenology associated with these objects opens a window into questions about models of quantum gravity and beyond the Standard Model physics from which they emerge.

To illustrate the impact of these features, we consider several examples and discuss their phenomenological implications. The unstable light rings of black holes and ultra compact objects, for instance, are responsible for the universal prompt ringdown when perturbed [94]. In contrast to black holes spacetimes, however, the absence of the perfectly absorbative horizon within black hole mimicking objects implies a partial reflection of massless perturbations propagating inwards; this results in modifications of the universal ringdown at sufficiently late times and imprinting signatures of the internal structure on the emitted gravitational wave radiation. Hence, the non-universal contribution is a smoking gun signature of black hole mimickers hidden in the gravitational wave signal, enabling us to probe the internal or near-horizon structures of astrophysical compact objects and distinguish a black hole from an ultra compact object. Furthermore, a linear instability associated with the presence of an ergoregion—the ergoregion instability—emerges as an exponentially growing accumulation of negative energy inside the ergoregion balanced by a positive energy flux at infinity [160, 264]. Spacetimes with ergoregions disconnected from any present horizons, i.e., including black hole mimicking objects, are suseptible to this exponential growth. The nonlinear development of this instability may result in smoking gun signatures through gravitational wave emissions (see, e.g., Ref. [48]). Finally, super-spinning ultra compact objects, i.e., those with dimensionless spin exceeding the Kerr-bound, exhibit deviations from the inspiral dynamics of binary black holes. These spin-interactions, which are enhanced towards the merger of a binary, imprinted in the emitted gravitational waveform, can be extracted from the gravitational wave data, and may be associated with black hole mimickers due to the Kerr-bound of spinning black holes in General Relativity.

Therefore, studying ultra compact and black hole mimicking objects in the strong-field and highly dynamical regime could fundamentally impact our understanding of classical and quantum gravity. Despite this discovery potential, even rough descriptions of the strong-field dynamical regime of these objects is lacking, limiting black hole tests that could be undertaken with current and future gravitational wave detectors such as LIGO, Virgo, KAGRA and LISA.

In recent years, boson stars have emerged as a particularly simple model of ultra compact spacetimes. These spacetimes are regular and asymptotically flat without horizons

sourced by a particular self-gravitating complex scalar field configuration. Interestingly, classes of these stars have been shown to harbor ergoregions, stable light rings, and super-extremal spins, while exhibiting high compaction [73, 220, 221]. Furthermore, compared with other models of ultra compact objects [97], boson stars have well-defined evolution equations associated with them—the Einstein-Klein-Gordon system of equations. Therefore, established evolution techniques from numerical relativity are readily applied to these objects, enabling the study of the nonlinear dynamics in the context of isolated and binary systems (see, Ref. [241] for a review). Hence, these objects are ideal candidates to explore the dynamics of black hole mimickers in the nonlinear regime. Despite this potential, the ability of boson stars to serve as proxies for a large class of ultra compact objects in the nonlinear regime hinges on their stability properties accross the relevant parts of parameter space, the correct, self-consistent, and accurate construction of binary boson star initial data, and their dynamical evolution during the inspiral, merger and ringdown. The study of these aspects is subject of the first part of this thesis.

1.2 Beyond the Standard Model physics

The Standard Model of particle physics is the most precise scientific theory, describing matter and its interactions to unprecedentedly high precision. Despite this remarkable success, the model is incomplete in various regards ranging from un-explained fine-tuning to questions about the fundamental nature of dark matter and even dark energy and quantum gravity. As a response, a series of minimal extensions beyond the Standard Model have been constructed to solve one or multiple of these problems. Of particular interest are new bosonic particles of masses $\lesssim 10^{-10}$ eV, as these are able to address several outstanding questions simultaneously. For instance, pseudo-scalar axion-like particles can solve the strong CP-problem [292], while also making up a significant fraction of the observed dark matter [23], whereas new ultralight vector bosons routinely emerge from low-energy expansions of models of quantum gravity [172]. Though substantial investment is being made in terrestrial experimental searches for these new particles, current astronomical observations have the potential to be much more sensitive probes.

Gravitational and electromagnetic signatures of the so-called black hole superradiance process are a uniquely efficient probe of ultralight particles that are weakly-coupled to ordinary matter (see, Ref. [80] for a review). The power of this mechanism as a probe of beyond the Standard Model physics lies in requiring only a minimal coupling to gravity. Hence, even without any coupling to the Standard Model, the resulting gravitational signatures are potentially observable. A scalar or vector ultralight bosonic field efficiently

extracts rotational energy from a spinning black hole through the superradiance process, forming a macroscopic oscillating condensate in the vicinity of the black hole. Especially, gravitational wave detectors, X-ray and gamma-ray telescopes, and radio efforts, possess large untapped discovery potential for finding evidence for the existence of well-motived extensions to the Standard Model inaccessible to other current observational techniques.

This potential can be leveraged, provided accurate predictions for the properties and types of signatures expected exist. Much development was devoted to determining the relevant dynamics, timescales, and frequencies for both minimally coupled massive scalar and vector particles; however, a gap between these results and the utilization of the latter in the context of observation campaigns emerged. Furthermore, embedding these scalar or vector degrees of freedom in the Standard Model, an extended dark sector, or low-energy limits of quantum gravity models, results in additional interactions that may impact the gravitational superradiance mechanism, and hence, the constraints obtained for minimially coupled models. In the second part of this thesis, we develop the gravitational waveform model `SuperRad` that aims to bridge the gab between theory and experiment, and study the impact of the lowest-order coupling of the ultralight vector boson to the Standard Model photon and the emerging phenomenology.

1.3 Summary and outline of the thesis

In the first part of this thesis, we focus on utilizing boson stars as proxies to study the linear and nonlinear dynamics of ultra compact and black hole mimicking objects. In particular, in Chapter 2 we investigate the stability properties of rotating scalar boson stars utilizing nonlinear numerical evolutions of the Einstein-Klein-Gordon system of equations, with focus on those solutions in models with several different types of nonlinear interactions. We show that a linear non-axisymmetric instability found in stars in models without self-interactions persists across the entire parameter space for these stars, with diverging timescale in the non-relativistic limit. Therefore, boson stars that are sufficiently non-relativistic, where the leading order mass term dominates, will be unstable, independent of the nonlinear scalar self-interactions. However, we do find classes of rotating bosons stars, where adding nonlinear interactions to the scalar potential quenches the non-axisymmetric instability. In Chapter 3, we place these stable rotatings boson stars, as well as non-spinning stars, in binary configurations. To that end, we utilize the conformal thin-sandwich formalism to construct constraint satisfying initial data for equal and un-equal mass binaries with and without spins in precessing and aligned confirgurations. Furthermore, spurious oscillations are suppressed by means of adapting existing and developing new methods

to modify the binary's free data and standard approaches to reduce residual orbital eccentricity are successfully applied to selected binaries; with these approaches, we reach residual eccentricities at the $\sim 10^{-3}$ level. As a result, we produce the first quasi-circular fully self-consistent inspiral-merger-ringdown gravitational waveforms from non-spinning and super-spinning binary boson stars. Finally, we comment on means to equilibriate the scalar matter making up the stars directly analogous to quasi-equilibrium methods developed for binary neutron star initial data. Finally, in Chapter 4 we study the impact of self-interactions of the scalar matter making up these stars in the context of binary boson star inspirals and mergers by performing a series of nonlinear evolutions of the corresponding Einstein-Klein-Gordon equations. Particular focus lies on the pivotal role the scalar phase and vortex structure plays during the late inspiral, merger, and ringdown. We find scalar interactions may substantially impact the inspiral gravitational wave amplitude and phase, as well as the length of a hypermassive phase potentially occuring shortly after merger. In addition, we develop a mapping that predicts the remnant type and properties of any given binary boson star merger approximately. Utilizing the predictions of this mapping, we use numerical evolutions to explicitly demonstrate, for the first time, that rotating boson stars can form as remnants from the merger of two spherical boson stars. We analyze this new formation mechanism, discuss its robustness, and comment on the implications for rotating vector boson stars.

In the second part of this thesis, we study the black hole superradiance phenomenon as means to detect or rule out viable extensions to the Standard Model of particle physics. In Chapter 5, we investigate the electrodynamics and observational implications of coupling a superradiant ultralight massive vector boson through the kinetic mixing to the Standard Model photon. This mixing results in a contribution of the vector boson cloud's fields to the visible electromagnetic fields coupling to the standard electromagnetic current. Hence, charged particles entering the cloud experience strong acceleration and initiate a pair production phase saturating in the formation of a pair plasma in the superradiant cloud around the black hole. We study the dynamics, emission mechanisms, and electromagnetic power output using resistive magnetohydrodynamics methods applicable in highly magnetized plasmas. We find that magnetic reconnection sites in the bulk of the cloud are locations of efficient dissipation and electromagnetic emissions with total luminosity as high as $10^{43}\,\mathrm{erg/s}$ for observationally-allowed parts of the coupling parameter space. Due to large ambient visible magnetic fields, the emission is expected to contain a large X-ray component with mild evidence of periodicity of the emission. We close by discussing detection strategies utilizing both gravitational wave and electromagnetic observations. Furthermore, in Chapter 6 we develop the gravitational waveform model `SuperRad`, which models the dynamics, oscillation frequency, quasi-monochromatic signal

emitted by both superradiant scalar and vector boson clouds. The model is valid across the relevant parameter space as it consistently combines state of the art analytic and numerical results. Particular focus lies on determining the accuracy of these methods for predicting the frequency evolution of the gravitational wave signal utilizing fully general-relativistic methods. As a first test-case, we estimate the prospects of conducting follow-up gravitational wave searches for ultralight vector clouds around supermassive black hole binary merger remnants using LISA. We find that vector masses in the range from 1×10^{-16} eV to 6×10^{-16} eV can, in principle, be probed using follow-up gravitational wave searches.

Throughout the first part of this thesis, we use units with $G = c = 1$ and the $(-+++)$ metric signature. However, neither units nor variable definitions carry over to the second part of this work. In the second part, we use units as indicated individually in each chapter.

Part I

Boson stars

Chapter 2

Stability of rotating scalar boson stars with nonlinear interactions

Executive summary: We study the stability of rotating scalar boson stars, comparing those made from a simple massive complex scalar (referred to as mini boson stars), to those with several different types of nonlinear interactions. To that end, we numerically evolve the nonlinear Einstein-Klein-Gordon equations in 3D, beginning with stationary boson star solutions. We show that the linear, non-axisymmetric instability found in mini boson stars with azimuthal number m = 1 persists across the entire parameter space for these stars, though the timescale diverges in the Newtonian limit. Therefore, any boson star with m = 1 that is sufficiently far into the non-relativistic regime, where the leading order mass term dominates, will be unstable, independent of the nonlinear scalar self-interactions. However, we do find regions of m = 1 boson star parameter space where adding nonlinear interactions to the scalar potential quenches the non-axisymmetric instability, both on the non-relativistic, and the relativistic branches of solutions. We also consider select boson stars with m = 2, finding instability in all cases. For the cases exhibiting instability, we follow the nonlinear development, finding a range of dynamics including fragmentation into multiple unbound non-rotating stars, and formation of binary black holes. Finally, we comment on the relationship between stability and criteria based on the rotating boson star's frequency in relation to that of a spherical boson star or the existence of a co-rotation point. The boson stars that we find not to exhibit instability when evolved for many dynamical times include rapidly rotating cases where the compactness is comparable to that of a black hole or neutron star.

2.1 Introduction

As outlined in Chapter 1, beside black holes (BHs) and neutron stars, a large class of exotic compact objects (ECOs) has been conceived [97]. The compactness of ordinary fluid stars, like neutron stars, is restricted by the Buchdahl limit [84] for spherically symmetric configurations, and more stringently by the requirement that the sound speed be less than the speed of light. However, these objects could capture and accrete dark matter from their environment, forming a composite object [170, 173, 191, 190, 236, 130], which could exceed these compactness limitations. Various models of ordinary matter also predict the existence of anisotropic stars with compactness levels arbitrarily close to those of BHs [75, 235, 196]. String theory inspired solutions, called fuzzballs, emerge as averages over microstates, generating horizonless, but highly compact, BH-like models [121, 57, 267, 45, 58]. There is speculation that quantum effects of a collapsing horizonless spacetime could halt the complete classical collapse to a BH and yield a highly compact configuration just outside the BH-limit [368, 104, 60, 41]. Furthermore, ultralight scalar or vector particles arise in compactifications of string theory, solutions to the strong CP-problem [183, 179], as well as as ultralight and fuzzy dark matter [201, 205, 237, 316, 47, 29]. If such particles exist in the universe, stationary boson stars (BSs) [215, 320, 333, 269, 307, 126, 241, 167] can be formed through a gravitational cooling mechanisms out of a diffuse distribution of bosonic matter [333, 323]. Lastly, there is an extended class of other ECOs like gravastars, wormholes, or firewalls [97]. The common feature of all these approaches is a certain "closeness," measured by the compactness and related features, to classical BHs.

Accurate predictions of the properties of BH mimickers, especially of their dynamics in the nonlinear regime in the case of mergers, is needed to confirm or disfavor the existence of BHs using GW or electromagnetic observations [217, 64, 46, 335, 246, 374]. However, for many ECO models, determining their nonlinear evolution is challenging or ill-posed, due to their vastly different physical and mathematical origins. BSs, on the other hand, obeying standard energy conditions (as long as their potential is non-negative), evolve according to well behaved wave-like equations, and can be treated numerically using the same techniques as the Einstein equations. Thus they provide a simple and tractable setting to explore dynamical properties of ECOs and BH mimickers [185, 241]. Stationary rotating BSs can have compactnesses approaching that of BHs, and therefore, capture the main gravitational features of a large set of ECOs. BSs can exhibit an innermost stable circular orbit, and unstable and stable photon orbits while being horizonless and regular everywhere. Therefore, these solutions provide an ideal test bed to study the nonlinear dynamics of a class of ultracompact objects.

However, while there is an extensive literature constructing stationary BS solutions in

general relativity, the number of studies that have looked at the dynamics or stability of these objects is more limited, in particular for BSs with angular momentum (see Ref. [241] for a recent review.) Recently, there has been increasing interest in studying the nonlinear dynamics of scalar and vector BSs in various scenarios (e.g. Refs. [280, 281, 107, 285, 188, 131, 277, 326] and see Ref. [241]). And in the past few years, several studies have presented evidence that rotating scalar BSs might be inherently unstable. In Refs. [285, 67], the inspiral and merger of binary scalar BSs settled, above a certain critical BH-threshold, into a *non*-rotating scalar BSs in the final state, shedding all angular momentum in the process. Similar results were found for the collapse of rotating clouds of scalar field [129]. Furthermore, Ref. [323] considered a number of rotating scalar BSs made of massive bosons without interactions, and found them all to be subject to a non-axisymmetric instability (NAI), rendering them little use, e.g., for studying the dynamics of a merger.

However, in this chapter, we show that this problem can be cured by considering nonlinear interactions for the scalar field, and present evidence for the stability of a large class of rotating BSs both in the relativistic (high compactness) *and* in the non-relativistic (dilute) regime. In particular, we show that when considering parameterized families of BSs for several different choices of the scalar field potential, the growth rate for the NAI approaches zero at certain critical values (e.g., of the frequency of the BS). Nonlinearly evolving select cases beyond these critical values for many dynamical times, we find no evidence for instability. (Though our methods do not allow us to rule out some instability operating on even longer timescales.) Hence, such rotating scalar BS solutions are promising candidates for studying the dynamics of isolated and binary ECOs in a nonlinear scenario, and comparing to BHs.

In Sec. 2.2, we outline the scalar field models we consider, describe the numerical techniques we use to construct rotating BS solutions in these models, and review the linear stability results in the literature. Following this, we present our numerical results in Sec. 2.3. We first identify the form and nature of the NAI in the linear regime, then measure the growth rates of the NAI for a set of BSs and potentials, and present select isolated rotating BSs that show no sign of instability. We also analyze the final state of the instability, and discuss various physical explanations for the onset of instability. Finally, we conclude in Sec. 2.4. Additional details on the numerical methods and error estimates from convergence studies are given in the appendices.

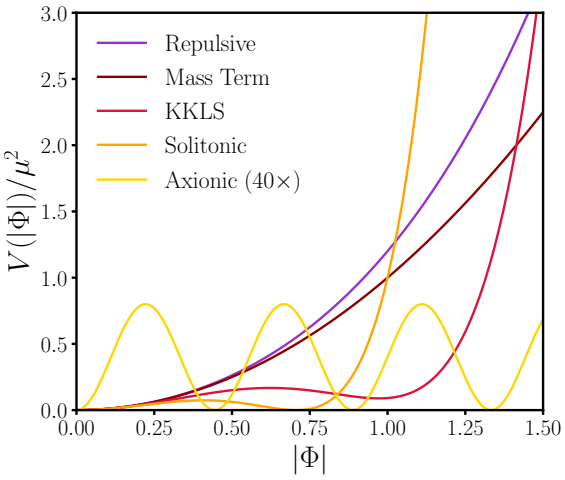

Figure 2.1: Examples of the nonlinear self-interactions, specified by $V(|\Phi|)$, considered here. We emphasize the characteristic features of each: The solitonic potential has a non-trivial vacuum state, the KKLS self-interaction has a metastable state, the axionic potential is periodic, and finally, the repulsive potential has a positive first correction to the mass term.

2.2 Stationary Scalar Boson stars

2.2.1 Models considered

In this chapter, we consider rotating scalar BSs in minimally coupled massive complex scalar models, comparing stars where the scalar potential only has a mass term (referred to as mini BSs) to stars where the potential has additional higher order terms, corresponding to non-trivial scalar self-interactions. The latter are motivated by axion-like particles, effective field theory descriptions of light scalar degrees of freedom, or simply by the finding that such models can produce highly compact BSs. As such, we consider a complex scalar field Φ, minimally coupled to the Einstein-Hilbert action, exhibiting a global U(1) symmetry:

$$S = \int d^4x\sqrt{-g}\left[\frac{R}{16\pi} - g^{\alpha\beta}\nabla_{(\alpha}\bar{\Phi}\nabla_{\beta)}\Phi - V(|\Phi|)\right]. \tag{2.1}$$

Here R is the curvature scalar, the overbar denotes complex conjugation, and the potential $V(|\Phi|)$ contains both the mass term and nonlinear self-interactions of the complex scalar

field. All such self-interactions considered here (see also Figure 2.1) reduce to the mass term[1], $V(|\Phi|) \to \mu^2|\Phi|^2$, in a small-coupling limit.

Solitonic potential: This potential is characterized by a single additional coupling parameter σ, such that [159]

$$V(|\Phi|) = \mu^2|\Phi|^2\left(1 - \frac{2|\Phi|^2}{\sigma^2}\right)^2, \tag{2.2}$$

reduces to the mass-term if $\sigma \to \infty$. As indicated in Figure 2.1, this potential has a negative first correction in the expansion in $|\Phi|$, and features a non-trivial vacuum state at $|\Phi| = \sigma/\sqrt{2}$. With these self-interactions, localized scalar field configurations (i.e., non-topological solitons) exist even in the absence of gravity [159], and spherically symmetric BSs of this type are sufficiently compact to support stable trapped null geodesics [285].

KKLS potential: The potential [220, 221],

$$V(|\Phi|) = \mu^2|\Phi|^2\left[1 - \frac{16\pi}{1.1\kappa}|\Phi|^2 + \frac{64\pi^2}{1.1\kappa^2}|\Phi|^4\right], \tag{2.3}$$

is parameterized by κ (see also Ref. [222]). It also exhibits a negative first correction beyond the mass-term, and a local minimum at a non-zero value of $|\Phi|$ (see also Figure 2.1). The KKLS potential simplifies to the mass term if $\kappa \to \infty$ [220]. After rescaling $|\Phi| \to (\kappa/(8\pi))^{1/2}|\Phi|$, BSs in this model reduce to non-gravitating non-topological Q-balls [111] in the $\kappa = 0$ limit.

Axionic potential: Inspired by ultralight particles predicted, for instance, by string theory compactifications, or to solve the QCD CP-problem, we consider a generic axion-like potential of the form

$$V(|\Phi|) = \mu^2 f^2\left\{1 - \cos[\sqrt{2|\Phi|^2}f^{-1}]\right\}. \tag{2.4}$$

This periodic potential is parameterized by the coupling f, reduces to the mass term if $f \to \infty$, and has a negative first correction, when expanded in small $|\Phi|$.

Repulsive potential: While all the above scalar self-interactions have attractive (i.e., negative) first corrections to the mass term, we also study the effects of a non-trivial *repulsive* first correction of the form

$$V(|\Phi|) = \mu^2|\Phi|^2 + \lambda|\Phi|^4, \tag{2.5}$$

[1]The scalar mass m_Φ and the mass parameter μ are related by $\mu = m_\Phi/\hbar$

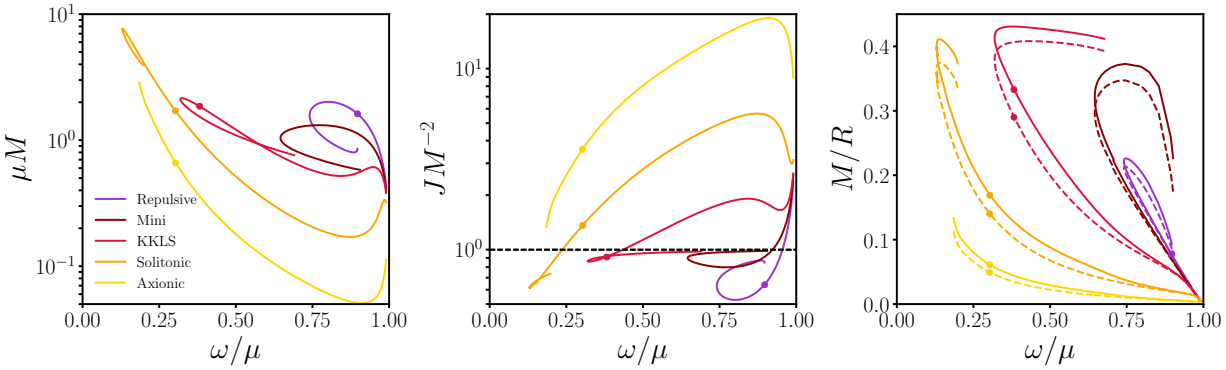

Figure 2.2: We present the main properties of five families of $m = 1$ rotating BSs in the above scalar models, for choices of coupling focused on in this work. The solitonic BS family has coupling $\sigma = 0.05$, the axionic family has coupling $f = 0.005$, the BSs in the KKLS model have $\kappa = 0.1$, the family of BSs with repulsive self-interactions have coupling $\lambda/\mu^2 = 5 \times 10^2$, while the mini BS family is given for reference. From left to right, the three plots show the total mass M in units of μ^{-1}, the dimensionless spin J/M^2, and the compactness M/R of each of these families of BSs as a function of the boson's frequency ω/μ. For determining the radius of the BSs in the last plot, we use either the surface containing 99% of the mass C^K (solid), or 99% of the U(1)-charge density C^Q (dashed), as discussed in Sec. 2.2.2. Based on the turning point argument described in the text, BSs past the maximum of the total mass are expected to be unstable. Notice that in the non-relativistic limit, i.e., when $\omega/\mu \to 1$, the behavior of all families of BSs with non-trivial self-interactions reduce to that of mini BSs [197, 122]. The individual data points indicate BSs that we evolve and where we find no sign of an instability (see Sec. 2.3.2). Note that, although not evident in the plot, the axionic family reaches a global maximum of μM at $\omega/\mu \approx 0.187$.

with $\lambda > 0$. In the following, we also briefly comment on the properties of BSs in a scalar model with a Liouville potential [328, 106],

$$V(|\Phi|) = \mu^2\alpha^2[e^{|\Phi|^2/\alpha^2} - 1], \tag{2.6}$$

which has the same form as Eq. (2.5) when expanded to quadratic order in $|\Phi|^2$.

2.2.2 Stationary solutions and classical observables

We consider BS solutions where the spacetime is regular, stationary, axisymmetric, and asymptotically flat. In Lewis-Papapetrou coordinates, the metric takes the general form

$$\begin{aligned} ds^2 = -f dt^2 + l f^{-1}\big\{ & g(dr^2 + r^2 d\theta^2) \\ & + r^2 \sin^2\theta \left(d\varphi - \Omega r^{-1} dt\right)^2 \big\}. \end{aligned} \tag{2.7}$$

Here all metric functions $\{f, l, g, \Omega\}$ depend only on (r, θ), in accordance with our assumptions. The complex scalar field is assumed to have the form $\Phi = e^{i\omega t + im\varphi}\phi(r,\theta)$, with $\phi \in \mathbb{R}$. This time and azimuthal dependency ensures that the scalar field stress-energy tensor is stationary and axisymmetric (maintaining the symmetry of the metric). In addition to the above five physical fields, we introduce two auxiliary fields $\rho(r,\theta)$ and $\omega_s(r,\theta)$, following Ref. [220], which aid in imposing certain conditions on the BSs (see appendix A.1 for details). With this ansatz, in conjunction with regularity conditions at the origin and asymptotic flatness conditions at infinity, the coupled system of Einstein-complex-Klein-Gordon equations

$$G_{\mu\nu} = 8\pi T_{\mu\nu}, \qquad \nabla_\alpha \nabla^\alpha \Phi + \Phi \partial_{|\Phi|^2} V(|\Phi|) = 0 \tag{2.8}$$

[together with Eq. (A.3)] reduce to an elliptic boundary value problem. Given a sufficiently accurate initial seed for a Newton-Raphson type relaxation scheme, the parameter space is explored by marching along the respective parameters. We give more details on how we numerically solve these equations to construct BS solutions in Appendix A.1.

In asymptotically flat, stationary spacetimes, the Komar mass integrated over a sphere at spatial infinity, and the ADM mass of a spatial slice Σ_t coincide. Both can be written as

$$M = \int_D dr d\theta d\varphi \sqrt{-g}(2T^t{}_t - T^\alpha{}_\alpha), \tag{2.9}$$

where the integral is over the Lewis-Papapetrou spatial coordinate domain D. The axisymmetry and regularity of Eq. (2.7) ensures that the total angular momentum of the spacetime is due to the scalar field through

$$J = -\int_D dr d\theta d\varphi \sqrt{-g} T^t{}_\varphi. \tag{2.10}$$

Finally, the global U(1) symmetry of the complex scalar theory gives rise to a conserved U(1)-Noether charge Q that measures the particle number (i.e., the occupation number of

the Bose-Einstein condensate[2]). The associated Noether current is

$$j^\mu = -i(\bar{\Phi}\partial^\mu\Phi - \Phi\partial^\mu\bar{\Phi}), \qquad \nabla_\mu j^\mu = 0. \tag{2.11}$$

Following immediately from noticing that $T^t{}_\varphi = mj^t$ (in terms of the Noether current Eq. (2.11)), the angular momentum of the system is "quantized" into integer increments of the scalar charge, $J = mQ$, dictated by the azimuthal number m. Of course, this relation is a purely classical constraint, but hints towards the quantum interpretation of the system as a coherent condensate of a set of bosons.

At sufficiently large radial coordinate, the scalar BS solution exhibits an exponential tail, $\phi \sim \exp(-\beta r)$, for some $\beta > 0$, making any notion of a radius for the star ambiguous. In the non-rotating case, the radius of a BS is typically defined by the *areal radius*, R_{99}, at which 99% of the BS's Komar mass Eq. (2.9) is contained within a coordinate 2-sphere of radius R_{99}. For rotating BSs, we introduce two distinct notions of size: *(i)* We define the R^K_{99} as the *circular radius*[3] $\tilde{r}$, for which $M(\tilde{r}) = 0.99M(\tilde{r} \to \infty)$, and *(ii)* we define R^Q_{99} as the circular radius, for which $Q(\tilde{r}) = 0.99Q(\tilde{r} \to \infty)$. Note that, while M contains both the scalar and the gravitational binding energy, Q measures only the scalar rest mass. Based on this notion of size, the compactness of a rotating BS is given either by $C^K = M/R^K_{99}$ or $C^Q = M/R^Q_{99}$. For comparison, for a non-rotating BH $C^K_{\rm BH} = 1/2$, while for a typical neutron star $C^K_{\rm NS} \sim 0.1$. For any given BS, the difference between C^Q and C^K is indicative of the ambiguity in defining its radius.

In Figure 2.2, we present these observables for several sets of families of solutions. The Newtonian limit is approached as the gravitational binding energy, of order M/R, is small. In that limit, the bosons' frequency ω approaches μ, the marginally bound value, since $\omega/\mu - 1 \sim M/R$.

2.2.3 Stability arguments

The stability of non-rotating BSs has been investigated by means of *(i)* analyzing the temporal dependence of individual modes or more general linear perturbations [234, 168, 169], *(ii)* applying catastrophe theory or thermodynamic stability to families of BS solutions [230, 355, 222, 346, 327], and *(iii)* evolving the Einstein-Klein-Gordon system of equations numerically to study the nonlinear stability of BSs [332, 44, 186, 365, 241]. The consensus of these methods is that spherically symmetric BSs switch their radial stability properties

[2]When quantizing the complex scalar field theory, the charge Q counts the (anti)-particles of a given state, making the relation manifest.

[3]The radius $\tilde{r}$ for which the proper length of a circle C in the equatorial plane is $C = 2\pi\tilde{r}$.

whenever the BS's mass reaches an extremum as a function of the central scalar field value $\phi(0)$: $dM/d\phi(0) = 0$. As such, non-rotating BSs have at least one stable branch reaching from the non-relativistic (i.e., dilute) limit, to the first maximum of M. Depending on the potential, non-rotating BSs can have a number of stable branches, analogous to the white dwarf and neutron star branches of fluid stars.

However, the stability analysis of *rotating* BSs is considerably more complex[4]. Even at the linear level, there is not expected to be a clean decoupling of the scalar and the gravitational modes, making a linear stability analysis difficult. Based on turning point arguments in Ref. [222] (see also Ref. [112] for a brief analysis of the stability of excited BSs with the KKLS potential), the stability of rotating BSs should switch, analogous to non-rotating BSs, at the extrema of $M(\omega)$. In Figure 2.2, we present the total mass, angular momentum, and compactness of five different potentials and families of $m = 1$ fundamental BSs. Applying the arguments above to these families of BSs, we see that mini BSs and those in the repulsive scalar model Eq. (2.5) exhibit a single (potentially) stable branch reaching from the non-relativistic limit, $\omega/\mu \lesssim 1$, to the frequency where M (or equivalently Q) reaches the global maximum, while all solutions past that maximum are unstable. Similarly, the family of BSs in the axionic, solitonic, and KKLS scalar models exhibit two distinct potentially stable branches. Since all these potentials reduce to the mass term in the non-relativistic limit, it is not surprising that BSs with these self-interactions are stable in the non-relativistic limit based on the turning point arguments. However, these BSs have another potentially stable branch in the relativistic (high-compactness) regime, between the first local minimum of M and its global maximum, where $\partial M/\partial\omega < 0$.

However, as seen, for instance, in Refs. [346, 327], turning points are only a *sufficient* condition for the existence of a thermodynamic instability, *not* a necessary condition. In fact, a thermodynamic instability could appear without the presence of a turning point. On top of this, thermodynamically unstable systems are not necessarily dynamically unstable: While there exists a preferred solution, there may not be a path through the solutions space that is dynamically achievable. Given these arguments, and the fact that some BSs are dynamically unstable in a regime not indicated by turning point arguments [323], a more detailed analysis of the dynamical nonlinear stability is necessary.

[4]Here we will not consider BSs with ergoregions, which would be subject to the ergoregion instability [160].

2.3 Results

In contrast to the stability analysis outlined in the last section, in Ref. [323], it was discovered that $m = 1$ scalar mini BSs are subject to a NAI in a regime where they are expected to be stable based on turning point arguments. In those cases, the evolution of the perturbed stationary scalar BSs revealed exponentially growing non-axisymmetric modes whose nonlinear evolution ultimately lead to the gravitational collapse of the BS to a BH. In the following, expanding on the work presented in Ref. [323] (see also Ref. [129] for the same instability present in dilute bosonic clouds), we study the nonlinear dynamical behavior of a large class of $m = 1$ (and some $m = 2$) mini BSs and BSs in the models presented in 2.2.1. To that end, we numerically evolve the Einstein-Klein-Gordon equations, Eq. (2.8), in 3D from stationary BS initial data that is perturbed only by numerical truncation error (see Appendix A.2 for details of the numerical evolution). In many cases, we find a similar NAI and determine its growth rate as a function of the BS parameters. However, we identify two distinct regions of the parameter space, where the NAI growth rate approaches zero. Past this point, rotating scalar BSs appear to be stable under nonlinear evolution. This is true for parts of the *relativistic branch*, identified in Sec. 2.2.3, as well as portions of the *non-relativistic branch*. Furthermore, we show that the instability growth rate for BSs in *any* scalar model, approaches zero (both in units of the BS mass and BS radius) in the dilute/Newtonian limit, where the nonlinear interactions can be neglected, and all BSs reduce to mini BSs.

In Sec. 2.3.1, we illustrate the linear characteristics of the NAI and explain how we extract the identifying features. In Sec. 2.3.2, we present the growth rates and other results on the unstable linear modes for a number of types of rotating BSs across the parameter space of the BSs' frequency and couplings, as well as explicitly demonstrate the stable evolution of a few example cases. In Sec. 2.3.3, we describe the ultimate fate of the unstable BSs, and finally, in Sec. 2.3.4, we examine several criteria for characterizing the onset of the NAI in BSs.

2.3.1 Characterization of the linear non-axisymmetric instability

In the linear regime, the NAI manifests as an exponentially growing, non-axisymmetric perturbation to both the scalar field and metric. We study this by evolving stationary BSs solutions in time, letting numerical truncation error seed the instability at a small amplitude that grows by several orders of magnitude before becoming nonlinear. This allows us to characterize the NAI during this extended linear phase.

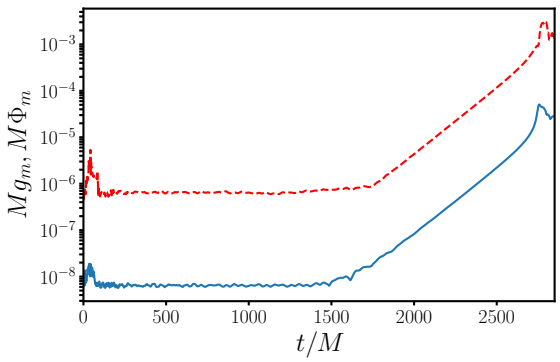

Figure 2.3: The evolution of the global maxima $g_m = \max|\partial_t g_{tt}|$ (red dashed) and $\Phi_m = \max|\partial_t|\Phi|^2|$ (blue) [see Eq. (2.13)] for an axionic $m = 1$ BS with $f = 5 \times 10^{-2}$ and $\omega/\mu = 0.425$. The NAI is evident as a linear instability beginning around $t/M \approx 1.75 \times 10^3$, and enters the nonlinear regime at roughly $t/M \approx 2.75 \times 10^3$. The perturbations present at early times originate from lower order interpolations at the mesh refinement boundaries (see Appendix A.2 for details).

We will be interested in monitoring perturbations to quantities that are stationary in the background BS solution, which has an axisymmetric and stationary spacetime. For example, linear perturbations to the magnitude squared of the BS complex scalar field $\Phi_{\rm BS}$ can be written as

$$|\Phi|^2 - |\Phi_{\rm BS}|^2 = e^{-i\tilde{\omega}t} e^{i\tilde{m}\varphi} \delta\Phi(r,\theta), \tag{2.12}$$

where $\tilde{\omega} = \tilde{\omega}_R + i\tilde{\omega}_I$ captures both the harmonic time dependence, $\tilde{\omega}_R > 0$, and possible (un)stable dynamical behavior with $\tilde{\omega}_I < 0$ (> 0), while $\tilde{m}$ is the azimuthal mode number. In the time domain setting, we are assuming[5] that a *single* perturbative mode (the most unstable) dominates the dynamics during the linear instability phase. We characterize the NAI by its azimuthal mode number, complex frequency, as well as the radial and polar dependency encoded in $\delta\Phi(r,\theta)$. We can extract the growth rates $\tilde{\omega}_I$ by fitting an exponential to the global maxima

$$\Phi_m := \max_{x\in\Sigma_t} |\partial_t|\Phi|^2| \qquad \text{and} \qquad g_m := \max_{x\in\Sigma_t} |\partial_t g_{tt}| \tag{2.13}$$

of a given time slice Σ_t, which quantify the divergence from a stationary solution. In Figure 2.3, we depict the typical dynamical behavior of Φ_m and g_m for an $m = 1$ scalar BS in the linear regime.

[5]We confirm explicitly that the φ-dependence of the linear perturbation has large support over only a single azimuthal mode $\tilde{m}$.

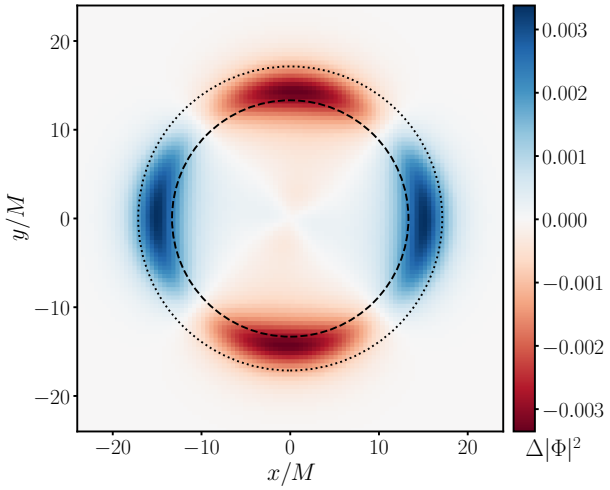

Figure 2.4: The radial dependence of the unstable mode from a typical case, in particular the axionic BS considered in Figure 2.3. We show $\Delta|\Phi|^2$ [defined in Eq. (2.14)] in the equatorial plane (parameterized by the Cartesian coordinates x and y), where we recall that $|\Phi(t=0)|^2$ is axisymmetric. This quantity is extracted at $t_{\rm NAI} = 2.5\times10^3 M$ which, as can be seen from Figure 2.3, is solidly in the linear instability regime. The depicted structure rotates about the center of the equatorial plane at an angular frequency $\tilde{\omega}_R M = 2.44\times10^{-2}$, while its magnitude grows exponentially with $\tilde{\omega}_I M = 6.4\times10^{-3}$. For reference, we also add the radii R^K_{99} (dotted circle) and R^Q_{99} (dashed circle) defined in Sec. 2.2.2.

Furthermore, in Figure 2.4, we present an example of the difference in magnitude of the scalar field, $\Delta|\Phi|^2$, during the linear phase (at $t = t_{\rm NAI}$) of the NAI, compared to the initial data (at $t = 0$), in the equatorial plane of the BS:

$$\Delta|\Phi|^2 := |\Phi(t=0)|^2 - |\Phi(t=t_{\rm NAI})|^2 \tag{2.14}$$

From this, we can extract the azimuthal mode number $\tilde{m}$, the radial dependence, and the harmonic part of the frequency $\tilde{\omega}_R$. The last-named is extracted by finding the radius R_m where the perturbation is largest, $\max_{x\in\Sigma_t}\Delta|\Phi|^2 = \Delta|\Phi(r=R_m,\theta=\pi/2)|^2$; we then fit $\cos(\tilde{m}\varphi+\phi(t))$ to $\Delta|\Phi(R_m,\theta=\pi/2,\varphi)|^2$ as a function of time during the exponential growth phase of the mode. The essentially constant time derivative of the phase $\dot{\phi}$ gives $\tilde{\omega}_R$ for the unstable mode. As can be seen in Figure 2.4, the azimuthal mode number $\tilde{m}$ is evident from $\Delta|\Phi|^2$, and shows large support only over a single mode $\tilde{m}$. These modes could equivalently be extracted from perturbations to the energy density, or other projections of the stress-energy tensor, due to the global U(1) symmetry. In the following section, we present the characteristics of the NAI extracted in this way from our time-domain

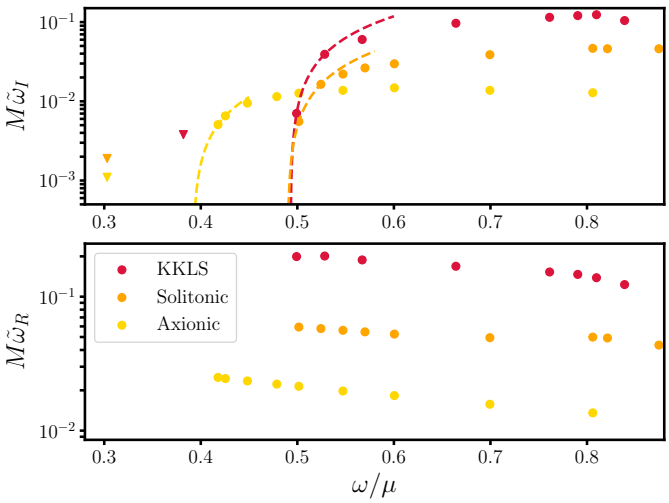

Figure 2.5: The imaginary (top) and real (bottom) components of the frequency of the $\tilde{m} = 2$ unstable mode as a function of the BS frequency ω/μ for three families of solutions shown in Figure 2.2. The axionic model has coupling $f = 5 \times 10^{-2}$, the solitonic potential has $\sigma = 0.05$, and the KKLS self-interactions are characterized by $\kappa = 0.1$. All three families are sequences of $m = 1$ rotating BSs. The dashed curves are linear interpolations considering only the two points with smallest ω/μ in each respective case. We also indicate the upper bounds on the growth rate of the cases considered in Table 2.1 by down-arrows.

evolutions for several different families of rotating BSs.

2.3.2 Results: Instability growth rates

In the following, we focus on finding the complex frequency $\tilde{\omega}$ for the unstable modes of the NAI. For all the families of BSs presented in Figure 2.2, we investigate how $\tilde{\omega}_I$ changes with the BS frequency or coupling. For self-interactions with an attractive first correction, we focus on the second potentially stable branch (based on turning point arguments, as discussed in Sec. 2.2.3), while for mini BSs and those in models with repulsive potentials, we focus on the only branch that is connected to the non-relativistic limit. In this limit, which corresponds to $\omega \to \mu$, the scalar field amplitude becomes small, and only the lowest-order term in the potential, i.e. the mass term, will be important. Ultimately, we identify critical points ω^c/μ and λ^c/μ^2 where $\tilde{\omega}_I$ tends toward zero, i.e. the NAI shuts off.

In Figure 2.5, we show the real and imaginary frequency of the unstable mode for

axionic, solitonic, and KKLS scalar rotating BSs with $m = 1$, as a function of the BS's frequency $\omega/\mu < 0.875$, for fixed coupling constants. All the cases shown exhibit an $\tilde{m} = 2$ NAI with a positive $\tilde{\omega}_I$ in the frequency ranges with ω/μ larger than the critical values:

$$\omega^c_{\rm A}/\mu = 0.392, \qquad \omega^c_{\rm S}/\mu = 0.493, \qquad \omega^c_{\rm K}/\mu = 0.490. \tag{2.15}$$

Here the subscripts stand for axionic, solitonic, and KKLS, respectively. From Figure 2.2, we see that all the BSs shown in Figure 2.5 are on the second branch that is nominally stable based on turning point arguments. Approaching these critical values from above, we find that the instability rate $\tilde{\omega}_I$ tends toward zero. Though it becomes more and more computationally expensive to measure longer and longer instability timescales, $\tilde{\omega}_I$ appears to be approaching zero roughly linearly in ω. This suggests that below this critical value, $\omega < \omega^c$ (and above the global maximum of the BS's mass), there is a range of BS solutions in the relativistic regime of the nonlinear interactions models we consider, that are free of the NAI. Again, consulting Figure 2.2, we see that such solutions have large compactness.

We also study the stability of $m = 1$ BSs with the repulsive nonlinear scalar interactions given by Eq. (2.5). We fix the BS frequency to $\omega/\mu = 0.897$ and vary the coupling constant λ. In the no-coupling limit, i.e., for $\lambda = 0$, the $\omega/\mu = 0.897$ mini BS exhibits a $\tilde{m} = 2$ NAI with growth rate $M\tilde{\omega}_I = 1.8 \times 10^{-2}$. As shown in Figure 2.6, as λ increases, the $\tilde{m} = 2$ NAI growth rate decreases (almost linearly), until it approaches zero at

$$\lambda^c/\mu^2 = 133.2. \tag{2.16}$$

Note, however, that there exists a small interval of λ/μ^2, for which the NAI is dominated by a $\tilde{m} = 1$ mode [which we ignore for the purposes of determining Eq. (2.16)]. This result seems to indicate that the NAI is turned off for $\lambda/\mu^2 > 133.2$, suggesting that BSs residing in this portion of the parameter space are stable. Finally, in contrast to the trend in growth rates of the relativistic branch, the real part of the perturbation's frequency $\tilde{\omega}_R M$ decreases *together* with $\tilde{\omega}_I M$ to zero at λ^c/μ^2, on this non-relativistic branch. When comparing the importance of the mass term $\mu^2|\Phi|^2$ to the repulsive potential $\lambda|\Phi|^4$ we see that the self-interactions dominate, i.e., $\lambda|\Phi|^2/\mu^2 > 1$ (around the maximum of the magnitude of the scalar field inside the star), for $\omega/\mu = 0.897$ repulsive BSs with couplings $\lambda/\mu^2 \geq 100$. This difference grows, with increasing coupling, allowing for the possibility of scalar BSs where the effect of the mass term is small in comparison to the quartic term, except at the outer and inner edges of the star.

In Figure 2.6, we also show the NAI growth rates of mini BSs in the regime between the global maximum of μM and the non-relativistic limit. The growth rates and harmonic frequencies $\tilde{\omega}_R$ both decrease approaching $\omega = \mu$. Fitting a generic quadratic ansatz to

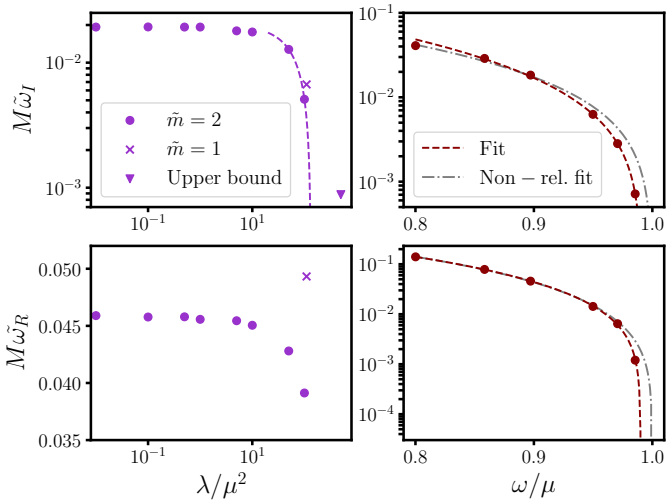

Figure 2.6: The top and bottom panel on the left show the complex frequency of the unstable modes of a family of repulsive potential BSs with fixed $\omega/\mu = 0.897$, but varying coupling constant λ. In all but one case, the unstable mode has the azimuthal number $\tilde{m} = 2$; for $\lambda/\mu^2 = 110$, the $\tilde{m} = 1$ mode is the (most) unstable. The dashed curve is a linear interpolation based on the two $\tilde{m} = 2$ cases with largest λ/μ^2 (ignoring the $\tilde{m} = 1$ case). The top and bottom panel on the right show the corresponding complex frequencies of the unstable modes of the family of mini BSs. We fit both a generic quadratic ansatz with three degrees of freedom (red dashed) and a quadratic ansatz (gray dash-dotted), which is fixed to $\tilde{\omega}_{R,I}|_{\omega=\mu} = 0$, to the data. Finally, we indicate the upper bounds on the growth rate of the case considered in Table 2.1 by down-arrows.

the $\tilde{\omega}_I M$ and $\tilde{\omega}_R M$ data, we find the respective critical boson frequencies where these two quantities would go through zero:

$$\omega^c_{\mathrm{I,m}}/\mu = 0.991, \qquad \omega^c_{\mathrm{R,m}}/\mu = 0.990. \tag{2.17}$$

We perform a resolution study on the mini BS with $\omega/\mu = 0.97$ (see Appendix A.2 for details) to determine the numerical uncertainty of our results, and hence, understand the stability of BSs with $\omega \approx \mu$. The relative numerical uncertainty for the $\tilde{\omega}_{R,I}M$ estimates is $\approx 3\%$. Comparing this with the extrapolated critical frequencies Eq. (2.17), implies that our results are consistent with $\tilde{\omega}_I$ and $\tilde{\omega}_R$ both reaching zero at $\omega = \mu$. The second fit presented in Figure 2.6, fixed to obey $\tilde{\omega}_I = 0$ as $\omega \to \mu$, is consistent with the free fit to within the numerical uncertainty. These results suggest that the timescales of the NAI grow at least as $\tilde{\tau}/M \sim (1 - \omega/\mu)^{-1}$ approaching the non-relativistic limit. Note also,

$V(\|\Phi\|)$	Coupl.	ω/μ	J/M^2	C^K	C^Q	$T_{\rm max}/M$
Axionic	$f = 0.005$	0.303	3.59	0.061	0.049	11.1×10^3
Solitonic	$\sigma = 0.05$	0.303	1.36	0.169	0.140	7.1×10^3
KKLS	$\kappa = 0.1$	0.382	0.91	0.333	0.290	3.7×10^3
Repulsive	$\lambda/\mu^2 = 500$	0.897	0.64	0.077	0.078	13.5×10^3

Table 2.1: We study the dynamical evolution of a set of $m = 1$ BSs, one for each set of scalar self-interactions that is expected to be stable based on the results obtain in Figure 2.5 and Figure 2.6. We evolve these cases up to $T_{\rm max}/M$ and find no sign of an instability arising.

when normalizing the frequencies by the BS radii, $\tilde{\omega}_{R,I} R_{99}^{K,Q}$, these quantities still tend to zero in the dilute limit (see Sec. 2.3.4 for a detailed discussion of this). We point out that these results are consistent with Ref. [129]; there a diffuse scalar cloud was evolved to form a rotating BS and then undergo the NAI. They find (notice a factor of two difference in the definition of the $|\Phi|^4$-term), a decrease of the instability timescales for larger λ, which is to be expected based on our results, because *(a)* the non-relativistic limit is unstable independent of the scalar self-interactions, and *(b)* the repulsive potential becomes more important the lower ω/μ. Therefore, the larger ω/μ, the larger the critical coupling λ^c/μ^2. In fact, one could conjecture: $\lim_{\omega\to\mu} \lambda^c \to \infty$.

To further test all these results, we pick one BS solution for each potential out of the regime conjectured to be free of the NAI (based on the trends in Figure 2.5 and Figure 2.6) and evolve it for many dynamical times. To that end, we evolve the cases summarized in Table 2.1 up to times $T_{\rm max}$, while monitoring Φ_m [defined in Eq. (2.13)] over time. In Sec. 2.3.1, we illustrated that tracking Φ_m captures the exponential growth during the linear phase of the NAI. While the truncation error introduces perturbations, these slowly decay away, and—in contrast to Figure 2.3—there is no sign of exponential growth for the cases presented in Table 2.1. From this we conclude that any instability develops on significantly longer timescales than the unstable cases with $\omega > \omega^c$ and $\lambda > \lambda^c$ found above. Based on these simulations, we place upper bounds on the growth rates of possible instabilities arising in those BSs. To that end, we use the unstable cases presented in Figure 2.5, and extrapolate the exponential growth backwards in time to $t = 0$ to estimate the initial amplitude at which truncation error seeds the unstable mode. Assuming that this amplitude is similar in the stars considered in Table 2.1, we extract approximate upper bounds on the possible growth rates for an instability not to be evident during the simulated time. We include these in Figure 2.5 and Figure 2.6.

Finally, we use nonlinear evolutions to explore the stability of individual $m = 2$ rotating

$V(\lvert\Phi\rvert)$	Coupl.	m	ω/μ	C^K	$\tilde{m}$	$M\tilde{\omega}_I$
KKLS	$\kappa = 0.1$	2	0.6	0.26	4	7.4×10^{-2}
Axionic	$f = 0.1$	2	0.9	0.08	2	1.1×10^{-2}
Solitonic	$\sigma = 0.05$	2	0.4	0.14	2	5.3×10^{-2}
Solitonic	$\sigma = 0.05$	2	0.9	0.03	4	8.5×10^{-2}
Solitonic	$\sigma = 0.1$	1	0.8	0.08	2	1.3×10^{-1}
Solitonic	$\sigma = 0.1$	1	0.4	0.28	–	$< 5.4 \times 10^{-3}$
Axionic	$f = 0.01$	1	0.8	0.03	2	4.5×10^{-2}
Axionic	$f = 0.01$	1	0.3	0.19	–	$< 5.3 \times 10^{-3}$
Liouville	$\alpha = 0.1$	1	0.9	0.07	2	1.0×10^{-2}
Liouville	$\alpha = 0.05$	1	0.9	0.07	–	$< 2.8 \times 10^{-3}$

Table 2.2: Properties of several additional rotating BSs are considered and their dynamical behavior studied. $\tilde{m}$ refers to the azimuthal number of the dominant (i.e., most unstable) non-axisymmetric mode. However, as pointed out in the text, for $m = 2$ BSs, the NAI is composed of several competing modes simultaneously. We estimate upper bounds on the growth rates for the cases, where no sign of an instability can be found. We describe in the text how these upper bounds are obtained.

BSs in different scalar models, as well as $m = 1$ BSs in various models with different couplings from the ones shown in Figure 2.5. The properties of the resulting evolutions are summarized in Table 2.2. In our small set of $m = 2$ BSs, we did not find a solution that does not develop a NAI. Note that, as will be discussed in the next section, the NAI for the $m = 2$ BSs has non-negligible support over several azimuthal modes. Therefore, the $\tilde{m}$ values for $m = 2$ BSs in Table 2.2 should be understood as rough estimates.

The result for $m = 1$ BSs shown in Table 2.2 solidify the conclusions drawn above. We show that even when changing the coupling constants in scalar models considered in Figure 2.5, there is an unstable (high frequency) regime, but also a seemingly stable (low frequency) regime, both in the solitonic and the axionic model. This shows that the coupling parameters chosen in Figure 2.5 are not special. In addition to this, we also study the stability of BSs in scalar models with a Liouville potential [328] [defined in Eq. (2.6)], a non-perturbative extension of the repulsive self-interactions. Analogous to the family of BSs in the repulsive model, studied in Figure 2.6, we fix the BS frequency to $\omega/\mu = 0.9$ and vary the coupling α. As seen from Table 2.2, there is a low-coupling range, for which an $\tilde{m} = 2$ NAI is present, but also a large coupling regime, where the NAI is quenched, and no sign of an instability can be found. Therefore, the addition of a $|\Phi|^4$ term in the scalar potential, is sufficient to stabilize rotating BS in a portion of the parameter space, and a

potential that has additional higher order terms does not affect this qualitative behavior.

2.3.3 Results: Endstate of the NAI

In the previous section, we identified two distinct regimes, the relativistic and non-relativistic branch, where the NAI is quenched and the stars appear stable when evolved nonlinearly. In what follows, we explore the end state of the instability of $m = 1$ and $m = 2$ BSs both in the relativistic regime and the non-relativistic regime.

In Ref. [323], it was found that a $m = 1$ mini BS with $\omega/\mu = 0.83$ was subject to a $\tilde{m} = 2$ NAI that lead to the formation of a BH. We study this family of mini BSs in more detail, following the growth and end state of the instability for the cases shown in Figure 2.6 with $\omega/\mu \in \{0.80, 0.86, 0.90, 0.95\}$. These stars undergo a $\tilde{m} = 2$ NAI, form two approximately non-rotating BSs that orbit around each other, and collapse to a binary BH (for $\omega/\mu \in \{0.80, 0.86\}$; see panel *a*) in Figure 2.7), or merge into a single non-rotating BS that then collapses to an isolated BH (for $\omega/\mu = 0.90$).

In the case of $\omega/\mu = 0.80$ mini BSs, the individual BSs collapse to BHs with negligible spin, and subsequently merge into a single BH $\approx 60M$ later. Additionally, we find that mini BSs with $\omega/\mu = 0.95$ undergo an $\tilde{m} = 2$ NAI and settle to a (highly perturbed) non-rotating BS (that does not collapse further), through the emission of scalar and gravitational waves, with non-zero linear momentum (see panel *b*) in Figure 2.7). This suggests that the contributions from the $\tilde{m} = 1$ unstable mode is non-negligible in this case. Similarly, repulsive self-interactions Eq. (2.5) with sufficiently large coupling can prevent the BSs from collapsing to BHs. Instead, the $m = 1$ BSs in the repulsive model, considered in Figure 2.6, undergoing the $\tilde{m} = 2$ NAI, collapse to BHs for couplings up to $\lambda/\mu^2 = 50$. For $\lambda/\mu^2 \geq 100$, however, we find that the $\tilde{m} = 2$ NAI eventually results in an approximately spherically symmetric BS, while the instability is quenched at Eq. (2.16). In Figure 2.7, we also depict the nonlinear evolution of a BS undergoing a $\tilde{m} = 1$ NAI.

This results in a highly perturbed, approximately non-rotating BS, with significant linear momentum, radiating both scalar and gravitational waves outwards. We can conclude that, the closer the BS is to the critical frequency/coupling, the less it seems to be prone to forming a BH. Therefore, we can also conclude that the end state of the NAI for $m = 1$ BSs on the branch directly connected to the non-relativistic limit depends both on the nonlinear scalar self-interactions, as well as the BS frequency. In contrast to this, we find a consistent outcome for the final fate of $m = 1$ BSs undergoing the NAI on the relativistic branch. *All* BSs presented in Figure 2.5 have the same final state, independent of the potential or their frequency: after the $\tilde{m} = 2$ NAI, two approximately non-rotating BSs

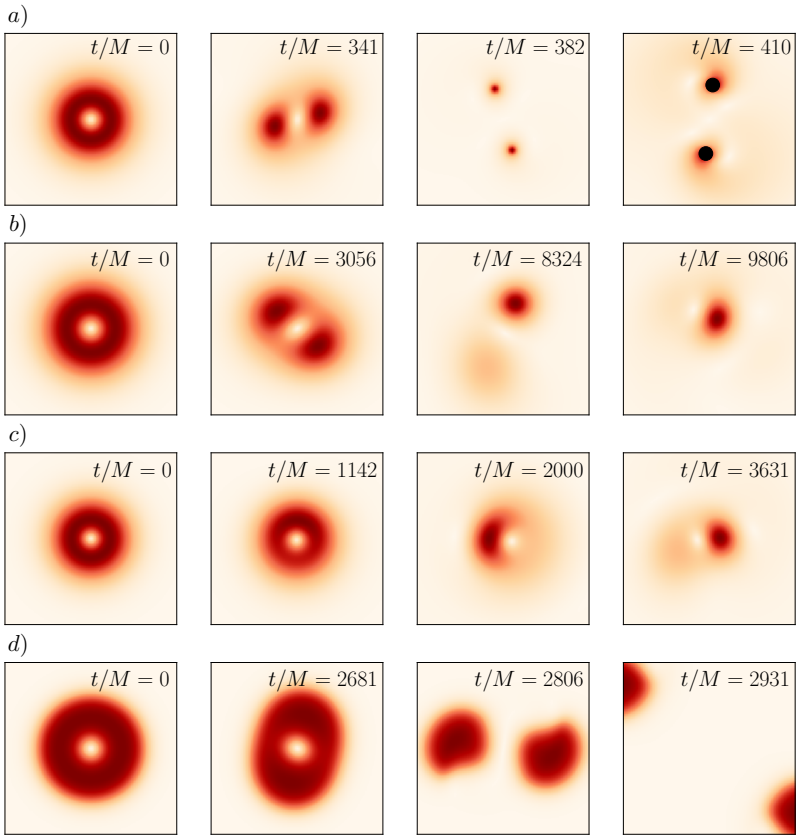

Figure 2.7: Series of snapshots (increasing in time from left to right) showing the evolution of $|\Phi|^2$ in four different scenarios where a BS undergoes a NAI. These are representative of the possible end states of all the unstable $m = 1$ BSs studied here. From top to bottom: *a*) Evolution of an $m = 1$ mini BS with $\omega/\mu = 0.8$ that collapses to a binary BH (the regions inside the apparent horizons are indicated in black). *b*) Snapshots of an $\omega/\mu = 0.95$ $m = 1$ mini BS resulting in a non-rotating BS with non-negligible linear momentum. *c*) The NAI of an $m = 1$ rotating BS, in the repulsive model with $\lambda/\mu^2 = 110$, and $\omega/\mu = 0.897$ (corresponding to the $\tilde{m} = 1$ case in Figure 2.6), yielding a non-rotating BS with large linear momentum. *d*) Finally, the evolution of an $m = 1$ axionic BS with $\omega/\mu = 0.425$ where the NAI results in the fragmentation of the star into two equal-mass non-rotating BSs.

are formed that are flung out into opposite directions at relativistic speeds. This behavior is illustrated in panel *d*) of Figure 2.7.

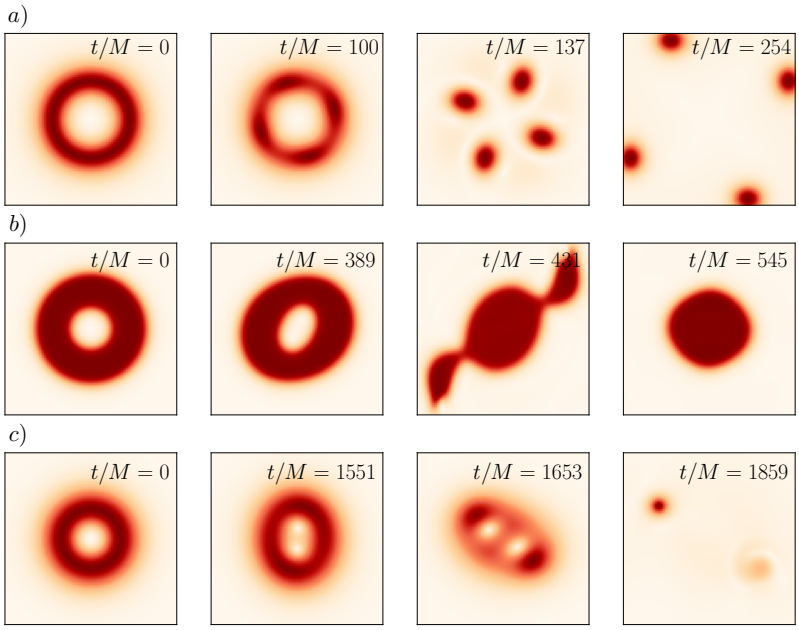

Figure 2.8: Analogous to Figure 2.7, here we present the dynamics of three $m = 2$ BSs undergoing a NAI (their properties can be found in Table 2.2). From top to bottom: *a*) The evolution of a rotating BS, in the KKLS model with $\kappa = 0.1$, and $\omega/\mu = 0.6$, results in four non-rotating equal mass BSs that are flung out from the center of mass. *b*) The fragmentation of a solitonic BS with $\sigma = 0.05$ and $\omega/\mu = 0.4$ into a large, oscillating, approximately spherically symmetric BS at the center, and two non-rotating BSs flung out at relativistic velocities. *c*) Finally, the NAI of an axionic BS with $f = 0.1$ and $\omega/\mu = 0.9$, undergoing a complex fragmentation process resulting in a single non-rotating BS with significant linear momentum.

We can conclude that the end state of the NAI in $m = 1$ BSs is clearly differentiated in the two branches. The first non-relativistic branch exhibits quasi stable bound non-stationary states after fragmentation of the original BS that either settle into a BH or to a single non-rotating BS. The second, relativistic branch consistently results in two non-rotating BSs that are flung out after fragmentation, independent of the frequency or the character of the nonlinear scalar self-interactions.

In Figure 2.8, we show the evolution of $m = 2$ BSs undergoing a NAI. The dynamics of the NAI in these stars is more complex, as more unstable non-axisymmetric modes are of non-negligible size. While the linear phase is still mostly dominated by a single azimuthal mode $\tilde{m}$ (see also Table 2.2), the nonlinear evolution of these $m = 2$ BSs is substantially

different from their $m = 1$ counterparts.

2.3.4 Results: Physical origin of the NAI

In this section, we investigate the possible physical mechanisms leading to stable regions in the BS parameter space. We focus on the case of $m = 1$ BSs and distinguish between stars on the relativistic branch and the non-relativistic branch, as the NAI of each has fundamentally different properties.

First, let us consider the non-relativistic branch, i.e., mini BSs and stars in the repulsive scalar model with frequencies between the non-relativistic limit $\omega/\mu = 1$ and the *global* maximum of the BS's mass. Since the solitonic, axionic, and KKLS scalar models reduce to the mass term in the Newtonian limit (for those cases, the non-relativistic branch extends from $\omega/\mu = 1$ to the *local* maximum of the BS's mass), the following also applies to that part of the BS parameter space in those models. From the previous section, we recall that the NAI timescales of mini BSs tend to infinity in the Newtonian limit, while BSs in the repulsive scalar model with fixed frequency $\omega/\mu = 0.897$ turn stable for coupling parameters with $\lambda > \lambda^c = 133.2\mu^2$. In Ref. [129], it was suggested that the presence of a co-rotation point (the radius at which angular velocity of the matter and the pattern speed of the unstable modes are equal) inside the star, is driving the NAI. There it was conjectured that, if the co-rotation point is outside the star (or it does not exist at all), then the star is stable, while if such a point exists within the star's radius, the star is unstable. Here we find this conjecture to hold for BSs on the non-relativistic branch. (Though not for the relativistic branch, as we shall discuss below.) The angular velocity $\tilde{\Omega}$ is defined in terms of the energy density ρ and angular momentum density J^μ, with respect to slices of constant time with unit normal n^μ and projector $\gamma_{\mu\nu} = g_{\mu\nu} + n_\mu n_\nu$:

$$\tilde{\Omega} = J^\varphi/\rho, \text{ with} \qquad J_i = \gamma_i^\mu n^\nu T_{\mu\nu}, \qquad \rho = n^\mu n^\nu T_{\mu\nu}. \tag{2.18}$$

(Note that we are only measuring this quantity with respect to our stationary and axisymmetric solutions.) We define the co-rotation radius to be the radius $r = R_{\rm cor}$ in the equatorial plane of a rotating BS where $\tilde{\Omega}(R_{\rm cor}) = \tilde{\omega}_R/\tilde{m}$.

In Figure 2.9, we show that $R_{\rm cor}$ approaches the radius of mini BSs, as well as BSs in the repulsive scalar model, as those families approach the critical frequency ω^c and critical coupling λ^c, respectively. This holds for either definition of the radius of the BS. In the repulsive scalar model, this is not surprising, since we already saw in Sec. 2.3.2 that the real part of the unstable mode's frequency (and therefore, the pattern speed $\tilde{\omega}_R/\tilde{m}$), tends to zero at λ^c. While the radius remains finite passing through λ^c, the decreasing pattern

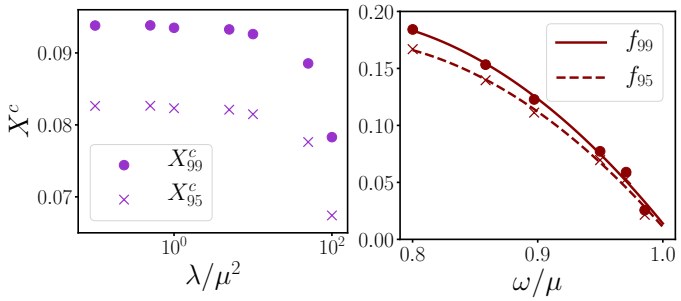

Figure 2.9: We plot the normalized difference $X^c_i = (R^K_i - R_{\rm cor})/R^K_i$, $i \in \{99, 95\}$, between the co-rotation point $R_{\rm cor}$ and the two radii R^K_{99} and R^K_{95} for the families of BSs considered in Figure 2.6. The left panel shows the repulsive potential cases, and the right shows the mini BS cases. The quantity R^K_{95} is defined, analogously to how R^K_{99} is in Sec. 2.2.2, as the circular radius $r = R^K_{95}$, where 95% of the energy resides in $r < R^K_{95}$. In the right panel, the solid and dashed lines are quadratic fits to the X^c_{99} and X^c_{95} data points.

speed is pushing $R_{\rm cor} \to \infty$, as $\lambda \to \lambda^c$. In the mini BS case, however, this is *not* the case. In the Newtonian limit, $\omega/\mu \to 1$, the radius of the BS diverges $R^K_{99} \to \infty$, while simultaneously, $\tilde{\omega}_R \to 0$. Therefore, there are two competing effects determining, whether $R^K_{99} < R_{\rm cor}$ or $R^K_{99} > R_{\rm cor}$. Despite this, the co-rotation point approaches the radius of the BS from inside the star, while the NAI growth rate decreases, as can be deduced from Figure 2.9. On top of this, we explicitly checked that $\lim_{\omega\to\mu}(\tilde{\omega}_{R,I} R^K_{99}) = 0$. This suggests that the presence of the co-rotation radius inside the star (independent of the notion of radius) is related to the instability of BSs on the non-relativistic branch. Lastly, this also seem to indicate that there is no finite regime with stable mini BSs in the Newtonian limit between the values in Eq. (2.17) and $\omega/\mu = 1$.

Let us now discuss the relativistic branch, i.e., axionic, solitonic, and KKLS BSs with frequencies between the local and the global maximum of M (see Figure 2.2): $0.3 \lesssim \omega/\mu \lesssim 0.9$. Recall from the discussion in Sec. 2.3.3 that these families of BSs undergo a $\tilde{m} = 2$ NAI that results in two equal-mass non-rotating BSs being flung out from the center of mass, for initial BS frequencies $\omega^c < \omega \lesssim 0.9\mu$. Fundamentally, the system posses three distinct conserved quantities: the ADM mass M, the angular momentum J about the symmetry axis, and the U(1)-charge Q. Given that the total number of bosons is conserved, we neglect scalar radiation and assume that the final state of the instability of a $m = 1$ BS with charge $Q_{\rm rot}$ is a binary $m = 0$ BS of total charge $2Q_{\rm sph} = Q_{\rm rot}$. From the difference in the initial BS mass, and that of the putative binary, we can calculate the normalized

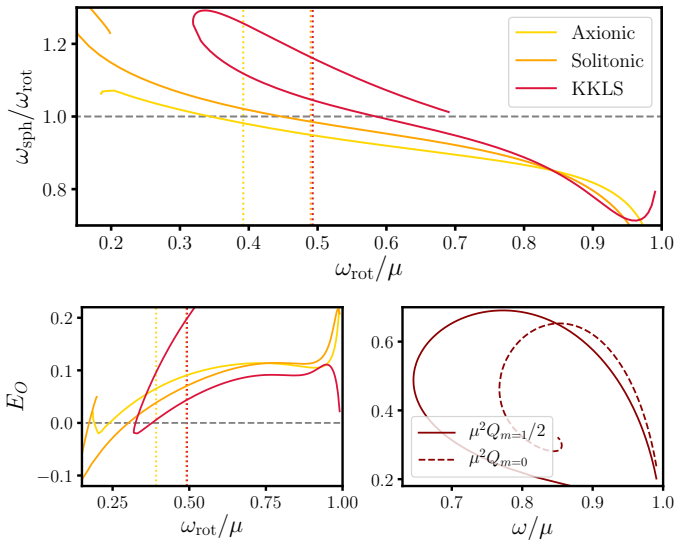

Figure 2.10: Top panel: The ratio $\omega_{\rm sph}/\omega_{\rm rot}$ of the boson frequency in $m = 1$ BSs with charge Q to the frequency of $m = 0$ BSs with charge $Q/2$ in several scalar models. The ratios pass through unity at $\omega_A^c/\mu = 0.34$, $\omega_S^c/\mu = 0.45$ and $\omega_K^c/\mu = 0.58$ for the axionic, solitonic and KKLS models, respectively. For comparison, we indicate the critical frequencies, in Eq. (2.15), by dashed vertical lines. Bottom left: The orbital energy E_O, defined in Eq. (2.19), of a $m = 0$ binary BS system with constituent charge $Q/2$ emerging from a single $m = 1$ BS with charge Q. (Legend from top panel also applies here.) Bottom right: Half the scalar charge $Q/2$ for $m = 1$ mini BSs (solid line), compared with the full charge Q of $m = 0$ mini BSs (dashed line), as a function of their respective frequencies.

orbital energy

$$E_O = (M_{\rm rot} - 2M_{\rm sph})/M_{\rm rot}, \tag{2.19}$$

as well as the frequency $\omega_{\rm sph}$ of BSs in the binary, as a function of initial boson frequency $\omega_{\rm rot}$. We show this in Figure 2.10. Based on the values shown there, the NAI fragments should be significantly unbound: $E_O = 0.1$ corresponds to a velocity of $\approx 0.4c$ at infinity. All the unstable solutions on the relativistic branch that we find occur in the regime where $E_O > 0$, which is consistent with the fact that the instability gives rise to two fragments which appear unbound. However, there is some part of the parameter space where $E_O > 0$, but we do not find the NAI.

The critical frequencies in Eq. (2.15), where the NAI instability approaches zero, seem to roughly align with those, where $\omega_{\rm sph} = \omega_{\rm rot}$ (see Figure 2.10). Due to the fragmentation,

and ignoring radiation, the bosons can fall into lower frequency/energy states within the stars (since there $\omega_{\rm sph} < \omega_{\rm rot}$), while for the regime where $\omega_{\rm sph} > \omega_{\rm rot}$, the bosons would have to climb up into higher frequency states, if the rotating BSs were to fragment into two non-rotating BSs. Hence, one can conjecture that the points, where $\omega_{\rm sph} = \omega_{\rm rot}$, indicate the switching of the stability properties. However, there is a discrepancy between the critical frequencies where $\omega_{\rm sph} = \omega_{\rm rot}$ in Figure 2.10, and those derived from the exponentially growing modes in Eq. (2.15) (even when including the numerical uncertainty), indicating that this criterion based on the relative frequency of the rotating and non-rotating equilibrium BS solutions is at most approximate. Furthermore, this approximate argument cannot be applied in the same way to the non-relativistic branch. Recall from Sec. 2.3.3 that the NAI in the case of mini BSs yields two orbiting pieces that either collapse to BHs or form a single non-rotating BS. Assuming these two orbiting scalar field distributions are roughly stationary isolated spherically symmetric BSs, i.e., applying the above argument, and consulting Figure 2.10 (bottom right), we notice two features. One is that $\omega_{\rm rot} < \omega_{\rm sph}$ for most of the parameter space, at least when comparing the turning-point stable branches. This may be related to the fact that the BS fragments collapse in some cases, which would be consistent with them being unstable spherical stars. The second feature to note is that for $m = 1$ stars with $\omega_{\rm rot}/\mu > 0.846$, there exists no corresponding non-rotating counterparts with half the U(1)-charge. Again, this may be related to the fact that for large enough $\omega_{\rm rot}$, the instability gives rise to a single BH or non-rotating BS. Additionally, we observe no significant qualitative change in the dynamics of the systems when moving across the point where both curves cross.

Finally, we note that the co-rotation argument discussed above in the context of non-relativistic BSs does not apply to the relativistic branch. This is because the real part of the unstable mode's frequency remain non-zero on the entire relativistic branch (see Figure 2.5), and hence the co-rotation point remains well inside the star for all unstable BSs. Even when extrapolating $\tilde{\omega}_R M$ deeper into the relativistic regime, the co-rotation point seems to only exit the star at the global maximum of the BS's mass.

2.4 Discussion and Conclusion

In this chapter, we study the stability of $m = 1$ and 2 BSs in various massive complex scalar models minimally coupled to gravity. We do this by numerically evolving the Einstein-Klein-Gordon system of equations, starting from stationary BS initial data. We consider a number of different types of scalar interactions, and explore the parameter space of BS solutions. We find that *all* $m = 1$ mini BSs are unstable to an exponentially-growing,

non-axisymmetric mode with azimuthal number $\tilde{m} = 2$, but that the growth rate scales as $\tilde{\omega}_I \propto (1 - \omega/\mu)$ when $\omega \to \mu$ (see Figure 2.6). Since all nonlinear scalar self-interactions reduce to the mass term for sufficiently small field values, this holds also for all $m = 1$ scalar BS that reside sufficiently deep in the Newtonian limit. This may have some relevance for rotating distributions of dark matter in models where they are composed of ultralight bosons.

We find that adding a nonlinear scalar potential can quench the instability in a number of cases, in the sense that the growth rate approaches zero as the BS frequency decreases towards a critical value (see Figure 2.5 and Figure 2.6). Studying the conjecture in Ref. [129], we relate the stability of the stars on the non-relativistic branch to the presence of the co-rotation point inside the star, and show that, when the BSs become stable, the co-rotation point moves outside of the star (independent of the notion of radius; see Figure 2.9). The stability of solutions on the relativistic branch seems unrelated to the co-rotation, though approximately related to the BS frequency; the final state of the instability is always an equal-mass binary BS of non-rotating constituents, and we find around where the rotating stars become stable, there is a transition from this final state having lower frequency to having higher frequency (see Figure 2.10 for the details). It would be interesting for future work to see if this argument could be sharpened. In Refs. [323, 129], it was argued that the stability of BSs is related to the morphology of surfaces of constant scalar energy. Stars with toroidal morphology were claimed to be unstable, while those with spherical surfaces of constant energy, stable. Here we find $m = 1$ scalar BSs that have toroidal morphology, but do not appear to be subject to this instability. Though we do not explore the parameter space of $m = 2$ BSs as thoroughly as the $m = 1$ case, we find all the examples we consider to be linearly unstable.

We choose several examples of $m = 1$ BSs with nonlinear interactions that are past the point where the NAI growth rate approaches zero, and evolve them for many dynamical times (in some cases $> 10^4 M$) and find no sign of a growing perturbation. These include cases with high compactness, rapid rotation, and—in the case of the KKLS BS in Table 2.1—unstable and stable photon orbits, which can be used for future studies of mergers, and compared to the mergers of black holes and neutron stars. Of course, our methods can not definitely rule out instabilities of any kind, in particular instabilities that arise on longer timescales than considered here. For example, in Ref. [216], it was conjectured that stable photon orbits may give rise to nonlinear instability, based on the slow timescales associated with the decay of linear perturbations. If such a nonlinear instability were to exist, it would likely operate on much longer timescales than the NAI, and so may not be evident here.

Another future direction is to see whether rotating scalar BSs could be formed dynam-

ically, through a non-spinning binary BS merger, or through the collapse of a rotating scalar cloud. The parameter space identified here could be used to choose favorable initial conditions that may dynamically give rise to a stable rotating BS. It would also be interesting to investigate scenarios where unstable rotating BS solutions may form, for example from the migration of a stable star to a unstable part of the parameter space, or through rapid collapse. In such cases, the nonlinear development of the instability will give rise to distinct gravitational wave signatures. For example, here we find cases where the NAI of a rotating BS gives rise to a binary BH which will subsequently merge, similar to the binary BH formation found to arise in the collapse of supermassive stars [309].

Chapter 3

Generic initial data for binary boson stars

Executive summary: Binary boson stars can be used to model the nonlinear dynamics and gravitational wave signals of merging ultracompact, but horizonless, objects. However, doing so requires initial data satisfying the Hamiltonian and momentum constraints of the Einstein equations, something that has not yet been addressed. In this chapter, we construct constraint-satisfying initial data for a variety of binary boson star configurations. We do this using the conformal thin-sandwich formulation of the constraint equations, together with a specific choice for the matter terms appropriate for scalar fields. The free data is chosen based upon a superposition of isolated boson star solutions, but with several modifications designed to suppress the spurious oscillations in the stars that such an approach can lead to. We show that the standard approach to reducing orbital eccentricity can be applied to construct quasi-circular binary boson star initial data, reducing the eccentricity of selected binaries to the $\sim 10^{-3}$ level. Using these methods, we construct initial data for quasi-circular binaries with different mass-ratios and spins, including a configuration where the spin is misaligned with the orbital angular momentum, and where the dimensionless spins of the boson stars exceeds the Kerr bound. We evolve these to produce the first such inspiral-merger-ringdown gravitational waveforms for constraint-satisfying binary boson stars. Finally, we comment on how equilibrium equations for the scalar matter could be used to improve the construction of binary initial data, analogous to the approach used for quasi-equilibrium binary neutron stars.

3.1 Introduction

The common practice in the literature, when constructing binary BS initial data, has been so far to simply superpose two boosted star solutions. More recently, in Refs. [189, 153], a modified superposition trick was utilized to reduce (but not eliminate) violations of the Hamiltonian and momentum constraints. While simple, superposed initial data leads to large constraint violations even at moderate separations, effectively excluding, for example, the quasi-circular binaries relevant to current GW observations of inspiral-merger-ringdown.

In this chapter, we develop and implement methods for constructing constraint-satisfying binary scalar BS initial data for a wide variety of configurations. (We also used these methods recently in Ref. [340].) We solve the constraint equations in the conformal thin-sandwich (CTS) formalism [373], using free data based on superposing stationary BS solutions, similar to what was done in Ref. [147] for black hole and fluid stars. However, considering scalar matter introduces several new complications which we address here, including the choice of which matter degrees of freedom to fix, as well as how to minimize spurious oscillations which may be induced in the BSs. Our approach is very flexible, and we use it to construct binary BSs with different mass-ratios, spin magnitudes, and spin orientations. We evolve several such binaries, including several cases where the BSs are super-spinning (i.e., have dimensionless spins exceed the Kerr bound of unity), through inspiral and merger. We do this both for physical interest, as well as to demonstrate that we can construct quasi-circular binaries by adapting eccentricity reduction techniques.

The remainder of this chapter is organized as follows. We briefly review the relevant physics of isolated stationary BSs in Sec. 2.2, and proceed in Sec. 3.2.1 to introduce our procedure to self-consistently solve the elliptic constraint equations in the CTS formalism [373] numerically, given an initial guess for the binary, utilizing the elliptic solver introduced in Ref. [147]. To that end, we identify the most suitable parameterization of the matter content of BSs in Sec. 3.2.2. We comment on possible equilibrium conditions for the scalar matter of these stars in Sec. 3.2.3, though we do not implement such an approach in this study. In Sec. 3.3.2, we analyze the quality of the constructed initial data and devise methods to reduce spurious oscillations in each star, as well as in the resulting gravitational radiation, and lastly, in Sec. 3.3.3, we test eccentricity reduction schemes in the context of binary BS inspirals and comment on their possible limitations. We consider binary configurations in two different scalar potentials, with equal and unequal masses, as well as non-spinning and spinning constituent stars with aligned and misaligned spins. Finally, in Sec. 3.4, we analyze the dynamics of selected eccentricity-reduced binary configurations, and present inspiral-merger-ringdown gravitational waveforms. We give details on the nu-

merical evolution scheme and present convergence results in Appendix B.1, and provide some further details on spurious high frequency components to the GWs and correcting for center-of-mass motion of the BS binaries in Appendices B.2 and B.3, respectively.

3.2 Methodology

3.2.1 Conformal thin-sandwich formulation

Moving now to the formalism used to construct constraint satisfying binary BS initial data, we introduce the CTS formulation of the Hamiltonian and momentum constraints of the Einstein equations. To that end, the spacetime is foliated into a series of spacelike hypersurfaces Σ_t, parameterized by the coordinate time t, with future-pointing unit-normal to the hypersurface n^μ. The tangent of lines of constant spatial coordinates is then

$$t^\mu = \alpha n^\mu + \beta^\mu, \tag{3.1}$$

with lapse function α and shift vector β^μ, with $n_\mu \beta^\mu = 0$. Furthermore, let $\gamma_{\mu\nu} = g_{\mu\nu} + n_\mu n_\nu$ be the projector onto the hypersurface Σ_t, such that γ_{ij} is the spatial metric induced on Σ_t. Lastly, the extrinsic curvature of Σ_t,

$$K_{ij} = -\frac{1}{2}\mathcal{L}_n \gamma_{ij}, \tag{3.2}$$

is defined by means of the Lie derivative $\mathcal{L}_n$ along the hypersurface normal. In this 3+1 language, the Hamiltonian and momentum constraints, i.e., the projections of the Einstein equations along the hypersurface normal, are

$$\begin{aligned} {}^{(3)}R + K^2 + K_{ij}K^{ij} &= 16\pi E, \\ D_j K^{ij} - D^i K &= 8\pi p^i, \end{aligned} \tag{3.3}$$

with trace $K = \gamma^{ij} K_{ij}$, Ricci scalar ${}^{(3)}R$ and derivative D_i defined with respect to the induced metric γ_{ij}, and finally, the energy density $E = n_\mu n_\nu T^{\mu\nu}$ and momentum density $p^i = -\gamma^i_\mu n_\nu T^{\mu\nu}$ of the matter content of the space in the Eulerian frame.

The CTS formulation [373] of the Hamiltonian and momentum constraints (3.3) relies on relating the constraint satisfying metric components γ_{ij} to a freely specifiable conformal metric $\tilde{\gamma}_{ij}$ as

$$\gamma_{ij} = \Psi^4 \tilde{\gamma}_{ij}, \tag{3.4}$$

with conformal factor Ψ. Furthermore, the traceless part of the extrinsic curvature A^{ij} is conformally decomposed as $A^{ij} = \Psi^{-10}\hat{A}^{ij}$ with

$$\hat{A}^{ij} = \frac{1}{2\tilde{\alpha}}\Big[(\tilde{\mathbb{L}}\beta)^{ij} + \partial_t\tilde{\gamma}^{ij}\Big], \tag{3.5}$$

in terms of the conformal Killing form $(\tilde{\mathbb{L}}\beta)^{ij} = \tilde{D}^i\beta^j + \tilde{D}^j\beta^i - 2\tilde{\gamma}^{ij}\tilde{D}_k\beta^k/3$. The conformal lapse and the time-derivative of the conformal metric are $\tilde{\alpha} = \Psi^{-6}\alpha$ and $\partial_t\tilde{\gamma}^{ij} = \Psi^4(\partial_t\gamma^{ij} - \gamma^{ij}\gamma_{kl}\partial_t\gamma^{kl}/3)$, respectively. Utilizing this decomposition, the metric constraints (3.3) are cast into the CTS equations

$$\begin{aligned} \tilde{D}_i\tilde{D}^i\Psi - \frac{\tilde{R}}{8}\Psi + \frac{\hat{A}_{ij}\hat{A}^{ij}}{8}\Psi^{-7} - \frac{K^2}{12}\Psi^5 &= -2\pi\Psi^5 E, \\ \tilde{D}_j\hat{A}^{ij} - \frac{2}{3}\Psi^6\tilde{D}^i K &= 8\pi\Psi^{10}p^i. \end{aligned} \tag{3.6}$$

The geometric free data (i.e., those metric variables that need to be specified) are comprised of the metric $\tilde{\gamma}_{ij}$ and its coordinate time derivative $\partial_t\tilde{\gamma}^{ij}$, as well as the trace K of the extrinsic curvature and the lapse function $\tilde{\alpha}$. This formulation is supplemented by a choice of energy and momentum densities, E and p^i, of the complex scalar matter, as well as the corresponding scalar free data. This will be discussed in detail in the next section.

To specify the metric free data, we proceed as follows. First, we solve for stationary isolated BSs in Lewis-Papapetrou coordinates, as outlined in Sec. 2.2. These solutions are subsequently transformed to Cartesian coordinates[1] and boosted using initial coordinate velocities $v^i_{(A)}$, where $A \in \{1, 2\}$ labels each star in the binary, and placed at coordinate positions $z^i_{(A)}$. Therefore, for each star we obtain the set of variables $\gamma^{(A)}_{ij}$, $\partial_t\gamma^{(A)}_{ij}$, $\alpha^{(A)}$, and $\beta^i_{(A)}$ (for both stars in Cartesian-type coordinates). For all binary configurations presented in this chapter, $z^i_{(A)}$ and $v^i_{(A)}$ are chosen such that the initial center-of-mass location coincides with the origin of the numerical grid, and the initial linear momentum of the center of mass vanishes (at the Newtonian level); limitations of this approach are discussed in Appendix B.3. These two solutions are then superposed as

$$\begin{aligned} \gamma^{\text{sup}}_{ij} &= \eta_{ij} + f_{(2)}\big[\gamma^{(1)}_{ij} - \eta_{ij}\big] + f_{(1)}\big[\gamma^{(2)}_{ij} - \eta_{ij}\big], \\ \partial_t\gamma^{\text{sup}}_{ij} &= f_{(2)}\partial_t\gamma^{(1)}_{ij} + f_{(1)}\partial_t\gamma^{(2)}_{ij}, \\ \alpha_{\text{sup}} &= 1 + f_{(2)}\big[\alpha^{(1)} - 1\big] + f_{(1)}\big[\alpha^{(2)} - 1\big], \\ \beta^i_{\text{sup}} &= f_{(2)}\beta^i_{(1)} + f_{(1)}\beta^i_{(2)}, \end{aligned} \tag{3.7}$$

[1]We transform from Lewis-Papapetrou to Cartesian coordinates by applying the usual flat relations between spherical and Cartesian coordinates.

where $\eta^i{}_j = \delta^i_j$ is the flat 3-metric, and $f_{(A)}$ is an attenuation function, which we introduce here for convenience and discuss in detail in Sec. 3.3.2. For now, we simply point out that the choice $f_{(A)} \equiv 1$ corresponds to a plain superposition of the isolated stars. As discussed in Ref. [147], the metric free data is then obtained from

$$\begin{aligned}
\tilde{\gamma}_{ij} &= \gamma^{\text{sup}}_{ij}, \\
\partial_t \tilde{\gamma}^{ij} &= -\tilde{\gamma}^{ik}\tilde{\gamma}^{jl}\left(\partial_t \gamma^{\text{sup}}_{kl} - \frac{1}{3}\tilde{\gamma}_{kl}\tilde{\gamma}^{mn}\partial_t \gamma^{\text{sup}}_{mn}\right), \\
\tilde{\alpha} &= \alpha_{\text{sup}}, \\
K &= \frac{1}{2\tilde{\alpha}}\left[2\partial_i \beta^i_{\text{sup}} + \tilde{\gamma}_{ij}\partial_t \tilde{\gamma}^{ij} + \tilde{\gamma}^{ij}\beta^k_{\text{sup}}\partial_k \tilde{\gamma}_{ij}\right].
\end{aligned} \tag{3.8}$$

The CTS equations admit solutions provided appropriate boundary conditions are specified. In the context of binary BSs, i.e., asymptotically flat spacetimes, we require that

$$\lim_{|\mathbf{x}|\to\infty} \Psi = 1, \qquad\qquad \lim_{|\mathbf{x}|\to\infty} \beta^i = \beta^i_{\text{sup}}|_\infty, \tag{3.9}$$

where $\beta^i_{\text{sup}}|_\infty$ is the shift of the free data at large distances. With these boundary conditions, we solve the CTS equations numerically using a multigrid scheme with fixed mesh refinement (further details can be found in Ref. [147]). In the context of axisymmetry, we employ a generalized Cartoon method that provides derivatives about the axis of symmetry by means of a the axisymmetric Killing field, allowing also for harmonic azimuthal dependencies in the scalar sector.

3.2.2 Binary boson star sources

So far, we have left the precise parameterization of the scalar matter sourcing the spacetime, E and p^i, unspecified. In principle, various choices of energy and momentum densities measured by an Eulerian observer, are possible for time-dependent complex scalar field matter. However, we find the precise choice to be crucial to achieve convergence of our numerical implementation. Therefore, in the following we outline possible matter source parameterizations, and especially, highlight the method we found to robustly yield consistent binary BS initial data in any considered context.

We begin by introducing the necessary projections of the nonlinear complex scalar energy-momentum tensor with respect to the foliation introduced in the previous section. The latter is readily obtained from (2.1) in covariant form:

$$T_{\mu\nu} = 2\partial_{(\mu}\bar{\Phi}\partial_{\nu)}\Phi - g_{\mu\nu}\left[g^{\alpha\beta}\partial_{(\alpha}\bar{\Phi}\partial_{\beta)}\Phi + V(|\Phi|)\right]. \tag{3.10}$$

For convenience, we define the conjugate momentum of the complex field with respect to a spatial slice as

$$\eta := \mathcal{L}_n \Phi = n^\alpha \partial_\alpha \Phi = \frac{1}{\alpha}(\partial_t \Phi - \beta^i D_i \Phi). \tag{3.11}$$

With this, the scalar energy-momentum tensor can be written in the Eulerian frame as

$$\begin{aligned} E &= n_\alpha n_\beta T^{\alpha\beta} = \eta\bar{\eta} + D^i\Phi D_i\bar{\Phi} + V(|\Phi|) \\ p^i &= -\gamma^i{}_\alpha n_\beta T^{\alpha\beta} = -\eta D^i\bar{\Phi} - \bar{\eta} D^i\Phi \\ S^{ij} &= \gamma^i{}_\alpha \gamma^j{}_\beta T^{\alpha\beta} = 2D^{(i}\Phi D^{j)}\bar{\Phi} \\ &\quad + \gamma^{ij}\Big[\eta\bar{\eta} - D_k\Phi D^k\bar{\Phi} - V(|\Phi|)\Big]. \end{aligned} \tag{3.12}$$

Starting from these expressions, we discuss possible approaches to parameterize the scalar matter, as well as the associated choices of scalar free data accompanying the metric free data (3.8). To that end, and before presenting the source parameterization that we found to work for any type of binary BS configuration, it is instructive to consider two other approaches that, while natural, exhibit fundamental issues.

Fixed energy and momentum densities

In the context of binary neutron star initial data, it is natural to choose the conformal Eulerian energy $\tilde{E}$ and momentum densities $\tilde{p}^i$ as free data for the CTS system of equations (3.6). The corresponding physical momentum density p^i is typically chosen to be $p^i = \Psi^{-10}\tilde{p}^i$. One choice for the conformal scaling of the energy is $E = \Psi^{-8}\tilde{E}$, which is motivated by uniqueness arguments and the preservation of the dominant energy condition (i.e., if the free data satisfies $\tilde{E} \geq \sqrt{\tilde{\gamma}^{ij}\tilde{p}_i\tilde{p}_j}$ so does the constraint satisfying initial data). In the case of fluid stars, the initial physical pressure P and density ρ are recovered by means of an algebraic relation between E, p^i, P, and ρ derived from the expression for the fluid energy-momentum tensor combined with the fluid equation of state. This provides a means to reconstruct the constraint satisfying fluid variable initial conditions directly from the free data and constrained data.

A complex scalar field, on the other hand, has kinetic and gradient energy, in addition to potential energy. The energy therefore depends on spatial gradients $D^i\Phi$ and time-derivatives $\partial_t\Phi$ of the scalar field, as can be seen in (3.12). Therefore, unlike in the binary neutron star scenario, the relation between the physical energy and momentum densities, and the matter field Φ, is not purely algebraic, but rather of differential form. This renders

the reconstruction of the scalar field initial data Φ and $\dot{\Phi}$ (or equivalently Φ and η) from the constraint satisfying energy and momentum densities non-trivial.

Irrespective of these shortcomings, we test this choice of matter source variables with a set of single isolated non-spinning and spinning BSs. The metric free data is constructed following the discussion in Sec. 3.2.1 (setting $\gamma^{(2)}_{ij} = 0$ etc.), while the scalar sources $\tilde{E}$ and $\tilde{p}^i$ are determined from (3.12). The CTS equations are then numerically solved iteratively as outlined above. We succeeded in recovering isolated, boosted, non-spinning and spinning BSs utilizing this approach, i.e., the elliptic CTS solver removed truncation error of the isolated solution to the precision allowed by the resolution of the discretization of the CTS equations. This shows that, within our numerical setup, solutions to isolated stars are in fact local attractors in the space of solutions using this scalar matter parameterization.

Fixed scalar initial data

In order to circumvent the issue discussed in the previous section, i.e., instead of fixing the energy and momentum densities directly, one could provide the scalar field initial data itself—Φ and $\dot{\Phi}$—as free data to the CTS equations. This makes the reconstruction of the scalar field trivial, ensuring that the metric and scalar initial data consistently solve the Hamiltonian and momentum constraints. To that end, we rewrite (3.12) in terms of the scalar fields Φ and $\dot{\Phi}$, leading to

$$\begin{aligned} E &= \frac{\Psi^{-12}}{\tilde{\alpha}^2}|\dot{\Phi} - \beta^i\partial_i\Phi|^2 + \Psi^{-4}\tilde{D}^i\bar{\Phi}\tilde{D}_i\Phi + V(|\Phi|), \\ p^i &= -\frac{\Psi^{-10}}{\tilde{\alpha}^2}\Big((\dot{\Phi} - \beta^i\partial_i\Phi)\tilde{D}^i\bar{\Phi} + (\dot{\bar{\Phi}} - \beta^i\partial_i\bar{\Phi})\tilde{D}^i\Phi\Big) \end{aligned} \tag{3.13}$$

in terms of the conformal variables. The different scaling of the kinetic, gradient, and potential energies with conformal factor Ψ, as well as the dependencies on the shift vector β^i indicate that this approaches differs from providing E and p^i as free data by more than a simple Ψ-rescaling.

We tested the above choice of sources within our numerical setup, similarly to our tests of the formulation presented in Sec. 3.2.2. We found robust convergence of the numerical schemes in the case of isolated boosted non-spinning BSs. However, we were unable to recover an isolated stationary rotating BS solution using (3.13) in the CTS equations. Despite the CTS equation residuals converging to zero at the expected order *before* the first iteration, the solution of the elliptic solver moves away from the true solution exponentially quickly with each iteration. This indicates that rotating BSs are not attractors in the space

of solutions when using (3.13) and our numerical framework, or suggests a break-down in the uniqueness of this solution for the given free and boundary data. Note, tests of uniqueness based on the maximum principle (see, e.g., Ref. [175]) are not applicable in this case, since the momentum constraint is not trivially satisfied by stationary rotating BS solutions[2].

Fixed scalar kinetic energy

We turn now to the choice of scalar matter free data that we found to robustly lead to constraint satisfying binary BS metric and scalar field initial data. Similar choices of free data were considered recently in cosmological contexts in Refs. [38, 115]. Here, instead of setting the scalar initial data $\{\Phi, \dot{\Phi}\}$ as free data for the CTS equations, we replace $\dot{\Phi}$ by the scalar field's conformal conjugate momentum $\tilde{\eta} = \Psi^6 \eta$ as free data. With this, and in terms of the above conformal decomposition, the energy and momentum densities turn into

$$\begin{aligned} E &= \Psi^{-12}\tilde{\eta}\bar{\tilde{\eta}} + \Psi^{-4}\tilde{D}^i\Phi\tilde{D}_i\bar{\Phi} + V(|\Phi|), \\ p^i &= -\Psi^{-10}(\tilde{\eta}\tilde{D}^i\bar{\Phi} + \bar{\tilde{\eta}}\tilde{D}^i\Phi). \end{aligned} \tag{3.14}$$

The scalar data satisfying the constraint equations can then be recovered via the *algebraic* relation

$$\dot{\Phi} = \tilde{\alpha}\tilde{\eta} + \beta^i\partial_i\Phi, \tag{3.15}$$

where β is the solution to the vector CTS equation provided the free data $\{\Phi, \tilde{\eta}\}$; notice $\alpha\eta = \tilde{\alpha}\tilde{\eta}$. For completeness, we include here also the expressions (3.14) in terms of $\Phi_R = (\Phi + \bar{\Phi})/2$, and $\Phi_I = (\Phi - \bar{\Phi})/(2i)$, as these are the variables used in our numerical implementation of the elliptic CTS solver, as well as the hyperbolic evolution scheme:

$$\begin{aligned} E = &\left[\Psi^{-12}\tilde{\eta}_R^2 + \Psi^{-4}\tilde{D}_i\Phi_R\tilde{D}^i\Phi_R + (R \leftrightarrow I)\right] \\ &+ V(\Phi_R^2 + \Phi_I^2), \\ p^i = &-2\Psi^{-10}\left[\tilde{\eta}_R\tilde{D}^i\Phi_R + (R \leftrightarrow I)\right]. \end{aligned} \tag{3.16}$$

[2]Even if the maximum principle could be applied in this case, perturbations ϵ away from a solution Ψ_0 to the Hamiltonian constraint follow to linear order the equation $\tilde{D}_i\tilde{D}^i\epsilon = \Gamma\epsilon$, with $\Gamma = \tilde{R}/2 - 14\pi\Psi_0^{-8}\tilde{\alpha}^{-2}|\dot{\Phi} - \beta^i\partial_i\Phi|^2 + \ldots$, where we ignored all positive-definite terms. Hence, non-vanishing kinetic energy and momentum densities p^i, present even in isolated rotating BSs, may result in violations of the maximum principle, i.e., in $\Gamma < 0$.

We found this matter source parameterization to robustly recover any kind of single BS solution in those tests outlined in Sec. 3.2.2. Given this parameterization passes these tests, we are now able to move to *binary* BS. To that end, we construct the scalar free data in a similar fashion to the superposed metric free data presented in (3.7). First, the scalar fields $\Phi^{(A)}$ of each star are boosted with the same boost as the metric, then the conjugate momenta $\tilde{\eta}^{(A)}$ are determined[3], and finally, the variables are superposed to obtain the scalar free data as follows:

$$\begin{aligned} \Phi^{\rm sup} &= \hat{f}_{(2)}\Phi^{(1)} + \hat{f}_{(1)}\Phi^{(2)}, \\ \tilde{\eta}^{\rm sup} &= \hat{f}_{(2)}\tilde{\eta}^{(1)} + \hat{f}_{(1)}\tilde{\eta}^{(2)}. \end{aligned} \tag{3.17}$$

Here $\hat{f}_{(A)}$ are attenuation functions (directly analogous to $f_{(A)}$, defined in Sec. 3.2.1), which we discuss in detail below and simply note here that $\hat{f}_{(A)} = 1$ corresponds to a simple superposition of the two star's scalar field variables. Notice, while the constraint equations are invariant under a global phase shift $\Phi \to \Phi e^{i\alpha}$, the source functions (3.14) are not invariant under the phase of a *single* constituent of a binary, e.g., $\Phi^{(1)} \to \Phi^{(1)}e^{i\alpha}$.

3.2.3 Scalar matter equilibrium

We focused so far on finding a scalar matter parameterization that robustly yields constraint satisfying binary BS initial data. Since no assumptions on the stars' trajectories, spin orientations, or mass-ratio were built into the formalism, this approach is very flexible. However, as we show in Sec. 3.3, the simple construction of the free data described above results in stars with large internal oscillations and ejected scalar matter. In the case of binary neutron stars, various methods have been introduced to alleviate these issues by explicitly equilibriating the fluid and metric degrees of freedom [71, 337, 358]. These approaches are based on assuming the existence of a helical Killing field ℓ^μ, which provides a notion of equilibrium not just for the metric, i.e., $\mathcal{L}_\ell g_{\mu\nu} = 0$, but also for the matter variables. In the case of binary neutron stars, combining the conservation of rest mass density, the conservation of the fluid's energy-momentum, and matter equilibrium with respect to ℓ^μ, results in an elliptic equation for the equilibriated initial velocity of the fluid. In the following, we apply these arguments qualitatively to the case of scalar field matter and outline approaches to equilibriating the scalar matter. However, as we are not testing these formalisms here explicitly, this is to be understood as a first step guiding more thorough future analyses.

[3]Recall, the scalar field has a non-trivial time-dependence [see also (4.1)], so that we first boost the vector $\partial_\mu\Phi$, and then determine its conjugate momentum in the boosted frame.

To that end, we assume the existence of a helical Killing field ℓ^μ, such that $\ell^\mu = \alpha n^\mu + \tilde{V}^\mu$. In the asymptotically inertial frame, the spatial velocity takes the form $\tilde{V}^\mu = \beta^\mu + \tilde{\Omega} m^\mu$, where m^μ is spacelike generating the azimuthal direction and $\tilde{\Omega}$ is the orbital period of the helical field ℓ^μ. On the other hand, in the co-rotating frame, the Killing field $\ell^\mu \to t^\mu$, such that $\tilde{V}^\mu \to \beta^\mu$ (for a discussion on the subtleties associated with this choice, see, e.g., Ref. [176]). From the perspective of the observer associated with n^μ, the Noether-current, decomposes as

$$j^\mu = \rho n^\mu + J^\mu, \tag{3.18}$$

$$\rho = -n_\mu j^\mu = i(\bar{\Phi}\eta - \Phi\bar{\eta}), \tag{3.19}$$

with local boson number density ρ, and spatial current

$$J^\mu = -i(\bar{\Phi} D^\mu \Phi - \Phi D^\mu \bar{\Phi}). \tag{3.20}$$

In direct analogy to the rest mass conservation equation for fluids, the global U(1) symmetry of the scalar theory implies the boson number conservation [see (2.11)]. With this above decomposition of the current, the conservation law (2.11) reduces to

$$\mathcal{L}_n \rho = \rho K - \frac{1}{\alpha} D_i(\alpha J^i). \tag{3.21}$$

Correspondingly, the evolution equation for the scalar field—the Klein-Gordon equation—is readily obtained from (2.1):

$$\left[\nabla_\mu \nabla^\mu - \partial_{|\Phi|^2} V(|\Phi|)\right] \Phi = 0. \tag{3.22}$$

Using the foliation defined by n^μ, the Klein-Gordon equation takes the form

$$\mathcal{L}_n \eta = \frac{1}{\alpha} D_i(\alpha D^i \Phi) + K\eta - \Phi \partial_{|\Phi|^2} V(|\Phi|), \tag{3.23}$$

and similarly for the conjugate equation. To proceed, a series of equilibrium conditions, utilizing the helical Killing vector, must be imposed on the matter variables.

Contrary to the matter variables relevant for fluid stars, the scalar matter making up BSs is not time-independent. To understand possible equilibrium conditions, recall that the scalar field ansatz (4.1), with $\eta \sim i(\omega - m\Omega/r)\Phi$, contains a harmonic time-dependence of the scalar variables due to the linear time-dependence of the scalar phase. Therefore, here we explore how the ansatz underlying the isolated BS solution, i.e.,

$$\mathcal{L}_\ell \Phi = i\tilde{\omega}\Phi, \tag{3.24}$$

may generalize to a binary system. To that end, we specialize to the co-rotating frame for the remainder of this section. This implies that $\mathcal{L}_\ell \alpha = 0$ and $\mathcal{L}_\ell \beta^\mu = 0$, which together with (3.24) imply that $\mathcal{L}_\ell \eta = i\tilde{\omega}\eta$. With these, the Klein-Gordon equation (3.23) reduces to the complex equation

$$-\beta^i D_i \eta + i\tilde{\omega}\eta - \alpha K \eta = D_i(\alpha D^i \Phi) - \alpha \Phi \partial_{|\Phi|^2} V(|\Phi|), \tag{3.25}$$

where $\eta = (i\tilde{\omega}\Phi - \beta^i D_i \Phi)/\alpha$ in the co-rotation frame. This second-order elliptic equation for Φ is directly analogous to the scalar equation obtained from plugging the metric and scalar field ansatz of an isolated stationary BS [given in (2.7) and (4.1), respectively] into the Klein-Gordon equation (3.22). Binary BS boundary conditions are $\lim_{|\mathbf{x}|\to\infty} \Phi = 0$.

In this approach, the frequency $\tilde{\omega}$ must be chosen. Even in the equal-frequency regime, we expect the binary's frequency $\tilde{\omega}$ to differ from the isolated star's frequency $\omega_1 = \omega_2 \neq \tilde{\omega}$ due to the increase in binding energy; hence, the naive expectation is that $\tilde{\omega} < \omega_1$. The frequency $\tilde{\omega}$ could be iteratively adjusted to achieve a desired property for the binary initial data (e.g. a value for the mass or scalar charge), or a new binary BS solution may be found at fixed $\tilde{\omega}$ (analogous to the case of an isolated BS). For unequal-mass binaries, the binary's frequency is spatially dependent since $\omega_1 \neq \omega_2$. A simple choice is to construct a differentiable $\tilde{\omega}$ transitioning from a fraction of ω_1 around the first star to the same (or different) fraction of ω_2 around the second star[4].

The previous ansatz, based on assumption (3.24), requires specifying the binary frequency $\tilde{\omega}$. An alternative is to specify some profile for the scalar field (or conjugate momentum) and then assume only the equilibrium conditions[5] $\mathcal{L}_\ell |\eta|^2 = \mathcal{L}_\ell \rho = 0$ [which are implied by (3.24)]. Assuming these equilibrium conditions, the two equations (3.21) and (3.23) reduce to

$$D_i \left[\alpha(\bar{\Phi} D^i \Phi - \Phi D^i \bar{\Phi})\right] = -(V^i D_i + \alpha K)(\bar{\Phi}\eta - \Phi\bar{\eta}), \tag{3.26}$$

as well as

$$\begin{aligned} &\bar{\eta} D_i(\alpha D^i \Phi) + \eta D_i(\alpha D^i \bar{\Phi}) \\ &= -(V^i D_i + 2\alpha K)|\eta|^2 + \alpha(\bar{\eta}\Phi + \eta\bar{\Phi})\partial_{|\Phi|^2} V(|\Phi|), \end{aligned} \tag{3.27}$$

[4]Instead of making an ad-hoc choice for $\tilde{\omega}$, the total charge of the binary may be kept fixed following the approach introduced in Ref. [220] for isolated BSs. While this approach is convenient for isolated solutions with spatially constant frequency, a generalization to unequal-frequency binary BSs with a spatially dependent frequency may be challenging.

[5]Notice, these approaches are manifestly slice-dependent. Due to the scalar time-dependence, the covariant equilibrium assumptions are $\mathcal{L}_\ell[\bar{\Phi}\Phi] = 0$, and $\mathcal{L}_\ell[\bar{\Phi}\partial_\mu \Phi] = 0$. This, in general, implies $\mathcal{L}_\ell \rho \neq 0$ in the co-rotating frame.

respectively. Notice, both equations are real. In the parameterization of Sec. 3.2.2, it is natural to interpret these equations as elliptic equations for either $\eta, \bar{\eta}$ or $\Phi, \bar{\Phi}$ (keeping the respective other fixed). Here, no choice of the binary's frequency is required, since the $\tilde{\omega}$-dependence in (3.25) is canceled when adding (3.25) and its complex conjugate to arrive at (3.27). Instead, the implicit assumption is that the free data provides a sufficiently accurate profile for either the conjugate momenta or scalar field to equilibriate the binary by adjusting the other using (3.26) and (3.27). In principle, either approach could be applied to constructing spinning binary BS initial data, assuming one starts with free data that is sufficiently close to the desired solution.

Ultimately, only the direct implementation of these approaches may test their applicability in reducing spurious perturbations and equilibriating the matter in binary configurations, which we leave to future work.

3.3 Quality of binary initial data

With the formalism in place to compute constraint satisfying binary initial data, we now assess the quality of the constructed data for some specific examples. Note, we are not equilibriating the scalar matter using the ansatz discussed in the previous section. To that end, we compare the physical properties of the free data with those of the constraint-satisfying initial data in Sec. 3.3.1. We proceed in Sec. 3.3.2 by addressing the spurious excitation of oscillation modes insides the BSs of the initial data, which shows up in the emitted GW signal, by using two prescriptions to systematically remove such artifacts. Finally, in Sec. 3.3.3, we utilize the standard procedure for reducing orbital eccentricity and discuss its limitations in the context of binary BSs.

3.3.1 Superposed free data

To assess the quality of the constructed initial data, we consider a series of binary BS configurations. For now, the focus is entirely on configurations obtained with $f_{(A)} = \hat{f}_{(A)} = 1$, i.e., the case of superposed *free* data, as defined in Secs. 3.2.1 and 3.2.2. The main properties of the considered configurations are summarized in Table 3.1. For binaries $\mathcal{B}_{1,2,3}$, we analyze the impact of solving the constraint equations on the physical properties of the resulting binary BS initial data as a function of coordinate separation. To that end, in the top panels of Fig. 3.1, we compare the ADM masses M, charges Q, and angular momenta J of the constraint-satisfying data to the corresponding quantities of the binary

at infinite separation labeled $M_0 = M_1 + M_2$ and $Q_0 = Q_1 + Q_2$. The physical properties of the initial data differ from the superposed configuration at infinite separation by up to $\sim 10\%$; these differences roughly scale as $\sim 1/D_0$ with the coordinate separation D_0 of the binary. Furthermore, in the bottom left panel of Fig. 3.1, we show how much the conformal factor Ψ differs from unity. Generally, this difference is at most a few percent for reasonable separations: $\max|\Psi - 1| \lesssim 0.02$.

Since the scalar matter is not equilibriated, solving the constraint equations (3.3) in this form with superposed free data leads to spurious oscillations in the constituents of the binary. In the case of binary neutron stars, these artifacts are identified by monitoring the central density of the stars during the subsequent evolution of the initial data. Here, we proceed analogously by tracking the global maximum of the magnitude of the scalar field $\max|\Phi|$ throughout the first few oscillation periods T_0 of excited modes in the stars. Specifically, we focus on those oscillation modes of the normalized maximum on each time

Label	Coupling	m	ω/μ	C_i	S_i/M_i^2	Setup	α
$\mathcal{B}_1$	$\sigma = 0.05$	1	0.4	0.12	2.0	Axi.	0
$\mathcal{B}_2$	$\lambda/\mu^2 = 10^3$	0	0.9	0.08	0	Axi.	0
$\mathcal{B}_3$	$\sigma = 0.05$	1	$0.3, 0.35$	$0.17, 0.14$	$1.37, 1.70$	3D	$\frac{\pi}{3}$
$\mathcal{B}_4$	$\lambda/\mu^2 = 10^3$	0	$0.86, 0.9$	$0.12, 0.08$	0	3D	0
$\mathcal{B}_5$	$\sigma = 0.05$	0	0.25	0.13	0	3D	$\frac{\pi}{2}$
$\mathcal{B}_6$	$\sigma = 0.05$	1	0.3	0.17	1.37	Axi.	–

Table 3.1: The properties of the isolated constituents of the binaries used throughout the remainder of this chapter. The configurations with coupling λ are solutions in the repulsive scalar model (2.5), while those with coupling σ are stars in the scalar theory with the solitonic potential (2.2). Here, ω is the star's frequency, m is the azimuthal index, C_i is the compactness, and S_i and M_i are its individual spin angular momentum and mass, respectively. Binaries $\mathcal{B}_{1,2,5,6}$ consist of identical stars, whereas $\mathcal{B}_{3,4}$ are made of two stars with different frequencies (and hence, masses, spins, etc.). The mass-ratio of the last mentioned binaries are $q = 1.43$ and $q = 1.13$, respectively. We also consider non-zero initial complex scalar phase offsets α (as defined at the end of Sec. 3.2.2) between the two stars. In the axisymmetric setup, the stars are boosted by the Newtonian free-fall velocity at the given coordinate separation, whereas in the 3D context, the stars are initialized with quasi-circular orbital frequency and spins aligned with the orbital angular momentum; note, however, we also consider a binary with the parameters of $\mathcal{B}_3$ with misaligned spins in detail in Sec. 3.4.3.

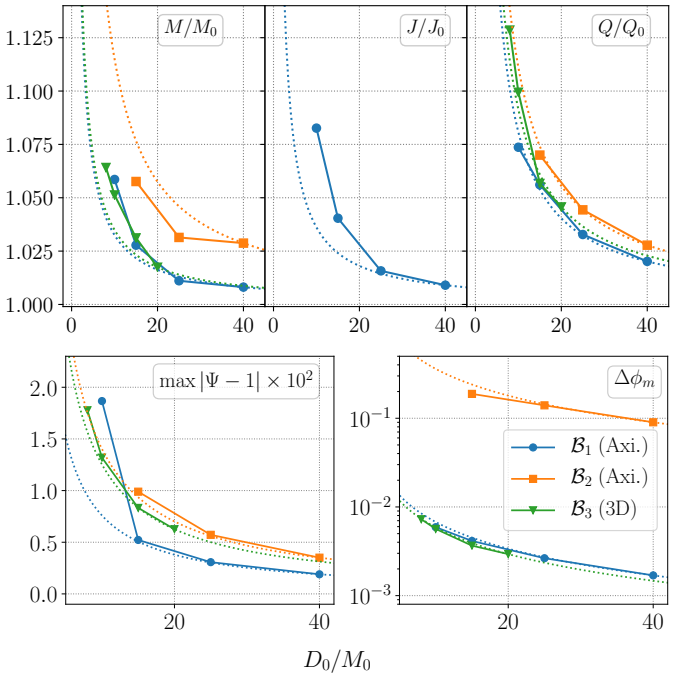

Figure 3.1: The properties of the constraint satisfying binary BS initial data as a function of coordinate separation D_0 of the stars. Here, M is the ADM mass, J the angular momentum (defined with respect to the axisymmetric Killing field), and Q the initial charge of the binary configurations with properties summarized in Table 3.1. These are compared with the corresponding quantities at infinite separation of the binary (e.g., $M_0 = M_1 + M_2$). The amplitude of the spurious oscillations in the stars emerging during the evolution of these binary initial data is defined in (3.28). Dotted lines indicate the $\propto 1/D_0$ fall-off matched to the point with the largest separations.

slice $\phi_m(t) = \max|\Phi|_t / \max|\Phi|_{t=0}$ and quantify the amplitude of these perturbations with

$$\Delta\phi_m = \frac{\max_{t\in[t_0,t_0+T_0]}\phi_m(t)}{\min_{t\in[t_0,t_0+T_0]}\phi_m(t)} - 1. \tag{3.28}$$

In the case of binaries in the repulsive scalar model, measuring $\Delta\phi_m$ with $t_0 = 0$ suffices, while for binary configurations in the solitonic scalar theory, we typically extract $\Delta\phi_m$ with $t_0 > 5T_0$ (once the binary settles into the dominant oscillation mode). We find the maximum of the gauge-dependent U(1)-charge density to track these oscillations equally well. In the bottom right panel of Fig. 3.1, we show $\Delta\phi_m$ for different binary configurations and initial separations. The amplitude of these oscillations increases with decreasing initial

binary separation. At large separations, $\Delta\phi_m \to 0$, indicating that the construction of the initial data (without assuming matter equilibrium) excites these oscillation modes. Notably, the magnitude of $\Delta\phi_m$ is much smaller in the case of binaries in the solitonic scalar model, compared with the repulsive scalar model. In the following section, we analyze spurious oscillations of this kind in more detail, and propose and test methods to help mitigate these effects.

3.3.2 Spurious Oscillations

We have seen that the naive choice for the metric and scalar free data, i.e., the superposed free data, leads to potentially significant spurious oscillations in the individual stars in the subsequent evolution of the initial data. To address this issue, it is instructive to consider possible physical mechanisms unique to scalar BSs causing these artifacts. The fundamental feature rendering the fluid star and the BS cases distinct is that the microphysical scales of the latter are *macroscopic*, leading to wave-like phenomena on scales of the star itself. Specifically, the BS can be thought of as composed of a collection of bosons with Compton wavelength $\lambda \sim 1/\mu$ satisfying $M/\lambda \sim CR/\lambda \sim \mathcal{O}(1)$, since $C \sim \mathcal{O}(0.1)$ in the relativistic regimes relevant for this chapter. Therefore, there may be distinct processes active in the context of binary BSs affecting the quality of the initial data.

Self-gravitating solitonic solutions such as BSs consist of a *single* coherent gravitationally bound state of bosons with energy[6] $\omega < \mu$. The marginally bound scenario, $\omega = \mu$, separates the bound states from unbound and *asymptotically* free states with energies $\omega > \mu$. Stationary isolated BSs are solutions with bosons of energy ω precisely in equilibrium with the gravitational field. However, perturbations introduced by superposing two stationary BSs and solving the Hamiltonian and momentum constraints based on such non-equilibriated free data disrupts this balance. Perturbations may elevate some fraction of the bound bosons of energy ω to *(i)* completely free states (dispersing away from the binary), *(ii)* states that are gravitationally bound to the binary (as opposed to one of the constituents); analogous to a wave dark matter halo with solitonic core (see, e.g., Ref. [204]), or *(iii)* states gravitationally bound to a single star, but with energy ω that is not at equilibrium with the gravitational sector. All these processes are, in principle, able to excite oscillation modes inside the star, as well as contaminate the GW signal at early times in a numerical evolution. Note, non-linear scalar self-interactions may also disturb equilibrium configurations. However, since since we mainly focus on high compact stars with $\omega \ll \mu$, these effects are suppressed (see, e.g., Ref. [340]).

[6]Note, here and in the following, we use boson "energy" and "frequency" interchangeably, implicitly setting $\hbar = 1$.

With these possible sources in mind, in the following we explore several prescriptions for reducing spurious oscillations in binary BSs. We first outline methods commonly used in the context of binary black hole and neutron star initial data and discuss their effectiveness in the BS context, before introducing and validating several methods specific to BSs.

Modified superposition

We begin by returning to the largest spurious oscillations in the bottom right panel of Fig. 3.1, i.e., those in the head-on collisions of non-rotating stars in the repulsive scalar model. As we demonstrate below, some of these spurious oscillation artifacts can be removed by choices of the attenuation functions $f_{(A)}$ and $\hat{f}_{(A)}$, introduced in Secs. 3.2.1 and 3.2.2, respectively. In the case of binary black hole or neutron star initial data, it is common practice to remove the metric variables of one star at the location of the other (analogous to approaches introduced in Refs. [251, 250, 72]), achieved by non-trivial attenuation functions $f_{(A)}$. This can reduce the effect of the superposition on the individual stars. In order to remove the metric and scalar free data due to one of the stars at the coordinate location of the other, we choose

$$f_{(1)}(\mathbf{x}) = 1 - \exp\left[-\frac{|\mathbf{x}-\mathbf{z}_{(2)}|^{\gamma}}{\sigma_{(1)}^{\gamma}}\right], \tag{3.29}$$

and the corresponding $(1) \leftrightarrow (2)$, as well as scalar attenuation functions $\hat{f}_{(A)}$ with associated length scales $\hat{\sigma}_{(A)}$. Here, $\mathbf{z}_{(2)}$ is the initial coordinate position of the second star (as defined in Sec. 3.2.1), whereas the length scales $\sigma_{(A)}$ and $\hat{\sigma}_{(A)}$ set the size of the attenuation region around each of the constituents of the binary. We consider $\gamma = 2$ and 4.

We find this approach to be effective in reducing spurious oscillations, as measured by $\Delta\phi_m$, only for BS solutions in the repulsive scalar model (2.5). In fact, applying this approach to stars in the solitonic models *worsens* the artificial oscillations, requiring a different prescription to handle the latter, as described in detail in the next section. In the left panels of Fig. 3.2, we show the time-dependence of the maximum of the scalar field magnitude, as well as the dependence of the amplitude of the spurious oscillations on the lengthscales associated with the attenuation function introduced in Eq. (3.29). As can be seen from the figure, increasing the attenuation length scales (at fixed separation), decreases the amplitude $\Delta\phi_m$. Around $\sigma_{(A)}/D_0 \approx 0.5$, the spurious oscillations are minimal, and increase in amplitude for $\sigma_{(A)}/D_0 \gtrsim 0.5$. Therefore, we find that in all cases considered, tuning the length scales relevant in (3.29) results in binary BS initial data with significantly

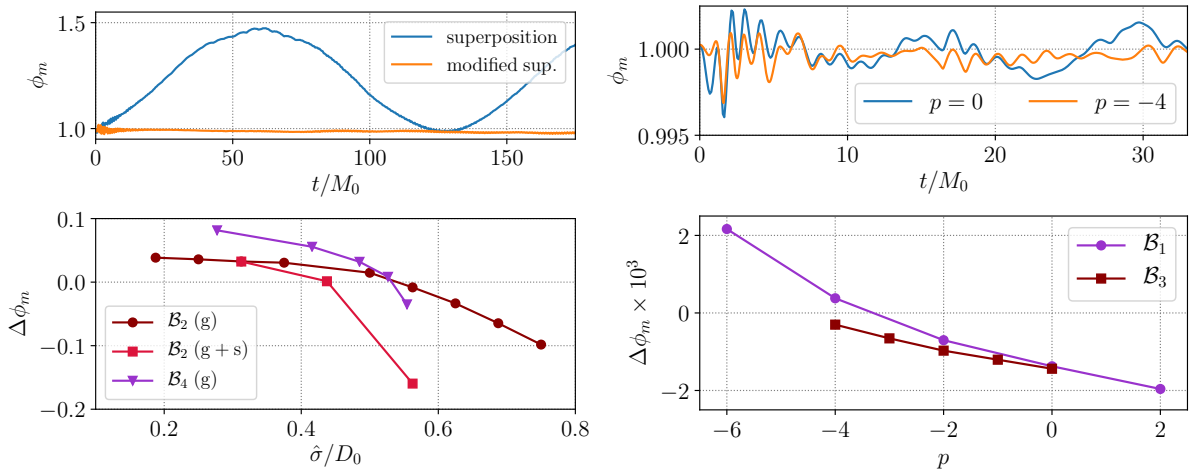

Figure 3.2: We show the temporal evolution of the normalized maximum on each time slice $\phi_m = \max|\Phi|/\max|\Phi|_{t=0}$ and amplitude of the perturbations $\Delta\phi_m$, defined in (3.28), for selected binary BS configurations. In all cases shown here, the exponent γ, defined in (3.29), is set to $\gamma = 2$. *(left top)* The behavior of the maximum ϕ_m during the evolution of the binary $\mathcal{B}_4$ (see Table 3.1) with initial coordinate separation $D_0 = 20M_0$, constructed with $f_{(A)} = \hat{f}_{(A)} = 1$ (labeled "superposition") contrasted with the case, where $\sigma_{(A)}/D_0 = 0.52$ and $\hat{\sigma}_{(A)} = 0$ (labeled "modified sup."). *(left bottom)* The amplitude $\Delta\phi_m$ of the spurious oscillations as functions of the lengthscale $\hat{\sigma}$. Cases indicated with "(g)" correspond to only metric attenuation, $\hat{\sigma}_{(A)} = 0$ and $\hat{\sigma} = \sigma_{(A)}$, while for those labeled "(g+s)" both the metric and scalar degrees of freedom are attenuated $\hat{\sigma} = \hat{\sigma}_{(A)} = \sigma_{(A)}$. The binary $\mathcal{B}_2$ has initial coordinate separation $D_0 = 40M_0$. *(top right)* The behavior of the maximum ϕ_m during the evolution of the binary $\mathcal{B}_3$ (see Table 3.1) with initial coordinate separation $D_0 = 12M_0$ (constructed with $f_{(A)} = \hat{f}_{(A)} = 1$) and rescaling the conformal kinetic energy in (3.30) with $p = 0$ as well as $p = -4$. *(bottom right)* We show the amplitude $\Delta\phi_m$ of spurious oscillations emerging during the evolution of binaries $\mathcal{B}_{1,3}$ with initial coordinate separations $D_0 = 40M_0$ and $D_0 = 12M_0$, respectively. For the latter, we were unable to construct binary BS initial data with $p < -4$.

reduced spurious oscillations. Finally, considering $\gamma = 4$ (as opposed to $\gamma = 2$) results in no qualitative difference to the behavior shown in left panels of Fig. 3.2.

Besides improving the binary BS initial data by removing spurious oscillations, this modified superposition approach turns out to be *necessary* in the case of highly compact binary inspirals at moderate separations within the repulsive scalar model (2.5). Specifically, we focus on a binary BS with $\omega_1 = \omega_2 = 0.86\mu$, at initial coordinate separation

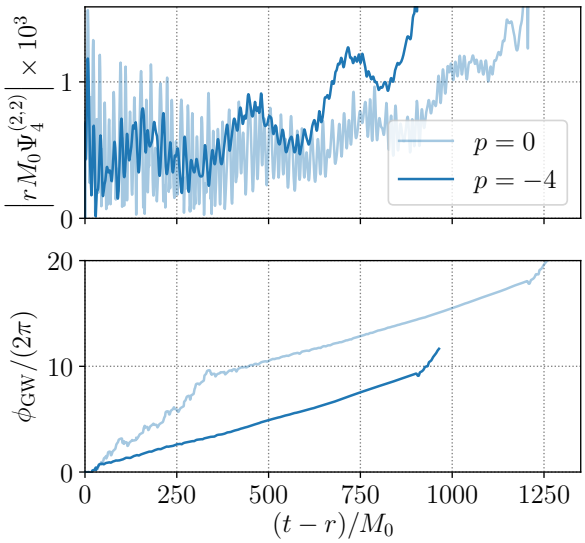

Figure 3.3: The GW amplitude *(top)* and phase *(bottom)* emitted by the (aligned-spin) binary $\mathcal{B}_3$ with initial separation $D_0 = 12M_0$. The two curves correspond to the evolution of initial data constructed using $p = 0$ or $p = -4$ in (3.30). Specifically, the GW phase $\phi_{\rm GW}$ is the complex phase of the Newman-Penrose scalar Ψ_4, whereas the GW amplitude is the magnitude of the projection of Ψ_4 onto the $(\ell, m) = (2, 2)$ mode of $s = -2$ spin-weighted spherical harmonics on a coordinate sphere at radius $r = 100M_0$. Note, the binary orbits are eccentric with eccentricity $e \approx 0.1$, resulting in modulations with period $\approx 250M_0$ as is most striking in the top panel (eccentricity reduction is discussed separately in Sec. 3.3.3).

$D_0/M_0 = 20$ and quasi-circular boost velocities. For this, we find that superposed free data, i.e., with $f_{(A)} = \hat{f}_{(A)} = 1$, results in premature collapse of each individual star to a black hole after $\approx 50M_0$. In contrast, with $\sigma_{(A)} = D_0/2$, the individual stars remain stable throughout the inspiral of length $\sim \mathcal{O}(10^3)M_0$ up to the point of contact. On the other hand, in Ref. [340], we found the simple choice $f_{(A)} = \hat{f}_{(A)} = 1$ to be sufficient to successfully evolve the binary with $\omega_1 = \omega_2 = 0.9\mu$ in the same family of solutions; hence, the attenuation is necessary for more relativistic BS solutions. Note, similar premature collapse was observed in Ref. [187].

Conformally rescaled kinetic energy

As alluded to above, we find attenuating the metric and scalar free data to only be beneficial in binary BSs in the repulsive scalar theory. For the solitonic case, we return to the notion

of energy levels determined by the frequency ω of the scalar bound state. In the context of the scalar variables, this frequency is set by $\dot{\Phi}$, which enters the kinetic energy $\sim |\eta|^2$ according to (3.11). For instance, for isolated BSs $\dot{\Phi} = i\omega\Phi$, and similarly $\eta \sim (\omega - m\Omega/r)\Phi$ (in the coordinates introduced in Sec. 2.2). To reduce the impact of the superposition on the BSs, as discussed in Sec. 3.3.2, we modify the kinetic energy of the scalar field[7]. The kinetic energy combines changes in the frequencies of the individual stars with changes in the local linear and angular momentum due to the orbital motion and the star's intrinsic spin. As such, increasing or decreasing the kinetic energy locally self-consistently within the CTS setup may help address spurious oscillations. To incorporate this in our initial data construction scheme discussed in Sec. 3.2.2, we rescale the physical conjugate moment η by an additional power p of the conformal factor:

$$\eta = \Psi^{-6-p}\tilde{\eta}. \tag{3.30}$$

In the right panel of Fig. 3.2, we illustrate the impact of the choice (3.30) for different p on the spurious oscillations in the individual stars of two types of binaries in the solitonic scalar model (in all binary BSs in the repulsive scalar model, we set $p = 0$). In the axisymmetric binary labelled $\mathcal{B}_1$, we find that the amplitude of the spurious oscillations can be minimized by adjusting the exponent p. In this case, a rescaling (3.30) with $-4 < p < -3$ minimizes the spurious oscillations measured by $\Delta\phi_m$. These oscillations can be addressed also in the case of the inspiraling binary $\mathcal{B}_3$; however, our numerical implementation robustly relaxes into a solution to the constraint equations only for $p \geq -4$. The oscillation amplitude is still decreasing with decreasing p for $p = -4$, and this leaves a residual oscillation amplitude roughly a factor of 5 smaller compared with the $p = 0$ initial data. While the spurious oscillation amplitude of all binaries in the solitonic scalar model considered is small, i.e., $|\Delta\phi_m| \sim 10^{-3}$, there is a correlation between reducing these small artifacts and removing a high-frequency contamination from the emitted gravitational waveform.

In Fig. 3.3, we show the GW amplitude and phase extracted from the binary evolution of $\mathcal{B}_3$ constructed using (3.30) with $p = 0$. We contrast this with the signal extracted from the same binary, but with initial data constructed using $p = -4$. Similar to the amplitude of the spurious oscillations described above, the high-frequency and large amplitude contamination of GWs at early times changes with the exponent p. As the period of the high-frequency contamination matches the period of the spurious oscillations in Fig. 3.2, we identify the latter as a source of the GW contamination. Therefore, the adjustment of the kinetic energy by the conformal rescaling (3.30) aids in reducing GW contamination. However, as for the spurious oscillations, the trend of the magnitude of this contamination with

[7]Note, in principle, one could modify $\dot{\Phi}$ iteratively, even when working with the parameterization of Sec. 3.2.2.

decreasing exponents $p < 0$ suggests that if initial data with $p < -4$ could be constructed, the contamination would be further inhibited. In this case, we find that the amplitude of the contamination is reduced by roughly a factor of 2 compared with the canonical choice $p = 0$. Additionally, the evolution of the GW phase shown in Fig. 3.3 indicates that in the $p = 0$ case the amplitude is dominated by the high-frequency contamination, while in the $p = -4$ case, the phase evolution is determined primarily by the binary orbit, as opposed to spurious oscillations. Finally, the choice (3.30) with $p < 0$, i.e., adjusted kinetic energy of the binary system, results in a shorter time-to-merger at fixed orbital parameters.

3.3.3 Eccentricity reduction

The flexibility of our approach to constructing the initial data allows us to, in principle, find constraint satisfying binary BS data resulting in any orbital configuration. Of particular interest in the case of compact binary inspirals are low-eccentricity orbits. Hence, in a last step to improve the quality of our binary BS initial data, we turn to applying common techniques to reduce the eccentricity of compact binary initial data to the binary BSs constructed here. To that end, we first define a notion of the BS coordinate location valid throughout the evolution, we then briefly review the eccentricity reduction methods introduced in Refs. [295, 76, 266], and finally, we apply these methods to selected spinning and non-spinning binary BSs.

To define the coordinate positions of the two BSs during a binary evolution, we employ a two-step procedure: first, a rough estimate of the star's position restricted to the initial equatorial plane is obtained by finding the coordinate locations of the local maxima of $|\Phi|$ for spherically symmetric stars, and local minima in the case of rotating BSs associated with each star (i.e., the intersection of the star's vortex lines and the equatorial plane). In a second step, the center of scalar field magnitude within a coordinate sphere B_A centered on the previously determined locations of extrema enclosing star A,

$$z^i_{(A)}(t) = \int_{B_A} d^3x |\Phi(t, \mathbf{x})| x^i, \tag{3.31}$$

is used as the coordinate position at the given coordinate time t[8]. The coordinate separation $d(t)$ of the binary is then simply $d(t) = |\mathbf{z}_{(1)}(t) - \mathbf{z}_{(2)}(t)|$. Note, the first step is sufficient for stars in the repulsive scalar potential (2.5), as the locations of the extrema are less prone to contamination by spurious oscillations within the stars. In the case of BSs in the solitonic

[8]Note, in the initial timeslice $z^i_{(A)}(0)$ agrees with the coordinate positions $z^i_{(A)}$ defined in Sec. 3.2.1 to a large degree; hence, we neglect any potential difference between the two in the following.

models, however, we find the second step to be crucial particularly for non-spinning stars, as $|\Phi|$ is roughly constant inside each star. In the remainder of this chapter, we use (3.31) to define the BS position.

The general procedure to reduce eccentricity, following Ref. [295], is to begin with a set of binary initial data, evolve these for a sufficiently long time to be able to confidently fit for the binary's orbital parameters, and then compute a correction to the initial radial velocity and orbital frequency to construct new initial data with lower eccentricity. This process is repeated until the desired eccentricity is reached. Specifically, we fit for the binary BS coordinate separation $d(t)$ using

$$\hat{d}(t) = A_{-1} + A_0 t + \frac{A_1}{2} t^2 + \frac{B}{\omega} \sin(\omega t + \varphi), \tag{3.32}$$

and correspondingly for the binary's radial velocity using the fit

$$\hat{v}_r(t) = A_0 + A_1 t + B \cos(\omega t + \varphi). \tag{3.33}$$

Based on this parameterization, the initial orbital frequency Ω_0 and initial radial velocity v_r are corrected by [295]

$$\begin{aligned} \Omega_0 &\to \Omega_0 + \frac{B\omega \sin(\varphi)}{2\Omega_0 d_0}, \\ v_r &\to v_r - B\cos(\varphi), \end{aligned} \tag{3.34}$$

at each eccentricity iteration step, where $d_0 = A_{-1}$[9]. Working entirely in flat space, in order to translate these orbital parameters to the initial coordinate positions $z^i_{(1)}$, $z^i_{(2)}$ and velocities $v^i_{(1)}$, $v^i_{(2)}$ of the binary constituents, as defined in Sec. 3.2.1, we utilize the Newtonian center-of-mass expressions

$$z^i_{(1)} = r^i \frac{M_2}{M_0}, \qquad z^i_{(2)} = -r^i \frac{M_1}{M_0}. \tag{3.35}$$

Here, r^i is the binary separation with $v^i = \dot{r}^i$, and the corresponding velocities $v^i_{(1)}$ and $v^i_{(2)}$ are given by the time derivatives of the above expressions. We decompose the center of mass velocity v^i into radial v_r and tangential v_t components as $v^i = v_r n^i + v_t \lambda^i$, where $n^i = r^i/r$ and $\lambda^i = \dot{n}^i$. The initial tangential component of the center-of-mass velocity is set by the initial orbital velocity as well as initial coordinate separation d_0 using $v_t = \Omega_0 d_0$.

[9] Note, in general $d_0 \neq D_0$, as we show below explicitly.

The constituents velocities are then reconstructed from v^i utilizing the time derivative of the expressions (3.35). In this context, the orbital eccentricity is defined to be

$$e = \frac{B}{\omega d_0}. \tag{3.36}$$

The formulas (3.34) are based only on Newtonian gravity, with radiation reaction and other general relativistic corrections assumed to be absorbed into the linear and quadratic time dependence in (3.32); we note that BSs will also have scalar interactions that become important during the late inspiral [340], particularly for stars with small compactness and $\omega \approx \mu$, which may introduce extra complications in performing eccentricity in this way at small separations.

Applying this machinery to binary BSs, we find that spurious oscillations of the stars and non-equilibriated scalar matter result in high-frequency oscillations of the coordinate separation $d(t)$, limiting the eccentricity reduction. Below eccentricities of $e \sim 10^{-2}$, the fit $\hat{v}_r(t)$ is too uncertain to confidently extract estimates for the subsequent iteration step. Instead, in these cases, we resort to using (3.32) to determine the corrections (3.34). For $e \lesssim 10^{-3}$, the amplitude of the modulation of d due to residual eccentricity reaches the amplitude of the oscillations in d introduced by these spurious oscillations. Therefore, even the fit $\hat{d}(t)$ to the coordinate separation d becomes uncertain, and we terminate eccentricity reduction at $e \gtrsim 10^{-3}$. Furthermore, it is, of course, crucial to minimize oscillations of the stars using the methods discussed in Sec. 3.3.2, i.e., find the exponent p of (3.30) and length scales $\{\sigma_{(A)}, \hat{\sigma}_{(A)}\}$ in (3.29), before attempting to reduce the eccentricity. Especially the choice of (3.30) alters the matter's kinetic energy and linear momentum, and hence, the orbital frequency and radial velocities.

In Fig. 3.4, we show the orbital parameters throughout the iterative reduction of the orbital eccentricity for two example binaries. In the case of the spinning and unequal-mass binary $\mathcal{B}_3$, the eccentricity decreases exponentially with the iteration step N_e down to $e \sim 10^{-3}$, where the fitting approach of (3.32) becomes unreliable. In the case of the non-spinning and equal-mass binary $\mathcal{B}_5$, however, the eccentricity decreases only slowly with each iteration step. Consulting the top panel of Fig. 3.4, the first iteration step for $\mathcal{B}_5$ resulted in a positive radial velocity. While v_r is a coordinate quantity, and hence, carries limited physical meaning, in binary black hole and neutron star initial data constructions, this is found to consistently satisfy $v_r < 0$. Both may be due to fitting to the $d(t)$ time series before all spurious perturbations of the initial data have decayed away sufficiently (e.g., fits of the $N_e = 1$ iteration contained only roughly 3/2 orbits), beyond which we cannot isolate a cause of the slow convergence of e for $\mathcal{B}_5$. Finally, in the case of the precessing $\mathcal{B}_3$ (details can be found in Sec. 3.4.3), we perform only a single iteration step and find

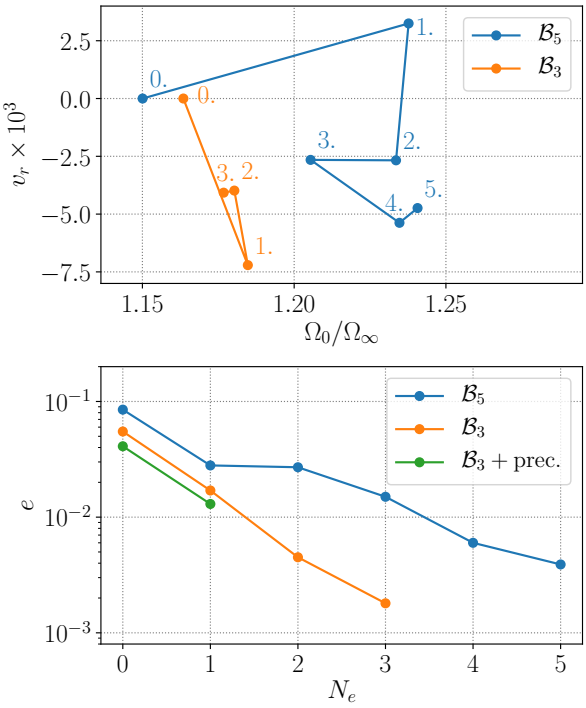

Figure 3.4: *(top panel)* The initial radial velocity component v_r and orbital angular frequency Ω_0 of the binary BS initial data corresponding to $\mathcal{B}_3$ and $\mathcal{B}_5$ (see Table 3.1), throughout the eccentricity reduction procedure, starting from iteration step 0. Here, $\Omega_\infty = (D_0^3/M_0)^{1/2}$. *(bottom panel)* The associated eccentricity, defined in (3.36), as a function of iteration step N_e. We only perform a single iteration step for the $\mathcal{B}_3$ binary with misaligned spins (this case is discussed further in Sec. 3.4.3).

similar convergence behavior as for the aligned-spin binary $\mathcal{B}_3$. Note, in precessing cases the spin-interactions (particularly for super-spinning compact objects as considered in $\mathcal{B}_3$) induce physical oscillations of the binary separation beyond residual eccentricity (see, e.g., Ref. [86]), which we, however, have not observed here. Lastly, in Appendix B.3, we discuss the linear motion of the center of mass away from the center of the numerical grid, and how to iteratively reduce this artifact, while simultaneously reducing eccentricity.

3.4 Binary evolutions

In this section, we illustrate our method for constructing binary BS initial data in the context of head-on collisions and quasi-circular inspirals, including a precessing system. In the case of head-on collisions, we demonstrate explicitly that equal-mass rotating binary BSs exhibit solitonic behavior (resembling the dynamics found in Ref. [281]), bouncing off each other when colliding along their spin axes, if the phase offset between the stars is precisely π. Furthermore, we consider two eccentricity-reduced, quasi-circular inspiraling binary BSs: one non-spinning equal-mass binary, and one super-spinning unequal-mass configuration. We analyze their inspiral dynamics, show that non-trivial scalar interactions result in strong deviations from the dynamics of binary black holes or neutron stars (analogous to what was found in Ref. [340]), and characterize the GW strain. Finally, we consider a super-spinning, precessing binary BS inspiral at moderately low eccentricity, analyze the merger dynamics, and show the resulting gravitational waveform.

3.4.1 Head-on collisions

In this section, we explore the merger dynamics of two rotating BSs during a head-on collision along their respective spin axes, focusing on the $\sigma = 0.05$ solitonic scalar model (2.2) and binaries composed of $m = 1$ rotating BSs. It is important to note that, in this setting, we evolve the binary BSs using a generalized Cartoon method, which explicitly assumes the scalar fields azimuthal dependence follows $\Phi \sim e^{im\varphi}$, in addition to an axisymmetric metric (see Appendix B.1 for details). As a result, any modes violating this condition will not appear in the evolution. In particular, this implies *(i)* any non-axisymmetric instability of the form found in Ref. [323] is suppressed, and *(ii)* the vortex structure of the solution on the symmetry axis is conserved throughout the evolution.

We begin by considering the predictions of the remnant map introduced in Ref. [340] for these head-on collisions. We do not repeat the details of the construction of the remnant map here (which are found in Ref. [340]), and simply summarize the key features in the context of the head-on collision of two $m = 1$ BSs. This map assumes U(1)-charge conservation ($Q_{\rm rem} = Q_1 + Q_2$) during the merger of two BSs to predict the qualitative and quantitative features of the merger remnant. In order to use the remnant map, one must provide a plausible candidate family of remnants. Due to our evolution methods, any binary composed of two $m = 1$ stars results in a remnant with $m = 1$ vortex along the symmetry axis. Therefore, it is natural to consider that the remnant of the two rotating BSs is another rotating BS of the same vortex index (unless the combined charge of the

binary surpasses the maximum charge of the family of $m = 1$ BSs in this scalar model, in which case the remnant is likely a black hole). In our axisymmetric setup, any known linear instability of the rotating BSs in the $\sigma = 0.05$ solitonic scalar model is suppressed, implying that this condition allows the merger remnant to be a $m = 1$ BS. Hence, we can map all properties of any given $m = 1$ binary BS, parameterized by their frequencies ω_1 and ω_2, into the properties of the resulting $m = 1$ BS assuming charge conservation. In particular, in order to consider the kinematics of the merger—and whether this favors the formation of a $m = 1$ BS remnant—we define the relative mass difference [340]

$$\mathcal{M} = \frac{M_1 + M_2 - M_{\rm rem}}{M_1 + M_2}. \tag{3.37}$$

Here, M_1 and M_2 are the masses of the individual stars, while $M_{\rm rem}$ is the mass of the rotating BS with charge $Q_{\rm rot} = Q_1 + Q_2$ obtained form the remnant map. If a binary configuration has $\mathcal{M} > 0$, then the formation of that $m = 1$ BS remnant of mass $M_{\rm rem}$ is energetically favorable. In Fig. 3.5, we show the relative mass difference $\mathcal{M}$ across the relevant binary BS parameter space. For all binary configurations shown, it is indeed energetically favorable to form a $m = 1$ rotating BS remnant after merger. Hence, the remnant map predicts the merger remnant to be a $m = 1$ rotating BS remnant. Note, if the initial phase offset α between the stars is exactly $\alpha = \pi$, then the remnant is not a (parity-even) $m = 1$ rotating BS, but rather a double rotating $m = 1$ star (i.e., a single, parity-odd rotating star), as we discuss in detail below.

To test this prediction, we perform a series of numerical evolutions of binary BSs in the axisymmetric setting described above. The initial data is constructed as discussed in the previous sections, where for simplicity, the conformal rescaling power in (3.30) is set to $p = 0$, and no modification of the form give in (3.29) is applied. The initial velocities are chosen based on the Newtonian free-fall velocity from rest at infinity, and the binary separation is chosen to be $D_0 = 10M_0$ initially. Finally, here the phase offset α (defined at the end of Sec. 3.2.2) between the phases of the rotating stars is set to vanish, $\alpha = 0$. (We consider scenarios varying the value of α below.) For each of the evolutions, we classify the remnants as either BSs ($m = 1$ rotating BSs) or spinning black holes. In Fig. 3.5, we show the binary configurations we numerically evolve, and indicate the remnant type. First, in the case of equal-mass binaries, i.e., those with $\omega_1 = \omega_2$, the remnant is consistent with the prediction of the remnant map, except for the case with $\omega_1 = \omega_2 = 0.2\mu$. In this case, and all other cases indicated as "BH" in Fig. 3.5, the merger product collapses to a black hole during the nonlinear merger process. The fact that the threshold for black hole formation is slightly lower than predicted by the remnant map is likely due to the extra compression and kinetic energy due to the collision. This explicitly demonstrates

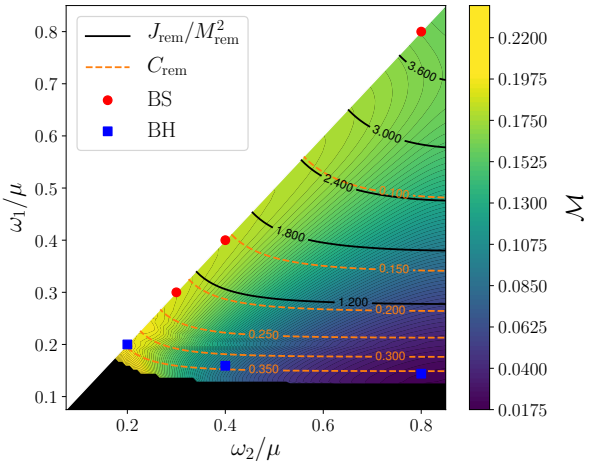

Figure 3.5: The remnant properties of a $m_1 = m_2 = 1$ spinning binary BS head-on collision (with frequencies ω_1 and ω_2) in the $\sigma = 0.05$ solitonic scalar model (2.2), assuming the remnant is a $m = 1$ rotating BS and using the remnant map of Ref. [340] (i.e., assuming U(1)-charge conservation to predict the remnants properties for each given binary configuration). The dimensionless angular momentum $J_{\rm rem}/M_{\rm rem}^2$ and the associated remnant compactness $C_{\rm rem}$ are shown as contours. The mass ratio $\mathcal{M}$ is defined in (3.37). We restrict to the $\omega_2 > \omega_1$ portion without loss of generality, and indicate the regions with $Q_{\rm rem} > Q_{\rm max}$, where $Q_{\rm max}$ is the maximum charge of the $m = 1$ family of BSs, in black. Finally, we classify the merger remnants into black holes ("BH") and $m = 1$ rotating BSs ("BS"), and mark the binary that gave rise to the respective remnant with dots. [Notice, the central (left) "BS" corresponds to binary $\mathcal{B}_1$ ($\mathcal{B}_6$), see Table 3.1.]

that the final remnant of the head-on collision of two rotating BSs along their mutual vortex line results in another rotating BS of the same vortex number (or a black hole if the individual stars are sufficiently compact). In Ref. [274], a similar analysis was performed in the Newtonian limit dropping all symmetry assumptions. Since they find that the central vortex line persists throughout the merger, their results are consistent with our findings here, and suggest that the latter generalize to 3D if linear instabilities are absent in both the merging BSs and the remnant BS.

Let us now return to considering head-on collisions of two $m = 1$ rotating binary BS configurations while varying the initial phase offset α. We perform a series of evolutions of the binary configuration $\mathcal{B}_6$ (with initial separation of $D = 10M_0$ and Newtonian free-fall velocities, as before), with initial phase offsets of $\alpha/\pi \in \{1/4, 1/2, 3/4, 8/9, 1\}$. Notice, the $\alpha = 0$ case was found to result in a rotating $m = 1$ BS as indicated in Fig. 3.5. In

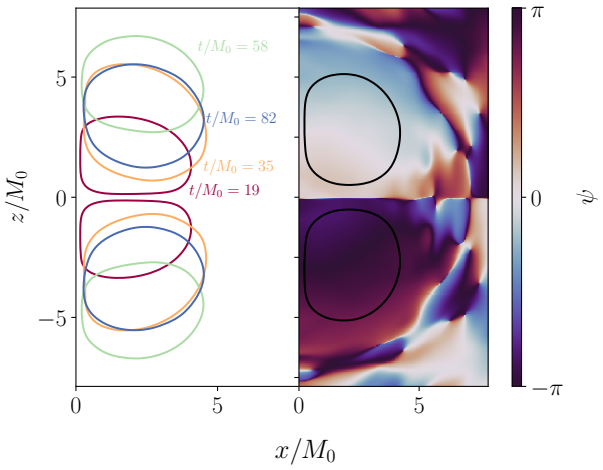

Figure 3.6: We show scalar field quantities on axial slices for the head-on collision of binary $\mathcal{B}_6$ with initial phase-offset of $\alpha = \pi$. The z-axis is the spin-axis and $z = 0$ corresponds to the center of mass of the system. *(left)* Surfaces of constant scalar field magnitude at various times during the head-on collision. *(right)* The solution after it has relaxed at late times ($t/M_0 = 856$). The black contour line indicates the surfaces of constant scalar field magnitude, while the color indicates the phase ψ of the scalar field. This end state resembles the parity-odd stationary double-BS solutions found in Refs. [221, 164].

Fig. 3.6, we show snapshots of the head-on collision of the binary with maximal phase offset, i.e., $\alpha = \pi$. As evident there, contrary to the expectation from the $\alpha = 0$ scenario, the two stars bounce off each other upon contact. After several bounces, the system settles into a state of two spatially separated scalar distributions with a persistent phase offset of π, as shown in the right panel of Fig. 3.6. The end state of this merger is plausibly a stationary solution analogous to those found in Refs. [221, 164]. These are parity-odd solutions resembling two rotating BSs, where gravitational attraction is balanced by scalar interactions. Physically, this solitonic behavior resembles the dynamics during the head-on collision of two *non-spinning* BSs with phase offset $\alpha = \pi$ reported in Ref. [281] (and associated stationary solutions of Ref. [375]).

Moving to the cases with $\alpha/\pi \neq 1$, we find that the remnant of the corresponding head-on collision is always a single $m = 1$ rotating BS at late times. In the case of $\alpha/\pi = 8/9$, the system performs a single bounce upon collision, but then merges to a perturbed rotating BS. This demonstrates that, similar to the head-on collision scenario of two non-spinning stars, only the $\alpha = \pi$ configuration exhibits a final state different from a $m = 1$ rotating BS. This, of course, limits the validity of the remnant map to those cases

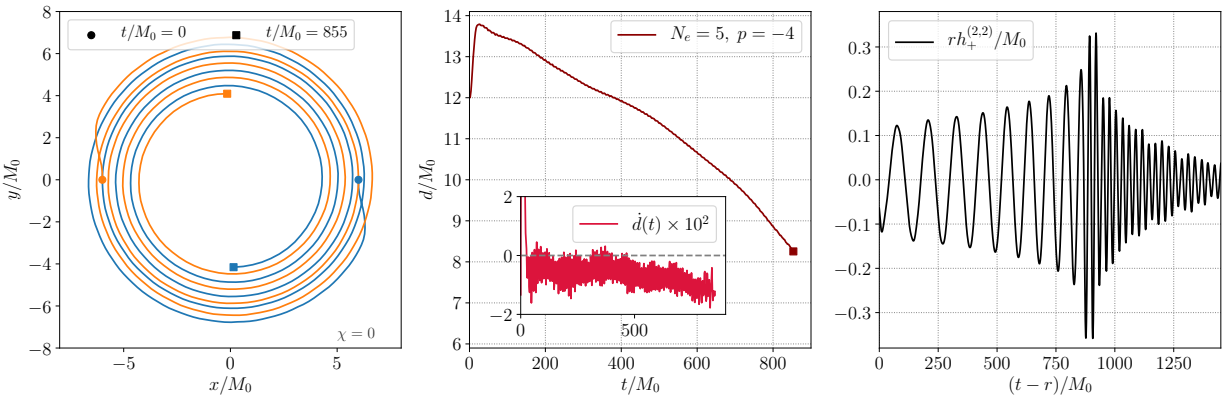

Figure 3.7: Trajectories and GWs from a quasi-circular binary BS mergers: an equal-mass, non-spinning binary labelled $\mathcal{B}_5$ (The binary properties are summarized in Table 3.1.) We show the BS trajectory in the orbital plane [defined according to (3.31)] throughout the evolution up to the point of contact *(left panel)*, the binary coordinate separation d as a function of time *(center panel)*, and the emitted $(\ell, m) = (2, 2)$ $s = -2$-weighted spherical harmonic component of the GW strain $h_+^{(2,2)}$ *(right panel)*. In the left and center panels, we indicate the initial time (round markers) and the time of contact (square markers). The dimensionless spins, χ, of the binary constituents can be found in the bottom right corners of the left panel. The legends in the center panels indicate the eccentricity reduction step N_e and the rescaling exponent p used in (3.30). After eccentricity reduction, $e \approx 4 \times 10^{-3}$ initially. In the center panel, we also show the time derivative of the separation d in the inset. Notice, the GW strain (right panel) contains residual high-frequency contamination as discussed in Sec. 3.3.2; this contamination is shown in detail in Appendix B.2. At the point of contact of the two stars, the GW frequency is roughly $\omega_c M_0 \approx 0.1$. For the post-merger phase, we estimate the dominant frequency and exponential decay timescale of $h_+^{(2,2)}$ to be $\omega_{\rm post} M_0 \approx 0.23$ and $\tau_{\rm post}/M_0 \approx 3 \times 10^2$, respectively.

with $\alpha/\pi \neq 1$; however, as this is an edge case (similar to two non-spinning stars with phase-offset of $\alpha = \pi$), the impact on the applicability of the remnant map even in these head-on scenarios is minimal.

3.4.2 Quasi-circular binaries

We return now to the eccentricity-reduced binary configurations discussed in Sec. 3.3.3, and provide further details on their orbital evolution as well as GW emission. In particular,

we consider the equal-mass, non-spinning binary $\mathcal{B}_5$, and the aligned-spin super-spinning binary $\mathcal{B}_3$ of mass-ratio $q = 1.43$ with details provided in Table 3.1. In both cases, we focus mainly on the last eccentricity-reduction iteration step shown in Fig. 3.4 (i.e., $N_e = 5$ and $N_e = 3$ for the non-spinning and spinning binaries, respectively) with eccentricity $e = 4 \times 10^{-3}$ in the case of $\mathcal{B}_5$ and $e = 1.8 \times 10^{-3}$ in case of the non-precessing binary $\mathcal{B}_3$. In Fig. 3.7 and Fig. 3.8, we show the orbital trajectories, binary separations and radial velocities, as well as the emitted GW strain for both configurations.

First, let us focus on the eccentricity reduced binary $\mathcal{B}_5$ (see Fig. 3.7). After initial gauge dynamics (we utilize damped harmonic gauge and the generalized harmonic formulation, see Appendix B.1 for details), the binary settles into a state with roughly 17% large coordinate separation of $d/M_0 \approx 14$. As can be seen from the center panel of Fig. 3.7, the time derivative $\dot{d}$ of the coordinate separation exhibits large, high-frequency features throughout the inspiral. These are likely a result of the residual low-amplitude perturbations of each star; the relative amplitude of the oscillations in this case is at the $\Delta\phi_m \sim 10^{-3}$ level. Clearly, further eccentricity reduction cannot rely on a fit to $\dot{d}$, but even a fit to d proves to be challenging at these eccentricities. Nonetheless, the inspiral dynamics follows a quasi-circular trajectory up to the point of contact, at a coordinate separation of roughly twice the star's radii: $d \approx 2R$. As the compactness of each star is $C = 0.13$, we expect qualitative similarities to the inspiral of a binary neutron star. After the point of contact at $t/M_0 = 855$, the two non-spinning stars merge into another *non-spinning* star. As shown in detail in Ref. [340], the binary $\mathcal{B}_5$ favors the formation of a $m = 1$ rotating remnant BS on purely energetic grounds. However, it lacks sufficient total angular momentum, and with a phase offset of $\alpha/\pi = 1/2$, is not expected to form a rotating BS remnant, but instead a non-rotating star, with the residual angular momentum shed in the form of scalar and gravitational radiation. Hence, after merger, the system rings down towards a single, non-spinning BS. This is reflected in the GW strain (right panel of Fig. 3.7), which exhibits a near exponential decay in the post-merger phase with a rough decay timescale of $\tau_{\rm post}/M_0 = 3 \times 10^2$ and a dominant ringdown frequency of $\omega_{\rm post} M_0 = 0.23$. It should be noted that, though not obvious from the figure, the GW strain shown in Fig. 3.7 and Figure 3.8 does contain some residual high-frequency GW contamination of the kind discussed in detail in Sec. 3.3.2. This is made more apparent in Appendix B.2.

We now turn to the inspiral of the binary $\mathcal{B}_3$ shown in Fig. 3.8, which exhibits several new features fundamentally different from either binary black hole or neutrons star coalescences. After the initial gauge dynamics, the system has a coordinate separation of roughly $d/M_0 \approx 14$. Before $t/M_0 = 1475$ (indicated in the figure with an x-marker), the binary exhibits a smooth inspiral with decreasing separation. In the center panel of Fig. 3.8, we compare the coordinate distance as functions of time to those cases with no eccentricity

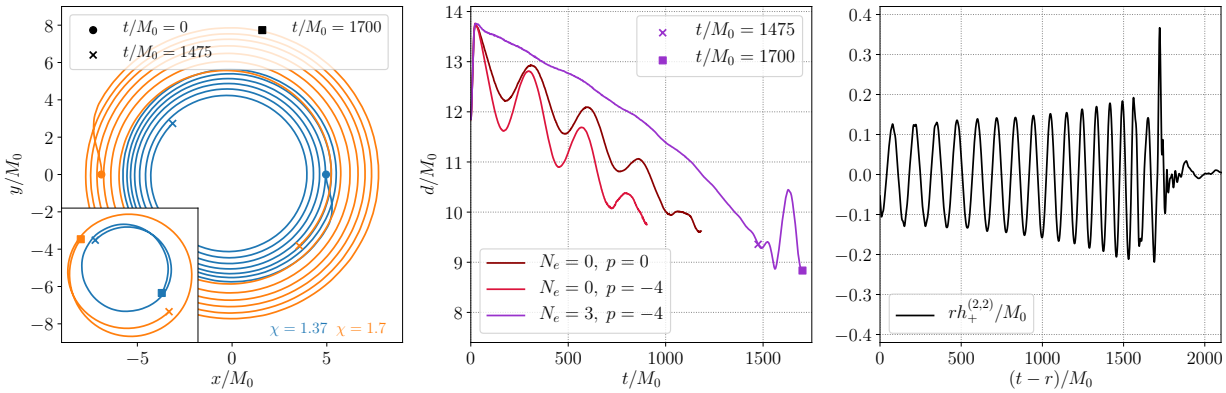

Figure 3.8: Same as in Figure 3.7 for binary $\mathcal{B}_3$. In the left and center panels, we also indicate the time $t/M_0 = 1475$ (x-marker) and show the subsequent in-plane star trajectories in the inset in the bottom left panel up to the point of contact, which is discussed in the main text. For comparison, in the center panel, we also show two cases with different values of p before eccentricity reduction ($N_e = 0$). After eccentricity reduction, the eccentricity is $e \approx 1.8 \times 10^{-3}$. At the point of contact of the two stars, the GW frequency is roughly $\omega_c M_0 \approx 0.1$ also for $\mathcal{B}_3$. There is a slight drift of the center of mass that is barely noticeable in bottom left panel corresponding to $v^x_{\rm com} \approx -1.2 \times 10^{-4}$ (all other components are $\lesssim 10^{-5}$; see Appendix B.3 for a discussion).

reduction and no conformal kinetic energy rescaling power p. Between the $N_e = 0$ cases, the binary with $p = -4$ conformally scaling for the scalar kinetic energy merges before the otherwise identical binary with $p = 0$. After several iterations of eccentricity reduction ($N_e = 3$), the merger occurs later. However, for $t/M_0 \gtrsim 1475$, the coordinate separation d exhibits oscillations, which culminate in the two stars moving away from each other, temporarily *increasing* the coordinate separation by approximately $\sim 10\%$ to $d/M_0 > 10$. After this sudden repulsion, the stars begin to merge at $t/M_0 = 1700$ (indicated by a square marker in Fig. 3.8). In the inset of the left panel in Fig. 3.8, we show the in-plane trajectories of both stars from $t/M_0 = 1475$ to merger. Qualitatively, the sudden repulsion of the two stars results in a sudden *increase* of orbital eccentricity for the last 3/2 orbits before merger (e.g., the orbital trajectories self-intersect). This repulsive behavior is likely due to strong scalar interactions between the two stars in the late stages of the inspiral. This behavior was first observed in Ref. [340] during the late inspiral and merger of two BSs in a scalar theory with repulsive scalar self-interactions. Despite the terminology, systems may exhibit repulsive behavior in both attractive and repulsive scalar models (see e.g. Ref. [281]). These scalar interactions are exponentially suppressed by the separation of

the binary BS and, hence, only become active in the late stages of the inspiral, depending on the constituent stars' compactnesses and frequencies. In contrast to the less relativistic binaries considered in Ref. [340], the constituents of binary $\mathcal{B}_3$ are highly compact, with scalar densities that rapidly decay away from the individual stars. As a result, the scalar interactions increase in importance over the gravitational interaction only roughly two orbits before the point of contact. At this stage, however, the strength of the scalar interactions surpasses that of the gravity, likely resulting in the rapid increase of the coordinate separation shown in the center and left panels of Fig. 3.8. This is a feature absent in mergers of compact binaries composed of black holes and neutron stars, and may serve as a smoking gun signature to distinguish BS binaries from such cases.

To understand the nonlinear merger dynamics of binary $\mathcal{B}_3$, recall that the initial phase offset of this binary is $\alpha/\pi = 1/3$ and that $\omega_1 \neq \omega_2$ (see Table 3.1). This latter renders the vortex structure of the binary time-dependent even at the linear level. Hence, a precise prediction and understanding of the merger outcome using the remnant map of Ref. [340] is challenging. However, the latter can still be utilized to qualitatively analyze the merger process. Due to the time-dependent scalar phase, there is no fixed vortex at the center of mass. Thus, the vortex structure does not prevent the formation of a single BS, and hence, the final remnant may be a combination of non-spinning stars including possibly only a single spherically symmetric BS. Both transitions, two $m = 1$ rotating BSs merging to two $m = 0$ BSs of the same charge, or a single $m = 0$ of the same charge, are energetically favorable (i.e., the corresponding quantity analogous to (3.37) satisfies $\mathcal{M} > 0$ in the relevant part of the parameter space). However, since the spins of the inspiraling superspinning BSs are aligned with the orbital angular momentum, the system contains large amounts of angular momentum. While it is plausible that a single non-spinning BS may shed this angular momentum sufficiently rapidly during the nonlinear merger (based on findings of e.g., Ref. [285]), we find that the final remnant is instead a *binary* of non-spinning stars, which are flung out away from the center of mass at high velocities (with the residual angular momentum likely being converted into orbital angular momentum as the stars come into contact). The binary separation continues to increase up until we terminate the evolution, at which point the separation increased to roughly $d/M_0 \approx 40$. The breakup of the spinning binary at the point of contact occurs at the locations of the vortices of each spinning star. As such, the nonlinear merger process of $\mathcal{B}_3$ is qualitatively similar to what in shown in Fig. 6 of Ref. [340].

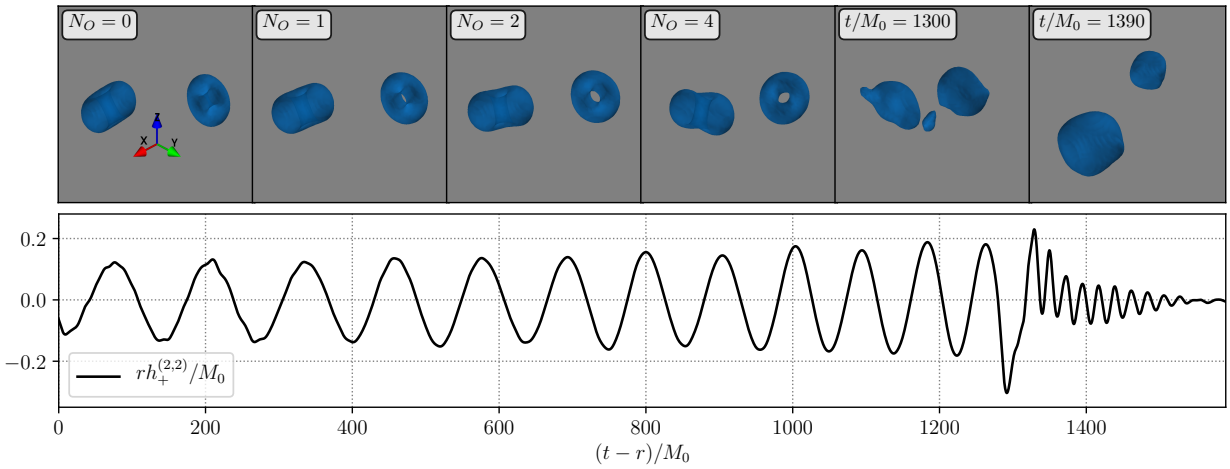

Figure 3.9: The inspiral and merger of the precessing binary configuration $\mathcal{B}_3$ (see Table 3.1) with initial coordinate separation $D_0 = 12M_0$ and initial spin-directions (defined in the main text) so the spin-vectors point away from the initial boost direction with a 45°-angle to the initial orbital plane. We show snapshots with surfaces of constant scalar field magnitude (3D rendering; *top row*) and the gravitational waveform extracted at $r/M_0 = 100$ *(bottom row)*. In the top row, the orientation of the axes (which is the same for all panels) is shown in the leftmost panel. The first four panels show the binary during the inspiral at roughly the same orbital phase after N_O orbits, while in the last two panels, the merger dynamics is presented roughly at coalescence time $t/M_0 = 1300$ and once the resulting non-spinning binary increase its coordinate separation $t/M_0 > 1350$. For this binary, the eccentricity and center-of-mass drift was reduced in a single iteration step to $e = 0.013$ and $v_{\rm com} \approx 9 \times 10^{-5}$.

3.4.3 Precessing binary

Finally, we turn to the precessing binary configuration $\mathcal{B}_3$ (see Table 3.1) mentioned throughout this chapter, and analyze its nonlinear dynamics in detail. The initial data for binary $\mathcal{B}_3$ is solved using an initial coordinate separation $D_0 = 12M_0$ and a conformal rescaling exponent $p = -4$. The spin of each star is chosen to make a 45°-angle with the plane containing the initial positions and velocities of the BSs, such that the component parallel to this plane is in the opposite direction to the initial tangential velocity. Recall, the dimensionless spins of *both* individual stars are above the Kerr-bound $S_i/M_i^2 > 1$. As indicated in Fig. 3.4, we perform a single eccentricity and center-of mass velocity reduction step, resulting in an eccentricity of $e = 0.013$ and linear center of mass drift of

$v_{\rm com} \approx 9 \times 10^{-5}$ (with $|v^z_{\rm com}| \approx 7 \times 10^{-5}$).

In Fig. 3.9, we show snapshots of the evolution of these binary BS initial data, as well as the gravitational waveform. Focusing first on the inspiral, recall that the spin of a rotating BS points along the vortex line through the center of the star, i.e., perpendicular to the torus formed by surfaces of constant scalar field magnitude. As can be seen from the top panel, the binary exhibits rapid precession of the star's spin vectors throughout the early inspiral. In fact, as the individual stars are super-spinning, the strength of the spin-orbit and spin-spin interactions surpasses that of any binary black hole during the inspiral. As the eccentricity is relatively large compared to the other quasi-circular cases, the initial separation is relatively close, and there is residual high-frequency GW contamination of the type discussed in Sec. 3.3.2, the typical modulation of the GW amplitude due to precession cannot be seen in the extracted gravitational waveform. The merger of this binary is qualitatively similar to the aligned-spin case discussed in Sec. 3.4.2: the two rotating BSs collide to form two non-spinning, highly perturbed BSs, which move outward from the center of mass. This is shown in the last two panels of the top row of Fig. 3.9. The coordinate separation surpasses $d/M_0 > 40$ before we terminate the evolution, and is not clear whether this new binary is gravitationally bound.

3.5 Conclusion

In this chapter, we tackled the problem of robustly constructing binary BS initial data satisfying the Hamiltonian and momentum constraints of the Einstein equations utilizing the CTS formulation. We analyzed and tested various approaches to specifying the scalar free data entering these equations based on superposing isolated boosted BS solutions. Among these approaches, we found considering the complex scalar field and its conformally rescaled kinetic energy as free data to robustly lead to constraint satisfying initial data that could be readily evolved without further reconstruction procedures. Beyond a simple superposition of BS solutions, we also reduce the spurious oscillations induced by non-equilibrium initial data using several methods. As suggested in previous studies, we attenuate the superposed free data of one compact object in the vicinity of the second compact object. In addition, here we introduce a new approach where we change the relation between the initial scalar kinetic energy and the conformally scaled version of this quantity which is specified as free data. This reduces the scalar kinetic energy, and hence, results in less perturbed scalar matter. Finally, we successfully reduce the orbital eccentricity of various mass ratio binary BSs down to the $e \sim 10^{-3}$ level.

Our procedure for constructing binary BS is highly generic, and thus, is ideally suited

to exploring a vast space of possible binary configurations. Here we test it for head-on and quasi-circular inspiral cases, including different mass-ratios, spin magnitudes, and spin orientations.

Ideally, instead of basing the scalar field configuration on superposed BS solutions, one would solve additional equations imposing a quasi-equilibrium of the scalar matter with respect to an approximate helical Killing field, analogous to approaches to construction of equilibriated binary neutron star initial data. In this chapter, we briefly discuss several ways in which one might approach this problem, and some of the complications that may arise, in particular if one wishes to tackle generic spinning binaries as considered here. However, we leave an implementation and testing of such an approach to future work.

While we were able to efficiently reduce spurious oscillations of the BSs in the binary, particularly for star solutions in the scalar theory with repulsive self-interactions, the residual perturbations limit the eccentricity reduction and contaminate the extracted gravitational waveform. In the cases we consider with eccentricities $\sim 10^{-3}$, we find further reduction of this quantity to be challenging as the spurious oscillations in each star induce high-frequency oscillations of the coordinate separation with comparable or larger amplitude as the eccentricity. Additionally, even small-amplitude perturbations in the scalar field making up BSs in scalar theories with solitonic potential induce large-amplitude high-frequency contamination in the gravitational radiation at early times during the numerical evolutions of the initial data. Both artifacts may be suppressed by solving the CTS constraint equations together with quasi-equilibrium scalar matter equations.

With the methods to construct binary BS initial data presented in this chapter, accurate waveforms of low-eccentricity non-spinning and (super-)spinning binary BSs can be obtained. Until the late inspiral, the binary evolution is largely model-independent, i.e., the inspiral-dynamics is driven by gravitational effects such as spin-interactions, rather than any mechanism specific to the scalar matter making up the stars. The resulting waveforms could be used in to validate and tune inspiral waveform models that would allow for binary parameters outside the ranges allowed by black holes and neutron stars (e.g., Ref. [231]). Likewise, current tests to distinguish binary black holes and neutron stars from exotic alternatives based on their GW signals [15] could be validated with accurate binary BS inspiral-merger-ringdown waveforms relying on the initial data constructed in this chapter. Another interesting avenue for future work is to study the impact of relativistic features such as stable light rings and ergoregions of exotic compact objects on the inspiral gravitational waveform using highly compact BSs.

Chapter 4

Binary boson stars: Merger dynamics and formation of rotating remnant stars

Executive summary: Scalar boson stars have attracted attention as simple models for exploring the nonlinear dynamics of a large class of ultra compact and black hole mimicking objects. Here, we study the impact of interactions in the scalar matter making up these stars. In particular, we show the pivotal role the scalar phase and vortex structure play during the late inspiral, merger, and post-merger oscillations of a binary boson star, as well as their impact on the properties of the merger remnant. To that end, we construct constraint satisfying binary boson star initial data and numerically evolve the nonlinear set of Einstein-Klein-Gordon equations. We demonstrate that the scalar interactions can significantly affect the inspiral gravitational wave amplitude and phase, and the length of a potential hypermassive phase shortly after merger. If a black hole is formed after merger, we find its spin angular momentum to be consistent with similar binary black hole and binary neutron star merger remnants. Furthermore, we formulate a mapping that approximately predicts the remnant properties of any given binary boson star merger. Guided by this mapping, we use numerical evolutions to explicitly demonstrate, for the first time, that rotating boson stars can form as remnants from the merger of two non-spinning boson stars. We characterize this new formation mechanism and discuss its robustness. Finally, we comment on the implications for rotating Proca stars.

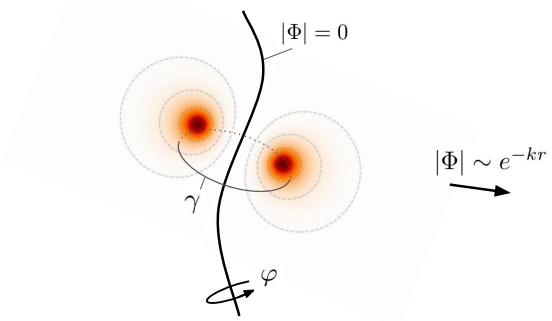

Figure 4.1: We show schematically an axial slice through a rotating BS at a fixed time. The scalar field magnitude $|\Phi|$ (red/yellow color) vanishes along the central vortex line, attains a maximum value some distance from the vortex line, and drops off exponentially towards large distances $\sim e^{-kr}$, with some $k > 0$. Surfaces of constant scalar field magnitude are indicated as gray dashed lines. Integrating the gradient of the scalar phase $\mathrm{Arg}(\Phi) = \psi$ along the path γ around the vortex in the azimuthal direction φ gives the vortex index q of the rotating BS, as defined in (4.2).

4.1 Introduction

As we noted in Chapter 2 and demonstrated explicitly in Chapter 3, the existence, stability, and formation of spherically symmetric stars from isolated or binary solutions is well-studied, the role of angular momentum in these systems is still poorly understood. It was noticed early on that spherical stars cannot rotate perturbatively [224] (i.e., they are not continuously connected to their non-rotating counterparts; notable exceptions exist in the Newtonian limit [223]). Later it was found that rotating BS [and their vector counterparts called Proca stars (PSs)] solutions with quantized angular momentum exist [220, 221, 77]. However, only stars in scalar models with self-interactions are perturbatively stable against a non-axisymmetric instability [323, 129, 339, 133]. Lastly, despite numerous efforts to form rotating BSs dynamically [285, 65, 66, 67, 117], even in those models with rotating stars without known instabilities [339], no rotating BSs has been formed from the merger of two non-spinning stars. If BSs mergers cannot form a (non-BH) rotating remnant, that would seem to place a serious impediment on their ability to mimic BHs without invoking horizons.

As we have seen in Chapter 2, BSs are stationary, non-topological solutions of a complex massive scalar field Φ with a global $U(1)$ symmetry minimally coupled to gravity (the generalization of Q-ball solutions to include self-gravity [158, 111]). The tendency of a

localized wave solution to disperse is balanced by gravitational attraction, while the gravitational decay of BSs (dissipation through gravitational radiation) is precluded by their conserved $U(1)$-charge Q, counting the number of bosons in the system. Generally, the scalar field of an isolated BS takes the form

$$\Phi = \phi e^{i(\omega t - m\varphi)}, \tag{4.1}$$

with magnitude ϕ, frequency ω, integer azimuthal index m, time coordinate t, and azimuthal coordinate φ (notice, this differs from the ansatz presented in sec. 2.2.2 by $m \to -m$). For spherical solutions, the scalar field magnitude is maximum at the origin, and exponentially decays towards spatial infinity. Their rotating counterparts with non-zero angular momentum $J = mQ$, on the other hand, exhibit vanishing scalar field magnitude at their centers and are classified by the index $|m| \geq 1$, leading to toroidal surfaces of constant scalar field magnitude. Therefore, rotating BSs can also be understood as *vortices* with gravitationally bound scalar matter. This is shown schematically in Figure 4.1. Within a spacelike slice of a spacetime with scalar field $\Phi = \phi e^{i\psi}$, we define a vortex to be the line L through the hypersurface such that the integral of the gradient of the scalar phase ψ along the oriented loop γ in a sufficiently small neighborhood around L is a non-zero integer q,

$$\frac{1}{2\pi} \oint_\gamma d\ell_i D^i \psi = q, \tag{4.2}$$

called the vortex index. Here, D_i is the covariant derivative in the hypersurface. Since for non-spinning BSs the phase ψ is constant in space, i.e., $D^i\psi = 0$, applying this definition gives $q = 0$. In the case of isolated rotating BSs, the gradient $D^i\psi$ is non-trivial. In fact, the vortex line is the line of vanishing $|\Phi|$ through the center of mass of these solutions (as shown in Figure 4.1). The vortex index q is exactly the azimuthal index m of the star, $|q| = m$. Hence, in the context of these rotating BS solutions, the connection between angular momentum and the vortex index is manifest. Lastly, reversing the orientation of γ implies $q \to -q$.

The appearance and role of vortices in various contexts have been the subject of extensive study for decades. In particular, quantized vortices are generic features in Bose-Einstein condensates [362], superfluids [228, 367, 330], wave-like dark matter [379, 344, 211, 313], or cosmic strings [218]; all of which are described by scalar models similar (or identical) to the scalar theories with BS solutions considered here. In these contexts, vortices appear dynamically, for instance, as the result of symmetry breaking phase transitions [218, 386, 125], or the introduction of angular momentum into the system [313, 362]. Therefore, from vortex lattices in trapped superfluids to cosmic string networks and spinning dark matter halos, vortices are important in a wide variety of phenomena. Here, we

show that vortices, their relation to angular momentum, and the evolution of the phase of the scalar field are also crucial ingredients in understanding and predicting the merger dynamics of binary BSs.

In this chapter, we numerically evolve the nonlinear Einstein-Klein-Gordon system of equations in 3D to study the role of the scalar field during the late inspiral, merger, and ringdown of spinning and non-spinning binary BSs in different nonlinear scalar models with a global $U(1)$ symmetry. As the scalar interactions are exponentially enhanced with decreasing binary separation, we find that the scalar phase plays a crucial role during the later inspiral and merger of binary BSs. We illustrate some cases where the nature of the endstate of a binary merger is determined by the relative phase of the stars at early times. Secondly, we provide a mapping that approximately predicts the outcome of any given binary (or multi) BS and PS merger. Utilizing this mapping to guide the choice of parameters, we show, for the first time, using numerical evolutions, cases where rotating BSs form dynamically from a non-spinning binary BS merger. We provide a set of necessary conditions for the formation of these rotating BS and PS remnants and identify the regions in parameter space where this formation channel is expected to be active.

The remainder of this chapter is organized as follows. In Sec. 4.2, we briefly review the role of scalar interactions in the dynamics of binary Q-balls, then proceed to apply these results to binary BS inspirals, first qualitatively, and then systematically, in the case of a non-spinning binary inspiral, and finally construct a mapping to approximately predict the remnant properties of any given binary BS inspiral. In Sec. 4.3, we begin by listing the necessary conditions for the formation of a rotating remnant BS from the merger of a non-spinning binary, explicitly demonstrate the formation of a rotating BS remnant by numerically evolving a suitable system, discuss the robustness and other characteristics of this formation channel, and study the remnant resulting from the merger of a spinning BS with a non-spinning BS. In Sec. 4.4, we further discuss our findings and conclude. Finally, in the appendices, we revisit a non-axisymmetric instability present in rotating BSs in light of our findings, and provide further details on our numerical setup.

4.2 Merger dynamics

During the merger of two BSs in a nonlinear scalar model, scalar interactions play an important role along with gravitational interactions. Due to the exponential fall-off of the scalar field amplitude at large distances from an isolated star, the scalar forces are also exponentially suppressed for a binary at large separations. Conversely, the scalar field

interaction is exponentially enhanced during the later inspiral and merger of two BSs, and is crucial to understanding the merger dynamics.

In Sec. 4.2.1, we briefly review known results for Q-balls and BSs, and conjecture how these results can be translated to the inspiral and merger dynamics of binary BSs. We apply this intuition to the inspiral of a representative binary BS in Sec. 4.2.2, and study the scalar interaction dependence on the scalar phase systematically in the context of a binary BS inspiral in Sec. 4.2.3. Lastly, in Sec. 4.2.4, we conjecture a mapping that identifies the remnant of any multi BS encounter and illustrate its utility in the context of an inspiraling spinning binary BS. (We also comment on the implications for PSs.)

4.2.1 Scalar interactions

On a flat background, a Q-ball can be decomposed, as in (4.1), into a spatial profile ϕ and a phase $\omega t - m\varphi \to \psi$. In the case of an isolated, non-spinning (i.e., $m = 0$) Q-ball, the spatial profile peaks at the center of the solution and decays exponentially as $\phi \sim e^{-kr}$ at large distances r from the center, while the complex phase exhibits a harmonic time dependence $\psi = \omega t$, together with the arbitrary constant phase-shift $\psi \to \psi + \alpha$, under which the model is symmetric. A binary Q-ball with separation $|\mathbf{x}_1 - \mathbf{x}_2| = D \gg 1/k_i$, with $i = 1$ and 2, is approximately given by the scalar field profile

$$\Phi \sim e^{i\omega_1 t}\phi_1(\mathbf{x}_1) + e^{i(\omega_2 t+\alpha)}\phi_2(\mathbf{x}_2). \tag{4.3}$$

The scalar self-interactions lead to momentum exchange—a scalar force—between the two solitons [39, 51, 74]. This force ultimately originates from the internal non-stationarity of the complex phase of the scalar field. For the binary defined in (4.3), the scalar force has a dependence given by [39, 74]

$$\tilde{F} \sim \cos[(\omega_1 - \omega_2)t + \alpha]e^{-D(k_1+k_2)}, \tag{4.4}$$

for $1/D \ll k_1, k_2$. The magnitude of $\tilde{F}$ is exponentially suppressed by the distance D between the solitons, while the sign of $\tilde{F}$ is determined by the phase evolution of the binary. This spatial dependence and importance of the complex phase is applicable also in the BS case, as we see below. In the limit of equal frequency, $\omega_1 = \omega_2$, the temporal dependence vanishes, and the sign of $\tilde{F}$ is determined solely by the phase-offset α. In the general case of $\omega_1 \neq \omega_2$, a breathing motion appears in response to the harmonically oscillating force applied on each Q-ball [39], independent of the constant offset α. Therefore, the complex phase dynamics determine the sign of the effective force applied, while the magnitude is exponentially suppressed by the distance between the solitons.

The dynamics of the complex phases ψ_1 and ψ_2 is non-trivial in the presence of nonlinear scalar interactions [51]. Integrating out the spatial degrees of freedom, assuming a large separation, and identical solitons, the evolution follows $\ddot{\psi}_1+\ddot{\psi}_2 = 0$ and $\ddot{\psi}_1-\ddot{\psi}_2 \sim \varepsilon^2 \sin(\psi_1-\psi_2)$, with the overlap $\varepsilon \sim e^{-D(k_1+k_2)}$. For the special case of $\psi_1 = \psi_2 + n\pi$, with $n \in \mathbb{Z}$, the evolution trivializes, i.e., $\dot{\psi}_1, \dot{\psi}_2 = \text{const.}$, and the soliton's phase-evolution is set by a single frequency. However, in general, an initial phase-offset $\alpha = (\psi_1 - \psi_2)|_{t=0} \in (0, \pi)$, implies $\ddot{\psi}_1, \ddot{\psi}_2 \neq 0$. Therefore, the phases start evolving towards $\dot{\psi}_1 > \dot{\psi}_2$, i.e., towards a state of different frequencies. The frequency evolution implies a change in charge of the two solitons, since the frequency uniquely parameterizes the family of Q-ball solutions of (in general) different charge. Hence, a non-trivial complex phase evolution ensues due to nonlinear scalar interactions, implying charge transfer between the two Q-balls, and altering the nature of the force (4.4).

Furthermore, in the presence of gravity (i.e., in the case of BSs), no nonlinear scalar potential is required for non-trivial interactions to occur. In Ref. [281], an effective repulsion was observed in the collision of two mini BSs (stars in linear scalar models) when comparing the case when the complex scalar field is *anti-symmetric* under star interchange, i.e., in (4.3), if $\alpha = \pi$, $\phi_1 = \phi_2$, and $\omega_1 = \omega_2$, then $\Phi \leftrightarrow -\Phi$ when $\mathbf{x}_1 \leftrightarrow \mathbf{x}_2$, to the symmetric case. Related to this, static spacetimes corresponding to BSs with two (or more) peaks have been constructed in the linear scalar model, which can be thought of as corresponding to two non-spinning BSs kept in equilibrium by the same relative phase difference [375, 194, 118]. In the following, we will refer to this equilibrium state as the dipolar BS (DBS) solution.

Lastly, angular momentum, present in rotating Q-balls, spinning BS solutions, or in inspiraling binary BSs, plays an important role in the evolution of the phase, since angular momentum and the appearance of vortices in a massive complex scalar theory are tightly connected. To illustrate this, we restrict to a flat spacetime, where we can use the symmetries of the background to define local notions of angular momentum. We define the angular momentum density ρ_A with respect to the Killing field η_A associated with the rotational symmetry in the A-th direction as $\rho_A = T_{0j}\eta^j_A$, in Cartesian coordinates. From the $U(1)$ complex scalar stress-energy tensor, we know that $T_{0i} = -2\dot{\phi}\partial_i\phi - 2\dot{\psi}\phi^2\partial_i\psi$, when decomposing $\Phi = \phi e^{i\psi}$. Therefore, the vorticity in the A-th direction, which we define as $\nu_A := \eta^j_A\partial_j\psi$, is related to the associated angular momentum density by

$$\rho_A \sim \phi^2\nu_A\partial_t\psi, \tag{4.5}$$

where we dropped the ψ-independent term. In the case of rotating Q-balls, with field profile $\psi = \omega t - m\varphi$, we find that the vorticity in all directions, excluding the spin-direction, vanishes. The latter is simply given by $\rho_{\text{spin}} = -2\omega\phi^2\nu_{\text{spin}} = 2m\omega\phi^2$. In the case of the rotating BS, the expression is modified only by curvature corrections. This makes

the connection between vorticity and angular momentum manifest, as the total angular momentum in the rotating Q-ball (and BS) solution is quantized by the vortex index m, as $J = mQ$. Note, a vortex in the $U(1)$ nonlinear scalar models considered here does *not*, by itself, contain energy. Hence, vortices can be created and destroyed spontaneously, as long as angular momentum is conserved. This is in stark contrast to, for instance, cosmic strings in global $U(1)$-Higgs or Higgs-Abelian models, where the string itself is a non-zero energy solution that is topologically protected.

Ultimately, the evolution of the complex phase of the scalar field determines the type of self-interaction-induced momentum and charge transfer between two Q-balls, as well as the angular momentum present in the solution, while these effects are exponentially suppressed by the distance between the solitons.

4.2.2 Scalar interactions in a binary BS inspiral

Let us translate the findings discussed in the previous section from the flat spacetime case, to the self-gravitating BS case in the context of a binary inspiral. For most of the early inspiral of a binary BS, the scalar interactions are exponentially suppressed, and hence, sub-dominant to the gravitational interactions. At this stage of the inspiral, the scalar phase of each star grows linearly according to the star's stationary frequency. In the late inspiral, i.e., when $D \sim 1/k_i$, scalar interactions increase in importance, and the phases of each star start to differ from the stationary prediction, i.e., $\ddot{\psi}_{1,2} \neq 0$. At this stage, linear predictions for the evolution of the scalar phase break down, and nonlinear simulations are necessary. Many of the effects present in Q-balls cannot be easily quantified in the context of dynamical gravity due to a lack of background symmetries and well-defined local quantities. Therefore, in the following we attempt to provide intuition for the scalar interaction-driven physical processes active during the later inspiral and merger of binary BS, and leave a more rigorous and systematic study to the later sections.

In order to understand the phase evolution within a binary BS during the late inspiral, it is instructive to begin by studying the phase of a single, boosted, non-spinning BS with field profile

$$\Phi = \phi(\mathbf{x}) e^{i(\omega t + \alpha)} \tag{4.6}$$

in the stationary frame. With the primed coordinates $(t', \mathbf{x}')$ denoting a boosted frame, defined by the boost vector β^i, the complex phase of the boosted BS in the $t' = 0$ slice is

$$\psi(\mathbf{x}') = \omega \beta^i x'_i + \alpha \mod 2\pi. \tag{4.7}$$

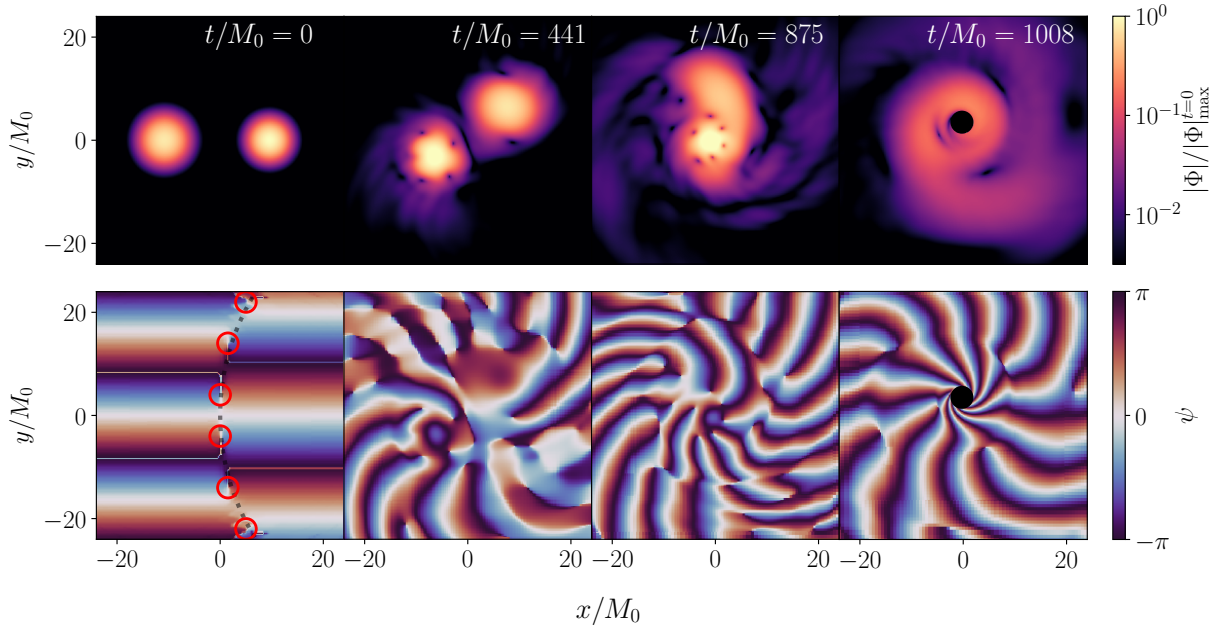

Figure 4.2: We show four snapshots of the equatorial plane during the merger of a non-spinning binary BS with frequencies $\omega_1/\mu = 0.9$ and $\omega_2/\mu = 0.86$, with no initial phase-offset $\alpha = 0$, total ADM mass M_0, an initial coordinate separation $D = 20M_0$, and in the repulsive scalar model (2.5) with $\lambda/\mu^2 = 10^3$. The compactness of the higher and lower frequency star is $C = 0.08$ and $C = 0.12$, respectively. The total angular momentum points into the page, and the orbit has Newtonian eccentricity $e = 0.13$. The final BH parameters are shown in Figure 4.3. *(top row)* We show the magnitude of the scalar field $|\Phi|$, normalized by the maximum magnitude of the scalar field in the initial time-slice $|\Phi|^{t=0}_{\max}$. *(bottom row)* We show the complex phase $\psi \in (-\pi, \pi)$ at the corresponding times in the equatorial plane. At $t/M_0 = 0$, we indicate the locations of the $q = 1$ vortices by red circles, while we indicate the surface of $\phi_1 \sim \phi_2$ defined below (4.9) with a black dashed line. Notice, the white lines in the first panel of the bottom row are interpolation artifacts and correspond to $\psi = \pm\pi$.

Therefore, due to the mixing of temporal and spatial degrees of freedom in the Lorentz boost, the complex phase of the scalar field is a monotonic function of *space* in the boosted frame, with slope determined by the star's frequency ω[1]. We now move to the case of an inspiraling binary BS. The construction of binary BS initial data satisfying the Hamiltonian and momentum constraints is outlined in Chapter 3, with further details in Chapter 3. Here, we simply note that the binary's scalar field is a superposition of two isolated stars, boosted with velocity v_1, v_2 along β_1^j, β_2^j. Explicitly, the constraint-solving scalar field profile in the initial time-slice in the center of mass frame is

$$\Phi_{\rm BBS} = \phi_1 e^{i(\omega_1 \beta_1^i x_i')} + \phi_2 e^{i(\omega_2 \beta_2^i x_i' + \alpha)}. \tag{4.8}$$

Therefore, in the center of mass frame, the spatial dependence of the complex phase $\psi_{\rm BBS}$ of $\Phi_{\rm BBS}$ is

$$\psi_{\rm BBS} \approx \begin{cases} \omega_1 \beta_1^i x_i', & \phi_1 \gg \phi_2, \\ \omega_2 \beta_2^i x_i' + \alpha, & \phi_2 \gg \phi_1. \end{cases} \tag{4.9}$$

In the regions with $\phi_1 \sim \phi_2$, an infinite set of $|q| = 1$ vortices appear. In fact, if the scalar field initial data of the binary BS is constructed by superposing the individual star's fields, then these vortices cannot be removed, unless all angular momentum is removed from the system (e.g., in a head-on collision). We find that a subset of these vortices becomes dynamically important in the binary evolutions discussed in the remainder of this chapter.

To illustrate this, and the subsequent evolution, we consider a non-spinning binary BS in the repulsive scalar model (2.5) with coupling $\lambda/\mu^2 = 10^3$. The stars of the binary are

[1]The magnitude ϕ is simply Lorentz contracted in the boost direction.

Frequency	C	x_0/M_0	v_x	J_0/M_0^2	α	e
$\omega_1/\mu = 0.90$	0.08	-10.69	0.12	0.9	0	0.13
$\omega_2/\mu = 0.86$	0.12	9.31	-0.10			

Table 4.1: The properties of the non-spinning binary BS initial data discussed in the main text. The two stars have frequencies $\omega_{1,2}$, with initial phase offset α, are positioned at coordinate locations x_0 and $y_0/M_0 = 0$, have boost velocities v_x and $v_y = 0$ (with Newtonian eccentricity e), compactness C, and mass-ratio $\tilde{q} = 1.13$. Here M_0 is the ADM mass, and J_0 is the similarly defined global angular momentum, the latter given by eq. (7.63) of Ref. [175]. Note, this definition of angular momentum, albeit commonly used, is not free from gauge-dependency (for further details, see Ref. [175]).

prepared with frequencies $\omega_1/\mu = 0.9$ and $\omega_2/\mu = 0.86$ and initial phase-offset $\alpha = 0$. The initial coordinate separation is $D = 20M_0$, with binary ADM mass M_0 (see Table 4.1 for details on the parameters of the initial data). In the language of the previous section, this choice enables phase evolution and breathing behavior. We comment on the former below, while the latter is likely a small effect on timescales larger than the orbital timescales of this binary. In Figure 4.2, we show the magnitude $\phi_{\rm BBS}$ and phase $\psi_{\rm BBS}$ of the equatorial plane of the binary BS at four different times throughout the evolution. We focus first on the initial time-slice. The less compact of the two stars, i.e., the star with smaller central scalar field magnitude, is the star with smaller charge and larger frequency, $\omega_1/\mu = 0.9$. The complex phase of this binary, shown in the bottom row of Figure 4.2, illustrates the structure discussed above. The phase is a monotonically increasing function of space in the boost direction on either side of the black dashed line, indicating where $\phi_1 \sim \phi_2$. The slope of the phase is different on either side of $\phi_1 \sim \phi_2$ in the equatorial plane, since $\omega_1 \neq \omega_2$. The surface of $\phi_1 \sim \phi_2$ is a 2-dimensional surface in the spatial hypersurface separating regions of $\phi_2 > \phi_1$ from those with $\phi_2 < \phi_1$. Lastly, in the equatorial plane, along the line of $\phi_1 \sim \phi_2$ there is a set of $q = 1$ vortices indicated with red circles.

The chosen boost parameters do not lead to a quasi-circular inspiral, but rather to an orbit with non-zero eccentricity. Therefore, the stars go through an initial orbital phase, during which their (coordinate) distance increases over time. During this time, the scalar interactions are exponentially suppressed, and the dynamics are largely dominated by gravitational interactions of the stars. Throughout this phase, the complex phase of each star increases approximately linearly, and independently, in time. After passing the apoapsis, the coordinate distance between the stars decreases, leading to enhanced scalar interactions. The closest approach is achieved around $t/M_0 = 350$. During the periapsis passage, there is significant overlap between the two scalar field profiles. The evolution of ψ is no longer approximately linear in time. The enhanced scalar interaction, in conjunction with the presence of the vortices in ψ between the two stars, leads to the transfer of these vortices onto *both* of the BSs. In the second snapshot of Figure 4.2, the vortices can be seen just after the closest approach. After the periapsis, the vortices orbit around each individual star in the same direction as the overall orbital motion. Qualitatively, the orbiting vortices indicate angular momentum transfer from the orbit to the spin angular momentum that can be assigned to each star. While stationary BSs cannot rotate perturbatively [224], time-dependent solutions may. During the second close encounter, the scalar interactions dominate the dynamics. The star with the larger frequency transfers large amounts of scalar charge onto its heavier companion. This process is shown in the third snapshot of Figure 4.2. As the heavier star accretes scalar matter, its charge and central scalar field magnitude increase. Ultimately, the lighter (and less compact) star is completely tidally

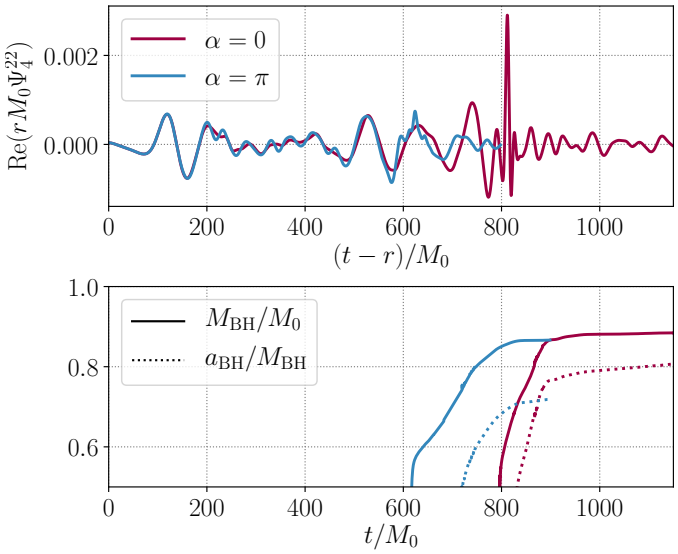

Figure 4.3: *(top panel)* We show the $(\ell, m) = (2, 2)$ mode of the $s = -2$- weighted spherical harmonic components of the Weyl Newman-Penrose scalar Ψ_4 (extracted at coordinate radius $r = 100M_0$) emitted during the binary BS inspiral of the case with initial phase-offset $\alpha = 0$ shown in Figure 4.2 and discussed in the main text. We compare this to the GWs from the same binary inspiral with initial phase-offset $\alpha = \pi$. *(bottom panel)* The mass $M_{\rm BH}$ (solid) and dimensionless spin parameter $a_{\rm BH}$ (dashed) measured from the apparent horizons of the remnant BHs formed in the inspiral of the top panel. We evolve the $\alpha = \pi$ case for only roughly $900M_0$.

disrupted and accretes rapidly onto the heaver companion. The mass of this companion increases beyond the maximum mass the star can stably support, and it collapses into a BH. This situation is shown in the fourth panel of Figure 4.2. The remnant BH moves through the surrounding residual scalar matter, continuing to accrete it.

The gravitational radiation, as well as the final BH parameters, are shown in Figure 4.3. There, we also compare to an evolution of the same binary BS initial data, except with initial phase-offset of $\alpha = \pi$. This case has two important features that distinguish it from the $\alpha = 0$ case: *(i)* The $\alpha = \pi$ case collapses to a BH roughly $200M_0$ earlier than the $\alpha = 0$ case, and *(ii)* the gravitational waveforms differ in amplitude from $t = 200M_0$ to $t = 500M_0$. The high-frequency features in the waveform shown in the top panel of Figure 4.3 originate from time-dependent features on scales smaller than the sizes of the stars. Comparing the orbital period of the vortices around the center of each star with the frequency of the small scale features in the emitted GWs, we can identify the orbiting

vortices as the source of the high-frequency GWs. The differing amplitudes indicate that the vortices in the $\alpha = \pi$ case are surrounded by larger $|\Phi|$ values. Consulting (4.5), this implies also a locally enhanced angular momentum density. This is consistent with finding *(i)*. Larger angular momentum transfer from the orbit to the spin implies earlier merger times, and hence, a more rapid transfer of charge to the heavy star and subsequent BH formation. The final BH parameters are, however, roughly independent of the initial phase offset. In fact, the spin angular momentum of the remnant BH is comparable to that formed by the merger of a binary neutron star or binary BH. Hence, beside the residual scalar matter, the remnant BH retains little memory of the type of binary it was made from.

A few remarks are in order. Many of the statements above are purely qualitative in nature, and are mainly made to provide intuition. In particular, the transfer of orbital to spin angular momentum deserves a more rigorous analysis (e.g., using techniques developed in Refs. [109, 116]). The evolution of the scalar phase during the second encounter is nonlinear, making it challenging to gain intuition from applying linear methods discussed in the previous section. In the following section, we return to the dependence of the GWs on the initial phase and a more systematic analysis of the phase evolution. Furthermore, the use of vortices as a tool to understand the nonlinear phase evolution and to predict the remnant is the subject of Secs. 4.2.4 and 4.3.

4.2.3 Gravitational wave imprints

In the previous two sections, we first reviewed the importance of the scalar phase evolution for the nonlinear dynamics of scalar solitons in the absence of gravity, and then qualitatively applied some of these concepts to the case of an inspiraling non-spinning binary BS. In this section, we investigate the role of the scalar phase in the inspiral and merger of a non-spinning binary BS and the emitted GWs more systematically. The variation of the scalar phase in binary BS mergers has been studied only in the case of head-on collisions in Refs. [232, 281, 280, 96, 153] (see Ref. [324] for a study in the PS case). Here, we consider the impact of the scalar interactions on the *inspiral* of a binary BS and connect our observations directly to the physical intuition provided in Sec. 4.2.1, for the first time. We find several significant differences between the head-on collisions studied in [232, 281, 280, 96, 153] and the inspirals considered here: *(i)* the effect of the scalar interactions accumulate secularly throughout the inspiral, eventually resulting in strong de-phasing and modulations of the emitted GW amplitudes; *(ii)* vortices appear due to the orbital angular momentum and drive dominant high-frequency features in the emitted GWs at late times during the merger; and *(iii)* the time to collapse to a BH post-merger depends

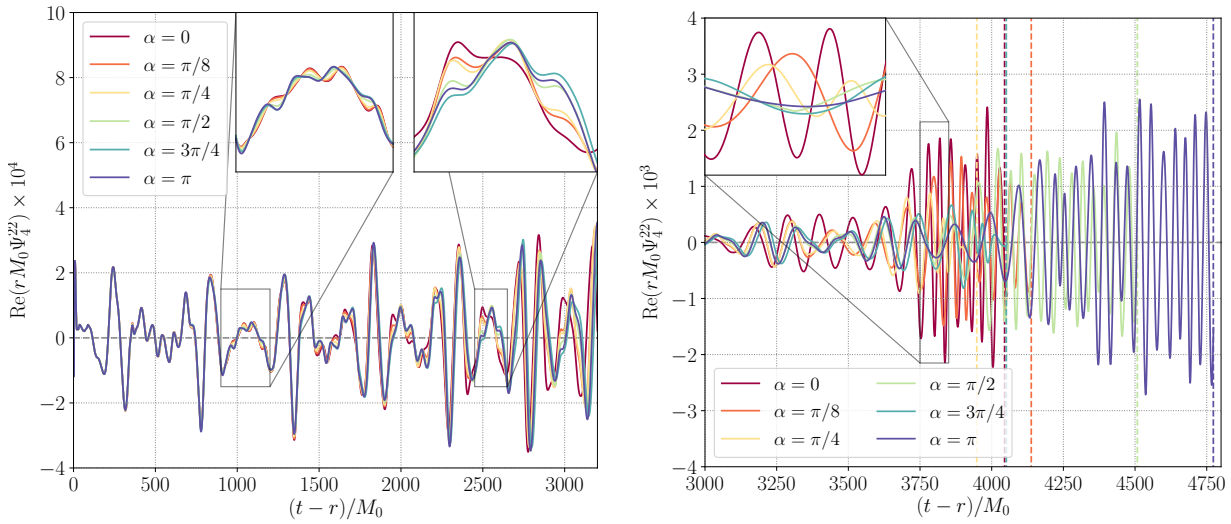

Figure 4.4: The GWs (extracted at a coordinate radius $r/M_0 = 100$) during the inspiral *(left)* and merger *(right)* of the binary BS described in the main text. The different cases correspond to identical initial binary systems, except with different values of the phase offset α in the range 0 to π. Specifically, we show the $(\ell, m) = (2, 2)$ $s = -2$-weighted spherical harmonic component of the Newman-Penrose scalar Ψ_4 as a function of retarded time $t - r$. The differences between the various α-cases are due to the enhancement of nonlinear scalar effects during each close encounter of the binary and towards merger, as the separation between the stars shrinks. Notice the different scale used on the left and the right. After merger, the waveforms are terminated around the time when the system collapses to a BH, which is indicated by a vertical dashed line. We show the GWs after gravitational collapse of the $\alpha = 0$ and π cases in Figure 4.5.

sensitively on the scalar interactions, while the remnant's properties are mostly insensitive to the scalar interactions driving the proceeding dynamics.

In order to illustrate the role of the scalar phase and vortex structure during the inspiral, merger, and ringdown, we consider a non-spinning binary BS in the repulsive scalar model given by (2.5) with $\lambda/\mu^2 = 10^3$, and focus on an equal frequency case with $\omega_1 = \omega_2 = 0.9\mu$. With a compactness of $C = 0.08$ for each star, the impact of the scalar interactions is enhanced compared with a system consisting of highly compact constituent BSs (and $\omega \ll \mu$), since at fixed separation of the stars' center of mass, the overlap of the two stars' scalar fields is larger. The constraint satisfying initial data is constructed using the methods outlined in Chapter 3. In the initial time slice, the binary system has ADM

mass M_0, the stars' coordinate positions are at $x_0/M_0 = \pm 10$ and $y_0/M_0 = 0$ (hence, initial coordinate separation $D = 20M_0$), and the initial coordinate velocities are $v_x = 0$ and $v_y = \mp 0.12$ (with these parameters the Newtonian eccentricity is $e = 0.15$). These initial velocities were chosen to result in an eccentric orbit, with multiple periapses before final merger. This allows us to observe the effects of repeatedly enhanced and suppressed scalar self-interactions on the GWs. In order to study the impact of the scalar field phase on the inspiral, we vary the initial phase-offset α between the BSs considering the values $\alpha \in \{0, \pi/8, \pi/4, \pi/2, 3\pi/4, \pi\}$. Note that in this strong-coupling regime of the repulsive scalar model, stable rotating $m = 1$ BSs were demonstrated to exist in Ref. [339] (and in Newtonian gravity in Ref. [133]). However, we choose binary BS parameters that are expected to result in the formation of a rotating BH since the sum of the charges of the constituent stars is larger than the maximum charge of *both* the $m = 0$ and $m = 1$ families of solutions, and indeed we find collapse postmerger.

In Figure 4.4, we show the GWs emitted during the inspiral of this binary BS for each initial phase offset α. Focusing first on the $\alpha = 0$ case, the non-negligible eccentricity in the binary is reflected in the gravitational waveform as periodic peaks around $(t - r)/M_0 \approx 250$, 750, 1300, 1800, 2300, and 2750, corresponding to the close encounters of the stars. In between these close encounters, the GW signal is characterized by a high-frequency component emerging from spurious oscillation modes excited in the individual stars due to the way the initial data is constructed. (Though we do not do so here, these spurious oscillations can be alleviated by modifying the superposition of the two isolated boosted stars and utilizing a different scaling for the conformal kinetic energy of the scalar field, as shown in Chapter 3.) Though the cases with different values of α initially have essentially indistinguishable orbits and GWs, following the first encounter around $(t-r)/M_0 \approx 250$, the differences in the GW amplitude $|\Psi_4^{22}|$ grow [2] (see also the two insets). During the periods of large separation between the stars, the scalar phase of each star evolves approximately linearly in time. However, scalar interactions are exponentially enhanced during each close encounter, and become more significant as the orbital period and periapse distance shrink due to GW emission during the course of the merger. Since the nonlinear interactions depend on, and affect the scalar phase of the star, as discussed in Sec. 4.2.1, they secularly affect the evolution and GWs of the binary BS system.

These differences in Figure 4.4 are primarily differences in the GW amplitude. However,

[2] All cases considered here were obtained with identical numerical setups both to construct the initial data and to evolve it, suggesting that the *relative* differences in the GWs of the evolutions shown in Figure 4.4 are driven by scalar interactions, rather than being due solely to numerical truncation error. However, as discussed in Appendix C.3, the estimated truncation error in the GW amplitude is comparable to the difference between the cases with different values of α.

as can already be seen there, at late times, there is also a non-negligible *de-phasing* between the waveforms. This can be clearly seen in Figure 4.4, where we show the GWs emitted during the late inspiral and merger of the binary systems. Though the exact point of contact for the two stars is not well-defined, As the stars begin to merge, the GW amplitude increases significantly—by up to an order of magnitude—as can be seen comparing the left and right panels of Figure 4.4 (note the difference in scales). While the exact point of contact for the two stars is not well-defined, one can loosely determine the merger time by this sudden increase in amplitude. It is clear from the right panel of Figure 4.4 that this time depends strongly on the initial phase offset α. For instance, the $\alpha = 0$ case merges around $(t - r)/M_0 \approx 3750$, while the binary with initial phase offset $\alpha = \pi$ merges at $(t - r)/M_0 \approx 4150$. After the merger, the system enters into a transient state consisting of a dynamical remnant star that is temporarily prevented from collapsing due to excess energy and/or angular momentum, analogous to what may happen post-merger in a binary neutron star. A series of scalar vortices (some of which still present from the initial data) rapidly orbit around the center of mass of the remnant indicating large perturbative angular momentum of the *hypermassive BS*. [3] These vortices are small scale features orbiting on the scale of the original constituent stars, which lead to high-frequency GW emission (similar to what we described in Sec. 4.2.2). This is reflected in the sudden increase in the GW frequency after the merger of the stars, as shown in Figure 4.4, which matches the orbital frequency of the vortices around the center of mass of the hypermassive BS. The length of this hypermassive state depends on the initial phase-offset, and hence, on the nonlinear scalar dynamics. For instance, the hypermassive phase in the $\alpha = \pi/4$ case only lasts $t/M_0 \approx 150$, while for the $\alpha = \pi$ case, it lasts $t/M_0 \approx 600$. The latter is longer lived, since the symmetry gives rise to a vortex at the center of mass throughout the evolution, which acts to delay the gravitational collapse of the hypermassive remnant. However, in all the cases with different values of α, we find eventual collapse to a BH, at times indicated by the vertical dashed lines in Figure 4.4. We cannot identify a clear trend in the dependence of the collapse time on initial scalar phase offset α. This may be explained by the fact that the intrinsic BS inverse frequency $\omega_{1,2}^{-1} \approx 1.4M_0$ is much shorter than the time to merger $T_m \sim \mathcal{O}(10^3 M_0)$, so that the repeated scalar interactions, operating on timescales $\sim 1/\omega$, accumulate differences nonlinearly throughout the inspiral of length T_m, leading to a significantly different states entering the hypermassive phase and subsequent gravitational collapse. Hence, any consistent α-trend present at early times appears lost in the accumulated nonlinear shift.

[3] In analogy with the neutron star case (see, e.g., Ref. [54]), here we use hypermassive to refer to an object with total mass above the maximum stable $m = 1$ rotating BS within the same scalar model. We use hypermassive BS to refer to the merger remnants even when these are highly perturbed, and far from equilibrium solutions.

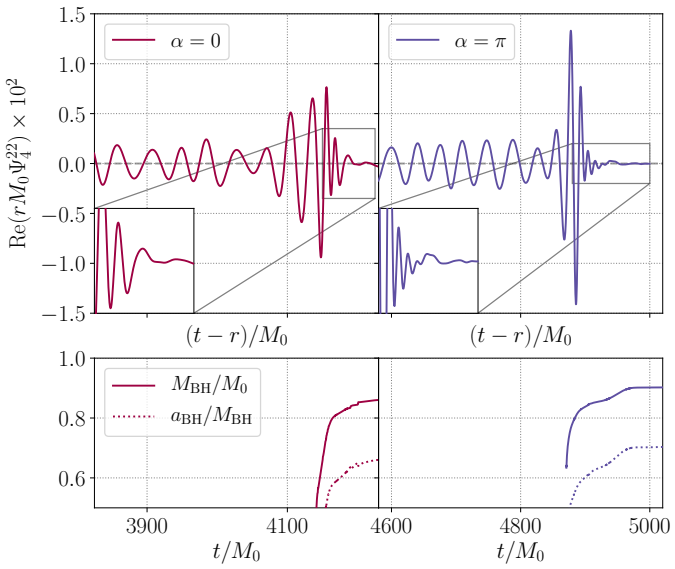

Figure 4.5: *(top panels)* We show the GWs emitted around the time of BH formation by the binary BS systems discussed in the main text and shown in Figure 4.4, for initial phase offsets $\alpha = 0$ and π. Notice the difference in scale compared with Figure 4.4. *(bottom panels)* The mass $M_{\rm BH}$ and spin parameter $a_{\rm BH}$ of the remnant BHs formed as functions of *coordinate time* t (corresponding to the retarded time $t - r$ in the top panels).

In Figure 4.5, we show the GWs through the collapse of the hypermassive BS state to the final remnant BH in the case of $\alpha = 0$ and $\alpha = \pi$. As pointed out above, the time of collapse is significantly different due to the accumulated nonlinear scalar (and gravitational) interactions. However, the GWs radiated during the collapse to a BH are qualitatively similar. The amplitude rapidly increases by a factor of a few and then decays. This sudden increase in amplitude is likely driven by the vortices in the hypermassive remnant being forced onto tighter orbits with higher orbital frequency just before horizon appearance. The subsequent ringdown differs somewhat from a spinning BH in vacuum due to the residual scalar matter (of mass $\sim 0.1 M_{\rm BH}$) orbiting the BH. As can be seen in the insets in the top panel of Figure 4.5, this has the effect of washing out the exponential decay of the GW amplitude. The mass and dimensionless spin parameters of the remnant BH are only slightly smaller, in the $\alpha = 0$ case compared to the $\alpha = \pi$ case. Therefore, despite the quantitatively different inspiral and merger dynamics, depending sensitively on the initial scalar phase configuration of the stars, the remnant BHs show only little memory of the initial BS binary from which they emerged. In fact, the dimensionless

spin of the remnant BHs are roughly $a_{\rm BH}/M_{\rm BH} \approx 0.7$, which is consistent with the quasi-circular merger of a non-spinning equal-mass binary BH, and the lower range of the values of $a_{\rm BH}/M_{\rm BH} \approx 0.7$–$0.8$ found for prompt collapse following a binary neutron star merger (see, e.g., Ref. [59, 99]).

In summary, we find that, during the late inspiral of a binary BS, scalar interactions, which depend on the scalar phase offset between the stars, have a significant, cumulative effect, resulting in modulations of the amplitude and de-phasing of the GWs, and affecting the merger time by hundreds of light crossing times of the system. The two stars merge into a hypermassive BS remnant that is characterized by a series of vortices orbiting rapidly around its center of mass, resulting in emitted high frequency GWs. Lastly, the hypermassive remnant collapses to a remnant BH with mass and spin which, despite the large difference in the inspiral dynamics, we find to be largely insensitive to the nonlinear scalar dynamics prior to collapse.

Here, we considered the special case of an equal frequency binary BS. Therefore, the scalar interactions in the initial binary BS are completely characterized by the scalar phase offset α between the stars. In a more complex scenario with $\omega_1 \neq \omega_2$, the different linear evolutions of both stars' phases would lead to oscillations in the nature of the scalar interactions at characteristic frequencies $\omega_1 \pm \omega_2$. The oscillatory nature of the interaction accumulates nonlinearly during the later inspiral, with the phase offset it leads to at the point of contact depending on the length of the inspiral. The value of this phase offset just before merger will likely have a strong effect on the qualitative behavior of the system after merger (when nonlinear interactions drive the dynamics), as it does in the scenario studied here. In fact, in Refs. [324, 153], it was noted that in the case of head-on collisions, the GW emission is predictably dependent on the phase-offset at early times and the point of contact. Our results, however, suggest that in the case of a BS inspiral, the nonlinear interactions prior to merger, which accumulate secularly, render a reliable prediction of the phase-offset at the point of contact challenging.

4.2.4 Remnant map

In the previous section, we demonstrated the complex dependence of the scalar and gravitational dynamics during the merger process on the binary BS parameters, in particular the scalar phase of the BSs. In order to provide a more straightforward understanding of these systems, here we outline and motive a small set of criteria, and an associated mapping, in order to guide predicting the outcome of a given merger of a binary BS, i.e., to determine whether a spinning BS, non-spinning BS, or a BH will be formed.

Details of the remnant map

Recall, within a given scalar (or vector) model, there exists a set of one-parameter families of BS (or PS) solutions $\mathbb{B}_m$ indexed by the azimuthal index m (excluding "excited" states with a higher number of radial nodes). A representative $\mathcal{B} \in \mathbb{B}_m$ (note, this is different from the notation in Chapter 3) of the one-parameter family of star solutions (for fixed m) is identified, in general, by its mass M, charge Q, frequency ω, and angular momentum J ($J = 0$ for spherical stars). Crucially however, if one restricts to the *stable* branches of a family of solutions, a particular BS (or PS) solution is *uniquely* identified by the charge alone $\mathcal{B}(Q)$.

During a binary BS (or PS) merger, energy and angular momentum will come both from the constituent stars, as well as from the orbit, and some fraction of these quantities will be carried away both by gravitational and scalar radiation. The total boson number (i.e., the $U(1)$-charge of the system), on the other hand, will only be affected by scalar radiation. We expect this to be subdominant to gravitational radiation since the scalar field is massive, and higher energy processes are required to elevate a bound boson into an asymptotically free state. Therefore we will make the approximation that the scalar charge is conserved during the merger here, but return to the implications of scalar particle loss below. Hence, a core assumption of the mapping from the binary's constituent BSs (formally, $\mathcal{B}_1 \in \mathbb{B}_{m_1}$ and $\mathcal{B}_2 \in \mathbb{B}_{m_2}$) with charges $Q_{1,2}$ into the remnant solution $\mathcal{B}_r$ of charge Q_r is charge conservation $Q_1 + Q_2 = Q_r$.

Combining the assumption of charge conservation, as well as restricting to the stable branches of the one-parameter families of solutions $\mathbb{B}_{m_{1,2}}$, enables us to introduce $\mathcal{R}_F$, which maps all properties of the merging binary BS (or PS), i.e., properties of $(\mathcal{B}_1, \mathcal{B}_2)$ into those of the remnant $\mathcal{B}_r$, formally written as

$$\mathcal{R}_F(\mathcal{B}_1, \mathcal{B}_2) = \mathcal{B}_r. \tag{4.10}$$

Since $\mathcal{B}_{1,2}$ are uniquely identified by any pair of the constituents properties (e.g., the frequencies $\omega_{1,2}$), the map $\mathcal{R}_F$ can take various explicit forms. For example, the explicit map of the frequencies of the inspiraling binary (ω_1, ω_2) into the frequency of the remnant ω_r is $\mathcal{R}_F^{\omega}(\omega_1, \omega_2) = Q_r^{-1}[Q_1(\omega_1) + Q_2(\omega_2)] = \omega_r$, using charge conservation and the inverse Q_r^{-1} of $Q_r(\omega_r)$ for a chosen family of solutions.

So far, we have not specified into which family of stationary solutions $\mathcal{B}_r \in F$ the remnant map $\mathcal{R}_F$ maps (this freedom is indicated by the subscript of $\mathcal{R}_F$). In principle, F could be *any* set of stationary solutions allowed in the scalar (or vector) theory at hand, i.e., (2.1) and (C.1), that satisfies the charge conservation assumption; for instance, a non-rotating BS, a DBS solution, a spinning BSs, etc. However, many of these possibilities can

be rejected using a series of conditions which the remnant has to approximately satisfy. Of course, it is possible that are no suitable remnant star solutions for a given binary. For example, the total charge of the binary may be above the maximum charge of any remnant non-vacuum family, $Q_1 + Q_2 > Q_r^{\max}$, in which case one may expect a BH to form. As we show below, the combination of these conditions and the remnant map (4.10) can be used to understand the outcome of even complex merger scenarios. In the following, we introduce the conditions first, and then return to a practical application of the formal map (4.10).

The first set of conditions, we call the *kinematic conditions*. The masses and angular momentum of the constituents of the binary, as well as the remaining orbital angular momentum at merger $J_{\rm orb}$, should satisfy

$$\begin{aligned} &1.\quad M_1 + M_2 \gtrsim M_r, \\ &2.\quad J_1 + J_2 + J_{\rm orb.} \gtrsim J_r, \end{aligned} \tag{4.11}$$

at the point of contact of the stars. Here, M_r and J_r are the remnant solution's total mass and angular momentum. This condition holds only for aligned-spin scenarios and here we are neglecting the correction from the orbital energy as being small.

Secondly, the *stability condition*, states that the remnant stationary solution must be free of any linear or nonlinear instability:

$$3.\quad \mathcal{B}_r \text{ is stable.} \tag{4.12}$$

Lastly, the *vortex condition* concerns the scalar phase dynamics. We conjecture that the vortex number m_r of the final remnant of the binary merger is given by the vortex number of a closed loop Γ enclosing the center of mass at the point of contact of the stars as well as all significant vortex lines of the merging binary:

$$4.\quad m_r = \frac{1}{2\pi}\oint_\Gamma d\ell_i D^i\psi. \tag{4.13}$$

By significant vortex lines, we mean to exclude, for example, those that may arise as perturbations to the constituent BSs during the inspiral (as in Fig. 4.2), though we will return to this below. Here, Γ is negatively oriented with respect to the total angular momentum[4] $J^\mu_{\rm ADM}$. These conditions are approximate, and we explicitly show below the degree to which they must be satisfied in example mergers.

[4]Note, paired with the choice of $J \to -J$ and $m \to -m$ (or $Q \to -Q$), the negative orientation of Γ with respect to the total angular momentum of the remnant is a convention.

The procedure to determine the family of stationary solutions F and identify the remnant $\mathcal{B}_r$ is as follows: *(i)* Construct $\mathcal{R}_F$ for a plausible family of remnants F, *(ii)* reject this mapping if it violates one of the four conditions listed above, and *(iii)* begin at step *(i)* with a different plausible family. Therefore, the map (4.10) is used to eliminate possibilities until the correct remnant remains. A priori, considering all plausible families F appears to be a daunting task. However, in practice, we find that only focusing on the families of non-spinning and $m = 1$ rotating isolated stars (within the considered model) suffices, with the vortex condition (4.13) efficiently discriminating between the two. For example, a DBS solution can be approximated by the sum of two non-spinning stars, particularly in the Newtonian limit (see Ref. [118]).

In Ref. [65], a similar set of criteria was considered (in particular conditions 1.–3.). However, crucially, here we add the vortex condition (4.13), and point out its vital role in the binary merger process below. Furthermore, while the "point of contact" is an ill-defined notion in the case of BSs (and PSs), the more relativistic the stars become, the easier it becomes to identify the point of contact. Similarly, the vortex condition should be regarded somewhat approximately, as we will show using examples of un-equal mass mergers of a rotating and a non-rotating BS. In the special case of a head-on collision (i.e., with exactly vanishing angular momentum), no vortex exists. Lastly, this map may be extended to PSs as well by the addition of another condition, which governs the relative *direction* of the vector fields of a given PS binary. We return to applying this remnant map to PS in Sec. 4.3.1, but leave a more detailed analysis to future work.

Applying the remnant map

We now illustrate the importance and utility of the above considerations with an example, in particular, of a binary BS where a single remnant is not formed at merger. We consider a spinning binary BS inspiral of identical $m_1 = m_2 = 1$ BSs with $\omega_1 = \omega_2 = 0.4\mu$ in the solitonic scalar model with $\sigma = 0.05$ [see (2.2)], of compactness $C = 0.12$, at an initial coordinate distance of $D = 10M_0$ and initial phase-offset of $\alpha = 0$. The orbit of the binary is set up such that $|J_{\text{orb.}}| < |J_1 + J_2|$, with $J_{\text{orb.}}$ anti-aligned with J_1 and J_2. Lastly, we note that, if the spinning binary BS initial data is prepared with a vanishing phase-offset initially, the symmetry of the binary fixes the location of a $q = -1$ vortex at the center of mass of the system throughout the inspiral. Notice that each *individual* spinning star has vortex number $m_{1,2} = 1$ (with respect to the total angular momentum).

We can now employ the remnant map (4.10), and consider possible outcomes of this inspiral. First, because of the vortex condition (4.13) with $m_r = q + m_1 + m_2 = 1$, no single non-spinning star can be formed, as that would require $m_r = 0$. Secondly, the total

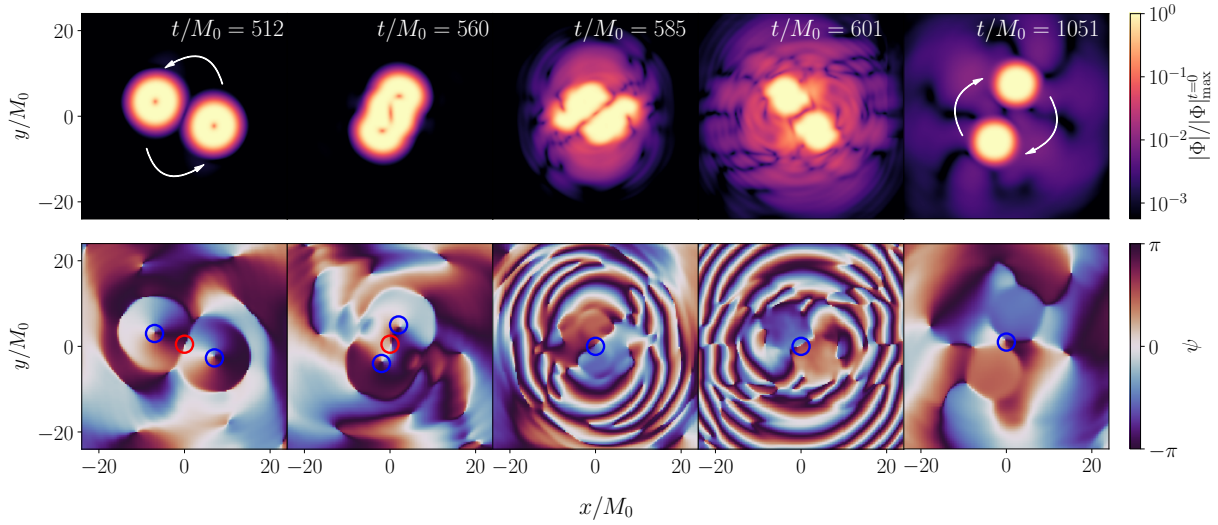

Figure 4.6: Five snapshots of the equatorial plane of the spinning binary BS inspiral discussed in Sec. 4.2.4. *(top row)* We show the magnitude of the scalar field in the equatorial plane, normalized by the initial maximum of the magnitude $|\Phi|^{t=0}_{\max}$. *(bottom row)* We present the corresponding scalar phase $\psi \in (-\pi, \pi)$. We indicate the location of all relevant $q = -1$ vortices by red circles, and all relevant $q = 1$ vortices by blue circles. (All vortex indices are measured with respect to the total angular momentum). The arrows indicate the direction of rotation of the inspiraling binary and the binary endstate.

angular momentum of the inspiraling system, $J_{\rm total} = J_1 + J_2 + J_{\rm orb.}$, is *smaller* than the angular momentum of a remnant spinning BS in the $|m_r| = 1$ family of solutions, as can be check explicitly using (4.10). Therefore, using the remnant map with (4.13) and conditions (4.11), we can already rule out that the remnant $\mathcal{B}_r$ is a single non-spinning BS or a $m_r \geq 1$ rotating BS [$|m_r| > 1$ would violate both the vortex condition and, likely, the stability condition (4.12)]. Hence, if the merger does not result in a BH, the only option is that the remnant consists of at least *two* stars. The reflection symmetry of the system with respect to the center of mass (due to the choice of identical stars with vanishing phase-offset in the initial data) suggests that the remnant is made up of an integer number of identical stars. Furthermore, as we show in Appendix C.5, a single isolated non-spinning BS is energetically favorable to a $m = 1$ spinning BS of the same charge. Therefore, two non-spinning remnant BSs are energetically favored over two spinning BSs. Finally, due to the $m_r = 1$ vortex of the remnant, the scalar phases of each non-spinning stars will be exactly out of phase with respect to each other. This implies they will be "bouncing" off each other due to the effective repulsion associated with this phase difference reviewed in Sec. 4.2.1,

analogous to the state found in [375, 281]. Lastly, the two stars (in a configuration similar to the DBS solution) will move around the common center of mass (and the $m_r = 1$ vortex) now with orbital angular momentum $J_{\rm total}$, i.e., they orbit in the *opposite* direction to the inspiraling orbit. Hence, using (4.10) we obtain a final state for the system that satisfies all of the above conditions. Therefore, using the remnant map (4.10) and the four conditions listed above, we were able to qualitatively predict large portions of the *nonlinear* dynamics of the binary system as well as the final remnant and its properties. Of course, we cannot rule out that the final state is composed of more than two stars, which, however, could be addressed in principle by considering, whether four stars as the remnant $\mathcal{B}_r$ is favored over two stars.

We confirm this picture by numerically evolving this spinning binary BS system, as shown in Figure 4.6. Before entering the regime of strong scalar interactions, i.e., for times $t/M_0 < 500$, the phases of each spinning star oscillate around the respective central vortex (marked in blue) roughly at the star's internal frequency. Notably, a $q = -1$ vortex is present at the center of mass by construction of the binary initial data (marked in red). From $t/M_0 \approx 550$ to $t/M_0 \approx 650$, the two stars interact nonlinearly, both gravitationally and through the scalar self-interaction. During this interaction, the two $m_{1,2} = 1$ vortices of the two spinning stars merge with the $q = -1$ vortex of the orbital angular momentum at the center of mass to form a single $m_r = q + m_1 + m_2 = 1$ remnant vortex fixed at the center of mass. Furthermore, the nonlinear interaction of the two spinning stars result in the formation of *two* (approximately) non-spinning BSs. This addition of vortex numbers can equivalently be understood using angular momentum conservation discussed in Sec. 4.2.1: The spin angular momenta of the two merging stars add to the *oppositely oriented* orbital angular momentum during the merger. The remnant stars are void of spin-angular momentum, such that the remaining vortex m_r must aligned with the total (and now only orbital) angular momentum. Finally, the $m_r = 1$ vortex at the center of mass remains and dictates that the two remnant stars are precisely out of phase. The latter can be seen in the last three snapshots of Figure 4.6. The outcome of the merger is a DBS solution [375, 281], however, with non-zero orbital angular momentum (implying the presence of the central $m_r = 1$ vortex). Hence, we find that this DBS state orbits around the central vortex with the remaining angular momentum (the arrows in Figure 4.6 indicating the sense of rotation about the center of mass). It is plausible that the final stationary state is a DBS solution with vanishing angular momentum (i.e., the system radiates the appropriate amount of energy and angular momentum to migrate towards a stationary DBS solution).

This explicitly demonstrates both the utility of the remnant map together with the kinematic, stability, and vortex conditions in predicting the outcome of highly nonlinear

mergers, as well as the important role the scalar interactions, in particular, the scalar phase evolution and vortex structures, play during the merger of binary BSs.

4.3 Formation of rotating boson stars

Finding a scenario where a rotating BS forms dynamically from the merger of two non-rotating stars has been an open problem. In the past, numerous attempts and configurations were considered to form a rotating BS remnant from a binary inspiral, most notably in Refs. [285, 65] (see also Refs. [280, 67, 325]). Here, we argue, that all of these attempts violate one or several of the conditions needed to form rotating BSs outlined in the previous section. In particular, we point out that the scalar phase and vortex structure play a pivotal role in forming a persistent rotating BS remnant.

To show this explicitly, we proceed by applying the remnant map and set of conditions from the previous section to this formation scenario in Sec. 4.3.1, and demonstrate by numerical evolutions in Sec. 4.3.2 that some appropriately chosen initial data satisfying these conditions do in fact lead to a rotating remnant. Hence, for the first time, we find rotating BS remnants that form dynamically from the merger of two non-spinning BSs. We then study the robustness of this formation mechanism to variations in angular momentum and scalar phase in Sec. 4.3.3, discuss the implications of these conditions on the characteristics of this new formation channel in Sec. 4.3.4, and finally, in Sec. 4.3.5 analyze the merger remnant of a binary where one BS is spinning and the other is non-spinning, showing that whether it is rotating or non-rotating depends on the binary's mass-ratio.

4.3.1 Formation criteria & parameter space

We begin by considering how the remnant map (4.10) relates two non-spinning BS solution to a $m = 1$ rotating BS solution, and in what range the kinematic and stability conditions, defined in (4.11) and (4.12) (discussed in Sec. 4.2.4), respectively, will be satisfied. We return to a discussion of the vortex condition below. To that end, we consider three different families of non-rotating stars: *(i)* a repulsive family of BSs with $\lambda/\mu^2 = 10^3$, *(ii)* a solitonic set of BSs with coupling $\sigma = 0.05$, and *(iii)* a family of non-rotating PSs (without vector self-interactions). For each of these families of solutions, a corresponding family of $m = 1$ rotating stars exists. We label the frequencies of the constituents of the initial non-spinning binary by ω_1 and ω_2 and choose, without loss of generality, that $\omega_2 \geq \omega_1$. For each combination of stationary stars (ω_1, ω_2) we use the charge conservation mapping

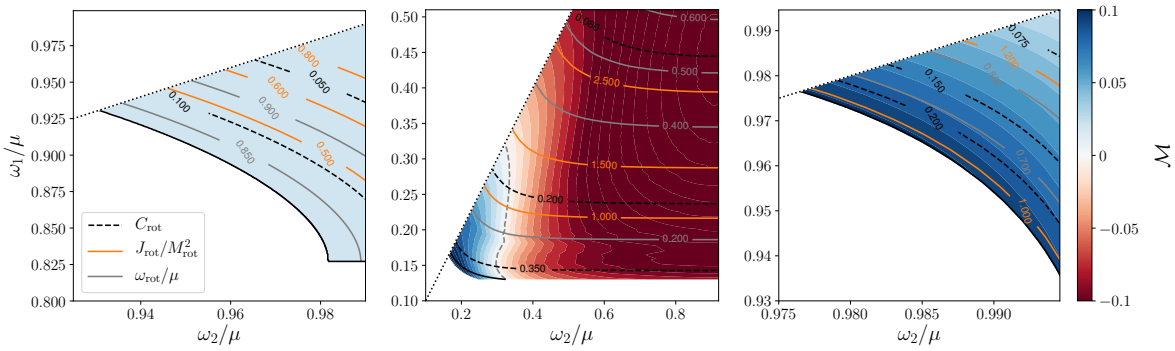

Figure 4.7: We plot the properties (dimensionless angular momentum $J_{\rm rot}/M_{\rm rot}^2$, frequency $\omega_{\rm rot}$, and compactness $C_{\rm rot} = M_{\rm rot}/R_{\rm rot}$) of a $m = 1$ rotating remnant star, assuming the remnant map (4.10), as a function of the initial non-spinning BS frequencies ω_1 and ω_2 (*contour lines*). In addition, we show the normalized mass difference $\mathcal{M} = (M_1 + M_2 - M_{\rm rot})/(M_1 + M_2)$ across the binary star parameter space (*contour plot*). Notice, the plot is symmetric under the interchange $\omega_1 \leftrightarrow \omega_2$, and we only consider the regime where $Q_1 + Q_2 < Q_{\rm rot}^{\rm max}$. *(left)* The binary parameter space in the repulsive scalar model with $\lambda/\mu^2 = 10^3$, *(middle)* the solitonic self-interactions with $\sigma = 0.05$, and *(right)* in the massive vector model without self-interactions. We explicitly restrict to only the radially stable Newtonian branches in the *left* and *right* panels, and the radially stable relativistic branch in the *middle* panel. In the *middle*, the dashed gray line indicates where $\mathcal{M} = 0$. Notice, for a $\sigma = 0.1$ solitonic scalar theory, no region with $\mathcal{M} > 0$ exists. The non-axisymmetric linear instability found in Ref. [323] is likely absent in the *right* panel; however, it is present in the *middle* for all $\omega_{\rm rot}/\mu > 0.5$, and may be present in the *left* panel for some solutions with $\omega_{\rm rot}/\mu < 0.9$, as shown in Ref. [339].

(4.10) combined with the one-to-one charge-frequency relation, $Q_r(\omega_r) \to Q_{m=1}(\omega_{\rm rot})$ for corresponding $m = 1$ family of rotating BSs (and PSs) in each of the three considered models to map all properties of the two stars in the initial binary system into the properties of a single *potential* $m = 1$ rotating remnant star.

In Figure 4.7, we show the results of the above constructed mapping for all three theories. Using this, we are able to apply the kinematic conditions to isolate the parts of the initial non-spinning binary parameter space that are suitable for the formation of a rotating remnant BS. First, we consider condition 1. in (4.11) (the kinematic condition). In order for the formation of a rotating remnant to be energetically favorable from a non-

spinning binary, we must require

$$\mathcal{M} = \frac{M_1 + M_2 - M_{\rm rot}}{M_1 + M_2} > 0. \tag{4.14}$$

Here M_1, M_2, and $M_{\rm rot}$ are the ADM masses of the stationary isolated non-spinning stars and the rotating star, respectively. From Figure 4.7, we can deduce that for models *(i)* and *(iii)*, the entire initial binary parameter space favors the formation of a rotating remnant on energetic grounds alone, while only the highly relativistic regime of the binary parameter space of model *(ii)* has $\mathcal{M} > 0$. This narrows down the possible initial binary configurations that might lead to the formation of a rotating remnant. Furthermore, for the formation, we must require that the orbit of the inspiral contains sufficient angular momentum, i.e., condition 2. in (4.11) dictates that

$$|J_{\rm orb.}| > |J_{\rm rot}|. \tag{4.15}$$

This restricts the binary orbit to a subset of all possible inspirals. In fact, as we discuss below in Sec. 4.3.3, it is not necessary for (4.15) to be strictly satisfied, and furthermore there is also an upper bound on $J_{\rm orb.}$ for the successful formation of a rotating remnant star, which we determine empirically below for an example inspiral.

According to the stability condition (4.12), the remnant rotating BS (or PS) must be a linearly (and non-linearly) stable solution. Despite the recent progress in understanding the stability properties of these rotating solutions, this is a subtle point, and we simply state that so far, no linear or nonlinear instability is known to exist in the parts of the rotating BS and PS parameter space we are interested in (see Figure 4.7 for an indication where known instabilities may be active). Finally, the last condition—the vortex condition—defined in (4.13), dictates that at the point of contact of the non-spinning binary, there must exist a $|q| = 1$ vortex in the phase in the vicinity of the center of mass of the system. This will be determined by the relative phases of the binary constituents. With these restrictions in hand, we are now able to explicitly determine whether a rotating remnant star is formed dynamically, when all the above conditions are met, in the next section.

4.3.2 Formation dynamics

Consulting the remnant map shown in Figure 4.7, we begin by constructing non-spinning binary BS initial data that satisfies the conditions of the previous section. Here, we focus exclusively on the repulsive and solitonic scalar models, with $\lambda/\mu^2 = 10^3$ and $\sigma = 0.05$, respectively, and return to a discussion of the vector case below. In order to ensure that the

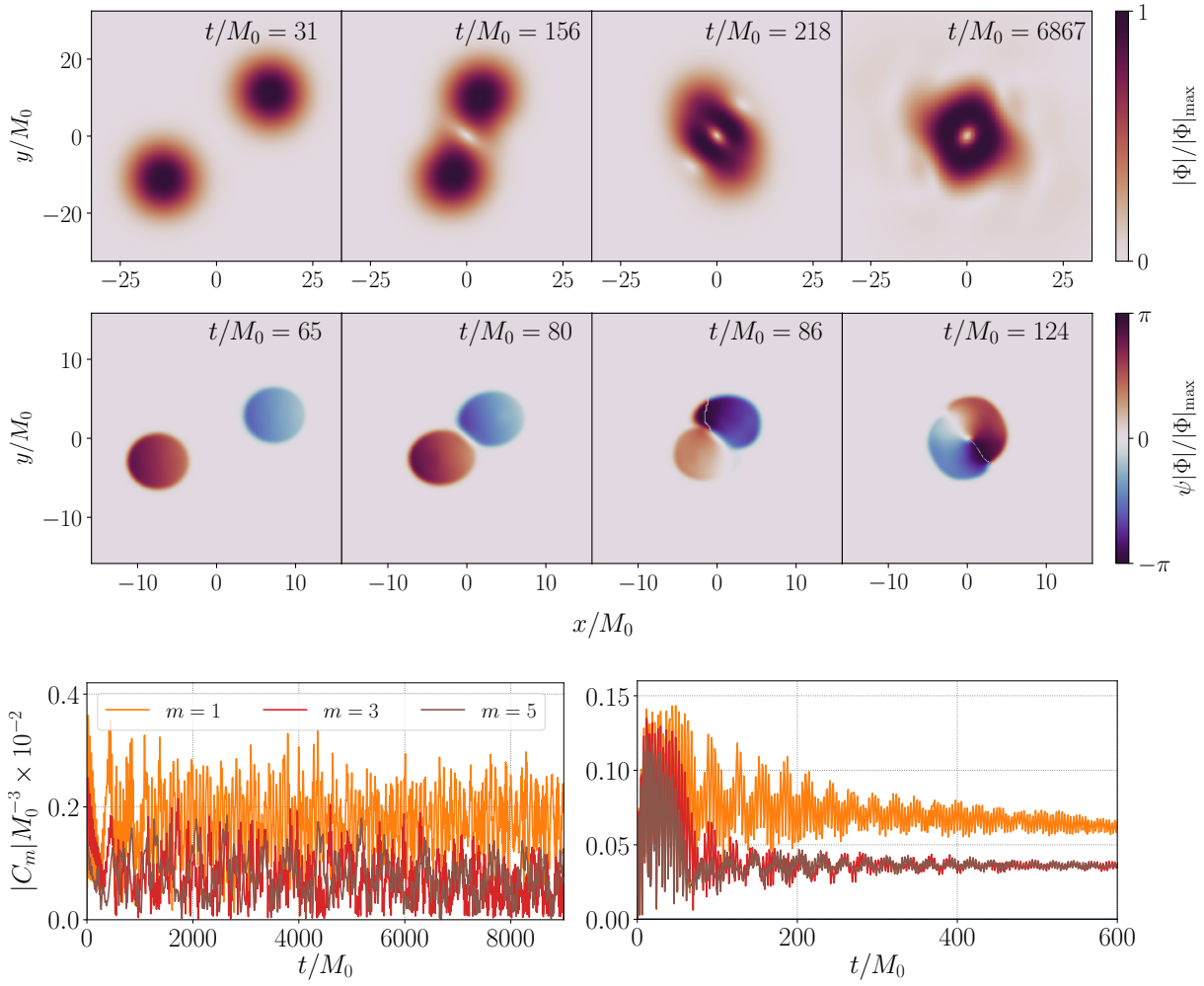

Figure 4.8: We illustrate the dynamics leading to the formation of $m = 1$ rotating BS remnants from the merger of two non-spinning BSs. *(top row)* Here, we focus on the binary star in the repulsive scalar model described in Table 4.2. We show the magnitude of the scalar field normalized by the maximum magnitude $|\Phi|/|\Phi|_{\max}$ in the equatorial plane at four different times during merger. *(middle row)* We plot the product of the scalar phase ψ and the maximum normalized scalar field magnitude $\psi|\Phi|/|\Phi|_{\max}$ in the equatorial plane at four different times during the merger. Here, we show the binary in the solitonic scalar theory with properties given in Table 4.2. *(bottom row)* The evolution of odd-m components of the azimuthal decomposition (4.16) of both binary mergers (the repulsive binary on the left, and the solitonic binary on the right). Notice, in the case of the solitonic binary, we show in Appendix C.3 that the $m = 3$ and 5 modes are dominated by truncation error at late times and converge to zero. The even–m modes are negligible throughout the evolution.

vortex condition (4.13) is satisfied at the point of contact, we restrict to a binary made up of identical stars, i.e., $\omega_1 = \omega_2 = \omega_{\rm sph}$, but with opposite initial phase, $\alpha = \pi$. The remaining characteristics of the initial data are summarized in Table 4.2. The frequency of the non-spinning stars are chosen to satisfy the kinematic and stability conditions. Specifically, comparing the properties presented in Table 4.2 with Figure 4.7, it is evident that these binaries satisfy $\mathcal{M} > 0$, and hence condition (4.14), and are in regions of the rotating BS parameter space without any known instabilities. The initial positions and velocities are set up in order to force the binary on a highly elliptical orbit and merge during the first encounter. The boost velocities are chosen to achieve sufficient angular momentum to form the rotating remnant star predicted by the remnant map: $J_{\rm rot}/M_{\rm rot}^2 = 0.56$ and $J_{\rm rot}/M_{\rm rot}^2 = 0.95$ for the stars in the repulsive and the solitonic scalar models, respectively. This ensures that condition (4.15) is satisfied at the point of contact. Finally, the center of mass of these binaries exhibits a $q = 1$ vortex throughout the evolution (measured with respect to the orbital angular momentum), by virtue of $\omega_1 = \omega_2$ and initial phase-offset $\alpha = \pi$, hence, satisfying the vortex condition (4.13). The details of the numerical construction of the constraint satisfying initial data are given in Appendix C.3.

In Figure 4.8, we show a few snapshots from the numerical evolution of the two sets of binary BSs constructed above, as well as the time evolution of the azimuthal mode decomposition of the real part, $\Phi_R = {\rm Re}(\Phi)$, of the scalar field around the center of mass, and along the angular momentum direction

$$C_m = \int d^3x \Phi_R e^{im\varphi}. \tag{4.16}$$

In the early stages of the evolution, $t/M_0 < 80$ and $t/M_0 < 150$, for the solitonic and repulsive cases, respectively, the phases of each stars evolve approximately linearly in time.

Model	$\omega_{\rm sph}/\mu$	J_0/Q_0	x_0/M_0	y_0/M_0	v_x	v_y	α
repulsive	0.95	2.12	± 15	± 10	∓ 0.06	± 0.02	π
solitonic	0.25	1.16	± 20	± 3	∓ 0.3	0	π

Table 4.2: The properties of non-spinning binary BS initial data leading to the formation of a rotating BS remnant. The two stars are identical, i.e., $\omega_1 = \omega_2 = \omega_{\rm sph}$, with initial phase offset α, are positioned at coordinate locations x_0 and y_0 (upper signs refer to the first star), and have boost velocities v_x and v_y. The initial orbital angular momentum is J_0, the ADM mass is M_0, and Q_0 refers to the initial $U(1)$-charge of the binary. The couplings are $\lambda/\mu^2 = 10^3$ and $\sigma = 0.05$ for the repulsive and solitonic scalar models, and the compactness of these stars is $C = 0.037$ and $C = 0.13$ in each of the models, respectively.

At the point of contact, the scalar and gravitational interactions are highly nonlinear. During this merger phase, the scalar matter attaches to the vortex line at the center of mass, and the system rings down to a state characterized by a single $m = 1$ mode in the scalar field—a rotating BS remnant. All other modes decay away over time. From the harmonic time-dependence of $\mathrm{Re}(C_1)$, we obtain the late-time rotating remnant frequency of $\omega_{\mathrm{rot}} M_0 = 0.78$ in the solitonic case. This is well approximated by the remnant map shown in Figure 4.7, which predicts $\omega_{\mathrm{rot}} = 0.75/M_0 = 0.22\mu$, with the difference being attributable to the (Richardson-extrapolated) charge loss of $\Delta Q/Q_0 = 0.04$ occurring during merger, as shown explicitly in Appendix C.3.

This explicitly demonstrates that, indeed, rotating BSs can be formed from the merger of two non-spinning BSs, given the conditions in Sec. 4.3.1 are met. In particular, in the following section, we show explicitly that (at least approximately) satisfying the vortex condition is crucial for successfully forming the rotating remnant. In the case of the formation of rotating PSs (instead of BSs), the vector phase may play a similarly important role. However, these solutions also possess an intrinsic preferred direction (due to the vector field), and hence, the merger dynamics might not only be governed by the vector phase, but also the vector direction.

4.3.3 Robustness of formation mechanism

Having demonstrated the dynamics leading to the formation of rotating BSs from the merger of two non-rotating stars in several cases, we now analyze the robustness of this formation channel to variations in both the total angular momentum and the phase offset of the binary. To that end, we focus on the binary BS in the solitonic scalar model we found to form a rotating BS remnant in the previous section, and vary its initial angular momentum and phase offset, while keeping all other parameters, in particular, the $U(1)$-charge, fixed. We show that there exists a set of binary BS initial data with non-zero measure that form a rotating BS remnant, demonstrating the robustness of the formation mechanism.

Variation of angular momentum

To quantify the robustness of the formation channel to variations in the binary angular momentum, we perform a series of simulations of the solitonic binary BS specified in Table 4.2 with varying initial boosts $|v_x| \in \{0.1, 0.25, 0.3, 0.35, 0.45\}$. This changes the initial angular momentum J_0 away from the value of the binary specified in Table 4.2. We evolve

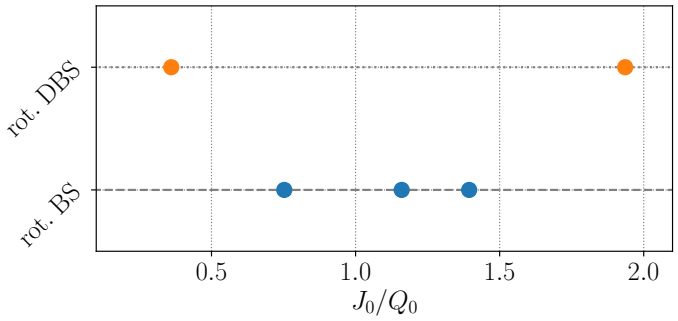

Figure 4.9: We classify the remnants of the mergers of a non-spinning binary BS into rotating DBS and rotating BS solutions as a function of the total (initial orbital) angular momentum J_0. The angular momentum is normalized by the $U(1)$-charge of the binary Q_0.

these sets of initial data through merger (see Appendix C.2 for snapshots of the evolution). In Figure 4.9, the remnant of the merger is classified as either a rotating DBS solution (consisting of two orbiting, non-spinning stars, as described in Secs. 4.2.1 and 4.2.4), or a $m = 1$ rotating BS solution. While both remnant classes posses a $|q| = 1$ vortex at the center of mass, the scalar field magnitude morphology is distinct; rotating BS solutions are stationary and exhibit toroidal surfaces of constant scalar field magnitude, in contrast to rotating DBS solutions, which exhibit two disconnected surfaces of constant scalar field magnitude[5]. Notice also, the rotating DBS remnant is *not* a stationary solution, as it continues to radiate energy and angular momentum. Consulting Figure 4.9, a variation of the initial angular momentum of up to $\Delta J_0/Q_0 \approx \pm 50\%$ still leads to the prompt formation of a rotating BS remnant[6]. However, if $|\Delta J_0|/Q_0$ is above some critical threshold (shown in Figure 4.9), then the system settles temporarily into a rotating DBS solution with long orbital period if $\Delta J_0 < 0$, and short orbital period if $\Delta J_0 > 0$. If both the initial angular momentum J_0 and total charge Q_0 of the binary system were conserved through merger, then only the initial data satisfying $J_0 = Q_0$ could form a $m = 1$ rotating remnant. However, due to scalar and gravitational radiation, both angular momentum and $U(1)$-charge may be carried away from the system resulting in the formation of a rotating BS remnant for initial data with a range of initial angular momenta. For instance,

[5]A more robust method to identify the remnants as rotating BSs (opposed to rotating DBSs) is to, for instance, explicitly check the consistency of $J_{\rm rem} = mQ_{\rm rem}$ of the remnant solution at late times (satisfied only by rotating BSs).

[6]Note, the initial angular momentum J_0 is determined using the *gauge-dependent* "ADM" angular momentum of the initial data.

based on the scalar field morphology, we find the binary configuration with $J_0/Q_0 \approx 0.75$ (shown in Figure 4.9) to settle into rotating BS after merger (see also Figure C.1). This highly perturbed remnant plausibly continues to emit residual energy and $U(1)$-charge, approaching $J/Q \approx 1$ at late times. Furthermore, the rotating DBS remnant with $J_0/Q_0 \lesssim 0.5$ may settle into a non-rotating DBS solution as suggested in Sec. 4.2.4, while the spinning DBS remnant with $J_0/Q_0 \gtrsim 1.5$ could plausibly settle into either a non-rotating DBS solution or a rotating BS as the system radiates angular momentum. Ultimately, the formation mechanism is robust against variations of binary orbital angular momentum to the degree shown in Figure 4.9.

Variations of scalar phase

Thus far, we have tested the robustness of the formation of a rotating BS from merger by varying the initial angular momentum of the binary BS's orbit, while keeping the initial scalar phase-offset between both stars fixed, i.e., $\alpha = \pi$. In this section, we fix $J_0/Q_0 = 1.16$ and instead vary the initial phase-offset between the two solitonic stars α. Hence, we considering binary mergers in the solitonic scalar model with parameters given in Table 4.2, but with different initial phases $\alpha/\pi \in [0, 63/64]$. We demonstrated in Sec. 4.3.2 that the $\alpha/\pi = 1$ case results in the formation of a $m = 1$ rotating BS remnant. The $\alpha = 0$ binary promptly leads to the formation of a *non-rotating* BS remnant, shedding all its orbital angular momentum. Hence, there exists a critical value, $0 < \alpha_{\rm crit} < \pi$, for which the remnant is marginally either a non-spinning or a rotating BS remnant.

In the bottom panel of Figure 4.10, we classify the remnants of the merger of the sequence of these binary BSs with varying initial phase into spherical and rotating BSs. We find all binaries with $\alpha/\pi \geq 7/8$ form a $m = 1$ rotating remnant at late times, while all binaries with $\alpha/\pi \leq 3/4$ result in a non-rotating BS remnant[7]. We find all remnant rotating stars persist, without further sign of instability, for the remainder of the evolutions of length $t \gtrsim 1000 M_0$.[8] Therefore, the formation scenario discussed in Sec. 4.3.1 does not require the phase offset of the merging binary to be fine-tuned, and is robust up to a phase variation of $|\Delta\alpha|/\pi \approx 0.12$ around $\alpha/\pi = 1$. In the top panel of Figure 4.10, we show a few snapshots of the evolution of the binary with $\alpha/\pi = 3/4$. In the first panel, the vortex is

[7] As another illustration of this type of behavior, we also considered the binary BS in the repulsive scalar model characterized in Table 4.2, with initial phase-offset $\alpha/\pi = 7/8$; this binary tends towards a non-rotating BS remnant at late times after merger.

[8] We note that at lower numerical resolutions, the rotating remnant formed when $\alpha/\pi \geq 7/8$ appears to have a growing perturbation that eventually ejects the central vortex from the star. However, this behavior disappears at sufficiently high resolutions. Details can be found in Appendix C.4.

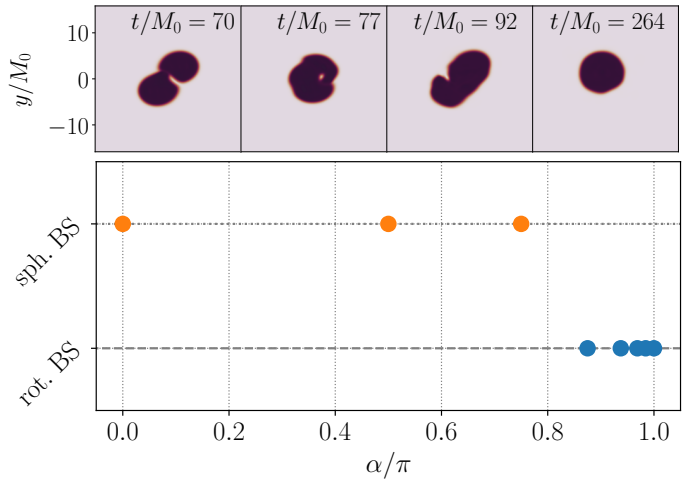

Figure 4.10: *(top)* We show the normalized magnitude of the scalar field $|\Phi|/|\Phi|^{t=0}_{\max}$ in the equatorial plane at four different times during the evolution of the binary BS merger with parameters given in Table 4.2, but with initial phase-offset $\alpha/\pi = 3/4$. *(bottom)* We classify the remnant solution of binary BSs with different values of the initial phase α into spherical or rotating ($m = 1$) BSs. We consider $\alpha/\pi \in \{1, 63/64, 31/32, 15/16, 7/8, 3/4, 1/2, 0\}$.

located to the right of the center of mass during the initial contact of the stars. The vortex then traverses the merging object in the second panel and is ejected in the third panel. The final state (fourth panel) is a perturbed non-rotating BS. This behavior is representative of all cases with $1/2 \leq \alpha/\pi \leq 3/4$. In the $\alpha = 0$ limit, any vortex present due to the non-vanishing orbital angular momentum stays *outside* the remnant star altogether.

4.3.4 Formation channel

In the previous sections, we demonstrated that rotating BSs can be formed from the merger of two non-spinning stars without fine tuning of the binary parameters for several examples. In this section, we consider more generally for what systems the approximate conditions for the formation of a rotating BS remnant listed in Sec. 4.3.1 are satisfied, and its implications for different formation channels for rotating BSs. We focus exclusively on binary mergers, and do not discuss, for example, formation of a rotating star from the collapse of coherent rotating cloud (as in, e.g., Ref. [323]).

First, from Figure 4.7, it is clear that the energy condition (4.14) is not restrictive for the repulsive scalar model and PSs (since $\mathcal{M} > 0$ across the parameter space). However, this

condition does restrict the solitonic scalar theory to a small $M_1/M_2 \sim \mathcal{O}(1)$ region in the highly relativistic part of the stable branch of the families of stars. Therefore, while in the former two models, the formation of a rotating star is possible in the entire parameter space, including the Newtonian limit, the situation is more complex in the solitonic scalar model. There, a spherical star would first have to be formed in the relativistic part of the family of BSs (i.e., in the region of parameter space in Figure 4.7 where $\mathcal{M} > 0$). If a star is formed on the Newtonian branch of the non-spinning solutions within the solitonic scalar model, then it can move towards the relativistic branch by gaining mass (e.g., through a sequence of binary BS mergers), which generically leads to a more compact, i.e., more relativistic, remnant. Once these stars have migrated to the relativistic branch, the formation of a rotating BS remnant is possible from a relativistic binary with mass-ratio close to unity.

Secondly, the stability condition (4.12) is the most restrictive, as all known $|m| > 1$ rotating BSs are linearly unstable [323, 339, 133], allowing only the formation of $m = 1$ rotating BS remnants in scalar models *with* self-interactions (i.e., in the limit of vanishing scalar self-interactions, all $m = 1$ BSs are likely linearly unstable). Furthermore, in the case of attractive scalar self-interactions (i.e., the solitonic scalar model), even the $m = 1$ BSs are linearly unstable in the Newtonian limit [133] and unstable to the ergoregion instability in the relativistic limit [160, 264], implying that in the solitonic model *only* those non-spinning stars in the relativistic part of the parameter space may form rotating BS remnants *without* ergoregions during merger. In the case of the repulsive scalar model (with sufficiently strong self-interactions), all $m = 1$ rotating BSs below the maximum mass of the family of solutions are linearly stable [339, 133]. The $m = 1$ rotating PSs were shown to be linearly stable using numerical simulations in [323], suggesting that also rotating PSs may be formed across a large part of the parameter space. The $m = 1$ rotating solutions in the repulsive scalar models and the massive vector theory exhibit ergoregions only near the maximum mass and in the strong coupling limit, only marginally affecting the parameter space in which the formation of a rotating remnant is possible.

Lastly, the angular momentum condition (4.15), restricts the types of orbits that could lead to a rotating remnant BS. In the following, we focus entirely on the equal mass limit of the inspiral binary for simplicity. In the Newtonian limit, a compact binary, composed of two point masses $M_{\rm sph}$ on circular orbits with separation d and orbital frequency $\Omega = \sqrt{2M_{\rm sph}/d^3}$, possesses orbital angular $J_{\rm orb} = \nu\Omega d^2$ with reduced mass $\nu = M_{\rm sph}/2$. Furthermore, if each compact object has a radius $R_{\rm sph}$ and compactness $C_{\rm sph} = M_{\rm sph}/R_{\rm sph}$, then the angular momentum of the binary, at the point of contact of the two objects, is $J_c = M_{\rm sph}^2/\sqrt{C_{\rm sph}}$. For a typical non-spinning neutron star, $C_{\rm sph} = 0.125$, the dimensionless orbital angular momentum at contact is $J_c/(2M_{\rm sph})^2 = 0.7$, which is roughly consistent with non-linear simulations [59, 99]. In Figure 4.11, we compare this quasi-circular orbit

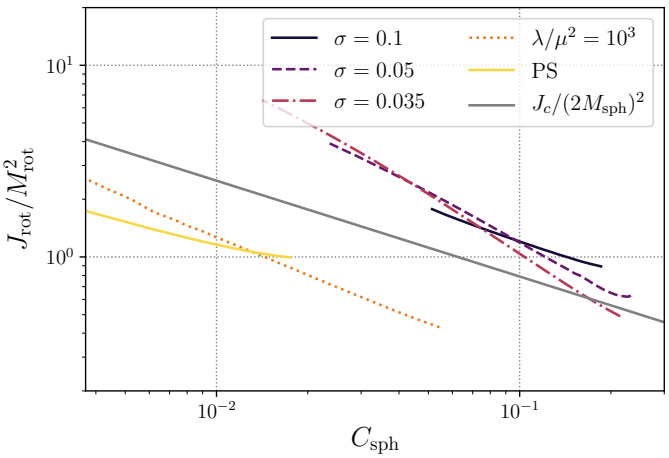

Figure 4.11: As a function of the compactness $C_{\rm sph}$ of two identical non-rotating stars in various models and couplings, we compare the dimensionless angular momentum of the corresponding $m = 1$ rotating BS and PS solution obtained using the remnant map (4.10). In particular, we compare three families of stars in the solitonic scalar model of coupling strength σ with the family of PSs, scalar BSs in the repulsive scalar model (labelled with its coupling λ), and the Newtonian quasi-circular angular momentum at the point of contact J_c, derived in the main text. We focus only on the solution branches below the maximum mass. Notice, however, that not all the solitonic cases that are plotted lie in the stable part of the $m = 1$ rotating BS parameter space.

estimate J_c to the spin angular momenta of four families of $m = 1$ BSs and the family of $m = 1$ PSs as a function of the compactness of the equal mass non-spinning binary they emerge from using the remnant map (4.10). From Figure 4.11, it is clear that the rotating non-relativistic stars (those in the repulsive scalar model and the PSs) require far less angular momentum than a quasi-circular orbit would provide, while on the other hand, the rotating relativistic stars (those in the scalar theory with solitonic potential) require far more angular momentum than a quasi-circular orbit could provide. While our estimate is purely Newtonian, and compares only the dimensionless spin at the point of contact (i.e., neglects radiation emitted during the merger process), it provides a rough estimate for the parameter space, where rotating BSs may form through quasi-circular inspirals. Therefore, from Figure 4.11 we conclude that in the solitonic and repulsive scalar models, as well as in the case of PSs, a quasi-circular orbit is unlikely to lead to the formation of a rotating remnant BS, with exceptions only in isolated and small parts of the parameter space.

Due to the non-relativistic nature of this estimate, there may be highly relativistic rotating solitonic BSs that could be formed through quasi-circular orbits, or the possibility that scalar interactions between diffuse repulsive stars radiate sufficient angular momentum during the late inspiral and merger leading to a rotating BS remnant. For instance, the binary inspiral in the repulsive scalar model shown to result in a rotating remnant BS in Sec. 4.3.2 possessed an oversupply of angular momentum, i.e., $J_0/Q_0 = 2.12$, and yet formed a (highly perturbed) $m = 1$ rotating BS remnant. This may similarly hold for merging PSs. However, it appears that the types of orbits that may robustly lead to the formation of a rotating remnant are relativistic, highly eccentric encounters of non-spinning relativistic stars in the solitonic scalar model, while only those stars with non-relativistic velocities and mild impact parameters may merge into rotating remnant PSs and BSs in the repulsive scalar model.

4.3.5 Merger of mixed spinning-non-spinning BS binaries

To further understand the formation of a rotating BS remnant from the merger of two isolated BSs, we now turn to mergers of binaries consisting of a non-spinning and a $m = 1$ spinning star. In this scenario, one can use the mass-ratio $\tilde{q} = M_{\rm rot}/M_{\rm sph}$, or equivalently the charge-ratio $\tilde{\zeta} = Q_{\rm rot}/Q_{\rm sph}$, to classify the system as an equal mass-ratio, $\tilde{q} \sim 1$, or extreme mass-ratio, $\tilde{q} \ll 1$ and $\tilde{q} \gg 1$, system. The types of BSs we consider here are perturbatively stable against known instabilities. Hence, in the $\tilde{q}, \tilde{\zeta} \to \infty$ limit, we expect the non-rotating star to be a small perturbation to the spinning star, and thus for the remnant to be spinning (i.e., the only relevant vortex line is that of the spinning star). Conversely, in the $\tilde{q}, \tilde{\zeta} \to 0$ limit, the remnant will be a non-spinning BS (hence, the vortex

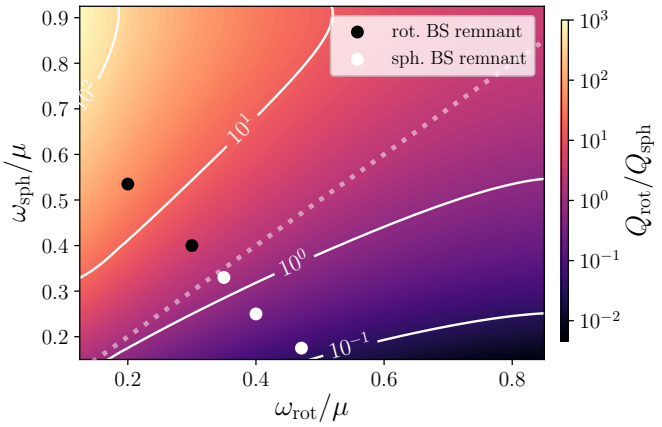

Figure 4.12: We plot the mass ratio $\tilde{q} = M_{\rm rot}/M_{\rm sph}$ (white contour lines) and charge ratio $\tilde{\zeta} = Q_{\rm rot}/Q_{\rm sph}$ (color) across the parameter space of a (superposed) binary BS consisting of a non-spinning star with frequency $\omega_{\rm sph}$ and an $m = 1$ rotating star with frequency $\omega_{\rm rot}$ in the $\sigma = 0.05$ solitonic scalar model. The dashed white line indicates where $\omega_{\rm sph} = \omega_{\rm rot}$. The mergers of binaries with parameters indicated by the black (white) points result in a single rotating (non-rotating) BS remnant.

line of the spinning star is perturbative and neglected in the vortex condition (4.13)). This is entirely consistent with the expectation based on the remnant map introduced in Sec. 4.2.4. In the intermediate regime, where $\tilde{q}, \tilde{\zeta} \sim 1$, the importance of the vortex from the spinning BS in ambiguous, and therefore, and the application of the remnant map is

$\omega_{\rm rot}/\mu$	$\omega_{\rm sph}/\mu$	$\tilde{q} = M_{\rm rot}/M_{\rm sph}$	$\tilde{\zeta} = Q_{\rm rot}/Q_{\rm sph}$
0.20	0.535	22	63
0.30	0.40	3.9	4.6
0.35	0.33	1.5	0.95
0.40	0.25	0.51	0.30
0.471	0.175	0.15	0.06

Table 4.3: The constituent BS frequencies, mass ratios, and charge ratios of the mixed spinning-non-spinning binary BS initial data discussed in the main text. The two stars have frequencies $\omega_{\rm rot}$ and $\omega_{\rm sph}$, (purely tangential) boost velocities $v_{\rm rot} = 0.85 M_{\rm sph} v_t/M_0$ and $v_{\rm sph} = -0.85 M_{\rm rot} v_t/M_0$ with $v_t = \sqrt{M_0/D_0}$, and coordinate separation $D_0 = 10 M_0$, in units of the ADM mass.

less clear. Instead of assuming the accuracy of the remnant map, here we simply perform a series of non-linear simulations of binary BSs in the solitonic scalar model with coupling $\sigma = 0.05$, covering the range of mass-ratios from $\tilde{q} = 22$ to $\tilde{q} = 0.15$. We summarize the properties of the constructed initial data in Table 4.3.

In Figure 4.12, we show the parameter space of such binary BSs consisting of one rotating and one non-rotating constituent together with the merger product of the binaries characterized in Table 4.3. By construction, the binaries merge after roughly one orbit in all cases considered. During the merger of the three cases with smallest mass-ratio, the vortex of the lighter spinning star is ejected from the system at the point of contact or shortly after. The merger dynamics become more violent with increasing initial mass-ratio, up to $\tilde{q} \sim 1$. The endstate in all three cases is a single, non-rotating star, while in the $\tilde{q} = 1.5$ case, a small scalar clump is ejected from the system similar to what was found in Ref. [65]. The two cases with largest mass- and charge-ratios merge into a single rotating BS remnant, identified by the $q = 1$ vortex at the center of the remnant star. The remnant star of the $\tilde{q} = 22$ binary persists for $t \gtrsim 600M_0$ without sign of instability, while the rotating remnant of the $\tilde{q} = 3.9$ remains non-perturbatively rotating for $t \approx 700M_0$. In the latter case, after this time in our simulation the central vortex is ejected in the same way as occurred at lower resolutions for the spinning remnant formed from the merger of non-spinning BSs described in Sec. 4.3.3 (see Appendix C.4 for details). Hence, we speculate that this is an artifact of the low resolution used to study this binary, and that at sufficiently high resolution simulations the star will remain stable after merger. However, we have not explicitly checked this for this case. In conclusion, we find that in the merger of a non-spinning and a rotating BS, the remnant is non-rotating roughly when the mass (or charge) ratio $\tilde{q} < 1$, and rotating when $\tilde{q} > 1$.

4.4 Discussion and Conclusion

In this chapter, we have studied the inspiral and merger dynamics of a large class of scalar binary BS systems in representative repulsive and attractive scalar potentials. To that end, we constructed constraint satisfying binary BS initial data using the conformal thin-sandwich approach and numerically evolved these data using the coupled Einstein-Klein-Gordon equations. We reviewed important results on the non-gravitational interactions between two Q-balls, and identified the impact of such interactions on the GW phenomenology of an inspiraling binary BS. We pointed out the pivotal role the scalar phase and vortex structure plays during the inspiral and merger process of a binary BS. In particular, in the cases we study we find that *(i)* the scalar interactions secularly accumu-

late throughout the late inspiral and drive strong de-phasing and amplitude modulations of the gravitational radiation, *(ii)* during the merger of a binary BS the GW signal is strongly affected by vortex dynamics, and that *(iii)* the nonlinear scalar interactions induce a prolonged hypermassive BS phase, and can delay the collapse to a BH by several hundred light crossing times of the remnant, though do not strongly affect the final BH's mass and spin. These findings demonstrate that, to have a consistent description of the late inspiral for such models that accurately predicts the emitted GWs, scalar interactions must be taken into account. Analogous to axion mediated forces in the inspiral of a binary neutron star considered in Refs. [200, 202, 382], the de-phasing and amplitude modulations from scalar interactions may enter at lower orders in a perturbative post-Newtonian expansion of the binary dynamics compared to tidal Love number effects, and hence, be a strong handle to efficiently distinguish binary BS mergers from binary neutron star ones. Additionally, our results suggest that predicting the GWs emitted during the nonlinear merger process (and of a potential hypermassive BS remnant) for a large class of binary constituents requires a substantial suite of nonlinear numerical evolutions, since the GW phenomenology is likely richer than even in the case of binary neutron stars, due to the star's internal scalar phase degree of freedom characterizing the merger. Lastly, if the final remnant of the merger is a BH, than the ringdown GW signal may be indistinguishable from that of a binary BH merger remnant (or a binary neutron star merger resulting in BH formation) in all but the least compact cases. If the constituent stars of the binary are less compact than typical neutron stars, then we show that accreting residual matter surrounding the remnant BH may alter the ringdown signal sufficiently to distinguish it from the typical exponential BH ringdown GW signals. On the other hand, if the remnant is a BS (spinning or non-rotating), then the ringdown signal is likely an efficient means of distinguishing the types of binaries, particularly if the total mass of the system is $M_0 \gtrsim \mathcal{O}(10)M_\odot$ (positioning the ringdown GW signal in the most sensitive band of ground-based GW detectors).

Furthermore, in this chapter, we have constructed a remnant map, augmented by several conditions, which approximately predicts the remnant star that results from a binary BS merger. We illustrated the utility of this mapping to qualitatively predict the outcome of the nonlinear dynamics of merging BSs using a particularly peculiar spinning binary BS inspiral. This inspiral results in the formation of a rotating dipolar BS solution (see, e.g., Refs. [281, 375]), as predicted by the remnant map. We also briefly commented on the implications of the remnant map on PS dynamics. We emphasize the central role of the scalar phase and vortex structure during the merger of binary BSs. In other areas of physics, vortices also play an important role, leading to phenomenology such as vortex reconnection and vortex lattices [228, 367, 330, 362]. These, and similar processes, may also arise in the context of BSs and are an interesting direction for the future. While the predictions

of the remnant map are most accurate for equal frequency stars, we find it to be a decent approximation even in more complex scenarios. However, in a few merger examples, we explicitly show the limitations of the remnant map. In particular, the classification of a vortex line as "significant" within the vortex condition is ambiguous. For instance, in the inspiral of a light spinning star and a heavy non-rotating star, the vortex line of the former must be classified as insignificant compared with the heavy companion in order for the vortex condition to be consistent with the formation of non-rotating remnant. However, as the relevant mass of the spinning star is increased, it is unclear, a priori, at exactly what mass ratio the vortex becomes significant to the remnant, and therefore there is no firm prediction for the exact threshold in the comparable mass regime where a rotating remnant will be formed. In this chapter, we primarily focused on the special case of a binary inspiral resulting in a single remnant star. However, this map could be extended to include more than two stars taking part in the merger and more than one remnant star.

Moreover, in this chapter we find, for the first time, examples where the merger of non-rotating stars results in the formation of a rotating BS. We achieve this by utilizing the remnant map paired with, in particular, the vortex condition, which is a crucial ingredient in understanding the formation of rotating BSs in mergers. We investigated the robustness of this new formation mechanism to changes in the binary's orbital angular momentum and initial scalar phase-offset, finding that variations of up to a factor of two of the orbital angular momentum and up to 12% of the initial phase-offset still result in the formation of a rotating remnant star. Hence, a large set of binary configurations may form rotating remnant stars, rather than non-spinning BSs or BHs. Furthermore, we find that quasi-circular orbits may inhibit the formation of rotating remnant BSs, since these orbits have either too little angular momentum (in the case of the solitonic scalar potential), or too much angular momentum (in the case of PSs and for stars in the repulsive scalar model considered). However, our results suggest that there may be limited regions of parameter space where a quasi-circular orbit leads to the formation of a rotating remnant star. Finally, regarding the merger remnant of a binary made up of a spinning and a non-spinning star, the mass-ratio (or charge-ratio) is a decent classifier of the remnant product: if the non-spinning star is heavier, than the remnant is a non-rotating star, while if the spinning star dominates the mass-ratio, then the remnant will be a rotating BS. We also briefly comment on the implications of the formation mechanism on PS dynamics and the formation of rotating PSs after a binary inspiral. Previous attempts at forming a rotating BS or PS remnant from the merger of two non-spinning stars have been unsuccessful, as they violated one or several of the conditions found here. The mergers of binary BSs considered in Refs. [280, 285, 67, 65] violated the vortex condition or stability condition, while the orbital PS mergers considered in Ref. [325] violated, at the least, the kinematic

and vortex conditions. Lastly, if an astrophysical population of these stars existed, then a subset of the binary inspirals may form rotating BS remnants, provided the scalar self-interactions allow it. In fact, using our results, one could quantify how many rotating boson star may be formed given the characteristics of a population of non-spinning binary stars. This formation mechanism could be used to study the inspiral, merger, and ringdown dynamics of BH mimicking ultra compact objects self-consistently in a nonlinear setting. In some cases, these rotating BS remnants are highly relativistic, exhibiting stable light rings and ergoregions. The impact of these features on the emitted gravitational waveform may be studied within these scenarios and extrapolated to a larger set of ultra compact objects.

Part II

Black hole superradiance

Chapter 5

Dark photon superradiance: Electrodynamics and multimessenger signals

Executive summary: We study the electrodynamics of a kinetically mixed dark photon cloud that forms through superradiance around a spinning black hole, and design strategies to search for the resulting multi-messenger signals. A dark photon superradiance cloud sources a rotating dark electromagnetic field which, through kinetic mixing, induces a rotating visible electromagnetic field. Standard model charged particles entering this field initiate a transient phase of particle production that populates a plasma inside the cloud and leads to a system which shares qualitative features with a pulsar magnetosphere. We study the electrodynamics of the dark photon cloud with resistive magnetohydrodynamics methods applicable to highly magnetized plasma, adapting techniques from simulations of pulsar magnetospheres. We identify turbulent magnetic field reconnection as the main source of dissipation and electromagnetic emission, and compute the peak luminosity from clouds around solar-mass black holes to be as large as 10^{43} erg/s for observationally-allowed dark photon parameter space. The emission is expected to have a significant X-ray component and to potentially be periodic, with period set by the dark photon mass. The luminosity is comparable to the brightest X-ray sources in the Universe, allowing for searches at distances of up to hundreds of Mpc with existing telescopes. We discuss observational strategies, including targeted electromagnetic follow-ups of solar-mass black hole mergers and targeted continuous gravitational wave searches of anomalous pulsars.

5.1 Introduction

As already briefly outlined in Chapter 1, ultralight fields arise in abundance in Beyond the Standard Model (SM) theories of particle physics. The most well-known and well-motivated such particle is the QCD axion [369, 372], proposed to solve the discrepancy between the observed and predicted magnitude of the neutron electric dipole moment arising from CP violation in the strong sector of the SM [292]. Beyond the QCD axion, light bosonic fields have been found to be ubiquitous in string theory [34, 351, 20, 172], and provide excellent candidates for the dark matter particle or a dark matter mediator [305, 10, 132, 178, 271, 31, 152, 23, 30], making this class of particles one of the most exciting candidates for new physics.

Black hole (BH) superradiance [380, 261, 348, 128, 56, 80] is a unique mechanism that enables searches for weakly interacting ultralight bosons [34, 35] that relies only on the boson's gravitational interaction. If a new light boson with Compton wavelength of order the BH horizon size exists in the theory—whether or not there is an initial abundance of the particle in the environment—the BH will spin down and source macroscopic, coherent, gravitationally-bound states of ultralight bosons [34, 35, 80]. These bosonic "clouds" carry up to several percent of the BH's initial mass, and have an energy density comparable to that of neutron star matter for stellar mass BHs [35, 145, 142]. The resulting large energy density of the cloud has time-dependent components, rotating around the BH axis at a frequency fixed by the particle mass, resulting in coherent, monochromatic gravitational wave (GW) radiation that depletes the cloud over parametrically longer times [35, 377, 33, 171].

The signatures of GW emission and BH spindown have been proposed to constrain and search for ultra-light bosons [35, 318, 289, 288, 377, 78, 33, 79, 80, 32, 141, 82, 81, 50, 142, 53, 338, 83, 384]. Bosons in the $10^{-13} - 10^{-11}$ eV range can lead to up to thousands of GW signals originating from our Galaxy alone [33, 32, 82, 81]. Blind continuous wave searches for monochromatic GW from scalar boson clouds [17, 19, 286, 120, 127, 384], as well as stochastic searches for an excess of GW power from spin-0 [364] and spin-1 [363] boson clouds around yet undiscovered BHs have been carried out with LIGO-Virgo-KAGRA (LVK) [5, 21, 36] data. These searches have produced some constraints; however, a robust underlying BH natal spin distribution is needed to conclusively exclude particle parameter space. Another search strategy is to follow up BHs with a measured mass and spin, which are newly born from binary BH mergers [32]; then the expected signals can be precisely computed, and a conclusive search performed. Directed searches for continuous GWs from a potential scalar boson cloud around Cygnus X-1 have also been carried out [350]. Currently, the sensitivity of GW searches is not sufficient to see follow-up signals from

spin-0 bosons around binary BH remnants [206], but they are promising for spin-1 bosons in upcoming observation runs, and especially in next-generation observatories [102, 342].

BH spin measurements have set constraints on ultralight bosons using measurements of BH properties from X-ray binaries [33, 93, 49, 256], as well as measurements of binary BH constituents using LVK observations [93, 272, 273]. The latter have produced constraints on spin-0 bosons of a factor of ~ 2 in mass [272, 273], and we expect slightly stronger constraints for spin-1 bosons, although such an analysis has not been carried out for the full data set. The X-ray binary measurements depend on BH accretion disk modeling, which may introduce additional systematics [239, 203]. In addition, while the gravitational interaction of the BH superradiance cloud and the accretion disk does not significantly affect the constraints [33], non-gravitational interactions of the cloud can perturb the disk dynamics, invalidating the constraints on the dark photon mass from BH spin measurements for the parameters considered in this chapter.

While the gravitational aspects of superradiance have been studied extensively, making contact with particle physics models of ultralight spin-0 or spin-1 particles can dramatically change this picture. For spin-0 axions, the relevant interaction at the next-order after the mass term is a quartic coupling (see e.g. [35, 376, 378, 182, 162]). This results in energy exchange between levels in the cloud [182, 49, 278], slowing down the spin extraction and resulting in lower-frequency gravitational waves from transitions and axion wave emission [49]. More complicated dark sectors can result in production of new dark states [50, 162, 252, 143, 144, 90]. Beyond interactions within the dark sector itself, interactions with SM particles can lead to additional energy loss channels [334], although for axion-like particles these are subdominant to the dynamics of self-interactions [49].

In this chapter, we focus on studying the effects of the lowest-order interactions one can write down for spin-1 dark photons: kinetic mixing with the SM photon [276, 199]. In the presence of such a mixing, the huge energy density of the cloud picks up a visible electromagnetic field component that interacts directly with electrons, leading to cascade production of charged particles and to the formation of a plasma. To study the plasma dynamics, we analyze an isolated, relativistic superradiance dark photon cloud, and compute the evolution of the visible electric and magnetic fields using a resistive-magnetohydrodynamic description, valid in the limit of a strongly magnetized, tenuous plasma, that we adapt from simulations of pulsar magnetospheres. See Fig. 5.1 for an example visualization of the resulting magnetic field strength around a rotating BH.

Our simulations show that the resulting system is a luminous multimessenger source: a BH system which emits an enormous electromagnetic flux, up to several orders of magnitude brighter than pulsars and magnetars. This radiation is generated by turbulent

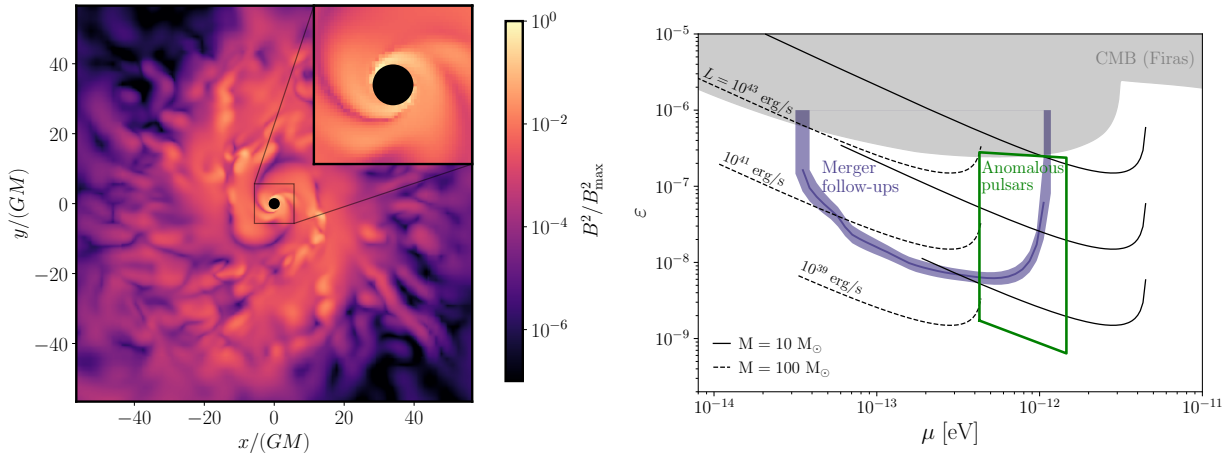

Figure 5.1: *(left)* We show the visible magnetic field strength B^2 (normalized by its maximum) in the equatorial plane of the central BH of mass M, dimensionless spin $a_* = 0.86$, and a dark photon mass $\mu = 0.3/(GM)$. The dark photon of the superradiance cloud forces the pair plasma into a circular motion resulting in magnetic field line twisting, which is released through magnetic field line reconnection, resulting in a turbulent plasma state (shown here) and efficient energy dissipation into the plasma, driving the luminous electromagnetic emissions from the system. *(right)* Kinetically mixed dark photon parameter space of interest in this chapter. The solid (dashed) black lines are contours of constant electromagnetic luminosity emitted from the superradiance cloud around a BH of mass 10 (100) $M_\odot$ and initial spin $a_* = 0.9$. The region above the blue contour is relevant for electromagnetic follow-ups of compact binary mergers, discussed in Sec. 5.7.1 (the shaded band on top of the contour is due to uncertainties on the merger rate). The area within the green contour is of interest for continuous gravitational waves searches targeted on anomalous pulsars, as described in Sec. 5.7.2. The gray shaded region is excluded by existing measurements of the CMB spectrum by COBE/FIRAS [154, 91].

field and plasma dynamics in the superradiance cloud, and is expected to have a large high-energy component. We find partial evidence for an intrinsic periodicity set by the mass of the dark photon particle, giving rise to a novel object that we call a "new pulsar." In Fig. 5.1, we show the parameter space of dark photon particles and the expected peak luminosity for illustrative BHs as a function of dark photon mass and kinetic mixing parameter.

Our results motivate a variety of novel astrophysical searches to discover these systems.

These include electromagnetic follow-ups of BH mergers that result in rotating BHs, most promising in the X-ray and radio bands. Another target is gravitational wave follow-ups of pulsars with coincident frequencies or positive frequency drifts, which could be superradiance cloud signals lasting thousands of years or more; see Fig. 5.1. In much of the parameter space, we find that the evolution of the cloud is still dominated by its gravitational dynamics, making the overall evolution free of electromagnetic modeling uncertainties. At small dark photon masses and large kinetic mixings, the electromagnetic emission has a larger power than the GWs, where we also have an exceptionally bright sources.

Some aspects of dark photon superradiance with a non-zero kinetic mixing have been explored in [92], and superradiance of the SM photon itself has been treated in [288, 70, 88, 89]. Ours is the first work to consistently take into account the dynamics of the SM plasma that is automatically generated by the kinetically-mixed cloud. The interactions with the plasma completely alter the behavior of the visible electromagnetic fields in the vicinity of the BH and the resulting signatures.

This chapter is organized as follows; in Sec. 5.2, we review gravitational spin-1 superradiance. In Sec. 5.3, we provide an executive summary of the dynamics of kinetically mixed superradiance, which we explore in detail in the subsequent sections. In Sec. 5.4, we describe the processes by which an isolated dark photon cloud generates its own plasma density. In Sec. 5.5, we study the dynamics of the coupled system of electromagnetic fields and charged currents. In Sec. 5.6, we describe the key electromagnetic emission mechanisms, including electromagnetic radiation and power dissipation in the plasma due to turbulent dynamics. In Sec. 5.7, we summarize the observational signatures and propose several detection strategies for this new class of astrophysical object, concluding and outlining future directions in Sec. 5.8.

This work spans the areas of particle physics, strong field electrodynamics, gravity, and astrophysical systems, thus introducing much notation, some non-standard; we collect definitions in App. D.7. We describe details of the numerical simulations of the superradiance cloud and electromagnetic fields and currents in App. D.1 and D.2, respectively. We present the resistive current prescription in App. D.3, the small conductivity regime in App. D.4, and aspects of the dark photon basis in App. D.5. We use the mostly-plus metric signature $(-,+,+,+)$ and natural units, with $\hbar = c = 1$ and non-reduced Planck mass $M_{\rm pl} = 1/\sqrt{G}$.

5.2 Black hole superradiance for vector fields

We begin by reviewing the BH superradiance of a massive vector (spin-1) boson that interacts predominantly through gravity. The kinetic and mass terms for this dark photon A'^{μ} are given by

$$\mathcal{L}' = -\frac{1}{4}F'_{\mu\nu}F'^{\mu\nu} - \frac{1}{2}\mu^2 A'^{\mu}A'_{\mu}. \tag{5.1}$$

We assume that the dark photon mass μ arises from the Stueckelberg mechanism [4] so in what follows, we do not discuss any dynamics that could originate from a Higgs sector [143, 144].

The superradiant instability is a purely gravitational process that can lead to the production of an exponentially large number of massive bosons around spinning BHs by extracting the BH's energy and angular momentum. The bosons occupy hydrogenic clouds characterized by a gravitational fine-structure constant $\alpha \equiv r_g\mu = GM\mu$, a principal quantum number n, and total, orbital, and magnetic angular momentum numbers j, l, and m. The total and orbital angular momentum can differ due to the boson's intrinsic spin: $j \in \{l-1, l, l+1\}$. Amongst the different cloud levels, the fastest-growing one for vector bosons is the $(j, n, l, m) = (1, 1, 0, 1)$ mode. Given its dynamical dominance, we focus for brevity exclusively on the study of this level. This will be sufficient for exploring the features that we wish to highlight in this work. The boson's energy in this level at leading-order in the gravitational coupling is given by

$$\omega \simeq \mu\left(1 - \frac{\alpha^2}{2}\right). \tag{5.2}$$

After the birth of the source BH, the number of dark photons in the cloud grows exponentially at a leading-α rate that, for our dynamically dominant mode, is set by

$$\Gamma_{\rm SR} \equiv \tau_{\rm SR}^{-1} \simeq 4\alpha^7(\Omega_{\rm BH} - \omega) \simeq 4a_*\alpha^6\mu, \tag{5.3}$$

where a_* is the BH's dimensionless spin and $\Omega_{\rm BH}$ its angular velocity

$$\Omega_{\rm BH} = \frac{1}{2}\left(\frac{a_*}{1+\sqrt{1-a_*^2}}\right) r_g^{-1}. \tag{5.4}$$

In the last equality of (5.3), we approximated $\Omega_{\rm BH} \gg \omega$ and took large-spin BHs $(1-a_*^2) \ll 1$. If, on the other hand, the BH's spin is small so that its angular velocity falls below the boson's energy

$$\Omega_{\rm BH} \leq \omega, \tag{5.5}$$

then $(j, n, l, m) = (1, 1, 0, 1)$ superradiance does not occur. Equation (5.5) implies a maximum possible value for the fine-structure constant (saturated for maximally spinning BHs)

$$\alpha \lesssim 1/2. \tag{5.6}$$

The above condition, together with the strong suppression of the superradiant rate at small α [see (5.3)] indicate that superradiance is most effective for gravitational couplings of order $\alpha \sim 10^{-1}$ or, equivalently, boson masses $\mu \sim 0.1/r_g$, which for stellar BHs corresponds to $\mu \sim 10^{-12}\,\mathrm{eV}$.

The growth of the cloud stops when sufficient spin has been extracted so that the condition Eq. (5.5) is saturated. The number of dark photons in the cloud can reach 10^{77} or more for a 10 solar mass BH, with the cloud mass

$$M_c \simeq 10^{-2}\left(\frac{\Delta a_*}{0.1}\right)\left(\frac{\alpha}{0.1}\right)M, \tag{5.7}$$

for $\alpha \ll 1$, where Δa_* is the difference between the initial BH spin and the final spin which saturates the superradiance condition. The cloud mass reaches up to 10% of the mass of the BH for large α and high initial BH spin [145]. The vector field profile around the BH, on the other hand, is given at leading order in the fine-structure constant by

$$\begin{aligned} A'_0 &= \frac{\sqrt{M_c}}{\sqrt{\pi}\mu^2 r_c^{5/2}} e^{-r/r_c} \sin\theta \sin(\omega t - \phi), \\ \mathbf{A'} &= -\frac{\sqrt{M_c}}{\sqrt{\pi}\mu r_c^{3/2}} e^{-r/r_c} \{\cos\omega t, \sin\omega t, 0\}, \end{aligned} \tag{5.8}$$

where $r_c = r_g/\alpha^2$ is the cloud's characteristic Bohr radius and we have taken the BH spin direction to lie along the z-axis. From Eq. (5.8), we see that the dark electric and magnetic fields $\mathbf{E'} \equiv -\nabla A'_0 - \partial_t \mathbf{A'}$ and $\mathbf{B'} \equiv \nabla \times \mathbf{A'}$ are in a proportion $|\mathbf{B'}|/|\mathbf{E'}| \sim \alpha$, so the cloud is electrically dominated. At leading order in α, the electric field corresponding to the potential Eq. (5.8) is unidirectional and equatorially oriented, and rotates on this plane at a frequency $\omega \simeq \mu$, while the magnetic field lines form concentric tori around the BH with a common axis perpendicular to the electric field direction and passing through the BH. Both fields decay exponentially away from the BH. We show these features in Fig. 5.2, where we present exact (in the test field limit) solutions for both the electric and magnetic fields, obtained by numerically solving the vector's equations of motion in the BH's Kerr metric. We refer the reader to Sec. 5.5 and App. D.1 for details on the simulations. We note that, close to the BH, the exact field solutions differ from the ones obtained from

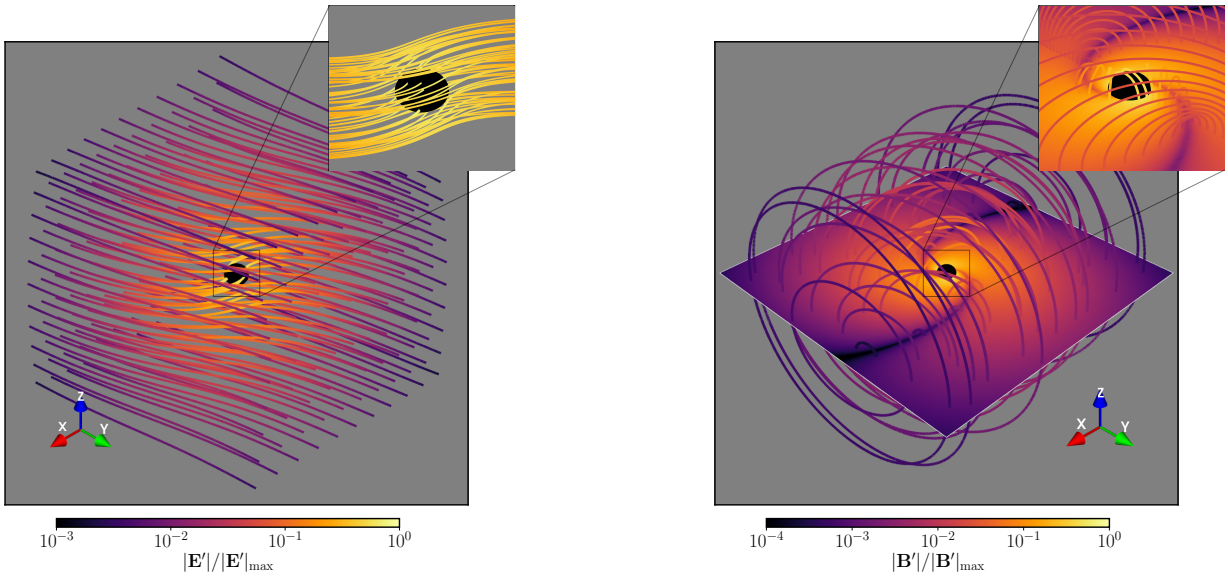

Figure 5.2: We plot representative sets of field lines of the electric *(left)* and magnetic fields *(right)* of the superradiant cloud around the central BH in Kerr-Schild coordinates (see App. D.1 for details). The $m = 1$ cloud is characterized by $\alpha = 0.3$, while the BH has a corresponding spin of $a_* = 0.86$ (further details can be found in Table D.1). The BH spin-axis points in the z-direction. Color indicates the field strength along each field line, normalized by the respective maximum field strength. On the right, we also plot the magnetic field strength inside the equatorial plane of the BH.

the approximations (5.8) due to corrections that arise at higher-order in the gravitational coupling.

Following its formation, the cloud decays via GW emission, which is the main observable signature of superradiance clouds composed of massive bosons that interact with the SM solely by gravitation. The GW emission power is given by

$$P_{\rm GW} \simeq 17 \frac{\alpha^{10}}{G} \left(\frac{M_c(t)}{M} \right)^2 \tag{5.9}$$

in the $\alpha \ll 1$ limit [50, 338]. The quadratic dependence of the emission power on the cloud mass leads to a power-law decay of the cloud set by

$$M_c(t) = \frac{M_c(t_0)}{1 + (t - t_0)/\tau_{\rm GW}}, \tag{5.10}$$

where $\tau_{\rm GW}$ is the gravitational-wave decay timescale, which is given by

$$\tau_{\rm GW} \simeq \frac{GM}{17\alpha^{11}\Delta a_*} \sim 30\,{\rm days}\left(\frac{0.1}{\Delta a_*}\right)\left(\frac{0.1}{\alpha}\right)^{11}\left(\frac{M}{10M_\odot}\right). \tag{5.11}$$

5.3 Kinetically-mixed superradiance clouds: an overview

So far, we have discussed a theory where vector bosons lack non-gravitational interactions. Going beyond this minimal setup, dark photons may interact with the SM at the renormalizable level via kinetic mixing with the SM U(1) gauge boson. In an effective theory below the electroweak scale, this interaction mixes the dark and SM photons via a Lagrangian term $\mathcal{L} \supset \varepsilon F'_{\mu\nu}F^{\mu\nu}/2$, where ε is a parameter that quantifies the mixing [276, 199]. This term can be equivalently written as a mass-mixing term by performing the field redefinition, $A'_\mu \to A'_\mu + \varepsilon A_\mu \equiv A'_\mu$, which results in the Lagrangian

$$\begin{aligned}\mathcal{L} = & -\frac{1}{4}F_{\mu\nu}F^{\mu\nu} - \frac{1}{4}F'_{\mu\nu}F'^{\mu\nu} \\ & -\frac{\mu^2}{2}A'_\mu A'^\mu - \varepsilon\mu^2 A'_\mu A^\mu + I_\mu A^\mu,\end{aligned} \tag{5.12}$$

where I^μ is the four-dimensional spacetime current. This choice of fields is referred to as the interaction basis; other choices of basis are discussed in App. D.5. Due to the mass mixing, the dark photon field acts as a source current for the visible fields and vice-versa, as can be seen either from the equations of motion

$$\nabla_\alpha F^{\alpha\beta} = -I^\beta + \varepsilon\mu^2 A'^\beta, \tag{5.13}$$

$$\nabla_\alpha F'^{\alpha\beta} = \mu^2 A'^\beta + \varepsilon\mu^2 A^\beta, \tag{5.14}$$

at leading order in the kinetic mixing parameter, or from the energy-momentum conservation relations, which manifestly show exchange of energy between the vector fields

$$\begin{aligned}\nabla_\alpha T^{\alpha\beta} &= -F^{\beta\gamma}(I_\gamma - \varepsilon\mu^2 A'_\gamma), \\ \nabla_\alpha T'^{\alpha\beta} &= \varepsilon\mu^2 F'^{\beta\gamma}A_\gamma\,.\end{aligned} \tag{5.15}$$

In the context of superradiance, the kinetic mixing term allows for the superradiance cloud to source electromagnetic fields[1]. Our objective in this chapter is to study the

[1]The induced coupling to SM electrons also results in a higher-dimensional self-interaction term for the dark photons of the Euler-Heisbenberg Lagrangian. Approximately extrapolating the results of self-interacting scalars [49], we estimate that the induced quartic coupling would start to affect the growth of the cloud for $\varepsilon \gtrsim \mathcal{O}(1)$, a value far greater than relevant for the dynamics discussed here, and that is already excluded.

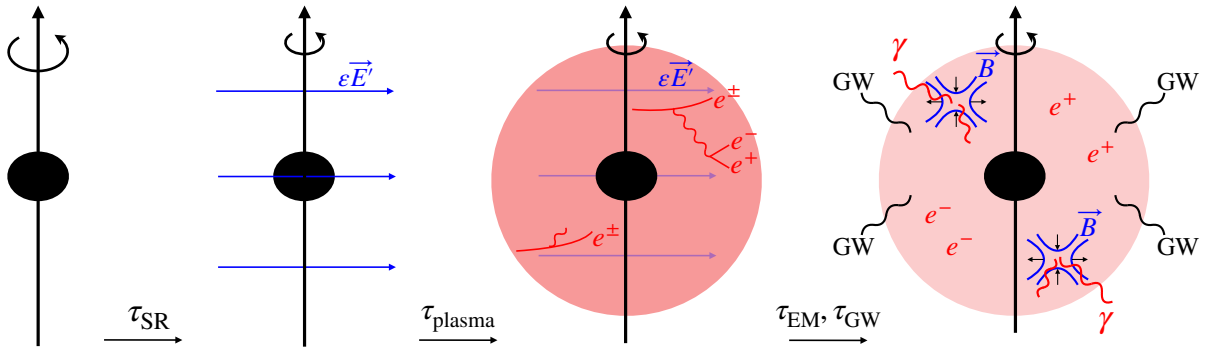

Figure 5.3: Schematic depiction of the evolution of a kinetically-mixed dark photon superradiance cloud. Starting from a spinning BH (*left*), a vector superradiance cloud forms on a timescale $\tau_{\rm SR}$ (*center-left*).The visible electric field sourced by the cloud accelerates environmental charged particles, leading to cascade production of electrons and positrons on a timescale $\tau_{\rm plasma}$; note that $\tau_{\rm SR} \gg \tau_{\rm plasma}$ and the cascade production occurs and completes before the superradiance instability completes (*center-right*). The cloud finally decays by GW emission on a timescale $\tau_{\rm GW}$, and by transferring energy to the plasma, which loses energy through electromagnetic emission on a timescale $\tau_{\rm EM}$(*right*). See text for further details.

corresponding electrodynamics, and we numerically solve Maxwell's equations with a superradiant source term in curved spacetime. This task is technically complex, but most of our results can be understood in simple physical terms, so to guide the reader through the discussion presented in the following sections, we will begin here by providing a simplified overview of our findings.

The evolution of a kinetically-mixed dark-photon superradiance cloud can be separated into several stages that are schematically depicted in Fig. 5.3. Starting with a spinning BH (leftmost panel), these stages correspond to the initial growth of the cloud (center-left panel), creation of a conducting plasma via particle acceleration and pair-creation due to the visible electric field induced by the cloud (center-right panel), and the establishment of an electromagnetic field and plasma configuration, which decays as the plasma radiates electromagnetically and the cloud emits GWs (rightmost panel). The initial growth of the cloud was reviewed in Sec. 5.2 for non-interacting dark photons. From Eq. (5.14), we see that the inclusion of kinetic mixing affects the dynamics of the superradiance cloud at order ε, which in turn leads to effects at order ε^2 in the visible fields via Eq. (5.13). Here, we will limit ourselves to computing the visible fields at leading (linear) order in ε, so in what follows we ignore the effects of kinetic mixing on the growth of the superradiance

cloud. Thus, the evolution of the cloud is governed purely by the gravitational dynamics as in the previous section (with a growth timescale $\tau_{\rm SR}$ given by Eq. (5.3)), and we may move on to the description of the creation of the plasma by the cloud-induced electric field. See also the text below Eq. (5.27) for a discussion of the negligible sub-leading corrections to the dark photon mass.

As discussed in Sec. 5.2, the cloud is dominated by an equatorially-oriented dark electric field, with a direction that rotates in the equatorial plane at frequency $\mu/(2\pi) \sim 10^2\,\text{Hz}\,(\mu/10^{-12}\,\text{eV})$. Due to kinetic mixing, the superradiance fields act as a source term in the visible field equations of motion, Eq. (5.13), and induce a visible electric field that is equal to the dark electric field times the mixing parameter. As the cloud grows through superradiance, the visible field grows concurrently. A fully-formed cloud would, in the absence of charged particles, have a visible electric field of magnitude

$$\begin{aligned} |\varepsilon \mathbf{E}'| &\simeq \frac{\varepsilon\sqrt{\Delta a_*}\,\alpha^{5/2}\mu}{\sqrt{G}} \\ &\simeq 2\cdot 10^{13}\ \text{V/m}\,\sqrt{\Delta a_*}\left(\frac{\varepsilon}{10^{-7}}\right)\left(\frac{\alpha}{0.1}\right)^{5/2}\left(\frac{\mu}{10^{-12}\,\text{eV}}\right) \end{aligned} \tag{5.16}$$

at distances of order the Bohr radius from the BH ($r_c \sim 1/\alpha\mu$). These large fields, however, cannot be achieved due to plasma screening.

Before the cloud reaches its full size, and when visible fields are still only a fraction of the value (5.16), environmental charged particles are accelerated to ultra-relativistic velocities. As illustrated in the middle-right panel in Fig. 5.3, the rotation of the electric field with the cloud curves the charged particle trajectories, which then emit synchrotron photons. These photons, in turn, interact non-perturbatively with the background electric field and produce additional electrons and positrons. The charge acceleration and pair production processes repeat in a cascade, until a conducting plasma is created. This mechanism is reminiscent of cascade production of electron-positron pairs in the strong magnetic field around supermassive BHs described by Blandford-Znajek [69], with the important difference that our system is electrically instead of magnetically dominated. An extended discussion of the plasma creation will be presented in Sec. 5.4. The effects of the plasma on the dark photon interactions with the visible fields are discussed in App. D.5.

Once the plasma is created, the electrodynamics can be studied by encoding the microscopic particle physics in an effective conductivity σ, which allows for the computation of spatial plasma currents from the electromagnetic fields using Ohm's law,

$$\mathbf{J} = \sigma(\mathbf{E} + \mathbf{v}\times\mathbf{B}), \tag{5.17}$$

where $\mathbf{v}$ is the plasma fluid velocity. This Ohmic prescription, which will be studied in detail in Sec. 5.5, is commonly used in magnetohydrodynamics [150], and has been proposed to treat dissipative currents in pulsars [227, 180, 181, 238, 282]. Pulsar magnetospheres are highly conducting, $\sigma/\omega \gg 1$ (where ω is the plasma angular frequency), so that in the bulk of the magnetosphere electromagnetic fields are shorted out and combine to cancel the Lorentz forces entering Eq. (5.17), resulting in a so-called "force-free" system that is mostly dissipationless [171, 68, 257]. Dissipative effects, however, do arise on specific two-dimensional planes called current sheets of thickness $\sim 1/\sigma$, which may be modelled using Eq. (5.17).

Our kinetically-mixed superradiance cloud shares many similarities with pulsars, and due to screening is also expected to have force-free regions. In fact, from numerical simulations presented in Sec. 5.5, we will see that if the plasma is highly conducting, $\sigma/\mu \gg 1$, plasma currents effectively redistribute charge to screen the rotating electric field induced by superradiance $\varepsilon\mathbf{E}'$. This leads to charge being separated into a dipole-like distribution, with a characteristic density that at the cloud radius is approximately given by,

$$\begin{aligned}\rho &\simeq \varepsilon \nabla\cdot\mathbf{E}' \simeq \pm\frac{\varepsilon\sqrt{\Delta a_*}\alpha^{7/2}\mu^2}{\sqrt{G}} \\ &\simeq \pm 5\cdot 10^7 \mathrm{cm}^{-3}\sqrt{\Delta a_*}\left(\frac{\varepsilon}{10^{-7}}\right)\left(\frac{\alpha}{0.1}\right)^{7/2}\left(\frac{\mu}{10^{-12}\,\mathrm{eV}}\right)^2,\end{aligned} \tag{5.18}$$

where the plus and the minus signs correspond to opposite ends of the dipole-like pattern. A crude, non-relativistic estimate indicates that the large magnitude of the charge density is consistent with large conductivities: for a non-relativistic collisionless plasma the conductivity is $\sigma \simeq \rho/\mu m_e$, which, using Eq. (5.18), gives $\sigma/\mu \sim 10^{12}$, where m_e is the electron mass.

Despite the utility of the pulsar analogy, the resemblance with our system is limited. First, in the absence of a plasma, the kinetically mixed superradiance cloud is electrically, instead of magnetically, dominated. Second, while in a pulsar the magnetic field is dipolar and decays away from the neutron star, in Sec. 5.5 we will show that in our system the resulting visible fields remain strong well outside of the light-cylinder $r_{\rm LC} \equiv 1/\mu$ (the radius out to which the plasma can corotate with the BH), up to the Bohr radius $r \gtrsim 1/\mu\alpha \gg r_{\rm LC}$. This means that in the bulk of our system, charges cannot move fast enough to perfectly screen the rotating source field. Electric dominance and imperfect screening suggest that in our cloud a steady-state force-free solution does not exist, unlike in pulsars where dissipative effects are confined to the current sheets. Instead, our numerical simulations, presented in Sec. 5.5, show a dynamical interplay between resistive and force-free regions where electric fields have been mostly screened.

Up to now, we have only discussed the electric field dynamics. Complementary insight into the electrodynamics can be gained by studying instead the magnetic fields induced by the plasma currents. The magnetic dynamics can be analyzed by combining Ohm's law Eq. (5.17), Faraday's, and Ampere's law (derived from Eq. (5.13)) to obtain the magnetic induction equation

$$\partial_t \mathbf{B} = \frac{\varepsilon\mu^2 \mathbf{B'}}{\sigma} + \frac{1}{\sigma}\nabla^2 \mathbf{B} + \nabla \times (\mathbf{v} \times \mathbf{B}), \tag{5.19}$$

where the first term on the right hand side accounts for the background superradiant magnetic field. The induction equation is used to study magnetic fields in a wide variety of astrophysical plasmas, where the electric displacement currents are smaller than plasma currents and can be neglected, an assumption that our simulations show to be valid. The three terms on the right-hand side of the induction equation describe different characteristic regions of the system. Closest to the BH, the superradiant driving field is large, and the first term on the right-hand side dominates the morphology of the magnetic fields. Away from the neighborhood of the BH, the magnetic field is non-trivially related to the superradiant driving fields, and the two remaining terms become dynamically relevant in a proportion set by a magnetic Reynolds number $R_m = \sigma|\mathbf{v}|\ell$, where $1/\ell$ characterizes the magnetic field gradients. In zones where $R_m \gg 1$, the last term on the right-hand side of Eq. (5.19), which represents pure field advection, is largest. The simulations presented in Sec. 5.5 show that large regions in the bulk of the plasma are dominated by advection, and are characterized by magnetic flux conservation, tight-coupling of the plasma and the magnetic fields, mostly screened electric fields, and some emission of electromagnetic radiation due to the time-dependent plasma charge and current densities.

Our simulations also show time-dependent regions, especially outside of the light-cylinder, where the plasma cannot corotate with the driving fields as advection would impose. This leads to differential rotation within the plasma and to the twisting and shearing of magnetic field lines, as well as to regions where the second (diffusive) term in Eq. (5.19) dominates due to large field gradients and/or small plasma velocities that result in $R_m \ll 1$. In these regions, we find that the interplay of advection and diffusion drives turbulent effects, such as breaking and reconnection of field lines, schematically shown in the rightmost panel of Fig. 5.3. Unscreened electric fields along the direction of plasma currents, expected from the simple kinematic arguments outlined above, are found at these sites. These electric fields lead to significant Ohmic dissipation $\mathbf{J} \cdot \mathbf{E}$, which in our simulation represent conversion of electromagnetic field energy into particle acceleration and radiation.

Our simulations thus show that dissipation is associated with magnetic field reconnection and unscreened electric fields, as in the pulsar current sheets. In contrast to the pulsar

system, however, in the kinetically mixed superradiance cloud the resistive effects are realized in dynamically evolving regions throughout the bulk of the plasma. As a consequence, while in pulsars most of the power emitted is due to the time-dependent nature of the currents in the force-free bulk, we find that in our system the comparative preponderance of dissipative effects leads to an emission power that is dominated by Ohmic losses.

Importantly, the simulations presented in Sec. 5.6.2 suggest that while increasing the conductivity reduces the size of the dissipative regions, it also increases their number, *i.e.* larger conductivities lead to "fragmentation" of the dissipative regions without changing their volumetric fraction. As a result, we find that the dissipative power tends to a σ-independent value (at large σ), allowing us to provide a prediction for the emitted power that is set entirely by the dark-photon model parameters and the BH mass. The power emitted by our system typically exceeds the emission power of pulsars by several orders of magnitude, and for clouds around stellar BHs can be as large as $L \simeq 10^{43}$ erg/s (an exact expression can be found in Eqns. (5.54) or (5.61)). We ascribe this difference to the rapid falloff of the dipolar magnetic field of the pulsar away from the neutron star, the large volume of the superradiance cloud when compared with the pulsar's emission regions $V_{\rm cloud}/V_{\rm lightcylinder} \sim 1/\alpha^3$, and to our system's dissipative features. Given the periodic rotation of the cloud, it is possible that the emitted power will have a pulsating component, and our simulations indeed show some limited evidence that supports this hypothesis (see Sec. 5.6.4). From our simulations we cannot compute the spectral decomposition of the emitted power; however, we can speculate based on results of kinetic treatments of turbulent plasmas (analogous to pulsar current sheet simulations) that charged particles will be highly boosted by the large electric fields resulting in a large component of high-energy radiation in the form of X- and gamma-rays [371, 383, 100, 101]; for further discussion see Sec. 5.6.5.

In the final stage of our system's evolution the cloud decays predominantly by gravitational-wave emission, accompanied by the novel electromagnetic emission outlined here, as depicted in the rightmost panel of Fig. 5.3. These emission channels lead to concrete observational signatures that we describe in Sec. 5.7, such as performing EM follow-up observations of compact binary mergers, searching for a population of same-frequency and/or positive-frequency drift pulsars, and targeting such anomalous pulsars with GW follow-up searches.

With this short summary in hand, we now move on to provide an in-depth discussion of the plasma and field dynamics at each stage of their evolution, starting with the production of the plasma.

5.4 Plasma production

In this section we describe the production of the conducting plasma within the superradiance cloud and determine the values of the mixing parameter ε for which a plasma is plausibly created. We identify two main processes that are crucial for the formation of the plasma, synchrotron radiation emitted by environmental electrons that are accelerated by the superradiance cloud, and subsequent photon-assisted Schwinger pair production in the background electric field. Here we estimate the rates of these two processes and show that they can effectively create the conducting plasma even for kinetic mixing parameters that are several orders of magnitude below current experimental bounds and of the region of interest for the observational prospects discussed later in this chapter. Several other mechanisms can produce charged particles in background fields and additionally contribute to the formation of the plasma, but for brevity we do not discuss them here (for a comprehensive list we refer the reader to [258]).

5.4.1 Synchrotron radiation

Any stray charged particle entering the kinetically mixed superradiance cloud will experience strong electromagnetic forces. Since the cloud's magnetic field is subdominant, $|\mathbf{B}'| \sim \alpha|\mathbf{E}'| < |\mathbf{E}'|$, we simply consider the motion of $e^{\pm}$ accelerated by the electric field (equivalently we can perform a boost into a frame with vanishing magnetic field and electric field amplitude reduced by a factor of $1-\alpha \simeq 1$). Inside a fully grown cloud (at distance r such that $r_g \ll r \lesssim 1/\alpha\mu$) the electric field has approximately constant amplitude given by Eq. (5.16) and rotates with angular velocity $\omega \simeq \mu$. The electrons/positrons are then approximately linearly accelerated over a time scale of $1/\mu$, reaching a maximum boost factor of

$$\begin{aligned}\gamma_e &\simeq \frac{e\varepsilon|\mathbf{E}'|}{m_e\mu} \simeq e\varepsilon\alpha^{5/2}\sqrt{\Delta a_*}\frac{M_{\rm pl}}{m_e} \\ &\simeq 10^{12}\left(\frac{\varepsilon}{10^{-7}}\right)\left(\frac{\alpha}{0.1}\right)^{5/2}\left(\frac{\Delta a_*}{0.1}\right)^{1/2}, \end{aligned} \tag{5.20}$$

where in the first line we made use of Eq. (5.16). As the electric field rotates, the electron/positrons trajectories bend with approximate radius of curvature $r_c \simeq \gamma_e m_e/(e\varepsilon|\mathbf{E}'|) \simeq 1/\mu$. During this circular motion the charged particles radiate synchrotron photons, predominantly at frequency $\omega_{\rm syn} = \gamma_e^3/r_c \simeq \gamma_e^3\mu$. We can estimate the rate for synchrotron

emission at this frequency as $P_{\rm syn}/\omega_{\rm syn}$, which gives

$$\Gamma_{\rm syn} \simeq \frac{2}{3}\frac{e^2\gamma_e}{r_c} \simeq \frac{2}{3}\frac{e^3\varepsilon|\mathbf{E}'|}{m_e} \simeq \frac{2}{3}e^3\varepsilon\,\alpha^{5/2}\sqrt{\Delta a_*}\mu\frac{M_{\rm Pl}}{m_e}, \tag{5.21}$$

where again, in the last equality we used (5.16). In order for the plasma to be phenomenologically relevant it must be created before the cloud is depleted by gravitational wave emission, on a timescale given by Eq. (5.11). To ensure that this occurs, we impose the sufficient requirement that the synchrotron and photon-assisted pair production rates (discussed in the next section) occur before any particle can escape the cloud, *i.e.*, that the synchrotron and pair-production timescales are shorter than the light-crossing time of the cloud, $1/\alpha\mu$, which is much smaller than the GW decay time (5.11). For the synchrotron emission rate of Eq. (5.21), this leads to the requirement

$$\varepsilon > \frac{1}{e^3\,\alpha^{5/2}\sqrt{\Delta a_*}}\frac{m_e}{M_{\rm Pl}} \simeq 10^{-18}\left(\frac{0.1}{\alpha}\right)^{5/2}\left(\frac{0.1}{\Delta a_*}\right)^{1/2} \tag{5.22}$$

As evident from Eq. (5.20), the above requirement also ensures that the accelerated electrons are highly relativistic ($\gamma_e \gg 1$).

5.4.2 Photon assisted Schwinger pair production

A static electric field can decay to electron-positron pairs through quantum tunneling, a process known as Schwinger pair production. The probability of scalar $e^\pm$ pair creation was first computed in Schwinger's seminal work [331], from vacuum decay in an external, slowly varying electric field $\mathbf{E}$. The rate per unit volume V is given by

$$\frac{\Gamma_{e^\pm}}{V} = \frac{(e|\mathbf{E}|)^2}{4\pi^3}\sum_n^\infty \frac{1}{n^2}\exp\left(-\frac{\pi m_e^2}{e|\mathbf{E}|}n\right), \tag{5.23}$$

and is exponentially suppressed for electric fields below the critical value $m_e^2/e \simeq 10^{18}$ V/m. Even the large electric field generated by the dark photon superradiance cloud, given in Eq. (5.16), falls short by a few orders of magnitude, making Schwinger pair production unlikely in our setup. However, pair creation can be greatly enhanced in the presence of highly energetic photons [329], such as the synchrotron photons described in the previous section. Photon assisted Schwinger pair production is similar to magnetic pair production [151] invoked in Blandford-Znajek processes [69], where radiation with energy above the threshold $2m_e$ can produces electron-positron pairs by scattering off of strong magnetic field.

Photon-assisted Schwinger pair creation can be viewed as a semiclassical tunneling process and the production rate has been computed with methods similar to the one used for metastable vacuum decay in Ref. [110]. The exponential factor in the rate is given by e^{-S_B}, where S_B is the Euclidean action evaluated on the bounce solution (the classical trajectory that extremizes the action). In our case [262, 139]

$$S_{\rm B} = -\gamma_\theta + \left(\frac{2m_e^2}{e\varepsilon|\mathbf{E}'|} + \frac{e\varepsilon|\mathbf{E}'|}{2m_e^2}\gamma_\theta^2\right)\arctan\frac{2m_e^2}{e\varepsilon|\mathbf{E}'|\gamma_\theta}, \tag{5.24}$$

where $\gamma_\theta = \sin\theta\ m_e\omega_\gamma/(e\varepsilon|\mathbf{E}'|)$, ω_γ is the photon frequency, and θ is the angle between the direction of the photon and the background electric field. As the synchrotron photons travel in the cloud, they will encounter electric fields that are almost perpendicular to their direction of propagation within a time scale of $1/\mu$, when the production rate is maximized. As a result, for a simple estimate of the rate we can take $\sin\theta \simeq 1$.

There are two limiting cases of Eq. (5.24) depending on the photon frequency. If $\omega_\gamma \ll 2m_e$, $S_B \simeq \pi m_e^2/(e\varepsilon|\mathbf{E}'|)$, which reduces to the standard Schwinger result of Eq. (5.23). Therefore if the photon energy is below the pair production threshold, the electric field still needs to be super-critical for the process not to be exponentially suppressed. On the other hand, if $\omega_\gamma \gg 2m_e$, as is the case for most of the synchrotron photons described in the previous section, $S_B \simeq 2m_e^3/(e\varepsilon|\mathbf{E}'|\omega_\gamma)$. The additional, potentially very small, factor of $2m_e/\omega_\gamma$ significantly enhances the probability of pair production. The full expression of the rate (including the prefactor of the exponential term) is given in Ref. [139] and is larger for photons with polarization perpendicular to the electric field. For the highly energetic synchrotron photons with perpendicular polarization, we have

$$\begin{aligned}\Gamma^\gamma_{e^\pm} &= \frac{\alpha_{\rm EM}}{2\pi}\frac{e\varepsilon|\mathbf{E}'|}{m_e}\exp\left(-\frac{2m_e^2}{e\varepsilon|\mathbf{E}'|}\frac{2m_e}{\omega_{\rm syn}}\right)\\ &= \frac{\alpha_{\rm EM}}{2\pi}\frac{e\varepsilon|\mathbf{E}'|}{m_e}\exp\left[-\frac{4m_e^6\mu^2}{(e\varepsilon|\mathbf{E}'|)^4}\right].\end{aligned} \tag{5.25}$$

For cascade production to occur in our system the term in the exponential must reach a magnitude of order unity when the cloud has reached its full size (or before) so that the exponential suppression of pair-production is lifted. This translates into a minimum value for the mixing parameter $\varepsilon \gtrsim m_e^{3/2}\mu^{1/2}/e|\mathbf{E}'|$. More precisely, in what follows we impose that the pair-production rate for a fully grown cloud is faster than the light crossing time of the cloud $1/\alpha\mu$, so that the synchrotron photons split into $e^\pm$ before escaping the superradiance cloud, ensuring a cascade production of the plasma, which translates into a

minimal mixing parameter

$$\begin{aligned}\varepsilon &\gg \left(\ln\frac{\alpha_{\rm EM}\gamma_e}{2\pi\alpha}\right)^{-1/4}\frac{m_e^{3/2}\sqrt{2\mu}}{e|\mathbf{E}'|}\\ &\approx \left(\ln\frac{\alpha_{\rm EM}\gamma_e}{2\pi\alpha}\right)^{-1/4}\frac{1}{e\alpha^{5/2}\sqrt{\Delta a_*}}\frac{m_e}{M_{\rm pl}}\sqrt{\frac{2m_e}{\mu}}\\ &\simeq 10^{-10}\left(\frac{0.1}{\alpha}\right)^{5/2}\left(\frac{0.1}{\Delta a_*}\right)^{1/2}\left(\frac{10^{-12}\text{ eV}}{\mu}\right)^{1/2}\left(\frac{\log\frac{\alpha_{\rm EM}\gamma_e}{2\pi\alpha}}{20}\right)^{-1/4},\end{aligned} \tag{5.26}$$

where in the logarithmic term we made use of (5.20), and in going to the second line we used Eq. (5.16). Notice that the above requirement also guarantees that $\omega_{\rm syn} \gg 2m_e$. For kinetic mixing parameters saturating the lower bound in Eq. (5.26), plasma production will be triggered when the cloud has reached a close-to maximal size, while for mixing parameters above this lower bound the plasma will be created before the cloud has fully grown. We show the smallest values of kinetic mixing parameters that allow for cascade pair creation in the superradiance cloud as a function of dark photon mass in the left panel of Fig. 5.4.

5.4.3 Dynamics leading to a quasi-steady state

The plasma begins to be populated once the pair-production cascade initiates, which as noted previously happens when the superradiance cloud has grown to a size such that the pair-production rate becomes of the order of the cloud's Bohr radius, *i.e.* $\Gamma^{\gamma}_{e^\pm} \simeq \alpha\mu$. For this to occur and up to a logarithmic correction, the superradiant field must reach a critical value $e\varepsilon|\mathbf{E}'_{\rm crit}| \simeq \sqrt{2}m_e^{3/2}\mu^{1/2}$. The superradiant field grows to $\mathbf{E}'_{\rm crit}$ in a few superradiance times $\tau_{\rm SR} \simeq 1/4\alpha^6 a_*\mu$. After that, the plasma is created by cascade production on the much shorter light-crossing timescale, over which the superradiant field and the cascade production rates are approximately fixed to $\mathbf{E}' \simeq \mathbf{E}'_{\rm crit}$ and $\Gamma^{\gamma}_{e^\pm} \simeq \alpha\mu$ respectively[2].

During cascade production, the charge density grows exponentially as $n_e = n_e^0 \exp\left(2\Gamma^{\gamma}_{e^\pm} t\right)$, where $n_e = n_e^- + n_e^+$ is the total number density of electrons and positrons. Pair production stops when the charged plasma effectively screens the critical electric field due to charge separation, which happens when the electron number density reaches $n_e^f \simeq \varepsilon\nabla\cdot\mathbf{E}'_{\rm crit}/e \simeq \sqrt{2}\alpha(m_e\mu)^{3/2}/e^2$. Assuming that when the cascade begins we start from one single electron

[2]For simplicity, throughout Secs. 5.4.1 and 5.4.2, we use the superradiant field value at saturation, Eq. (5.16), instead of the critical field, $\mathbf{E}'_{\rm crit}$. The latter will be as large as the saturation field only for the smallest values of ε allowed, given numerically in Eqs. (5.22) and (5.26).

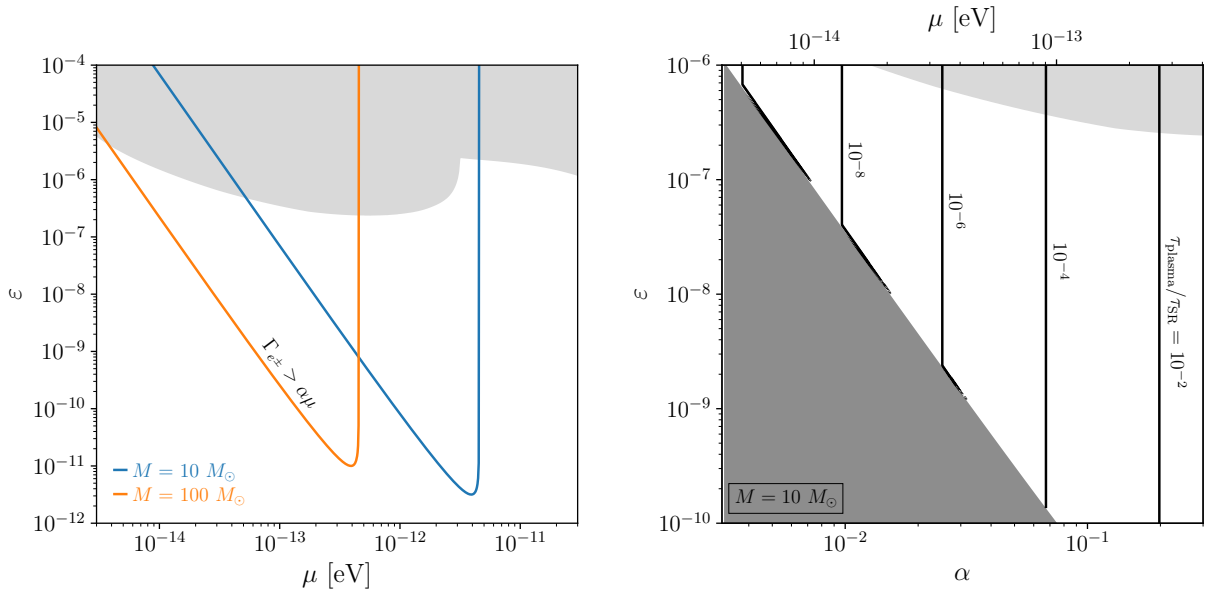

Figure 5.4: *(left)* Smallest values of the kinetic mixing parameter ε that allows for efficient $e^\pm$ pair production in the superradiance cloud as a function of dark photon mass μ, for BH masses of $10\,M_\odot$ (blue) and $100\,M_\odot$ (orange), with initial BH spin of $a_* = 0.9$. The rate for photon stimulated Schwinger pair production, given in Eq. (5.25), is required to be greater than the size of the cloud, $\alpha\mu$, when the cloud has fully grown. Smaller dark electric fields at small μ, require larger ε to initiate the cascade. The sharp cutoff corresponds to the highest dark photon mass that satisfies the superradiance condition for the fastest growing level. *(right)* Ratio of the time needed to populate the plasma over the superradiance e-folding time as a function of the kinetic mixing parameter ε and the gravitational coupling α for a BH mass of $10\ M_\odot$ and initial BH spin of $a_* = 0.9$ (the ratio is independent of M and only mildly dependent on a_*). An estimate of the ratio is given in Eq. (5.27), while in the plot $\tau_{\rm plasma}$ is evaluated using the electric field value at the time that the cascade pair production is initiated. In the dark gray shaded region, the electric field is always too small to produce $e^\pm$. When the cascade is efficient, the plasma is filled within a small fraction of one superradiance e-folding time ($\tau_{\rm SR}$ grows steeply at small α). In both panels, the light gray shaded region is excluded by measurements of the CMB spectrum by COBE/FIRAS [154, 91]

in the cloud, $n_e^0 \simeq (\alpha\mu)^3$, the plasma grows n_e^f/n_e^0 e-folds before the cascade stops, so that

the plasma formation time can be estimated as

$$\tau_{\rm plasma} \simeq \frac{1}{2\Gamma^{\gamma}_{e^\pm}} \ln\left(\frac{n_e^f}{n_e^0}\right) \simeq \frac{1}{2\alpha\mu} \ln \frac{m_e^{3/2}}{e^2\alpha^2\mu^{3/2}} \quad .$$

The plasma production time is thus parametrically shorter than the superradiance timescale by a factor

$$\frac{\tau_{\rm plasma}}{\tau_{\rm SR}} \simeq 2a_*\alpha^5 \ln \frac{m_e^{3/2}}{e^2\alpha^2\mu^{3/2}} \tag{5.27}$$

In the right panel of Fig. 5.4 we show the above ratio of timescales for the values of ε and α that satisfy the plasma pair production requirement from Eq. 5.26.

As the dark photon cloud continues to grow and the electric field increases, more charged particles will be created and the plasma will rearrange itself in the screening configuration, until $\mathbf{E}'$ has reached its maximum value Eq. (5.16) after $\approx 180\ \tau_{\rm SR}$, at which point the charge density achieves its maximal value Eq. (5.18). The numerical simulation presented in the next sections will show how charge separation in the cloud and electric screening are indeed good approximations. Note that the formation of the plasma induces a plasma mass for the SM photon ($\omega_p = e\sqrt{n_e/m_e}$), but does not significantly affect the dark photon mass. In fact, in the limit $\mu \to 0$, a massless mode must remain in the theory even in the presence of the plasma, which indicates that the leading contribution to the dark photon mass is simply μ, up to ε^2 corrections. The plasma frequency does not affect the mixing between the dark and visible photons either, nor the propagation of visible fields in the plasma, the reason being that in our system the energy density in the visible electromagnetic fields greatly exceeds the energy density in the charged $e^\pm$ plasma (by a factor $\sqrt{m_e/\mu}$), so the tenuous plasma cannot impede the propagation of the comparatively larger EM fields. This is different from the case in [138], where the EM fields are a small perturbation on top of a comparatively dense charged plasma. A more detailed discussion of plasma effects on the dark photon is presented in App. D.5. Note also that the total mass of the plasma,

$$\begin{aligned} M_{\rm plasma} \approx & \frac{m_e\rho}{e(\alpha\mu)^3} \simeq \varepsilon\alpha^{1/2}(\Delta a_*)^{1/2}\frac{m_e M_{\rm pl}}{\mu} \\ \simeq & 10^{-29} M_\odot \left(\frac{\epsilon}{10^{-7}}\right)\left(\frac{\alpha}{0.1}\right)^{1/2}\left(\frac{\Delta a_*}{0.1}\right)^{1/2}\left(\frac{10^{-12}\ \text{eV}}{\mu}\right) \end{aligned} \tag{5.28}$$

is much smaller than the mass of the cloud, $M_c = \alpha^2\Delta a_* M_{\rm pl}^2/\mu$, leaving the gravitational potential unaltered. We can then safely assume that the growth and dynamics of the superradiance cloud is not affected by the presence of the standard model plasma.

In the left panel of Fig. 5.4, we show the range of ε and μ where fast cascade production occurs and the plasma is populated, $\Gamma^{\gamma}_{e^{\pm}} > \alpha\mu$. Much slower processes can also populate this plasma in the parameter spaces where the fast cascade production is inactive. Assuming, for example, Bondi accretion and $\mathcal{O}(1)$ sound speeds c_s, it takes roughly

$$\begin{aligned}\tau_{\rm acc} = \frac{M_{\rm plasma}}{\dot{M}_{\rm Bondi}} &\approx \varepsilon\alpha^{-3/2}(\Delta a_*)^{1/2}\frac{c_s^3 M_{\rm pl}\mu}{\pi n_M} \\ &\simeq 10 \text{ years}\left(\frac{\varepsilon}{10^{-7}}\right)\left(\frac{\alpha}{0.1}\right)^{-3/2}\left(\frac{\Delta a_*}{0.1}\right)^{1/2}\left(\frac{\mu}{10^{-12}\text{ eV}}\right)\left(\frac{1/\text{cm}^3}{n_M}\right)\left(\frac{c_s}{1}\right)^3\end{aligned} \tag{5.29}$$

to populate enough charged particles inside the superradiance cloud, where n_M is the matter number density in the interstellar medium. Such a time scale suggests that for parameters where the cascade production is active, accretion from interstellar medium can be safely ignored during dark photon superradiance and plasma generation. On the other hand, in the parameter space where the cascade production is inactive, such processes can be fast enough to populate a plasma inside the superradiance cloud around isolated BHs inside our galaxy, which are most likely more than thousands if not millions of years old.

Finally, it is worth pointing out that the transient process of cascade particle production discussed in this section only produces a small and unobservable amount of emission. The transient effects discussed in [92], for example, occur when $|\mathbf{E}|^2 \sim m_e^3\mu$, which amounts to a total energy of $10^{32}(10^{-12}\text{ eV}/\mu)^2(0.1/\alpha)^3$ ergs (independent of ε). As we will demonstrate in section 5.6.2, this is about 20 orders of magnitude smaller than the total electromagnetically dissipated power from the superradiance cloud. Similarly, photon superradiance [288, 95, 70, 88, 89] will saturate long before the field strengths and energy densities in the photon superradiance cloud reaches sizes relevant for observation.

5.5 Field configurations

We have shown that a pair production cascade ensues on short timescales, once the superradiance dark photon cloud surpasses a critical electric field strength during the exponential growth of the cloud. The generated charges form a highly conducting plasma that is subject to the electromagnetic fields of the dark photon cloud. In this section, we study the macroscopic state this plasma equilibrates into. To that end, we consider, numerically, the superradiance cloud of a kinetically mixed dark photon on a fixed Kerr spacetime of mass M and dimensionless spin parameter a_*. As outlined throughout secs. 5.3 and 5.4,

it is crucial to work with an Ohm's law that accounts for the energy dissipation into the plasma inside the cloud. Building on the analytical discussions in the previous section, we first examine the structure of the visible electromagnetic fields of the cloud-plasma system on large scales. On small scales, we demonstrate that, in the high conductivity limit, turbulent dynamics emerges accompanied by efficient magnetic field line reconnection in the bulk of the dark photon cloud. Throughout the section, we study the system considering all relativistic effects of the background spacetime in the interaction basis.

We begin by introducing the plasma model in the context of a kinetically mixed massive vector field with the SM photon in Sec. 5.5.1. We establish that within this model, a quasi-stationary end state of the pair production cascade is reached and characterize its large scale behavior in Sec. 5.5.2, and small-scale dynamics in Sec. 5.5.3. In Sec. 5.5.4, we briefly summarize the main findings.

5.5.1 Plasma model

We study the kinetically mixed field equations (5.13) of the visible field A_μ in the interaction basis (5.12). A strongly magnetized, highly-conducting pair plasma, is well-described by the force-free limit of ideal magnetohydrodynamics (see, e.g., Ref. [155] for a review). Specifically, force-free electrodynamics is applicable when *(i)* resistive effects are negligible, *(ii)* the magnetic field strength is larger than the electric field's, i.e., $B^2 > E^2$, and *(iii)* the plasma mass density ρ_p and pressure P_p are much smaller than the electromagnetic energy density, i.e., $B^2 \gg \rho_p, P_p$ (see e.g., [171, 68]). In force-free electrodynamics, one can numerically evolve only the electromagnetic fields, without keeping track of the fluid quantities, with the current being uniquely determined from the electromagnetic fields by the requirement that the Lorentz force vanishes (see, e.g., Refs. [291, 226] for details on the force-free limit). In essence, $F_{\alpha\beta}I^\alpha = 0$ allows $\nabla_\beta F^{\alpha\beta} = I^\alpha$ to be rewritten as $F_{\alpha\gamma}\nabla_\beta F^{\alpha\beta} = 0$. (More details, include the equations of force-free electrodynamics in terms of electric and magnetic fields can be found in App. D.3.)

As discussed in the previous sections, the superradiant system considered here satisfies condition *(iii)* [see (5.28)], but *a priori* violates conditions *(i)* and *(ii)*. Exactly how and why these violations persist, even at large conductivities is the subject of the following subsections. However, one can already anticipate that in the limit of vanishing backreaction of the pair plasma onto the visible electromagnetic fields, the magnetic dominance is lost by virtue of the superradiant solution being electrically dominated: $B^2 = \varepsilon^2 B'^2 < \varepsilon^2 E'^2 = E^2$. Since electric dominance implies that there is no frame where the electric field, and hence the acceleration on any charges, vanishes, it is furthermore not surprising that dissipative

processes also become important. Therefore, in order to relax assumptions *(i)* and *(ii)*, we modify the force-free equations to explicitly allow for dissipation by introducing an Ohm's law with finite conductivity σ, while still requiring the current to be a function of the electromagnetic fields. This is done in such a way that, under a certain set of assumptions, the force free limit can be recovered as $\sigma \to \infty$. Slightly abusing terminology, we shall refer to this as resistive force-free electrodynamics. Several variations of this approach have been applied to simulating pulsar magnetospheres [227, 180, 238, 290, 247], and in particular the electrically dominated current sheet [238, 247], and here we generalize these to the kinetically mixed case (see also App. D.3 for more details). In the following, we will describe how we set up the coordinate system, the Maxwell equations, the fluid of charged particles and the Ohm's law in a fully relativistic simulation of the plasma of electrons and positrons inside the superradiance cloud.

Space-time decomposition: We begin by discussing how the kinetically-mixed Maxwell's equations for the visible fields can be decomposed according to a given choice of time slicing of a spacetime, which for this study will be given by the Cartesian Kerr-Schild coordinate time t. Using the (future-pointing) unit normal to slices of constant time n^μ, the visible electric and magnetic fields defined with respect to this slicing are

$$E^i \equiv n_\nu F^{i\nu}, \qquad B^i \equiv n_\nu (*F)^{i\nu} = \frac{1}{2} n_\nu \varepsilon^{i\nu\alpha\beta} F_{\alpha\beta}. \tag{5.30}$$

where $\varepsilon^{\alpha\beta\gamma\delta}$ is the Levi-Civita tensor. These are the quantities that we evolve on the BH spacetime. Projecting the kinetically mixed Maxwell equations (5.13) into components orthogonal and parallel to the time slice, one obtains the evolution equations in terms of three-dimensional spatial quantities. We give the explicit form of these equations that we use to carry out the numerical evolution in App. D.2.

In order to evolve the electric and magnetic fields, we also need to specify the electromagnetic current. The four dimensional current I^μ can be decomposed into a spatial component J^i, and a component perpendicular to the slices of constant time

$$J^i = I^i - \rho_q n^i, \qquad \rho_q = -n_\mu I^\mu, \tag{5.31}$$

where ρ_q is the Eulerian frame (i.e., with respect to the slices of constant time) charge density. We directly calculate the charge density from the divergence of the electric field,

$$\rho_q = D_i E^i - \varepsilon \mu^2 n_\mu A'^\mu, \tag{5.32}$$

using the Gauss's law constraint equation obtained from projecting the kinetically mixed Maxwell equations for the visible fields (5.13) onto the time slice. However, we still need to specify the spatial part of the current J^i.

Ohm's law: As discussed above, we introduce the effect of finite conductivity using a simple Ohm's law in the frame of the fluid (plasma)

$$j^\mu = \sigma e^\mu, \tag{5.33}$$

where j^μ and and e^μ are, respectively, the electromagnetic current and visible electric field in the fluid frame. The latter is defined in terms of the fluid velocity u^μ,

$$e^\mu \equiv u_\nu F^{\mu\nu}, \qquad\qquad j^\mu \equiv I^\mu + (u^\nu I_\nu) u^\mu, \tag{5.34}$$

in an analogous way to the Eulerian frame quantities. With this prescription, we are neglecting anisotropic magnetic field effects. However, as the superradiance cloud system is characterized by strong electric fields, this is the dominant contribution away from the force-free limit. Note that the Ohm's law (5.33) instantaneously relates currents and electric fields, a prescription that is valid for low-inertia plasmas such as ours. In eq. (5.33), the conductivity σ is a phenomenological parameter that allows for energy dissipation via mechanisms that are set by the microphysics, which is left unspecified. While without a microphysical description it is not possible to determine the value of the conductivity, we expect that the conductivity of the pair plasma considered here is large when measured in terms of the system's natural length scale (the inverse dark-photon mass), i.e., $\sigma/\mu \to \infty$ [see also a brief discussion below eq. (5.18)]. Note that in this limit, other charge transport mechanism such as diffusion due to charge gradients can be safely neglected.

The resistive relation (5.33) allows us to compute the fluid-frame currents from the visible electromagnetic fields. However, since we are not directly evolving the fluid, and in particular its velocity, this is not sufficient to give the Eulerian current entering into the evolution equations. In ideal magnetohydrodynamics (including the limiting case of force-free), given the electromagnetic fields, one can reconstruct one component of the velocity, referred to as the drift velocity

$$v^i_{d,\text{ideal}} = \frac{\varepsilon^{ijk} E_j B_k}{B^2}, \tag{5.35}$$

where here we use v^i to refer to the Eulerian spatial velocity of the fluid $v_i = -u_i/(n_\mu u^\mu)$, though not the component of the velocity parallel to the magnetic field. In our resistive extension, following [181] (see also Ref. [227]), we use a drift velocity that is augmented with an electric component to allow for electrically dominated regions to be treated self-consistently,

$$\begin{aligned} v^i_d &= \frac{\varepsilon^{ijk} E_j B_k}{B^2 + E_0^2}, \quad E_0^2 = B_0^2 + E^2 - B^2, \\ B_0^2 &= \frac{1}{2}\left[B^2 - E^2 + \sqrt{(B^2 - E^2)^2 + 4(E_i B^i)^2}\right]. \end{aligned} \tag{5.36}$$

This ensures that the drift velocity is bounded by the speed of light, even in electrically dominated regions, and is further reduced in regions with non-vanishing resistive effects, i.e., $E_i B^i \neq 0$. We note that, while the quantities above are written in terms of E and B fields, $B^2 - E^2 = F_{\mu\nu}F^{\mu\nu}/2$ and $E_i B^i = F_{\mu\nu}(*F)^{\mu\nu}/4$ are spacetime scalars.

In general, the full fluid velocity cannot be determined from the electromagnetic fields alone, without extra conditions. Here, following [238], we identify $v^i = v^i_d$, i.e., we set the non-drift velocity component to zero in the BH frame defined by n^μ. With the fluid velocity specified, we can transform (5.33) into the Eulerian frame, giving

$$J^i = \rho_q v^i_d + \sigma E_0 \sqrt{\frac{B^2 + E_0^2}{B_0^2 + E_0^2}} \left(\frac{E_0 E^i + B_0 B^i}{B^2 + E_0^2} \right) . \tag{5.37}$$

This is the kinetically mixed extension of the current considered in [238]. In App. D.3, we further discuss the advantages and limitations of this choice of current, and contrast it with other currents developed in the literature. Notice, however, this ansatz is merely a prescription to extend the regime of validity of the force-free paradigm to resistive regions (such as current sheets), which has physical meaning only in the high-conductivity limit, where $B^2 > E^2$, $E_i B^i = 0$, and $\sigma E_0 < \infty$, such that $v^i_d \to v^i_{d,\text{ideal}}$. Hence, while different choices of currents may result in different physics at moderate conductivity, for $\sigma \to \infty$ all prescripts converge towards the well-defined force-free limit. Therefore, we primarily focus on the trend towards this limit.

Numerical setup: The visible fields E^i and B^i are numerically evolved on a fixed Kerr spacetime in Cartesian Kerr-Schild coordinates. The massive vector field solutions on this background spacetime, which enter as source terms in the evolution equations, are constructed numerically (this is discussed in App. D.1). We restrict our attention to solutions where the superradiant instability has been saturated, which occurs when the cloud oscillation frequency is synchronized with the horizon frequency $\omega_R = \Omega_{\text{BH}}$. The computational domain extends from the BH horizon to spatial infinity through the use of compactified coordinates, and mesh refinement is used to concentrate resolution in the central region, enabling us to resolve the BH-cloud system sufficiently up to $r = 10 r_c$. The conductivity σ is set to be constant in space and time, as is serves merely as a proxy for the local resistivity present in the cloud. In light of the lack of a microphysically motivated conductivity, and the success of analogous choices in the case of the pulsar magnetosphere (see e.g., [238]), this choice, while unphysical, is a first step towards a more complete analysis. We also note that, any choice of spatially dependent conductivity that varies on a macroscopic length scale likely results in similar qualitative and quantitative behavior of the system.

This follows provided the system's state is independent of conductivity for sufficiently high values, because resistive features (magnetic reconnection, energy dissipation, etc.) are active on scales below the macroscopic scales of the system. Finally, we evolve the system of equations forward in time using a higher-order explicit Runge-Kutta algorithm. The limitations of this choice in the context of stiff equations in the large conductivity limit, as well as further details of the numerical methods, are discussed in App. D.2. We evolve the system, starting from suitably chosen initial data, for a sufficiently long period of time ($\sim 200/\mu$ or longer) such that it relaxes towards an approximate equilibrium, as measured by the Poynting flux at large radii becoming nearly constant. Details are given in App. D.2.

5.5.2 Field solutions: Large scale behaviors

In the following, we demonstrate how in the quasi-steady state solution, the strong electric field of the superradiance cloud is mostly screened by locally produced charges at large conductivities, and the visible magnetic field begins to play an important role in the system. As noted above, the physical value of the plasma conductivity σ will be set by a microphysical scale (due to scattering, synchrotron radiation, pair production and annihilation, etc.) that we expect to be much smaller than the other physical length or time scales in the system that we consider (e.g., $1/\mu$). However, due to numerical limitations, we only consider values up to $\sigma/\mu = 20$. Therefore, in order to make qualitative and quantitative statements about the properties of the quasi-endstate, we proceed by discussing the behavior of the system as a function of conductivity, focusing primarily on $\sigma/\mu \geq 1$ (though we include the low-conductivity limit in App. D.4 for completeness), and extrapolate trends towards $\sigma \to \infty$ if possible. This is the approach typically used to study resistive effects in pulsar magnetospheres [238, 290, 247]; we discuss possible shortcomings of these methods below.

We begin by considering the behavior of the visible electric field E^i of the quasi-stationary endstate of the pair cascade as function of conductivity in Figure 5.5. In the vacuum limit, $\sigma/\mu = 0$, there is no electric field generated by a charged plasma, and the depicted field lines are just an equatorial slice of the electric field $E^i = \varepsilon E'^i$ shown in Figure 5.2. For $\sigma/\mu \geq 1$, the main qualitative feature, as summarized in Sec. 5.3, is the buildup of the dipolar screening charge density leading to a significant reduction of the visible electric field compared to the vacuum case. As the conductivity increases, this suppression of E^2 grows and the component of E^i along the BH spin-axis becomes more important, as $E^z/E \sim \mathcal{O}(1)$ in the $\sigma/\mu = 20$ panel of Figure 5.5.

Another important qualitative feature we find is that the visible electric field exhibits a global de-phasing of $\pi/2$ with respect to the dark electric field at large conductivities.

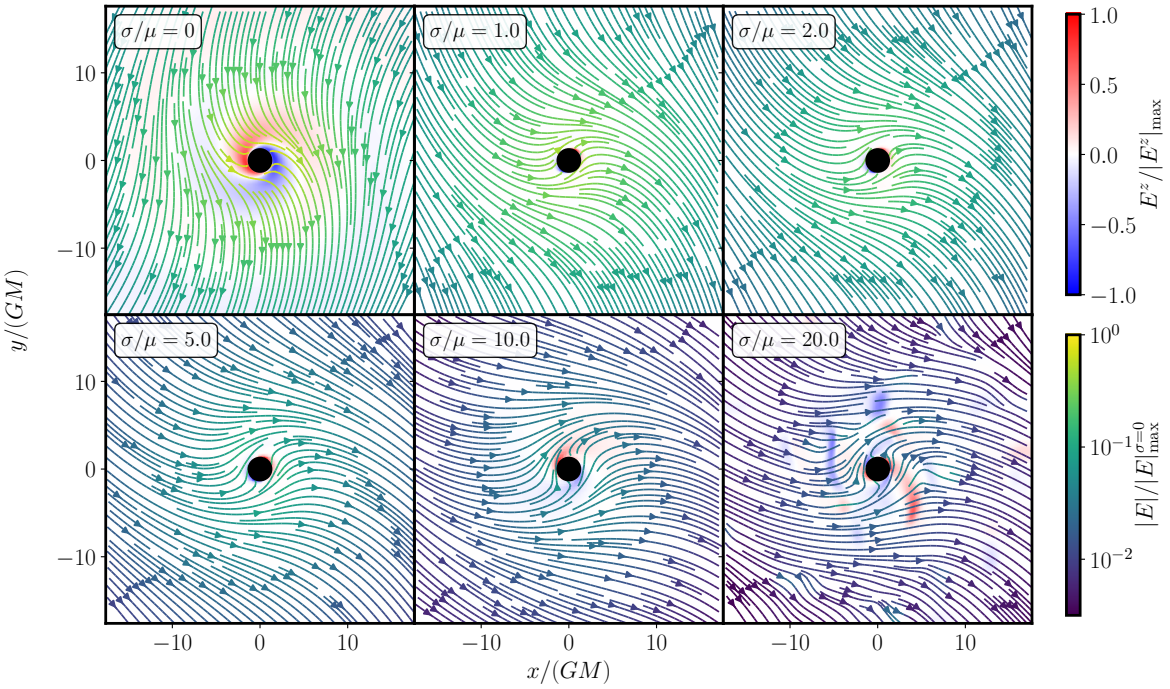

Figure 5.5: We show the visible electric field geometry, E^i, and magnitude as a function of the plasma conductivity σ in the equatorial plane of the BH. The superradiance cloud's phase is the same in each panel. Color (red/blue) correspond to the magnitude of the component along the spin axis, i.e., in the z-direction, normalized by the maximal magnitude of that component at the given conductivity. Field lines are projections of the electric field onto the equatorial plane, while the color of the field lines (yellow/green) indicates the magnitude of the visible electric field normalized by the maximal magnitude at $\sigma = 0$. The BH and cloud parameters are as in Figure 5.2, i.e., $\alpha = 0.3$ and $a_* = 0.86$. With increasing conductivity, the electric field magnitude decreases compared with the vacuum limit, and $E^z/E \sim \mathcal{O}(1)$ for $\sigma/\mu = 20$. The field geometry undergoes a phase-shift of $\pi/2$ between vacuum and large conductivity limits.

This de-phasing can be understood analytically in the non-relativistic limit, $\alpha \ll 1$. In this limit, a spatial derivative, which is set by the inverse cloud size ($\nabla \sim \alpha\mu$), is much smaller than the time derivative ($\partial_t \sim \mu$). For electric fields with similar or larger strengths compared to the magnetic field, as indicated by our numerical simulations at small and moderate conductivities (see Figure 5.7 below), the Maxwell equations in the interaction

basis (D.8) reduce to

$$\partial_t E^i \approx -\sigma E^i + \varepsilon \mu^2 A'^i, \tag{5.38}$$

where we assume the same Ohm's law as before in (5.33). With the non-relativistic superradiant field solutions A'_i in (5.8), we see that the visible electric field is driven towards the inhomogeneous solution

$$\mathbf{E} \propto \begin{pmatrix} \sigma + i\mu \\ \mu - i\sigma \\ 0 \end{pmatrix} e^{-i\omega t} + c.c. \tag{5.39}$$

over timescales of $1/\sigma$. Hence, as conductivity increases towards $\sigma \sim \mu$, the visible electric field direction rotates with respect to a fixed superradiance cloud phase, such that at large conductivities, $\sigma/\mu \gg 1$, the visible and superradiant electric fields exhibit a phase-offset of $\pi/2$. Notice, however, at very large conductivity, this analytic approximation, in principle, is no longer valid, as it neglects the magnetic field effects, which become important as the electric field is screened, for $\sigma/\mu \gg 1$. These effects induce the appearance of small scale structures visible in the last panel of Figure 5.5. We will elaborate on the break down of this approximation and the emergence of small scale features in more detail in Sec. 5.5.3.

As the conductivity grows, the electric field decreases in amplitude and the magnetic field plays a more important role. The field line geometry and magnitude of the visible magnetic fields are shown as a function of conductivity in Figure 5.6. At vanishing σ, the solutions are identical to the vacuum solution, and the snapshot in Figure 5.6 simply represents a slice of the geometry shown in Figure 5.2. The magnetic null line (i.e., where $B^i = 0$) crosses this slice once on either side of the BH as they spiral away from the BH. The field lines close around this null line, and the magnetic field strength is largest close to the BH and decays exponentially towards spatial infinity. In the vacuum limit, the dark photon field exhibits an exact helical symmetry about the BH spin-axis[3]. For $\sigma = \mu$, the magnetic field pattern still exhibits this helical symmetry approximately on the spatial scales depicted in Figure 5.6. This symmetry is broken for $\sigma/\mu > 1$. Therefore, the last two snapshots of Figure 5.6, while representing the magnetic field geometry qualitatively, are not indicative of the full three-dimensional field geometry. Qualitatively, at large conductivities, the plasma turns into a highly conducting pair plasma attaching to the visible magnetic field lines. This implies a differential rotation of the magnetic field lines

[3]The helical Killing field is $k^\mu = \xi^\mu - \Omega_{\rm BH}\varphi^\mu$ in terms of the stationary and axisymmetric Killing vectors. The superradiant field A'_μ strictly retains this symmetry, at leading order in the kinetic mixing, i.e. $\mathcal{L}_{\mathbf{k}} A'_\mu \sim \mathcal{O}(\varepsilon^2)$.

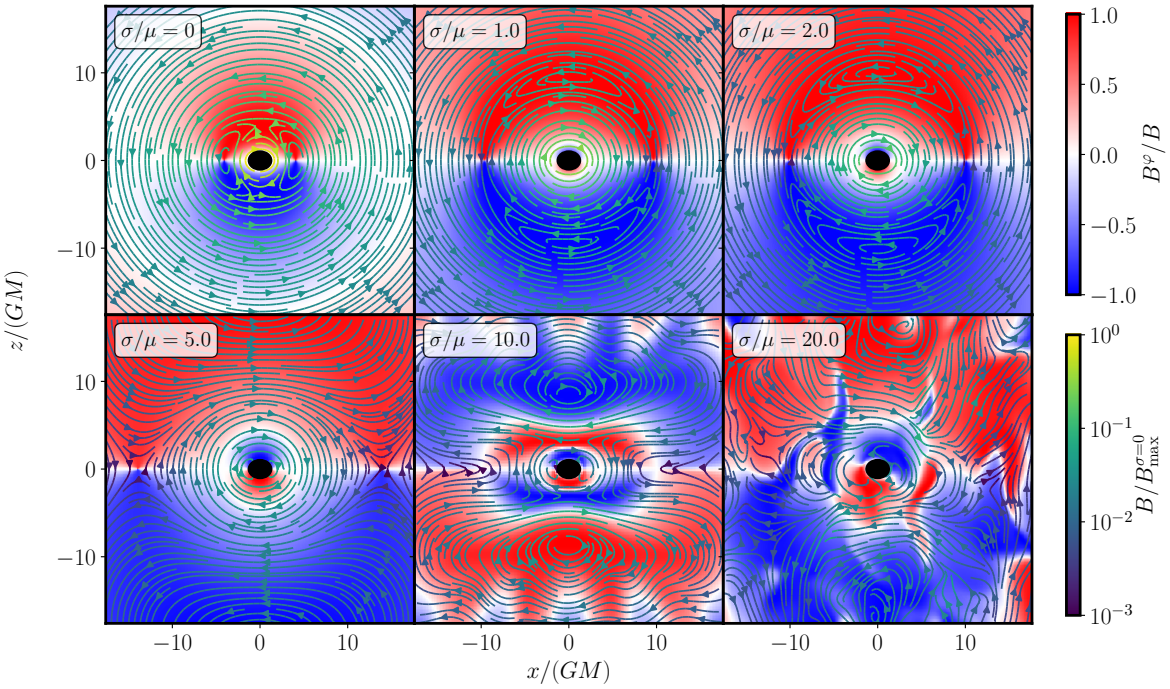

Figure 5.6: Magnetic field lines B^i and magnitudes in a coordinate slice spanned by the BH spin (pointing in the z-direction), and an arbitrarily chosen superradiance cloud phase. The six panels show the field configurations in the same slice for successively larger conductivities σ. The background colors (red/blue) indicate the magnitude of the component perpendicular to the slice B^φ in the φ-direction around the BH normalized by the magnitude of the visible magnetic field. The colors of the field lines (yellow/green) indicate the magnitude of the visible magnetic field along the field lines normalized by the maximal magnitude in the vacuum case $B^{\sigma=0}_{\max}$. The BH and cloud parameters in all panels are as in Figure 5.2, i.e., $\alpha = 0.3$ and $a_* = 0.86$. The magnitude of the magnetic field, while exponentially decaying in the vacuum limit, is roughly uniform at large conductivities $\sigma/\mu = 20$. The small-scale features are discussed in detail in Sec. 5.5.3

at large and small distances from the BH, which breaks the helical geometry into a more complex configuration presenting small-scale features, that are further discussed in the next section. For both the electric and magnetic field, the presence of the plasma leads to field strengths that are relatively uniform in magnitude within the Bohr radius (as can be seen in the $\sigma/\mu = 20$ panel of Figure 5.5). The small-scale features, crucial for the high-conductivity dynamics of the system, are discussed in detail in the next section.

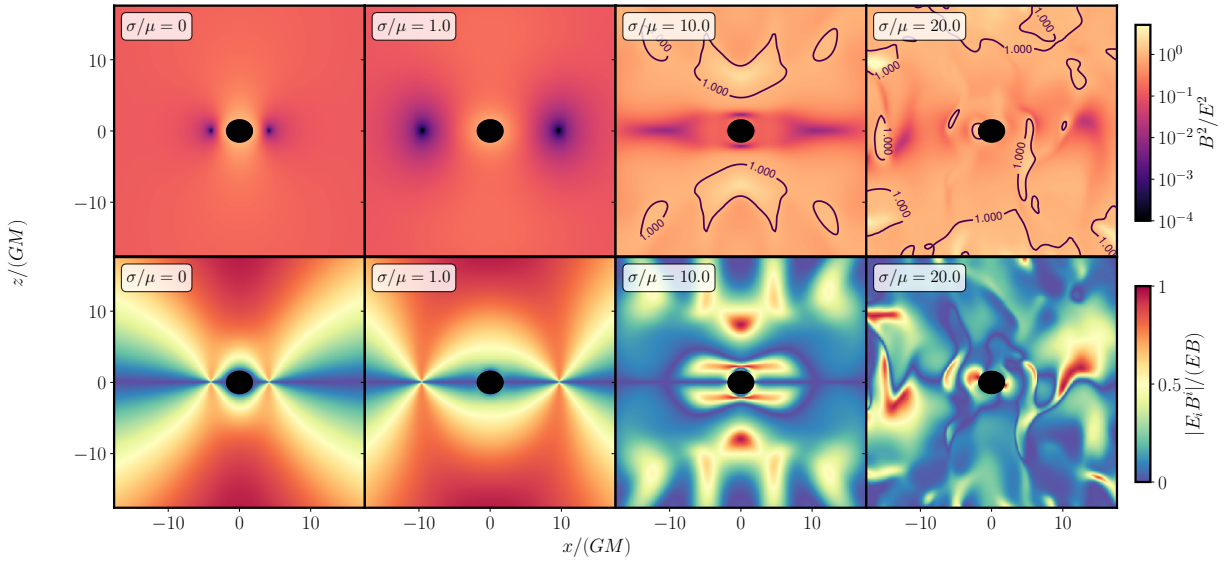

Figure 5.7: *(top row)* The ratio between visible magnetic and electric field strengths, B^2 and E^2, respectively, as function of conductivity σ in the same slices as in Figure 5.6 (i.e., spanned by the BH spin-axis in the z-direction and an arbitrary superradiant phase). Contour lines indicate, where $B^2/E^2 = 1$. *(bottom row)* The magnitude of the visible electric field component in the direction of the visible magnetic field, $|E_iB^i|$, normalized by both magnitudes. The slices of the top and bottom rows are identical. The BH and cloud parameters in all panels are as in Figure 5.2, i.e., $\alpha = 0.3$ and $a_* = 0.86$. For $\sigma/\mu \lesssim 1$, the electric field is dominant everywhere and the violations of $|E_iB^i| = 0$ is strong, while for $\sigma/\mu \gtrsim 1$, the magnetic field begins to dominate in some regimes and $|E_iB^i| = 0$ is violated only in isolated regions.

In order to understand the degree to which our solutions approach a force-free solution in the $\sigma \to \infty$ limit, we consider how violations of the force-free conditions $E_iB^i = 0$ and $B^2 > E^2$ (respectively, conditions *(i)* and *(ii)* discussed in the beginning of subsection 5.5.1), change with increasing conductivity. In Figure 5.7, we show, in representative slices, pointwise measures of the violations of these conditions, while in Figure 5.8 we show how volume integrated measures of these violations decrease with increasing conductivity.

Examining a volume integral of E_iB^i as a function of conductivity, shown in rightmost panel of Figure 5.8, we find that it begins to decrease like $1/\sigma$ for $\sigma/\mu \geq 1$. From the bottom panels of Figure 5.7, we can see that, in contrast to low and moderate value of σ/μ, at high conductivity, large values of E_iB^i (relative to the magnitude of the fields) occur only in isolated, smaller-scale regions.

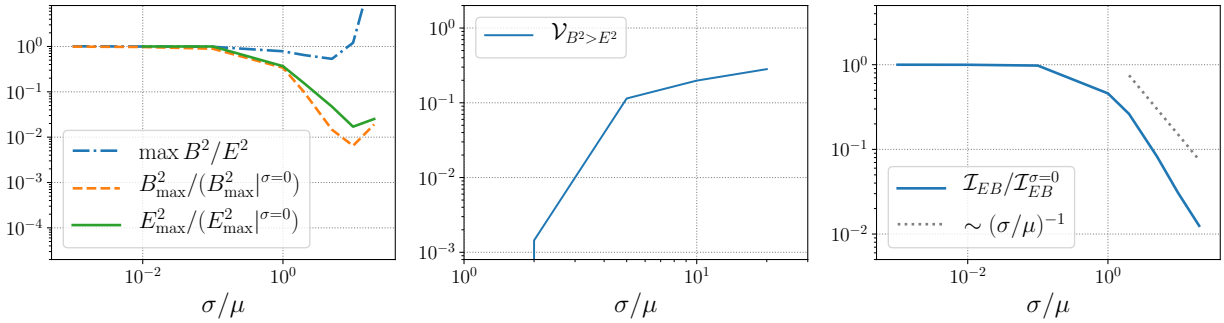

Figure 5.8: *(left)* We plot the maximal ratio of visible magnetic to electric field magnitudes $\max B^2/E^2$, and the maximal magnetic and electric field magnitudes, $B^2_{\rm max}$ and $E^2_{\rm max}$, normalized by their maximal vacuum values, as a function of plasma conductivity $\sigma/\mu \in \{0.001, 0.01, 0.1, 1, 2, 5, 10, 20\}$. *(middle)* The fractional coordinate volume $\mathcal{V}_{B^2>E^2}$ of magnetically dominated regions inside a coordinate sphere of radius $4/(\alpha\mu)$ around the central BH as function of conductivity. *(right)* We show the behavior of the volume integral of $|E^i B_i|$ over a coordinate sphere of radius $10r_c$, $\mathcal{I}_{EB}$, as a function of conductivity, normatlized to its vacuum value $\mathcal{I}_{EB}^{\sigma=0}$. As above, we consider here a BH-cloud system with $\alpha = 0.3$ and spin $a_* = 0.86$ in all panels.

We also find that the fraction of the volume that is magnetically dominated increases with increasing conductivity, as shown in the middle panel of Figure 5.8, in particular, for a coordinate sphere of radius $4/(\alpha\mu)$. For $\sigma = 0$, none of this volume is magnetically dominated (as expected, since $B' \sim \alpha E'$, $B = \varepsilon B'$, and $E = \varepsilon E'$), while for $\sigma/\mu = 20$, approximately one-third of the volume is. The spatial extent of these magnetically dominated regions can be seen in the top panels of Figure 5.7. Similarly, as shown in the left panel of Figure 5.8, the global maximum visible electric and magnetic field strengths are comparable, while the value of $\max B^2/E^2$ increases to large values with large conductivities.

Naïvely, one might expect that in the infinite conductivity limit, the visible electric field in the fluid frame is completely shorted out by large scale charge separation, leading to $e^\mu \to 0$, and hence a magnetically dominated solution everywhere (recalling that magnetic dominance is equivalent to the existence of a frame where the electric field vanishes, i.e., $B^2/E^2 > 1$). The results above suggest that a force-free solution might exist for $\sigma \to \infty$, at least in a significant fraction of the total volume taken up by the plasma and superradiance cloud. However, given the slow increase in the magnetically dominated fraction of the volume with increasing conductivity, it seems plausible that electrically dominated regions with non-zero volume may persist as $\sigma \to \infty$. Electric dominance implies an unscreened

electric field in the fluid frame, allowing for strong particle acceleration, and the dissipation of field energy. This is consistent with our force-free simulations (without a guide field), which always evolve towards developing electrically dominated regions (see Figure D.3 in App. D.3 for a discussion on these force-free simulations), and will be discussed further in the following section. In the next section, we will also discuss how the violations of the force-free conditions are connected to the turblent behavior the plasma.

5.5.3 Field solutions: Small scale turbulence

In the previous section, we found that a large-scale charge separation screens the superradiant electric field, lifting the importance of the visible electric field and leading to magnetically dominated regions. In what follows, we focus on the magnetic field dynamics in the large-conductivity regime. We show that, in this regime, the dark photon superradiance cloud-plasma system is characterized by turbulent plasma dynamics in the bulk of the system. A trend towards small-scale features can already be seen in Figure 5.6, and becomes more apparent in Figure 5.7 in the previous section. The turbulent regions emerge not in isolated and clearly structured lower-dimensional regions, but rather across the bulk of the cloud. This is in contrast to the pulsar magnetosphere, where, at least in the high conductivity limit, small scale features and dissipation are expected to be contained mostly in a two-dimensional current sheet.

In order to understand the turbulent behavior of the visible magnetic field dynamics at moderate and large conductivities, it is instructive to consider the visible magnetic induction equation in the presence of a finite kinetic mixing with the massive vector field. For simplicity, we focus on the flat spacetime limit only, noting that the following qualitative arguments are unchanged on curved backgrounds. Furthermore, for clarity, we assume that the fluid (i.e., the plasma) is mostly non-relativistic, and that at large σ, the plasma is conduction (as opposed to advection) dominated, as explicitly shown in App. D.4. Finally, we can neglect the displacement current $\partial_t E^i \sim \mu E^i$, as it is suppressed compared to the conduction term $\sim \sigma E^i$, if $\sigma \gg \mu$. All qualitative arguments outlined below translate to the fully-relativistic case. Making these assumptions, the evolution equations of the (kinetically mixed) Maxwell equations (D.8) together with the current (5.33) reduce to the visible magnetic induction equation

$$\partial_t B^i = \frac{\varepsilon \mu^2 B'^i}{\sigma} + \frac{1}{\sigma}\partial_j \partial^j B^i + \varepsilon^{ijk}\varepsilon_{klm}\partial_j v^l B^m, \tag{5.40}$$

where $B'^i = \varepsilon^{ijk}\partial_j A'_k$ and v^i is the fluid velocity that we identify with the drift velocity $v^i = v^i_d$, such that $v^i E_i = 0$. For later convenience, we define the Cartesian Kerr-Schild

coordinate radius $\hat{\rho} = (x^2 + y^2 + z^2)^{1/2}$ (see App. D.2 for details). With a characteristic length scale $\ell = 1/\mu$ of the system, we are able to define an effective *magnetic Reynolds number*, $R_m = \ell v_d \sigma = \sigma v_d/\mu$, of the effective plasma defined in (5.37)[4]. For $R_m \gg 1$, the magnetic field dynamics is dominated by the third term in Eq. (5.40), which represents field advection. In this regime the magnetic field dynamics is entirely determined by the plasma, as both are strongly coupled (i.e., the magnetic field is comoving with the plasma). For $R_m \ll 1$, the second term in the induction equation is most important, which accounts for magnetic field diffusion. In this case the magnetic field decouples from the plasma motion and relaxes to a diffusive state. The effects of the superradiant driving fields are included explicitly in the first term of Eq. (5.40) and implicitly in the plasma velocity, which depends on the driving electric fields, and in the visible magnetic field themselves, which are sourced by electrically induced currents.

To illustrate the different domains of the magnetic field dynamics, in Figure 5.9 we show the magnetic field magnitude inside the equatorial plane as a function of conductivity. In the vacuum limit, $\sigma/\mu = 0$, the magnetic field coincides with the superradiant magnetic driving field shown in Figure 5.2. With increasing conductivity, i.e., $\sigma/\mu \gtrsim 1$, from Figure 5.9 we see that the regions where the morphology of the magnetic field resembles the superradiant magnetic fields are confined to distances from the BH that are smaller than a characteristic radius r_*, which we heuristically find to be

$$r_* \approx 80\mu GM/\sigma. \tag{5.41}$$

Inside this critical radius, the superradiant driving field B'^i is exponentially large, and the first term of (5.40) dominates, compared with the terms it induces in the diffusion and advection contributions[5]. Note also that at large conductivities an overall phase-offset of $\pi/2$ between the superradiant and visible magnetic fields appears, similar to the behavior of the electric field case (see Figure 5.5); at the level of the magnetic field, this phase-offset emerges from the first term in the induction equation (5.40).

For radii larger than r_* we see that the magnetic fields are non-trivially related to the driving superradiant electric and magnetic fields. At large distances from the BH and on scales of order $1/\mu$, the magnetic field strength increases with growing conductivity. On smaller scales, on the other hand, and especially at large conductivities, we see that a series of small scale features appear. These features, which arise on scales of order $1/\sigma$, emerge

[4]One could instead chose $\ell = r_c$. However, the qualitative arguments are unaffected by the precise choice of magnetic Reynolds number.

[5]Note, the superradiant components of the visible magnetic fields in the second and third term in the induction equation (5.40), are α^2 and α suppressed, respectively, to the leading contribution at intermediate conductivities.

from the interplay of the diffusion and advection components of the magnetic induction equation. At large conductivities and due to the large plasma velocities, most regions with $\hat{\rho} > r_*$ are advection dominated. As a result, the oscillating superradiant driving fields source visible magnetic fields that couple strongly to the plasma, while conversely, the plasma cannot back react onto the superradiant driving fields. Our results show that for radii $\hat{\rho} > r_*$, and on spatial scales of the entire cloud (i.e., $> 1/\mu$), the plasma is unable to corotate with the driving fields; hence, differential rotation between plasma cells at different radii occurs. This shear velocity results in twisting of the magnetic field lines on scales of the cloud. The twist builds up magnetic energy that is dissipated through turbulent magnetic reconnection in regions of large magnetic diffusion, i.e., $R_m \ll 1$ (as we illustrate in detail below). Thus, the small scale features in Figure 5.9 are a result of this turbulent reconnection. The radius r_* may saturate at the light cylinder of the system for $\sigma \to \infty$ as inside it the plasma could rotate rigidly with the superradiant driving fields. However, we do not find the light cylinder to be a location of special importance for the largest conductivity that we considered: $\sigma/\mu = 20$.

Another qualitative feature is the disappearance of the magnetic null line of the superradiant magnetic field for moderate conductivities, $\sigma/\mu > 5$, outside the critical radius r_*, as can be seen in Figure 5.9. Vanishing magnetic field strength implies vanishing plasma bulk velocity, i.e., $R_m \approx 0$, and equivalently the presence of strong magnetic diffusion. Hence, we find that the magnetic null line is quickly filled by magnetic field lines diffusing into the null line from surrounding areas with finite magnetic field strength. This process efficiently removes the null line outside the critical radius r_*.

In addition to the large scale differential rotation about the BH, in advection dominated regions (where the plasma and magnetic field are co-moving) we observe localized roughly uniform *oscillatory* motion of the plasma within the equatorial plane (with oscillation radius given by $1/\mu$), as well as periodic *longitudinal* motion of the plasma along the BH spin-axis[6]. This periodic motion is likely driven by the large scale superradiant electric field throughout the plasma, in conjunction with large scale charge separation of the pair plasma for $\sigma/\mu \gtrsim 1$. Charges are accelerated along the large scale superradiant electric field. However, the orbital frequency μ of the field's direction forces the charges into a circular trajectory with radius of $1/\mu$. This is reflected in the circular motion of features in the magnetic field of scale $1/\mu$ inside the equatorial plane. The circular motion of negative and positive charges is exactly out of phase by π, resulting in out-of-phase oscillatory motion of the plasma on either side of the BH due to the large scale charge dipole screening the superradiant electric field. The longitudinal periodic motion along the spin axis is more

[6]Even in the force-free simulations, this periodic oscillatory motion of the magnetic field strength in the equatorial plane can be observed.

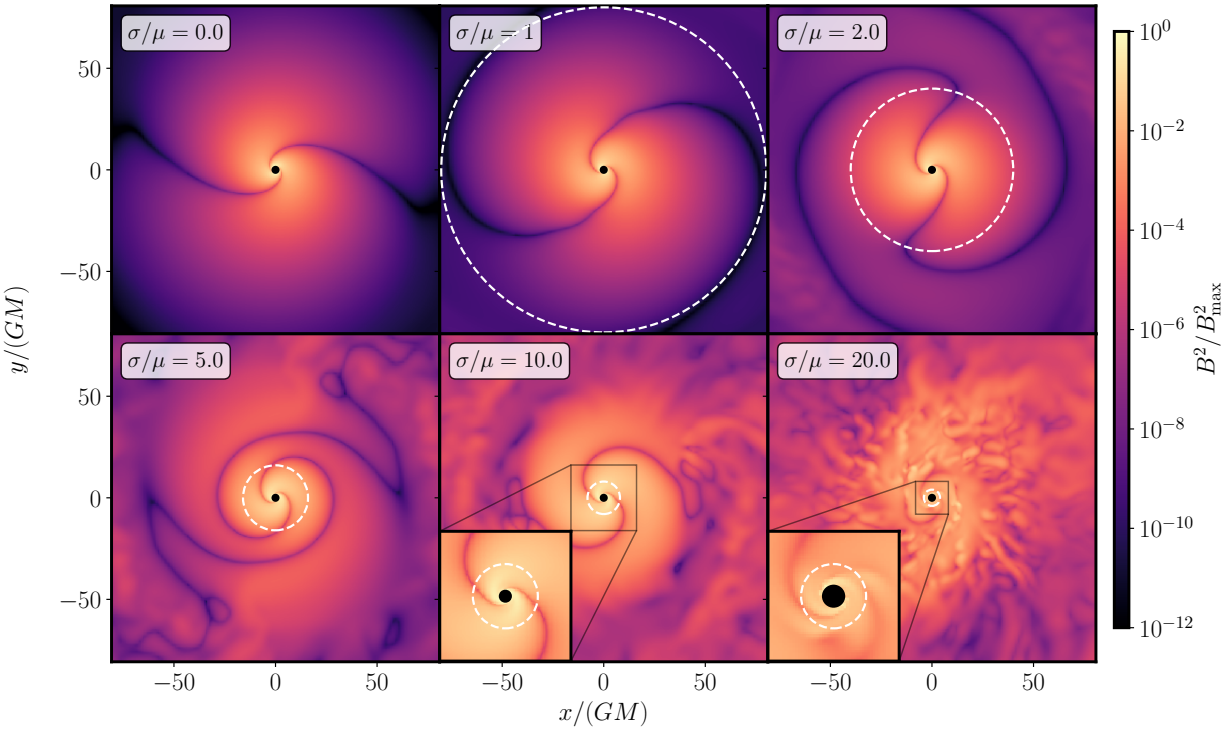

Figure 5.9: We plot the visible magnetic field strength B^2 in the equatorial plane of the system in the vacuum limit, $\sigma = 0$, as well as at moderate to high plasma conductivities, i.e., $\sigma/\mu \gtrsim 1$. The BH and cloud parameters are as in Figure 5.2, i.e., $\alpha = 0.3$ and $a_* = 0.86$. The superradiance cloud phase is identical in each of the panels. The color is normalized by the maximal visible magnetic field strength at each conductivity. The white dashed line indicates the critical coordinate radius $r_* = 80\mu GM/\sigma$, discussed in the main text. The region $\hat{\rho} < r_*$ is dominated by superradiant driving, while the regions with $\hat{\rho} > r_*$ are characterized by an interplay of advective and diffusive regions. The flat spacetime light cylinder for this system is roughly $R_{\rm LC} = GM/\alpha \approx 3.33GM$. Notice, the resolution of our numerical methods decreases with increasing coordinate distances $|x|$ and $|y|$, resulting in, for instance, a suppression of small-scale features in the $\sigma/\mu > 2$ cases for $|x|, |y| > 50GM$.

complex, and likely a result of the electric field driving within the equatorial plane. We will discuss the observational consequence of this motion of charge densities in Sec. 5.6.4.

Let us illustrate some of these observations explicitly in Figure 5.10. In panel (a), we show the three-dimensional geometry of the visible magnetic field lines in the vicinity of the

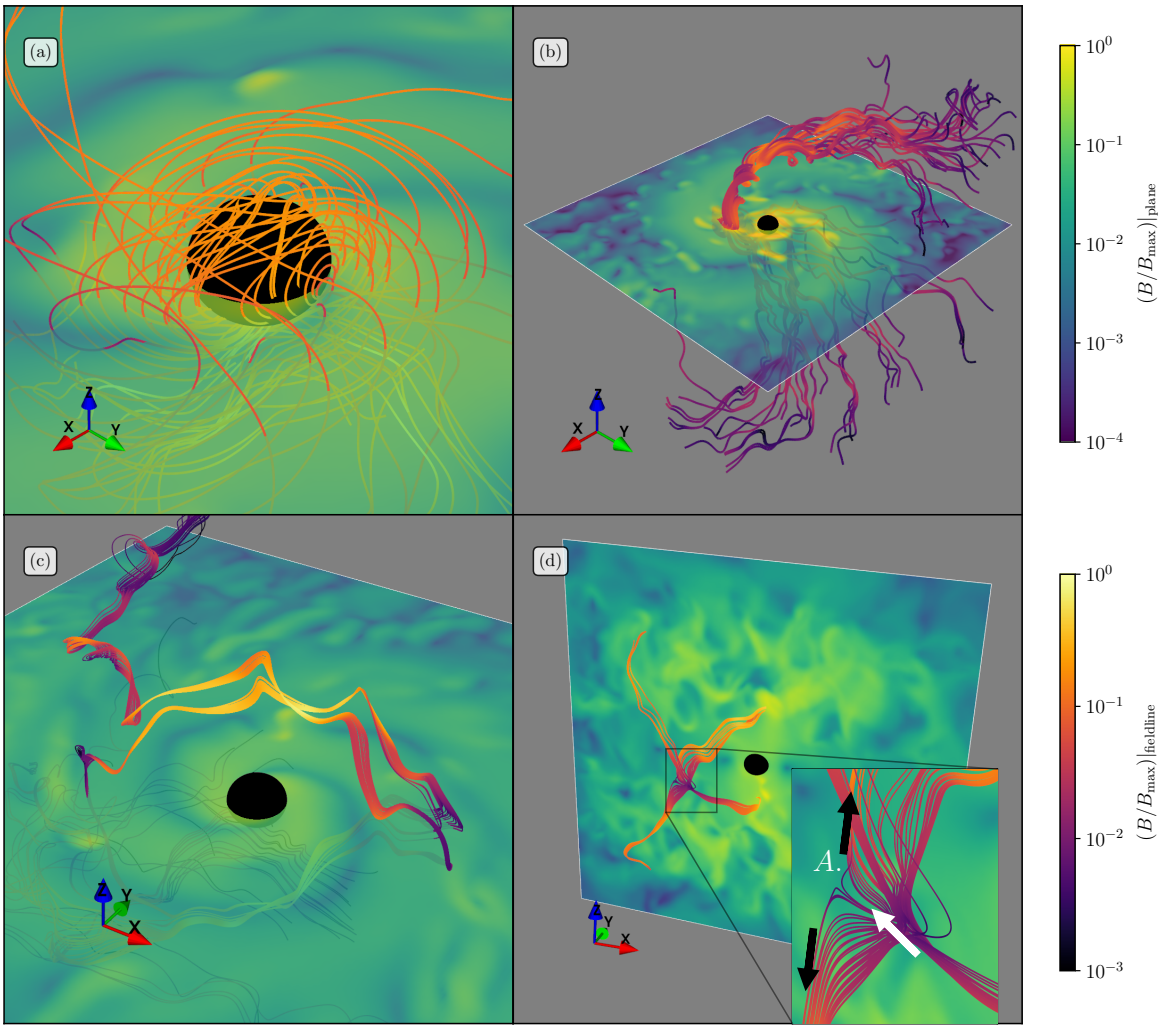

Figure 5.10: We plot a selection of visible magnetic field lines of the superradiance cloud-plasma system with conductivity $\sigma/\mu = 20$, $\alpha = 0.3$, and $a_* = 0.86$. In panels (a), (b) and (c) we also plot the visible magnetic field strength within the equatorial plane, while in panel (d) we show the visible magnetic field strength in the plane spanned by the BH spin and an arbitrary superradiance cloud phase. We discuss this plot in detail in the main text. The main macroscopic scales involved are the BH-scale, set by the mass M, the superradiance cloud's oscillation timescale $1/\mu \approx 3.33GM$, and the cloud's Bohr radius $r_c \approx 11.1GM$.

central BH. The field lines are mostly closed around the BH, and only occasionally thread the event horizon. This confirms the discussion above, as these field lines are roughly inside $\hat{\rho} < r_* \approx 4GM$ for the choice of parameters in the figure, and hence, are approximately set by the superradiant driving field (compare also to Figure 5.2).

The large-scale differential rotation and twisting of magnetic field lines on scales of the entire cloud is shown in panel (b) of Figure 5.10. There, we focus on a few representative field lines crossing the equatorial plane. Both above and below the equatorial plane, we find that the azimuthal angular velocity of the magnetic field lines decreases with increasing distance from the BH's spin axis, leading to a lag of portions of the field lines far away from the BH compared to those closer to the center. This lag causes twisting of the field lines roughly around the spin-axis[7] on scales of the superradiance cloud, which, ultimately, results in the opening of the visible magnetic field lines at large distances.

In addition to this large scale feature, the field line geometry also exhibits features on scales of roughly $1/\mu$, as can be seen in panel (c) of Figure 5.10 (notice, this scale compared with the BH mass is $1/(\mu GM) \approx 3.33$). There we show two collections of field lines exhibiting variations on spatial scales set by the superradiance oscillation frequency. These arise likely as a result of the periodic motion of the plasma in the large scale superradiant electric field, twisting the field lines on scales of $1/\mu \ll r_c$ as well. Both the twisting on scales of the cloud, and small scales, $1/\mu$, builds up magnetic energy that is dissipated by means of magnetic reconnection.

In panel (d) of Figure 5.10, we isolate one such reconnection sight, representative for a class of reconnection processes active throughout the bulk of the cloud. We leave the details to the discussion in Sec. 5.6.3, and just point out here that the visible magnetic field lines entering the reconnection region along the white arrow, diverge away into *two* distinct directions along the black arrows. This indicates that the connectivity of the field lines is discontinuously changed at the location labelled as A. Another indication of magnetic reconnection at location A in panel (d) of Figure 5.10, is the appearance of *four* bundles of field lines from the region around A. In the highly conducting and highly magnetized plasma limit, (at least one of) the dimensions of the reconnection regions are expected to scale as $1/\sigma$. Speculating about the $\sigma \to \infty$ limit, we hypothesize that these reconnection sites turn into one- or two-dimensional highly fragmented localized filaments and current sheets, where potentially large amounts of electromagnetic energy is injected into the plasma (as typically observed in turbulent highly magnetized plasmas, e.g., [383, 113, 303]). We discuss the connection between significant energy dissipation into the plasma and magnetic reconnection in Sec. 5.6.3 in detail.

[7] This is only roughly true, since the plasma motion is more complex as pointed out above.

5.5.4 Summary of turbulent plasma scales

Before concluding this section, we provide a summary of the main features of the quasi-equilibrium endstate of the pair production cascade. We begin with the largest scales first, and work towards small scales:

- On spatial scales of the superradiance cloud, $\sim r_c = 1/(\mu\alpha)$, the superradiant electric field is efficiently screened by a roughly dipolar charge distribution. A significant fraction of the cloud's volume is magnetically dominated at $\sigma/\mu = 20$ with trend towards larger fractional volumes for larger plasma conductivities. This increases the importance of the magnetic field dynamics for the cloud-plasma system. For sufficiently high conductivity, the magnetic field and the plasma become strongly coupled except in isolated diffusion regions. Hence, at large distances from the central BH's spin axis, the plasma rotates around the BH with period much longer than the superradiant cloud's period, inducing differential rotation on the scale of the entire cloud. The resulting shearing magnetic field lines reconnect inside the bulk of the cloud.

- On spatial and temporal scales set by the Compton wavelength of the dark photon, $1/\mu$, a variety of features appear. The plasma orbits with the superradiance cloud in circular motion with radius given by roughly $1/\mu$. This is likely due to the large scale electric field set by the superradiance cloud. Hence, negative and positive components of the local charge density orbit exactly out of phase due to the large charge dipole. In the large conductivity regime, this circular motion implies circular motion of the visible magnetic field due to the strong coupling in advection dominated regions. Features of size $1/\mu$ in the global visible magnetic field geometry appear due to the built-up magnetic field twisting, which is released in magnetic field line reconnection sites.

- Besides the two macroscopic scales discussed above, the conductivity σ sets the size of non-ideal features, which are expected to be of microscopic size. We found that at moderately large conductivities $\sigma/\mu = 20$, these non-ideal regions begin to form filaments inside the superradiance cloud's plasma, setting the scale of the turbulent behavior. Speculating, for very large conductivities, $\sigma/\mu \gg 20$, the non-ideal regions may fragment into a large number of current sheet-like structures filling the turbulent plasma[8]. Below, in Sec. 5.6.2, we elaborate on this and identify these regions as sites of enhanced energy dissipation.

[8]This is typically found in treatments of turbulent magnetized plasmas, e.g., [113, 383, 303].

Therefore, the superradiance cloud-plasma system is characterized by differential rotation, as well as periodic plasma motion with period given by the boson mass scale $1/\mu$, leading the magnetic field lines to be twisted both on cloud size scales $1/(\mu\alpha)$, and on scales set by the dark photon mass $1/\mu$. This twisting is relaxed through magnetic reconnection in the bulk of the superradiance cloud in features with size set by $1/\sigma$. These processes likely lead to strong electromagnetic transients with periodicity set by the dark photon mass μ. Characterizing the power and periodicity of these transients is the subject of the next section.

5.6 Electromagnetic emission

The pair production cascade within the superradiance cloud saturates in a turbulent, differentially-rotating plasma surrounding the central BH with a partially screened electric field and magnetic field line reconnection in the bulk. In highly-magnetized astrophysical plasmas, particles are efficiently accelerated at reconnection sites, leading to high-energy electromagnetic emission. Therefore, we expect strong electromagnetic signatures from the superradiance cloud system.

In the following, we illustrate the radiation and dissipation channels in our setup in Sec. 5.6.1, quantify the emitted electromagnetic luminosity in Sec. 5.6.2, identify the dominant emission mechanism in Sec. 5.6.3, discuss the periodicity of the emission pattern in Sec. 5.6.4, and comment on the possible emission spectra in Sec. 5.6.5.

5.6.1 Radiation and dissipation channels

The effective description of the pair plasma that we use, introduced in the previous sections, includes only the leading-order resistive correction to the force-free limit of ideal magnetohydrodynamics. In the context of this formalism, any microphysical processes (e.g. pair production, scattering, photon emission, or other QED effects) are averaged over, or only roughly approximated by the macroscopic conductivity σ that characterizes the local dissipation in the plasma, and not included from first principles[9]. However, our approximation is sufficient to reliably estimate the total electromagnetic power output of the system through the outgoing Poynting flux, as well as through dissipation due to macroscopic spatial currents along the visible electric field. The Poynting flux is typically

[9]To some degree, this could be achieved within the context of kinetic theory and particle-in-cell simulations. However, we leave exploring this avenue to future work.

invoked, within the force-free paradigm to estimate the rotational energy extraction rates of pulsars [171, 114, 227, 347, 321, 293, 98] (which have been confirmed within kinetic theory in [101, 299, 298]). For typical pulsars, this macroscopic coherent energy flux is expected to be emitted from the system in the form of lower-energy radio waves, as well as dissipate in particle acceleration processes in current sheets resulting in X-rays and gamma-rays. While in the pulsar magnetosphere, dissipation is mainly confined to roughly two-dimensional current sheets, the superradiance cloud exhibits reconnection in the bulk, enabling efficient energy transfer into high-energy emission. The dissipation of electromagnetic energy can be interpreted as sourcing local particle acceleration, synchrotron and curvature radiation, and plasma heating. Therefore, estimating the total emitted Poynting flux and dissipative energy losses of the superradiant system is crucial to understand the overall electromagnetic signatures. In the following, we briefly outline how these quantities are computed in our setup.

Modified Poynting theorem: The conservation of energy in the interaction basis, (5.15), can be used to identify the macroscopic sources and types of energy flows present in the system. The background Kerr spacetime has an asymptotically-timelike Killing field ξ^μ, endowing the system with a local energy conservation law. Therefore, we define the total energy $\mathcal{E}$ of A_μ, with respect to ξ^μ, within the (coordinate) domain D as

$$\mathcal{E} = \int_D d^3x \sqrt{\gamma} T^\alpha{}_\mu n_\alpha \xi^\mu, \tag{5.42}$$

with the volume form $d^3x\sqrt{\gamma}$ of a t =const. slice of Kerr spacetime (see App. D.2 for details), and the energy-momentum tensor $T_{\mu\nu}$ of the *visible* fields

$$T_{\mu\nu} = F_\mu{}^\lambda F_{\lambda\nu} - \frac{1}{4} g_{\mu\nu} F^{\alpha\beta} F_{\alpha\beta}. \tag{5.43}$$

Throughout this chapter, the domain D of consideration is the exterior of the BH up to a coordinate sphere $S^2_{\hat{\rho}}$ at coordinate radius $\hat{\rho} = \sqrt{x^2+y^2+z^2}$ in Kerr-Schild coordinates (defined in App. D.2). In the following, we focus entirely on the *visible* electromagnetic field. Intuitively, this visible field is a superposition of the massless (i.e., the SM photon) and the massive vector fields. The former is propagating freely, and sourced only by the plasma, while the latter is gravitationally bound to the BH, and non-radiative. Given this, and the energy-momentum conservation (5.15), we can relate the change of the total energy of the visible electromagnetic fields within D, $\partial_t \mathcal{E}$, to the energy fluxes across the boundary of the domain, ∂D, as well as the work done on the plasma within D, by the

modified Poynting theorem, written as

$$\partial_t \mathcal{E} = -P_{\rm EM} - \dot{\mathcal{E}}_{\rm BH} - L_{\rm diss} + \dot{\mathcal{E}}_{\rm A'}. \tag{5.44}$$

The first two terms on the right-hand side correspond to the Poynting flux emitted towards infinity, $P_{\rm EM}$, and the visible electromagnetic field flux across the event horizon of the BH, $\dot{\mathcal{E}}_{\rm BH}$, respectively. The third term describes the energy loss of the visible fields to the pair plasma through resistive processes, $L_{\rm diss}$. Lastly, the source of energy of the superradiant system is the energy injection of the massive vector field $\dot{\mathcal{E}}_{A'}$. Notice, we assumed that the energy of the visible electromagnetic fields is much larger than the energy contained in the pair plasma, i.e., $T_{\mu\nu} \gg T^{\rm plasma}_{\mu\nu}$. Hence, any finite mass loss due to the accretion or emission of fermions is not contained in the above analysis, which was shown to be a good approximation in (5.28). In the following, we consider each component on the right hand side of Eq. (5.44) and take the flat spacetime limit to connect to familiar expressions.

Poynting fluxes: The electromagnetic luminosity—the Poynting flux—through a coordinate sphere at radius $\hat{\rho}$, is

$$P_{\rm EM} = -\oint_{S^2_{\hat{\rho}}} d\Omega_\mu T^\mu{}_\nu \xi^\nu \overset{\rm flat}{=} \oint_{S^2_{\hat{\rho}}} d\Omega\, \hat{\boldsymbol{\rho}} \cdot (\boldsymbol{E} \times \boldsymbol{B}). \tag{5.45}$$

Here, $d\Omega_\mu$ is the oriented area element of $S^2_{\hat{\rho}}$ pointing outwards, $\hat{\boldsymbol{\rho}}$ the radial unit vector, and $d\Omega$ the solid angle. Hence, positive $P_{\rm EM}$ implies visible electromagnetic energy leaving the domain D. Since the massive linear combination of A_μ and A'_μ is gravitationally bound to the BH and decays as $\sim \exp(-r/r_c)$, at large distances, the visible Poynting flux, $P_{\rm EM}$, will receive a contribution only from the massless linear combination (corresponding to the SM photon) for sufficiently large $\hat{\rho}$. Analogously, the energy flux across the BH's event horizon is

$$\dot{\mathcal{E}}_{\rm BH} = -\oint_{S^2_{\rm BH}} d\Omega_\mu T^\mu{}_\nu \xi^\nu, \tag{5.46}$$

where $S^2_{\rm BH}$ is the event horizon, and $d\Omega_\mu$ the oriented area element pointing outwards. Hence, negative $\dot{\mathcal{E}}_{\rm BH}$ implies visible electromagnetic energy accreting onto the BH. This, of course, vanishes in the $\alpha \ll 1$ limit (i.e., in the flat spacetime limit). At the saturation point, i.e., if $\omega = \Omega_{\rm BH}$, the massive field has vanishing flux across the horizon, such that $\dot{\mathcal{E}}_{\rm BH}$ contains only massless fluxes. We can therefore interpret (5.46) as a measure of the amount of accretion, or energy extraction from the BH (e.g. the Blandford-Znajek process [69]), triggered by the plasma and superradiance cloud.

Dissipative energy losses: Besides these fluxes of energy across the boundary of the domain, the resistive pair plasma is able to dissipate energy in the bulk of D. This macroscopic dissipation is captured by the dissipative losses[10]

$$L_{\rm diss} = -\int_D d^3x\sqrt{-g}F^{\alpha\beta}\xi_\alpha I_\beta \overset{\rm flat}{=} \int_D d^3x \boldsymbol{E}\cdot\boldsymbol{J}. \tag{5.47}$$

Here g is the metric determinant of Kerr spacetime. In the flat spacetime limit, this expression reduces to the Joule heating within D. For later convenience, we define the local dissipation density

$$\rho_{\rm diss} = NF^{\alpha\beta}\xi_\alpha I_\beta, \tag{5.48}$$

where $N = \sqrt{-g/\gamma}$ is the lapse providing a macroscopic measure of the local rate at which energy is lost to heating, particle acceleration, etc.

Energy transfer from superradiance cloud: The main energy source, driving the radiation and dissipation, is the superradiance cloud, which extracted a non-negligible amount of rotational energy from the BH. The rate of replenishment of $\mathcal{E}$ from the superradiance cloud A'_μ is given by the last term in (5.44):

$$\dot{\mathcal{E}}_{\rm A'} = -\varepsilon\mu^2\int_D d^3x\sqrt{-g}F^{\alpha\beta}\xi_\alpha A'_\beta \overset{\rm flat}{=} \varepsilon\mu^2\int_D d^3x\boldsymbol{E}\cdot\boldsymbol{A}'. \tag{5.49}$$

This describes the energy transfer from superradiant to the visible fields.

Most important for our discussion in the following sections are the Poynting flux $P_{\rm EM}$ and the dissipation rate $L_{\rm diss}$. These determine the total electromagnetic power output of the system, and provide insights into the characteristics of the emission, such as the primary emission mechanism, the time-dependence, and the emission spectrum.

5.6.2 Power output

We find that the cloud-plasma system settles into a driven turbulent state with a large electric dipole screening the superradiant electric field and bulk magnetic field reconnection.

[10] Again, due to the kinetic mixing, both the massive and massless linear combinations of A_μ and A'_μ dissipate energy.

We demonstrate below that the dipole results in coherent electromagnetic Poynting flux, while the magnetic reconnection is associated with strong energy dissipation from the visible electromagnetic fields into the plasma. As we show in the following, due to the turbulent nature of the dissipation in the bulk of the cloud, the dissipative losses dominate over the Poynting flux from the system by orders of magnitude.

In the vacuum limit, i.e., for $\sigma = 0$, there is no dissipation and electromagnetic modes propagate freely. However, both the dark and visible electromagnetic fields fall off exponentially at large distances away from the BH, and there is no flux to infinity. At non-zero conductivities of the medium, on the other hand, any Poynting flux is re-absorbed by the plasma on scales set by the skin-depth of the effective fluid, which is a complex function of propagating mode frequencies, conductivity, background electromagnetic field strengths, and local Ohmic losses. As we show below, this leads the Poynting flux to go to zero in the intermediate regime $\sigma/\mu \sim \mathcal{O}(1)$. In this regime, the energy dissipation is expected to be largest, while any freely propagating electromagnetic modes are re-absorbed on the skin depth length scales. In the limit where $\sigma/\mu \gg 1$, the regime in which the cloud-plasma system is expected to reside, the Poynting flux is expected to mostly decouple from the plasma, except in locations of large dissipation into the plasma, and propagate freely.

To understand the high-conductivity regime, we compute the quantities $P_{\rm EM}$, $L_{\rm diss}$, and $\dot{\mathcal{E}}_{\rm BH}$ in our numerical simulations for $\alpha = 0.3$ and various different conductivities $\sigma/\mu \gtrsim 1$ (note, in App. D.4, we discuss the small-σ regime for completeness). In Figure 5.11, we present the visible Poynting flux and dissipative losses as functions of conductivity and coordinate radius for the superradiant cloud-plasma system. We postpone a discussion on time-dependence of the electromagnetic emission to Sec. 5.6.4, and focus here on quantities time-averaged over one period of the superradiance cloud. As anticipated, the energy dissipation into the plasma is largest for intermediate conductivities, $\sigma \sim \mu$. As a result, the visible Poynting flux is efficiently re-absorbed by the fluid and decays exponentially as it propagates away from the BH. The sinusoidal features of $P_{\rm EM}$ for $\sigma/\mu \lesssim 1$ are discussed in detail in App. D.6. The local energy dissipation follows the radial profile of the superradiant cloud $\sim \exp(-\sqrt{2(\mu^2 - \omega^2)}\hat{\rho})$, driving the energy injection into the plasma, at large distances from the BH. Moving towards larger conductivities, $\sigma/\mu > 1$, the weakening of the dissipative losses roughly follows a $\sim 1/\sigma$ scaling, however, with important corrections at $\sigma/\mu \gtrsim 5$ discussed below. As can seen in the left panel of Figure 5.11, energy flows into the BH for $\sigma/\mu \geq 1$ (though the horizon is actually a source of energy for lower conductivies, see App. D.4) at rate comparable to the total Poynting flux to the wavezone. The radial re-absorption length scale of the electromagnetic flux increases significantly with conductivity for $\sigma/\mu > 1$, enabling efficient transfer of propagating modes from the center of the superradiance cloud to the emission zone far away from the BH.

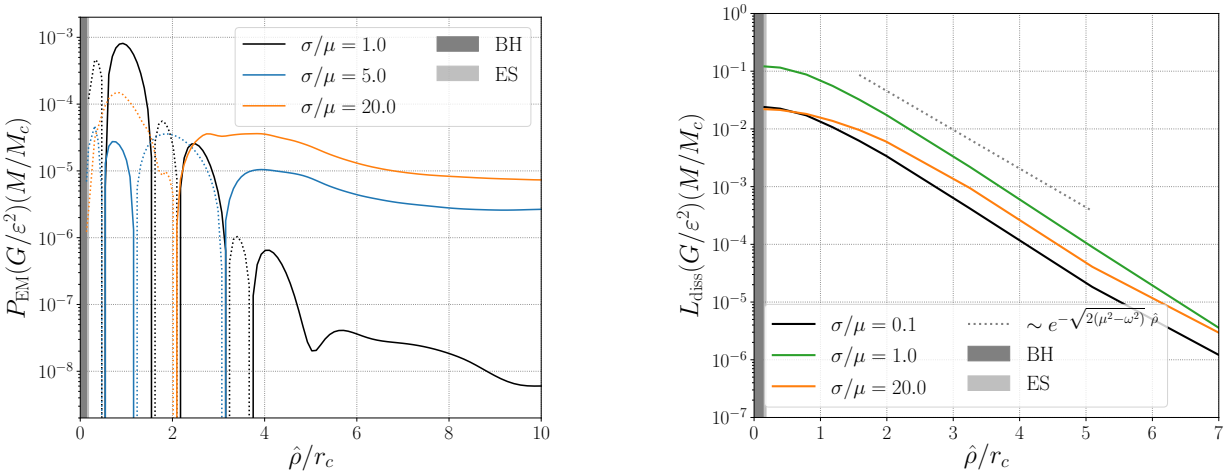

Figure 5.11: *(left)* We plot the total visible, time-averaged, Poynting flux $P_{\rm EM}$, defined in (5.45), through a coordinate sphere at radius $\hat{\rho}$ around the BH, for various conductivities σ. Solid lines are positive (locally outgoing) fluxes, whereas dotted lines are negative (locally ingoing) fluxes. The interior of the BH and the ergosphere (ES) in the equatorial plane are indicated by shaded regions; the smallest radius value indicates the flux through the event horizon $\dot{\mathcal{E}}_{\rm BH}$. *(right)* We plot the total energy dissipation rate due to Ohmic losses $L_{\rm diss}$, defined in (5.47), everywhere *outside* a coordinate radius $\hat{\rho}$ for various conductivities. In both panels, we focus on an $\alpha = 0.3$ cloud with a BH of spin $a_* = 0.86$, and Bohr radius of the superradiance cloud of $r_c = 1/(\mu\alpha)$; notice, $\sqrt{2(\mu^2 - \omega^2)} \to \alpha\mu$ for $\alpha \ll 1$. Note, our simulations assume a conductivity constant everywhere in space. At intermediate conductivities, $\sigma \sim \mu$, the Poynting flux is efficiently absorbed by the effective plasma, while towards large conductivity, the electromagnetic modes propagate freely. The energy injection into the plasma $L_{\rm diss}$ follows the profile of the cloud for all but the highest conductivities considered here.

Focusing on the outgoing Poynting fluxes at large distances, $\hat{\rho} = 10r_c$, a trend emerges, from small fluxes at intermediate conductivities to large power at large conductivity, saturating at a conductivity-independent outgoing electromagnetic emission.

The conductivity of the pair plasma within the superradiance cloud is expected to be set by a micro-physical scale far smaller than any macroscopic scale of the system, $\sigma \gg \mu$. Therefore, in the left panel of Figure 5.12, we consider the trends of total dissipation $L_{\rm diss}$ and Poynting flux at large radii $P_{\rm EM}$ towards the large-σ limit. As pointed out above, the coherent electromagnetic flux emitted from the system increases rapidly from $\sigma \sim \mu$ towards a non-zero value for $\sigma \gg \mu$. The blue band in the left panel of Figure 5.12,

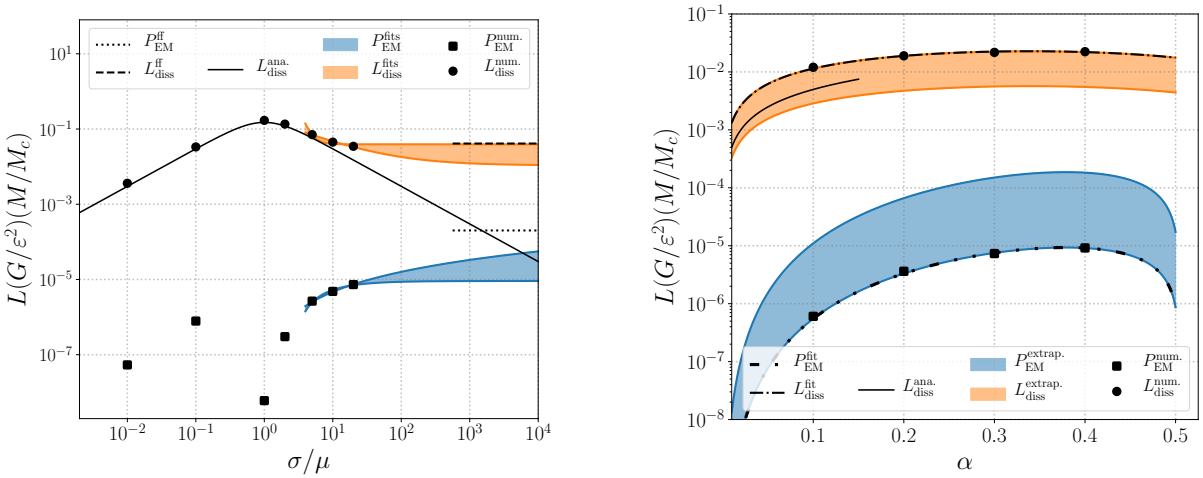

Figure 5.12: We show the energy dissipation rate, integrated over the entire cloud $L_{\rm diss}$, and the total (time-averaged) Poynting flux $P_{\rm EM}$ extracted at $\hat{\rho} = 10r_c = 10/(\mu\alpha)$. *(left)* Focusing on $\alpha = 0.3$ and $a_* = 0.86$, we plot the quantities obtained from our resistive force-free simulations, black circles representing $L_{\rm diss}^{\rm num.}$, and black squares representing $P_{\rm EM}^{\rm num.}$, as functions of conductivity. The orange and blue bands, labelled $L_{\rm diss}^{\rm fits}$ and $P_{\rm EM}^{\rm fits}$, respectively, are a series of fits of the form $a_1 + a_2(\mu/\sigma)^p$ to the simulation results with the three largest conductivities. The fits are motivated by the discussion in the main text that the energy dissipation remains finite at infinite conductivities. The bands are bounded by the most optimistic and pessimistic fits to the data. The black dotted and dashed lines show the force-free estimates for the emitted Poynting flux and total dissipation, labelled $P_{\rm EM}^{\rm ff}$ and $L_{\rm diss}^{\rm ff}$, valid formally at $\sigma \to \infty$ (how these are obtained is discussed in the main text). Lastly, we show the analytical approximations (5.52), labelled as $L_{\rm diss}^{\rm ana.}$, for comparison. *(right)* We also show $L_{\rm diss}^{\rm num.}$ and $P_{\rm EM}^{\rm num.}$ from the simulations, but now fixing $\sigma/\mu = 20$ and varying α, assuming $\omega = \Omega_{\rm BH}$. The two fits in (5.54) to the numerical data $L_{\rm diss}^{\rm num.}$ (dash-dotted line) and $P_{\rm EM}^{\rm num.}$ (sparse-dashed line) are labelled as $P_{\rm EM}^{\rm fit}$ and $L_{\rm diss}^{\rm fit}$ (and use the ansatz $a_1\alpha^3 + a_2\alpha^4$ and $a_1\alpha^1 + a_2\alpha^2$, respectively). The orange and blue bands, labelled $L_{\rm diss}^{\rm extrap.}$ and $P_{\rm EM}^{\rm extrap.}$, are the $\sigma/\mu \to \infty$ extrapolations of the corresponding bands in the plot on the left (there for $\alpha = 0.3$) applied to the two fits $P_{\rm EM}^{\rm fit}$ and $L_{\rm diss}^{\rm fit}$. Lastly, the analytic estimate (5.52) is indicated as $L_{\rm diss}^{\rm ana.}$. A discussion of both plots can be found in the main text.

indicates possible fits with various σ-scalings of the trend, extrapolating to physically relevant regimes, $\sigma \gg \mu$. We discuss the behavior of $P_{\rm EM}$ for $\sigma/\mu < 1$ in App. D.6. Turning to the dissipation of energy into the plasma, the behavior in the low to medium

conductivity regime, $\sigma/\mu \lesssim 1$, is as expected. The energy injection at the macroscopic level increases as $\sim \sigma$ from the vacuum limit towards intermediate resistivity levels. Beyond the peak dissipation power around $\sigma \sim \mu$, a decay following $L_{\rm diss} \propto 1/\sigma$ is predicted by simple arguments of the bulk dissipation inside the cloud (outlined below). However, instead of following this behavior, the energy dissipation rate deviates from this trend. In order to extrapolate to large σ, we can therefore split the dissipation into two different components:

$$L_{\rm diss} = L_{\rm diss}^{\rm bulk} + L_{\rm diss}^{\rm turb}, \tag{5.50}$$

heuristically representing the bulk and the turbulent dissipation, respectively. Based on analytic estimates (discussed below) the bulk dissipation $L_{\rm diss}^{\rm bulk}$ is expected to decrease as $\sim 1/\sigma$ towards small resistivity, while the turbulent dissipation component $L_{\rm diss}^{\rm turb}$ will have a non-zero value in the infinite conductivity limit. To capture this, in Figure 5.12, we fit the results from the simulations with $L_{\rm diss} \sim a_1 + a_2(\mu/\sigma)^p$, considering $p \in [1, 0.025]$, finding $L_{\rm diss} = L_{\rm diss}^{\rm turb} \approx 5 \times 10^{-2}(\varepsilon^2/G)(M_c/M)$ for $\alpha = 0.3$ and $\sigma \to \infty$. The orange band in Figure 5.12 represents the range of values for the conductivity dependence, and is bounded by the most optimistic and pessimistic fits considered, to illustrate the uncertainty of this extrapolation.

We compare these extrapolations with the results from force-free simulations, valid formally at $\sigma \to \infty$, (see App. D.3 for details on the numerical implementation and setup; in particular the current is given by (D.13)). In the force-free simulations, the continually development of electrically dominated regions (where the evolution equations breakdown) must be handled in an ad hoc manner, by reducing the magnitude of the electric field by hand, which gives rise to an artificial type of dissipation in regions where current sheets might develop in a more complete description of the plasma dynamics. Nevertheless, we can determine the effective dissipation rate by assuming energy conservation (5.44), as is common in the literature (e.g. [265]), and also compute the Poynting flux given by the force-free simulations at large distances and across the BH horizon. Encouragingly, these infinite conductivity results are in good agreement with the extrapolation of the resistive plasma simulations towards large conductivity, shown as the orange bands in the left panel of Figure 5.12. As we discuss in below, this turbulent dissipation component is associated with magnetic reconnection and other small scale features of the solution, and hence, is expected to remain finite even at very large bulk conductivities, $\sigma \to \infty$. The Poynting flux at large distances from the central BH in the force-free setting, shown in Figure 5.12, is consistent with the large-σ extrapolations of $P_{\rm EM}$ (i.e., is within the blue band in the left panel of Figure 5.12).

The bulk dissipation is linked to the large-scale visible electric field induced by the superradiance cloud, while the turbulent dissipation emerges from higher-order magnetic

field corrections. The former can be understood analytically in the non-relativistic limit, i.e., for $\alpha \ll 1$, by means of the solutions derived in (5.39). Given this solution and neglecting magnetic field effects, we can determine the electromagnetic current density of the plasma to be

$$\begin{aligned} \mathbf{J} &= \sigma \mathbf{E} \\ &= -\frac{e^{-r/r_c}\sqrt{M_c \mu}\alpha^{3/2}\varepsilon\sigma\omega^2}{2\sqrt{\pi}(\sigma^2+\omega^2)} \begin{pmatrix} \sigma + i\omega \\ -\omega + i\sigma \\ 0 \end{pmatrix} e^{-i\omega t} + c.c. \end{aligned} \tag{5.51}$$

In the non-relativistic limit, the spatial extend r_c of the superradiance cloud is large compared with the oscillation frequency $1/\mu$, implying local charge neutrality $\rho_q = 0$. Hence, the spatial dependence of J^i is a large scale modulation of the locally neutral plasma for $\alpha \ll 1$. Using the flat spacetime limit of (5.47), together with the above current density and the visible electric field solution (5.39), the bulk dissipation rate of the cloud in the $\alpha \ll 1$ limit is

$$L_{\rm diss}^{\rm bulk} = \frac{\sigma\alpha\varepsilon^2}{\mu(1+(\sigma/\mu)^2)}\frac{M_c}{GM} \ . \tag{5.52}$$

As expected, this quantity goes to zero in both the insulating and highly conducting limits, leading to free propagation of Poynting flux away from the system. From Figure 5.12, we can see that this expression provides a good approximation for the total dissipation for $\sigma \lesssim 2\mu$ for $\alpha = 0.3$, while for higher conductivities, the turbulent contributions, i.e., the magnetic field driven component, to J^i are more important.

Most relevant for determining the potentially observable electromagnetic signatures of superradiant systems are the $\sigma \to \infty$ estimates for $L_{\rm diss}$ and $P_{\rm EM}$ as functions of α. In the right panel of Figure 5.12, we show our results for $L_{\rm diss}$ and $P_{\rm EM}$ in simulations with $\sigma/\mu = 20$ as functions of α. Focusing on the numerical results first, it is evident from the right panel of Figure 5.12 that the Poynting flux and the total dissipation power have different scalings with α. The analytic estimate (5.52) for $L_{\rm diss}^{\rm bulk} \sim \alpha M_c/M$ suggests a leading order α-scaling of $L_{\rm diss}^{\rm num.} \sim \alpha M_c/M$, which we find in Figure 5.12 to provide the best fit to the data. For the Poynting flux, we find a leading-order scaling of $P_{\rm EM} \sim \alpha^3$ to

fit best. The two fits shown in the right panel of Figure 5.12, are[11]

$$L_{\rm diss}^{\rm fit} = \varepsilon^2 F(\alpha)\frac{M_c}{GM}, \tag{5.53}$$

$$P_{\rm EM}^{\rm fit} = \varepsilon^2 G(\alpha)\frac{M_c}{GM}, \tag{5.54}$$

with

$$\begin{aligned} F(\alpha) &= 1.31\times 10^{-1}\alpha - 1.88\times 10^{-1}\alpha^2, \\ G(\alpha) &= 6.86\times 10^{-4}\alpha^3 - 1.36\times 10^{-3}\alpha^4. \end{aligned} \tag{5.55}$$

Determining whether these scalings are also valid in the $\sigma\to\infty$ limit requires simulations with larger conductivities across a larger range of values for α. Hence, we estimate the theoretical uncertainties of the fits (5.53) and (5.54), indicated as orange and blue bands in the right panel of Figure 5.12, as follows. For $\alpha = 0.3$ (i.e., the left panel of Figure 5.12), we obtain a series of different $\sigma\to\infty$ extrapolations for both the total dissipation and the Poynting flux (blue and orange bands in the left panel of Figure 5.12). The spread of these $\sigma\to\infty$ extrapolating fits in the left panel of Figure 5.12, corresponds to the width of the orange/blue bands at $\alpha = 0.3$ in the right panel of Figure 5.12. We then use this relative uncertainty of the large-σ extrapolation at $\alpha = 0.3$ and apply it to the fits for total dissipation and Poynting flux, i.e., (5.53) and (5.54), for all α, hence, obtaining the orange and blue bands in the right panel of Figure 5.12. Therefore, the fit in (5.53) for $L_{\rm diss}$ is likely an over-estimate of the $\sigma\to\infty$ result (the lower bound of this extrapolation uncertainty is given by $L_{\rm diss}^{\rm fit}/4$), while the fit in (5.54) for $P_{\rm EM}$, is likely under-estimating the true flux at $\sigma\to\infty$. It is clear from Figure 5.12, that the turbulent dissipation power dominates over the total Poynting flux across the entire parameter space of the $m = 1$ superradiant state. Furthermore, the relatively flat α-scaling of the total power output is in stark contrast to the dependence of the total emitted gravitational wave energy flux $P_{\rm GW}\propto\alpha^{10}M_c^2/M^2$ from the oscillating dark photon cloud in the $\alpha\ll 1$ limit. Lastly, for comparison, the superradiant instability growth rate of the $m = 1$ state scales as $\Gamma\sim a_*\alpha^6\mu$.

5.6.3 Dissipation mechanism

Given the importance of the turbulent dissipation power, even at large conductivity, we next discuss the spatial dependence of the energy dissipation density $\rho_{\rm diss}$, defined in (5.48),

[11]Note, fits of the form $L_{\rm diss}^{\rm fit}\sim\alpha^p+\alpha^{2p}$ with $p\in(0.7,1)$ are plausible based on the numerical data and result in louder signals for $\alpha<0.1$. Fits with $p\in(1,1.2)$ are equally plausible, however, are entirely consistent with the large-σ extrapolation uncertainty of (5.53) down to $\alpha\sim 10^{-4}$.

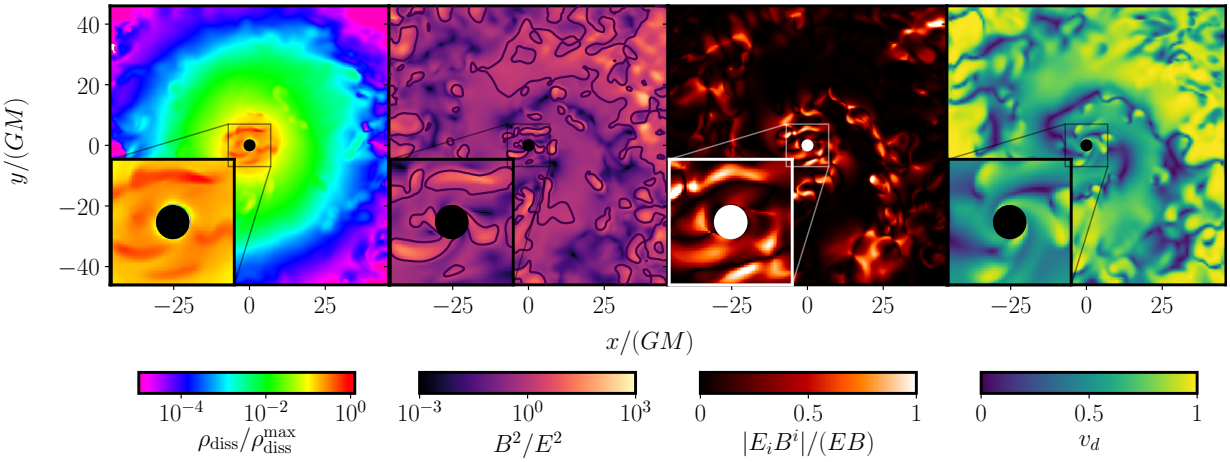

Figure 5.13: We plot the dissipation density $\rho_{\rm diss}$ (defined in (5.48)) normalized by the maximal density $\rho_{\rm diss}^{\rm max} = \max \rho_{\rm diss}$, the ratio of visible electromagnetic fields B^2/E^2, the violations of the force-free condition $E_i B^i = 0$ normalized by the magnitude of the visible electric and magnetic fields, and the magntiude of the plasma velocity $v_d = |\boldsymbol{v}_d|$ in the equatorial plane of the central BH. All panels correspond to the same coordinate time and a BH of spin $a_* = 0.86$, cloud with $\alpha = 0.3$, and plasma conductivity of $\sigma/\mu = 20$. We indicate where $B^2/E^2 = 1$ by a contour line. Regions of small plasma velocities, i.e., large magnetic diffusion, are also sites of large $E_i B^i \neq 0$ and locally enhanced energy injection density $\rho_{\rm diss}$. This implies that magnetic reconnection sites are locations of enhanced energy injection into the plasma.

and demonstrate that regions of high dissipation are associated with magnetic reconnection. This density captures the macroscopic energy injection of the electromagnetic fields into the plasma, driving dissipative processes at the microscopic level. Recall, magnetic reconnection sites are regions, where the connectivity of the otherwise frozen-in magnetic field is changed, resulting in large spatial current along the visible electric fields dissipating energy. In the following, we focus on the $\alpha = 0.3$, $a_* = 0.86$ and $\sigma/\mu = 20$ case, while commenting on how these results extrapolate to the physically relevant limit of high conductivity.

In the left panel of Figure 5.13, we show the local dissipation rate per volume $\rho_{\rm diss}$ [defined in (5.48)]. On large scales, this quantity follows the same exponential fall-off in the radial direction as the superradiance cloud (at $\sigma/\mu = 20$), while on smaller scales, strong variation associated with turbulent features is apparent[12]. We focus on the latter

[12]These two spatial components are naturally associated with the bulk and turbulent dissipation powers

since, as argued in the previous subsection, we expect these to persist (though develop smaller scales) in the $\sigma \to \infty$ limit. From Figure 5.13, it is clear that the regions of local enhancement in the dissipation are associated with magnetic dominance (second panel) combined with $|E_i B^i| \sim EB$ (third panel), or with electric dominance. From Eq. (5.37), the plasma either allows for a significant component of the current parallel to the electric field. Focusing on the insets showing the neighborhood of the BH, locations of the locally enhanced dissipation density, in addition to having large $|E_i B^i|$ and being magnetically dominated, are also bordered by zones of low drift velocity v_d (or equivalently, small magnetic Reynolds number R_m; fourth panel), which are associated with efficient magnetic reconnection. Farther away from the BH, large regions (at $\sigma/\mu = 20$) are strongly electrically dominated, and associated with enhanced dissipation and low drift velocity (in contrast to the magnetically dominated regions which have $v_d \sim 1$), again indicating strong magnetic diffusion and reconnection.

The magnetic field geometry within the plasma is set by the three different spatial scales discussed in Sec. 5.5.4. The differential rotation on scales of the cloud induces a shearing of the magnetic field lines on scales of the cloud r_c around the spin-axis of the BH, while the intermediate scale oscillations of the plasma (both in the equatorial plane and longitudinally along the BH spin axis) drive twisting of the field lines on scales of $1/\mu$. This combined macroscopic build-up of magnetic field twisting is released in magnetic diffusion regions associated with currents along the visible electric fields of thickness $1/\sigma$. As discussed in more detail in Sec. 5.5.3, regions of small magnetic Reynolds number $R_m = \sigma v_d/\mu$ are characterized by efficient magnetic diffusion. In these diffusive regions, the connectivity of the magnetic field lines changes, i.e. reconnection occurs, which drives enhanced dissipation and accounts for the dominant channel for the loss of electromagnetic energy in the superradiance cloud-plasma system.

To illustrate this connection explicitly, we show two example magnetic reconnection events in Figure 5.14. In panel (b) of Figure 5.14, magnetic field lines enter the reconnection region (labelled "3.") from the top along the white arrow (and from behind the semi-transparent plane on which $\rho_{\rm diss}$ is plotted). These same field lines exit the region in *two* directions along the two black arrows (similarly for the lines entering from behind the semi-transparent plane). The point where the field lines diverge is associated with the magnetic field magnitude dropping to near zero (indicated by the color of the magnetic field lines) and locally enhanced dissipation density $\rho_{\rm diss}$ (indicated by the color in the semi-transparent plane). This is characteristic of discontinuous reconnection, where the magnetic field lines change connectivity discontinuously along a line or plane where the magnetic field goes to zero. In two dimensions, X-point reconnection is the canoncial

$L^{\rm bulk}_{\rm diss}$ and $L^{\rm turb}_{\rm diss}$, driven by electric and magnetic fields, respectively (as discussed in the previous section).

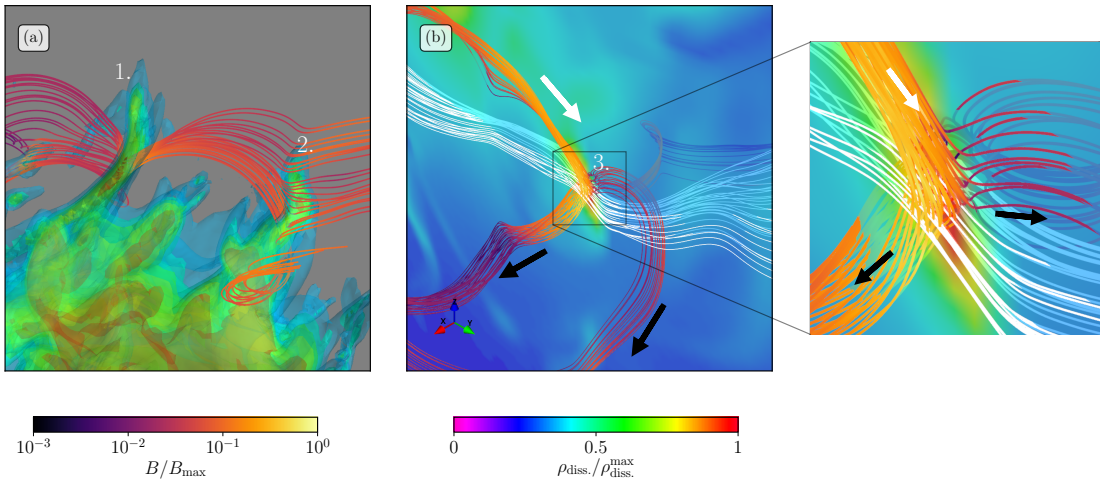

Figure 5.14: We show the visible magnetic field lines (in dark/yellow, color indicating the visible magnetic field strength normalized by the global maximum $B/B_{\rm max}$) and electric field lines (in white), as well as the local dissipation density $\rho_{\rm diss}$ (all colors) in two different contexts. Both panels show a close-up of the plasma roughly $15GM$ away from the central BH of spin $a_* = 0.86$, as well as $\alpha = 0.3$ and $\sigma/\mu = 20$. In *(a)*, the dissipation density is shown as semi-transparent isosurfaces. The BH is located towards the bottom of the plot. In *(b)*, the dissipation density is plotted on a semi-transparent plane spanned by the z and y directions. Here the BH is located towards the top left of the plot. The numbers in both panels indicate regions of large energy injection into the plasma. The arrows show the divergence of magnetic field lines away from the reconnection site. A detailed discussion can be found in the main text.

example of discontinuous reconnection, and most prominent in current sheets of the pulsar magnetosphere powering the high-energy component of the electromagnetic emissions. In particular, the field line geometry shown in panel (b) of Figure 5.14 resembles spine-fan type magnetic reconnection [240, 302].

We show a second example of reconnection in panel (a) of Figure 5.14, where we isolate two sites of large magnetic field gradients. There, we show a set of visible magnetic field lines that are strongly twisted as they connect two regions of locally enhanced $\rho_{\rm diss}$ (labelled as "1." and "2."), separated by a distance of $\sim 1/\mu$. Within each dissipation region, the field lines are curved on smaller scales (plausibly set by $1/\sigma$). The strong field gradients in these regions, as well as the fact that the magnetic field magnitude does not go to zero, make this example more consistent with continuous reconnection, where magnetic field

lines pass through each other in a diffusion dominated region of small plasma velocity[13] (see also Figure 5.13).

Therefore, we find that the visible magnetic field line connectivity changes discontinuously (and we find evidence for continuous reconnection) at various places in the bulk of the cloud. Both types are accompanied by enhanced energy injection into the plasma. The reconnection is fundamentally driven by the fixed orbital frequency of the superradiant magnetic field, suggesting that, for even larger conductivities, $\sigma/\mu \gg 20$, the qualitative picture is unchanged. We expect that, in this limit, though the size of the diffusion regions may decrease as $\sim 1/\sigma$ down to micro-physical scales, the rate of energy dissipation, which is driven by reconnection, remains roughly constant. Identifying the changing connectivity of the magnetic field as the driver of dissipation allows us to make a connection with existing kinetic analyses to roughly estimate the particle and emission spectrum of the system, which is the subject of Sec. 5.6.5.

5.6.4 Periodicity of emission

So far, we have discussed the total time-averaged Poynting flux and turbulent energy injection into the plasma, ignoring the time-dependence of the emission. In the case of a pulsar, the beamed radio emission, as well as the pulsed high-energy component of the spectrum are characteristics that emerge from the oscillation of the magnetic dipole field around the spin-axis of the star. Since even in the well-studied pulsar case, the radio emission mechanism is a topic of debate, we ignore it in the following, returning to a brief discussion of this low-frequency component in Sec. 5.6.5. The pulsed X-ray component of the pulsar spectrum requires a large-scale, coherent magnetic field geometry deep inside the light cylinder, along which charges are accelerated and radiate, or an oscillating current sheet outside the light cylinder [43, 42, 101, 298, 212]. In the context of the superradiant system considered here, we do not find such coherent and persistent field or current sheet structures, at least at the conductivities we consider in this study. Instead, we find the plasma surrounding the BH to be in a turbulent state without persistent large-scale magnetic or electric fields. However, since this is driven periodically by the superradiant fields at a frequency ω one may naïvely expect the electromagnetic emission to still be periodic as well. Because modeling the light curve, as is done in the pulsar case (see e.g., Refs. [42, 101]), is challenging for the superradiant system, we consider

[13] Continuous type reconnection typically occurs at quasi-separatrix layers with large, but bounded, squashing degree [240, 302, 140]. We do not attempt to identify quasi-separatrix layers, instead resort to identifying reconnection zones based on field diffusivity, magnetic field curvature and dissipation density.

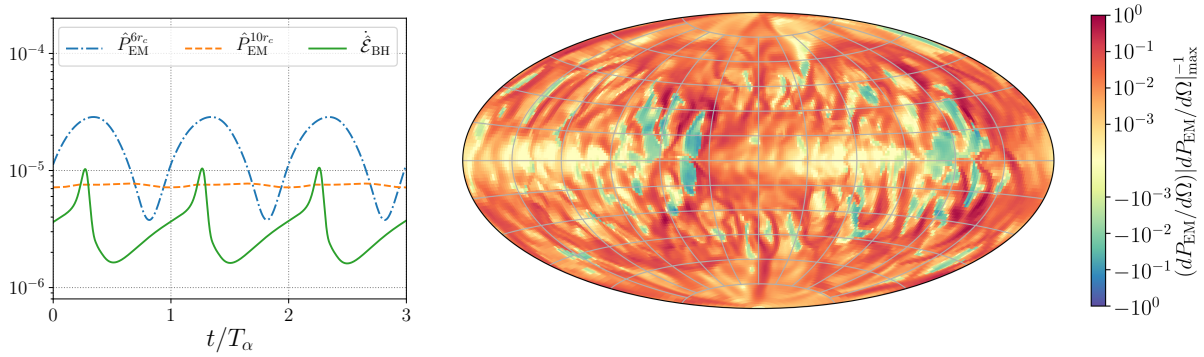

Figure 5.15: Here we consider a system with a BH of spin $a_* = 0.86$, a superradiant cloud with $\alpha = 0.3$, and a plasma conductivity of $\sigma/\mu = 20$. *(left)* We show the time dependence of the total visible Poynting flux entering the BH $\dot{\hat{\mathcal{E}}}_{\rm EH}$ and the outward flux $\hat{P}_{\rm EM}$ through spheres of coordinate radii of $6r_c$ and $10r_c$. Hats indicates the rescaling $\hat{P} = P(G/\varepsilon^2)(M/M_c)$. Time is normalized by the period of the superradiance cloud $T_\alpha = 2\pi/\omega$. *(right)* We show a snapshot of the visible Poynting flux per solid-angle (centered on the BH) through a coordinate sphere at $6r_c$, normalized by the maximum value. Due to the differential rotation of the turbulent plasma, this pattern only rotates slowly along the azimuthal direction, i.e., with period $T \gg T_\alpha$. At a coordinate radii of $10r_c$, the periodic modulation of the amplitude of the Poynting flux is mostly gone, indicating that the dissipation in the interior region is periodic. The small-scale features in the angular distribution $dP_{\rm EM}/d\Omega$ is a result of the formation of current sheets and turbulence in the plasma.

the time-dependence of the macroscopic Poynting flux at large distances, as well as the energy dissipation density throughout the bulk of the cloud in order to understand the temporal evolution of the electromagnetic emission. We find that the (sub-dominant) Poynting flux shows signs of periodicity, and the dissipation density locally exhibits weak evidence of periodicity. We close this section by discussing techniques which could improve our understanding of the temporal and viewing angle dependence of the electromagnetic emission.

We begin by discussing the time-dependence of the amplitude and angular distribution of the total Poynting flux. In the left panel of Figure 5.15, we demonstrate that both the total Poynting flux entering the BH, and the flux passing through a coordinate sphere at distance $6r_c$ from the central BH, vary periodically on timescales set by the cloud's

frequency[14]. The periodic absorption of electromagnetic energy by the BH is driven by the longitudinal periodic plasma motion in the vicinity of the event horizon elaborated on below. The plasma density is expected to roughly follow the profile of the superradiance cloud (compare (5.18)), and thus the conductivity should decrease exponentially away from the central BH. This, paired with the decreasing contribution of the periodic component of $P_{\rm EM}$ with increasing distance[15] (as shown in Figure 5.15), suggest that the Poynting flux periodically injects energy into the plasma $\sim \mathcal{O}(r_c)$ away from the BH. Hence, the periodicity of the total emitted Poynting flux is suggestive of periodic electromagnetic emission.

We now turn to the temporal variation of the energy injection density $\rho_{\rm diss}$ into the plasma. Generally, the dissipation density follows the motion of the plasma on scales of $1/\mu$ and r_c. Close to the BH, the most relevant periodic motion of the plasma is the longitudinal motion (discussed in Sec. 5.5.3) along the spin-axis of the BH. In the first panel of Figure 5.16, the dissipation density is peaked in pockets above and below the BH, moving along the spin-axis towards the equatorial plane, as indicated by the arrows. This corresponds to the time when the overall maximum of the dissipation density is at its lowest value per period, as shown in the bottom plot in Figure 5.16. Subsequently, two regions of enhanced dissipation density (and the associated plasma) collide within the equatorial plane, as show in the middle panel of the top row, leading to locally and temporally large amplitudes of the energy injection rate $\rho_{\rm diss}$. Finally, the regions of enhanced dissipation density begin to move away from the equatorial plane along the spin-axis in the last panel in the top row of Figure 5.16, and the associated maximum of the dissipation density decreases. This process repeats on timescales of the cloud's period. It is non-trivial to translate this behavior directly into observable variations of the electromagnetic signature. We may speculate, however, that this periodic enhancement of the dissipation density could lead to a periodic flaring of the superradiance cloud (analogous to e.g., [265, 270, 314]). It should be noted though, that the total integrated turbulent energy dissipation does not show significant temporal modulations.

In summary, both the Poynting flux and the local dissipation rate exhibit weak evidence of periodicity on timescales set by the dark photon mass $1/\mu$. Ultimately, our large-scale macroscopic description of the system is insufficient to resolve and understand the micro-

[14]Notice, the *visible* Poynting flux at finite distances from the BH contains propagating massive dark photon states that are bound to the BH. This component is exponentially suppressed at large distances. Hence, we have made sure that the contribution to $P_{\rm EM}^{6r_c}$ in Figure 5.15 from the massive states is negligible.

[15]Recall, the conductivity is spatially constant in our simulations. At $\hat{\rho} = 10r_c$, the conductivity is several orders of magnitude smaller compared with (5.18); hence, the physical relevance of the Poynting flux at those large distances should be interpreted with caution.

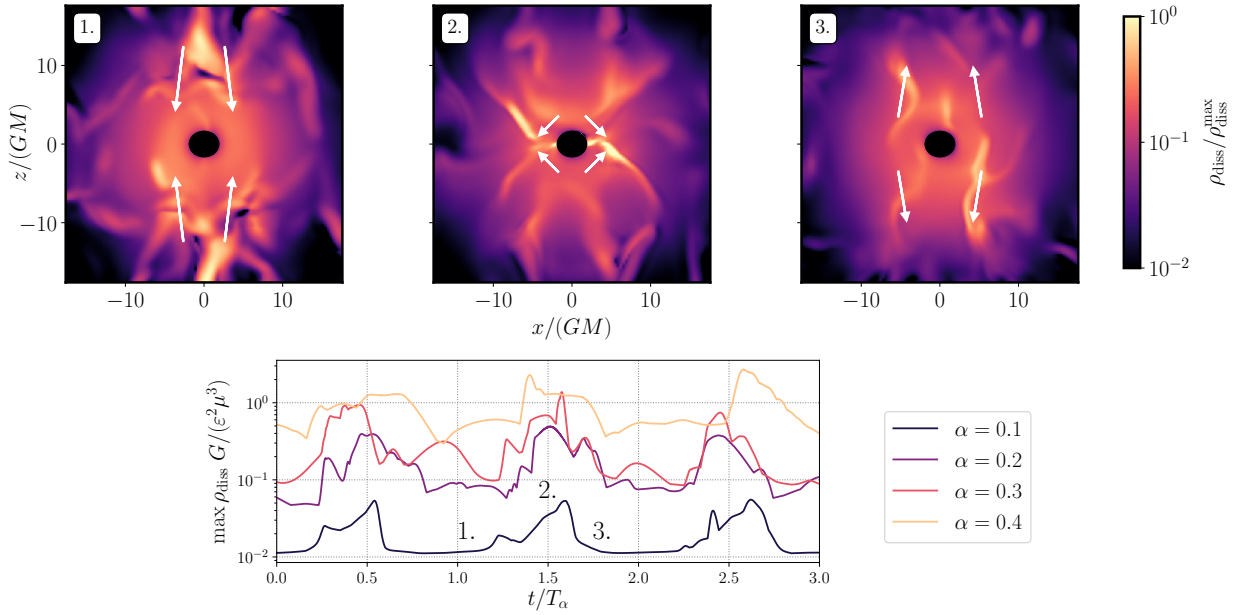

Figure 5.16: *(top row)* We show the dissipation density $\rho_{\rm diss}$ in the plane spanned by the BH spin and a fixed direction in the equatorial plane at three instances during a single superradiance cloud period. Here we focus on a BH with spin $a_* = 0.86$, $\alpha = 0.3$, and plasma conductivity $\sigma/\mu = 20$. The arrows indicate the direction of the motion of the features, and are discussed in detail in the main text. *(bottom)* We plot the maximum of the dissipation density $\max \rho_{\rm diss}$ as a function to time (normalized by the cloud's period $T_\alpha = 2\pi/\omega$) for different values of $\alpha \in \{0.1, 0.2, 0.3, 0.4\}$ (and associated saturated BH spins satisfying $\omega = \Omega_{\rm BH}$, see Tab. D.1). In the bottom panel, we also indicate the times of the snapshots in the top panels by their corresponding number labels. Over the course of a single period of the superradiance cloud, the plasma undergoes periodic motion along the BH's spin axis (as indicated by the arrows in 1. and 3. in the top row), leading to peaks in the local dissipation density, when the plasma from below and above the BH collide in the equatorial plane (corresponding to snapshot 2.).

scopic particle acceleration processes active in the turbulent plasma. As well, with our current treatment, we are unable to determine how the local dissipation rate translates into observing-angle-dependent radiation, though naïvely one expects this to be strongly modulated by the oscillation of the superradiance cloud. This could be improved by consider a small domain near the BH and using higher resolution to resolve higher values of conductivity than considered in this study, e.g., using local resistive force-free techniques.

This could determine whether coherent magnetic and electric field geometries remain inside the light cylinder, even at very large conductivities. These sufficiently large scale field geometries may then be used to perform light curve modeling paralleling the advances made in understanding high-energy pulsar light curves. Another avenue could be to utilize particle-in-cell (PIC) simulations of the turbulent regions of the plasma. This would recover the particle acceleration and non-thermal heating within the plasma, and could therefore be utilized to understand the time- and angular-dependence of the X-ray/gamma-ray sky map of the superradiant system.

5.6.5 Emission spectra

The plasma is characterized by differential rotation on scales of the entire cloud, superradiant driving on scales of $1/\mu$, and turbulence down to microscopic scales accounted for in our setup by the inverse conductivity $1/\sigma$. Visible electromagnetic energy is dissipated into the pair plasma by resistive processes. Likely this dissipation occurs primarily through particle acceleration, with the subsequent synchrotron emission of highly boosted particles leading to high energy photons that escape the system. Besides this non-thermal component at the high-energy end of the emission spectrum, various coherent low-energy radio emission processes may be active in regions of the superradiance cloud. In the following, we briefly review existing kinetic theory results for the spectra of turbulent pair plasma and possible low-frequency radio emission mechanisms that may be relevant to the emission spectrum for the system considered here.

In the pulsar magnetosphere, resistive processes occur mainly in current sheets outside the light cylinder. There, magnetic dominance is lost, and electromagnetic energy is efficiently dissipated by accelerating and heating the plasma. In order to gain insight into the microphysical processes in these accelerating regions, kinetic approaches based on numerical PIC methods are typically utilized [275]. Within this framework, the distributions of charged particles are evolved in time according to the Lorentz force of the local electromagnetic field, while back-reacting on the ambient fields through the charge and current they source. Local simulations resolve microphysical scales such as the Lamour radius $r_L = m_e\gamma/(eB)$ of an electron with mass m_e and boost factor $\gamma = E_e/m_e$ in an ambient magnetic field of strength B. Therefore, these methods are powerful tools to determine the classical particle kinetic spectrum self-consistently from first principles. On the other hand, radiative corrections to the particle motion, pair production, are neglected, or added in an ad-hoc fashion, and the expensive nature of these simulations make it difficult to apply in a global setting, while still achieving sufficient resolution to accurately approximating the microphysics. Nonetheless, PIC methods have successfully recovered the global pulsar

magnetosphere, the expected non-thermal particle spectrum, and have played a central role in studies of the radio emission mechanism of pulsars [299, 101, 381].

In the case of magnetic reconnection, PIC approaches have found that the local electron acceleration results in a particle distribution $N_e(\gamma)$ with a high-energy, power-law tail below a cutoff γ_c, of the form $dN_e/d\gamma \propto \gamma^{-p} e^{-\gamma/\gamma_c}$ [371, 345, 184], for $\gamma \gtrsim 1$ (see also Refs. [210, 370, 100, 101, 298]). The size of the resistive region ℓ sets the high-energy cutoff γ_c as the boost factor where ℓ equals the Lamour radius. Most applicable to the superradiant system at hand are studies focusing on three-dimensional turbulent pair plasmas [383, 113], determining the power-law to be roughly $p = 2.8$, for large plasma magnetizations. We leave a detailed investigation of the kinetic spectrum in the context of a kinetically mixed superradiance cloud to future work, and in the following make a crude estimate of the high-energy component of the emission associated with this electron kinetic spectrum based on the characteristic length scales and field strengths. The high-energy cutoff $\gamma_c = e\ell\langle B^2\rangle^{1/2}/m_e$ is set by the average ambient magnetic field strength $\langle B^2\rangle^{1/2}$, defined by $\langle B^2\rangle = 1/S_{2r_c}\int_{S_{2r_c}} dV B^2$, where S_{2r_c} is a coordinate volume of a sphere of radius $2r_c$ centered on the BH. From the resistive force-free simulations with $\sigma/\mu = 20$, we extract this root-mean-square magnetic energy for each value of α we consider. Fitting the α-dependence by[16] $\sim \alpha^{5/2}$, the average magnetic field is

$$\langle B^2\rangle^{1/2} = 2.5\times 10^8 \text{ Gauss}\left(\frac{\varepsilon}{10^{-7}}\right)\left(\frac{M_\odot}{M}\right)\left(\frac{\alpha}{0.1}\right)^{5/2}. \tag{5.56}$$

With this, the cutoff electron and positron boost factor, with $\ell = 1/\mu$, is given by

$$\gamma_c \approx 2.2\times 10^7 \left(\frac{\varepsilon}{10^{-7}}\right)\left(\frac{\alpha}{0.1}\right)^{3/2}. \tag{5.57}$$

The size of the resistive region could be set by smaller length scales than the $1/\mu$ value used above. However, for most the parameter space of interest, the effects of the radiation reaction will become important for much lower boost factors than in (5.57). Synchrotron backreaction becomes significant, when the radiation reaction timescale $\tau_R = E_e/P_e^{\rm sync}$, where $P_e^{\rm sync}$ is the total single electron synchrotron power, is comparable to, or smaller than, the Lamour timescale $\tau_L = 2\pi r_L$. Hence, this radiation reaction becomes important for $\gamma > \gamma_r = (3m_e^2/(e^3\langle B^2\rangle^{1/2}))^{1/2}$ with

$$\gamma_r = 3\times 10^3 \left(\frac{10^{-7}}{\varepsilon}\right)^{1/2}\left(\frac{M}{M_\odot}\right)^{1/2}\left(\frac{0.1}{\alpha}\right)^{5/4}. \tag{5.58}$$

[16] Functions of the form $\sim \alpha^2$ or $\sim \alpha^3$ provide worse fits, but are plausible given the numerical and theoretical uncertainty.

Therefore, in the regime $1 \lesssim \gamma < \min(\gamma_r, \gamma_c)$, the power-law electron and positron kinetic spectrum results in a synchrotron photon spectral power-law $P(\nu) \propto \nu^{-s}$ with spectral index $s = 0.9$ [322] (assuming $p = 2.8$ [113]), making up the non-thermal tail of the high-energy component of the emitted photon spectrum, while above this range the synchrotron spectral index is modified. The synchrotron spectrum from a single electron or positron in this non-thermal distribution with $\gamma \leq \gamma_r$ peaks at emission frequencies

$$\nu_{\rm peak} = 12 \text{ keV} \left(\frac{\gamma}{10^2}\right)^2 \left(\frac{\varepsilon}{10^{-7}}\right) \left(\frac{M_\odot}{M}\right) \left(\frac{\alpha}{0.1}\right)^{5/2}, \tag{5.59}$$

where the value of γ is chosen inspired by simulations presented in [101] and a dedicated PIC simulation will be helpful to determine the exact spectrum, and an electron with kinetic energy of $m_e\gamma_r$ radiates mostly at $\nu_r = 6.4$ MeV.

In summary, in the superradiance cloud, the electromagnetic fields lose energy predominantly through magnetic reconnection in a strong ambient magnetic field with strength on the order of (5.56). We can expect that this efficiently accelerates electrons and positron to large boost factors, $\gamma \sim \mathcal{O}(10^3)$, as given by the minimum of the values in (5.57) and (5.58), and that these high-energy particles then radiate synchrotron photons in the process, with spectrum ranging from a few keV up to MeV [see (5.59)]. Therefore, it is likely that there will be strong non-thermal high-energy component of the emission spectrum from the kinetically mixed superradiance clouds.

We turning now to the low-frequency, i.e., radio, end of the spectrum, where the emission mechanisms are far less well-understood. Even in the well-studied pulsar case, this a topic of debate. Low-frequency electromagnetic phenomena such as pulsar radio emissions and fast-radio bursts are thought to be sourced through a shock induced synchrotron maser emission mechanism in the pulsar wind, reconnection driven radio emission, or near field processes [381]. In, for instance, Refs. [248, 297], plasmoids forming from the discontinuous reconnection of the pulsar current sheet was demonstrated to result in the emission of fast magnetosonic waves, plausibly escaping as radio emission to infinity. Therefore, the efficient magnetic reconnection of the superradiant plasma, some of which occurs through the discontinuous reconnection channel, suggests that the cloud is a source of continuous radio flux as part of the total power output[17]. Furthermore, as discussed above in Sec. 5.6.4, the plasma performs periodic longitudinal motion along the BH spin axis with frequency $1/\mu$, resulting in collisions of regions with enhanced dissipation density within the equatorial plane close to the central BH. If these collisions, at the microphysical level, manifest as

[17]We note that, near the BH, the plasma frequency is on the order of a GHz, but it is expected to decrease exponentially away from the BH with the superradiance cloud density (see Sec. 5.4.3).

colliding shock waves and trigger a synchrotron maser mechanism in the process (see, e.g. Refs. [259, 301]), then one would expect periodically enhanced radio flux from these shocks. Hence, the naïve expectation is that the plasma-filled superradiance cloud is a source of continuous radio flux, together with periodic peaks in the radio power with pulse period set by the dark photon mass $1/\mu$.

5.7 Multimessenger Signals

The system studied thus far motivates a novel target for multimessenger searches: a new bright, possibly periodic, source with specific, unusual properties. In this section, we summarize the relevant dynamics and observational signatures of the kinetically-mixed dark photon superradiance cloud. The numerical simulations performed in this chapter give us an estimate of the total electromagnetic power emitted, but do not directly provide the spectrum of the emitted radiation, nor conclusively establish its periodicity.

Nevertheless, the unique properties of the system and the analogy with the well-studied neutron star pulsars allow us to identify promising search strategies based on our system's combination of electromagnetic and GW emission. Given reasonable assumptions, outlined below, we expect current and planned telescopes and GW observatories to reveal dark photons in the $10^{-14} - 10^{-11}$ eV mass range, with kinetic mixing below the current cosmological bound $\varepsilon \lesssim 3 \times 10^{-7}$.

The evolution of our new pulsar begins with the birth of a new, rotating, BH. Around this BH, the superradiance instability populates a cloud of dark photons in $\mathcal{O}(100)$ superradiance times[18],

$$t_{\rm growth} \sim \ln(M_c/\mu)\tau_{\rm SR} \approx 10^4\,{\rm s}\left(\frac{M}{10\ M_\odot}\right)\left(\frac{0.7}{a_*}\right)\left(\frac{0.1}{\alpha}\right)^7. \tag{5.60}$$

The resulting large electromagnetic fields will, for large enough values of the kinetic mixing parameter, $\varepsilon \gtrsim 10^{-10}$, build up a dense plasma of charged particles in the last few e-folds before saturation (see Sec. 5.4). The rotation of the cloud and resulting turbulent electromagnetic processes in the plasma lead to a large flux of electromagnetic emission from the system, as described in Secs. 5.5 and 5.6.2. The energy output is dominated by the

[18] The results in this section are obtained using the gravitational waveform model `SuperRad` [342] for the superradiant vector cloud, with approximate expressions for the timescales, etc. given to guide the reader.

dissipative losses in the turbulent regions, which we infer from our numerical simulations (see Eq. (5.53)) to be

$$\begin{aligned} L_{\rm EM} &= \varepsilon^2 F(\alpha)\frac{M_c}{GM} \simeq \varepsilon^2\frac{\alpha^2\Delta a_*}{G} \\ &\simeq 4\times 10^{41}{\rm erg/s}\left(\frac{\varepsilon}{10^{-7}}\right)^2\left(\frac{\alpha}{0.1}\right)^2\left(\frac{\Delta a_*}{0.1}\right), \end{aligned} \tag{5.61}$$

where $F(\alpha) = 0.13\alpha - 0.19\alpha^2$ is a polynomial fit to the simulations, and we used the mass of the superradiance cloud at its maximum and the small α limit. The luminosity can be up to five orders of magnitude brighter than the Crab pulsar's bolometric luminosity [198], and up to ten orders of magnitude brighter than the solar luminosity. In the following, we will assume the luminosity to be given by Eq. (5.61) also for $\alpha < 0.1$, below the smallest simulated value.

The cloud slowly decays through emission of GWs and electromagnetic radiation on a timescale generally dominated by the gravitational dissipation of the cloud, except at small dark photon masses and large mixing, as shown in the left panel of Fig. 5.17. The observable electromagnetic signal lasts for $\sim \min\{\tau_{\rm GW}, \tau_{\rm EM}\}$,

$$\begin{aligned} \tau_{\rm GW} &\approx \frac{GM}{17\alpha^{11}\Delta a_*} \approx 10^6\,{\rm s}\left(\frac{M}{10M_\odot}\right)\left(\frac{0.1}{\alpha}\right)^{11}\left(\frac{0.1}{\Delta a_*}\right), \\ \tau_{\rm EM} &\approx \frac{GM\ln 2}{\varepsilon^2 F(\alpha)} \approx 10^{11}{\rm s}\left(\frac{M}{10M_\odot}\right)\left(\frac{10^{-7}}{\varepsilon}\right)^2\left(\frac{10^{-2}}{F(0.1)}\right). \end{aligned} \tag{5.62}$$

The decay is power-law in time when more energy is released in GWs than electromagnetic radiation and exponential otherwise,

$$\frac{M_c(t)}{M_c(t_0)} = \begin{cases} [1+(t-t_0)/\tau_{\rm GW}]^{-1} & \tau_{\rm GW} \ll \tau_{\rm EM} \\ e^{-(t-t_0)/\tau_{\rm EM}\ln 2} & \tau_{\rm GW} \gg \tau_{\rm EM}. \end{cases} \tag{5.63}$$

At small α and large enough ε, the superradiance growth time $\tau_{\rm SR}$ can become slower than $\tau_{\rm EM}$, possibly preventing the cloud from reaching its full size. A detailed study of the cloud saturation in this case is beyond the scope of this work and we always require $\tau_{\rm SR} < \tau_{\rm EM}$, which applies to most of the open parameter space (see Fig. 5.17).

To summarize, the evolution of a kinetically mixed cloud is fully fixed by the dark photon mass μ, which sets the overall fundamental scale, and the dimensionless couplings ε and

α. Over the lifetime of the cloud, the electromagnetic and GW signals grow exponentially—at a rate fixed uniquely by the dark photon mass and α—until the cloud reaches its maximum size, and then decrease on longer timescales as the cloud disappears.[19] If the GW radiation dominates, there is a unique relation between the growth and decay timescales, $\tau_{\rm SR}$ and $\tau_{\rm GW}$. For $\alpha \ll 1$ (for which the GW timescale is given by Eq. (5.11)) it takes the approximate form

$$\tau_{\rm SR} \simeq 0.98\, \tau_{\rm GW}^{7/11} r_g^{4/11} \left[a_* \left(\frac{\Delta a_*}{0.5} \right)^{7/11} \right]. \tag{5.64}$$

We show the characteristic electromagnetic luminosities and their time evolution due to GW emission in the right panel of Fig. 5.17.

Clearly, the observational prospects of this system depend heavily on the spectral shape of the electromagnetic radiation; unfortunately, our simulations do not give us this information. However, given the similarities of our system to pulsars, which have been observed across electromagnetic bands in many systems, and have PIC simulations in agreement with aspects of the observations, we can make educated guesses as to the expected emission in different bands.

In analogy with neutron star pulsars, one dominant emission mechanism could be synchrotron radiation. As discussed in Sec. 5.6.5, the boost factor of electrons and positrons in the cloud peaks in the range $\gamma \sim \mathcal{O}(10-100)$, giving typical electron radiation frequencies ranging from keV to a few MeV. Depending on the value of the kinetic mixing and BH mass, most of the spectrum would fall within the range of X-ray telescopes, such as Chandra [3] and Swift [87] of $\mathcal{O}(0.1-10\,{\rm keV})$ or Fermi-GBM (8 keV to 1 MeV) [37].

GW emission from the system is monochromatic with frequency $f_{\rm GW} = \omega/\pi$, and the electromagnetic emission is also expected to have periodicity on timescales of $1/\omega$ (Sec 5.6.4). Here, ω is the energy per dark photon, given by its rest mass with $\Delta\omega/\mu \approx -\alpha^2/2 - \mathcal{O}(\alpha^4)$ corrections due to the gravitational potential energy of the BH [53] and $\Delta\omega_c/\mu \approx -(5/8)\alpha^2 M_c/M$ the gravitational self-energy of the cloud [342]. The combination of the decrease of the BH mass as the cloud grows, and the decrease of the cloud mass as it decays, result in a monotonically increasing frequency correction. In other words, the cloud period *decreases* during the whole evolution of the cloud [342], in stark contrast with conventional pulsars, for which the period increases in time. Thus, rotating BHs can host an anomalously bright "pulsar" which spins up over time [33].

This new type of pulsar has several unique features and a peculiar evolution history. While there are a variety of signatures that can be looked for, here we highlight two

[19] The electromagnetic signal is only present for large enough cloud sizes M_c and kinetic mixings ε which are needed to generate the plasma, Sec. 5.4.

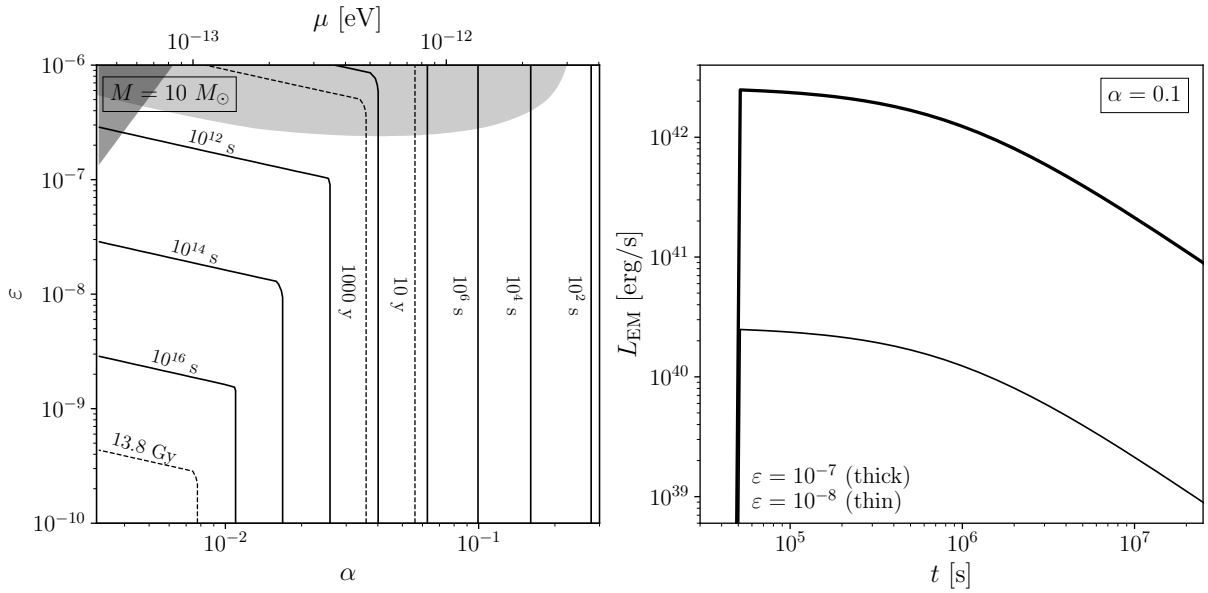

Figure 5.17: *(left)* Lifetime of the superradiance cloud as a function of the kinetic mixing parameter ε and the gravitational coupling α for a BH with an initial mass of 10 $M_\odot$ and spin of $a_* = 0.9$. At large α, the cloud decays through GW emission, and the lifetime is independent of ε. When α is too small, the power emitted in electromagnetic radiation overcomes the GW power and the cloud depletes faster for larger ε (see Eq. 5.62). In both regimes, the lifetime is proportional to the BH mass, $\tau \propto M$, so the transition is independent of the value chosen. The initial BH spin determines the largest value of α that satisfies the superradiance condition, but otherwise has a mildly effect on the lifetime of the cloud. In the dark gray shaded region $\tau_{\rm SR} > \tau_{\rm EM}$, while the light shading corresponds to parameters excluded by measurements of the CMB spectrum by COBE/FIRAS [154, 91]. *(right)* Time evolution of the superradiance cloud's electromagnetic luminosity (see Eq. 5.61) for two different values of ε, for $M = 10\ M_\odot$ and $a_* = 0.9$ (the luminosity is independent of M and only mildly dependent on a_*, while the decay time will increase for heavier BHs). After the spinning BH is formed, the energy emitted in radiation quickly grows exponentially with the superradiance cloud, and later slowly decreases due to the cloud mass decay through GW emission.

distinct observational prospects: searching for the emergence of a bright electromagnetic source from a known rotating BH remnant (with or without a periodic component), or searching for continuous GWs emitted by anomalous pulsars. These two observational strategies are best-suited to regimes of large and small α, respectively.

Name	Final BH mass [$M_\odot$]	Final BH spin	Dist. [Mpc]	$\Delta\Omega$ [deg^2]
GW170814 [9]	53.2	0.72	600	87
GW190814 [12]	25.7	0.28	230	19
GW200202_154313 [14]	16.76	0.69	410	170

Table 5.1: List of example compact binary merger events observed by LIGO-Virgo-KAGRA that are promising candidates for a dark photon superradiance search through electromagnetic follow up observations and corresponding central values of their parameters. See Fig. 5.18 for the observational prospects.

Given the signal uncertainties, we propose discovery oriented searches rather than exclusions. It is possible that the absence of a large number of ultraluminous X-ray sources already places limits on dark photon parameter space; however, given uncertainties in natal BH spin distributions, as well as in the emission spectrum of the dark photon cloud, such a constraint would not be robust. Similarly, we can speculate that such kinetically mixed superradiance clouds may account for some of the ultraluminous X-ray sources already observed [352, 300].

5.7.1 Electromagnetic follow-ups of black hole mergers

Most of the compact binary mergers detected by the LVK observatories result in a BH remnant with a mass between 10 to a 100 $M_\odot$ and high spin, due to the capture of a significant component of the binary's orbital angular momentum [85]. Electromagnetic follow-up observations of the mergers could reveal the existence of a dark photon superradiance cloud around the BH remnant. We select three illustrative events from the LSC O1-3 catalogs [9, 12, 14] and forecast the sensitivity of radio and X-ray searches in Fig. 5.18. The best targets and their inferred parameters are listed in Table 5.1; they correspond to the closest mergers with the best sky localization and one high mass and one low mass event, to cover the widest range of dark photon masses. We also include the possible neutron star–BH merger GW190814 [11], for which an electromagnetic counterpart was not found in the radio [135, 134, 174], optical, and near-infrared [219, 123, 359, 22, 366], and X-ray [279]. These null results could exclude new dark photon parameter space, provided a more reliable prediction for the emission spectra from the superradiance system.

For our projections, we assume an $\mathcal{O}(1)$ of the superradiance cloud luminosity (5.61) is emitted into X-rays and a $\mathcal{O}(10^{-4})$ fraction into radio frequencies, in analogy with the spectrum of standard pulsars [214, 249]. For the follow-up to detect the EM emission,

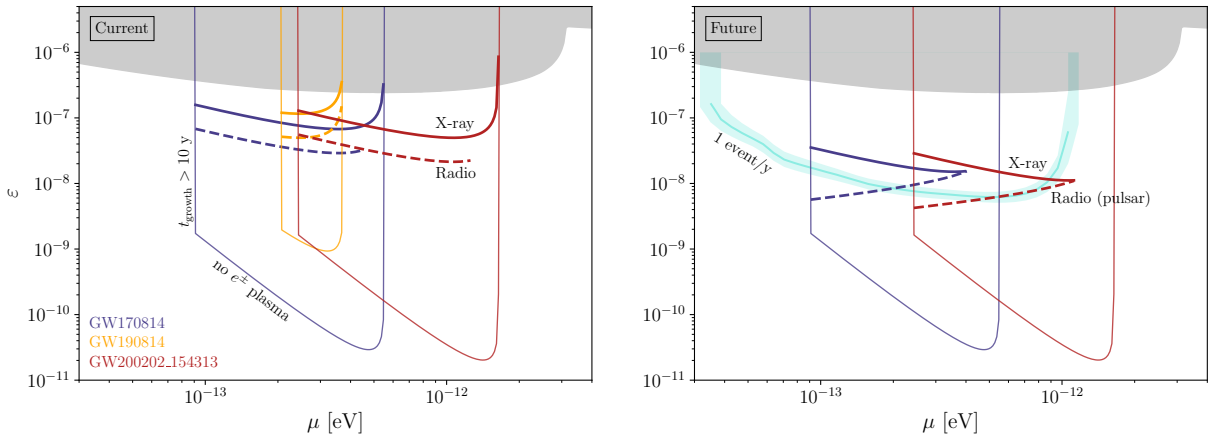

Figure 5.18: Range of dark photon kinetic mixing parameter ε and mass μ producing a visible signal for electromagnetic follow-up observations of LVK compact binary merger events with a BH remnant. As an example, we choose the three best target events: GW170814 (blue), GW190814 (yellow), GW200202_154313 (red) (measured parameters are given in Table 5.1). The thin solid lines show the regions where a signal could exist, which are bounded from below by the requirement that the visible electric field is large enough to produce the plasma (see Sec. 5.4 and Eq. (5.26)), to the left by the requirement that the cloud grows within 10 years (see Eq. (5.60)), and to the right by the superradiant condition for the fastest-growing bound state (see Sec. 5.2). The reach is further limited on the right by the signal duration falling below a minimum observational time. The gray shaded region is excluded by measurements of the CMB spectrum by COBE/FIRAS [154, 91]. *(left)* Current prospects for an X-ray [87] (solid) and radio transient [134] (dashed) search. *(right)* Future prospects for an X-ray search (solid) and a radio search for a pulsating source (dashed). See the text for more details. The cyan contour corresponds to one merger event per year visible in the X-ray, with shaded band indicating the error due to the uncertainty in the BH merger rate.

the cloud needs to grow within a reasonable observational timescale; for concreteness we impose the requirement $t_{\rm growth} < 10$ years (c.f. Eq. (5.60)), which translates into a large-α requirement given by $\alpha \gtrsim 0.036, 0.04$, and 0.03 for our three selected candidates. The left panel of Fig. 5.18 shows how current instruments could already measure a signal, taking a radio flux sensitivity of 40 μJy at 944 MHz for an observation time of 10 h, achievable by ASKAP searching for transient events [134], and an X-ray detection sensitivity of 2×10^{-14} erg cm^{-2}s^{-1} in 10^4 s, attainable by Swift-XRT [87] as it scans through the sky (eROSITA has similar performance [304]). Better reach can be achieved with Chandra,

which however requires prior angular localization. For instance, for sources with angular localization from radio observations, Chandra could probe almost an order of magnitude smaller X-ray fluxes [208].

The sky localization is expected to improve during O4 with the Advanced LIGO, Virgo, and KAGRA network, with about 10% of the events localized within 5 deg^2 [8], improving the prospects of detecting an electromagnetic counterpart. In the right panel of Fig. 5.18, we assume smaller positional errors that would allow a Chandra-like X-ray search sensitive to 10^{-15} erg $\mathrm{cm}^{-2}\mathrm{s}^{-1}$ fluxes in 10^5 s. In the same panel we also indicate with a cyan contour the region of parameter space above which more than one X-ray event per year from BH mergers could be observed with the same X-ray sensitivity. To obtain this contour we made use of the BH merger rate as a function of primary BH mass measured by LVK [16], assuming a final BH spin of 0.7, and a final mass equal to twice the primary mass. The shaded band around the cyan contour indicates the uncertainty in the merger rate.

The searches discussed so far in this subsection are aimed at a steady source that shines for as long as the required observational time, without assuming any periodicity. If we further assume partial or total periodicity in the electromagnetic emission power, a search for a long lasting pulsating radio signal could be performed. We estimate that the prospect of such a search with a sensitivity of 10 μJy at 1 GHz with 500 MHz bandwidth for 15 minute observations daily over the lifetime of the cloud,[20] which is comparable to the performances of FAST [268] and slightly better than CHIME [105].

The superradiance cloud could also have higher energy emission, up to γ-rays. Telescopes with nearly all sky coverage, such as *Fermi*-LAT [37], are well suited to perform follow-up observations of compact binary coalescences (which have been done and are planned during O4 [310]). Current flux sensitivities result in reach in kinetic mixing comparable to current constraints, but a signal could be detected in the event of an exceptionally close merger.

In the event of a positive detection of a new luminous source following a binary BH merger, there are non-trivial cross checks that can be used to confirm the superradiance origin of the signal. First, by measuring the peak luminosity of the different sources, the luminosity's unique dependence on the parameter α—Eq. (5.61)—can be verified. For a dark photon with a given mass and kinetic mixing, the luminosity will only depend on the BH mass and spin, which are measured in the merger. Secondly, the measured light curve should be consistent with an exponential growth as dictated by superradiance, and power-law decay, as expected from GW emission, with growth and decay timescales satisfying the non-trivial relation Eq. (5.64). Thirdly, if a pulsating electromagnetic signal

[20] Private communications with Kendrick Smith.

is observed, the measurement of the period, given by $2\pi/\mu$, can be used to extract the dark photon mass and verify the signal growth and decay times dependence on the parameter α—see Eqs. (5.60) and (5.62). Multiple sources will have the same period up to Doppler shifts of $\mathcal{O}(10^{-3})$, and gravitational potential corrections of up to a few percent. Finally, the superradiance system also emits continuous GWs with frequency ω/π, which could be detected with a search targeted on the luminous source [32, 206, 102, 342]. The GW has the same signal growth and decay times as the electromagnetic emission, which, together with the period coincidence, constitute unmistakable signatures of dark photon superradiance.

The discovery of such an ultraluminous source depends crucially on our ability to localize the newly formed BH. In particular, for sources with short duration (large α), it is important that the source is located hours before the merger to allow telescope observation coincident with the merger. Space-based, mid-band detectors can locate stellar mass BH merger events similar to GW150914 to an angular area of ~ 0.01 deg^2 an hour before the merger [177, 336]. Similar angular localization can be reached with the Laser Interferometer Space Antenna (LISA) and similar space missions for intermediate mass and supermassive BH mergers [119, 319]. These missions could significantly improve the chances of finding the X-ray and radio signals from the dark photon superradiance cloud.

5.7.2 Gravitational follow-ups of anomalous pulsars

If the superradiance electromagnetic emission is periodic, old galactic BHs dressed with a dark photon cloud could look like a neutron star pulsar, and be detected by ongoing surveys of pulsating sources. Such "fake" pulsars appear to be rotating at a single frequency f set by the dark photon mass, spin up over time, and emit continuous GWs with frequency $f_{\rm GW} = 2f$. Their GW strain is up to several orders of magnitude larger than the neutron star spin down limit and can be searched for with targeted continuous GW analyses.

We select two types of potential candidates in the ATNF pulsar catalogue [249, 1]. The first type is a set of frequency multiplets, *i.e.* sources i with at least one other pulsar j that satisfies $|f_i - f_j|/f_i < 10^{-3}$, which takes into account the spread in frequency due to Doppler shifts of $\mathcal{O}(10^{-3})$. The second type is a source with $\dot{f}_{\rm obs} > 0$ that is not known to be in a binary system, to avoid spurious positive spin frequency derivatives due to the source's acceleration in a binary orbit.

Since all these pulsars are within our Galaxy, the BH formation event must have occurred long enough ago so that it was not observed. We therefore impose $\tau_{\rm GW} > 10^3$ yr, which translates into a maximum value for $\alpha \lesssim 0.03 - 0.05$ for the selected sources. For each system, the dark photon mass is fixed to be $\mu = 2\pi f$ (gravitational corrections to

the dark photon energy are negligible in the small α limit). A lower bound on α is set by the smallest possible BH mass, which we take to be 3 $M_\odot$, resulting in $\alpha \gtrsim 0.05 - 0.005$ across the range of frequencies considered. We take the initial BH spin to be 0.5. A better choice for the BH spin would be to sample it from the spin distribution of the Galactic BH population; however, this is not well known.

We only consider sources with $f > 50$ Hz, since for a stellar mass BH, smaller frequencies would correspond to a very small α, and correspondingly small signal. Above this threshold, the ATNF catalogue contains 229 sources with measured f, distance, and with positive or unknown $\dot{f}_{\rm obs}$. Among these, there are 3 frequency triplets and 26 frequency doublets (19 of the doublets have a non-zero allowed range of α between the upper and lower bound), statistically compatible with the number of accidental multiplets expected for a uniform frequency distribution between 50 and 500 Hz. For each fake pulsar in a multiplet, the emitted GW strain cannot be uniquely predicted, since the BH mass and age (that sets the remaining superradiance cloud mass, and thus affects the GW emission power) are unknown. In the left panel of Fig. 5.19, we show the maximum possible strain for the allowed range of α values, for two example BH ages of 10^3 and 10^6 years. As pointed out previously, we do not consider younger systems. These young systems are excluded by all-sky searches for continuous GWs [17, 13], but strains below the current bounds are possible for older systems, and within the reach of a targeted search [18].

With the same selection criteria as above, but without requiring frequency multiplets, we find 20 sources with $\dot{f}_{\rm obs} > 0$, with values between 4×10^{-17} Hz/s and 5×10^{-14} Hz/s. Only 16 of these sources have a non-zero range of α values between the upper and lower bound. Interestingly, four of these sources (J0024-7204Z [157], B0021-72G [315, 157], J1801-0857C [244, 287], and B0021-72M [315, 157]) *also* belong to a frequency doublet. The frequencies of the four doublets are approximately 219.6, 247.5, 267.4, and 272.0 Hz. These candidates could be further strengthened (or disfavored) by performing spin derivative measurements of the other component of each of the doublets, which at present do not have $\dot{f}$ measurements, and that are J0514-4002D [312], J1824-2452J [156], J0024-7204ad [311], and J0125-2327 [263], respectively.

If the spin-up is due to the superradiance cloud decay through GW emission, we expect an intrinsic spin frequency derivative [342]

$$\dot{f}_{\rm int} \simeq \frac{5}{8\pi} \alpha \mu^2 G P_{\rm GW}. \tag{5.65}$$

The observed frequency derivative could differ from the intrinsic one due to additional positive contributions from acceleration along the line of sight. Thus, one should interpret the measured spin derivative $\dot{f}_{\rm obs}$ only as an *upper limit* on the intrinsic spin derivative.

Here, however, our intention is to provide a first example of how spin derivative measurements could be used to discover anomalous pulsars, so in what follows we simply neglect accelerations along the line of sight and assume $\dot{f}_{\rm obs} \simeq \dot{f}_{\rm int}$. With this assumption, the measured value of $\dot{f}_{\rm obs}$ fixes the power emitted in GWs $P_{\rm GW}$ for any given α. Since the power emitted decreases as the cloud's mass decays, there is a minimum α that allows for a spin up rate as large as the one observed when the cloud is as young as possible, i.e., at least 1000 yr. This lower bound on α is stronger than the one described above from the minimum BH mass for $f \lesssim 270$ Hz . Therefore, the observable strain is *predicted* to be within a small range given by the small spread of α values allowed, as shown on the left of Fig. 5.19 with the short segments bounded by the downward and upward pointing blue triangles.

We find that most sources should have already been seen by all-sky searches for continuous waves, but one candidate pulsar with a frequency around 600 Hz remains unconstrained, which could be an interesting candidate for a targeted search. We note that if the assumption $\dot{f}_{\rm obs} \simeq \dot{f}_{\rm int}$ is correct, the four previously mentioned events that are frequency multiplets and have $\dot{f}_{\rm obs} > 0$ would be excluded, since their $\dot{f}_{\rm obs} > 0$ measurement leads to a strain prediction that is already ruled out by existing GW searches. These sources, however, could certainly be compatible with data if $\dot{f}_{\rm int} < \dot{f}_{\rm obs}$, due to the source accelerations along the line of sight that we have neglected.

For each anomalous pulsar, the kinetic mixing parameter could lie within a range of allowed values, which are shown in the right panel of Fig. 5.19. In the prediction of the strain described above, we assumed that the cloud decays through GW emission, and that the power emitted in electromagnetic radiation is subdominant at all times, giving an upper bound on ε of around a few times 10^{-7} for a system that is 1000 years old (see Fig. 5.17)—a different time evolution for the cloud is, in principle, allowed and would give a different observable strain. The lower bound on ε shown in Fig. 5.19 comes from requiring the superradiance cloud to pair produce the plasma, as described in Sec. 5.4. This bound, however, can be relaxed since the BH was formed long ago, and charged particles could be slowly accreted and build up the plasma over time (see Sec. 5.4.3). In this case, ε as small as 10^{-12} could produce a pulsating source that is luminous enough to be observed at galactic distances. Finally, we notice that a few of the pulsating sources used here have a measured luminosity, which could be used to fix the value of ε if the emission spectra were known (see Sec. 5.6.5). Taking the fraction of total luminosity that goes in the radio band to be between 10^{-4} and 10^{-6} gives ε between approximately 10^{-12} and 10^{-11} [249, 214].

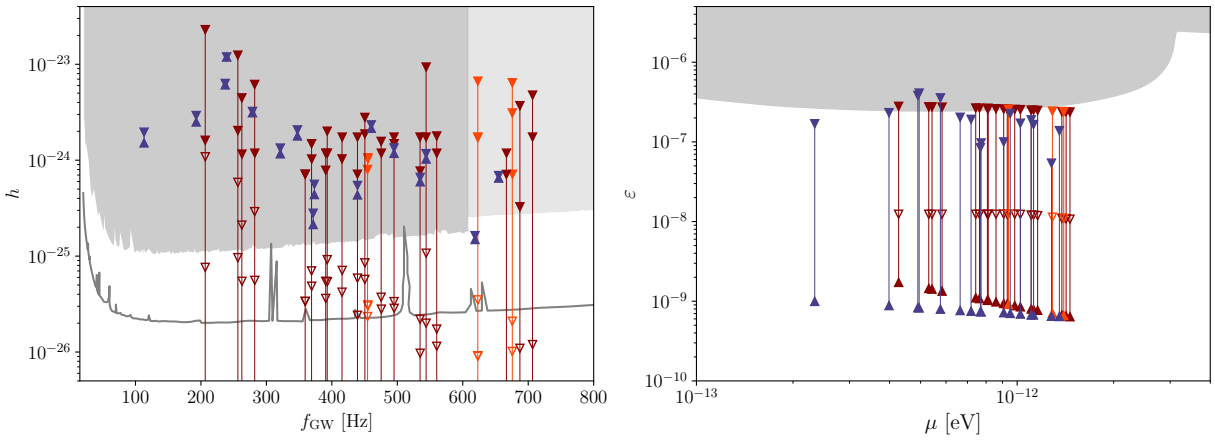

Figure 5.19: *(left)* We show the projected gravitational wave strain of observed pulsating sources whose luminosity could be powered by the kinetically mixed dark photon superradiance cloud. The potential candidates are selected from the ATNF pulsar catalogue [249], as described in Sec. 5.7.2, and are frequency doublets (dark red), frequency triplets (light red), and pulsars with positive measured frequency derivative (blue). The filled (empty) triangles correspond to the largest possible strain that a source in a frequency multiplet could produce if the cloud were created 10^3 (10^6) yr ago. The strain could take any value below that upper bound (thin solid lines) down to a minimum strain outside of the range shown here. The blue down-pointing and up-pointing triangles denote the range of strains allowed assuming that the spin-up is due to gravitational wave emissions from the cloud. The 95% C.L. upper limits on the signal strain amplitude from Refs. [17] and [13] are shown in dark and light gray shading, respectively. The solid gray line corresponds to the expected sensitivity of a targeted search with LIGO Livingston derived in [18]. *(right)* Range of kinetic mixing parameters allowed for each pulsar, with frequency doublets (dark red), frequency triplets (light red), and pulsars with positive measured frequency derivative (blue). For the frequency multiplets, filled (empty) down-pointing triangles correspond to the largest ε that allows the cloud to decay through GW emission for at least 10^3 (10^6) yr. For the sources that are spinning up, down-pointing triangles give the largest ε that allows the cloud to decay through GW emission up to their current age (which is fixed by $\dot{f}_{\rm obs}$). For all the sources, up-pointing triangles denote the smallest mixing parameter that allows for plasma pair production in the cloud (see Sec. 5.4 and Eq. (5.26)).

5.7.3 Concluding remarks

In the last two subsections, we discussed two detection strategies which take advantage of the multimessenger signals from a dark photon superradiance cloud around a spinning BH. In both cases, a combination of the electromagnetic and GW observations allow us to perform highly non-trivial cross checks to uniquely identify our system and measure the dark photon mass and kinetic mixing parameter. Our analysis can be strengthened by dedicated numerical studies which

- extend our analysis to smaller gravitational coupling α and larger conductivity σ/μ,
- provide robust information about the electromagnetic emission spectrum,
- show robust evidence for or against periodicity in the electromagnetic emission in different electromagnetic bands.

In addition to the signals mentioned above, our system may host a plethora of phenomena, including ultraluminous X-ray sources (ULX) [352], as well as transient processes such as fast radio bursts (FRB) [28, 294] and X-ray flares and giant flares [108]. Follow-up GW observations of these events could identify their origin as a dark photon superradiance cloud. With electromagnetic observations alone, more dedicated numerical studies are needed to determine the similarities and differences in the spectral properties and transient dynamics between our system and a neutron star pulsar or magnetar [299], or other astrophysical sources. If BH superradiance is discovered with continuous GW searches at LVK and future GW observatories, follow-up electromagnetic observations can discover the kinetically mixed phenomena presented in this chapter or put robust constraints on the dark photon parameter space.

Finally, note that in this chapter we have exclusively focused on signals from stellar BHs, but the computations and the results for the luminosity presented in Eq. (5.61) also apply to the case of isolated supermassive BHs, which would be of relevance for follow-up signatures of mergers detected by LISA.

5.8 Discussion and Conclusions

In this chapter, we performed a detailed analytical and numerical study of the dynamics of a kinetically-mixed, dark photon superradiance cloud and the resulting multimessenger signatures. If a dark photon with Compton wavelength on the order of the radius of a stellar

mass black hole exists, isolated, rotating black holes turn into very bright electromagnetic sources for kinetic mixings on the order of $\varepsilon \sim 10^{-10} - 10^{-6}$. We summarize our approach, discuss the unique dynamics and observational signatures of the system, and outline future directions for investigation below.

A dark photon superradiance cloud is a dark electromagnetic field rotating at a frequency fixed by the dark photon energy. Charged particles in the interstellar medium enter the rotating cloud and, in the presence of a kinetic mixing, initiate a transient phase of cascade particle production, resulting in a dense plasma. The stable rotation of the cloud, large strength of the visible electromagnetic fields, and the appearance of the charged plasma resemble pulsar magnetospheres. We use resistive electrodynamic methods that interpolate between the vacuum and the force-free limit. Our methods are adapted from those originally developed to model resistive effects in the pulsar magnetosphere, here applied to a fixed Kerr spacetime and the kinetically mixed case.

Due to the system's large conductivity, plasma currents redistribute charge in an approximately dipolar form on large scales in order to screen the coherent visible electromagnetic field set up by the rotating superradiance cloud. We find that, due to the electric dominance of the oscillating superradiance cloud, the charged plasma cannot completely screen the electromagnetic field. Our numerical simulations of the field electrodynamics indicate that the differential rotation between the background fields and the plasma leads to the emergence of small-scale turbulence in the form of magnetic field reconnection and unscreened electric fields (Sec. 5.5.3). We establish that the electromagnetic emission from the system is dominated by such small-scale turbulent dissipation into the standard model plasma, with a peak luminosity of up to 10 orders of magnitude larger than the solar luminosity, as described in Sec. 5.6.2 (see Eqs. (5.54) and (5.61)). In addition, we find a Poynting flux component to the emission. Though subdominant, $\sim 10^2 - 10^4$ times smaller than the local dissipation, this may also be significant for the observational signatures of the system. These are the main results of this chapter.

Given the rotation of the superradiance cloud, we expect that at least a fraction of our system's emission is periodic (with period $T \approx 2\pi/\mu$), a property that would extend the analogy with pulsars into the observational domain. Our simulations show some evidence for such a periodicity, as discussed in Sec. 5.6.4, but cannot conclusively verify this expectation. By analogy with the results for pulsar magnetospheres and findings from PIC simulations of turbulent plasmas, we expect that the emission spectrum contains a non-thermal X-ray component for kinetic mixing parameters $\varepsilon \gtrsim 10^{-7}$, softer spectra for smaller mixing parameters, and likely a radio component (see Sec. 5.6.5). Our simulations cannot directly determine the spectrum of the emitted luminosity, so given the differences between our system and pulsars, both in field profile morphology and strength, more investigations

are essential to conclusively establish the spectral shape.

Based on the system's large luminosity, characteristic time evolution, and expected periodicity, we propose several search strategies for dark photon superradiance clouds. The first strategy relies on the extreme brightness of our system: electromagnetic follow-up searches targeting binary BH mergers observed by the LVK Collaboration (Sec. 5.7.1). Based on our expectations of the spectrum, the most promising reach is achieved by X-ray and radio observations. In addition to the spatial and temporal correlation of a merger and the resulting electromagnetic emission, one could discriminate between superradiance clouds and standard astrophysical sources by requiring a fast exponential rise, and $1/t$ power-law fall-off of the light curve, consistent with superradiant growth and subsequent decay by GW emission. Given the measured remnant BH mass and spin from the gravitational waveform, these timescales are fully determined by the dark photon mass; for the parameters necessary to see these signals over cosmological distances, the electromagnetic power is subdominant to the GW power and does not affect the time evolution. This results in a non-trivial relation between the rise and decay times (see Eq. (5.64)), which if experimentally confirmed, would provide a smoking gun signature of superradiance.

Further assuming periodicity, a variety of additional signatures can be explored. For the proposed electromagnetic follow-ups, the periodicity alone could be used to measure the dark photon mass μ, as the periodicity is set by the dark photon mass up to a few-percent binding energy corrections from the BH potential. This would further strengthen the evidence for the new physics hypothesis by requiring consistency between the period-based measurement of μ and the light curve rise and decay times.

Another observational strategy targets known pulsars, either by selecting those with positive frequency derivative, or by selecting those with the same measured period up to $\mathcal{O}(10^{-3})$ due to Doppler shifts. Interestingly, by surveying existing pulsar catalogues we find four candidate sources for which a partner with the same frequency exist, *and* that have a positive frequency derivative measurement. Our computation of the GW power with the measured "pulsar" period and spin-up rate suggest that many of these objects would emit continuous gravitational wave with strain above the LVK threshold if their origin is dark photon superradiance. Many potential sources could be excluded with blind continuous wave searches while others could be further probed with targeted continuous wave searches (section 5.7.2).

Apart from these multi-messenger signatures of correlated EM and GW emission, at small α and large ε the dark photon cloud depletion is dominated by EM emission, leading to persistent ultra-bright sources of X-rays. Observation of several periodic sources with periods within a few percent of each other would be strong evidence for the origin of these

objects being a dark photon superradiance cloud. The absence of these sources in the Universe may already imply constraints on the dark photon parameter space assuming a natal black hole mass and spin distribution; given the uncertainties in BH properties and the EM signal spectral shape, we leave this study to future work.

We close with a discussion of future directions. In this chapter, we studied the case of an isolated BH and a single new particle with a minimal interaction, the kinetically-mixed dark photon. In the presence of a more complex dark sector, such as the existence of a dark Higgs, the dynamics may be altered further. Recently, some of the authors showed that in the higgsed dark photon scenario, vortex lines can form and deplete the cloud before it reaches its maximum size [143, 144]. Further study is needed to understand how the vortex production and evolution is affected by the presence of plasma (see, e.g., Refs. [24, 144]).

Furthermore, many BHs are not isolated: they are surrounded by an accretion disk, leading to additional dynamics. While it is a negligible perturbation to the background dark photon field, a dense accretion disk affects the visible electromagnetic field and resulting electromagnetic dynamics and emission. BH systems affected by these dynamics include accreting supermassive black holes, X-ray binaries, etc. Preliminary studies show that even a small superradiance cloud (or a small $\varepsilon \sim 10^{-12}$ for a maximal cloud) affects the disk properties, and would invalidate the ISCO-based spin measurements [239, 255, 308]; we leave further details to a future publication [203].

This work sets the stage for the exploration of kinetically-mixed dark photon superradiance. We have established numerical simulation techniques to understand the electrodynamics of the cloud and its electromagnetic emission. The parameter space of possible signatures is vast, from weak, long-lasting signals to bright, short signals, across the electromagnetic spectrum. We have detailed several possible observations, and a more wide-ranging study of search strategies is warranted. Utilizing different simulation approaches to better understand the electromagnetic emission spectrum would be invaluable to pin down observables. Finally, given the similarities between our system and a magnetar, it is conceivable that the dark photon superradiance cloud could host a wide range of astrophysical phenomena, such as X-ray flares and fast radio bursts. Due to the differences in the magnetic field structures, further investigations are clearly needed, and would be of great interest.

Chapter 6

`SuperRad`: Modeling the black hole superradiance gravitational waveform

Executive summary: Gravitational signatures of black hole superradiance are a unique probe of ultralight particles that are weakly-coupled to ordinary matter. The existence of an ultralight boson would lead spinning black holes with size comparable to the Compton wavelength of the boson to become superradiantly unstable to forming an oscillating cloud, spinning down the black hole, and radiating gravitational waves in the process. However, maximizing the chance of observing such signals or, in their absence, placing the strongest constraints on the existence of such particles, requires accurate theoretical predictions. In this chapter, we introduce a new gravitational waveform model, `SuperRad`, that models the dynamics, oscillation frequency, and gravitational wave signals of these clouds by combining numerical results in the relativistic regime with fits calibrated to analytical estimates, covering the entire parameter space of ultralight scalar and vector clouds with the lowest two azimuthal numbers ($m = 1$ and 2). We present new calculations of the gravitational wave frequency evolution as the boson cloud dissipates, including using fully general-relativistic methods to quantify the error in more approximate treatments. Finally, as a first application, we assess the viability of conducting follow-up gravitational wave searches for ultralight vector clouds around massive black hole binary merger remnants. We show that LISA may be able to probe vector masses in the range from 1×10^{-16} eV to 6×10^{-16} eV using follow-up gravitational wave searches.

6.1 Introduction

In Chapter 5, we introduced the BH superradiance process, and how it can be used to search for ultralight bosons extending the SM of particle physics. To leverage the observational potential of ground- and space-based GW detectors, however, accurate predictions for the involved spin-down timescales, as well as GW frequency and amplitudes are required. Much effort has gone into determining these for scalar bosons [356, 385, 128, 136, 35, 377, 33, 32, 79, 378], vector bosons [318, 288, 289, 93, 50, 141, 142, 53, 338], and spin-2 fields [78, 83] (see Ref. [79] for a review). Scalar bosons exhibit the longest spin-down timescales, as well as weakest and longest GW signal after cloud formation. Vector bosons, on the other hand, are amplified more efficiently, leading to faster cloud growth rates and stronger, but hence shorter, GW emissions. In modified theories of gravity, massive spin-2 fields grow the fastest around BHs.

To bridge the gap between these developments and their implementation in search campaigns, we introduce `SuperRad`, an open source BH superradiance waveform model incorporating state-of-the-art theoretical predictions for BH spin-down and GW observables across the entire relevant parameter space in a simple, ready-to-use `python` package[1]. A primary goal is to provide a tool to efficiently and accurately interpret GW search results of current and future ground- and space-based GW observatories. As part of this work, we present new calculations of the frequency evolution of the boson cloud oscillations and attendant GWs due to the changing mass of the boson cloud. We compare the analytic frequency evolution in the non-relativistic limit to both approximate quasi-relativistic calculations, as well as fully general-relativistic ones, to determine their accuracy in the relativistic regime.

As a first application, we use `SuperRad` to show that the Laser Interferometer Space Antenna (LISA) should in principle be able to probe ultralight boson masses from 1×10^{-16} eV to 6×10^{-16} eV by performing follow-up searches for GWs from boson clouds arising around the remnants of massive BH binary mergers. Such follow-up searches have been previously discussed in the context of stellar mass BH mergers [166, 206, 102], and are especially promising because the observation of the binary BH merger waveform gives definitive information on the properties of the remnant BH, allowing one to place constraints in the absence of a signal without further assumptions. By contrast, other search methods outlined above rely on further assumptions and are subject to various uncertainties: electromagnetic spin measurements are contingent on astrophysical uncertainties and may be invalidated by weak couplings of the ultralight boson to the SM [343], spin measure-

[1] Available at `www.bitbucket.org/weast/superrad` .

ments of constitutents of inspiraling binary BHs have large statistical uncertainties, and constraints based on blind continuous waves and stochastic gravitational wave background searches rely on BH population assumptions.

We begin in Sec. 6.2 by providing a broad overview over the expected GW signals from BH superradiance of scalar and vector clouds. In Sec. 6.3, we discuss in detail how `SuperRad` determines the cloud's oscillation frequency and the superradiance instability timescales. Furthermore, we analyze the frequency shift due to the finite self-gravity of the cloud around the BH in Sec. 6.4 using Newtonian, quasi-relativistic, and fully relativistic approaches. The GW amplitude and waveform is discussed in Sec. 6.5. Following this, we outline the linear evolution of the cloud as well as the accompanying GW signature in Sec. 6.6, and close with the application of `SuperRad` to analyze the prospects of follow-up searches with LISA in Sec. 6.7. We use $G = c = 1$ units throughout this chapter (note this is different from our definitions in Chapter 5).

6.2 Overview and Example

We begin with an example to illustrate the expected GW signal from superradiant clouds, and give an overview of the different effects that go into calculating it. We consider parameters consistent with the remnant from a GW150914-like binary BH merger. In particular, we consider a BH with mass $M = 62\ M_\odot$ and dimensionless spin[2] $a_* = 0.67$ at a distance of 410 Mpc [7] and determine the resulting GW signal if there were an ultralight boson—scalar or vector—with mass $\hbar\mu = 3.6 \times 10^{-13}$ eV (hence $\alpha \approx 0.17$). For simplicity, here we assume the angular momentum points in the direction of the observer—hence both GW polarizations are equal—and ignore redshift effects. The GW strain and frequency calculated with `SuperRad` for both the scalar boson case and the vector case are shown in Fig. 6.1.

There are a number of different parts that go into these calculations. First, one determines the superradiant instability timescale by solving for the fastest growing mode of the massive scalar or vector equations of motion on the BH spacetime as described in Sec. 6.3. This gives the timescale over which the boson cloud mass, and hence the GW amplitude, grows exponentially in time. From Fig. 6.1, it can be seen that the e-folding time of the cloud mass (half the e-folding time of the field τ_I) is much slower for the scalar case ($\tau_I/2 \sim 10$ days) compared to the vector case ($\tau_I/2 \sim 3$ minutes). Taking into account the resulting decrease in the mass and spin of the BH as the boson cloud grows, as described in

[2]Defined by the ratio of angular momentum J to the mass square of the BH: $a_* = J/M^2$.

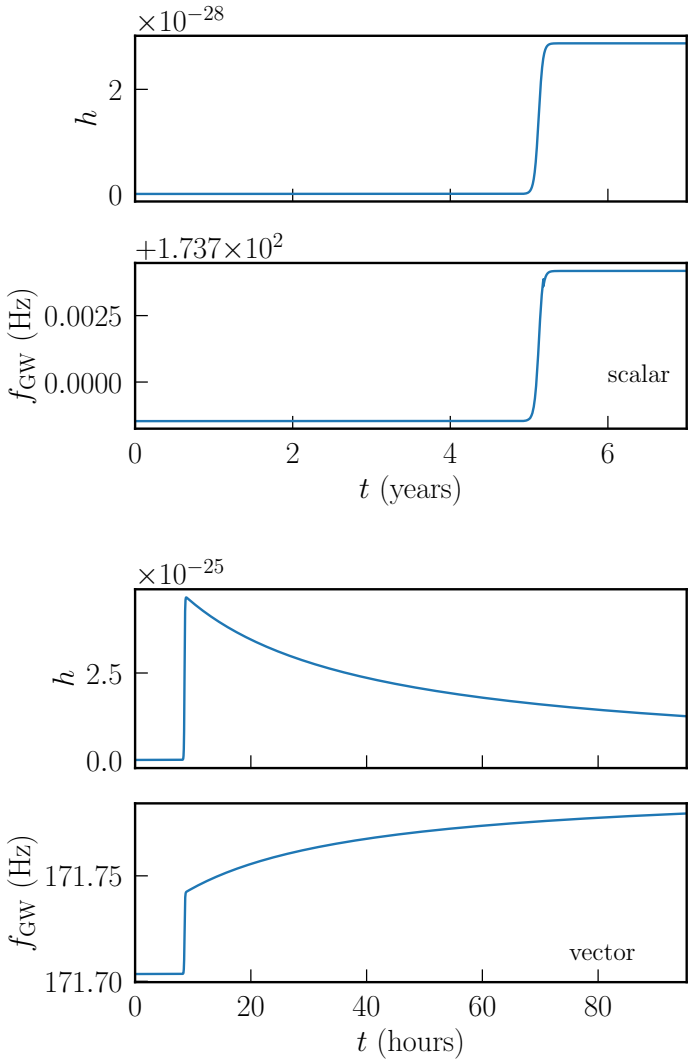

Figure 6.1: The GW strain h and frequency $f_{\rm GW}$ as a function of time for a BH with $M = 62\ M_\odot$ and $a_* = 0.67$ at a distance of 410 Mpc subject to the superradiant instability of a boson with mass 3.6×10^{-13} eV. The top set of panels shows the scalar boson case, while the bottom set shows the vector case. Note the difference in timescales shown, since in the scalar (vector) case the cloud grows on timescales of ~ 5 years (9 hours) and decays through GW radiation on timescales of ~ 9000 years (1 day). Time is measured since the BH was formed, assuming the cloud started as a single boson.

Sec. 6.6, the instability timescale becomes longer and longer as the horizon frequency of the BH approaches the oscillation frequency of the cloud. As the instability saturates, and the cloud mass reaches its maximum value, the dissipation of the cloud through gravitational radiation becomes dominant, leading to a slow decrease in cloud mass. The rate at which energy is lost through gravitational radiation $P_{\rm GW}$, as well as the two strain polarizations h_+ and $h_\times$, are calculated by solving for linearized metric perturbations on the BH spacetime, sourced by the oscillating cloud solution, as described in Sec. 6.5. As can be seen in Fig. 6.1, in the scalar case the decay of GW amplitude is negligible on any reasonable observing timescale, taking on the order of 10^4 years, while in the vector case, the cloud mass and GW amplitude decrease on timescales of days.

The gravitational frequency shown in Fig. 6.1 exhibits an increase or "chirp" in frequency, first as the BH loses mass and the cloud grows exponentially, and then more slowly as the boson cloud dissipates. Calculating this frequency shift requires accounting for the self-gravity of the boson cloud, which slightly red-shifts the oscillation frequency of the cloud, and hence the gravitational waves (which have twice the frequency of the cloud oscillations), as described in Sec. 6.4. Though the change in frequency is small, because the GW signal persists for many cycles, this is still an important effect.

6.3 Cloud properties

In this section, we outline the superradiant cloud properties relevant for observational signatures such as BH spin-down or GW emission. This includes a brief discussion of how estimates for the superradiant instability timescale τ_I and the emitted GW frequency $f_{\rm GW}$ are obtained for different values of the BH mass, spin, and the gravitational fine structure constant α. We defer the analysis of the dependency of the cloud frequency on cloud mass, and the cloud dynamics to Secs. 6.4 and 6.6, respectively. `SuperRad` combines analytic and numerical predictions, valid for $\alpha \ll 1$ and $\alpha \sim \mathcal{O}(1)$, and utilizes numerically calibrated higher-order expansions to interpolate between the two regimes.

In most of the following calculations, we assume a fixed Kerr BH spacetime $g_{\mu\nu}$, and consider scalar and vector bosonic fields, as well as linear metric (GW) perturbations on this background. The exception to this is the calculation of the frequency shift due to the self-gravity of the boson-cloud. We will discuss the validity of this assumption further in Secs.6.5.2 and 6.4. Furthermore, we neglect field self-interactions and non-minimal couplings to the SM throughout, which have been investigated in Refs. [376, 162, 49, 143, 144, 278]. Depending on the coupling strength, these can alter the superradiance dynamics. However, here we assume that we are in the weak coupling limit, which reduces

to the purely gravitational case. Therefore, the relevant field equations to solve in order to obtain the desired observables are the scalar and vector massive wave equations on the spacetime $g_{\mu\nu}$, which are given by

$$(\Box_g - \mu_S^2)\Phi = 0, \qquad \nabla_\mu F'^{\mu\nu} = \mu_V^2 A'^{\nu}, \tag{6.1}$$

where $\mathcal{M}_S = \hbar\mu_S$ and $\hbar\mu_V = \hbar\mu_V$ are the scalar and vector boson masses, respectively. Due to various symmetries of the Kerr spacetime, solutions to the field equations (6.1) can be written in the form

$$A'_\mu, \Phi \sim e^{-i(\omega t - m\varphi)}, \tag{6.2}$$

where we introduced the azimuthal mode number m and complex frequency ω. Here, and in the following, we refer to the Boyer-Lindquist time, radius, polar and azimuthal coordinate as t, r, θ, and φ. Without loss of generality, we assume the azimuthal index to satisfy $m \geq 0$ throughout. Lastly, we label all quantities defined both for scalar and vector fields with $\sigma \in \{S, V\}$. The fields A'_μ and Φ are susceptible to the superradiance instability, if the superradiance condition

$$0 < \omega_R < m\Omega_H, \tag{6.3}$$

is satisfied, where Ω_H is the horizon frequency of the BH. In the ansatz (6.2), the frequency $\omega = \omega_R + i\omega_I$ encodes both the oscillation frequency of the cloud, which is half of the characteristic GW frequency $f_{\rm GW} = 2\omega_R/(2\pi)$ (up to self-gravity corrections), and the instability growth timescale $\tau_I = 1/\omega_I$. For fixed mode number m_σ, these observables (in units of M) depend only on α and spin a_*, i.e., $\omega(\alpha, a_*)$.

In what follows, we begin by outlining `SuperRad's` coverage of the (α, a_*) parameter space in Sec. 6.3.1, and then we illustrate how analytic and numerical results are used to calibrate `SuperRad` in the intermediate regime in Secs. 6.3.2 and 6.3.3.

6.3.1 Parameter space

In Figure 6.2, we show the parameter space for the $m_V = 1$ massive vector as an illustrative example. For a given quantity $q(\alpha, a_*) \in \{\omega_R, \omega_I, \partial_t\omega_R\}$ (in units of M), we numerically calculate its value in the relativistic regime, but for computational reasons, do not extend our calculations deep into the small-α regime. We want to match on to analytic results q_N that are valid only in the Newtonian limit, when $\alpha \ll 1$. We do this by dividing the parameter space in (α, a_*) into two regions. In the relativistic regime, labelled $\mathcal{D}_{\rm int}$,

we merely interpolate between the numerically computed points using the interpolation polynomial $I_R(\alpha, a_*)$. In the regime where α is smaller, labelled $\mathcal{D}_{\rm fit}$, we use a subset of the numerical results in $\mathcal{D}_{\rm int}$ (corresponding to the red points in Fig. 6.2) and fit the difference between these results and the analytic ones in a way that is guaranteed to recover the latter at sufficiently small α. That is, we let

$$q(\alpha, a_*) = \begin{cases} q_N(\alpha, a_*) + g(\alpha, a_*), & (\alpha, a_*) \in \mathcal{D}_{\rm fit}, \\ I_R(\alpha, a_*), & (\alpha, a_*) \in \mathcal{D}_{\rm int}. \end{cases} \tag{6.4}$$

where g is a fitting function chosen to give $q_N(\alpha, a_*) + g(\alpha, a_*) \to q_N(\alpha, a_*)$ as $\alpha \to 0$. The specific choices of $\mathcal{D}_{\rm fit}$ and $\mathcal{D}_{\rm int}$ depend on the field and azimuthal mode in question, and are determined by the accuracy of the underlying methods (these are defined in App. E.3). Note also that we are only interested in the part of the parameter space where $\omega_R \leq m_\sigma \Omega_H$, since outside this range the cloud will be exponentially decaying through absorption by the BH.

In the relativistic part of the parameter space $\mathcal{D}_{\rm int}$, a set of 320^2 waveforms are generated for the azimuthal modes $m_\sigma = 1$ and 2, and for both the scalar and the vector case. The grid of waveforms is uniformly spaced in the coordinates (y, a_*), with $y \in [0, 1]$, defined by

$$y = \frac{\alpha - \alpha_0}{\alpha_1 - \alpha_0}, \tag{6.5}$$

where $\alpha_0^{m_\sigma=1} = 0.05$ and $\alpha_0^{m_\sigma=2} = 0.25$, while α_1 is the solution to

$$\beta\alpha_1 \left[1 - \frac{\alpha_1^2}{2n_\sigma^2}\right] = m_\sigma M \Omega_H(a_*), \tag{6.6}$$

with $\beta = 0.9$, and n_σ is the cloud's principle number defined below in (6.9). This choice of α_1 is made so as to guarantee that $y = 1$ lies outside the superradiant regime, and thus that the saturated state $\omega_R = m_\sigma \Omega_H$ lies within the grid. The boundary $y = 1$ corresponds to the large-α boundary of the numerical data in Figure 6.2, beyond the superradiant saturation.

6.3.2 Oscillation frequencies

The real part of the superradiantly unstable field's frequency determines the cloud's oscillation about the BH

$$A'_\mu, \Phi \sim \cos(\omega_R t), \tag{6.7}$$

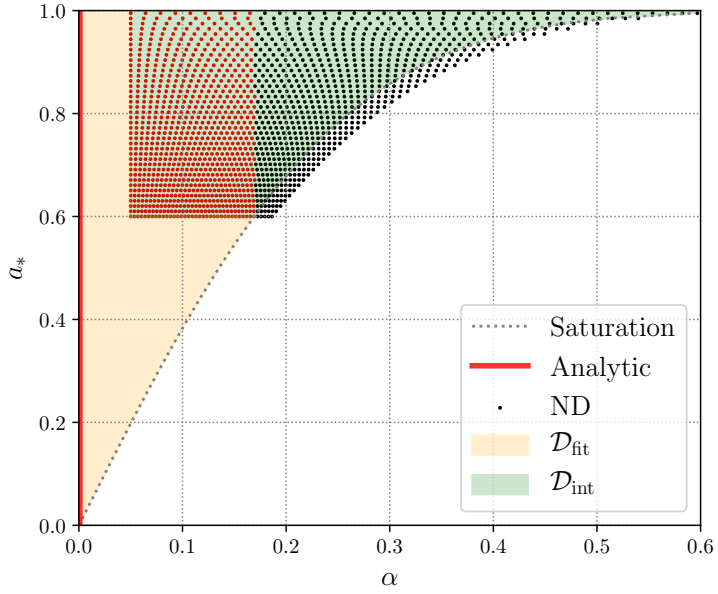

Figure 6.2: The parameter space of the superradiant $m_V = 1$ vector mode. It is made up of relativistic regime $\mathcal{D}_{\rm int}$, where `SuperRad` employs interpolation functions based on the numerical data (labelled ND) to determine a given quantity $q(\alpha, a_*)$ and a lower α region $\mathcal{D}_{\rm fit}$, where numerical calibration is necessary to augment the expressions valid in the Newtonian limit $\alpha \to 0$ (indicated by a red line). For illustration purposes, we show only 40^2 of the 320^2 data points used in `SuperRad`. The gray dashed line marks the saturation point of the superradiance instability, i.e., $\omega_R = \Omega_H(a_*)$. In this case, the red data points are used for calibration in $\mathcal{D}_{\rm fit}$.

and also sets the characteristic GW frequency $f_{\rm GW} = \omega_R/\pi$ (up to self-gravity corrections). Because of the BH's gravitational potential, a bound massive particle has a frequency $\omega_R < \mu$. Expanding (6.1) to leading order in α yields a Schrödinger-type equation with potential $U \sim \alpha/r$, at a radius r away from the BH. In this regime, the solutions are simple hydrogen-like bound states for scalar and vector fields [128, 289]. The scalar states are characterized by their angular momentum quantum number ℓ_S, as well as azimuthal mode number $-\ell_S \leq m_S \leq \ell_S$ and radial node number $\hat{n}_S \geq 0$, while the vector states are identified by an analogous definition of radial node number $\hat{n}_V \geq 0$, angular momentum number ℓ_V and azimuthal index m_V, in addition to the polarization state $\hat{S} \in \{-1, 0, 1\}$. With this, the oscillation frequencies of the scalar and vector clouds are, in the non-

relativistic limit,

$$\omega_R = \mu\left(1 - \frac{\alpha^2}{2n_\sigma^2} + C_\sigma[\alpha]\right), \tag{6.8}$$

where $C_\sigma[\alpha]$ includes higher order corrections. In particular, we include terms of up to $\mathcal{O}(\alpha^5)$, obtained by keeping sub-leading contributions in α when solving (6.1) [53], with the full expressions for C_σ given in appendix E.2 [in particular (E.4) and (E.11)]. The state label n_σ, depends on the intrinsic spin of the field and is given by

$$n_S = \ell_S + 1 + \hat{n}_S, \qquad\qquad n_V = m_V + \hat{n}_V + \hat{S} + 1. \tag{6.9}$$

Notice, in the case of the scalar field, we follow the conventions of Ref. [53], while in the vector case, we follow Ref. [137]. In the language of the previous section, the expressions (6.8) are the Newtonian estimates $q_N(\alpha, a_*)$.

We numerically estimate ω_R using the methods discussed in appendix E.2, without assuming an expansion in small α. These estimates are calculated for $m_\sigma \in \{1, 2\}$ for both scalar and vector fields. Here, we simply summarize that our numerical methods are more accurate and precise than the analytic estimates everywhere in $\mathcal{D}_{\rm int}$. The waveform model provides accurate values for ω_R in $\mathcal{D}_{\rm fit}$ using a fit to the numerical results. We perform this fit using the ansatz

$$\frac{\omega_R}{\mu} - 1 + \frac{\alpha^2}{2n_\sigma^2} - C_\sigma[\alpha] = \sum_{q,p} \alpha^p \hat{a}_{p,q} (1 - a_*^2)^{q/2}, \tag{6.10}$$

with appropriately chosen ranges for p and q, to the numerical data in a subset of $\mathcal{D}_{\rm int}$ (see appendix E.3 for details). The right-hand side of (6.10) corresponds to $g(\alpha, a_*)$, defined in the previous section. This ansatz explicitly assumes the analytic estimates in the $\alpha \ll 1$ regime. Within `SuperRad`, we combine all three of these ingredients as described in (6.4) to determine ω_R in the parameter space. Therefore, we ensure that `SuperRad` provides the most accurate and precise estimate for frequencies of a given superradiant bosonic field around a fixed Kerr BH background across the entire parameter space. The correction of these frequency estimates due to the self-gravity of the superradiant cloud is discussed in Sec. 6.4.

In Figure 6.3, we compare the available analytic estimates, given in (6.8) [together with (E.4) and (E.11)], with those provided by `SuperRad`. As expected, the relative difference between the analytic estimates and `SuperRad`'s decay as $\sim \alpha^6$ [the order of the leading-in-α unknown coefficient in the expansion of (6.8)] in the Newtonian regime. For large spins a_* and large α, i.e., in the relativistic regime, the analytic estimates have relative errors up to $D_R(\omega_R) \lesssim 10^{-2}$. In comparison to the vector results, the analytic estimates for ω_R^S are more accurate in the most relativistic regime.

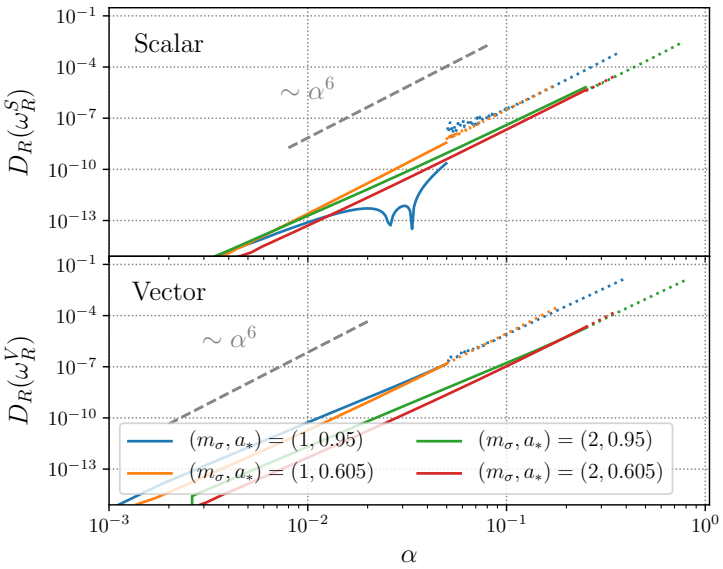

Figure 6.3: The relative difference D_R, between the prediction for ω_R provided by `SuperRad`, and purely analytical non-relativistic estimates given in (6.8) together with (E.4) and (E.11). Dotted lines indicate the $\mathcal{D}_{\rm int}$ region in `SuperRad`. We focus on a few representative cases.

6.3.3 Instability timescales

The imaginary part of the frequency ω_I sets the superradiant instability timescale $\tau_I = 1/\omega_I$ of the bosonic cloud,

$$A'_\mu, \Phi \sim e^{\omega_I t}. \tag{6.11}$$

In the non-relativistic limit $\alpha \to 0$, the cloud sits far away from the BH and the flux across the horizon, and hence the instability growth rate, tends towards zero. For small, but non-zero α, the rates scale with a characteristic power κ, i.e., $\omega_I M \sim \alpha^\kappa$. This scaling depends on the type of field (scalar or vector) and the mode considered. Furthermore, at saturation, i.e., when $\omega_R = m_\sigma \Omega_H$, the ultralight particles cease extracting rotational energy from the BH, such that the growth rate vanishes. Combining these two limits, the general behavior of the instability growth rates for both the scalar and the vector cases is

$$\omega_I M = \alpha^\kappa (\omega_R - m_\sigma \Omega_H) 2 r_+ G_\sigma(a_*, \alpha). \tag{6.12}$$

Here, $G_\sigma(a_*, \alpha)$ is a function of the BH spin, as well as α, and determines the leading order and sub-dominant-in-α contributions to ω_I. The scaling power κ, for scalar and vector fields are [128, 288]

$$\kappa_S = 4m_S + 5, \qquad \kappa_V = 4m_V + 2\hat{S} + 5, \tag{6.13}$$

for the fastest growing configurations[3], and depend on the azimuthal index m_σ and the vector polarization state $\hat{S}$. The leading order contributions in the scalar case [128] and the vector case [318, 289, 50, 53] to $G_\sigma(a_*, \alpha)$ that we use are given in Appendix E.2 [in particular (E.6) and (E.14), respectively]. These are Newtonian estimates that we use [$q_N(\alpha, a_*)$ in the language of Sec. 6.3.1] for the imaginary frequency.

Similarly to the previous section, we utilize numerical techniques to obtain accurate predictions for ω_I in the relativistic regime $\mathcal{D}_{\rm int}$ of the parameter space. The methods and their accuracy are outlined in Appendix E.2. Here, we simply note again that the numerical predictions are more accurate than the analytic Newtonian expressions everywhere in $\mathcal{D}_{\rm int}$. Similar to the real part of the cloud's frequency, the analytic results obtained in the Newtonian limit are connected with the numerical estimates in the $\alpha \sim 1$ regime by fitting[4] the ansatz

$$\begin{aligned} &\frac{\omega_I M \alpha^{-\kappa} G_\sigma^{-1}(a_*, \alpha)}{2r_+(\omega_R - m_\sigma \Omega_H)} - 1 \\ &\qquad = \sum_{p,q} \alpha^p \left[\hat{b}_{p,q} a_*^{q+1} + \hat{c}_{p,q}(1 - a_*^2)^{q/2}\right], \end{aligned} \tag{6.14}$$

with appropriately chosen ranges for p and q, to the numerical data obtained in $\mathcal{D}_{\rm int}$ (see Appendix E.3 for details). The right-hand-side of (6.14) serves as $g(\alpha, a_*)$ in the construction (6.4) for ω_I. Analogously to the oscillation frequency, with this construction we ensure `SuperRad` provides the most accurate and precise estimates for the superradiance growth rate ω_I everywhere in the cloud's parameter space.

In Figure 6.4, we illustrate the relative differences between the analytic estimates using only (6.12) together with (E.6) and (E.14), and the estimates provided by `SuperRad`. In the Newtonian regime, the relative difference approaches zero, while in the relativistic regime, the relative error in the analytic estimates becomes $D_R(\omega_I) \sim \mathcal{O}(1)$ in both the scalar and the vector cases. Hence, using non-relativistic analytic estimates in the relativistic regime can lead to large systematic uncertainties in the instability rate. We indicate the

[3] Notice, in the relativistic regime, it is non-trivial to identify the most unstable mode.

[4] Notice a typo in eq. (A.2) of [338]; it is fixed by $C_m \to 2C_m r_+$.

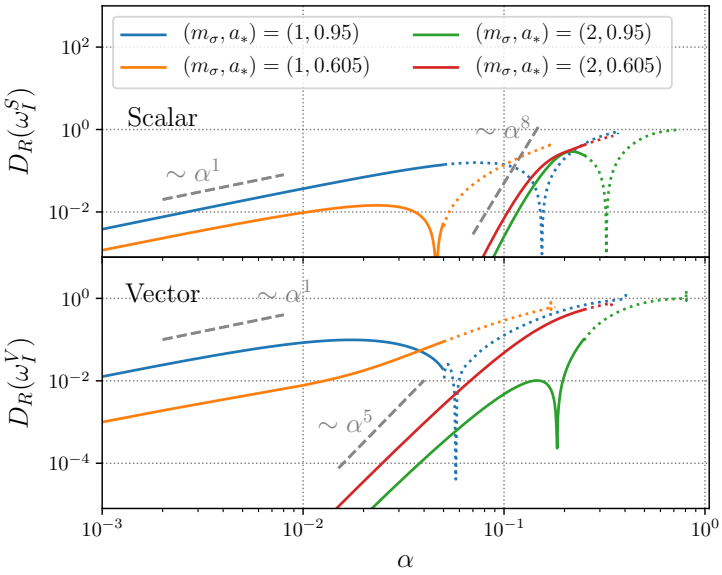

Figure 6.4: The relative difference D_R between the prediction for ω_I provided by `SuperRad`, and purely analytical non-relativistic estimates given in (6.12) together with (E.6) and (E.14). Dashed lines indicate the $\mathcal{D}_{\text{int}}$ region in `SuperRad`. We show the same representative cases as in Figure 6.3.

leading-in-α scaling of the difference for each m_σ. An $\sim \alpha^1$-scaling is expected in principle for both $m_\sigma = 1$ and $m_\sigma = 2$, however, due to our choices of p and q in (6.14) (see also Appendix E.3), the leading power is > 1 for $\alpha \ll 1$ in the $m_\sigma = 2$ case. For $\alpha \gtrsim 0.1$, the scaling decreases to the expected $\sim \alpha^1$.

6.4 Frequency shift

So far, we have considered calculations that assume the bosonic field can be treated as a test field on a Kerr background. Even for cases where the boson cloud mass reaches $M_c \sim 0.1M$, treating the spacetime as Kerr, with quasi-adiabtically changing parameters, gives a good approximation to the nonlinear treatment [145, 142]. However, in this section, we address the effect of the self-gravity of the cloud, focusing in particular on how it causes the characteristic increase in frequency of the cloud oscillation, and hence the frequency of the emitted GW radiation. Though the cloud-mass induced shift in the frequency is small, it will change as the cloud slowly dissipates through gravitational radiation, affecting how

long the GW signal can be coherently integrated without taking this effect into account. Quantitatively estimating the contribution to the frequency from the finite cloud mass

$$\Delta\omega(M_c) = \omega(M_c) - \omega(M_c = 0) \tag{6.15}$$

(which we will assume to be real) is the subject of this section. We employ a Newtonian approach, recovering and extending known results in the literature. We then compare these results in the scalar case to a fully nonlinear approach using synchronized complex fields around BHs.

6.4.1 Newtonian approach

The Newtonian approach, utilized to estimate the cloud mass correction to the frequency in Refs. [50, 206, 49], exploits the fact that in the non-relativistic limit, the energy density[5] ρ is spread out over large scales away from the BH, minimizing curvature effects. In this limit, the cloud itself sources a Newtonian gravitational potential Ψ, which follows the Poisson equation:

$$\Delta_{\rm flat}\Psi = 4\pi\rho, \qquad\qquad \Psi(\mathbf{r}) = -\int d^3\mathbf{r}' \frac{\rho(\mathbf{r}')}{|\mathbf{r}-\mathbf{r}'|}. \tag{6.16}$$

Here, the coordinates $\mathbf{r}$ can be identified with spatial slices of Kerr, where gauge ambiguities disappear in the $\alpha \ll 1$ limit. Furthermore, while one might choose $d^3\mathbf{r}' = \sqrt{\gamma}d^3x'$, with the determinant of the metric of a spatial slice of Kerr, a priori this is not more consistent than simply setting $\gamma \to \gamma_{\rm flat}$, which is our choice. In this weak-field limit, the scalar wave equation (6.1) is given by

$$(\omega - \mu_S)\Phi(\mathbf{r}) \approx \left(-\frac{\nabla^2}{2\mu_S} - \frac{\mu_S M}{r} + \mu_S\Psi\right)\Phi(\mathbf{r}) \ , \tag{6.17}$$

with $r = |\mathbf{r}|$. Taking the usual approximation that the shift in frequency at leading order in α is given by evaluating the perturbed operator on the unperturbed eigenfunction, the self-gravity of a cloud with mass $M_c = \int d^3\mathbf{r}\rho(\mathbf{r})$ contributes a shift in frequency of

$$\begin{aligned}\Delta\omega\frac{M_c}{\mu} &\approx \int d^3\mathbf{r}\rho\Psi \\ &= 2\int d^3\mathbf{r}\int_{|\mathbf{r}'|<|\mathbf{r}|} d^3\mathbf{r}'\frac{\rho(\mathbf{r})\rho(\mathbf{r}')}{|\mathbf{r}-\mathbf{r}'|} = 2W.\end{aligned} \tag{6.18}$$

[5] In a spacetime, like Kerr, with asymptotically timelike Killing field ξ^μ and time-slice normal vector n^μ, the energy density is defined as $\rho = n_\alpha\xi_\beta T^{\alpha\beta}$ through the scalar or vector field's energy-momentum tensor $T^{\alpha\beta}$.

We used the non-relativistic approximation that $\rho \approx \mu^2|\phi|^2$, and in the last line introduced the total potential energy W in the cloud. We note that this factor of 2 (from restricting the inner integral) is missing from some references [50, 206], but included in Ref. [49]. An equivalent derivation gives the same expression (6.18) in the vector case as well.

We can further simplify the frequency shift calculation by considering a low multipole approximation. The denominator of (6.18) can be expanded in terms of spherical harmonics $Y_{\ell m}(\Omega)$, where $(\Omega) = (\theta, \varphi)$ describes the angular dependence, as

$$\frac{1}{|\mathbf{r} - \mathbf{r}'|} = \sum_{\ell=0}^{\infty} \sum_{m=-\ell}^{\ell} \frac{r'^{\ell}}{r^{\ell+1}} \frac{4\pi}{2\ell+1} Y_{\ell m}(\Omega) \bar{Y}_{\ell m}(\Omega'), \tag{6.19}$$

assuming $|\mathbf{r}'| < |\mathbf{r}|$. If we keep only the monopolar, i.e., the $\ell = 0$, component of the density, which we can write in terms of the radial mass function $m_c(r) = \int d\Omega' \int_0^r dr' r'^2 \rho(\mathbf{r}')$, then (6.18) simplifies to

$$\Delta\omega = -\frac{2\mu}{M_c} \int d^3\mathbf{r} \frac{m_c(|\mathbf{r}|)\rho(\mathbf{r})}{|\mathbf{r}|}. \tag{6.20}$$

In general, there are non-vanishing higher order multipoles due to the non-trivial azimuthal and polar dependencies of the cloud's energy densities that are neglected above. However, for the $m_S = 1$, the error in the calculation of W associated with making this monopole approximation, as opposed to considering higher multipole corrections, is $\approx 2\%$ at leading order in α [6]. In the $m_V = 1$ case, all higher-order multipolar contributions are sub-leading in α, since the Newtonian energy density is spherically symmetric. While the cloud states with larger azimuthal number have strong polar dependencies, the corrections from high-order multipoles is moderate. For the $m_V = 2$ state, the quadrupolar contribution is $\approx 2\%$ of the monopolar piece, at leading order in α. The frequency shift $\Delta\omega$ is then calculated for different modes of the non-relativistic solutions to (6.17) for scalar clouds, and for corresponding non-relativistic vector cloud solutions. Expressions for $\Delta\omega$, valid for any azimuthal index m_σ, as well as a table listing the first few values, are given in (E.15) and in Table E.1, respectively.

6.4.2 Quasi-relativistic

These analytic expressions (E.15) are accurate in the Newtonian limit, i.e., $\alpha \ll 1$. Here, we extend the validity to the $\alpha \sim \mathcal{O}(1)$ regime, with the caveat that a more accurate non-linear treatment, discussed in the next section, is ultimately necessary. Within `SuperRad`,

[6] At leading order in α, only the quadrupole $\ell = 2$ contributes non-trivially.

we compute the frequency shift in the relativistic regime $\mathcal{D}_{\rm int}$ in a quasi-relativistic approximation, as in Ref. [338]. We take the relativistic field configurations (derived in Appendix E.2) in Boyer-Lindquist coordinates and use them to compute the energy density ρ, which we then use to compute the frequency shift $\Delta\omega$ using the monopolar Newtonian expression (6.20). This approach explicitly assumes a linear dependence of the frequency shift on the cloud mass: $\Delta\omega \sim M_c$. Given these quasi-relativistic results in the relativistic regime of the parameter space, we follow the approach taken in Secs. 6.3.2 and 6.3.3, to calibrate a fit that assumes the analytic expressions (E.15) against the quasi-relativistic results in $\mathcal{D}_{\rm int}$. The fit ansatz is

$$\frac{M^2\Delta\omega}{-\alpha^3 M_c} + F_\sigma = \sum_{p\geq 1} \alpha^p \hat{d}^\sigma_p, \tag{6.21}$$

where F_σ contains the leading-in-α contribution, computed above and explicitly given in Appendix E.4.

As a figure of merit for comparing how relevant this will be in GW observations of boson clouds, we can calculate the extra accumulated phase shift due to the frequency drift, using that $\omega_{\rm GW} = 2\omega_R$,

$$\Delta\phi_{\rm GW} = 2\int_{t_{\rm max}}^{t_{\rm max}+\tau} [\omega_R(t) - \omega_R(t_{\rm max})]\, dt, \tag{6.22}$$

where $t_{\rm max}$ is the time the cloud mass is at its maximum. We show this for the scalar and vector case in Fig. 6.5, taking the total time $\tau = \min(\tau_{\rm GW}, 1{\rm yr})$ to be either the characteristic time over which the GW signal decays $\tau_{\rm GW}$, or one year, when $\tau_{\rm GW} > 1$ yr (assuming a 50 $M_\odot$ BH). From the figure, we can see that $\Delta\phi_{\rm GW} \gg 1$ across the parameter space, except for the scalar case when $\alpha \lesssim 0.1$. Thus, properly accounting for this frequency shift is important to be able to coherently integrate the GW signal. The diverging behavior of the $\tau = \tau_{\rm GW}$ curves in Fig. 6.5 at low α is due to the steeper α-scaling of the GW timescales compared with the frequency shift's scaling.

6.4.3 Comparison to fully relativistic approach

To gauge the error in the quasi-relativistic frequency shifts described above, we compare them to numerically constructed, fully relativistic solutions. Following Herdeiro & Radu [195], we construct stationary and axisymmetric spacetime solutions to the full Einstein-Klein-Gordon field equations consisting of a massive complex scalar field cloud

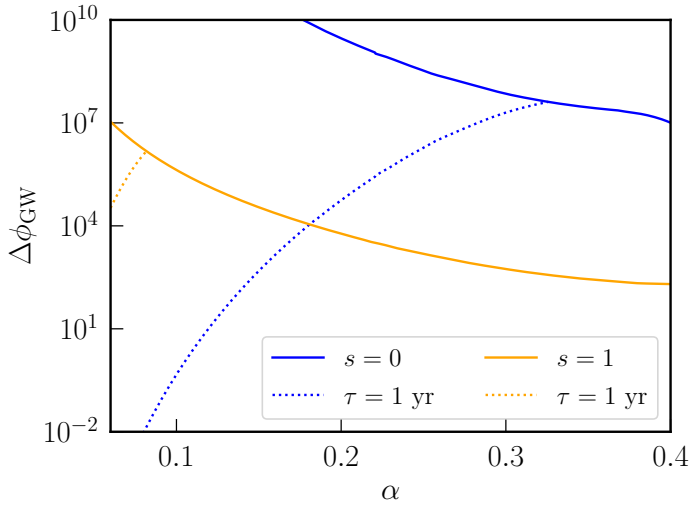

Figure 6.5: The additional accumulated GW phase $\Delta\phi_{\rm GW}$ due to the increase in frequency as the boson cloud mass decreases [defined in (6.22)] for scalar (blue curves) and vector (orange curves) bosons. This phase is calculated beginning from when the cloud mass is maximum for a duration of $\tau_{\rm GW}$ (solid curves) and for one year (when $\tau_{\rm GW} > 1$ yr; dotted curves). We assume a BH with $M = 50\ M_\odot$ and $a_* = 0.99$.

with $\Phi \sim e^{im_S\phi - i\omega_R t}$ around a BH, satisfying the synchronization condition $\omega_R = m_S\Omega_H$. These can be thought of as oscillation (or, equivalently, azimuthal angle) averaged versions of the scalar cloud solutions. By calculating how the frequency of the solution changes with M_c at fixed M and α, we can obtain a fully-relativistic estimate for the frequency shift $\Delta\omega$. The frequency shift is the part of the real frequency that is dependent on the boson cloud mass, $\omega(M_c) = \omega(M_c = 0) + \Delta\omega(M_c)$. For the values of cloud mass relevant to superradiance, $\Delta\omega$ is, to a good approximation linear in M_c, as expected from the non-relativistic results above. Therefore, here we compute a numerical estimate of $\partial\omega/\partial M_c$ at $M_c = 0$ and fixed α (which is $\approx \Delta\omega/M_c$, to within $\sim 1\%$ for $M_c < 0.04M$). In Fig. 6.6, we show how this compares, for $m_S = 1$, to the non-relativistic and quasi-relativistic results for the frequency shift. From there it can be seen that the quasi-relativistic estimate used by `SuperRad` is slightly more accurate than the non-relativistic expressions, but still noticeably underestimates the frequency decrease, by $\approx 32\%$, for $\alpha = 0.4$. For small α, all three calculations give similar results, as expected. In particular, for $\alpha < 0.15$, the difference in the quasi- versus the fully relativistic calculation is $< 7\%$.

We plan to include the fully relativistic frequency corrections in a future version of

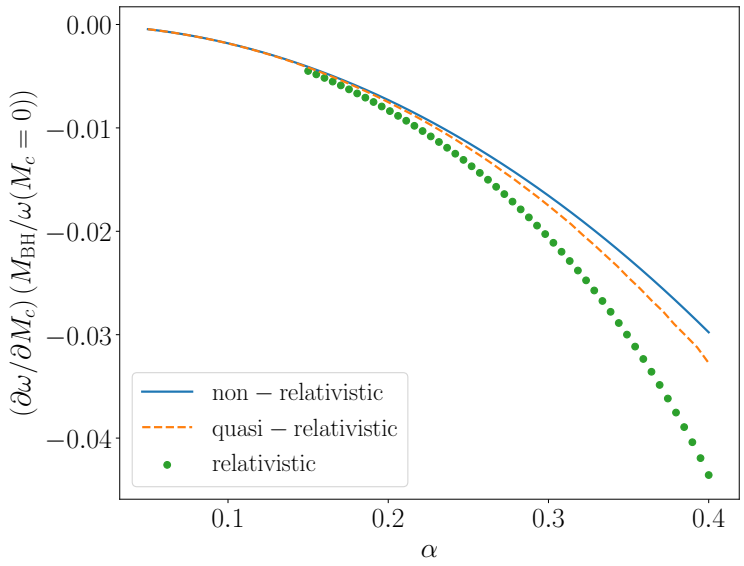

Figure 6.6: A comparison of different approximations of the frequency shift due to the boson cloud's self-gravity for a scalar field with $m_S = 1$. We compare the non-relativistic (see Sec. 6.4.1) and quasi-relativistic (see Sec. 6.4.2) approximations to the (leading order in M_c part) fully relativistic (labelled "relativistic") relative frequency shift. In particular, we show, for fixed α, $(\partial\omega/\partial M_c)(M_c = 0) \approx \Delta\omega/M_c$, where the equality is exact for the non-relativistic and quasi-relativistic approximations.

`SuperRad`, and we defer details on constructing the BH-complex boson cloud solutions, as well as the massive vector case (where we expect comparable, if somewhat larger, relativistic corrections) to upcoming work [253]. We note that with such relativistic solutions, there is still theoretical error associated with taking a complex instead of real field (and hence axisymmetric spacetime). However, we can estimate this by comparing $\Delta\omega$ calculated from (6.18) using the axisymmetric energy density calculated from the complex scalar field solution, to the same quantity calculated from just taking the real part, scaled to give the same energy $\Phi \to \sqrt{2}\mathrm{Re}[\Phi]$. We find the relative difference to be 5×10^{-5}, indicating the theoretical error in the frequency shift should be $< 0.01\%$ for these relativistic results.

6.5 Gravitational waves

In the previous sections, we focused primarily on the conservative sector, neglecting GW dissipation from the system. In what follows, we outline the computation of the GW

strain from the oscillating boson cloud in the source frame. The general procedure is to consider superradiant solutions to the field equations (6.1) as sources for the linearized Einstein equations. These source linear metric perturbations around the BH, which then propagate on an (approximately) fixed Kerr spacetime towards the observer. Analogous to the approach outlined in Sec. 6.3, we use numerical calculations of the emitted GWs that are valid in the relativistic regime, and combine those with input from analytic calculations that are valid in the Newtonian regime, $\alpha \ll 1$, to cover the entire parameter space. In contrast, however, to the quantities calculated in Sec. 6.3, in several cases only the leading order scaling of the GW power and strain with α is known, while the coefficient can be fixed accurately only with numerical methods.

In the following, we begin by outlining the conventions used in the literature and in `SuperRad` in Sec. 6.5.1. We then discuss the emitted GW energy flux and the polarization waveform, as well as the GW modes in the source frame in Sec. 6.5.2.

6.5.1 Conventions

At a large distance r away from the source, the GWs in the source frame are captured by the polarization waveform

$$h = h_+ - ih_\times = \frac{\mathcal{A}}{r} e^{-i\phi_{\rm GW}(t)} \psi(\theta) e^{im_{\rm GW}\varphi}. \tag{6.23}$$

The GW frequency is just twice the cloud oscillation frequency, hence

$$\phi_{\rm GW}(t) = 2 \int \omega_R(t) dt. \tag{6.24}$$

As discussed in Sec. 6.4, the frequency will change over time as the cloud first grows exponentially, and then decays through GW dissipation. The azimuthal dependence is fixed exactly by that of the cloud in question: $|m_{\rm GW}| = 2m_\sigma$, whereas the polar contribution $\psi(\theta)$ is dominated by the $\ell_{\rm GW} = m_{\rm GW}$ spin-(-2)-weighted spherical harmonic mode, except in the relativistic regime of the parameter space. The overall amplitude $\mathcal{A}$ of the signal scales with a leading power in the gravitational fine structure constant of the system: $\mathcal{A} \sim \alpha^q$. This amplitude is approximately independent of BH spin and is proportional to the cloud's mass: $\mathcal{A}(t) \propto M_c(t)$.

We decompose the polarization waveform h into GW modes $h^{\ell m}$ with ${}_{-2}Y_{\ell m}(\theta, \varphi) =$

${}_{-2}S_{\ell m}(\theta)e^{im\varphi}$, the -2-weighted spherical harmonics[7], leading to:

$$h^{\ell m} = \int_{S^2} d\Omega h_{-2}\bar{Y}^{\ell m}(\theta,\varphi). \tag{6.25}$$

Here, and in the following, we drop the subscripts "GW" on the GW mode labels (ℓ, m) for brevity, and distinguish these from the corresponding cloud labels by referring to the latter with (ℓ_σ, m_σ). The polarization waveform can be reconstructed as

$$\begin{aligned} h_+ = \frac{1}{r}\sum_{\ell\geq m} |h^{\ell m}| \left[{}_{-2}S_{\ell m} + (-1)^\ell {}_{-2}S_{\ell -m}\right] \\ \times \cos(\phi_{\rm GW} + m\varphi + \tilde{\phi}_{\ell m}), \\ h_\times = -\frac{1}{r}\sum_{\ell\geq m} |h^{\ell m}| \left[{}_{-2}S_{\ell m} - (-1)^\ell {}_{-2}S_{\ell -m}\right] \\ \times \sin(\phi_{\rm GW} + m\varphi + \tilde{\phi}_{\ell m}), \end{aligned} \tag{6.26}$$

where we used $h^{\ell,-m} = (-1)^\ell \bar{h}^{\ell m}$, and defined $\tilde{\phi}_{\ell m}$ as the complex phase-offsets between different $h^{\ell m}$. Finally, the total GW energy flux is

$$P_{\rm GW} = \int d\Omega \frac{r^2(2\omega_R)^2|h|^2}{16\pi}, \tag{6.27}$$

and can be decomposed into the power emitted in each polar GW ℓ-mode as

$$P_{\rm GW} = P_{\rm GW}^{\ell=m} + P_{\rm GW}^{\ell=m+1} + P_{\rm GW}^{\ell=m+2} + \dots. \tag{6.28}$$

Due to the amplitude scaling $\mathcal{A} \propto M_c$, it is convenient to factor out the dependence on the cloud's mass, and quote results only for the rescaled GW power:

$$\tilde{P}_{\rm GW} = P_{\rm GW} M^2/M_c^2. \tag{6.29}$$

6.5.2 Gravitational wave power and strain

There are two main avenues to determine the strain h in the context of BH superradiance. On the one hand, there are frequency-domain approaches, solving a type of differential eigenvalue problem that assumes a BH background with linear perturbations, while on the

[7]Normalized as $\int d\cos\theta\ {}_{-2}\bar{S}_{\ell m}(\theta)\ {}_{-2}S_{\ell m}(\theta) = 1$.

other hand, there are time-domain numerical methods, which solve the full nonlinear Einstein equations. The former are readily extended across the entire relevant parameter space, but do not capture nonlinear effects, while the latter make no approximations, but carry relatively large numerical uncertainties, and are not easily extended to cover large parts of the parameter space. In this chapter, we mainly leverage frequency-domain methods, and validate these against time-domain estimates, where applicable. These frequency-domain methods can be classified into the "flat" and the "Schwarzschild" approximations, as well as what we call the "Teukolsky" approximation. The former two are analytic estimates, valid only in the non-relativistic regime, $\alpha \ll 1$, while the last named is a numerical approach, which is computationally efficient only when α is not too small. The details of these approximations are given in Appendix E.5. Ultimately, as done above, `SuperRad` combines the best of both worlds and provides the most accurate estimates across the entire parameter space.

In the non-relativistic limit, the currently available results are of the form

$$\tilde{P}_{\rm GW} = H\alpha^{\eta}. \tag{6.30}$$

The respective α scalings for the GW power from scalar and vector superradiant clouds are [35, 377, 79, 50]

$$\eta_S = 4m_S + 10, \qquad \eta_V = 4m_V + 6, \tag{6.31}$$

while the numerical coefficient H depends on the type of approximation employed. We quote all available results in Appendix E.5, and focus here solely on those associated with $m_\sigma = 1$ cloud states. The Schwarzschild approximation has been studied only in the $m_\sigma = 1$ case, resulting in [79, 50]

$$(H_S)^{m_S=1}_{\rm Schw.} = \frac{484 + 9\pi^2}{23040}, \qquad (H_V)^{m_V=1}_{\rm Schw.} = 60. \tag{6.32}$$

These overestimate the true emitted GW power, while the "flat" approximation [377, 50]

$$(H_S)^{m_S=1}_{\rm flat} = \frac{1}{640}, \qquad (H_V)^{m_V=1}_{\rm flat} = \frac{32}{5}, \tag{6.33}$$

is expected to underestimate the total energy flux. From comparing the Schwarzschild with the flat approximation, it is clear that the non-relativistic approximations have systematic uncertainties of roughly one order of magnitude. Hence, even for $\alpha \ll 1$, numerical techniques are required to reduce the uncertainty in the coefficient H.

For this reason, and to extend the validity of the GW power and strain predictions of `SuperRad` to the part of the parameter space with the loudest signals, we utilize frequency-domain numerical techniques in the Teukolsky approximation. We outline the methods we use in Appendix E.5. Here, we simply state that our numerical results are more accurate than either of the analytic approximation techniques, even for moderately small α.

As evident from (6.30), the GW emission is independent of the BH spin a_* in the Newtonian regime, while in the relativistic regime, the GWs exhibit mild spin-dependence [377, 338]. To simplify the parameter space, we restrict to clouds in the saturated state; that is, we assume $\omega_R = m_\sigma \Omega_H$ [8], removing the spin-dependence from the parameter space. As in the discussion in Sec. 6.3, there exists a relativistic regime, $\tilde{\mathcal{D}}_{\rm int}$, in which accurate numerical predictions can be obtained. For $\alpha \ll 1$, the function

$$\tilde{P}_{\rm GW} = b\alpha^\eta + c\alpha^{\eta+1} + \dots , \tag{6.34}$$

is used to fit against the numerical results. In general, $b \neq H_\sigma$; that is, we fit even the leading order coefficient from the numerically obtained Teukolsky estimates. However, we check explicitly that $(H_\sigma)_{\rm flat} < b < (H_\sigma)_{\rm Schw.}$ for both the scalar and vector $m_\sigma = 1$ cloud states in the $\alpha \ll 1$ regime. `SuperRad` employs cubic-order interpolation in $\tilde{\mathcal{D}}_{\rm int}$, and uses fits of the type (6.34) for $\alpha \in \tilde{D}_{\rm fit}$.

In Figure 6.7, we compare the various calculation of the the GW power to the predictions by `SuperRad`. In the Newtonian limit, `SuperRad` differs from (6.30) due to the fit (6.34), allowing different leading-α coefficients. The underlying numerical results are more accurate (see Appendix E.5 for details), allowing us to conclude that the estimates provided by `SuperRad`, are more accurate than the Schwarzschild or flat approximations. The analytic estimates for $\tilde{P}_{\rm GW}$ are worse for $m_\sigma = 2$; we use those results only to inform the leading-α scaling behavior. We also show time-domain results from evolving the full nonlinear Einstein-Proca equations [141, 142] for a few points. These agree with the Teukolsky calculations to within the numerical error of the simulations.

In Figure 6.8, we show the GW modes provided by `SuperRad`, as defined in (6.25), over the entire parameter space, assuming the saturation condition. As expected from the non-relativistic results, the quadrupolar contribution h_{22} dominates throughout most of the parameter space, except in the most relativistic regime, where h_{32} increases in importance (and equivalently for h_{44} and h_{54}). This behavior implies a constant phase shift between the two involved multipolar components. Hence, there is an α-range where $|h_{22}| \sim |h_{32}|$ (and $|h_{44}| \sim |h_{54}|$), which means that the phase difference $\tilde{\phi}_{22}$ (and $\tilde{\phi}_{44}$), defined in (6.26), introduces a non-trivial phase-offset between the two involved polar modes.

[8] The validity of this last condition is discussed below in Sec. 6.6.

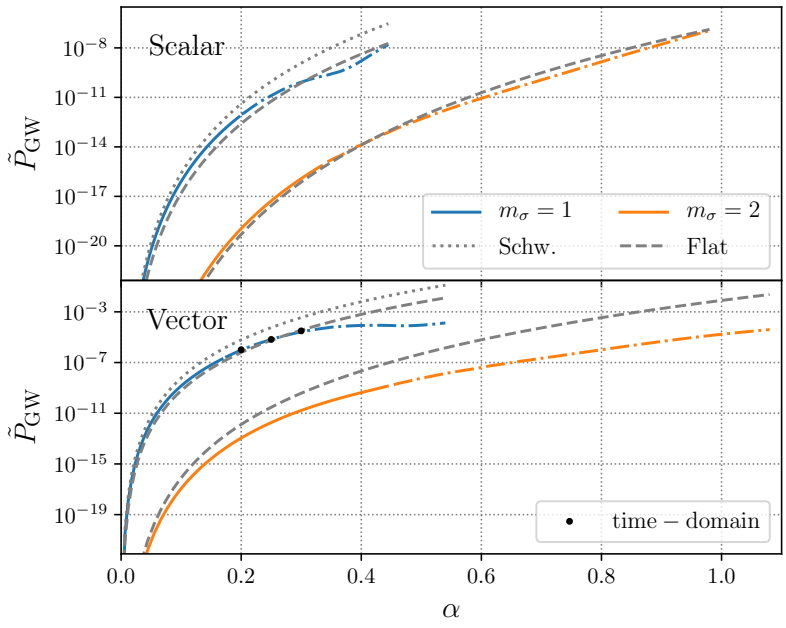

Figure 6.7: We show the mass-rescaled GW power $\tilde{P}_{\rm GW}$, defined in (6.29), emitted by the scalar and vector clouds with azimuthal number $m_\sigma = 1$ and 2 at the saturation point, $\omega_R = m_\sigma \Omega_H$, comparing the Schwarzschild "Schw." and the flat approximations to `SuperRad` *(colored lines)*, and time-domain estimates obtained in [141, 142]. Dash-dotted colored lines indicate where `SuperRad` uses interpolation of numerical results over fits of the type (6.34).

6.6 Growth and decay of boson cloud

In this section, we address how the superradiant instability and GW calculations can be combined to calculate the evolution of the boson cloud, which determines the evolution of the amplitude and frequency of the GW signal.

A boson cloud around a spinning BH evolves as the cloud extracts energy and angular momentum from the BH through the superradiant instability. During this process, the cloud also loses energy and angular momentum to gravitational radiation. In a quasi-

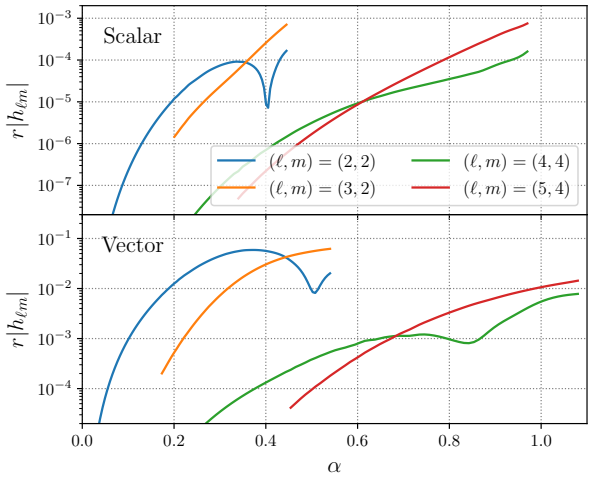

Figure 6.8: We show the magnitudes of the GW modes $h_{\ell m}$, defined in (6.25), which are sourced by $m_\sigma = 1$ and 2 scalar and vector boson clouds at saturation ($\omega_R = m_\sigma \Omega_H$) as functions of α. Notice that $\ell \geq 2m_\sigma$.

adiabatic approximation, the evolution of this system is given by

$$\begin{aligned} \dot{M}_c &= 2\omega_I M_c + P_{\rm GW}, \\ \dot{M} &= -2\omega_I M_c, \\ \dot{J} &= -\frac{2m_\sigma \omega_I}{\omega_R} M_c, \end{aligned} \tag{6.35}$$

where ω_R, ω_I, and $P_{\rm GW}$ are functions of the cloud mass and BH mass and spin. The evolution of the boson cloud can be roughly divided into two phases. In the first phase, the cloud grows exponentially, with the mass going like $M_c \sim \exp(2\omega_I t)$, with the growth eventually saturating as the BH is spun down and ω_I becomes small as $m_\sigma \Omega_H$ decreases towards ω_R. This is followed by the gradual dissipation of the boson cloud through gravitational radiation. Since during this time $-\dot{M}_c \approx P_{\rm GW} \propto M_c^2$,

$$M_c(t) \approx \frac{\bar{M}_c}{1 + (t - t_{\rm max})/\tau_{\rm GW}} \tag{6.36}$$

where the cloud mass reaches a maximum $\bar{M}_c$ at $t = t_{\rm max}$ and $\tau_{\rm GW} := \bar{M}_c / P_{\rm GW}$.

In Figure 6.9, we plot an example of the evolution of the cloud mass for both scalar and vector bosons. In both cases, $\tau_I \ll \tau_{\rm GW}$, so that the exponential growth phase takes place

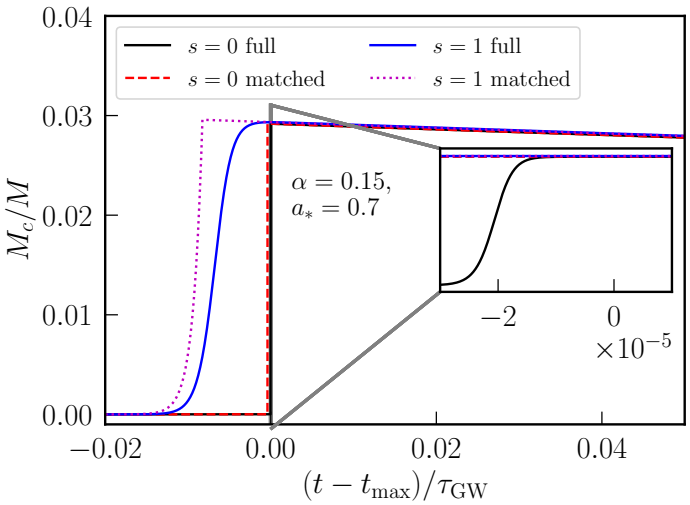

Figure 6.9: An example evolution of the boson cloud mass as a function of time for scalars ($s = 0$) and vectors ($s = 1$) with $\alpha = 0.15$ and $a_* = 0.7$. The plot compares the evolution determined by evolving the full equations (6.35) (solid lines, labelled "full"), to an approximation that matches together constant exponential growth to GW-dominated decay (dotted and dashed lines, labelled "matched"). Time is normalized by the gravitational dissipation timescale in either case, and the offset adjusted so that the maximum value of M_c occurs at zero for the full evolution cases, and the matching value of M_c is obtained for the corresponding matched evolution cases. The inset shows a zoom in of the end of the exponential growth phase for the scalar case (in particular the full evolution).

on a much shorter time scale than GW dissipation. However, the ratio $\tau_I/\tau_{\rm GW}$ is markedly smaller in the scalar case compared to the vector one. In addition to the full evolution of the cloud as determined by (6.35), in Figure 6.9 we also plot a simple approximation where the maximum cloud mass is determined by solving for the BH parameters where $\omega_R = m_\sigma \Omega_H$, and the evolution of M_c after the maximum is given solely by gravitational radiation, and the evolution of M_c before the maximum is given by exponential growth with a fixed value ω_I given by the initial parameters.

The `SuperRad` waveform model implements options for both the full cloud evolution and the matched approximation. While the latter approximation is less computationally expensive, as can be seen in Figure 6.9, it slightly overestimates the maximum cloud mass (by $\approx 0.04\%$ and 0.8%, respectively, for the scalar and vector cases shown in the figure), and underestimates the time for the cloud to reach its maximum. Thus, the more accurate

full cloud evolution is appropriate for scenarios when the signal before the time when the cloud reaches saturation makes a non-negligible contribution. However, as noted above, our calculation of $\tilde{P}_{\rm GW}$ assumes $m_\sigma \Omega_H = \omega_R$, which is not strictly valid before the saturation of the instability. Hence, there will be a discrepancy in the BH spin used for the computation of the GW power. This discrepancy is negligible (i.e., below the numerical error of the methods, discussed in Appendix E.5) for $m_\sigma = 2$, and for $m_\sigma = 1$ assuming $a_* < 0.9$. It should be noted that this affects the GW emission before saturation only, and also only systems with initial spin $a_* \gtrsim 0.9$. In the vector $m_V = 1$ case, the largest discrepancy occurs for $\alpha \approx 0.46$ and extremal spins, where the relative error from assuming the saturation condition in the mass-rescaled GW power $\tilde{P}_{\rm GW}$ is $\approx 55\%$ (see Fig. 7 in [338]). For the scalar $m_S = 1$ case this discrepancy is at most $\approx 24\%$ around $\alpha \approx 0.36$.

6.7 LISA follow-up searches

The two main observational signatures of superradiant clouds, BH spin down and GW emission, are sensitive to various systematic and statistical uncertainties. Spin measurements have been used to exclude scalar and vector mass ranges. Most of these constraints, however, rely on BH-spin estimates from electromagnetic observations with significant systematic uncertainties. Spin measurements of BHs in inspiraling binaries using GWs exhibit large statistical uncertainties and make assumptions about the proceeding history of the binary. Constraints from the stochastic GW background, assuming a population of BH-cloud systems, rely on assumptions regarding the BH mass and spin population, in addition to position and distance uncertainties. Lastly, searches for GWs from existing BHs observed in the electromagnetic channel make assumptions about the past history of the observed BH, introducing large systematic uncertainties. Clearly all of these methods rely on modeling or assumptions with potentially substantial systematic uncertainties.

One search strategy for GWs from superradiant clouds, however, evades these assumptions: BH merger follow-up searches. These searches target BH remnants of previously detected compact binary coalescences. The key advantages are the knowledge of the complete past history of the targeted BH, as well as measurements of sky-position, spin, mass, and distance. Given these quantities, accurate predictions of the subsequent superradiance instability and GW emission are possible, enabling a targeted search for the latter in the days/weeks/years following the merger. This removes the assumptions affecting other search strategies, reduces the uncertainties to those coming from the merger GW signal measurement of the remnant, and those of the waveform model (discussed in the case of `SuperRad` below), and enables one to put confident constraints on relevant parts of the

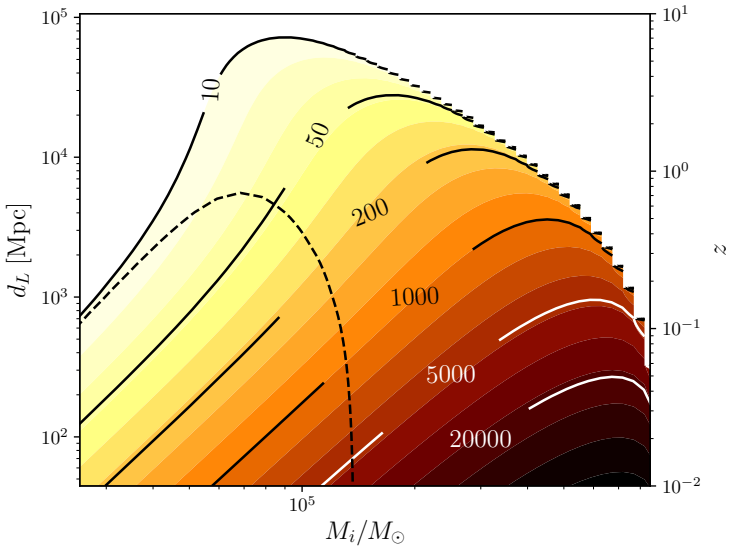

Figure 6.10: We show the SNR *(contour lines and color)* of GWs from vector superradiant clouds around a fiducial BH of initial remnant source frame mass of M_i and spin $a_{*,i} = 0.8$ as a function of luminosity distance d_L and redshift z, assuming a standard ΛCDM cosmology and $\alpha = 0.2$. For comparison, we also consider an initial spin of $a_{*,i} = 0.7$ showing the $\rho_{\rm SNR} = 10$ contour *(dashed black line)*, assuming $\alpha = 0.15$.

ultralight boson parameter space, or potentially to make a confident discovery.

In the context of the current generation of ground-based GW detectors, follow-up searches for GWs from scalar superradiant clouds are likely infeasible due to the small strain amplitudes [206]. On the other hand, because of their faster growth rates and orders of magnitude stronger signals, vector boson clouds are ideal candidates for these types of searches [209]. At design sensitivity, the advanced LIGO [5], advanced Virgo [21], and KAGRA [36] observatories will in principle be sensitive to systems out to ~ 1 Gpc at a typical remnant BH spin of $a_* = 0.7$ and masses of $M \sim 100 M_\odot$ [102, 209]. Undertaking follow-up searches targeting BHs falling into this parameter range could target vector boson masses roughly in the range of $\mathcal{M}_V \in (1 \times 10^{-11}, 1 \times 10^{-13})$ eV. In a similar fashion, LISA could be sensitive to GWs from vector boson clouds with boson masses in the $\mathcal{M}_V < 10^{-15}$ eV regime, inaccessible by ground-based detectors.

In the following, we analyze the prospects of follow-up searches for GWs from vector superradiant clouds around supermassive binary BH merger remnants with LISA. The fundamental assumption of follow-up searches is that a *new* superradiant cloud forms

around the remnant after merger. If either of the constituents already posses a superradiant cloud, it is expected to be depleted before or during merger for nearly equal mass-ratio ($q \sim 1$) systems [52]. Even for $q > 1$, depending on α, clouds around the constituents of the binary are efficiently removed before merger [52, 62, 353, 354]. LISA is expected to see at least a handful of such mergers over the mission lifetime of four years [61, 260]. Therefore, to estimate the detection horizon, we assume a fiducial supermassive binary BH merger remnant detection that occurs one year into the mission. After merger at redshift z, residual ultralight vector densities around the remnant, or quantum fluctuations, trigger the superradiance instability[9] leading to the complete cloud formation, and hence the peak of the GW signal, on timescales of at most $t_c \approx \tau_I(1+z)\log(M_c/\mathcal{M}_V)/2$ in the detector frame. Over most of the parameter space, these signals will last for longer than the remaining three years of the LISA mission, leaving an observing time of $T_{\rm obs} = 3 - t_c$ years. We determine the maximum detection horizon of GWs from vector superradiant clouds by considering the optimal signal-to-noise ratio (SNR) $\rho_{\rm SNR}$ with the LISA sensitivity curve (details can be found in Appendix E.1). Making these assumptions, we illustrate the detection horizon of LISA for such events in Figure 6.10.

From Figure 6.10, we conclude that parts of the vector boson mass parameter space can be probed with idealized follow-up GW searches from supermassive binary BH remnants. Even for moderate initial spins of $a_{*,i} = 0.7$, GWs can be detected up to $z \lesssim 0.8$, while for slightly more favorable initial spins of $a_{*,i} = 0.8$, the GW emission is observable out to $z \lesssim 8$. The merger rate of massive BH binaries is expected to peak around $M \sim 10^6 M_\odot$ for equal mass ratio systems, $q \lesssim 1$, and at $z \approx 2$ [254, 192, 207]. For initial BH masses $M_i > 10^6\ M_\odot$, the cloud formation timescales are larger than the mission duration, $t_c > 3$ years, leading to a drop in SNR. At high redshifts, the sensitivity of LISA is primarily limited by the short effective observation times in the detector frame. Larger BH masses (lower boson masses) can be accessed only with larger initial spins, or significantly longer mission durations. Vector boson masses roughly around $\mathcal{M}_V \in (1 \times 10^{-16}, 6 \times 10^{-16})$ eV are within reach of these follow-up search strategies with LISA.

These prospects are subject to a few caveats. First, we determined the detection horizon and sensitivity of LISA to GW from vector clouds around remnant supermassive BHs using the optimal matched filter SNR. What fraction of this total available SNR could be recovered from the data by a realistic search algorithm is an open question, even for ground-based detectors [209]. Secondly, the merger rate of massive BH binaries has large uncertainties. If the true merger rate were peaked at redshifts of $z > 5$, a realistic follow-up search would require a very favorable initial BH spin $a_{*,i} > 0.8$ to access a meaningful part of the vector boson parameter space directly, or an outlier event much closer.

[9] Notice, an equal-mass, non-spinning binary BH merger results in remnant BH with $a_* \approx 0.7$.

6.8 Discussion

We have introduced a new BH superradiance gravitational waveform model called `SuperRad`. This provides the superradiance instability growth timescale τ_I, the cloud oscillation frequency ω_R, the GW frequency $f_{\rm GW}(t)$ and strain $h_{\times/+}$ in the source frame as a function of time, the GW power $P_{\rm GW}$, and the evolution of the boson cloud. The `SuperRad` model makes use of all available analytic and numerical estimates for these observables, and calibrates analytic fits against the numerical data to extend the applicability across the *entire* parameter space of the $m = 1$ and 2 scalar and vector superradiant clouds. The waveform model `SuperRad` can be used to inform and interpret the results of GW searches for ultralight scalar and vector BH superradiance. This includes both blind and targeted searches for resolved continuous wave signals, as well as searches for a stochastic GW background from BH-boson cloud systems. It can also be used when interpreting BH spin measurements using GW or electromagnetic observations. Importantly, `SuperRad` is accurate in the relativistic regime where the observable signals will be the strongest.

As the ultralight boson cloud dissipates through gravitational radiation, there is a small increase in the frequency of the GWs due to the changing self-gravity contribution of the cloud. As illustrated above, even though this frequency drift is small, because of the large number of GW cycles that make up a typical superradiance signal, not properly accounting for it can lead to the signal model going out of phase in a fraction of the observing time. Fully including this second-order effect within BH perturbation theory is challenging, and the results in `SuperRad` for the frequency evolution of the GW signal use non-relativistic approximations. By comparing these to fully-relativistic numerical calculations for the scalar boson case, we found that the former underestimates the value of $\dot{f}_{\rm GW}$ by $\sim 30\%$ for the most relativistic (i.e. $\alpha \sim O(1)$) cases, though the differences are smaller for more typical parameters. In future work, we plan to include the fully-relativistic results for the cloud-mass contribution to the frequency for both scalar and vector bosons in `SuperRad`. Though, given the stringent accuracy requirements imposed by the typical signal timescales (see Fig. 6.5), it is likely that fully-coherent signal analysis techniques (e.g., match filtering) will still not be feasible in much of the parameter space, better predictions for the GW frequency evolution are nevertheless important in guiding the application of semi-coherent techniques.

Furthermore, we investigated the viability of follow-up searches for GWs from ultralight vector superradiant clouds with LISA targeting remnants of observed massive binary BH mergers. We found that these searches are confident probes of the ultralight vector boson parameter space around $\mathcal{M} \in (1 \times 10^{-16}, 6 \times 10^{-16})$ eV. With current estimates of the merger rate of massive BH binaries, LISA will be sensitive to GWs from vector boson

clouds around remnants of these mergers out to redshift $z \lesssim 8$ at mass-ratio $q \lesssim 1$ and remnant black hole masses of roughly $M \in (6 \times 10^4, 2 \times 10^5) M_\odot$. Our basic analysis leaves various questions unanswered. We assumed the total available signal-to-noise ratio can be recovered by a realistic search algorithm, which is an overestimate even in the case of ground-based detectors [209]. As well, a more detailed study folding in massive black hole binary merger rates with superradiant cloud growth timescales and emitted GW luminosities could provide an estimate for the expected number and mass ranges of merger events where LISA would be sensitive to the GW signal from an ultralight vector boson.

Chapter 7

Conclusion and outlook

In this thesis, we addressed multiple questions important for probing aspects of fundamental physics with current and future gravitational wave detectors and electromagnetic observations. In this first part, we focused on understanding the stability of boson stars and exploring their dynamics in the context of various binary configurations. Our work explicitly demonstrates the viability of boson stars as linearly stable highly-compact testbeds to investigate potential linear and non-linear instabilities associated with relativistic features such as the Ergoregion [160] or stable light-rings [216]. These phenomena, common amongst black hole mimicking objects, may encode smoking gun signatures for the existence of ultra compact objects in the emitted gravitational waves. Furthermore, as a result of the linear stability of some highly-compact boson stars, another interesting avenue forward is to study the merger and ringdown of ultra compact object mergers and their gravitational wave emission. A large body of research has been devoted to the study of the ringdown of black hole mimicking objects (see, e.g., Ref. [97]), while, to the best of our knowledge, no self-consistent nonlinear evolution of a binary inspiral consisting of ultra compact objects has been performed to date. This leaves questions about the impact of nonlinear and finite-size effects and their imprint on the inspiral dynamics and resulting gravitational waveform un-answered. Another intersting direction forward is to leverage highly accurate binary boson star inspiral-merger-ringdown gravitational waveforms in order to validate test of the black hole paradigm or tests of general relativity currently used by the LIGO-Virgo-KAGRA collaboration. While binary boson stars are, of course, solutions to general relativity, these tests may or may not be able to distinguish between beyond-general relativity compact binary inspirals and highly-compact binary boson star gravitational waveforms. To that end, a thorough analysis of equilibrium equations for scalar matter making up the binary's stars at the level of the initial data may aid to im-

prove the quality and reduce the impact of spurious artifacts of binary boson star initial data, and hence, produce cleaner waveforms.

In the second part, we studied the superradiance phenomenon of ultralight fields around black holes to understand the impact of non-vanishing couplings to the Standard Model of particle physics, and developed a waveform model for the emitted gravitational radiation for the use in future observation campaigns of ground- and space-based gravitational wave detectors. Utilizing this waveform model, we analyzed prospects of performing searches for signals from vector boson clouds around known black holes adapting continuous wave methods subject to current gravitational wave detection sensitivities in Ref. [209]. Follow-up work could perform an actual search for gravitational waves following up previously detected binary black hole mergers (both in previous and future gravitational wave observing runs), either making a detection in the process, or placing strong constraints on a collection of ultralight vector boson models. In the context of vector boson clouds with non-vanishing kinetic mixing with the Standard Model photon, searches outlined here could be performed in order to access untapped regions of the dark photon parameter space. In particular, following up binary black hole mergers with X- or γ-ray telescopes could prove fruiteful in constraining the existence of the dark photon one to two orders of magnitude below the current constraints in the relevant mass-range. Furthermore, an interesting direction for future work is the study of these systems with accretion disks. Depending on the parameter space, the superradiant cloud periodically perturbs the disk, potentially leading to observable smoking gun signatures in the emitted electromagnetic spectrum. Active galactic nuclei, in particular, are observable to large distances, rendering this a fruitful avenue to probe complementary regimes of beyond the Standard Model physics associated with a new ultralight vector boson of masses $\lesssim 10^{-14}$ eV.

References

[1] http://www.atnf.csiro.au/research/pulsar/psrcat.

[2] Black Hole Perturbation Toolkit. (bhptoolkit.org).

[3] Chandra proposers observatory guide, cycle 25. https://cxc.cfa.harvard.edu/proposer/POG/.

[4] Die Wechselwirkungskräfte in der Elektrodynamik und in der Feldtheorie der Kernkräfte (Teil II und III) [40]. In *E.C.G. Stueckelberg, An Unconventional Figure of Twentieth Century Physics*, page 273. 2009.

[5] J. Aasi et al. Advanced LIGO. *Classical and Quantum Gravity*, 32:074001, 2015.

[6] B. P. Abbott et al. Observation of Gravitational Waves from a Binary Black Hole Merger. *Phys. Rev. Lett.*, 116(6):061102, 2016.

[7] B. P. Abbott et al. Properties of the Binary Black Hole Merger GW150914. *Phys. Rev. Lett.*, 116(24):241102, 2016.

[8] B. P. Abbott et al. Prospects for observing and localizing gravitational-wave transients with Advanced LIGO, Advanced Virgo and KAGRA. *Living Rev. Rel.*, 21(1):3, 2018.

[9] B.P. Abbott et al. GWTC-1: A Gravitational-Wave Transient Catalog of Compact Binary Mergers Observed by LIGO and Virgo during the First and Second Observing Runs. *Phys. Rev. X*, 9(3):031040, 2019.

[10] L. F. Abbott and P. Sikivie. A Cosmological Bound on the Invisible Axion. *Phys. Lett. B*, 120:133–136, 1983.

[11] R. Abbott et al. GW190814: Gravitational Waves from the Coalescence of a 23 Solar Mass Black Hole with a 2.6 Solar Mass Compact Object. *Astrophys. J. Lett.*, 896(2):L44, 2020.

[12] R. Abbott et al. GWTC-2: Compact Binary Coalescences Observed by LIGO and Virgo During the First Half of the Third Observing Run. 10 2020.

[13] R. Abbott et al. All-sky search for continuous gravitational waves from isolated neutron stars in the early O3 LIGO data. *Phys. Rev. D*, 104(8):082004, 2021.

[14] R. Abbott et al. GWTC-3: Compact Binary Coalescences Observed by LIGO and Virgo During the Second Part of the Third Observing Run. 11 2021.

[15] R. Abbott et al. Tests of General Relativity with GWTC-3. 12 2021.

[16] R. Abbott et al. The population of merging compact binaries inferred using gravitational waves through GWTC-3. 11 2021.

[17] R. Abbott et al. All-sky search for gravitational wave emission from scalar boson clouds around spinning black holes in LIGO O3 data. *Phys. Rev. D*, 105(10):102001, 2022.

[18] R. Abbott et al. Narrowband Searches for Continuous and Long-duration Transient Gravitational Waves from Known Pulsars in the LIGO-Virgo Third Observing Run. *Astrophys. J.*, 932(2):133, 2022.

[19] R. Abbott et al. Search for continuous gravitational wave emission from the Milky Way center in O3 LIGO-Virgo data. *Phys. Rev. D*, 106(4):042003, 2022.

[20] S. A. Abel, M. D. Goodsell, J. Jaeckel, V. V. Khoze, and A. Ringwald. Kinetic Mixing of the Photon with Hidden U(1)s in String Phenomenology. *JHEP*, 07:124, 2008.

[21] F. Acernese et al. Advanced Virgo: a second-generation interferometric gravitational wave detector. *Classical and Quantum Gravity*, 32(2):024001, 2015.

[22] K. Ackley et al. Observational constraints on the optical and near-infrared emission from the neutron star–black hole binary merger candidate S190814bv. *Astron. Astrophys.*, 643:A113, 2020.

[23] C. B. Adams et al. Axion Dark Matter. In *Snowmass 2021*, 3 2022.

[24] Eric Adelberger, Gia Dvali, and Andrei Gruzinov. Photon mass bound destroyed by vortices. *Phys. Rev. Lett.*, 98:010402, 2007.

[25] Kazunori Akiyama et al. First M87 Event Horizon Telescope Results. I. The Shadow of the Supermassive Black Hole. *Astrophys. J. Lett.*, 875:L1, 2019.

[26] Miguel Alcubierre, Steven Brandt, Bernd Bruegmann, Daniel Holz, Edward Seidel, Ryoji Takahashi, and Jonathan Thornburg. Symmetry without symmetry: Numerical simulation of axisymmetric systems using Cartesian grids. *Int. J. Mod. Phys. D*, 10:273–290, 2001.

[27] Daniela Alic, Philipp Mosta, Luciano Rezzolla, Olindo Zanotti, and Jose Luis Jaramillo. Accurate Simulations of Binary Black-Hole Mergers in Force-Free Electrodynamics. *Astrophys. J.*, 754:36, 2012.

[28] Mandana Amiri et al. Observations of fast radio bursts at frequencies down to 400 megahertz. *Nature*, 566(7743):230–234, 2019.

[29] Lorenzo Annulli, Vitor Cardoso, and Rodrigo Vicente. Response of ultralight dark matter to supermassive black holes and binaries. *Phys. Rev. D*, 102(6):063022, 2020.

[30] D. Antypas et al. New Horizons: Scalar and Vector Ultralight Dark Matter. 3 2022.

[31] Paola Arias, Davide Cadamuro, Mark Goodsell, Joerg Jaeckel, Javier Redondo, and Andreas Ringwald. WISPy Cold Dark Matter. *JCAP*, 06:013, 2012.

[32] Asimina Arvanitaki, Masha Baryakhtar, Savas Dimopoulos, Sergei Dubovsky, and Robert Lasenby. Black Hole Mergers and the QCD Axion at Advanced LIGO. *Phys. Rev.*, D95(4):043001, 2017.

[33] Asimina Arvanitaki, Masha Baryakhtar, and Xinlu Huang. Discovering the QCD Axion with Black Holes and Gravitational Waves. *Phys. Rev.*, D91(8):084011, 2015.

[34] Asimina Arvanitaki, Savas Dimopoulos, Sergei Dubovsky, Nemanja Kaloper, and John March-Russell. String Axiverse. *Phys. Rev.*, D81:123530, 2010.

[35] Asimina Arvanitaki and Sergei Dubovsky. Exploring the String Axiverse with Precision Black Hole Physics. *Phys. Rev.*, D83:044026, 2011.

[36] Yoichi Aso, Yuta Michimura, Kentaro Somiya, Masaki Ando, Osamu Miyakawa, Takanori Sekiguchi, Daisuke Tatsumi, and Hiroaki Yamamoto. Interferometer design of the kagra gravitational wave detector. *Phys. Rev. D*, 88:043007, Aug 2013.

[37] W. B. Atwood et al. The Large Area Telescope on the Fermi Gamma-Ray Space Telescope Mission. ApJ, 697(2):1071–1102, June 2009.

[38] Josu C. Aurrekoetxea, Katy Clough, and Eugene A. Lim. CTTK: A new method to solve the initial data constraints in numerical relativity. 7 2022.

[39] Minos Axenides, Stavros Komineas, Leandros Perivolaropoulos, and Manolis Floratos. Dynamics of nontopological solitons: Q balls. *Phys. Rev. D*, 61:085006, 2000.

[40] Stanislav Babak, Antoine Petiteau, and Martin Hewitson. LISA Sensitivity and SNR Calculations. 8 2021.

[41] Valentina Baccetti, Robert B. Mann, and Daniel R. Terno. Role of evaporation in gravitational collapse. *Class. Quant. Grav.*, 35(18):185005, 2018.

[42] Xue-Ning Bai and Anatoly Spitkovsky. Modeling of Gamma-ray Pulsar Light Curves Using the Force-free Magnetic Field. *ApJ*, 715(2):1282–1301, June 2010.

[43] Xue-Ning Bai and Anatoly Spitkovsky. Uncertainties of Modeling Gamma-ray Pulsar Light Curves Using Vacuum Dipole Magnetic Field. *ApJ*, 715(2):1270–1281, June 2010.

[44] Jayashree Balakrishna, Edward Seidel, and Wai-Mo Suen. Dynamical evolution of boson stars. 2. Excited states and selfinteracting fields. *Phys. Rev. D*, 58:104004, 1998.

[45] Vijay Balasubramanian, Jan de Boer, Sheer El-Showk, and Ilies Messamah. Black Holes as Effective Geometries. *Class. Quant. Grav.*, 25:214004, 2008.

[46] Cosimo Bambi. Testing black hole candidates with electromagnetic radiation. *Rev. Mod. Phys.*, 89(2):025001, 2017.

[47] Nitsan Bar, Diego Blas, Kfir Blum, and Sergey Sibiryakov. Galactic rotation curves versus ultralight dark matter: Implications of the soliton-host halo relation. *Phys. Rev. D*, 98(8):083027, 2018.

[48] Enrico Barausse, Richard Brito, Vitor Cardoso, Irina Dvorkin, and Paolo Pani. The stochastic gravitational-wave background in the absence of horizons. *Class. Quant. Grav.*, 35(20):20LT01, 2018.

[49] Masha Baryakhtar, Marios Galanis, Robert Lasenby, and Olivier Simon. Black hole superradiance of self-interacting scalar fields. *Phys. Rev. D*, 103(9):095019, 2021.

[50] Masha Baryakhtar, Robert Lasenby, and Mae Teo. Black Hole Superradiance Signatures of Ultralight Vectors. *Phys. Rev.*, D96(3):035019, 2017.

[51] Richard Battye and Paul Sutcliffe. Q-ball dynamics. *Nucl. Phys. B*, 590:329–363, 2000.

[52] Daniel Baumann, Horng Sheng Chia, and Rafael A. Porto. Probing Ultralight Bosons with Binary Black Holes. *Phys. Rev.*, D99(4):044001, 2019.

[53] Daniel Baumann, Horng Sheng Chia, John Stout, and Lotte ter Haar. The Spectra of Gravitational Atoms. *JCAP*, 12:006, 2019.

[54] Thomas W. Baumgarte, Stuart L. Shapiro, and Masaru Shibata. On the maximum mass of differentially rotating neutron stars. *Astrophys. J. Lett.*, 528:L29, 2000.

[55] Yilber Fabian Bautista and Nils Siemonsen. Post-Newtonian waveforms from spinning scattering amplitudes. *JHEP*, 01:006, 2022.

[56] Jacob D. Bekenstein and Marcelo Schiffer. The Many faces of superradiance. *Phys. Rev. D*, 58:064014, 1998.

[57] Iosif Bena and Nicholas P. Warner. Black holes, black rings and their microstates. *Lect. Notes Phys.*, 755:1–92, 2008.

[58] Iosif Bena and Nicholas P. Warner. Resolving the Structure of Black Holes: Philosophizing with a Hammer. 11 2013.

[59] Sebastiano Bernuzzi, Tim Dietrich, Wolfgang Tichy, and Bernd Brügmann. Mergers of binary neutron stars with realistic spin. *Phys. Rev. D*, 89(10):104021, 2014.

[60] Clément Berthiere, Debajyoti Sarkar, and Sergey N. Solodukhin. The fate of black hole horizons in semiclassical gravity. *Phys. Lett. B*, 786:21–27, 2018.

[61] Emanuele Berti. Lisa observations of massive black hole mergers: event rates and issues in waveform modelling. *Class. Quant. Grav.*, 23:S785–S798, 2006.

[62] Emanuele Berti, Richard Brito, Caio F. B. Macedo, Guilherme Raposo, and Joao Luis Rosa. Ultralight boson cloud depletion in binary systems. *Phys. Rev. D*, 99(10):104039, 2019.

[63] Emanuele Berti, Vitor Cardoso, and Marc Casals. Eigenvalues and eigenfunctions of spin-weighted spheroidal harmonics in four and higher dimensions. *Phys. Rev. D*, 73:024013, 2006. [Erratum: Phys.Rev.D 73, 109902 (2006)].

[64] Emanuele Berti et al. Testing General Relativity with Present and Future Astrophysical Observations. *Class. Quant. Grav.*, 32:243001, 2015.

[65] Miguel Bezares, Mateja Bošković, Steven Liebling, Carlos Palenzuela, Paolo Pani, and Enrico Barausse. Gravitational waves and kicks from the merger of unequal mass, highly compact boson stars. *Phys. Rev. D*, 105(6):064067, 2022.

[66] Miguel Bezares and Carlos Palenzuela. Gravitational Waves from Dark Boson Star binary mergers. *Class. Quant. Grav.*, 35(23):234002, 2018.

[67] Miguel Bezares, Carlos Palenzuela, and Carles Bona. Final fate of compact boson star mergers. *Phys. Rev. D*, 95(12):124005, 2017.

[68] R. D. Blandford. To the lighthouse. In *MPA / ESO / MPE / USM Conference on Lighthouses of the Universe: The Most Luminous Celestial Objects and their use for Cosmology*, 2 2002.

[69] R. D. Blandford and R. L. Znajek. Electromagnetic extractions of energy from Kerr black holes. *Mon. Not. Roy. Astron. Soc.*, 179:433–456, 1977.

[70] Diego Blas and Samuel J. Witte. Quenching Mechanisms of Photon Superradiance. *Phys. Rev. D*, 102(12):123018, 2020.

[71] Silvano Bonazzola, Eric Gourgoulhon, and Jean-Alain Marck. A Relativistic formalism to compute quasiequilibrium configurations of nonsynchronized neutron star binaries. *Phys. Rev. D*, 56:7740–7749, 1997.

[72] Erin Bonning, Pedro Marronetti, David Neilsen, and Richard Matzner. Physics and initial data for multiple black hole space-times. *Phys. Rev. D*, 68:044019, 2003.

[73] Mateja Bošković and Enrico Barausse. Soliton boson stars, Q-balls and the causal Buchdahl bound. *JCAP*, 02(02):032, 2022.

[74] Peter Bowcock, David Foster, and Paul Sutcliffe. Q-balls, Integrability and Duality. *J. Phys. A*, 42:085403, 2009.

[75] Richard L. Bowers and E.P.T. Liang. Anisotropic Spheres in General Relativity. *Astrophys. J.*, 188:657–665, 1974.

[76] Michael Boyle, Duncan A. Brown, Lawrence E. Kidder, Abdul H. Mroue, Harald P. Pfeiffer, Mark A. Scheel, Gregory B. Cook, and Saul A. Teukolsky. High-accuracy comparison of numerical relativity simulations with post-Newtonian expansions. *Phys. Rev. D*, 76:124038, 2007.

[77] Richard Brito, Vitor Cardoso, Carlos A. R. Herdeiro, and Eugen Radu. Proca stars: Gravitating Bose–Einstein condensates of massive spin 1 particles. *Phys. Lett. B*, 752:291–295, 2016.

[78] Richard Brito, Vitor Cardoso, and Paolo Pani. Massive spin-2 fields on black hole spacetimes: Instability of the Schwarzschild and Kerr solutions and bounds on the graviton mass. *Phys. Rev. D*, 88(2):023514, 2013.

[79] Richard Brito, Vitor Cardoso, and Paolo Pani. Black holes as particle detectors: evolution of superradiant instabilities. *Class. Quant. Grav.*, 32(13):134001, 2015.

[80] Richard Brito, Vitor Cardoso, and Paolo Pani. Superradiance: New Frontiers in Black Hole Physics. *Lect. Notes Phys.*, 906:pp.1–237, 2015.

[81] Richard Brito, Shrobana Ghosh, Enrico Barausse, Emanuele Berti, Vitor Cardoso, Irina Dvorkin, Antoine Klein, and Paolo Pani. Gravitational wave searches for ultralight bosons with LIGO and LISA. *Phys. Rev. D*, 96(6):064050, 2017.

[82] Richard Brito, Shrobana Ghosh, Enrico Barausse, Emanuele Berti, Vitor Cardoso, Irina Dvorkin, Antoine Klein, and Paolo Pani. Stochastic and resolvable gravitational waves from ultralight bosons. *Phys. Rev. Lett.*, 119(13):131101, 2017.

[83] Richard Brito, Sara Grillo, and Paolo Pani. Black Hole Superradiant Instability from Ultralight Spin-2 Fields. *Phys. Rev. Lett.*, 124(21):211101, 2020.

[84] Hans A. Buchdahl. General Relativistic Fluid Spheres. *Phys. Rev.*, 116:1027, 1959.

[85] Alessandra Buonanno, Lawrence E. Kidder, and Luis Lehner. Estimating the final spin of a binary black hole coalescence. *Phys. Rev. D*, 77:026004, 2008.

[86] Alessandra Buonanno, Lawrence E. Kidder, Abdul H. Mroue, Harald P. Pfeiffer, and Andrea Taracchini. Reducing orbital eccentricity of precessing black-hole binaries. *Phys. Rev. D*, 83:104034, 2011.

[87] David N. Burrows et al. The Swift X-ray Telescope. *Space Sci. Rev.*, 120:165, 2005.

[88] Enrico Cannizzaro, Andrea Caputo, Laura Sberna, and Paolo Pani. Plasma-photon interaction in curved spacetime I: formalism and quasibound states around nonspinning black holes. *Phys. Rev. D*, 103:124018, 2021.

[89] Enrico Cannizzaro, Andrea Caputo, Laura Sberna, and Paolo Pani. Plasma-photon interaction in curved spacetime. II. Collisions, thermal corrections, and superradiant instabilities. *Phys. Rev. D*, 104(10):104048, 2021.

[90] Enrico Cannizzaro, Laura Sberna, Andrea Caputo, and Paolo Pani. Dark photon superradiance quenched by dark matter. *Phys. Rev. D*, 106(8):083019, 2022.

[91] Andrea Caputo, Hongwan Liu, Siddharth Mishra-Sharma, and Joshua T. Ruderman. Dark Photon Oscillations in Our Inhomogeneous Universe. *Phys. Rev. Lett.*, 125(22):221303, 2020.

[92] Andrea Caputo, Samuel J. Witte, Diego Blas, and Paolo Pani. Electromagnetic signatures of dark photon superradiance. *Phys. Rev. D*, 104(4):043006, 2021.

[93] Vitor Cardoso, Óscar J. C. Dias, Gavin S. Hartnett, Matthew Middleton, Paolo Pani, and Jorge E. Santos. Constraining the mass of dark photons and axion-like particles through black-hole superradiance. *JCAP*, 03:043, 2018.

[94] Vitor Cardoso, Edgardo Franzin, and Paolo Pani. Is the gravitational-wave ringdown a probe of the event horizon? *Phys. Rev. Lett.*, 116(17):171101, 2016. [Erratum: Phys.Rev.Lett. 117, 089902 (2016)].

[95] Vitor Cardoso, Wen-Di Guo, Caio F. B. Macedo, and Paolo Pani. The tune of the Universe: the role of plasma in tests of strong-field gravity. *Mon. Not. Roy. Astron. Soc.*, 503(1):563–573, 2021.

[96] Vitor Cardoso, Seth Hopper, Caio F. B. Macedo, Carlos Palenzuela, and Paolo Pani. Gravitational-wave signatures of exotic compact objects and of quantum corrections at the horizon scale. *Phys. Rev. D*, 94(8):084031, 2016.

[97] Vitor Cardoso and Paolo Pani. Testing the nature of dark compact objects: a status report. *Living Rev. Rel.*, 22(1):4, 2019.

[98] Federico Carrasco, Carlos Palenzuela, and Oscar Reula. Pulsar magnetospheres in General Relativity. *Phys. Rev. D*, 98(2):023010, 2018.

[99] Kutay A. Çokluk, Kadri Yakut, and Bruno Giacomazzo. General Relativistic Simulations of High-Mass Binary Neutron Star Mergers: rapid formation of low-mass stellar black holes. 1 2023.

[100] Benoît Cerutti, Alexander Philippov, Kyle Parfrey, and Anatoly Spitkovsky. Particle acceleration in axisymmetric pulsar current sheets. *Mon. Not. Roy. Astron. Soc.*, 448(1):606–619, 2015.

[101] Benoît Cerutti, Alexander A. Philippov, and Anatoly Spitkovsky. Modelling high-energy pulsar light curves from first principles. *Mon. Not. Roy. Astron. Soc.*, 457(3):2401–2414, 2016.

[102] Kelvin H. M. Chan and Otto A. Hannuksela. Extracting ultralight boson properties from boson clouds around post-merger remnants. 9 2022.

[103] Saptarshi Chaudhuri, Peter W. Graham, Kent Irwin, Jeremy Mardon, Surjeet Rajendran, and Yue Zhao. Radio for hidden-photon dark matter detection. *Phys. Rev. D*, 92(7):075012, 2015.

[104] Pisin Chen, William G. Unruh, Chih-Hung Wu, and Dong-Han Yeom. Pre-Hawking radiation cannot prevent the formation of apparent horizon. *Phys. Rev. D*, 97(6):064045, 2018.

[105] CHIME/Pulsar Collaboration. The CHIME Pulsar Project: System Overview. ApJS, 255(1):5, July 2021.

[106] Gongjun Choi, Hong-Jian He, and Enrico D. Schiappacasse. Probing Dynamics of Boson Stars by Fast Radio Bursts and Gravitational Wave Detection. *JCAP*, 10:043, 2019.

[107] Matthew W. Choptuik and Frans Pretorius. Ultra Relativistic Particle Collisions. *Phys. Rev. Lett.*, 104:111101, 2010.

[108] T. L. Cline, U. D. Desai, G. Pizzichini, B. J. Teegarden, W. D. Evans, R. W. Klebesadel, J. G. Laros, K. Hurley, M. Niel, and G. Vedrenne. Detection of a fast, intense and unusual gamma-ray transient. ApJ, 237:L1–L5, April 1980.

[109] Katy Clough. Continuity equations for general matter: applications in numerical relativity. *Class. Quant. Grav.*, 38(16):167001, 2021.

[110] Sidney R. Coleman. The Fate of the False Vacuum. 1. Semiclassical Theory. *Phys. Rev. D*, 15:2929–2936, 1977. [Erratum: Phys.Rev.D 16, 1248(E) (1977)].

[111] Sidney R. Coleman. Q Balls. *Nucl. Phys. B*, 262:263, 1985. [Erratum: Nucl.Phys.B 269, 744 (1986)].

[112] Lucas G. Collodel, Burkhard Kleihaus, and Jutta Kunz. Excited Boson Stars. *Phys. Rev. D*, 96(8):084066, 2017.

[113] Luca Comisso and Lorenzo Sironi. Particle Acceleration in Relativistic Plasma Turbulence. *Phys. Rev. Lett.*, 121(25):255101, 2018.

[114] Ioannis Contopoulos, Demosthenes Kazanas, and Christian Fendt. The axisymmetric pulsar magnetosphere. *The Astrophysical Journal*, 511(1):351, jan 1999.

[115] Maxence Corman and William E. East. Starting inflation from inhomogeneous initial conditions with momentum. 12 2022.

[116] Robin Croft. Local Continuity of Angular Momentum and Noether Charge for Matter in General Relativity. 3 2022.

[117] Robin Croft, Thomas Helfer, Bo-Xuan Ge, Miren Radia, Tamara Evstafyeva, Eugene A. Lim, Ulrich Sperhake, and Katy Clough. The Gravitational Afterglow of Boson Stars. 7 2022.

[118] P. Cunha, C. Herdeiro, E. Radu, and Ya. Shnir. Two boson stars in equilibrium. 10 2022.

[119] Curt Cutler. Angular resolution of the LISA gravitational wave detector. *Phys. Rev. D*, 57:7089–7102, 1998.

[120] S. D'Antonio et al. Semicoherent analysis method to search for continuous gravitational waves emitted by ultralight boson clouds around spinning black holes. *Phys. Rev. D*, 98(10):103017, 2018.

[121] Justin R. David, Gautam Mandal, and Spenta R. Wadia. Microscopic formulation of black holes in string theory. *Phys. Rept.*, 369:549–686, 2002.

[122] Sacha Davidson and Thomas Schwetz. Rotating Drops of Axion Dark Matter. *Phys. Rev. D*, 93(12):123509, 2016.

[123] S. de Wet et al. GW190814 follow-up with the optical telescope MeerLICHT. *Astron. Astrophys.*, 649:A72, 2021.

[124] A. Dedner, F. Kemm, D. Kröner, C. D. Munz, T. Schnitzer, and M. Wesenberg. Hyperbolic Divergence Cleaning for the MHD Equations. *Journal of Computational Physics*, 175(2):645–673, January 2002.

[125] Adolfo del Campo and Wojciech H. Zurek. Universality of phase transition dynamics: Topological Defects from Symmetry Breaking. *Int. J. Mod. Phys. A*, 29(8):1430018, 2014.

[126] Maksym Deliyergiyev, Antonino Del Popolo, Laura Tolos, Morgan Le Delliou, Xiguo Lee, and Fiorella Burgio. Dark compact objects: an extensive overview. *Phys. Rev. D*, 99(6):063015, 2019.

[127] Vladimir Dergachev and Maria Alessandra Papa. Sensitivity improvements in the search for periodic gravitational waves using O1 LIGO data. *Phys. Rev. Lett.*, 123(10):101101, 2019.

[128] Steven L. Detweiler. KLEIN-GORDON EQUATION AND ROTATING BLACK HOLES. *Phys. Rev. D*, 22:2323–2326, 1980.

[129] F. Di Giovanni, N. Sanchis-Gual, P. Cerdá-Durán, M. Zilhão, C. Herdeiro, J.A. Font, and E. Radu. On the dynamical bar-mode instability in spinning bosonic stars. 10 2020.

[130] Fabrizio Di Giovanni, Saeed Fakhry, Nicolas Sanchis-Gual, Juan Carlos Degollado, and José A. Font. Dynamical formation and stability of fermion-boson stars. 6 2020.

[131] Tim Dietrich, Serguei Ossokine, and Katy Clough. Full 3D numerical relativity simulations of neutron star–boson star collisions with BAM. *Class. Quant. Grav.*, 36(2):025002, 2019.

[132] Michael Dine and Willy Fischler. The Not So Harmless Axion. *Phys. Lett. B*, 120:137–141, 1983.

[133] A. S. Dmitriev, D. G. Levkov, A. G. Panin, E. K. Pushnaya, and I. I. Tkachev. Instability of rotating Bose stars. *Phys. Rev. D*, 104(2):023504, 2021.

[134] D. Dobie et al. A comprehensive search for the radio counterpart of GW190814 with the Australian Square Kilometre Array Pathfinder. *Mon. Not. Roy. Astron. Soc.*, 510(3):3794–3805, 2022.

[135] Dougal Dobie et al. An ASKAP Search for a Radio Counterpart to the First High-significance Neutron Star–Black Hole Merger LIGO/Virgo S190814bv. *Astrophys. J. Lett.*, 887(1):L13, 2019.

[136] Sam R. Dolan. Instability of the massive Klein-Gordon field on the Kerr spacetime. *Phys. Rev. D*, 76:084001, 2007.

[137] Sam R. Dolan. Instability of the Proca field on Kerr spacetime. *Phys. Rev.*, D98(10):104006, 2018.

[138] Sergei Dubovsky and Guzmán Hernández-Chifflet. Heating up the Galaxy with Hidden Photons. *JCAP*, 12:054, 2015.

[139] Gerald V. Dunne, Holger Gies, and Ralf Schutzhold. Catalysis of Schwinger Vacuum Pair Production. *Phys. Rev. D*, 80:111301(R), 2009.

[140] P. Démoulin. Extending the concept of separatrices to qsls for magnetic reconnection. *Advances in Space Research*, 37(7):1269–1282, 2006. Reconnection at Sun and in Magnetospheres.

[141] William E. East. Superradiant instability of massive vector fields around spinning black holes in the relativistic regime. *Phys. Rev.*, D96(2):024004, 2017.

[142] William E. East. Massive Boson Superradiant Instability of Black Holes: Nonlinear Growth, Saturation, and Gravitational Radiation. *Phys. Rev. Lett.*, 121(13):131104, 2018.

[143] William E. East. Vortex String Formation in Black Hole Superradiance of a Dark Photon with the Higgs Mechanism. *Phys. Rev. Lett.*, 129(14):141103, 2022.

[144] William E. East and Junwu Huang. Dark photon vortex formation and dynamics. 6 2022.

[145] William E. East and Frans Pretorius. Superradiant Instability and Backreaction of Massive Vector Fields around Kerr Black Holes. *Phys. Rev. Lett.*, 119(4):041101, 2017.

[146] William E. East, Frans Pretorius, and Branson C. Stephens. Hydrodynamics in full general relativity with conservative AMR. *Phys. Rev. D*, 85:124010, 2012.

[147] William E. East, Fethi M. Ramazanoglu, and Frans Pretorius. Conformal Thin-Sandwich Solver for Generic Initial Data. *Phys. Rev. D*, 86:104053, 2012.

[148] William E. East and Huan Yang. Magnetosphere of a spinning black hole and the role of the current sheet. *Phys. Rev. D*, 98(2):023008, 2018.

[149] William E. East, Jonathan Zrake, Yajie Yuan, and Roger D. Blandford. Spontaneous decay of periodic magnetostatic equilibria. *Phys. Rev. Lett.*, 115(9):095002, 2015.

[150] Carl Eckart. The thermodynamics of irreversible processes. iii. relativistic theory of the simple fluid. *Physical review*, 58(10):919, 1940.

[151] Thomas Erber. High-energy electromagnetic conversion processes in intense magnetic fields. *Rev. Mod. Phys.*, 38:626–659, 1966.

[152] Rouven Essig et al. Working Group Report: New Light Weakly Coupled Particles. In *Community Summer Study 2013: Snowmass on the Mississippi*, 10 2013.

[153] Tamara Evstafyeva, Ulrich Sperhake, Thomas Helfer, Robin Croft, Miren Radia, Bo-Xuan Ge, and Eugene A. Lim. Unequal-mass boson-star binaries: Initial data and merger dynamics. 12 2022.

[154] D. J. Fixsen, E. S. Cheng, J. M. Gales, John C. Mather, R. A. Shafer, and E. L. Wright. The Cosmic Microwave Background spectrum from the full COBE FIRAS data set. *Astrophys. J.*, 473:576, 1996.

[155] Jose A. Font. Numerical Hydrodynamics and Magnetohydrodynamics in General Relativity. *Living Rev. Rel.*, 11:7, 2008.

[156] P. C. Freire. Pulsars in globular clusters. *Pulsars in globular clusters*, 2008.

[157] P. C. C. Freire et al. Long-term observations of the pulsars in 47 Tucanae – II. Proper motions, accelerations and jerks. *Mon. Not. Roy. Astron. Soc.*, 471(1):857–876, 2017.

[158] R. Friedberg, T. D. Lee, and A. Sirlin. A Class of Scalar-Field Soliton Solutions in Three Space Dimensions. *Phys. Rev. D*, 13:2739–2761, 1976.

[159] R. Friedberg, T.D. Lee, and Y. Pang. Scalar Soliton Stars and Black Holes. *Phys. Rev. D*, 35:3658, 1987.

[160] John L. Friedman. Ergosphere instability. *Comm. Math. Phys.*, 63(3):243–255, 1978.

[161] Valeri P. Frolov, Pavel Krtous, David Kubiznak, and Jorge E. Santos. Massive Vector Fields in Rotating Black-Hole Spacetimes: Separability and Quasinormal Modes. *Phys. Rev. Lett.*, 120:231103, 2018.

[162] Hajime Fukuda and Kazunori Nakayama. Aspects of Nonlinear Effect on Black Hole Superradiance. *JHEP*, 01:128, 2020.

[163] R. Genzel, A. Eckart, T. Ott, and F. Eisenhauer. On the nature of the dark mass in the centre of the Milky Way. *MNRAS*, 291(1):219–234, October 1997.

[164] Romain Gervalle. Chains of rotating boson stars. *Phys. Rev. D*, 105(12):124052, 2022.

[165] A.M. Ghez, B.L. Klein, M. Morris, and E.E. Becklin. High proper motion stars in the vicinity of Sgr A*: Evidence for a supermassive black hole at the center of our galaxy. *Astrophys. J.*, 509:678–686, 1998.

[166] Shrobana Ghosh, Emanuele Berti, Richard Brito, and Mauricio Richartz. Follow-up signals from superradiant instabilities of black hole merger remnants. *Phys. Rev. D*, 99(10):104030, 2019.

[167] Gian F. Giudice, Matthew McCullough, and Alfredo Urbano. Hunting for Dark Particles with Gravitational Waves. *JCAP*, 10:001, 2016.

[168] Marcelo Gleiser. Stability of Boson Stars. *Phys. Rev. D*, 38:2376, 1988. [Erratum: Phys.Rev.D 39, 1257 (1989)].

[169] Marcelo Gleiser and Richard Watkins. Gravitational Stability of Scalar Matter. *Nucl. Phys. B*, 319:733–746, 1989.

[170] I. Goldman and S. Nussinov. Weakly Interacting Massive Particles and Neutron Stars. *Phys. Rev. D*, 40:3221–3230, 1989.

[171] Peter Goldreich and William H. Julian. Pulsar Electrodynamics. ApJ, 157:869, August 1969.

[172] Mark Goodsell, Joerg Jaeckel, Javier Redondo, and Andreas Ringwald. Naturally Light Hidden Photons in LARGE Volume String Compactifications. *JHEP*, 11:027, 2009.

[173] Andrew Gould, Bruce T. Draine, Roger W. Romani, and Shmuel Nussinov. Neutron Stars: Graveyard of Charged Dark Matter. *Phys. Lett. B*, 238:337–343, 1990.

[174] K. Gourdji, A. Rowlinson, R. A. M. J. Wijers, J. W. Broderick, A. Shulevski, and P. G. Jonker. Searching for low radio-frequency gravitational wave counterparts in wide-field LOFAR data. *Mon. Not. Roy. Astron. Soc.*, 509(4):5018–5029, 2021.

[175] Eric Gourgoulhon. 3+1 formalism and bases of numerical relativity. 3 2007.

[176] Eric Gourgoulhon, Philippe Grandclement, and Silvano Bonazzola. Binary black holes in circular orbits. 1. A Global space-time approach. *Phys. Rev. D*, 65:044020, 2002.

[177] Peter W. Graham and Sunghoon Jung. Localizing Gravitational Wave Sources with Single-Baseline Atom Interferometers. *Phys. Rev. D*, 97(2):024052, 2018.

[178] Peter W. Graham, Jeremy Mardon, and Surjeet Rajendran. Vector Dark Matter from Inflationary Fluctuations. *Phys. Rev. D*, 93(10):103520, 2016.

[179] Giovanni Grilli di Cortona, Edward Hardy, Javier Pardo Vega, and Giovanni Villadoro. The QCD axion, precisely. *JHEP*, 01:034, 2016.

[180] Andrei Gruzinov. Dissipative Strong-Field Electrodynamics. 10 2007.

[181] Andrei Gruzinov. Strong-Field Electrodynamics. 2 2008.

[182] Andrei Gruzinov. Black Hole Spindown by Light Bosons. 4 2016.

[183] Davide Guerra, Caio F.B. Macedo, and Paolo Pani. Axion boson stars. *JCAP*, 09:061, 2019.

[184] Fan Guo, Hui Li, William Daughton, and Yi-Hsin Liu. Formation of Hard Power-laws in the Energetic Particle Spectra Resulting from Relativistic Magnetic Reconnection. *Phys. Rev. Lett.*, 113:155005, 2014.

[185] F.S. Guzman and J.M. Rueda-Becerril. Spherical boson stars as black hole mimickers. *Phys. Rev. D*, 80:084023, 2009.

[186] F.Siddhartha Guzman. Evolving spherical boson stars on a 3-D Cartesian grid. *Phys. Rev. D*, 70:044033, 2004.

[187] Thomas Helfer, Eugene A. Lim, Marcos A. G. Garcia, and Mustafa A. Amin. Gravitational Wave Emission from Collisions of Compact Scalar Solitons. *Phys. Rev. D*, 99(4):044046, 2019.

[188] Thomas Helfer, David J. E. Marsh, Katy Clough, Malcolm Fairbairn, Eugene A. Lim, and Ricardo Becerril. Black hole formation from axion stars. *JCAP*, 03:055, 2017.

[189] Thomas Helfer, Ulrich Sperhake, Robin Croft, Miren Radia, Bo-Xuan Ge, and Eugene A. Lim. Malaise and remedy of binary boson-star initial data. 8 2021.

[190] A.B. Henriques, Andrew R. Liddle, and R.G. Moorhouse. COMBINED BOSON - FERMION STARS. *Phys. Lett. B*, 233:99, 1989.

[191] A.B. Henriques, Andrew R. Liddle, and R.G. Moorhouse. Combined Boson - Fermion Stars: Configurations and Stability. *Nucl. Phys. B*, 337:737–761, 1990.

[192] Bruno M. B. Henriques, Simon White, Peter Thomas, Raul Angulo, Qi Guo, Gerard Lemson, Volker Springel, and Roderik Overzier. Galaxy formation in the Planck cosmology – I. Matching the observed evolution of star formation rates, colours and stellar masses. *Mon. Not. Roy. Astron. Soc.*, 451(3):2663–2680, 2015.

[193] C. Herdeiro, I. Perapechka, E. Radu, and Ya. Shnir. Asymptotically flat spinning scalar, Dirac and Proca stars. *Phys. Lett. B*, 797:134845, 2019.

[194] C. A. R. Herdeiro, J. Kunz, I. Perapechka, E. Radu, and Y. Shnir. Chains of Boson Stars. *Phys. Rev. D*, 103(6):065009, 2021.

[195] Carlos Herdeiro and Eugen Radu. Construction and physical properties of Kerr black holes with scalar hair. *Classical and Quantum Gravity*, 32(14):144001, July 2015.

[196] L. Herrera, A. Di Prisco, J. Martin, J. Ospino, N.O. Santos, and O. Troconis. Spherically symmetric dissipative anisotropic fluids: A General study. *Phys. Rev. D*, 69:084026, 2004.

[197] Mark P. Hertzberg and Enrico D. Schiappacasse. Scalar dark matter clumps with angular momentum. *JCAP*, 08:028, 2018.

[198] J Jeff Hester. The crab nebula: an astrophysical chimera. *Annu. Rev. Astron. Astrophys.*, 46:127–155, 2008.

[199] Bob Holdom. Two U(1)'s and Epsilon Charge Shifts. *Phys. Lett. B*, 166:196–198, 1986.

[200] Anson Hook and Junwu Huang. Probing axions with neutron star inspirals and other stellar processes. *JHEP*, 06:036, 2018.

[201] Wayne Hu, Rennan Barkana, and Andrei Gruzinov. Cold and fuzzy dark matter. *Phys. Rev. Lett.*, 85:1158–1161, 2000.

[202] Junwu Huang, Matthew C. Johnson, Laura Sagunski, Mairi Sakellariadou, and Jun Zhang. Prospects for axion searches with Advanced LIGO through binary mergers. *Phys. Rev. D*, 99(6):063013, 2019.

[203] Junwu Huang, Geoffrey Ryan, and Nils Siemonsen. in preparation.

[204] Lam Hui. Wave Dark Matter. *Ann. Rev. Astron. Astrophys.*, 59:247–289, 2021.

[205] Lam Hui, Jeremiah P. Ostriker, Scott Tremaine, and Edward Witten. Ultralight scalars as cosmological dark matter. *Phys. Rev. D*, 95(4):043541, 2017.

[206] Maximiliano Isi, Ling Sun, Richard Brito, and Andrew Melatos. Directed searches for gravitational waves from ultralight bosons. *Phys. Rev.*, D99(8):084042, 2019.

[207] David Izquierdo-Villalba, Silvia Bonoli, Massimo Dotti, Alberto Sesana, Yetli Rosas-Guevara, and Daniele Spinoso. From galactic nuclei to the halo outskirts: tracing supermassive black holes across cosmic history and environments. *MNRAS*, 495(4):4681–4706, July 2020.

[208] Amruta Jaodand et al. LIGO/Virgo S190814bv: Chandra X-ray non-detection of ASKAP J005547-270433 / AT2019osy. *GRB Coordinates Network*, 25822:1, September 2019.

[209] Dana Jones, Ling Sun, Nils Siemonsen, William E. East, Susan M. Scott, and Karl Wette. Methods and prospects for gravitational wave searches targeting ultralight vector boson clouds around known black holes. 4 2023.

[210] Daniel Kagan, Lorenzo Sironi, Benoit Cerutti, and Dimitrios Giannios. Relativistic magnetic reconnection in pair plasmas and its astrophysical applications. *Space Sci. Rev.*, 191(1-4):545–573, 2015.

[211] Ben Kain and Hong Y. Ling. Vortices in Bose-Einstein Condensate Dark Matter. *Phys. Rev. D*, 82:064042, 2010.

[212] Constantinos Kalapotharakos, Gabriele Brambilla, Andrey Timokhin, Alice K. Harding, and Demosthenes Kazanas. Three-dimensional Kinetic Pulsar Magnetosphere Models: Connecting to Gamma-Ray Observations. *Astrophys. J.*, 857(1):44, 2018.

[213] Constantinos Kalapotharakos, Ioannis Contopoulos, and Demos Kazanas. The extended pulsar magnetosphere. MNRAS, 420(4):2793–2798, March 2012.

[214] Victoria M. Kaspi and Andrei Beloborodov. Magnetars. *Ann. Rev. Astron. Astrophys.*, 55:261–301, 2017.

[215] David J. Kaup. Klein-Gordon Geon. *Phys. Rev.*, 172:1331–1342, 1968.

[216] Joe Keir. Slowly decaying waves on spherically symmetric spacetimes and ultracompact neutron stars. *Class. Quant. Grav.*, 33(13):135009, 2016.

[217] Michael Kesden, Jonathan Gair, and Marc Kamionkowski. Gravitational-wave signature of an inspiral into a supermassive horizonless object. *Phys. Rev. D*, 71:044015, 2005.

[218] T. W. B. Kibble. Topology of Cosmic Domains and Strings. *J. Phys. A*, 9:1387–1398, 1976.

[219] Charles D. Kilpatrick et al. The Gravity Collective: A Search for the Electromagnetic Counterpart to the Neutron Star–Black Hole Merger GW190814. *Astrophys. J.*, 923(2):258, 2021.

[220] Burkhard Kleihaus, Jutta Kunz, and Meike List. Rotating boson stars and Q-balls. *Phys. Rev. D*, 72:064002, 2005.

[221] Burkhard Kleihaus, Jutta Kunz, Meike List, and Isabell Schaffer. Rotating Boson Stars and Q-Balls. II. Negative Parity and Ergoregions. *Phys. Rev. D*, 77:064025, 2008.

[222] Burkhard Kleihaus, Jutta Kunz, and Stefanie Schneider. Stable Phases of Boson Stars. *Phys. Rev. D*, 85:024045, 2012.

[223] Felix Kling, Arvind Rajaraman, and Freida Liz Rivera. New solutions for rotating boson stars. *Phys. Rev. D*, 103(7):075020, 2021.

[224] Y. Kobayashi, M. Kasai, and T. Futamase. Does a boson star rotate? *Phys. Rev. D*, 50:7721–7724, 1994.

[225] S. S. Komissarov. On the properties of time dependent, force-free, degenerate electrodynamics. *Mon. Not. Roy. Astron. Soc.*, 336:759, 2002.

[226] S. S. Komissarov. Electrodynamics of black hole magnetospheres. *Mon. Not. Roy. Astron. Soc.*, 350:407, 2004.

[227] S. S. Komissarov. Simulations of axisymmetric magnetospheres of neutron stars. *Mon. Not. Roy. Astron. Soc.*, 367:19–31, 2006.

[228] Joel Koplik and Herbert Levine. Vortex reconnection in superfluid helium. *Phys. Rev. Lett.*, 71:1375–1378, Aug 1993.

[229] Pavel Krtouš, Valeri P. Frolov, and David Kubizňák. Separation of Maxwell equations in Kerr–NUT–(A)dS spacetimes. *Nucl. Phys.*, B934:7–38, 2018.

[230] Fjodor V. Kusmartsev, Eckehard W. Mielke, and Franz E. Schunck. Gravitational stability of boson stars. *Phys. Rev. D*, 43:3895–3901, 1991.

[231] Michael LaHaye, Huan Yang, Béatrice Bonga, and Zhenwei Lyu. Efficient fully precessing gravitational waveforms for binaries with neutron stars. 12 2022.

[232] Chi-Wai Lai. A Numerical study of boson stars. Other thesis, 9 2004.

[233] E. W. Leaver. An Analytic representation for the quasi normal modes of Kerr black holes. *Proc. Roy. Soc. Lond. A*, 402:285–298, 1985.

[234] T.D. Lee and Yang Pang. Stability of Mini - Boson Stars. *Nucl. Phys. B*, 315:477, 1989.

[235] Patricio S. Letelier. Anisotropic fluids with two-perfect-fluid components. *Phys. Rev. D*, 22(4):807, 1980.

[236] S.C. Leung, M.C. Chu, and L.M. Lin. Dark-matter admixed neutron stars. *Phys. Rev. D*, 84:107301, 2011.

[237] Bohua Li, Tanja Rindler-Daller, and Paul R. Shapiro. Cosmological Constraints on Bose-Einstein-Condensed Scalar Field Dark Matter. *Phys. Rev. D*, 89(8):083536, 2014.

[238] Jason Li, Anatoly Spitkovsky, and Alexander Tchekhovskoy. Resistive Solutions for Pulsar Magnetospheres. *Astrophys. J.*, 746:60, 2012.

[239] Li-Xin Li, Erik R. Zimmerman, Ramesh Narayan, and Jeffrey E. McClintock. Multi-temperature blackbody spectrum of a thin accretion disk around a Kerr black hole: Model computations and comparison with observations. *Astrophys. J. Suppl.*, 157:335–370, 2005.

[240] Ting Li, Eric Priest, and Ruilong Guo. Three-dimensional magnetic reconnection in astrophysical plasmas. *Proceedings of the Royal Society of London Series A*, 477(2249):20200949, May 2021.

[241] Steven L. Liebling and Carlos Palenzuela. Dynamical Boson Stars. *Living Rev. Rel.*, 20(1):5, 2017.

[242] Lee Lindblom and Bela Szilagyi. An Improved Gauge Driver for the GH Einstein System. *Phys. Rev.*, D80:084019, 2009.

[243] Oleg Lunin. Maxwell's equations in the Myers-Perry geometry. *JHEP*, 12:138, 2017.

[244] Ryan S. Lynch, Scott M. Ransom, Paulo C. C. Freire, and Ingrid H. Stairs. Six New Recycled Globular Cluster Pulsars Discovered with the Green Bank Telescope. ApJ, 734(2):89, June 2011.

[245] Maxim Lyutikov. Explosive reconnection in magnetars. *Mon. Not. Roy. Astron. Soc.*, 346:540, 2003.

[246] Caio F.B. Macedo, Paolo Pani, Vitor Cardoso, and Luís C. B. Crispino. Astrophysical signatures of boson stars: quasinormal modes and inspiral resonances. *Phys. Rev. D*, 88(6):064046, 2013.

[247] J. F. Mahlmann, M. A. Aloy, V. Mewes, and P. Cerdá-Durán. Computational General Relativistic Force-Free Electrodynamics: II. Characterization of Numerical Diffusivity. *Astron. Astrophys.*, 647:A58, 2021.

[248] J. F. Mahlmann, A. A. Philippov, A. Levinson, A. Spitkovsky, and H. Hakobyan. Electromagnetic fireworks: Fast radio bursts from rapid reconnection in the compressed magnetar wind. *Astrophys. J. Lett.*, 932:L20, 2022.

[249] R N Manchester, G B Hobbs, A Teoh, and M Hobbs. The Australia Telescope National Facility pulsar catalogue. *Astron. J.*, 129:1993, 2005.

[250] Pedro Marronetti, Mijan Huq, Pablo Laguna, Luis Lehner, Richard A. Matzner, and Deirdre Shoemaker. Approximate analytical solutions to the initial data problem of black hole binary systems. *Phys. Rev. D*, 62:024017, 2000.

[251] Pedro Marronetti and Richard A. Matzner. Solving the initial value problem of two black holes. *Phys. Rev. Lett.*, 85:5500–5503, 2000.

[252] Anubhav Mathur, Surjeet Rajendran, and Erwin H. Tanin. Clockwork mechanism to remove superradiance limits. *Phys. Rev. D*, 102(5):055015, 2020.

[253] Taillte May, Nils Siemonsen, and William E. East. in prep.

[254] Giovanni Mazzolari, Matteo Bonetti, Alberto Sesana, Riccardo M. Colombo, Massimo Dotti, Giuseppe Lodato, and David Izquierdo-Villalba. Extreme Mass Ratio Inspirals triggered by Massive Black Hole Binaries: from Relativistic Dynamics to Cosmological Rates. 4 2022.

[255] Jeffrey E. McClintock, Ramesh Narayan, and James F. Steiner. Black Hole Spin via Continuum Fitting and the Role of Spin in Powering Transient Jets. *Space Sci. Rev.*, 183:295–322, 2014.

[256] Viraf M. Mehta, Mehmet Demirtas, Cody Long, David J. E. Marsh, Liam Mcallister, and Matthew J. Stott. Superradiance Exclusions in the Landscape of Type IIB String Theory. 11 2020.

[257] David L Meier. Ohm's law in the fast lane: general relativistic charge dynamics. *The Astrophysical Journal*, 605(1):340, 2004.

[258] Peter Mészáros. *High-energy radiation from magnetized neutron stars*. University of Chicago press, 1992.

[259] Brian D. Metzger, Ben Margalit, and Lorenzo Sironi. Fast radio bursts as synchrotron maser emission from decelerating relativistic blast waves. *Mon. Not. Roy. Astron. Soc.*, 485(3):4091–4106, 2019.

[260] Miroslav Micic, Kelly Holley-Bockelmann, Steinn Sigurdsson, and Tom Abel. Supermassive Black Hole Growth and Merger Rates from Cosmological N-body Simulations. *Mon. Not. Roy. Astron. Soc.*, 380:1533, 2007.

[261] C. W. Misner. Interpretation of Gravitational-Wave Observations. *Physical Review Letters*, 28:994, 1972.

[262] A. Monin and M. B. Voloshin. Semiclassical Calculation of Photon-Stimulated Schwinger Pair Creation. *Phys. Rev. D*, 81:085014, 2010.

[263] V. Morello et al. The High Time Resolution Universe survey – XIV. Discovery of 23 pulsars through GPU-accelerated reprocessing. *Mon. Not. Roy. Astron. Soc.*, 483(3):3673–3685, 2019.

[264] Georgios Moschidis. A Proof of Friedman's Ergosphere Instability for Scalar Waves. *Commun. Math. Phys.*, 358(2):437–520, 2018.

[265] Elias R. Most and Alexander A. Philippov. Electromagnetic precursors to gravitational wave events: Numerical simulations of flaring in pre-merger binary neutron star magnetospheres. *Astrophys. J. Lett.*, 893(1):L6, 2020.

[266] Abdul H. Mroue, Harald P. Pfeiffer, Lawrence E. Kidder, and Saul A. Teukolsky. Measuring orbital eccentricity and periastron advance in quasi-circular black hole simulations. *Phys. Rev. D*, 82:124016, 2010.

[267] Robert C. Myers. Pure states don't wear black. *Gen. Rel. Grav.*, 29:1217–1222, 1997.

[268] Rendong Nan, Di Li, Chengjin Jin, Qiming Wang, Lichun Zhu, Wenbai Zhu, Haiyan Zhang, Youling Yue, and Lei Qian. The Five-Hundred-Meter Aperture Spherical Radio Telescope (FAST) Project. *Int. J. Mod. Phys. D*, 20:989–1024, 2011.

[269] Gaurav Narain, Jurgen Schaffner-Bielich, and Igor N. Mishustin. Compact stars made of fermionic dark matter. *Phys. Rev. D*, 74:063003, 2006.

[270] Antonios Nathanail, Christian M. Fromm, Oliver Porth, Hector Olivares, Ziri Younsi, Yosuke Mizuno, and Luciano Rezzolla. Plasmoid formation in global GRMHD simulations and AGN flares. *Mon. Not. Roy. Astron. Soc.*, 495(2):1549–1565, 2020.

[271] Ann E. Nelson and Jakub Scholtz. Dark Light, Dark Matter and the Misalignment Mechanism. *Phys. Rev. D*, 84:103501, 2011.

[272] Ken K. Y. Ng, Otto A. Hannuksela, Salvatore Vitale, and Tjonnie G. F. Li. Searching for ultralight bosons within spin measurements of a population of binary black hole mergers. *Phys. Rev. D*, 103(6):063010, 2021.

[273] Ken K. Y. Ng, Salvatore Vitale, Otto A. Hannuksela, and Tjonnie G. F. Li. Constraints on Ultralight Scalar Bosons within Black Hole Spin Measurements from the LIGO-Virgo GWTC-2. *Phys. Rev. Lett.*, 126(15):151102, 2021.

[274] Y. O. Nikolaieva, Y. M. Bidasyuk, K. Korshynska, E. V. Gorbar, Junji Jia, and A. I. Yakimenko. Stable vortex structures in colliding self-gravitating Bose-Einstein condensates. 12 2022.

[275] Kenichi Nishikawa, Ioana Dutan, Christoph Koehn, and Yosuke Mizuno. PIC methods in astrophysics: Simulations of relativistic jets and kinetic physics in astrophysical systems. *Liv. Rev. Comput. Astrophys.*, 7:1, 2021.

[276] L. B. Okun. LIMITS OF ELECTRODYNAMICS: PARAPHOTONS? *Sov. Phys. JETP*, 56:502, 1982.

[277] Hector Olivares, Ziri Younsi, Christian M. Fromm, Mariafelicia De Laurentis, Oliver Porth, Yosuke Mizuno, Heino Falcke, Michael Kramer, and Luciano Rezzolla. How to tell an accreting boson star from a black hole. *Mon. Not. Roy. Astron. Soc.*, 497:521–535, 2020.

[278] Hidetoshi Omiya, Takuya Takahashi, Takahiro Tanaka, and Hirotaka Yoshino. Impact of multiple modes on the evolution of self-interacting axion condensate around rotating black holes. 11 2022.

[279] K. L. Page et al. *Swift*-XRT follow-up of gravitational wave triggers during the third aLIGO/Virgo observing run. *Mon. Not. Roy. Astron. Soc.*, 499(3):3459–3480, 2020.

[280] C. Palenzuela, L. Lehner, and Steven L. Liebling. Orbital Dynamics of Binary Boson Star Systems. *Phys. Rev. D*, 77:044036, 2008.

[281] C. Palenzuela, I. Olabarrieta, L. Lehner, and Steven L. Liebling. Head-on collisions of boson stars. *Phys. Rev. D*, 75:064005, 2007.

[282] Carlos Palenzuela. Modeling magnetized neutron stars using resistive MHD. *Mon. Not. Roy. Astron. Soc.*, 431:1853–1865, 2013.

[283] Carlos Palenzuela, Travis Garrett, Luis Lehner, and Steven L. Liebling. Magnetospheres of Black Hole Systems in Force-Free Plasma. *Phys. Rev. D*, 82:044045, 2010.

[284] Carlos Palenzuela, Luis Lehner, Oscar Reula, and Luciano Rezzolla. Beyond ideal MHD: towards a more realistic modeling of relativistic astrophysical plasmas. *Mon. Not. Roy. Astron. Soc.*, 394:1727–1740, 2009.

[285] Carlos Palenzuela, Paolo Pani, Miguel Bezares, Vitor Cardoso, Luis Lehner, and Steven Liebling. Gravitational Wave Signatures of Highly Compact Boson Star Binaries. *Phys. Rev. D*, 96(10):104058, 2017.

[286] Cristiano Palomba et al. Direct constraints on ultra-light boson mass from searches for continuous gravitational waves. *Phys. Rev. Lett.*, 123:171101, 2019.

[287] Zhichen Pan, Xiaoyun Ma, Lei Qian, Lin Wang, Zhen Yan, Jintao Luo, Scott M. Ransom, Duncan R. Lorimer, and Peng Jiang. Three pulsars discovered by FAST in the globular cluster NGC 6517 with a pulsar candidate sifting code based on dispersion measure to signal-to-noise ratio plots. *Res. Astron. Astrophys.*, 21(6):143, 2021.

[288] Paolo Pani, Vitor Cardoso, Leonardo Gualtieri, Emanuele Berti, and Akihiro Ishibashi. Black hole bombs and photon mass bounds. *Phys. Rev. Lett.*, 109:131102, 2012.

[289] Paolo Pani, Vitor Cardoso, Leonardo Gualtieri, Emanuele Berti, and Akihiro Ishibashi. Perturbations of slowly rotating black holes: massive vector fields in the Kerr metric. *Phys. Rev. D*, 86:104017, 2012.

[290] Kyle Parfrey, Anatoly Spitkovsky, and Andrei M. Beloborodov. Simulations of the magnetospheres of accreting millisecond pulsars. *Mon. Not. Roy. Astron. Soc.*, 469(3):3656–3669, 2017.

[291] Vasileios Paschalidis and Stuart L. Shapiro. A new scheme for matching general relativistic ideal magnetohydrodynamics to its force-free limit. *Phys. Rev. D*, 88(10):104031, 2013.

[292] R. D. Peccei and Helen R. Quinn. CP Conservation in the Presence of Instantons. *Phys. Rev. Lett.*, 38:1440–1443, 1977.

[293] J. Petri. General-relativistic force-free pulsar magnetospheres. *Mon. Not. Roy. Astron. Soc.*, 455(4):3779–3805, 2016.

[294] E. Petroff, J. W. T. Hessels, and D. R. Lorimer. Fast Radio Bursts. *Astron. Astrophys. Rev.*, 27(1):4, 2019.

[295] Harald P. Pfeiffer, Duncan A. Brown, Lawrence E. Kidder, Lee Lindblom, Geoffrey Lovelace, and Mark A. Scheel. Reducing orbital eccentricity in binary black hole simulations. *Class. Quant. Grav.*, 24:S59–S82, 2007.

[296] Harald P. Pfeiffer and Andrew I. MacFadyen. Hyperbolicity of Force-Free Electrodynamics. 7 2013.

[297] Alexander Philippov, Dmitri A. Uzdensky, Anatoly Spitkovsky, and Benoît Cerutti. Pulsar Radio Emission Mechanism: Radio Nanoshots as a Low Frequency Afterglow of Relativistic Magnetic Reconnection. *Astrophys. J. Lett.*, 876(1):L6, 2019.

[298] Alexander A. Philippov and Anatoly Spitkovsky. Ab-Initio Pulsar Magnetosphere: Particle acceleration in Oblique Rotators and High-energy Emission Modeling. *Astrophys. J.*, 855(2):94, 2018.

[299] Alexander A. Philippov, Anatoly Spitkovsky, and Benoit Cerutti. Ab-initio pulsar magnetosphere: three-dimensional particle-in-cell simulations of oblique pulsars. *Astrophys. J. Lett.*, 801(1):L19, 2015.

[300] F. Pintore et al. A new Ultraluminous X-ray source in the galaxy NGC 5907. *Mon. Not. Roy. Astron. Soc.*, 477(1):L90–L95, 2018.

[301] Illya Plotnikov and Lorenzo Sironi. The synchrotron maser emission from relativistic shocks in Fast Radio Bursts: 1D PIC simulations of cold pair plasmas. *Mon. Not. Roy. Astron. Soc.*, 485(3):3816–3833, 2019.

[302] D. I. Pontin. Theory of magnetic reconnection in solar and astrophysical plasmas. *Philosophical Transactions of the Royal Society of London Series A*, 370(1970):3169–3192, July 2012.

[303] D. I. Pontin, A. L. Wilmot-Smith, G. Hornig, and K. Galsgaard. Dynamics of braided coronal loops. II. Cascade to multiple small-scale reconnection events. A&A, 525:A57, January 2011.

[304] P. Predehl. eROSITA on SRG. *Astronomische Nachrichten*, 338(159):159–164, March 2017.

[305] John Preskill, Mark B. Wise, and Frank Wilczek. Cosmology of the Invisible Axion. *Phys. Lett.*, 120B:127–132, 1983.

[306] Frans Pretorius. Numerical relativity using a generalized harmonic decomposition. *Class. Quant. Grav.*, 22:425–452, 2005.

[307] Martti Raidal, Sergey Solodukhin, Ville Vaskonen, and Hardi Veermäe. Light Primordial Exotic Compact Objects as All Dark Matter. *Phys. Rev. D*, 97(12):123520, 2018.

[308] M. J. Reid, J. E. McClintock, J. F. Steiner, D. Steeghs, R. A. Remillard, V. Dhawan, and R. Narayan. A Parallax Distance to the Microquasar GRS 1915+105 and a Revised Estimate of its Black Hole Mass. *Astrophys. J.*, 796:2, 2014.

[309] C. Reisswig, C.D. Ott, E. Abdikamalov, R. Haas, P. Moesta, and E. Schnetter. Formation and Coalescence of Cosmological Supermassive Black Hole Binaries in Supermassive Star Collapse. *Phys. Rev. Lett.*, 111:151101, 2013.

[310] Chongyang Ren and Zhongxiang Wang. Searching for γ-ray Emission from Binary Black-Hole Mergers Detected in LIGO/Virgo O3 Run. *Universe*, 8(10):517, 2022.

[311] A. Ridolfi et al. Eight new millisecond pulsars from the first MeerKAT globular cluster census. *Mon. Not. Roy. Astron. Soc.*, 504(1):1407–1426, 2021.

[312] A. Ridolfi et al. TRAPUM discovery of 13 new pulsars in NGC 1851 using MeerKAT. *Astron. Astrophys.*, 664:A27, 2022.

[313] Tanja Rindler-Daller and Paul R. Shapiro. Angular Momentum and Vortex Formation in Bose-Einstein-Condensed Cold Dark Matter Haloes. *Mon. Not. Roy. Astron. Soc.*, 422:135–161, 2012.

[314] Bart Ripperda, Fabio Bacchini, and Alexander Philippov. Magnetic Reconnection and Hot Spot Formation in Black Hole Accretion Disks. *Astrophys. J.*, 900(2):100, 2020.

[315] Clive Robinson, A. G. Lyne, R. N. Manchester, M. Bailes, N. D'Amico, and S. Johnston. Millisecond pulsars in the globular cluster 47 Tucanae. MNRAS, 274(2):547–554, May 1995.

[316] Victor H. Robles and Tonatiuh Matos. Flat Central Density Profile and Constant DM Surface Density in Galaxies from Scalar Field Dark Matter. *Mon. Not. Roy. Astron. Soc.*, 422:282–289, 2012.

[317] Travis Robson, Neil J. Cornish, and Chang Liu. The construction and use of LISA sensitivity curves. *Class. Quant. Grav.*, 36(10):105011, 2019.

[318] Joao G. Rosa and Sam R. Dolan. Massive vector fields on the Schwarzschild spacetime: quasi-normal modes and bound states. *Phys. Rev. D*, 85:044043, 2012.

[319] Wen-Hong Ruan, Chang Liu, Zong-Kuan Guo, Yue-Liang Wu, and Rong-Gen Cai. The LISA-Taiji network: precision localization of massive black hole binaries. 10 2019.

[320] Remo Ruffini and Silvano Bonazzola. Systems of selfgravitating particles in general relativity and the concept of an equation of state. *Phys. Rev.*, 187:1767–1783, 1969.

[321] Milton Ruiz, Vasileios Paschalidis, and Stuart L. Shapiro. Pulsar spin-down luminosity: Simulations in general relativity. *Phys. Rev. D*, 89(8):084045, 2014.

[322] George B. Rybicki and Alan P. Lightman. *Radiative Processes in Astrophysics*. 1986.

[323] N. Sanchis-Gual, F. Di Giovanni, M. Zilhão, C. Herdeiro, P. Cerdá-Durán, J.A. Font, and E. Radu. Nonlinear Dynamics of Spinning Bosonic Stars: Formation and Stability. *Phys. Rev. Lett.*, 123(22):221101, 2019.

[324] Nicolas Sanchis-Gual, Juan Calderón Bustillo, Carlos Herdeiro, Eugen Radu, José A. Font, Samson H. W. Leong, and Alejandro Torres-Forné. Impact of the wave-like nature of Proca stars on their gravitational-wave emission. 8 2022.

[325] Nicolas Sanchis-Gual, Carlos Herdeiro, José A. Font, Eugen Radu, and Fabrizio Di Giovanni. Head-on collisions and orbital mergers of Proca stars. *Phys. Rev. D*, 99(2):024017, 2019.

[326] Nicolas Sanchis-Gual, Miguel Zilhão, Carlos Herdeiro, Fabrizio Di Giovanni, José A. Font, and Eugen Radu. Synchronised gravitational atoms from mergers of bosonic stars. 7 2020.

[327] Joshua S. Schiffrin and Robert M. Wald. Turning Point Instabilities for Relativistic Stars and Black Holes. *Class. Quant. Grav.*, 31:035024, 2014.

[328] Franz E. Schunck and Diego F. Torres. Boson stars with generic selfinteractions. *Int. J. Mod. Phys. D*, 9:601–618, 2000.

[329] Ralf Schutzhold, Holger Gies, and Gerald Dunne. Dynamically assisted Schwinger mechanism. *Phys. Rev. Lett.*, 101:130404, 2008.

[330] K. W. Schwarz. Three-dimensional vortex dynamics in superfluid ^{4}He: Homogeneous superfluid turbulence. *Phys. Rev. B*, 38:2398–2417, Aug 1988.

[331] Julian S. Schwinger. On gauge invariance and vacuum polarization. *Phys. Rev.*, 82:664–679, 1951.

[332] Edward Seidel and Wai-Mo Suen. Dynamical Evolution of Boson Stars. 1. Perturbing the Ground State. *Phys. Rev. D*, 42:384–403, 1990.

[333] Edward Seidel and Wai-Mo Suen. Formation of solitonic stars through gravitational cooling. *Phys. Rev. Lett.*, 72:2516–2519, 1994.

[334] Srimoyee Sen. Plasma effects on lasing of a uniform ultralight axion condensate. *Phys. Rev. D*, 98(10):103012, 2018.

[335] Noah Sennett, Tanja Hinderer, Jan Steinhoff, Alessandra Buonanno, and Serguei Ossokine. Distinguishing Boson Stars from Black Holes and Neutron Stars from Tidal Interactions in Inspiraling Binary Systems. *Phys. Rev. D*, 96(2):024002, 2017.

[336] Brian C. Seymour, Hang Yu, and Yanbei Chen. Multiband Gravitational Wave Cosmography with Dark Sirens. 8 2022.

[337] Masaru Shibata. A Relativistic formalism for computation of irrotational binary stars in quasiequilibrium states. *Phys. Rev. D*, 58:024012, 1998.

[338] Nils Siemonsen and William E. East. Gravitational wave signatures of ultralight vector bosons from black hole superradiance. *Phys. Rev. D*, 101(2):024019, 2020.

[339] Nils Siemonsen and William E. East. Stability of rotating scalar boson stars with nonlinear interactions. *Phys. Rev. D*, 103(4):044022, 2021.

[340] Nils Siemonsen and William E. East. Binary boson stars: Merger dynamics and formation of rotating remnant stars. *Phys. Rev. D*, 107(12):124018, 2023.

[341] Nils Siemonsen and William E. East. Generic initial data for binary boson stars. 6 2023.

[342] Nils Siemonsen, Taillte May, and William E. East. Modeling the black hole superradiance gravitational waveform. *Phys. Rev. D*, 107(10):104003, 2023.

[343] Nils Siemonsen, Cristina Mondino, Daniel Egana-Ugrinovic, Junwu Huang, Masha Baryakhtar, and William E. East. Dark photon superradiance: Electrodynamics and multimessenger signals. *Phys. Rev. D*, 107(7):075025, 2023.

[344] P. Sikivie and Q. Yang. Bose-Einstein Condensation of Dark Matter Axions. *Phys. Rev. Lett.*, 103:111301, 2009.

[345] Lorenzo Sironi and Anatoly Spitkovsky. Relativistic Reconnection: an Efficient Source of Non-Thermal Particles. *Astrophys. J. Lett.*, 783:L21, 2014.

[346] Rafael Sorkin. A Criterion for the onset of instability at a turning point. *Astrophys. J.*, 249:254–257, 1981.

[347] Anatoly Spitkovsky. Time-dependent force-free pulsar magnetospheres: axisymmetric and oblique rotators. *Astrophys. J. Lett.*, 648:L51–L54, 2006.

[348] A. A. Starobinsky. Amplification of waves reflected from a rotating "black hole". *Sov. Phys. JETP*, 37(1):28–32, 1973.

[349] Leo C. Stein. qnm: A Python package for calculating Kerr quasinormal modes, separation constants, and spherical-spheroidal mixing coefficients. *J. Open Source Softw.*, 4(42):1683, 2019.

[350] Ling Sun, Richard Brito, and Maximiliano Isi. Search for ultralight bosons in Cygnus X-1 with Advanced LIGO. *Phys. Rev. D*, 101(6):063020, 2020. [Erratum: Phys.Rev.D 102, 089902(E) (2020)].

[351] Peter Svrcek and Edward Witten. Axions In String Theory. *JHEP*, 06:051, 2006.

[352] Douglas A. Swartz, Kajal K. Ghosh, Allyn F. Tennant, and Kin-Wah Wu. The Ultraluminous x-ray source population from the Chandra archive of galaxies. *Astrophys. J. Suppl.*, 154:519, 2004.

[353] Takuya Takahashi, Hidetoshi Omiya, and Takahiro Tanaka. Axion cloud evaporation during inspiral of black hole binaries: The effects of backreaction and radiation. *PTEP*, 2022(4):043E01, 2022.

[354] Takuya Takahashi and Takahiro Tanaka. Axion clouds may survive the perturbative tidal interaction over the early inspiral phase of black hole binaries. *JCAP*, 10:031, 2021.

[355] Takashi Tamaki and Nobuyuki Sakai. How does gravity save or kill Q-balls? *Phys. Rev. D*, 83:044027, 2011.

[356] I. M. Ternov, V. R. Khalilov, G. A. Chizhov, and Alex B. Gaina. Finite Movement of Massive Particles in Kerr and Schwarzschild Fields. *Sov. Phys. J.*, 21:1200–1204, 1978. [Izv. Vuz. Fiz.21N9,109(1978)].

[357] Saul A. Teukolsky. Perturbations of a rotating black hole. 1. Fundamental equations for gravitational electromagnetic and neutrino field perturbations. *Astrophys. J.*, 185:635–647, 1973.

[358] Saul A. Teukolsky. Irrotational binary neutron stars in quasiequilibrium in general relativity. *Astrophys. J.*, 504:442, 1998.

[359] A. L. Thakur et al. A search for optical and near-infrared counterparts of the compact binary merger GW190814. *Mon. Not. Roy. Astron. Soc.*, 499(3):3868–3883, 2020. [Erratum: Mon.Not.Roy.Astron.Soc. 501, 2821 (2021)].

[360] M J Thatcher and M J Morgan. Vortex scattering in the abelian higgs model. *Classical and Quantum Gravity*, 14(11):3161–3175, nov 1997.

[361] K. S. Thorne. Multipole Expansions of Gravitational Radiation. *Rev. Mod. Phys.*, 52:299–339, 1980.

[362] Makoto Tsubota, Kenichi Kasamatsu, and Masahito Ueda. Vortex lattice formation in a rotating bose-einstein condensate. *Phys. Rev. A*, 65:023603, Jan 2002.

[363] Leo Tsukada, Richard Brito, William E. East, and Nils Siemonsen. Modeling and searching for a stochastic gravitational-wave background from ultralight vector bosons. *Phys. Rev. D*, 103(8):083005, 2021.

[364] Leo Tsukada, Thomas Callister, Andrew Matas, and Patrick Meyers. First search for a stochastic gravitational-wave background from ultralight bosons. *Phys. Rev.*, D99(10):103015, 2019.

[365] Susana Valdez-Alvarado, Carlos Palenzuela, Daniela Alic, and L.Arturo Ureña-López. Dynamical evolution of fermion-boson stars. *Phys. Rev. D*, 87(8):084040, 2013.

[366] Nicholas Vieira et al. A Deep CFHT Optical Search for a Counterpart to the Possible Neutron Star–Black Hole Merger GW190814. *Astrophys. J.*, 895(2):96, 2020.

[367] W. F. Vinen, Makoto Tsubota, and Akira Mitani. Kelvin-wave cascade on a vortex in superfluid ^{4}He at a very low temperature. *Phys. Rev. Lett.*, 91:135301, Sep 2003.

[368] Matt Visser, Carlos Barcelo, Stefano Liberati, and Sebastiano Sonego. Small, dark, and heavy: But is it a black hole? *PoS*, BHGRS:010, 2008.

[369] Steven Weinberg. A New Light Boson? *Phys. Rev. Lett.*, 40:223–226, 1978.

[370] G. R. Werner, D. A. Uzdensky, M. C. Begelman, B. Cerutti, and K. Nalewajko. Non-thermal particle acceleration in collisionless relativistic electron–proton reconnection. *Mon. Not. Roy. Astron. Soc.*, 473(4):4840–4861, 2018.

[371] G. R. Werner, D. A. Uzdensky, B. Cerutti, K. Nalewajko, and M. C. Begelman. The extent of power-law energy spectra in collisionless relativistic magnetic reconnection in pair plasmas. *Astrophys. J. Lett.*, 816(1):L8, 2016.

[372] Frank Wilczek. Problem of Strong P and T Invariance in the Presence of Instantons. *Phys. Rev. Lett.*, 40:279–282, 1978.

[373] James W. York, Jr. Conformal 'thin sandwich' data for the initial-value problem. *Phys. Rev. Lett.*, 82:1350–1353, 1999.

[374] S. Yoshida, Y. Eriguchi, and T. Futamase. Quasinormal modes of boson stars. *Phys. Rev. D*, 50:6235–6246, 1994.

[375] Shijun Yoshida and Yoshiharu Eriguchi. New static axisymmetric and nonvacuum solutions in general relativity: Equilibrium solutions of boson stars. *Phys. Rev. D*, 55:1994–2001, 1997.

[376] Hirotaka Yoshino and Hideo Kodama. Bosenova collapse of axion cloud around a rotating black hole. *Prog. Theor. Phys.*, 128:153–190, 2012.

[377] Hirotaka Yoshino and Hideo Kodama. Gravitational radiation from an axion cloud around a black hole: Superradiant phase. *PTEP*, 2014:043E02, 2014.

[378] Hirotaka Yoshino and Hideo Kodama. The bosenova and axiverse. *Class. Quant. Grav.*, 32(21):214001, 2015.

[379] R. P. Yu and M. J. Morgan. Vortices in a rotating dark matter condensate. *Class. Quant. Grav.*, 19:L157–L166, 2002.

[380] Ya. B. Zel'Dovich. Generation of Waves by a Rotating Body. *Soviet Journal of Experimental and Theoretical Physics Letters*, 14:180, August 1971.

[381] Bing Zhang. The Physical Mechanisms of Fast Radio Bursts. *Nature*, 587:45–53, 2020.

[382] Jun Zhang, Zhenwei Lyu, Junwu Huang, Matthew C. Johnson, Laura Sagunski, Mairi Sakellariadou, and Huan Yang. First Constraints on Nuclear Coupling of Axionlike Particles from the Binary Neutron Star Gravitational Wave Event GW170817. *Phys. Rev. Lett.*, 127(16):161101, 2021.

[383] Vladimir Zhdankin, Gregory R. Werner, Dmitri A. Uzdensky, and Mitchell C. Begelman. Kinetic Turbulence in Relativistic Plasma: From Thermal Bath to Nonthermal Continuum. *Phys. Rev. Lett.*, 118(5):055103, 2017.

[384] Sylvia J. Zhu, Masha Baryakhtar, Maria Alessandra Papa, Daichi Tsuna, Norita Kawanaka, and Heinz-Bernd Eggenstein. Characterizing the continuous gravitational-wave signal from boson clouds around Galactic isolated black holes. *Phys. Rev. D*, 102(6):063020, 2020.

[385] T. J. M. Zouros and D. M. Eardley. INSTABILITIES OF MASSIVE SCALAR PERTURBATIONS OF A ROTATING BLACK HOLE. *Annals Phys.*, 118:139–155, 1979.

[386] W. H. Zurek. Cosmological Experiments in Superfluid Helium? *Nature*, 317:505–508, 1985.

APPENDICES

Appendix A

Rotating boson star construction and evolution

A.1 Numerical construction of stationary boson stars

Here we provide the details of the numerical methods employed in order to construct stationary BS solutions. We assume an axisymmetric and stationary metric $g_{\mu\nu}$, which can be written in Lewis-Papapetrou coordinates as in Eq. (2.7), where all free functions depend only on the r and θ coordinates. Additionally, we use a harmonic scalar field ansatz $\Phi = e^{i\omega t + im\varphi}\phi$ (note, this differs from (4.1) by $m \to -m$), where ϕ carries the r and θ dependence, that is compatible with the metric ansatz. Plugging these expressions into the Einstein-Klein-Gordon equations, Eq. (2.8), results in a set of five coupled partial differential equations in r and θ. Imposing regularity at the origin, $r = 0$, and asymptotic flatness at $r \to \infty$ provides the boundary conditions for the elliptic set of equations. See, for instance, Ref. [220] for the explicit form of the equations and boundary conditions for the metric ansatz Eq. (2.7) chosen here. Notice a typo in their Eq. (B1): The second to last term should be $-2l(\partial_r f)^2$. Additionally, we find our axisymmetric system of equations to agree if, in the equation for $f(r,\theta)$ (i.e., Eq. (B6) in Ref. [220]):

$$-\frac{1}{2}\partial_\theta f \;\to -\frac{1}{2}\frac{\partial_\theta f \partial_\theta l}{l}, \tag{A.1}$$

$$-2r^2\kappa l U(\phi) \;\to -2r^2\kappa l g U(\phi). \tag{A.2}$$

As mentioned in the main text, we introduce the *auxiliary* functions ω_s and ρ. Following the arguments in Ref. [220], these obey the equations

$$\Delta_g \omega_s = 0, \qquad \Delta_g \rho = j^t/\omega_s, \tag{A.3}$$

where $\Delta_g := g^{ij}\nabla_i\nabla_j$ is the Laplacian associated with the spacetime metric $g_{\mu\nu}$, and j^t is proportional to the charge density defined by the Noether current associated with the global U(1) symmetry. Here we have also promoted the scalar field's frequency ω to the scalar function ω_s, which, however, is fixed to be constant by the Laplace equation (with the appropriate boundary conditions given below). Introducing ω_s and ρ in such a fashion enables us to impose *either* the BS's frequency ω, *or* the total U(1)-Noether charge Q, as boundary conditions at spatial infinity (outlined below). This way, we are able to explore the full parameter space, even, when the family of solutions develops two different branches for a fixed frequency ω or charge Q.

We solve these equations using a relaxation method, which requires a sufficiently good guess for the field configurations. In order to obtain such an initial guess, we begin by exploiting the fact that Eq. (2.3) admits solitonic solutions even in the absence of gravity. In the non-rotating limit, the above set of elliptic partial different equations reduces to a single *ordinary* differential equation for $\phi(r)$. We compactify the radial coordinate to $\bar{r} \in (0,1)$ with $\bar{r} = r/(1+r)$. Given the boundary conditions for ϕ, we use a shooting method, starting at the origin, and integrating outwards to $\bar{r} = 1$, to generate the non-gravitating scalar solitons (known as Q-balls) in the non-relativistic regime (i.e., where $\omega/\mu \approx 1$). We use these Q-ball solutions as the starting point for solving the equations including gravity. In anticipation of the rotating case, we use a Newton-Raphson-type relaxation code with fifth order finite differences to solve for these spherically symmetric BSs. In order to be able to impose either the BS frequency ω/μ, *or* its U(1)-charge Q at $r \to \infty$, we introduce the two equations Eq. (A.3) into the relaxation scheme. The boundary conditions for these auxiliary functions are

$$\partial_r \rho|_{r=0} = 0, \qquad \lim_{r\to\infty} \rho = \rho_\infty, \tag{A.4}$$

where ρ_∞ is arbitrary (we set $\rho_\infty = 1$). We can then impose the BS frequency ω as a boundary condition given

$$\lim_{r\to\infty} \omega_s = \omega, \tag{A.5}$$

or the U(1)-charge by

$$\lim_{r\to\infty} 8\pi r^2 \omega_s \partial_r \rho = Q. \tag{A.6}$$

This follows directly from a volume integration of the ρ-equation in Eq. (A.3). Finally, in both cases $\lim_{r\to 0}\partial_r\omega_s = 0$. Gravity can be incorporated slowly starting from the Q-ball solutions in the non-relativistic limit by increasing κ from 0 incrementally. Depending on the convergence properties of the individual solutions in the relaxation scheme, the step size $\delta\kappa$ must be adjusted. We find that $\delta\kappa = 0.01$ is typically sufficient.

Using these non-rotating BS solutions in the non-relativistic limit as a starting point, the rest of the parameter space can be explored by marching iteratively in the ω/μ direction: We start from a solution with $\omega = \omega_0$, take a sufficiently small step $\omega_1 = \omega_0 - \delta\omega$ (with $\delta\omega > 0$) towards small frequencies, use the solution with ω_0 as an initial guess, and then relax using the above established relaxation scheme into the new solution imposing $\omega = \omega_1$. Due to the spiral feature of the solutions in the (ω, Q) plane, we can follow this approach only up to a global minimum, $\omega_{\rm min}$, at which point no new solutions can be found at $\omega < \omega_{\rm min}$. At these turning points, we switch from imposing the frequency ω_∞, to imposing the corresponding BS U(1)-charge with Eq. (A.6). We then proceed by incrementally decreasing (or increasing) the charge until we reach the next turning point, where we switch back to imposing the frequency with Eq. (A.5), until the family of BS solutions is generated across the parameter space. Spherically symmetric BSs with different potentials can be generated using this family of KKLS BSs as an initial seed for the relaxation into the BS solution with a different potential in the non-relativistic limit (for a given κ). We find this works, even if the two potentials cannot be continuously deformed into each other, as long as the coupling parameters are chosen such that the potentials are similar.

For rotating BSs, we proceed in much the same fashion. In this case, however, we cannot obtain the initial rotating Q-balls using a shooting method, as the equation is no longer an *ordinary* differential equation, but a partial differential equation in r and θ. We found that generating analytic seeds based on the results of Ref. [220] for $m > 0$ rotating Q-balls provided sufficiently good initial guesses to be able to relax into the correct rotating Q-ball solutions in the non-relativistic regime. Once these solutions are generated, we follow the same procedure as in the $m = 0$ case. We find that the necessary resolution varies significantly with the properties of the BS considered. For less compact BSs, $C < 0.2$, a resolution of $N_{\bar{r}} \times N_\theta = 350 \times 50$ (or even lower resolution) was sufficient, while for BSs with high compactness, resolutions up to 500×100 were necessary for a successful relaxation. In general, we find a resolution of $N_{\bar{r}} \times N_\theta = 500 \times 200$ is sufficient to generate initial data that accurate enough so that the evolution errors are dominant, even for the highest resolution simulations we consider.

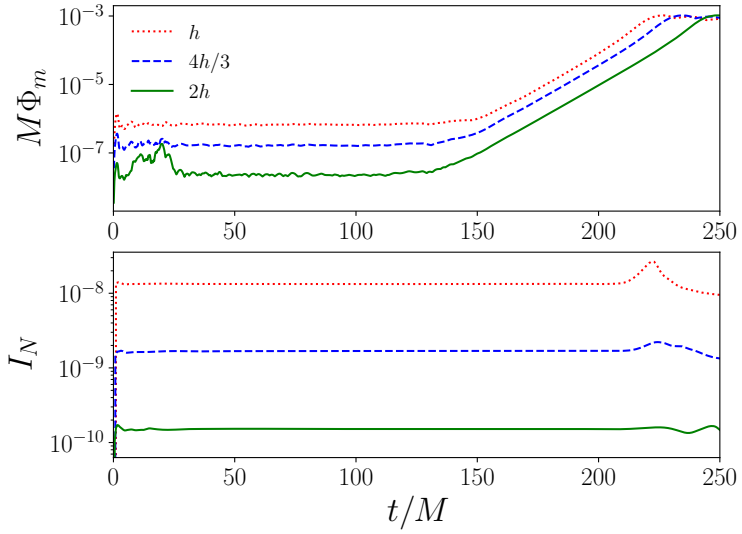

Figure A.1: Time evolution of Φ_m (top panel), defined in Eq. (2.13), at the three different resolutions specified in the text. We also show the integrated norm of the generalized harmonic constraint violation $I_N := \int_{\Sigma_t} d^3\sigma |H_\mu - \Box x_\mu|$ (bottom panel). Both quantities converge to zero at the expected fourth order. The origin of the perturbations of Φ_m at early times is discussed in the text. The units for I_N are arbitrary since here our purpose is just to demonstrate convergence.

A.2 Numerical evolution of stationary boson stars

Once the stationary solutions are generated, we evolve the Einstein-Klein-Gordon equations in the generalized harmonic formulation [306]. We utilize standard fourth order accurate finite difference stencils and fourth order Runge-Kutta time integration, and use adaptive mesh refinement (AMR). Our computational grid extends to spatial infinity, where we apply boundary conditions that the metric is flat and the scalar field is zero, through the use of compactified coordinates. More details can be found in Ref. [146]. We use a gauge where we fix the source functions H^a to be equal to those calculated from the stationary solution, and constant in time. For those mini BSs that collapse to binary (or single) BHs, we utilize a damped harmonic gauge [242, 107]. We consider a range of cases where the BS compactness varies significantly from $\sim 10^{-3}$ to $\approx 1/3$. Therefore, we employ grid hierarchies with between five and eight levels of mesh refinement (using a 2:1 refinement ratio) centered on the BS.

We perform resolution studies, using three different resolutions, on $m = 1$ axionic and

KKLS BSs with $\omega/\mu = 0.6$ (and $M/R^K_{99} = 0.02$) and $\omega/\mu = 0.7$ (and $M/R^K_{99} = 0.14$), respectively, as well as a mini BS with $\omega/\mu = 0.97$, to check convergence and determine the numerical accuracy of our results. In Figure A.1, we present the time evolution of the magnitude of the scalar field, captured by Eq. (2.13), and the integrated norm of the constraint violations of the KKLS BS case. For this case, the lowest resolution is 49^3 with six levels of mesh refinement and a spatial resolution of $dx/M \approx 0.26$ on the lowest level. The medium and high resolutions are, respectively, a factor of 4/3 and 2× larger than the lowest resolution. Both quantities are converging to zero, consistent with the fact that the instability is seeded only by truncation error. The resolution studies for the other cases showed similar behavior. We note that there is transient perturbation to the global maximum Φ_m that is briefly evident in the highest resolution of Fig. A.1 that is not converging at the expected rate. This is due to the time interpolation on the AMR boundaries, and in particular an inaccuracy in how the "past" time level used to perform this interpolation at the initial time is set.

The medium resolution used in the resolution studies is equivalent to the resolution we use for all the other cases studied here. We place the mesh refinement such that both radii of the BS (defined in Sec. 2.2.2) reside inside the finest AMR level, and set the spatial resolution to be roughly $dx/R^K_{99} \approx 0.04$ or greater in all cases considered in the text. For most cases, we fix the mesh refinement to be that of the initial time slice. In those cases where the NAI yields binary BHs or binary BSs, however, we employ AMR set by the truncation error estimates between different refinement levels to track the fragments. Using Richardson extrapolation, we are able to determine the numerical accuracy of the NAI growth rate and harmonic frequency estimates both on the relativistic and the non-relativistic branch of BS solutions. Based on the respective resolution studies of the $m = 1$ KKLS, axionic, and mini BSs, we estimate the relative numerical error in $\tilde{\omega}_I$ to typically be 2.5% (3%) on the relativistic (non-relativistic) branch. The error in $\tilde{\omega}_R$ is smaller; the relative numerical error in this quantity is $< 0.5\%$ (3%) on the relativistic (non-relativistic) branch.

Appendix B

Binary boson star initial data quality

B.1 Numerical setup

In this appendix, we discuss the details of the numerical evolution of the binary BS initial data, which we perform using the same methods as in Refs. [339, 340]. We evolve the Einstein-Klein-Gordon system of equations, derived from (2.1), using the generalized harmonic formulation of the Einstein equations [306]. The spatial fourth-order accurate discretization is achieved using finite-difference stencils over a compactified grid containing spatial infinity. At these boundaries, we impose asymptotically flat boundary conditions both on the metric and the scalar variables. In order to track the individual stars of a given binary, we utilize adaptive mesh refinement of the Cartesian grid with a 2:1 refinement ratio (see Ref. [146]). The time-stepping is achieved using a fourth-order accurate Runge-Kutta integration. As briefly mentioned in Sec. 3.4.1, the axisymmetric evolutions are performed using a generalized Cartoon method [26, 306], which explicitly assumes an azimuthal Killing field k^μ, such that $\mathcal{L}_k g_{\mu\nu} = 0$ and $\mathcal{L}_k \Phi = im\Phi$. Typically, we require seven mesh refinement levels with grid spacing $\Delta x/M_0 = 0.08$ on the finest level when evolving an inspiraling binary BSs; in the case of axisymmetric evolutions the grid spacing on the finest level is typically $\Delta x/M_0 = 0.01$. For all evolutions considered here, the gauge is specified by setting the source functions $H^\mu = \Box x^\mu$ according to the damped harmonic gauge [242, 107].

We perform convergence tests in order to validate our numerical methods and quantify the truncation error. Specifically, we measure the constraint violation given by $\mathcal{C} = M_0 \sum_\mu |(H^\mu - \Box x^\mu)|/4$ throughout the evolutions by computing $\max \mathcal{C}$, as well as the integrated norm $\mathcal{I}_\mathcal{C} = M_0^{-2} \int d^3x \sqrt{\gamma} \mathcal{C}$ (in a coordinate sphere of radius $100 M_0$). In the

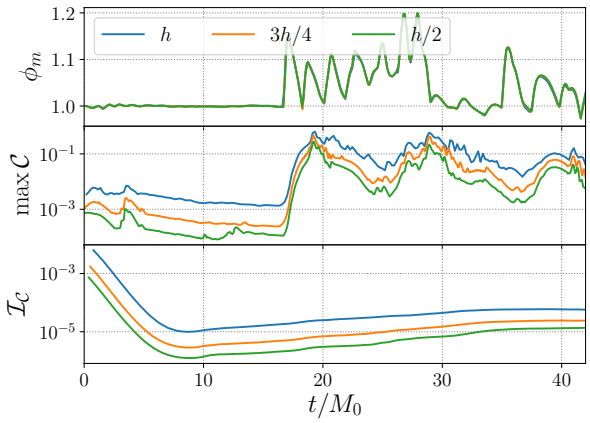

Figure B.1: Convergence study of the numerical evolution of the axisymmetric binary $\mathcal{B}_1$ with properties summarized in Table 3.1 (and initial coordinate separation $D = 10M_0$), at three different numerical resolutions, where h is the grid spacing of the lowest resolution. The top panel shows $\phi_m = \max|\Phi|/\max|\Phi|_{t=0}$, the normalized maximum of the scalar field magnitude, while the lower panels show two different measures of the constraint violation, $\max\mathcal{C}$ and $\mathcal{I}_\mathcal{C}$ (defined in the text). The constraint violation is converging to zero at roughly third and fourth order in the middle and bottom panels, respectively.

generalized harmonic formulation, any violation of the Hamiltonian and momentum constraints on the initial time slice will lead $\mathcal{C}$ to evolve to a non-zero value (as does truncation error). In Fig. B.1, we present the typical convergence behavior of $\mathcal{I}_\mathcal{C}$ and $\max\mathcal{C}$ for an axisymmetric binary BS evolution starting from constraint satisfying initial data using the above numerical evolution setup. In Fig. B.2, we present a convergence study of the constraint violation of the binary initial data associated with $\mathcal{B}_5$ (see Table 3.1). In the case of the axisymmetric settings, the maximum of the constraint violation $\max\mathcal{C}$ is mainly set by the third-order accurate time-interpolation performed on the mesh refinement boundaries, and as a result, converges at roughly third order or better in Fig. B.1. In the three-dimensional evolutions, $\max\mathcal{C}$ is typically reached in the interior of the stars. Hence, in those cases, we expect a roughly fourth-order convergence behavior (as seen in Fig. B.2). In both settings, however, the integrated norm $\mathcal{I}_\mathcal{C}$ converges at approximately fourth order, as it is less affected by the lower-order interpolation on the mesh refinement boundaries.

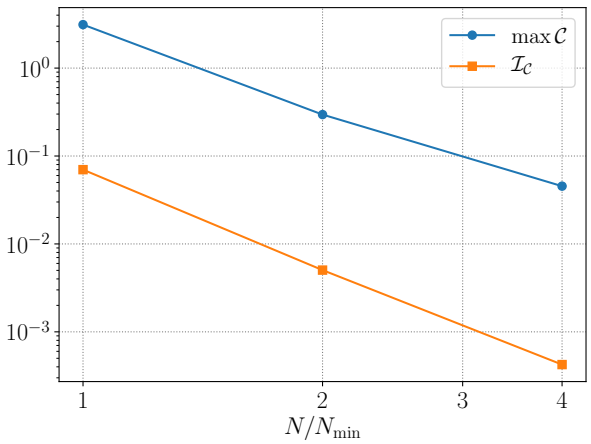

Figure B.2: The convergence with behavior of the two norms, $\max \mathcal{C}$ and $\mathcal{I}_{\mathcal{C}}$ (defined in the main text), of the constraint violation of the binary initial data associated with $\mathcal{B}_5$ (see Table 3.1) with increasing resolution N, the number of grid points in each linear dimension, compared with the lowest resolution considered $N_{\rm min}$. Both norms exhibit (as expected) roughly fourth-order accurate convergence towards zero.

B.2 GW contamination

In this appendix, we briefly return to the high-frequency contamination in the GW emission from the binaries presented in Sec. 3.4.2. This contamination emerges from the residual perturbations present in the eccentricity reduced binaries $\mathcal{B}_3$ and $\mathcal{B}_5$ constructed with conformally rescaled kinetic energy using (3.30) with $p = -4$. In Fig. B.3, we present the $(\ell, m) = (2, 2)$ spherical harmonic component of the Newman-Penrose scalar Ψ_4, which can be compared to the corresponding GW strain shown in the right panels of Fig. 3.7 and Fig. 3.8. Since Ψ_4 is related to the strain by two time derivatives, it accentuates the high-frequency component from the perturbed BSs. As shown in Sec. 3.3.2, this contamination is reduced by means of the rescaling (3.30) of the conformal kinetic energy. However, with the lowest exponent with which the elliptic solver was able to find a solution, $p = -4$, some oscillations remain in the stars, and lead to the high frequency component to Ψ_4 evident at early times in Fig. B.3.

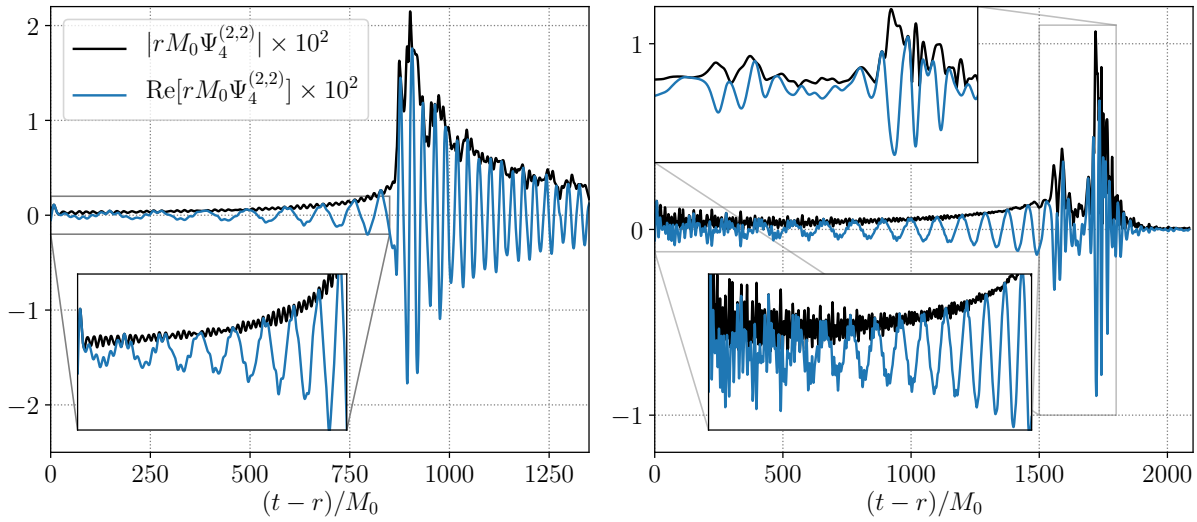

Figure B.3: We show the $(\ell, m) = (2, 2)$ spin-weighted spherical harmonic components of the Newman-Penrose scalar Ψ_4 extracted on a coordinate sphere of radius $100M_0$. The top panel corresponds to the $N_e = 5$ and $p = -4$ binary $\mathcal{B}_5$ shown in the top row of Fig. 3.7 and Fig. 3.8, while the bottom panel shows the $N_e = 3$ and $p = -4$ binary $\mathcal{B}_3$ shown in the bottom row of Fig. 3.7 and Fig. 3.8. This shows the high-frequency contamination of the gravitational waveform from the binaries at early times due to residual spurious oscillations and unbound scalar matter in and around the constituents of the binaries.

B.3 Center-of-mass motion

Within our approach, the initial linear momentum is set to zero using Newtonian expressions for the initial boost velocities (as discussed in Sec. 3.3.3). We find this to be sufficient for non-spinning binaries, i.e, the center-of-mass velocity throughout the evolution of the initial data remains below $v_{\rm com} < 10^{-7}$. For highly-spinning quasi-circular binary initial data, the center of mass of the system exhibits larger drifts with constant velocity away from origin of the numerical grid. For the aligned-spin binary $\mathcal{B}_3$, the magnitude of the in-orbital-plane coordinate velocity of the center of mass is $v_{\rm com} = 6 \times 10^{-3}$ (the out-of-plane component is $< 10^{-10}$). Leading post-Newtonian corrections to the center-of-mass and center-of-momentum velocities, used to initialize the binaries in this work, are roughly an order of magnitude too small to account for $v_{\rm com}$. This strong drift may be the result of spurious gravitational and scalar radiation emitted during the first few light crossing times of the binary, as well as the large spins of the super-spinning binary $\mathcal{B}_3$. We address this by measuring the in-plane components $v^i_{\rm com}$ of the center-of-mass coordinate velocity

and subtracting this from the initial binary velocities $v^i_{(A)}$ of the free data as defined in Sec. 3.2.1. This is done in tandem with the eccentricity reduction. Hence, the linear momentum of the binary can be iteratively reduced in this way. After two iteration steps, the velocity is reduced by more than an order of magnitude to $v_{\rm com} = 1 \times 10^{-4}$ for the binary $\mathcal{B}_3$ with aligned spins. In the case of the precessing binary $\mathcal{B}_3$, discussed in Sec. 3.4.3, the center-of-mass motion in the direction of the orbital angular momentum dominates; this we treat iteratively in precisely the same manner as the in-plane center-of-mass velocity.

Appendix C

Proca star construction and binary boson star evolution

C.1 Isolated Proca star solutions

The details of the construction of isolated scalar BSs are presented in Ref. [339]. Hence, here we focus on our approach to constructing the PS solutions considered in this work. PSs are, analogous to scalar BSs, solutions to a massive complex field—in this case a vector field A_α of mass μ—minimally coupled to general relativity as [77]

$$S = \int d^4x\sqrt{-g}\left[\frac{R}{16\pi} - \frac{1}{4}F_{\alpha\beta}\bar{F}^{\alpha\beta} - \frac{1}{2}\mu^2 A_\alpha \bar{A}^\alpha\right]. \tag{C.1}$$

Here $F_{\alpha\beta} = \nabla_\alpha A_\beta - \nabla_\beta A_\alpha$ is the field strength, while the overbar denotes complex conjugation. This theory is also invariant under a global $U(1)$ transformation $A_\beta \to A_\beta e^{i\theta}$. The associated Noether current and Noether charge are

$$j^\mu = \frac{i}{2}(\bar{F}^\mu{}_\alpha A^\alpha - F^\mu{}_\alpha \bar{A}^\alpha), \qquad\qquad Q = -\int d^3x\sqrt{-g}j^0, \tag{C.2}$$

respectively. The Lorenz relation, $\nabla_\alpha A^\alpha = 0$, is identically satisfied due to the anti-symmetry in the field-strength, assuming $\mu \neq 0$ (and no vector self-interactions). The stress-energy associated with the action (C.1) is given by

$$\begin{aligned} T_{\mu\nu} = & -F_{\alpha(\mu}\bar{F}_{\nu)}{}^\alpha - \frac{1}{4}g_{\mu\nu}F^{\alpha\beta}\bar{F}_{\alpha\beta} \\ & + \mu^2 \bar{A}_{(\mu}A_{\nu)} - \frac{1}{2}\mu^2 g_{\mu\nu}A_\alpha\bar{A}^\alpha. \end{aligned} \tag{C.3}$$

With this, the Einstein equations, sourced by the vector matter, and the vector field equations are given by

$$G_{\alpha\beta} = 8\pi T_{\alpha\beta}, \qquad \nabla_\alpha F^{\alpha\beta} = \mu^2 A^\beta, \tag{C.4}$$

where $G_{\alpha\beta}$ is the Einstein tensor. Rotating PSs are asymptotically flat, axisymmetric solutions to the above system of equations. Hence, we make the ansatz

$$\begin{aligned} ds^2 = -f dt^2 \ &+ l f^{-1}\{j(dr^2 + r^2 d\theta^2) \\ &+ r^2 \sin^2\theta (d\varphi - \Omega r^{-1} dt)^2\}, \end{aligned} \tag{C.5}$$

where f, l, j, and Ω are functions of r and θ. The corresponding ansatz for the vector 1-form is given by

$$\mathbf{A} = e^{i\omega t}(V dt + iB dr) \tag{C.6}$$

for spherically symmetric solutions, and

$$\mathbf{A} = e^{i\omega t} e^{im\varphi} \left(iV dt + \frac{H_1}{r} dr + H_2 d\theta + i \sin\theta H_3 d\varphi \right) \tag{C.7}$$

for rotating solutions. Here, in direct analogy to scalar BSs, this approach yields an infinite set of families of solution indexed by their azimuthal mode m, and parameterized by their frequency ω. The boundary conditions for the vector field are $A_\mu \to 0$ for $r \to \infty$. However, in order to obtain non-trivial solutions to the field equations and these boundary conditions, we promote the frequency to a field $\omega \to \omega_s(r, \theta)$ and introduce the second auxiliary field $\rho(r, \theta)$, following Ref. [220], where this was applied in the scalar case (see also Ref. [339]). Both fields follow $\Box_g = g^{\mu\nu}\nabla_\mu \nabla_\nu$ of the spacetime $g_{\mu\nu}$:

$$\Box_g \omega_s = 0, \qquad \Box_g \rho = \frac{j^t}{\omega_s}. \tag{C.8}$$

Through the boundary conditions $\omega_s(r \to \infty) \to \omega$, where ω is the solution's frequency, we ensure that the solution is non-trivial. Integrating over the entire three-volume of a time-slice, we see that ρ encodes the total $U(1)$-charge in its boundary data:

$$\lim_{r\to\infty} r^2 \partial_r \rho(r, \theta) = -\frac{Q}{4\pi\omega}. \tag{C.9}$$

Conversely, using (C.9), we can impose Q as a boundary condition, and solve for ω_s. Hence, within this formalism, either the solution's frequency ω, or the solution's charge Q

can be imposed as a boundary condition. The list of boundary conditions for the metric variables and auxiliary functions are given in Ref. [339], while the boundary conditions of the vector components are listed in Ref. [77]. One subtlety arises for $B(r)$ (in the spherically symmetric case), which follows a first order differential equation. We promote this equation trivially to a second order equation by $B(r) \to \partial_r \tilde{B}(r)$, and then impose the boundary condition $\lim_{r\to\infty} \tilde{B}(r) = \tilde{B}_\infty$ (the solution is independent of $\tilde{B}_\infty$), while requiring $\partial_r \tilde{B}(r)|_{r=0} = 0$.

To numerically solve the system of equations introduced above subject to the boundary conditions, we follow the implementation for scalar BSs in Ref. [339]. We compactify the radial coordinate $r \to \bar{r} = r/(1+r)$, such that $\bar{r} \in (0,1)$, and restrict to the upper-half plane, i.e., $\theta \in (0, \pi/2)$. We utilize fifth-order accurate finite differences both in the radial and polar directions, and consider a uniformly spaced grid in the compactified coordinates $(\bar{r}, \theta)$. We utilize a Newton-Raphson-type relaxation procedure that iteratively approaches the true solution given a sufficiently close initial guess. The initial guess is constructed from plots given in Ref. [193]. Once a solution is found at ω_1, we explore the parameter space of each family m, by imposing the boundary conditions $\omega_2 = \omega_1 + \delta\omega$ (or analogously the vector charge), where $\delta\omega$ is chosen sufficiently small such that the solution at ω_1 is a good enough initial guess to obtain the solution at ω_2. For spherically symmetric stars, we found that a resolution of $N_r = 1000$ was sufficient for all considered cases, while in the rotating case we typically use $N_r \times N_\theta = 500 \times 100$.

C.2 Angular momentum variation

In Figure C.1, we present snapshots of the evolution of the sequence of non-spinning binary BSs of varying initial orbital angular momentum discussed in Sec. 4.3.3.

C.3 Numerical setup

Given initial data (see Chapter 3) for a scalar binary BS, we evolve the Einstein-Klein-Gordon equations (following from the scalar action (2.1)) forward in time employing the generalized harmonic formulation of the Einstein evolution equations [306] with methods outlined in Appendix A.2. The compactness of the stars sets the number of levels required to resolve the stars sufficiently; for low-compactness solutions [typically stars in the repulsive scalar model, (2.5)], we require five to six refinement levels, while for the high-compactness solutions [usually those in the solitonic scalar model, (2.2)], we require six to

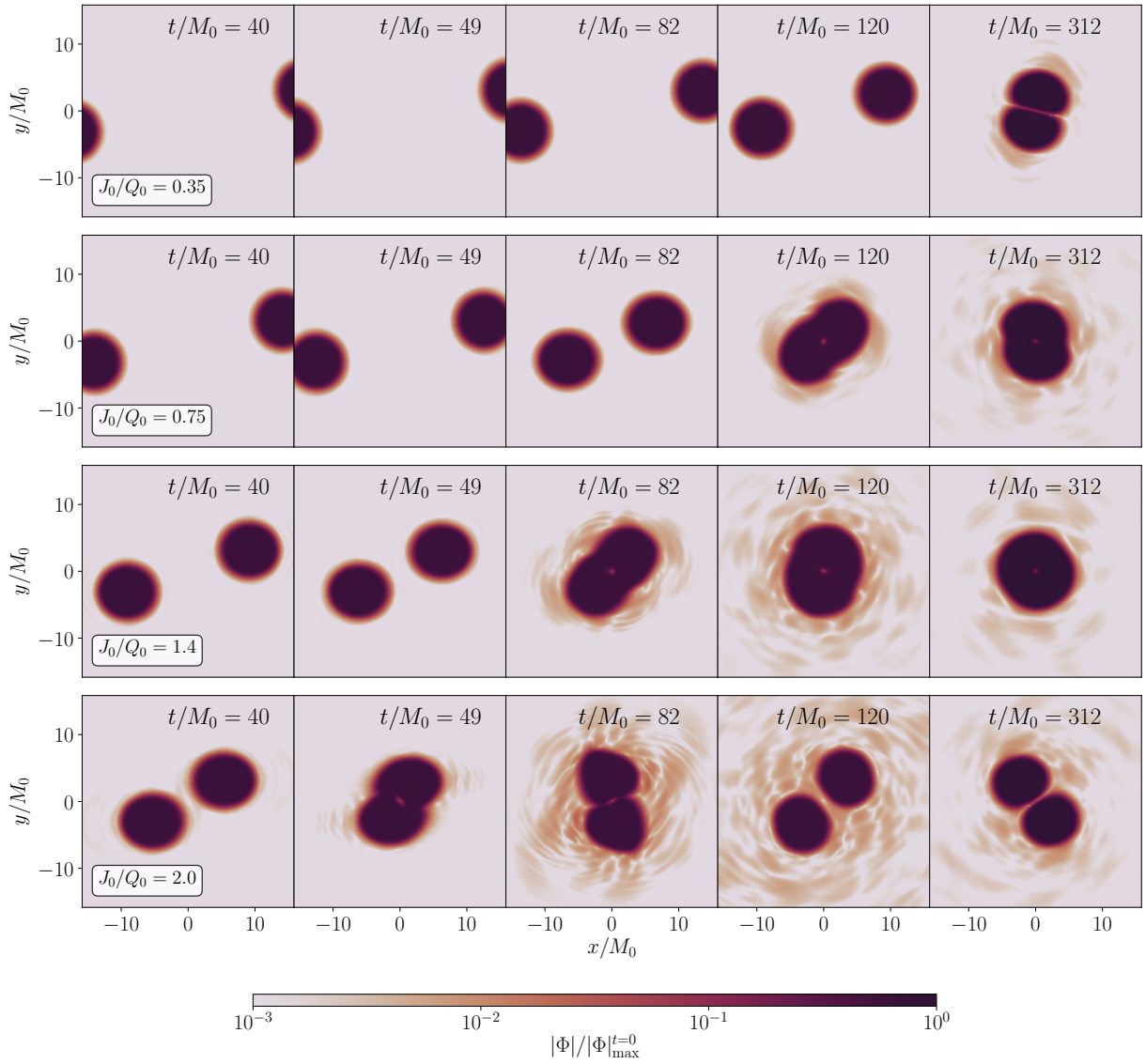

Figure C.1: We show the scalar field magnitude $|\Phi|$ (normalized by the maximum in the initial time-slice) in a few snapshots of the equatorial slice of the binary BS simulations discussed in Figure 4.9. We label each sequence of time-slices by the initial angular momentum J_0 in units of initial charge Q_0. In the top and bottom rows, the binary merges into a rotating DBS solution (i.e. two non-rotating BSs separated by scalar interactions, as discussed in Sec. 4.2.1). Compared with the top row, the binary in the bottom row rotates at high angular velocities around the center of mass at late times, i.e., $t/M_0 > 300$. The case shown in the middle two rows merge to form a remnant with $q = 1$ vortex at the center of mass at late times. Notice, we find that the $J_0/Q_0 = 0.75$ case relaxes to a rotating BS at late times $t/M_0 > 300$.

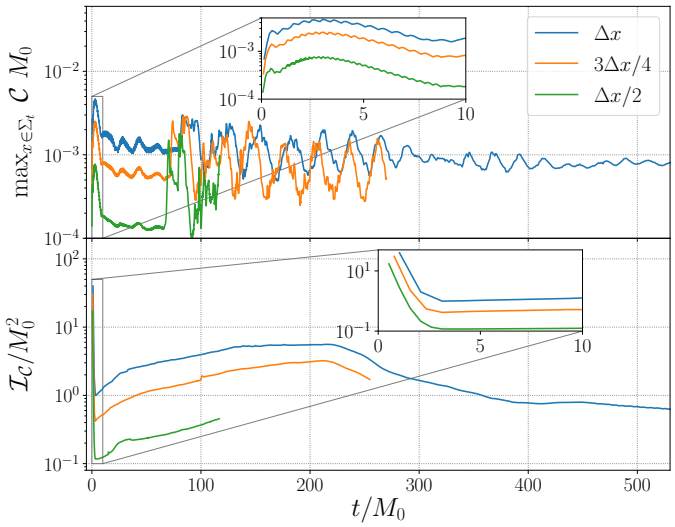

Figure C.2: Here we consider the convergence behavior of the binary BS in the $\sigma = 0.05$ solitonic scalar model, with properties summarized in Table 4.2, with decreasing grid spacing. The quantities $\mathcal{C}$ and $\mathcal{I}_\mathcal{C}$ (defined in the text) are a positive definite measure of the constraint violation, which we track throughout the simulation. The rapid variation of the constraints is driven by gauge dynamics at early times. The maximum of the constraint violation $\mathcal{C}$ occurs during the merger of the binary at around $t/M_0 \approx 75$. The binary merges earlier with increasing resolution, and only the medium and high resolutions capture small-scale features present in the remnant after merger. The quantity $\max \mathcal{C}$ converges to zero roughly at third order, as expected, since it is primarily set by the third-order accurate time interpolations on the mesh refinement boundaries. On the other hand, the integrated quantity $\mathcal{I}_\mathcal{C}$ converges at the expected forth order, as it is largely insensitive to the lower-order time interpolations.

seven levels. In the cases with black hole formation, we add refinement levels dynamically to resolve the gravitational collapse and apparent horizon (this requires seven to nine levels). The resolution on the finest mesh refinement level for the binary evolutions presented in Sec. 4.2.3 is $\Delta x/M_0 = 0.15$. The resolution for the solitonic cases shown in Sec. 4.3.2 is $\Delta x/M_0 = 0.075$ on the finest refinement level, while for the binaries in the repulsive model it is $\Delta x/M_0 = 0.2$. Throughout, we use the standard damped harmonic gauge condition to set the generalized harmonic source functions H_μ [107, 242].

We present resolution studies of two exemplary binary mergers. First, we focus on the $\sigma = 0.05$ solitonic scalar model and the binary with parameters given in Table 4.2.

We consider three resolutions, corresponding to Δx, $3\Delta x/4$, and $\Delta x/2$, where the lowest resolution corresponds to a grid spacing of $\Delta x/M_0 \approx 0.1$ on the finest level, and the medium resolution is the default resolution for all simulations discussed in Sec. 4.3. In order to explicitly demonstrate that we are solving the Hamiltonian and momentum constraints, we track the violations of the constraints, given by $C_\mu = H_\mu - \Box x_\mu$, in time. In Figure C.2, we plot the evolution of the constraints at these different resolutions of the binary with parameters given in Table 4.2. To track the constraint violations, we define $\mathcal{C} = \sum_\mu |(C_\mu)^2|/4$, and consider the global maximum $\max \mathcal{C}$ in each time-slice, as well as the integrated norm $\mathcal{I}_\mathcal{C} = \int d^3x \sqrt{\gamma}\mathcal{C}$. In Figure C.3, we show the convergence behavior of the total $U(1)$-charge of the system. Overall, the constraint violations converge to zero at the expected forth order of our numerical methods. The violation of the conservation of the $U(1)$ charge Q, shown in Figure C.3, also converges towards zero. Likely, due to the compactness ($C = 0.13$) of the BSs, rapid exponential decay of the scalar field outside the stars, i.e., $\Phi \sim \exp(-\sqrt{\mu^2 - \omega^2}r)$, with $\omega/\mu = 0.25$, and the large initial separation (of $D = 40M_0$), the low and medium resolutions exhibit relatively large drifts in the total conserved charge. Hence, the scalar field gradients on the surface of the stars, as well as the spatial scales of perturbations, require relatively high resolution.

Secondly, we discuss the numerical convergence of one of the binaries considered in Sec. 4.2.3. In particular, we focus on the $\alpha = \pi/2$ case, and compare its convergence behavior to that of the $\alpha = \pi$ binary evolution. In Figure C.4, we present the convergence of the constraint violations with increasing resolution of the $\alpha = \pi/2$ evolution. Again, this demonstrates explicitly that we are solving the Hamiltonian and momentum constraints consistently within the $t = 0$ slice. In the subsequent evolution up to $t/M_0 = 100$, the constraints converge at the expected orders. For numerical stability purposes, we have to increase the size of the second coarsest mesh-refinement level in the lowest resolution run, moving the outer boundary of this level from $|x_i|/M_0 = 100$ to $|x_i|/M_0 \approx 241$. This explains the disagreement between the Δx and the $3\Delta x/4$ as well as $\Delta x/2$ resolutions in Figure C.4, *after* $t/M_0 \approx 100$ (as at this time constraint violations propagating outward reach the mesh-refinement boundary in the medium and high resolution runs, but not yet in the low-resolution case). Furthermore, this different mesh-refinement layout in the low resolution case alters the convergence behavior, such that this case mergers much earlier compared with the medium and high resolution runs. However, we have checked explicitly that the merger delay between the $\alpha = \pi/2$ and $\alpha = \pi$ cases *increases* from low (of $\Delta t/M_0 \approx 43$) to medium resolution evolutions (of $\Delta t/M_0 \approx 262$). Hence, the dephasing, delayed merger and black hole collapse discussed in Sec. 4.2.3 are physical, and we are likely *underestimating* their impact on the GWs. Notice also, identical numerical setups were used for *all* cases presented Sec. 4.2.3, both for the initial data construction and evolution.

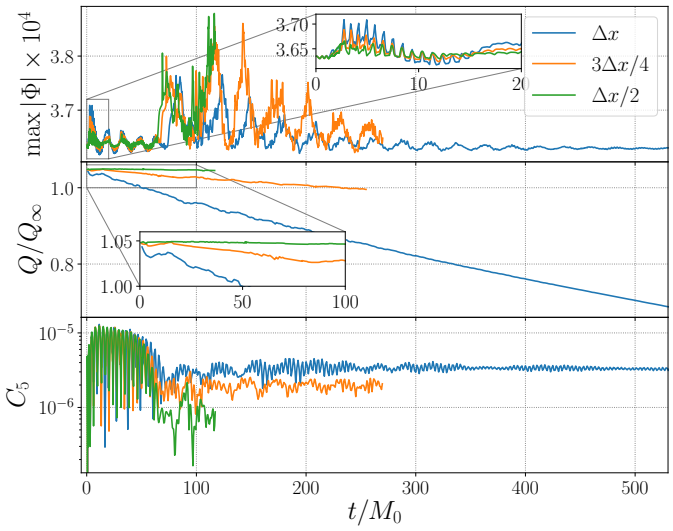

Figure C.3: We consider the convergence behavior of the global maximum of $|\Phi|$, the total $U(1)$-charge Q, and the azimuthal mode C_5 of the scalar field for the binary BS shown in Figure C.2. The total charge Q is calculated in a coordinate sphere of radius $100M_0$ around the center of mass of the system. We normalize Q by Q_∞, the sum of the BSs' isolated charges $Q_\infty = Q_1 + Q_2$. As the initial separation between the two stars increases, the total charge approaches the superposed charge: $Q \to Q_\infty$. Lastly, we also show the convergence behavior of the C_5 mode [defined in (4.16)] during the binary evolution. The $m = 5$ perturbations remaining after the merger (and the formation of an $m = 1$ rotating remnant) at around $t/M_0 \approx 75$ are converging towards zero with increasing resolution at roughly the expected fourth order.

Therefore, while *absolute* differences are not resolved, this is suggestive that the *relative* difference in amplitude in the GW waveform between the α-cases are driven by the scalar interactions, rather than numerical truncation error.

C.4 Vortex ejection as an artifact of numerical resolution

We find that in our simulations of the rotating BS formed from the merger of two non-rotating BS with a phase variation of $63/64 \geq \alpha/\pi \geq 7/8$ exhibit a growing perturbation leading to vortex ejection at low resolutions, but that this behavior disappears at sufficiently

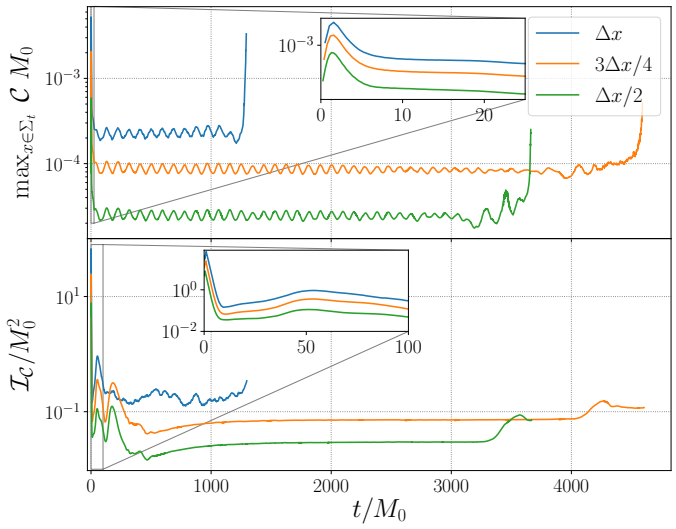

Figure C.4: We consider the convergence behavior of the $\alpha = \pi/2$ case of Sec. 4.2.3 with decreasing grid spacing Δx. The quantities $\mathcal{C}$ and $\mathcal{I}_\mathcal{C}$ are defined in the text. The low resolution evolution is based on a different mesh-refinement layout (as discussed in the text,) and, hence, exhibits slightly different convergence behavior. At early times, the convergence orders of these quantities are the same as those discussed in the caption of Figure C.2.

high resolution. In order to understand this behavior, it is instructive to consider an azimuthal mode decomposition of the real part of the scalar field, $\Phi_R = \mathrm{Re}(\Phi)$, defined in (4.16). In Figure C.5, we show the scalar field modes C_m during the merger of the binary BS specified in Table 4.2 with initial phase variation $\alpha/\pi = 63/64$. During, and shortly after, the merger around $t/M_0 = 75$, the $m = 1$ mode is the most dominant mode representing the formation of a $m = 1$ rotating BS, and indicating the formation of a $q = 1$ central vortex. Additionally, the amplitude of the even-m modes right after merger is consistent across resolutions. On the other hand, the even-m modes begin to grow exponentially right after formation of the rotating remnant (the representative $m = 0$ mode is shown in Figure C.5) in the evolution with *lowest* resolution. Furthermore, we find that with increasing α, the amplitude of the even-m modes after merger decreases, but in all cases the artificial instability appears at lowest resolution; in fact, even in the $\alpha = \pi$ case, where the even-m modes are seeded at amplitudes consistent with floating point roundoff, we find this behavior. In all cases considered, this growing perturbation at low resolution saturates in the vortex ejection of the solution. However, we performed higher resolution evolutions

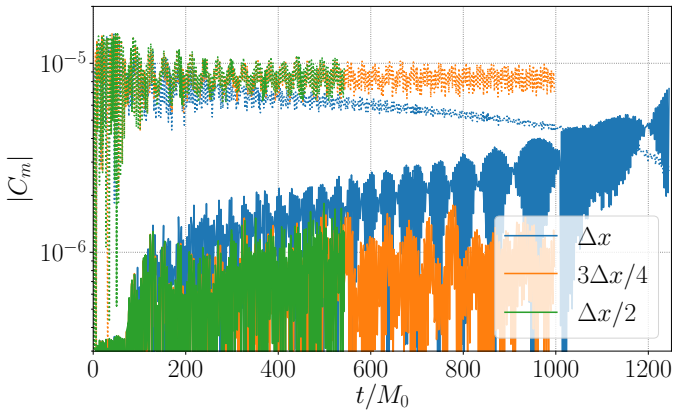

Figure C.5: The evolution of the scalar field modes C_m (dotted and solid lines corresponding to $m = 1$ and 2, respectively) defined in (4.16) for the binary BS merger specified in Table 4.2 with phase variation $\alpha/\pi = 63/64$. The merger occurs roughly at $t/M_0 \approx 75$, after which the even-m modes promptly begin to grow exponentially in the evolution with the *lowest* resolution (the $m = 0$ mode is representative of all even-m modes). This apparent instability is an artifact of low numerical resolution, and disappears with increasing resolution.

in the binaries with $\alpha/\pi \in \{63/64, 31/32, 7/8\}$ and explicitly checked that the unstable behavior disappears. This is illustrated for $\alpha/\pi = 63/64$ in Figure C.5.

C.5 Phase evolution of the non-axisymmetric instability

In this appendix, we briefly revisit the non-axisymmetric instability (referred to as NAI in the following) discovered in [323], focusing on the importance of the scalar phase and vortex structure in these solutions. To gain intuition, we re-analyze two unstable BSs with $m = 1$ and 2, in the solitonic and repulsive scalar theories introduced in (2.2) and (2.5), respectively, originally considered in Ref. [339], and discuss the instability in light of the remnant map constructed in Sec. 4.2.4.

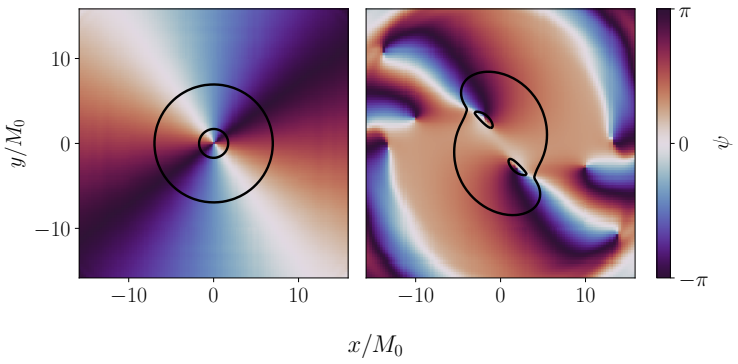

Figure C.6: We show the scalar phase in two equatorial slices of the $m = 2$ rotating BS of frequency $\omega/\mu = 0.4$ in the $\sigma = 0.05$ solitonic scalar model undergoing the NAI (first discussed in Ref. [339]). The left panel shows the scalar phase at $t/M_0 = 0$, while the right panel shows the scalar phase during the nonlinear saturation of the NAI. The black lines indicate arbitrarily chosen level surfaces of the scalar field magnitude within the equatorial plane.

C.5.1 Instability of a $m = 2$ boson star

We begin with the phase evolution during the development and saturation of the NAI of a $m = 2$ rotating BS solution. Specifically, we evolve the $m = 2$ rotating BS of frequency $\omega/\mu = 0.4$ in the $\sigma = 0.05$ solitonic scalar model in (2.2). The NAI of this stationary solution exhibits characteristic growth timescales of $\tau_{\rm NAI}/M_0 \approx 19$, leading to the ejection of two blobs of scalar matter in opposite directions, leaving behind a single non-spinning remnant star at the center of mass (see panel b of Fig. 8 in Ref. [339] for snapshots of the saturation of the NAI in this star). In Figure C.6, we show the scalar phase in the equatorial slice at the start of the evolution, and during the non-linear saturation of the NAI. Initially, the vortex at the center of the star is a $q = 2$ vortex (as expected for a $m = 2$ star). However, during the non-linear saturation of the NAI shown on the right in Figure C.6, this $q = m = 2$ vortex at the center of mass breaks up into *two* $q = 1$ vortices, which are quickly ejected from the star, leaving only a non-spinning star at late times (not shown in Figure C.6). This is reminiscent of, for instance, the break-up of a $m = 2$ string in the Abelian-Higgs model (see, e.g., Ref. [360]).

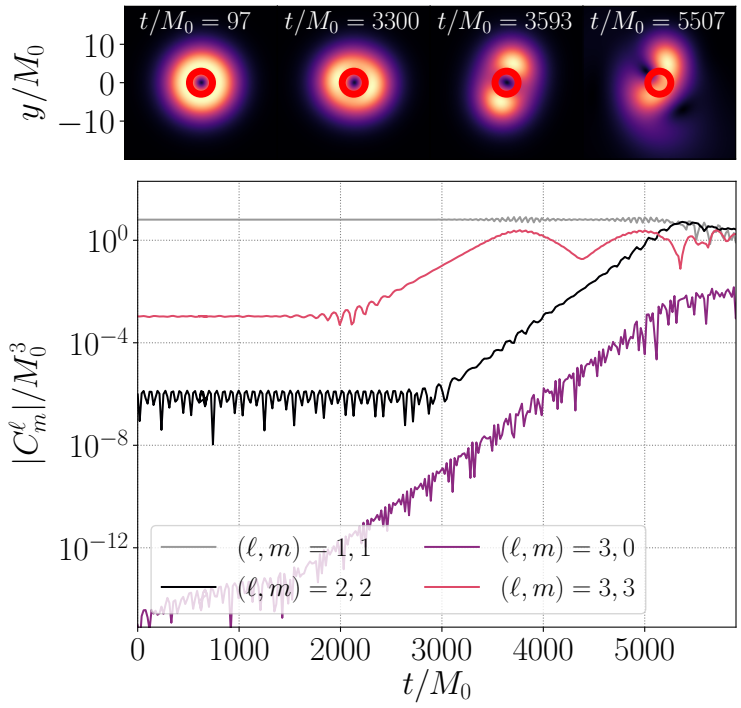

Figure C.7: *(top)* We show the normalized scalar field magnitude $|\Phi|/|\Phi|^{t=0}_{\rm max}$ in four equatorial slices at different times during the evolution of an isolated $m = 1$ rotating BS of mass M_0 in the repulsive model with $\lambda/\mu^2 = 10^2$ and frequency $\omega/\mu = 0.9$. The star was shown to be unstable to the NAI in Ref. [339]. Red circles indicate the coordinate location of the vortex at early times in all snapshots. *(bottom)* The evolution of some of the spherical harmonic modes C_m^ℓ, defined in (C.10), corresponding to the same star as in the top panel.

C.5.2 Instability of a $m = 1$ boson star

We turn now to the NAI active in a $m = 1$ rotating BS of frequency $\omega/\mu = 0.9$ in the repulsive scalar model with coupling $\lambda/\mu^2 = 10^2$. In the top panel of Figure C.7, we show four snapshots of the evolution throughout the development and saturation of the NAI. At early times, the scalar field magnitude morphology is toroidal (first panel), while at intermediate times (second and third panel), the scalar field magnitude exhibits a quadrupolar pattern, which is broken up at late times (fourth panel) and eventually becomes a monopolar (i.e., perturbed spherically symmetric) remnant BS. It is clear from the top panel of Figure C.7 that the $q = 1$ vortex of the stationary BS solution remains at the center of mass even during the *first* fragmentation (first and second panel) until the

second fragmentation phase, when this vortex is ejected from the system (last panel).

In order to understand this two-staged fragmentation process, we decompose the scalar field $\Phi_R = \mathrm{Re}(\Phi)$ into coordinate spherical-harmonic components C^ℓ_m as

$$C^\ell_m = \int_D d^3x \Phi_R Y^\ell_m(\theta, \varphi), \tag{C.10}$$

centered on the center of mass and aligned with the spin-axis of an isolated star. (Here, the domain of integration D is the ball of coordinate radius $r/M_0 = 25$). In the bottom panel of Figure C.7, we show the evolution of some of the spherical harmonic components during the development and saturation of the NAI. First, the $(\ell, m) = (1, 1)$ component dominates throughout the evolution, since this is a $m = 1$ (toroidal) BS. Secondly, the even-m components are seeded roughly at the level of floating point roundoff at $t = 0$, while the odd-m components (except for $m = 1$) have amplitudes set by the truncation error (orders of magnitude larger than the floating point roundoff). While the even- and odd-m components shown in the bottom panel of Figure C.7 all exhibit the same e-folding growth rate, suggesting that they are all associated with the same unstable mode, the NAI has a much larger overlap with the $(\ell, m) = (3, 3)$ component than the other components. During the first fragmentation phase around $t/M_0 \approx 3500$, the quadrupolar patter of $|\Phi|$ can be understood by considering the bottom panel of Figure C.7. In this phase, the odd-m components dominant in the initial non-linear phase. In particular, the $(\ell, m) = (3, 3)$ perturbation mixes with the $(\ell, m) = (1, 1)$ background solution into a $\tilde{m} = 3 \pm 1$ mode of $|\Phi|$, corresponding precisely to the quadrupolar pattern observed in the top panel of Figure C.7. During the second fragmentation around $t/M_0 \approx 5000$, the even-m components also become significant and their presence results in the ejection of the central vortex and the formation of the non-spinning, i.e., $m = 0$, BS remnant. The numerical convergence of this instability was checked in Ref. [339].

From this, we conclude that the NAI is dominated by odd-m perturbations of Φ_R and does not significantly affect the scalar vortex, even as the unstable mode starts to become large (and nonlinear). However, in the subsequent evolution in the nonlinear phase, even-m perturbations continue to grow and eventually lead to the ejection of the central vortex.

C.5.3 The instability and the remnant map

For completeness, we briefly discuss the transition from a $m = 1$ rotating BS to a non-spinning star of the same scalar model with the remnant map described in Sec. 4.2.4. This transition (similar to the NAI and its non-linear saturation) corresponds to the decay

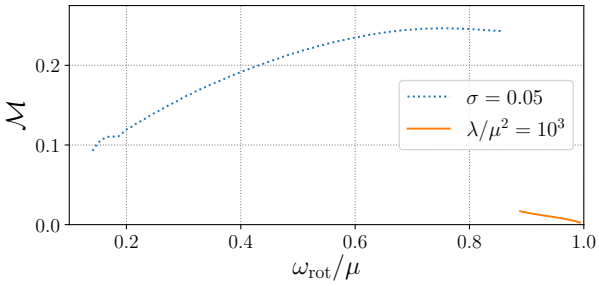

Figure C.8: We show the normalized mass difference $\mathcal{M} = (M_* - M_{\rm rot})/M_*$ between the mass $M_{\rm rot}$ of an isolated $m = 1$ spinning star of frequency $\omega_{\rm rot}$ and a non-rotating star of mass M_* in the same models, when assuming the remnant map described in Sec. 4.2.4. We do this for the solitonic and repulsive scalar models, with couplings σ and λ, respectively. Therefore, for each $\omega_{\rm rot}$ shown, $\mathcal{M}$ indicates the energy gained by transitioning the $m = 1$ rotating star to a non-rotating star of the same charge. We show only the branches below the maximum mass of the families of solutions.

of a rotating solution to a non-rotating solution, which may be dynamically achieved by means of an instability in the $m = 1$ star. In Figure C.8, show the energy gained by such a transition assuming the remnant map, i.e., assuming no scalar radiation. Clearly, it is energetically favorable to decay from a $m = 1$ rotating star to a non-rotating star. However, whether this is a hint of a linear instability everywhere in the parameter space shown in Figure C.8 is non-trivial. Furthermore, a dynamical transition requires the ejection of all angular momentum from the system, which may break the assumption of local charge conservation around the star. On the other hand, this demonstrates that the transition of two identical $m = 1$ BSs into two identical non-spinning stars is also energetically favorable, a scenario we explicitly found performing a nonlinear evolution in Sec. 4.2.4.

Appendix D

Dark Photon Superradiance: Framework and numerical setting

D.1 Construction of massive vector cloud

To construct the superradiantly unstable massive vector field modes on a fixed Kerr spacetime of mass M and dimensionless spin a_*, we follow Refs. [243, 161, 229], as well as [137, 338]. Neglecting all non-linear effects both on the massive vector field A'_μ, as well as in the gravitational sector, we treat A'_μ as a test field on a fixed Kerr background spacetime. In this Ricci-flat geometry, the vector field satisfies the massive vector wave equation

$$g^{\alpha\beta}\nabla_\alpha\nabla_\beta A'^\gamma = \mu^2 A'^\gamma, \tag{D.1}$$

with $g^{\alpha\beta} = g^{\alpha\beta}_{\rm Kerr}$ and mass parameter μ. The Kerr family of BH spacetimes, a special case of the Kerr-NUT-(A)dS class of spacetime, admits additional symmetries beyond stationarity and axisymmetry generated by the timelike and axial Killing fields, $\boldsymbol{\xi}$ and $\boldsymbol{\eta}$, respectively. These "hidden" symmetries were utilized in Ref. [161] to construct an ansatz for the field A'_μ, satisfying the massive vector wave equation, that separates radial and angular dependencies. The ansatz makes use of the Killing-Yano symplectic 2-form $\boldsymbol{h}$, whose tensor components satisfy $\nabla_\mu h_{\nu\gamma} = 2g_{\mu[\nu}\xi_{\gamma]}$. The vector field ansatz of frequency ω and azimuthal index m reads [161]

$$A'^\mu = B^{\mu\nu}\nabla_\nu Z, \qquad\qquad Z = R(r)S(\theta)e^{-i(\omega T - m\varphi)} \tag{D.2}$$

in Boyer-Lindquist (BL) coordinates (T, r, θ, φ). The polarization tensor $B^{\mu\nu}$ is implicitly defined by $B^{\alpha\beta}(g_{\beta\gamma} + ih_{\beta\gamma}) = \delta^\alpha_\gamma$ utilizing the Killing-Yano 2-form. Due to the presence of

$\boldsymbol{\xi}$ and $\boldsymbol{\eta}$ in the spacetime, the temporal and azimuthal dependencies are trivially satisfied. The radial and polar dependencies are determined by solving a nonlinear ordinary differential eigenvalue problem with eigenfunctions $R(r)$ and $S(\theta)$ and complex eigenvalues ω and ν of the form, $\mathcal{D}^r_{\omega,\nu}R(r) = 0$ and $\mathcal{D}^\theta_{\omega,\nu}S(\theta) = 0$, where $D^{r,\theta}_{\omega,\nu}$ are second order ordinary differential operators depending on r and θ only. Bound state solutions are obtained by imposing ingoing radiation boundary conditions at the horizon, and asymptotically flat boundary conditions at spatial infinity. For details on how the polar equation is solved, see Ref. [137]. The radial solution is expanded around the outer horizon, $r \geq r_+$, with $r_\pm = M \pm \sqrt{M^2 - a^2}$, in a Frobenius series of the form [137]

$$R_{\rm near}(r) = \hat{r}^{i\kappa}(1 + \hat{a}_1\hat{r} + \hat{a}_2\hat{r}^2 + \dots), \tag{D.3}$$

with $\kappa = 2mr_+(\omega - m\Omega_{\rm BH})/(r_+ - r_-)$, coefficients $\hat{a}_i$, and $\hat{r} = (r - r_+)(r_+ - r_-)^{-1}$. The coefficients $\hat{a}_i$ can be solved for by plugging $R_{\rm near}(r)$ into the radial equation $\mathcal{D}^r_{\omega,\nu}R(r) = 0$. The near-horizon solution (D.3) is then used to numerically integrate the radial second order ordinary differential equation outwards from $r_s = r_+ + \epsilon$ towards large $r \gg 10/(\alpha\mu)$, with $\epsilon = 10^{-4}M$ typically, in the spirit of the shooting method. Integration cannot start at $r = r_+$, as the BL coordinates are singular on the event horizon. For further details, see Refs. [137, 338]. The superradiantly unstable vector cloud can then be reconstructed with Eq. (D.2).

Our numerical setup, outlined in App. D.2, utilizes the Kerr spacetime in Cartesian Kerr-Schild (KS) coordinates (t, x, y, z). Therefore, the relevant spacelike hypersurface is the surface of constant KS coordinate time t, not BL time T; these are two *different* slices of the Kerr spacetime. Therefore, we transform the above constructed vector field A'^μ from BL coordinates to KS coordinates. The two gauges are related by

$$\begin{aligned} t &= T + \frac{M^2 \log\frac{r-r_+}{r-r_-}}{\sqrt{M^2 - a^2}} + M\log\Delta, \\ x &= \sin\theta(r\cos\bar{\phi} - a\sin\bar{\phi}), \\ y &= \sin\theta(a\cos\bar{\phi} + r\sin\bar{\phi}), \\ z &= r\cos\theta, \end{aligned} \tag{D.4}$$

where $\Delta = a^2 - 2Mr + r^2$. The inverse of these relations is

$$\begin{aligned} T &= t - \frac{M^2 \log \frac{r-r_+}{r-r_-}}{\sqrt{M^2-a^2}} - M \log \Delta, \\ r &= 2^{-1/2}\Big[-a^2 + x^2 + y^2 + z^2 \\ &\qquad + \sqrt{4a^2z^2 + (a^2 - x^2 - y^2 - z^2)^2}\Big]^{1/2}, \\ \phi &= \arctan\left[\frac{rx + ay}{-ax + ry}\right] - \frac{a \log \frac{r-r_+}{r-r_-}}{2\sqrt{M^2-a^2}}, \quad x > 0 \\ \theta &= \arccos \frac{z}{r}, \end{aligned} \tag{D.5}$$

where $\bar{\phi} = \phi + (2\sqrt{M^2-a^2})^{-1} a \log[(r-r_+)(r-r_-)^{-1}]$, valid outside the event horizon $r > r_+$. Using these coordinate transformations, we transform the massive vector field to KS coordinates for $r > r_+ + \epsilon$. Subtleties arise for $r < r_+ + \epsilon$. However, it is necessary for the successful evolution of the system of equations in the interaction basis that the source term is defined (at the very least) everywhere outside the event horizon $r \geq r_+$, and while *all* modes on the horizon are marginally trapped, the finite difference length scale (potentially) allows for values at points inside the horizon to numerically affect points just outside the horizon. Furthermore, the exponential blue-shift captured in the transformation rules (D.4) and (D.5) of the type $\cos \log(r - r_+)$ for $r > r_+$ leads to an exponential amplification of any truncation error in the numerical solution of the radial and angular equations $\mathcal{D}^r_{\omega,\nu} R(r) = 0$ and $\mathcal{D}^\theta_{\omega,\nu} S(\theta) = 0$. Hence, any power-like converging numerical truncation error is exponentially enhanced for $r \to r_+$, and dominates the solution for some r_d with $r_d > r > r_+$. To address this subtlety, we employ a C^4-transition function $f_t(r)$ that matches the Frobenius solution $R_{\text{near}}(r)$, valid for $r \gtrsim r_+$ and the numerical solution $R_{\text{num.}}(r)$, valid for $r > r_+ + \epsilon$, in the overlap region $r_+ + \epsilon < r < r_+ + 10^2\epsilon$: $R_{\text{matched}}(r) = f_t R_{\text{near}}(r) + (1 - f_t) R_{\text{num.}}(r)$. In addition to these manipulations at small radii, we also need to address the exponential fall-off as $r \to \infty$. Due to finite floating point precision, the shooting method will inevitably switch from the exponentially decaying solution into the exponentially diverging solution at some large $r = r_{\text{max}}$. Therefore, in order to provide sensible estimates also for $r > r_{\text{max}}$ (which is necessary since we are working with a compactified setup that includes spacelike infinity, as outlined below in App. D.2), we fit an exponential of the form ae^{-br} for $b > 0$ to the solution $R_{\text{num.}}(r)$ in the range $r \in (0.9 r_{\text{max}}, r_{\text{max}})$. With this, we obtain a $R_{\text{matched}}(r)$ that is valid for $r \in (r_+, \infty)$.

Finally, the 3+1 superradiant vector variables are projected with respect to the t=const. spacelike hypersurface using the hypersurface normal n^μ and the projector $\gamma^\alpha{}_\beta = \delta^\alpha_\beta +$

$n^\alpha n_\beta$ (further details can be found in App. D.2). In this framework, the vector field decomposes into $\chi_\phi \equiv -n_\mu A'^\mu$ and $\chi^i \equiv \gamma^i{}_\mu A'^\mu$, which are reconstructed from the matched and extrapolated radial solution, in conjunction with the polar solution, the transformation rules (D.5) and (D.4), and ansatz (D.2), everywhere in the $t = \text{const.}$ spacelike hypersurface with $r > r_+$. Lastly, we find better convergence properties of the $D_i B^i = 0$ constraint close to the BH event horizon if a buffer region between the event horizon and the excision surface in the BH interior is used. To that end, we utilize second order extrapolation of all 3+1 variables along lines of constant θ, φ, t from $r > r_+$ to $r_- < r < r_+$ to ensure well-defined gradients at r_+, we utilize zeroth order extrapolation from a distance of $\delta = 10^{-4}M$ away from the spin-axis to set the cloud values *on* the axis in KS coordinates, since the BL coordinates also exhibit a coordinate singularities at the poles. The time-dependence of the cloud in KS coordinates is then simply $\chi_\phi, \chi_i \sim e^{i\omega t}$. In this work, we consider only those superradiance clouds that arose from the fast growing modes, and subsequently saturated the superradiance condition, i.e., satisfying $\omega = m\Omega_{\rm BH}$. That is, we focus on $m = 1, \hat{n} = 0$, and $S = -1$ clouds, in the language of [338] (corresponding to $(j, n, l, m) = (1, 1, 0, 1)$, introduced in Sec. 5.2). Properties of the clouds considered in this work are given in Table D.1. These states are expected to be the endstate of the instability to a good approximation [141, 145], and hence, exhibit vanishing growth rates.

We test our numerical implementation of the above described reconstruction of the cloud in KS coordinates by considering the numerical truncation error τ of the massive vector wave equation (D.1) in KS coordinates: $\tau = \sum_\alpha |(\Box_{\rm Kerr,KS} - \mu^2)(\chi_\phi n_\alpha + \chi_\alpha)|$. Inside the event horizon, the truncation error τ is divergent with decreasing grid spacing h, which is likely due to inaccuracies in the extrapolation procedure described above. On the event horizon, the truncation error shows marginal point-wise convergence $\tau|_{r=r_+} \sim \mathcal{O}(h^{1/2})$ or better. To quantify the convergence behavior outside the event horizon, in the coordinate

α	ωM	a_*
0.1	0.099485	0.382787
0.2	0.195543	0.678411
0.3	0.283390	0.857953
0.4	0.357498	0.946250

Table D.1: The properties of the four clouds used in the main text. We consider only the $m = 1, \hat{n} = 0$ and $S = -1$ superradiant vector boson clouds in the language of Ref. [338] [corresponding to $(j, n, l, m) = (1, 1, 0, 1)$ used in Sec. 5.2] around spinning BHs of mass M and dimensionless spin a_*. The saturation condition, $\omega = \Omega_{\rm BH}$, fixes the spin a_* for each α.

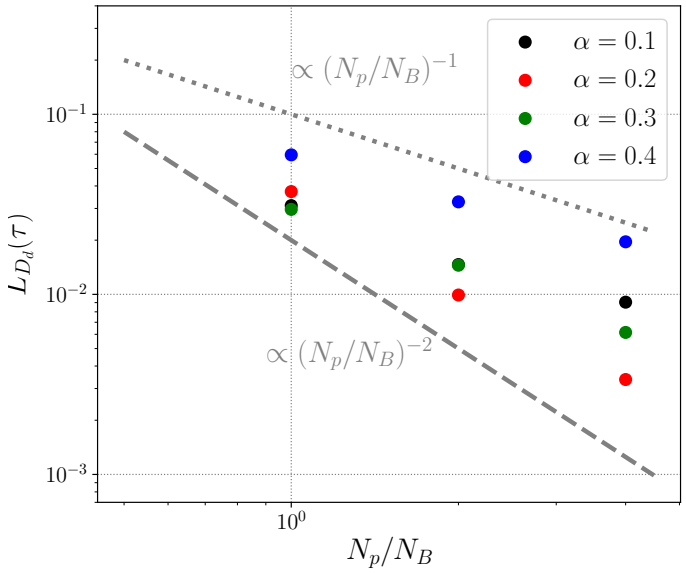

Figure D.1: The norm $L_{D_d}(\tau)$ of the residual of the massive vector wave equation, defined in (D.6), as a function of the number of grid points N_p considered with respect to the base resolution N_B. The default resolution used for each of the configurations given in table D.1 and presented throughout the main text is $N_p/N_B = 2$.

domain D, we introduce the norm $L_D(f)$ of function f as

$$L_D(f) \equiv \int_D d^3x\sqrt{\gamma}|f|, \tag{D.6}$$

where $d^3x\sqrt{\gamma} = d^3x\sqrt{\det\gamma_{ij}}$ is the volume form of the spacelike hypersurface. Here, and in the following, the domain $D = D_d$ is the coordinate shell defined by the radii $10r_c > r > r_+$ (recall, $r_c = 1/(\mu\alpha)$ is the cloud's Bohr radius). The norm of the truncation error converges approximately as $L_{D_d}(\tau) \sim \mathcal{O}(h^2)$ for $\alpha \in \{0.2, 0.3\}$ and as $L_{D_d}(\tau) \sim \mathcal{O}(h^1)$ for $\alpha \in \{0.1, 0.4\}$, see Figure D.1. We use second order accurate methods to compute the residual τ. This convergence behavior can be explained by considering the shooting method underlying the reconstructed solution. As discussed above, any remaining truncation error close to the horizon is exponentially amplified, while at large radii, the shooting method inevitable switches from the exponentially decaying solution to the exponentially increasing solution due to finite floating point accuracy (see also a discussion of this in [338]). While our shooting method implementation makes use of higher-than double-precision floating point arithmetic, the convergence is ultimately limited, especially for small α. Further, the extrapolation of the cloud to the spin-axis in KS coordinates, and the exponential

extrapolation at large radii, can further reduce the convergence rate, especially at large α. Therefore, even slow convergence is a good sign of correct implementation of the superradiant source terms in our compactified KS evolution implemented discussed next.

D.2 Numerical evolution setup

Our calculations are carried out on a fixed rotating BH background of mass M and dimensionless spin a_*. We adopt the Kerr metric $g_{\alpha\beta}$ in Cartesian Kerr-Schild coordinates (t, x, y, z), with line element

$$\begin{aligned} ds^2 = & -dt^2 + dx^2 + dy^2 + dz^2 \\ & + \frac{2Mr^3}{r^4 + a^2M^2z^2}\Big[dt + \frac{z}{r}dz \\ & + \frac{r(xdx + ydy)}{r^2 + a^2M^2} - \frac{aM(xdy - ydx)}{r^2 + a^2M^2}\Big]^2, \end{aligned} \tag{D.7}$$

where r satisfies $(x^2 + y^2)/(r^2 + a^2) + z^2/r^2 = 1$. However, we evolve the fields using a $3 + 1$ space–time decomposition, making using of several such geometric quantities. This includes the unit normal to slices of constant time, which can be decomposed as $n^\mu = (1, -\beta^i)/N$, where N and β^i are the lapse and shift vector, respectively. There is also the spatial metric/projection operator $\gamma_{\mu\nu} = n_\mu n_\nu + g_{\mu\nu}$, the extrinsic curvature tensor $K_{ij} = -(D_t\gamma_{ij})/(2N)$, where $D_t = \partial_t - \mathcal{L}_\beta$ with $\mathcal{L}_\beta$ the Lie derivative along the shift. In a Minkowski spacetime in Cartesian coordinates these 3+1 variables would be $N = 1$, $\beta^i = 0$, $\gamma_{ij} = \delta_{ij}$, and $K_{ij} = 0$. For convenience, we also define also the covariant derivative D_i defined with respect to γ_{ij}, as well as the trace of the extrinsic curvature $K = K_{ij}\gamma^{ij}$.

The kinetically mixed Maxwell's equations, presented in covariant from in (5.13), in terms of the visible electric and magnetic fields are given by

$$\begin{aligned} D_tE^i &= NKE^i + \varepsilon^{ijk}D_j(NB_k) - NJ^i + N\varepsilon\mu^2\gamma^i{}_\mu A'^\mu, \\ D_tB^i &= NKB^i - \varepsilon^{ijk}D_j(NE_k), \\ D_iE^i &= \rho_q + \varepsilon\mu^2 n_\mu A'^\mu, \\ D_iB^i &= 0, \end{aligned} \tag{D.8}$$

where $\varepsilon^{ijk} = \varepsilon^{ijk\alpha}n_\alpha$ is the 3-dimensional Levi-Civita tensor. These evolution equations (D.8) are discretized using fourth-order accurate spatial finite-difference stencils, in conjunction with fourth-order Runge-Kutta integration in time [149, 148]. All simulations are

performed on a 3D Cartesian grid that includes spatial infinity through the use of compactified coordinates (details can be found in [306]). Sixth-order, Kreiss-Oliger-type numerical dissipation is applied to the evolution variables for numerical stability. This further dissipates shorter wavelength features at large distances beyond the compactification scale, minimizing reflection off spatial infinity. We use between ten and seven mesh-refinement levels centered on the BH, with refinement ratio $2:1$, for $\alpha = 0.1$ through $\alpha = 0.4$, respectively. We choose the finest level to have length roughly twice the diameter of the BH in each linear dimension. The system is rescaled so that $20\mu^{-1}\alpha^{-1} = 20r_c$ is roughly equal to the compactification scale (recall r_c is the cloud's Bohr radius). This allows us to resolve both the scale set by the BH, as well as that set by the superradiance cloud, for sufficiently long times as to ensure relaxation into a quasi-equilibrium state. For all cases, we use a grid spacing of $\Delta x \approx 0.03M$ on the finest mesh refinement level. Due to this scaling, radiation extraction can be done up to a distance of $r \leq 10r_c$; beyond this distance, high-frequency radiation modes are no longer sufficiently resolved in the wave extraction zone due to the compactification of the domain. The Maxwell equations with an Ohm's law become stiff in the high conductivity limit (discussed further in App. D.3). Hence, at conductivies of $\sigma/\mu > 2$, we adjust the time-step Δt to account for this behavior. For $\alpha = 0.3$, we decrease it gradually with increasing conductivity from $\Delta t/\Delta x = 0.5$ down to $\Delta t/\Delta x = 0.075$ to achieve a robust numerical evolution. For $\alpha \in \{0.1, 0.2, 0.4\}$ and $\sigma/\mu = 20$, we scale Δt, such that $\sigma\Delta t$ remains as small, or smaller than, the value of $\sigma\Delta t$ for $\alpha = 0.3$, everywhere in the relevant computational domain. The construction of the superradiance cloud is described in detail in App. D.1. As we are neglecting backreaction of the presence of the plasma and massless electromagnetic fields, the superradiance cloud is not evolved numerically, rather it is a pre-prescribed function of time.

The set of equations (D.8) is comprised of the two constraints, the Gauss law for electric and magnetic fields, and the Faraday equation and Ampere's law as evolution equations. Numerically, we damp possible violations of the constraint equations by means of two constraint-damping fields Φ and Ψ [124, 284]. To that end, we perform the replacements $D_t B^i \to D_t B^i - N D^i \Phi$ and $D_t E^i \to D_t E^i - N D^i \Psi$ at the level of the evolution equations in (D.8). Furthermore, we promote the constraint equations to evolution equations for these auxiliary fields, following Refs. [124, 284]:

$$\begin{aligned} D_t \Psi &= -N(D_i E^i - \varepsilon\mu^2 n_\mu A'^\mu - \rho_q) - N\kappa\Psi, \\ D_t \Phi &= -N D_i B^i - N\kappa\Phi. \end{aligned} \tag{D.9}$$

This ensures that any numerical violation of the constraints $D_i E^i - \varepsilon\mu^2 n_\mu A'^\mu - \rho_q = 0$ and $D_i B^i = 0$ are damped exponentially over timescales $1/\kappa$. For all (resistive) force-free simulations, the constraint $D_i E^i - \varepsilon\mu^2 n_\mu A'^\mu - \rho_q = 0$ is trivially satisfies since the charge

density is *defined* to be $\rho_q = D_i E^i - \varepsilon\mu^2 n_\mu A'^\mu$. Hence, unless we explicitly assume vacuum (and in particular, set $\sigma = 0$), Ψ is identically zero. In all cases, the initial conditions for these auxiliary fields is $\Phi = \Psi = 0$. In addition, we perform ideal force-free simulations by means of two ad-hoc field modifications applied at each grid point after an evolution step [284, 283] (see Ref. [27] for a discussion):

$$E^i \to E^j \left(\delta^i_j - \frac{B_j B^i}{B^2}\right), \tag{D.10}$$

$$E^i \to E^i \left\{1 - \hat{\theta}(\lambda) + \hat{\theta}(\lambda)\frac{B}{E}\right\}, \tag{D.11}$$

where $\lambda = E^2 - B^2$ and $\hat{\theta}$ is the Heaviside function. This prescription enforces the two force-free conditions, $E_i B^i = 0$ and $B^2 > E^2$, by explicitly rescaling the electric field at each grid point. The rescaling is a form of ad-hoc numerical dissipation that is not physically motivated and reproduces physical dissipation behavior only in special cases. Therefore, as pointed out in the main text, the dissipation estimates provided by these force-free evolution schemes should be interpreted with caution.

The evolution of the system proceeds as follows. We evolve the system towards its equilibrium state in several steps. Initially, we set the fields to visible fields to zero $E^i = B^i = 0$ and evolve until time $t = t_s$ assuming vacuum $I^\alpha = 0$. With $t_s \approx 5/\mu$, this allows the system to equilibrate at roughly $E^i = \varepsilon E'^i$ and $B^i = \varepsilon B'^i$, which is purely the superradiance cloud's contribution to the visible fields. During this time, we utilize both the electric and magnetic field's Gauss constraint cleaning potentials Φ and Ψ. These ensure that constraint violations in the magnetic field are kept small, as well as efficiently remove constraint violations of the $E^i = 0$ initial data on timescales $1/\kappa \ll t_s$. At $t = t_s$, the resistive current (5.37) is discontinuously turned on, and the system is evolved until the total Poynting flux at the largest radii where we extract it is relaxed to a quasi-constant value. For $\alpha = 0.4$, we found that this required the system to be evolved for $\sim 8t_{\rm LC}$ light crossing times of the entire cloud, defined as $t_{\rm LC} = 10r_c$, whereas for $\alpha = 0.1$, we evolved the system for $\sim 3t_{\rm LC}$. During the evolution of the system, we monitor the behavior of the Gauss constraint $D_i B^i = 0$ throughout the entire domain. This provides a measure for the rate of convergence of the numerical solution, and the self-consistency of the numerical implementation.

To test the numerical implementation of the kinetically mixed force-free Maxwell equations, together with the reconstruction of the massive vector field modes, we begin by considering the $\alpha = 0.3$ vacuum case $\sigma = 0$. To that end, we consider (D.8) with $I^\mu = 0$, and perform a series of simulations with increasing resolution starting from vacuum initial

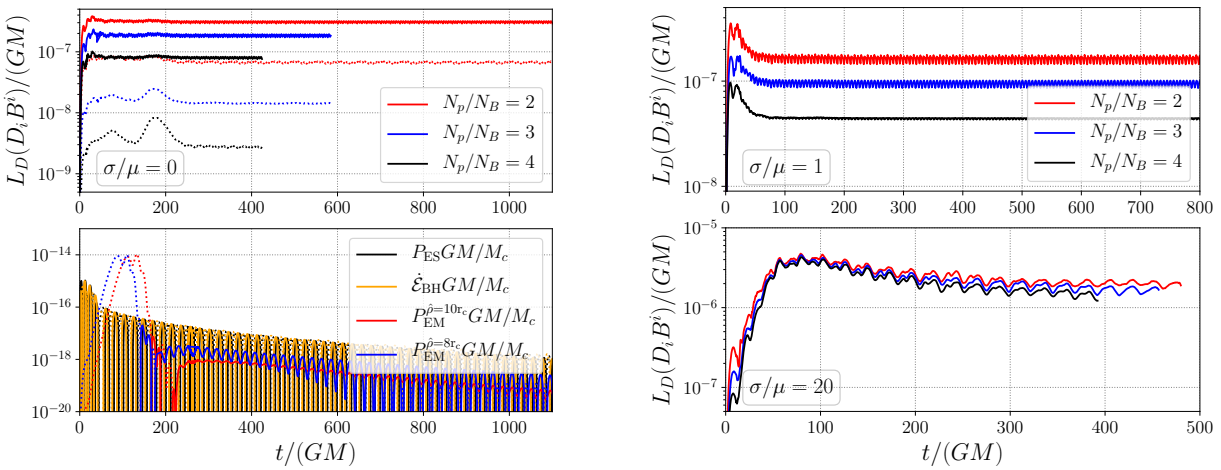

Figure D.2: *(right and top left)* We present the convergence of the norm (D.6) of the Gauss constraint D_iB^i within domains D_s (solid lines) and D_d (dashed lines) for the $\alpha = 0.3$ system at three different conductivities σ. The former is the entire domain outside the outer horizon with $r > 1/\mu$ (i.e., neglecting the near-horizon behavior), whereas the latter is the entire domain outside the BH $r > r_+$. N_p/N_B is defined as in Figure D.1, and we set $\varepsilon = 10^{-6}$. *(bottom left)* We plot the Poynting fluxes across the ergosurface, $P_{\rm ES}$, the event horizon, $\dot{\mathcal{E}}_{\rm BH}$, as well as the flux $P_{\rm EM}$ coordinate radii $r = 8r_c$ and $r = 10r_c$ in the $\alpha = 0.3$ cloud with $I^\mu = 0$ and $\varepsilon = 10^{-6}$.

data: $B_i = E_i = 0$. To demonstrate the correct implementation of the equations, we monitor the evolution of the constraints $D_iB^i = 0$. In Figure D.2, we show the convergence of this Gauss constraint with grid spacing h utilizing the norm defined in (D.6). As can be seen there, roughly $L_{D_s}(D_iB^i) \sim \mathcal{O}(h^{3.5})$, whereas $L_{D_d}(D_iB^i) \sim \mathcal{O}(h^2)$. Therefore, in the bulk of the vector cloud, the convergence is roughly fourth order, as expected. Close to the event horizon, convergence is slower. This may be attributed to the presence of the excision surface close to the event horizon, as well as the lower convergence order of the massive vector cloud residual τ just outside the horizon. The constraint $D_iE^i - \varepsilon\mu^2 n_\mu A'^\mu = 0$ (not shown here) is violated by the initial data, but quickly becomes dominated by converging truncation error after a few periods of the cloud. This could be improved upon, by choosing constraint satisfying initial data. However, the goal of this work is to investigate the system with non-vanishing charge density, and at late times, the latter constraint is satisfied to floating point accuracy if $I^\mu \neq 0$. Moving to cases with non-vanishing conductivity, we show in Figure D.2 the convergence properties of $\alpha = 0.3$ systems for $\sigma/\mu = 1$ and $\sigma/\mu = 20$. The former exhibits the same convergence behavior as the vacuum case, whereas

the latter follows roughly $L_{D_d}(D_i B^i) \sim \mathcal{O}(h^{0.6})$. This can be explained by considering the scales of the features that need to be resolved. As we showed in the main text, the scale of the features is roughly given by $1/\sigma$, which translates into a length scale of $\ell \approx 0.17M$ for $\alpha = 0.3$. On the finest level, the grid spacing, $\Delta x = 0.03GM$, is sufficient to resolve these features, while on coarser levels, numerical dissipation likely dampens these scales efficiently. This damping is numerical, rather than physical, in nature, and does not obey the Maxwell equations, and therefore, leads to a larger violation of the Gauss constraint and worse convergence properties.

Apart from the convergence of the constraints, the vacuum quasi-stationary state, after several $t_{\rm LC}$, should exhibit no energy flux across the event horizon, as it is, by construction, synchronized with the BH angular velocity. In practice, there are various sources of numerical error that can spoil this property. The synchronization condition $\omega = \Omega_{\rm BH}$ can be achieved only up to finite precision, when solving for the superradiance cloud. Finite resolution both in the evolution scheme, as well as in the cloud construction scheme, may also leave room for the solution to develop a small, but finite, energy flux across the horizon and towards spatial infinity. To quantify this, and to obtain a rough estimate for the time at which the system is truly settled, $t_{\rm settle}$, we monitor the energy fluxes across the horizon, the BH ergosurface, and coordinate spheres of radius $\hat{\rho} = 8r_c$, and $\hat{\rho} = 10r_c$ in Figure D.2. In the continuum limit, with $\omega = \Omega_{\rm BH}$ exactly, we expect all these fluxes to be zero. Therefore, the flux evolution presented in Figure D.2 can be used to establish $t_{\rm settle}$, i.e., when the system has reduced the superradiance cloud's emission powers to the degree necessary.

We briefly comment on issues related to performing simulations of the superradiance cloud system in the small-α limit. In the Newtonian limit, the massive vector wave equation on a Kerr background is obtained by expanding in small α to leading order. All spin-effects are subleading in this expansion, and the leading contribution is solely given by the far-zone Newtonian potential of the BH $\sim GM/r$. In this limit, the vector wave equation reduces to a radial Schrödinger-type equation with solution (5.8). Within a numerical time-domain evolution setup, the singular behavior of the Newtonian potential at the location of the BH poses challenges. However, there are subtleties associated with replacing the far-zone weak-field metric by Minkowski both in the interaction and mass eigenbases ((5.12) and (D.21), respectively). Within the mass eigenbasis, the force-free condition (or resistive generalization thereof) $F^{\alpha\beta} I_\beta = 0$, depends on the electric and magnetic field components of (5.8). The non-relativistic field (5.8) and its electric and magnetic field components are multivalued, i.e., discontinuous, at the origin, leading to a breakdown in the validity of numerical schemes around the origin. Additionally, the usual force-free current would require modification, as it requires the field (5.8) to satisfy the

corresponding Maxwell equations on a weak-field background spacetime. As noted above, a weak-field metric is numerically challenging to implement, such that the choice of a flat background introduces inconsistencies when using the (resistive) force-free current. These could be remedied, however, by including terms involving higher order derivatives of the massive vector field (5.8) in the equations, but this would add further complications at the origin. By contrast, the evolution equations in the interaction basis depend only on A'_μ, and not on its spatial derivatives; hence, the interaction basis evolution approach allows one to evolve the system self-consistently on a flat background. On the other hand, this choice is accompanied by subtleties associated with the photon-dark photon interaction term in (5.12). The massless state can mix into the massive state as it radiates towards infinity. In a weak-field metric, this mixing prevents the massive component of the visible field A_μ from radiating to infinity, as it is bound to the central gravitational potential. In the flat spacetime limit, leakage of the massive state into radiation emitted to infinity is not prevented (an illustration of this behavior is presented in Figure D.4). Therefore, in this context, any radiated Poynting flux is to be understood as an upper bound for the total emitted power. All these subtleties are absent in the fully-relativistic calculations we use as our main results, where the relativistic clouds constructed in App. D.1 is considered on a Kerr BH background spacetime as described above.

D.3 Resistive force-free currents

In this appendix, we discuss different resistive generalizations of force-free electrodynamics used in the literature to identify the approach most applicable in the kinetically-mixed scenario at hand. In the main text, we demonstrated that the system is characterized by turbulence and magnetic reconnection with efficient energy dissipation into the plasma. In principle, there are two feasible approaches for capturing these effects: resistive magneto-hydrodynamics and kinetic PIC methods. PIC methods, which capture the macro- and micro-physics, are ideally suited to tackle the magnetosphere of the kinetically mixed super-radiance cloud. However, as we are interested in the overall electromagnetic power-output and large scale features of the system in three dimensions, PIC simulations are prohibitively computationally expensive, especially on a curved background BH spacetime. Full resistive magnetohydrodynamics, on the other hand, is notoriously difficult to apply to regimes in which the plasma mass density is far below the energy density of the electromagnetic field, which is the case for the superradiant system considered here. Hence, we choose to use a resistive approach where the plasma dynamics is not directly tracked, and rely only on the electromagnetic field's evolution. A few approaches have been developed in the literature,

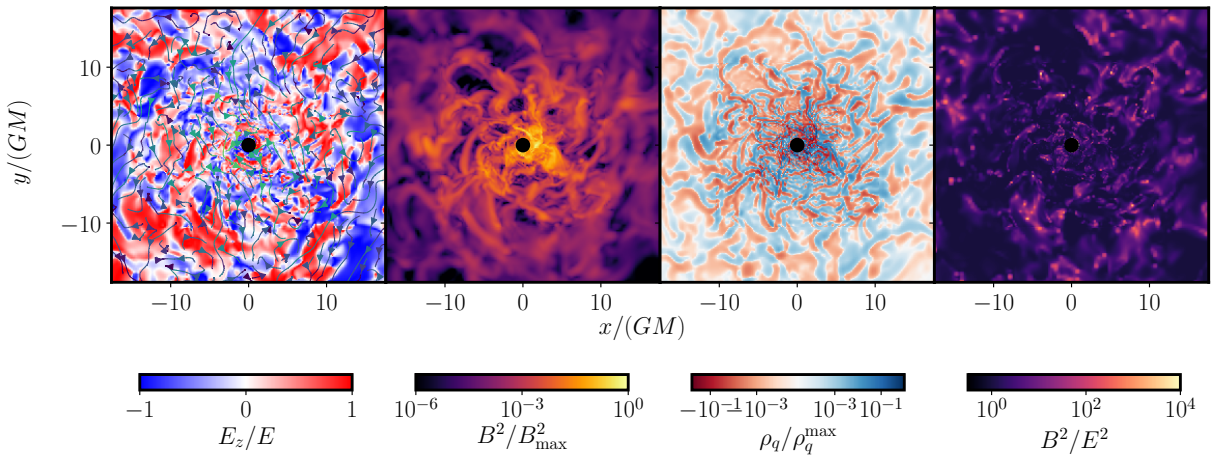

Figure D.3: We show the visible electric and magnetic fields, charge density, and the ratio of electromagnetic field magnitudes obtained from a force-free simulation using the current (D.13), with prescription (D.11) for a superradiance cloud system with $\alpha = 0.3$ and a BH spin of $a_* = 0.86$. In the case of the visible electric field, the field line color code is the same as in Figure 5.5.

particularly to model the resistive regions of pulsar magnetospheres [227, 180, 238, 290, 213] (see also Refs. [284, 282]). All are based on an electromagnetic current J^i that aims to capture the physics of a highly conducting plasma in strong electromagnetic fields, while being specified solely in terms of the electromagnetic fields. Generally, this current can be decomposed into a piece describing the drift velocity of the charges, v_d^i, and a contribution orthogonal to the drift velocity

$$J^a = \rho_q v_d^a + J_\perp^a. \tag{D.12}$$

In all (resistive) force-free approaches, the charge density is defined using the (kinetically-mixed) electric Gauss law: $\rho_q = D_i E^i - \varepsilon\mu^2 n_\mu A'^\mu$. In the following, we briefly review the currents considered in the literature, apply these to kinetically-mixed superradiance clouds in the non-relativistic limit, and compare our findings with the vacuum and force-free limits in order to evaluate their applicability.

We begin with a discussion of the commonly invoked force-free paradigm, which assumes vanishing Lorentz force $F^{\mu\nu} I_\nu$, as well as $F_{\mu\nu}F^{\mu\nu} > 0$ and $F_{\mu\nu}(*F)^{\mu\nu} = 0$. In terms of electric and magnetic fields, the last two conditions are, respectively, equivalent to magnetic dominance $B^2 > E^2$ and $E_i B^i = 0$. With these assumptions, the corresponding force-free current is given by (the relativistic contributions in the form of the extrinsic curvature K

and covariant derivative D_i are defined in App. D.2)

$$\begin{aligned} v_d^a &= \frac{\varepsilon^{ajk} E_j B_k}{B^2}, \\ J^a_{\perp,\mathrm{FF}} &= \frac{B^a}{B^2}\Big[2K B_i E^i - 2K_{ij} E^i B^j + B_i \epsilon^{ijk} D_j B_k \\ &\quad - E_i \epsilon^{ijk} D_j E_k + \varepsilon \mu^2 B_i \gamma^i_\mu A'^\mu\Big]. \end{aligned} \tag{D.13}$$

The current is perpendicular to the electric field, and there is no dissipation of electromagnetic energy. Therefore, the force-free limit of ideal magnetohydrodynamics excludes resistive processes or transfer of electromagnetic energy to the plasma (e.g., particle acceleration, magnetic reconnection, plasma heating, etc.), which however, are active throughout the superradiance cloud due to the *electric* dominance of the fields A'_μ in vacuum. Notice, the plasma drift velocity v_d^a is entirely determined by the dynamics of the electromagnetic fields. While the force-free approximation is, in principle, ideal, it can break down at current sheets and places where magnetic dominance is lost. Numerically, this is handled with numerical dissipation which is particularly large in turbulence driven regimes (due to the cascade to short, unresolved wavelengths), as well as by (as noted in App. D.2) enforcing the force-free conditions by rescaling the visible electric field, as shown in (D.11). We perform a set of force-free simulations of the $\alpha = 0.3$ and $a_* = 0.86$ cloud-plasma system. As the turbulent features reach scales much below the grid scale of our simulations, numerical dissipation and the prescription (D.11) efficiently remove energy that was sourced by the superradiance cloud. Therefore, it serves as an artificial source of dissipation, that nonetheless agrees well with the $\sigma \to \infty$ extrapolations shown in Figure 5.12. Regardless, results from these force-free simulations should be interpreted with caution and in light of the un-physical dissipation mechanism. In Figure D.3, we show the force-free solution the system attains at late times (with strong numerical dissipation in the bulk of the cloud). In all cases, the magnetic Gauss constraint is non-convergent, while the time-averaged outgoing Poynting flux and energy injection from the superradiance cloud are roughly consistent across resolutions to within an $\mathcal{O}(1)$-factor (the Poynting flux estimates is shown in Figure 5.12). For all the numerical resolutions we considered, features emerged on the grid scale, suggesting the endstate of the pair production cascade is a bulk turbulent state. As can be seen in Figure D.3, no large scale electric field and charge separation persists, while $E_z/E \sim \mathcal{O}(1)$. The numerical implementation, by construction, removes any violation of $B^2 > E^2$ at each grid point after each timestep, such that the ratio B^2/E^2, shown in last panel in Figure D.3, is strictly larger than unity. Similarly, the violations of $E_i B^i = 0$ are at the level of floating point error.

In the context of resistive magnetohydrodynamics, a macroscopic resistivity is intro-

duced by means of a suitably chosen Ohm's law with conductivity σ. In order to recover the force-free approximation in the $\sigma \to \infty$ limit and to maintain a form for the electrodynamics that does not require one to also keep track of the fluid dynamics, all resistive force-free approaches assume the drift velocity v_d^i of the charges is altered as [180] (see also Ref. [227] for a similar approach)

$$\begin{aligned} v_d^i =& \frac{\varepsilon^{ijk} E_j B_k}{B^2 + E_0^2}, \qquad E_0^2 = B_0^2 + E^2 - B^2, \\ B_0^2 =& \frac{1}{2}\left[B^2 - E^2 + \sqrt{(B^2 - E^2)^2 + 4(E_i B^i)^2}\right]. \end{aligned} \tag{D.14}$$

Thus, even for fields with $E^2 > B^2$, the drift velocity v_d^i is bounded by the speed of light due to the additional electric field contribution E_0^2 in the denominator compared with the force-free prescription (D.13). Non-vanishing $E_i B^i$ can only reduce the resulting drift velocity further. This ensures that around current sheets within a strongly magnetized plasma, the characteristic speeds remain physical. Three distinct methods to construct $J_\perp^i$ have been considered in the literature. In Ref. [181], the Ohm's law was applied in the frame of vanishing charge density, referred to as *(A)* in the following. In Ref. [238] (see also Ref [245]), the Ohm's law was applied in the minimal velocity (with respect to the "lab" or simulation frame) fluid frame, labeled as *(B)* in what follows. Lastly, the approach of Ref. [290] introduces resistive effects with a prescription driving $E_i B^i$ towards $J^i B_i/\sigma$ over some arbitrary timescale $1/\kappa$, called approach *(C)* from here on. Beyond the drift velocity, the three approaches *(A)*, *(B)*, and *(C)* differ.

Comparing the three currents, method *(A)* is manifestly covariant, but lacks a well-defined vacuum limit, while both *(B)* and *(C)* exhibit $J^i \to 0$ as $\sigma \to 0$. Since the superradiant system is well-understood a priori only in the vacuum limit, we focus on *(B)* and *(C)* in this discussion. Explicitly, the orthogonal component of the current *(B)* constructed in Ref. [245, 238] reads

$$J^a_{\perp,(B)} = \sigma E_0 \sqrt{\frac{B^2 + E_0^2}{B_0^2 + E_0^2}} \frac{E_0 E^a + B_0 B^a}{B^2 + E_0^2}. \tag{D.15}$$

The prescription, *(C)* modifies the force-free contribution as [290]

$$J^a_{\perp,(C)} = \frac{\sigma}{(\sigma + \kappa)} \left(J^a_{\perp,\mathrm{FF}} + \kappa E^i B_i \frac{B^a}{B^2} \right). \tag{D.16}$$

Here, the driving timescale $1/\kappa$ can be understood by contracting the above current by

B^a, using the Maxwell equations to arrive at

$$D_t(E_iB^i) = -\kappa N\left(E^i - \frac{1}{\sigma}J^i\right)B_i, \tag{D.17}$$

such that E_iB^i is driven towards J_iB^i/σ. Note, we assume the resulting system to be hyperbolic (see e.g., Refs. [225, 296] for a discussion).

Physically, these currents describe the interaction of an effective plasma with the visible electromagnetic fields, assuming $E^2, B^2 \gg \rho_p, P_p$, where ρ_p and P_p are the plasma's mass density and pressure. The $\sigma \to 0$ limit corresponds to the vacuum limit. To understand this, consider the charge conservation $\nabla_\mu I^\mu = 0$. In the Eulerian frame, together with (5.31), this leads to

$$D_t\rho_q = N\rho_q K - D_i(NJ^i) = N\rho_q K - D_i(N\rho_q v_d^i) = 0. \tag{D.18}$$

Hence, if the initial conditions satisfy $\rho_q = 0$, then the system does not acquire a non-trivial charge distribution dynamically, i.e., in a medium with small conductivity charges cannot separate. This implies that the resistive currents above reduce to $I^\mu = 0$, assuming the initial data is neutral. Therefore, the $\sigma = 0$ regime is the vacuum limit of the system. Moving away from this limit to non-zero, but small conductivities, $\sigma \ll \mu$, the effective fluid coupling to the visible electromagnetic fields is an efficient insulator. The current I^μ is timelike, and J^i is advection dominated. Due to the residual conductivity, the charges in the insulating fluid can move along the electric field with mobility $\sim \sigma/\mu$, i.e., the charge mobility in the fluid frame is conductivity suppressed. However, since the system is advection dominated, no large charge gradients can build up, unless the fluid is compressible. In our case, the fluid velocity in the Eulerian frame is $D_iv_d^i \neq 0$, resulting in potential charge pile-up in regions of large v_d-gradients and compressibility. At intermediate resistivity, $\sigma \sim \mu$, the insulating fluid transitions to a moderately conducting plasma. Here, the current I^μ is both locally spacelike and timelike in different places, and the system has advection and conduction dominated regions. For $\sigma \gg \mu$, the plasma turns into a highly-conducting plasma with only residual resistivity. Here, the advection of the fluid is a negligible contribution to the overall charge distribution. Large scale charge separation is enabled by large conduction currents along the electromagnetic fields. In this regime, the conductivity sets the diffusion length scale $\ell = 1/\sigma$ that governs residual resistive features such as current sheets and tearing modes. Finally, assuming that in the $\sigma \to \infty$ limit, the system becomes largely magnetically dominated and $E_iB^i \to 0$ while σE_0 remains finite, then all three currents reduce to the familiar and physically well-defined force-free limit. This is discussed further in the context of the superradiance system in App. D.4.

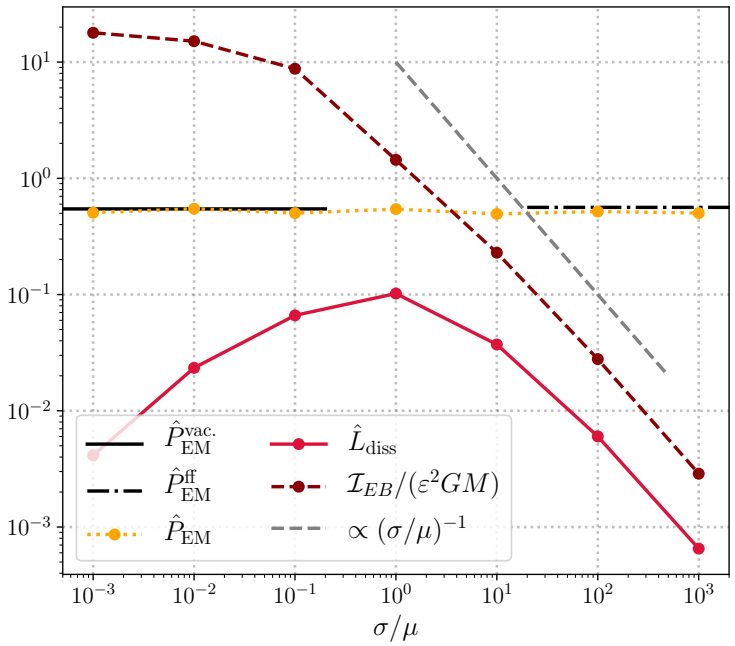

Figure D.4: We show the rescaled energy emission rates, $\hat{P} = P(G/\varepsilon^2)(M/M_c)$, of the Poynting flux $P_{\rm EM}$ (extracted at $r = 10r_c$), the Joule heating $L_{\rm diss}$, and $\mathcal{I}_{EB} = \int d^3\sqrt{\gamma}|E_i B^i|$, as functions of conductivity σ/μ for model *(C)* with a superradiance cloud of $\alpha = 0.3$ on a Minkowski background with magnetic guide field $B_z = 3 \times 10^4 B'_{\rm max}$. The corresponding Poynting fluxes in the vacuum $P^{\rm vac.}_{\rm EM}$ and force-free limits $P^{\rm ff}_{\rm EM}$ are indicated for reference.

In all cases, the conductivity σ is to be understood as a proxy for a class of dissipative processes and is chosen to be constant in space and time (primarily due to the lack of a physically motivated prescription for the spatial dependence of conductivity in this setup), as as typically done, for instance in [238, 247] (see [290] for a notable exception). The advantage of current *(C)* is its numerical properties in the high-conductivity limit. There, due to the prefactor $\sigma/(\sigma + \gamma)$ multiplying the orthogonal component, the magnitude of the source of the Maxwell equations remains small, ensuring that the evolution equations do not become stiff. This ultimately allows us to evolve the system even at relatively large conductivities with moderate resolution within an explicit forward integration scheme. However, a drawback of approach *(C)* is that $J^i_{\perp,(C)}$ diverges wherever $B^2 = 0$. In a magnetically dominated pulsar magnetosphere, this does not lead to problematic behavior, while in the case of an electrically dominated superradiance cloud, this causes issues at moderate and high conductivities, since within the equatorial plane, the magnetic field

of the superradiance cloud smoothly transitions through zero. We tested explicitly, that this magnetic null line causes the current (D.16) to diverge in the intermediate and high conductivity regime, leading to non-convergent features orbiting in the equatorial plane (particularly on mesh-refinement boundaries). As the resistive methods outlined above are designed to remove non-converging behavior in, for instance, current sheets, and we require convergence of our numerical implementation in order to validate our findings, approach *(C)* is not well-suited to tackle the kinetically-mixed superradiance cloud without modification. Therefore, we resort to approach *(B)* and current (D.15) to model resistive processes and the electromagnetic field geometries throughout the superradiance cloud. This evolution method has a stiffness problem at large conductivities, as outlined in App. D.2, which ultimately limits our ability to explore the $\sigma/\mu > 20$ parameter space.

We briefly illustrate the shortcomings of performing simulations on Minkowski spacetime, and the extent to which current *(C)* can be used in the context of a magnetic guide field removing magnetic null lines. To that end, we consider a $\alpha = 0.3$ superradiance cloud of the form (5.8) on a fixed Minkowski background. The constant magnetic guide field is initialized at the beginning of the simulations as $B_0^i = (0, 0, B_z)^i$ (where $\hat{z}$ is the spin-direction of the cloud), with magnitude $B_z = 3 \times 10^4 B'_{\rm max} \gg \varepsilon |\mathbf{E}'| M$. We test that the following results are independent of the choice of B_z, as long as the guide field magnitude is larger than a threshold, $B_z > B_t$. Below this threshold, the electric field $\varepsilon \mathcal{E}'$ starts dominating around the origin of the cloud. With this construction, a series of simulations is performed varying the conductivity from $\sigma/\mu = 10^{-3}$ to 10^3 within the context of the resistive methods *(C)* introduced above. In addition, we also study the vacuum limit $J^a = 0$, as well as the force-free limit on this flat background.

In Fig. D.4, we show the behavior of the total power output of the system as function of bulk conductivity in the model *(C)* in (D.16). Let us compare these quantities to those obtained on Kerr spacetime *without* a guide field and using model *(B)* [given by Eq. (D.15)] shown in Figure 5.12 and Figure 5.8. The flat spacetime guide field setup recovers the correct bulk dissipation component $L_{\rm diss} = L_{\rm diss}^{\rm bulk}$, both in amplitude and in conductivity dependence, while the turbulent component $L_{\rm diss}^{\rm turb}$ is absent. The latter is due to the magnetic guide field removing any magnetically diffusive regions that might form due to turbulence. The behavior of $\mathcal{I}_{EB}$ in Figure D.4 is entirely analogous to the corresponding quantity in Figure 5.8. Lastly, the outgoing Poynting flux in Figure D.4 is constant across decades of conductivities, and agrees well with both the vacuum and the force-free limits. This illustrates the leakage discussed above due to the lack of gravitational confining potential in flat spacetime, filtering out the massive propagating states. This demonstrates that, within the interaction basis, the flat space solution cannot be used to estimate physical observables associated with the outgoing Poynting flux. Hence, we

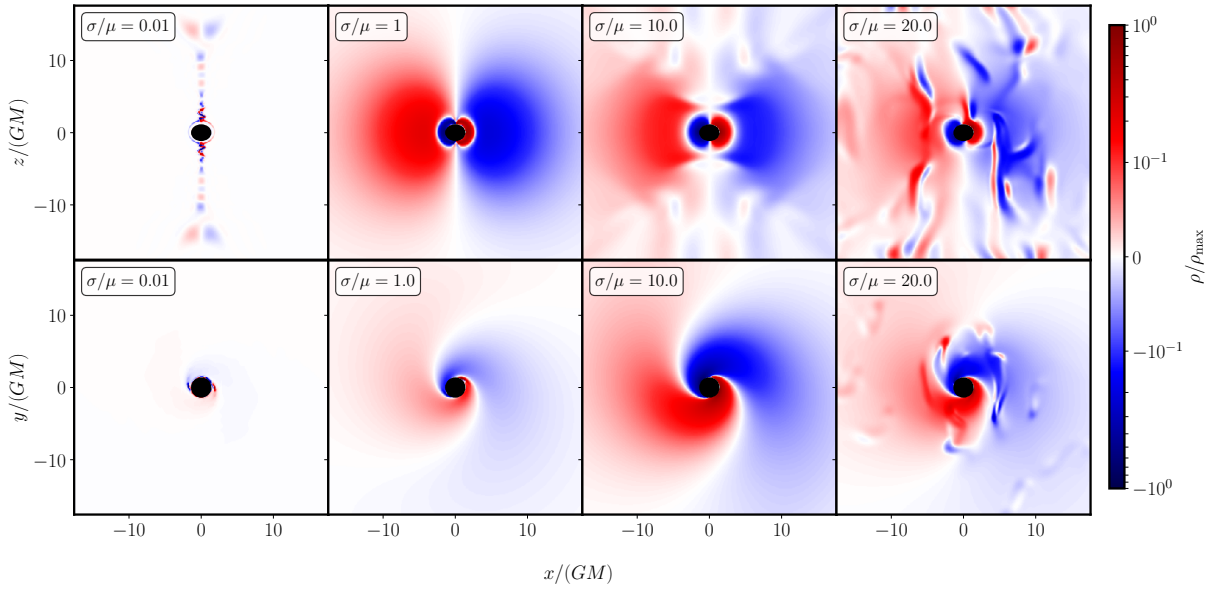

Figure D.5: The charge distribution ρ_q for various small to large conductivities in the equatorial plane (bottom row) and in a plane spanned by the BH spin and an arbitrary superradiance cloud phase (top row). The slices at varying conductivities correspond to the same superradiance cloud phase. We focus on a $\alpha = 0.3$ and $a_* = 0.86$ BH-cloud system.

cannot use model *(C)* without a guide field, as discussed above. However, using a guide field also does not give the correct answer, as this artificially removes the turbulent dynamics characterizing the high-conductivity limit of the system.

D.4 Charge distribution and small conductivity regime

In Figure D.5, we illustrate the spatial charge distribution ρ_q of the solution at low and intermediate conductivities. At low conductivity, the largest charge separation occurs along the spin-axis of the BH. This may be interpreted as follows: Charge separation is suppressed at high resistivity, $1/\sigma \gg 1$. However, any residual conductivity can separate charges on scales $\sim \sigma/\mu$ (assuming vanishing charge diffusion). Any separated charge distribution advects with the drift velocity of the fluid. In the presence of sufficiently large fluid velocity gradients (with finite fluid compressibility) large charge densities may build up. In the superradiance cloud context, regions of high velocity gradients coincide

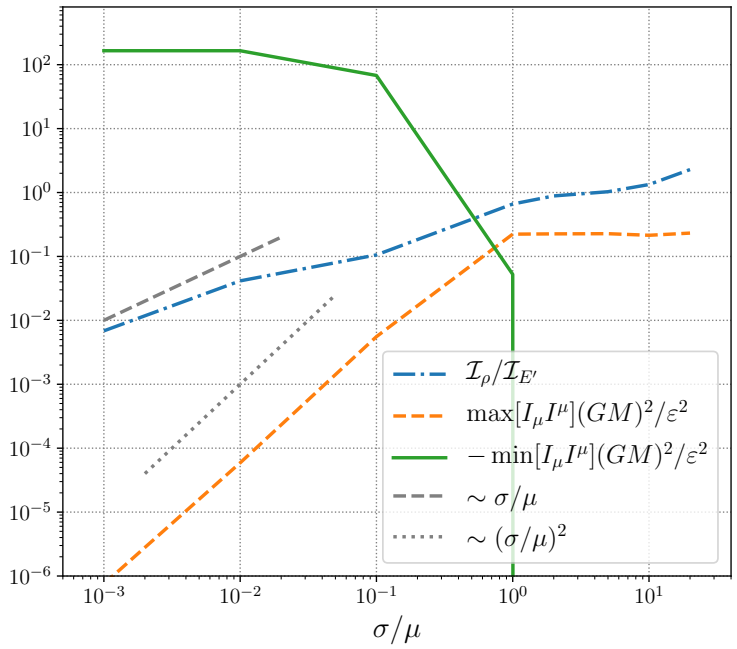

Figure D.6: We show the charge separation $\mathcal{I}_\rho$ [defined in (D.19)] as a function of conductivity in units of $\mathcal{I}_{E'}$ [defined in (D.20)], as well as the global maximum $\max[I_\mu I^\mu]$ of the electromagnetic 4-current (5.37) and global minimum $-\min[I_\mu I^\mu]$ (recall, we are using the $-+++$ signature). We focus on a $\alpha = 0.3$ and $a_* = 0.86$ BH-cloud system and consider conductivities $\sigma/\mu \in \{0.01, 0.1, 1, 2, 5, 10, 20\}$.

with regions where the charge density is largest for $\sigma/\mu = 10^{-2}$. Once the charge density is accumulated, and the fluid velocity varies on scales larger than the charge distribution scale, the latter is frozen into the flow of the former and is carried away from the BH along the spin axis. At moderate and large conductivity, $\sigma/\mu \gtrsim 1$, the resistivity is sufficiently small as to enable large scale charge separation. While for $\sigma/\mu = 1$, the charge density follows roughly the superradiant electric field morphology (compare with (5.18)), for $\sigma/\mu = 20$, small scale features begin to appear, likely driven by the turbulent dynamics inside the plasma.

Let us demonstrate explicitly that at large resistivity, the plasma cannot charge separate across scales larger than the charge separation scale $\sim \sigma$ and that the superradiant electric field is screened efficiently at large conductivity. To that end, we define the quantity

$$\mathcal{I}_\rho = \int_D d^3x \sqrt{\gamma} |\rho_q|, \tag{D.19}$$

measuring the charge separation in a coordinate volume D extending out to $\hat{\rho} = 10 r_c$ within the slice Σ_t with volume form $\sqrt{\gamma} d^3x$. This is compared with the charge separation required screen the superradiant electric field E'_i entirely [see also (5.18)]:

$$\mathcal{I}_{E'} = \int_D d^3x \sqrt{\gamma} \varepsilon |D_i E'^i|. \tag{D.20}$$

We show the behavior of $\mathcal{I}_\rho$ as a function of conductivity, compared with $\mathcal{I}_{E'}$, in the right panel of Figure D.6 (recall, $\mathcal{I}_{E'}$ is conductivity independent). For $\sigma/\mu \ll 1$, we find that $\mathcal{I}_\rho \to 0$, indicating that the system tends to the vacuum solution set by the superradiance cloud. At intermediate conductivity, the charge separation scales roughly as $\mathcal{I}_\rho \sim \sigma/\mu$. At large conductivity, $\mathcal{I}_\rho \sim \mathcal{I}_{E'}$, supporting the conclusion that, for $\sigma/\mu \gg 1$, the solution exhibits large scale charge separation that screens the field E'_i efficiently, even in the turbulent regime. Furthermore, we also show the behavior of the norm $I_\mu I^\mu$ of the electromagnetic 4-current (5.37) in Figure D.6. As outlined in App. D.3, for $\sigma \ll \mu$, the current is fluid advection dominated, where a residual charge distribution is flowing with the fluid on timelike trajectories. Conversely, for large conductivities the conduction part of the current starts to dominate, the current becomes spacelike, and the solution begins to asymptote towards a conductivity independent value of $\max[I_\mu I^\mu]$.

In Figure D.7, we show the spatial distribution of $\rho_{\rm diss}$ at small and large σ/μ. For $\sigma/\mu < 10$, the dissipation density roughly follows the shape of the superradiance cloud. This is consistent with (5.48), since the visible electric field is dominated by the superradiance electric field component E'^i for $\sigma/\mu \ll 1$. Hence, any small dissipation density traces out the superradiance cloud's electric field E'^i; in the main text, this component is referred to as $L^{\rm bulk}_{\rm diss}$. This is the relativistic result corresponding to the approximation (5.51). In Figure D.7, for $\sigma/\mu = 10$, the dissipation density deviates from the superradiance cloud's electric field; more precisely, the dissipation density is set by the superradiance cloud for $r < r_*$, and set by the plasma dynamics for $r > r_*$, with r_* defined in (5.41). Therefore, the appearance of r_* marks the breakdown of approximation (5.51), and the onset of the reconnection driven regime, leading to the turbulent dissipation component $L^{\rm turb}_{\rm diss}$. The latter dominates over the dissipation density component provided by the contribution of the dark photon electric field to the visible electric fields in practically all regions outside the BH, for $\sigma/\mu = 20$, as can be seen in Figure D.7. The dissipation density develops features on the scale $1/\mu$, set by the boson mass, and $1/\sigma$, set by the conductivity. This is consistent with the discussion in Sec. 5.5.3, where local magnetic field line twisting, on scales of $1/\mu$ and scales of the entire cloud, are relaxed by reconnection events, dissipating energy through a locally enhanced $\rho_{\rm diss}$. For completeness, we show the ratio of visible electromagnetic fields in Figure D.7 at low to moderate conductivities. This completes the

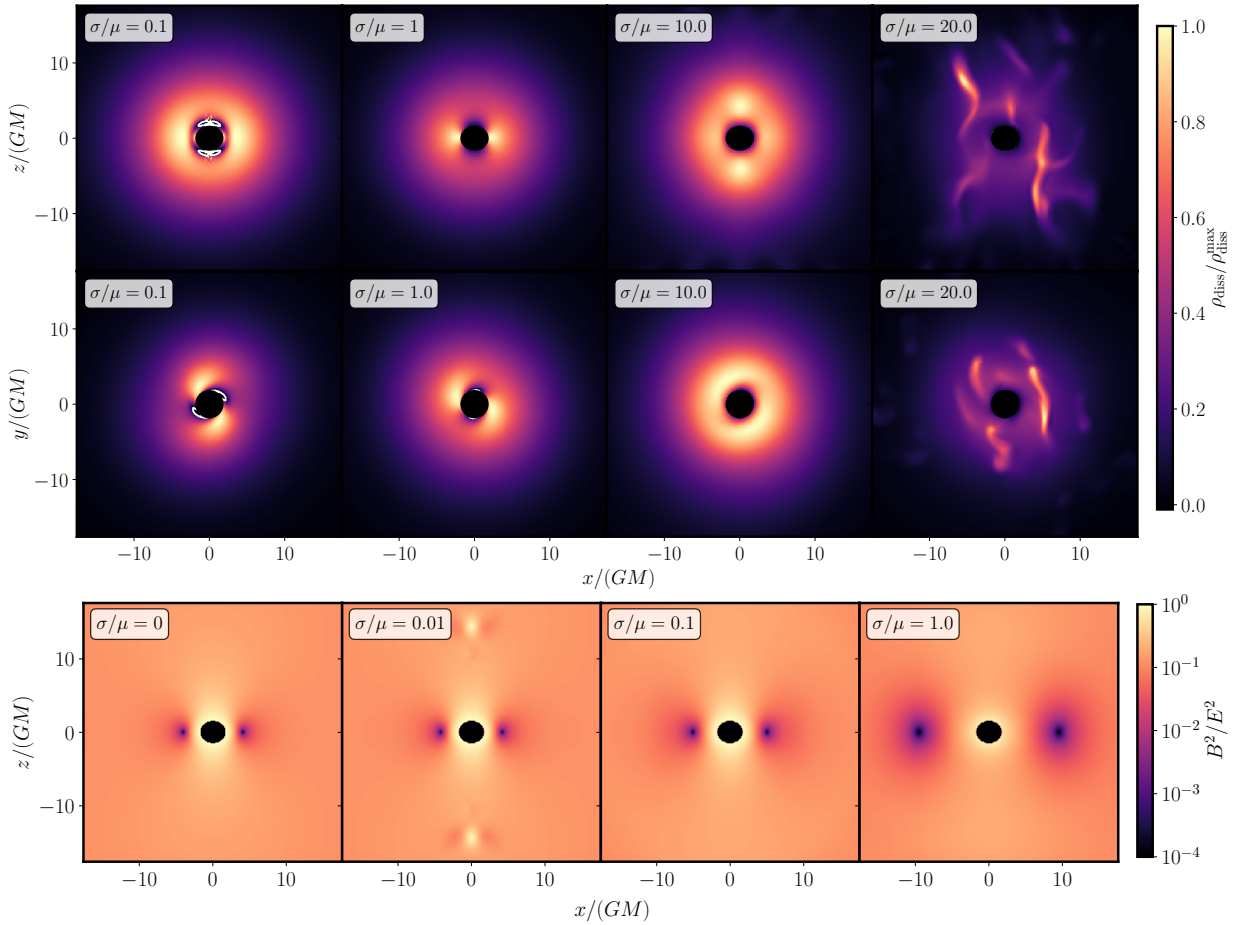

Figure D.7: *(top and middle row)* We show the energy dissipation density $\rho_{\rm diss}$, defined in (5.48), as a function of conductivity in a slice spanned by the BH spin and an arbitrary superradiance cloud phase *(top row)*, as well as in the equatorial plane of the BH *(middle row)*. The color scale is normalized by the global maximum dissipation density at each conductivity. All slices correspond to the same superradiance cloud phase. White contour lines indicate where the density goes through zero. We focus on a $\alpha = 0.3$ and $a_* = 0.86$ BH-cloud system. *(bottom row)* We show the ratio of visible electromagnetic fields, B^2/E^2, in a plane spanned by the BH spin and an arbitrary superradiance cloud phase for various small and moderate conductivies. The $\sigma/\mu > 1$ regime is shown in Figure 5.7. We compare the plasma cases to the vacuum case, i.e., $\sigma/\mu = 0$.

low-conductivity regime of the behavior shown in Figure 5.9. As evident from Figure D.7,

the field structure is affected at the $\mathcal{O}(1)$-level only at intermediate conductivities, $\sigma \sim \mu$. For $\sigma/\mu < 1$, the two magnetic null lines inside the equatorial plane are unchanged. In the case of $\sigma/\mu = 10^{-2}$, the charge distribution accumulating along the spin-axis of the BH, leaves mild imprints on B^2/E^2.

D.5 Dark photon basis

A kinetic mixing between the SM photon and a dark massive photon enters as $\mathcal{L} = \mathcal{L}_{\rm SM} + \mathcal{L}_{\rm Proca} + \varepsilon F'_{\mu\nu}F^{\mu\nu}/2$ at low energies. Under the field redefinition $A_\mu \to A_\mu + \varepsilon A'_\mu =: \mathcal{A}_\mu$ this turns into the Lagrangian in the mass eigenbasis

$$\begin{aligned}\mathcal{L}_{\rm mass} = &-\frac{1}{4}\mathcal{F}_{\mu\nu}\mathcal{F}^{\mu\nu} - \frac{1}{4}\mathcal{F}'_{\mu\nu}\mathcal{F}'^{\mu\nu} \\ &- \frac{\mu^2}{2}\mathcal{A}'_\mu\mathcal{A}'^\mu + I_\mu(\mathcal{A}^\mu + \varepsilon\mathcal{A}'^\mu),\end{aligned} \tag{D.21}$$

or, using $A'_\mu \to A'_\mu + \varepsilon A_\mu =: A'_\mu$ into the interaction basis

$$\begin{aligned}\mathcal{L}_{\rm inter} = &-\frac{1}{4}F_{\mu\nu}F^{\mu\nu} - \frac{1}{4}F'_{\mu\nu}F'^{\mu\nu} \\ &- \frac{\mu^2}{2}A'_\mu A'^\mu - \varepsilon\mu^2 A'_\mu A^\mu + I_\mu A^\mu.\end{aligned} \tag{D.22}$$

In both bases, the current I_μ is the current of the SM charged particles. These lead to the field equations, in the mass eigenbasis,

$$\begin{aligned}\nabla_\alpha\mathcal{F}^{\alpha\beta} &= -I^\beta, \\ \nabla_\alpha\mathcal{F}'^{\alpha\beta} &= \mu^2\mathcal{A}'^\beta - \varepsilon I^\beta,\end{aligned} \tag{D.23}$$

and interaction basis

$$\begin{aligned}\nabla_\alpha F^{\alpha\beta} &= -I^\beta + \varepsilon\mu^2 A'^\beta, \\ \nabla_\alpha F'^{\alpha\beta} &= \mu^2 A'^\beta + \varepsilon\mu^2 A^\beta,\end{aligned} \tag{D.24}$$

when working to leading order in the kinetic mixing ε. The mixing of the SM and the dark fields at the level of the electromagnetic current I^α is manifest in (D.21). Hence, both

the SM fields and the dark fields can accelerate charged particles. This is reflected in the energy-momentum conservation of (D.21):

$$\begin{aligned} \nabla_\alpha \mathcal{T}^{\alpha\beta} &= -\mathcal{F}^{\beta\gamma} I_\gamma, \\ \nabla_\alpha \mathcal{T}'^{\alpha\beta} &= -\varepsilon \mathcal{F}'^{\beta\gamma} I_\gamma. \end{aligned} \tag{D.25}$$

In the mass eigenbasis, no energy is transferred from the dark to the SM field, while both transfer energy to and from charge particles. In the interaction basis, we have

$$\begin{aligned} \nabla_\alpha T^{\alpha\beta} &= -F^{\beta\gamma}(I_\gamma - \varepsilon\mu^2 A'_\gamma), \\ \nabla_\alpha T'^{\alpha\beta} &= \varepsilon\mu^2 F'^{\beta\gamma} A_\gamma, \end{aligned} \tag{D.26}$$

where the energy transfer between fields is manifest.

Furthermore, at leading order in ε this implies the Lorenz condition on A'_μ, as well as the current conservation

$$\nabla^\mu A'_\mu = 0, \qquad\qquad \nabla_\mu I^\mu = 0. \tag{D.27}$$

In the main text, in particular after Sec. 5.3, we work out all the dynamics in the interaction basis, which is most convenient for the analysis since, inside the dense plasma, A_μ has equations of motion which are potentially sensitive to the scale σ and ω_p, both of which are much larger than the dark photon mass μ. This manifests in the simulation as short distance turbulent dynamics of the field A_μ, while the background A'_μ has only dynamics on length scales of order $1/\mu$. Therefore, inside this dense plasma, the interaction basis of the plasma modes A_μ and the dark photon A'_μ is also the *mass* basis. Clearly, the interaction basis is more convenient for our simulations. In the following, we emphasize some of the important physical intuition that is hidden in Eqs. (D.23), (D.24), (D.25) and (D.26) and clarifying some points of confusion.

A first confusion comes from searching for static solutions by inspection. From Eqs. (D.23) and (D.25), it seems apparent that there is a solution of $I_\mu = 0$ while Eqs. (D.24) and (D.26) would naively suggest that there is a solution of $I^\beta = \varepsilon\mu^2 A'^\beta$. Both of these two solutions we have in fact discussed in the main text. The solution $I_\mu = 0$ is the vacuum solution, which corresponds to a dark photon cloud with zero charged plasma. Such a solution is, however, unstable due to pair production instabilities described in Sec. 5.4. The solution of $I^\beta = \varepsilon\mu^2 A'^\beta$ in the interaction basis corresponds to the naive physical picture of a rotating electric dipole, which is not viable due to the fact that the cloud is electrically dominated (with size that is much larger than the light cylinder radius).

A second confusion pertains to the common lore that in a dense plasma, the effect of the dark photon is suppressed by the ratio of the dark photon mass and the plasma mass of the photon, usually in the form of $(\mu/\omega_p)^2$. However, this suppression assumes that the dark photon field weakly perturbs a dense fluid of SM particles, which is not true in our case. Rather, in the superradiance cloud, the dark photon cloud energy density scales as $|\mathbf{E}'|^2$, the visible electric field energy density scales as $\varepsilon^2|\mathbf{E}'|^2$, while the charged particle energy density we obtain in the simulation is $\mathcal{O}(m_e\mu\varepsilon|\mathbf{E}'|)$. Given that $\varepsilon|\mathbf{E}'| \approx m_e^{3/2}\mu^{1/2}$ when pair production starts, the pair produced plasma carries energy density that is at most $\mathcal{O}((\mu/m_e)^{1/2})$ of the energy density of the electromagnetic field. In this case, the dark photon field is no longer a small perturbation and the SM plasma, as a result, is very far from an equilibrium state at zero field. As a result, the intuition developed in Refs. [138, 103] fails.

D.6 Flux discussion

In Sec. 5.6.2, we extrapolated the electromagnetic power through the Poynting flux $P_{\rm EM}$ and the energy dissipation $L_{\rm diss}$ from our numerical data at moderate conductivities $\sigma/\mu \leq 20$ to very large conductivities $\sigma \to \infty$. In Figure 5.11, we showed, however, only those scenarios with conductivities resulting in qualitatively different behavior of the Poynting flux. Therefore, for completeness, we show the electromagnetic emission power for all values of the conductivity considered in Figure D.8, as function of the radial coordinate distance $\hat{\rho}$ from the BH. The exponential decay and oscillatory behavior of $P_{\rm EM}$ in the low-conductivity regime reflects the exponential decay and oscillatory behavior of the electromagnetic waves in a medium with low conductivity. These electromagnetic waves are eigenstates of the Helmholtz equation in spherical coordinates, with eigenvalues of $\pm i\sqrt{\sigma\mu + i\mu^2}$. The eigenfunctions are spherical Hankel functions of the first kind, which have a similar spatial dependence (this oscillatory behavior can be observed also in e.g. B^2 in the equatorial plane of the BH-cloud system for $\sigma/\mu < 1$, which is not shown here). Such exponential decay and oscillatory behavior is evident in Figure D.8 close to the BH at low and intermediate conductivities. In this regime, low frequency oscillations on large scales dominate, which gives rise to the same oscillatory features in $P_{\rm EM}$. Finally, in the right panel of Figure D.8, we show the total time-averaged Poynting flux for $\sigma/\mu = 20$ as a function of coordinate distance from the BH for each of the values of α considered in this work.

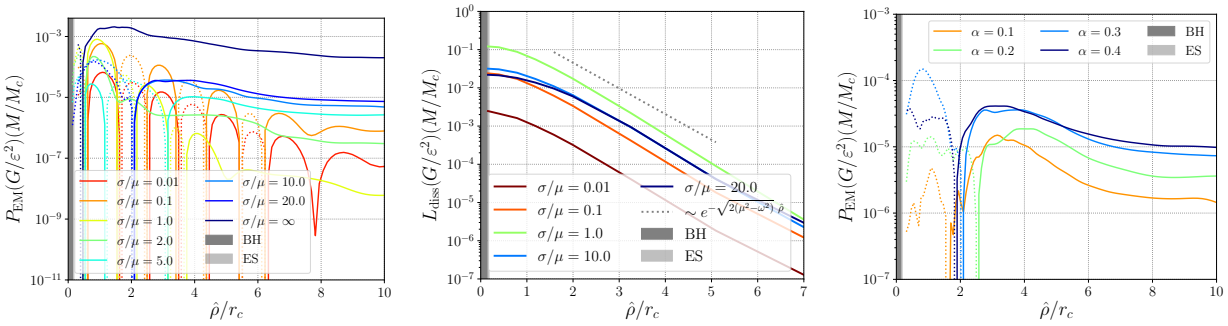

Figure D.8: *(left and middle)* The total (time-averaged) electromagnetic power emitted or injected into the plasma as a function of coordinate radius $\hat{\rho}$ in terms of the cloud's Bohr radius r_c for various plasma conductivities σ/μ. The flux obtained in the force-free context is labelled as $\sigma/\mu = \infty$. Here, we focus on the $\alpha = 0.3$ case with a BH spin of $a_* = 0.86$, and indicate the BH horizon and ergosurface by shaded regions labelled BH and ES, respectively. *(left)* We show the total time-averaged visible Poynting flux $P_{\rm EM}$, defined in (5.45), through spheres at radii $\hat{\rho}$ starting from the horizon and extending to large distances [here solid (dashed) lines indicate locally radially outwards (inwards) going fluxes]. *(middle)* We show the total dissipation power $L_{\rm diss}$, defined in (5.47), integrated from $\hat{\rho} \to \infty$ to $\hat{\rho}$. Recall that our simulations assume spatially constant plasma conductivity σ. *(right)* Here, we show the total time-averaged Poynting flux $P_{\rm EM}$ for all values of α, keeping $\sigma/\mu = 20$ fixed.

D.7 Notation

We list the variable definitions used throughout the text in Table D.2.

Variable	Description
ε	Kinetic mixing
μ	Massive vector field mass
r_c	Cloud's Bohr radius
a_*	Black hole dimensionless spin
Δa_*	Loss of black hole dimensionless spin
M	Black hole mass
r_g	Half black hole Schwarzschild radius
ω	Superradiance cloud angular frequency
f	Superradiance cloud frequency
$\Omega_{\rm BH}$	Black hole horizon frequency
M_c	Superradiance cloud mass
α	Gravitational fine structure constant
t, x, y, z	Cartesian Kerr-Schild coordinates
σ	Plasma conductivity
γ_e	Electron/positron Lorentz factor
m_e	Electron/positron mass
e	Positron charge
$\tau_{\rm plasma}$	Timescale to populate the $e^{\pm}$ plasma
ω_p	Plasma frequency
A'_μ	Dark vector potential (interaction basis)
$E'^i, \mathbf{E}'$	Dark electric field (interaction basis)
$B'^i, \mathbf{B}'$	Dark magnetic field (interaction basis)
A_μ	Visible vector potential (interaction basis)
$E^i, \mathbf{E}$	Visible electric field (interaction basis)
$B^i, \mathbf{B}$	Visible magnetic field (interaction basis)
I^μ	Electromagnetic 4-current
J^i	Electromagnetic spatial current
ρ_q	Charge density
v_d^i	Plasma drift velocity in Eulerian frame
$f_{\rm GW}$	Gravitational wave frequency
$P_{\rm GW}$	Gravitational wave luminosity
$\tau_{\rm GW}$	Gravitational radiation timescale
$\tau_{\rm SR}$	Superradiance instability timescale
$P_{\rm EM}$	Visible Poynting flux
$L_{\rm diss}$	Visible energy dissipation power
$\tau_{\rm EM}$	Electromagnetic radiation timescale
ν	Spectral frequency of electromagnetic emissions

Table D.2: List of the variables used most commonly throughout the main text, as well as a brief description.

Appendix E

Black hole superradiance field solutions and gravitational radiation

E.1 LISA signal-to-noise ratio

For a given an initial BH spin and mass, as well as ultralight boson mass, `SuperRad` provides predictions for the GW strain $h_{+/\times}(t, R, \theta, \phi)$ at time t, (luminosity) distance r, and angles (θ, φ) in the source frame. In the case of LISA, the detector response functions $\tilde{X}_{+/\times}(\Theta, \Phi, \psi, f)$ relate the GW strain in the source frame to the strain in the detector. The latter depend on the source's sky-position (Θ, Φ), polarization ψ, and frequency[1] f. Hence, the GW amplitude in the detector, $\tilde{h}_{\rm det.}(f)$, in the frequency domain is given by

$$\tilde{h}_{\rm det.}(f) = \tilde{X}_{+}\tilde{h}_{+}(f) + \tilde{X}_{\times}\tilde{h}_{\times}(f), \tag{E.1}$$

where $\tilde{h}_{+/\times}(f)$ are the Fourier-transforms of $h_{+/\times}(t, R, \theta, \varphi)$. Let $\langle \dots \rangle$ be the sky/polarization average over Θ, Φ, and ψ, and let $\mathcal{R}(f)$ be the frequency-dependent transfer function defined by the sky/polarization average of the detector response $\langle \tilde{h}^{*}_{\rm det.}\tilde{h}_{\rm det.}\rangle = \mathcal{R}(f)[|\tilde{h}_{\times}(f)|^2 + |\tilde{h}_{+}(f)|^2]$. Then the SNR $\rho_{\rm SNR}$ is (see e.g., Refs. [317, 40])

$$\frac{\rho^2_{\rm SNR}}{4} = \int_0^\infty df \frac{\langle \tilde{h}^{*}_{\rm det.}\tilde{h}_{\rm det.}\rangle}{S_n(f)} = \int_0^\infty df \frac{|\tilde{h}_{\times}(f)|^2 + |\tilde{h}_{+}(f)|^2}{S_h(f)}, \tag{E.2}$$

where $S_n(f)$ is the noise power spectral density of LISA, and $S_h(f) = S_n(f)/\mathcal{R}(f)$ is the LISA sensitivity curve. For all estimates, we use the conservative six months confusion noise projections.

[1] We neglect the motion of LISA and the source with respect to each other.

Since `SuperRad` provides the time domain GW strain in the source frame, we add the appropriate redshift factors and use fast-Fourier-transform algorithms to numerically transform into the frequency domain. This is feasible for shorter signals considered in follow-up searches. However, it becomes increasingly computationally expensive with longer signals at smaller α.

E.2 Superradiant field solutions

In this appendix, we briefly summarize the numerical methods we use to obtain the scalar and vector estimates for the oscillation frequencies ω_R and instability growth rates ω_I discussed in Secs. 6.3.2 and 6.3.3, respectively. We also provide bounds on the precision of our methods, and comment on the resulting uncertainties.

E.2.1 Scalar field

The real massive scalar wave equation (6.1) has been extensively studied in the context of asymptotically flat BHs. On a Kerr background of mass M and spin parameter a, Detweiler [128] first derived expressions for the superradiance instability rates and oscillation frequencies. These results were refined in various other works, e.g., Refs. [136, 377, 53]. In this subsection, ω, ℓ, n, and m refer exclusively to the scalar mode numbers, hence, we drop the subscripts used throughout the main text, for brevity.

Generally, due to the backgrounds symmetries, the most convenient scalar field ansatz is of the form $\Phi = \mathrm{Re}[R_s(r)S_s(\theta)e^{-i(\omega t - m\varphi)}]$. With this ansatz, the field equations separate into a pair of polar and radial second-order ordinary differential equations. The polar equation can be identified with the spheroidal harmonic equation of spin-weight $s = 0$ and spheriodicity $c^2 = -k^2a^2$, with $k^2 = \mu_S^2 - \omega^2$; the solutions to this equation is the set of spheroidal harmonics, ${}_s\tilde{S}_{\ell m}(\theta; c)$, of spin-weight $s = 0$. Hence, the polar solution is simply the spheroidal harmonic $S_s(\theta) = {}_0\tilde{S}_{\ell m}(\theta; c)$ associated with the polar eigenvalue $A_{\ell m}(c)$ that reduces to $A_{\ell m}(c \to 0) = \ell(\ell+1)$ in the Schwarzschild limit (see, for instance, Ref. [63]). The radial equation turns out to be the source-free $s = 0$ radial Teukolsky equation

$$\begin{aligned} &\frac{d}{dr}\left(\Delta \frac{dR_s}{dr}\right) \\ &\quad + \left(\frac{(r^2+a^2)\omega - am}{\Delta} - \lambda_{\ell m} - \mu_S^2 r^2\right) R_s = 0, \end{aligned} \tag{E.3}$$

where $\lambda_{\ell m} = A_{\ell m} + a^2\omega^2 - 2am\omega$ depends on the radial eigenvalue $\omega = \omega_R + i\omega_I$, and $\Delta = r^2 - 2Mr + a^2$.

The radial eigenvalue ω can be obtained, together with the radial solution $R_s(r)$ satisfying ingoing boundary conditions at the horizon, and asymptotically flat boundary conditions at spatial infinity. At leading order in α, the above radial equation reduces to a type of Laguerre equation, yielding Hydrogen-like radial states, together with the associated energy spectrum ω [136, 128]. Higher order corrections at the level of the radial and polar equations are solved for in an order-by-order fashion perturbatively around $\alpha = 0$. Solving the eigenvalue problem in this way leads to the higher order corrections to the real part of the superradiantly unstable scalar modes, defined in (6.8), [53]

$$C_S[\alpha] = -\frac{\alpha^4}{8n^4} + \frac{f^S_{n\ell}\alpha^4}{n^3} + \frac{h^S_\ell a_* m\alpha^5}{n^3} + \mathcal{O}(\alpha^6), \tag{E.4}$$

where

$$\begin{aligned} f^S_{n\ell} &= -\frac{6}{2\ell+1} + \frac{2}{n}, \\ h^S_\ell &= \frac{16}{2\ell(2\ell+1)(2\ell+2)}. \end{aligned} \tag{E.5}$$

The corresponding instability growth rates, defined in (6.12), are [128]

$$\begin{aligned} G_S(a_*, \alpha) &= \frac{2^{4\ell+1}(n+\ell)!}{n^{2\ell+4}(n-\ell-1)!} k^S_{n\ell} g^S_{m\ell} \\ k^S_{n\ell} &= \left[\frac{\ell!}{(2\ell)!(2\ell+1)!}\right]^2, \\ g^S_{m\ell} &= \prod_{o=1}^{\ell} \left[o^2(1-a_*^2) + (a_* m - 2r_+\omega_R)^2\right]. \end{aligned} \tag{E.6}$$

for the most unstable mode in the non-relativistic limit. The principle quantum number n is defined in (6.9).

In this work, we compute the eigenvalue $\omega = \omega_R + i\omega_I$ numerically in the relativistic regime $\mathcal{D}_{\rm int}$ where the analytic methods break down. The typical approach employed to solve differential eigenvalue problems of this type goes back to Leaver [233], and was applied to massive scalar fields in Kerr spacetime in Refs. [136, 377]. There, the radial solution is assumed to be written in power series form as

$$R(r) = (r - r_+)^{-i\beta}(r - r_-)^{i\beta+\gamma-1} \sum_{n\geq 0} a_n \left(\frac{r - r_+}{r - r_-}\right)^n, \tag{E.7}$$

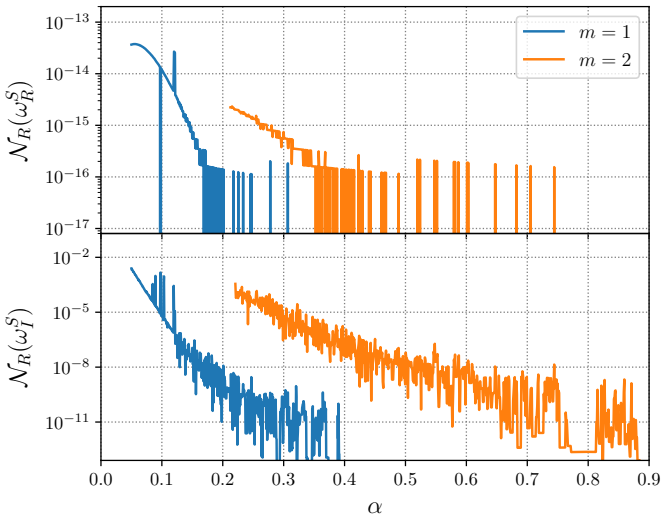

Figure E.1: The relative numerical error $\mathcal{N}_R$, defined in (E.8), of the real and imaginary parts of the frequency of the scalar $m = 1$ and $m = 2$ superradiant states around a BH of spin $a_* = 0.985$.

with $\beta = 2Mr_+(\omega - m\Omega_H)/(r_+ - r_-)$ and $\gamma = M(2\omega^2 - \mu_S^2)/k$. Plugging this into the radial equation (E.3), one obtains a recurrence relation between the coefficients a_n. This relation is used to obtain a continued fraction constraint on the frequency ω for each $\{\ell, m, a, \mu_S\}$. This constraint is an implicit equation for the eigenvalues ω_R and ω_I, which can be solved for numerically using a minimization algorithm over the complex ω-plane. With the recurrence relation and ω, the radial solution is constructed using (E.7). Details can be found in Refs. [136, 377]. In the non-relativistic limit, we found that a total number of $N \geq 5000$ terms in the series expansion is necessary for our desired accuracy, while in the relativistic regime, a lower number, i.e., $N \leq 1000$, is sufficient. We construct the spheroidal harmonics ${}_0S_{\ell m}(\theta; c)$ and associated eigenvalues $A_{\ell m}$ using `qnm`, a python implementation of a Leaver-like continued fraction method developed in Ref. [349].

In order to estimate the numerical uncertainty of this method, we determine the frequency ω in a range of α and fixed BH spin, using the above approach with successively increasing N, up to the $N_{\rm max} = 8000$ used throughout the entire parameter space in `SuperRad`. The numerical error is then estimated by

$$\mathcal{N}_R(\omega) = \frac{|\omega_{N_{\rm max}} - \omega_{N_{\rm max}/2}|}{\omega_{N_{\rm max}}}. \tag{E.8}$$

The results are shown in Figure E.1. We ensure that the minimization algorithm has termination conditions at the floating point level. The real part of the frequency is obtained to one part in $\sim 10^{14}$, whereas the imaginary part is determined less precisely. However, even for $\alpha \gtrsim 0.05$, the latter is more precise or comparable to the theoretical uncertainty of the analytic estimates in (6.8) together with (E.4). This establishes the numerical uncertainties of the methods used to extend `SuperRad` into the relativistic regime. However, it does not show the overall uncertainty of `SuperRad` in this regime due to interpolation error, which is discussed in Appendix E.3.

E.2.2 Vector field

The massive vector wave equation (6.1) has been studied more recently in [289, 93, 137, 161]. The non-separability of the vector field equation was a fundamental problem until a series of works by Lunin [243] and Frolov et al. [161]. There, an ansatz, referred to as FKKS in the following, was constructed that separates the polar and radial parts of the field equation (6.1), and hence, significantly simplifies the problem. We briefly summarize this ansatz and quote analytic results for the oscillation frequency and instability growth rates, $\omega = \omega_R + i\omega_I$, obtained with it. Similarly to the previous subsection, we drop the subscripts of ω, ℓ, n, and m, used in the main text, and use these exclusively for vector modes and frequencies.

The FKKS ansatz exploits a hidden symmetries of Kerr spacetime $g_{\mu\nu}$. This symmetry is captured by a Killing-Yano 2-form $\mathbf{k}$, with tensor components that satisfy $\nabla_\alpha k_{\beta\gamma} = 2g_{\alpha[\beta}\xi_{\gamma]}$. Using this, the vector field ansatz takes the form

$$A^\mu = B^{\mu\nu}\nabla_\nu Z, \qquad\qquad Z = R_V(r)S_V(\theta)e^{-i(\omega t - m\varphi)}, \tag{E.9}$$

with polarization tensor $B^{\mu\nu}(g_{\nu\gamma} + i\nu k_{\nu\gamma}) = \delta^\mu_\gamma$ and angular eigenvalue ν. Plugging this ansatz into (6.1) yields ordinary differential equations for the radial and polar dependencies, respectively. The angular equation is a deformed spheroidal harmonic equation for spin-weight $s = -1$ that does not, a priori, possess known solutions. In the Schwarzschild limit, $a \to 0$, the solutions reduce the usual spherical harmonics $S_V(\theta) = Y_{\ell m}(\theta)$, with a relation between the polar eigenvalue $\Lambda = \ell(\ell+1)$ and the separation constant $\nu \to \nu_\ell$ (see Ref. [137] for details). In this limit, the spatial components of the vector field are then given by $A^i_{a\to 0} \propto Y^i_{j,jm}(\theta)$ where $Y^i_{j,jm}(\theta)$ are the vector spherical harmonics with $j = \ell - \hat{S}$ (see Ref. [361]). When the BH spin is non-zero, there is a mixing of the polar mode number ℓ, such that, in general $S_V(\theta) = Y_{|m|,m}(\theta) + b_1 Y_{|m|+1,m}(\theta) + \ldots$. The radial equation for

$R_V(r)$ takes the form

$$\mathcal{D}_{\nu,\omega,m,a} R_V(r) = 0, \tag{E.10}$$

with a second order differential operator $\mathcal{D}_{\nu,\omega,m,a}$ [161, 137]. In the $a \to 0$ limit, and at leading order in α, this equation reduces to a Schrödinger-type equation for $R_V(r)$ with the eigenvalue spectrum (6.8) [50]. This FKKS ansatz was used in [53] to go beyond the leading orders in both a and α. They found the sub-leading corrections to the spectra (6.8) to be

$$C_V[\alpha] = -\frac{\alpha^4}{8n^4} + \frac{f^V_{n\ell\hat{S}}\alpha^4}{n^3} + \frac{h^V_{\ell\hat{S}} a_* m \alpha^5}{n^3} + \mathcal{O}(\alpha^6), \tag{E.11}$$

with

$$f^V_{n\ell\hat{S}} = -\frac{4(6\ell(\ell-\hat{S}+1)-3\hat{S}+2)}{(2\ell-\hat{S})(2\ell-\hat{S}+1)(2\ell-\hat{S}+2)} + \frac{2}{n}, \tag{E.12}$$

$$h^V_{\ell\hat{S}} = \frac{16}{(2\ell-\hat{S})(2\ell-\hat{S}+1)(2\ell-\hat{S}+2)}. \tag{E.13}$$

The corresponding instability growth rates (6.12) are [49, 53]

$$\begin{aligned} G_V(a_*,\alpha) &= \frac{2^{4\ell-2\hat{S}+1}(n+\ell)!}{n^{2\ell+4}(n-\ell-1)!} k^V_{\ell\hat{S}} d^V_{\ell\hat{S}} g^V_{\ell\hat{S}} \\ k^V_{\ell\hat{S}} &= \left[\frac{\ell!}{(2\ell-\hat{S})!(2\ell-\hat{S}+1)!}\right]^2, \\ d^V_{\ell\hat{S}} &= \left[1 + \frac{2(1+\hat{S})(1-\hat{S})}{2\ell-\hat{S}}\right]^2, \\ g^V_{\ell\hat{S}} &= \prod_{o=1}^{\ell-\hat{S}} \left[o^2(1-a_*^2) + (a_* m - 2r_+\omega_R)^2\right]. \end{aligned} \tag{E.14}$$

for the most unstable mode in the non-relativistic limit, $\ell = m + \hat{S}$ and $\hat{S} = -1$.

In this work, we obtain numerical data in the relativistic regime $\mathcal{D}_{\rm int}$ by solving (E.10) and the associated polar equation numerically following Refs. [137, 338]. To that end, the angular equation is expanded in regular spherical harmonics ${}_0S_{\ell m}(\theta; c=0)$, while the radial equation is integrated numerically outwards from the horizon to large distances. Therefore,

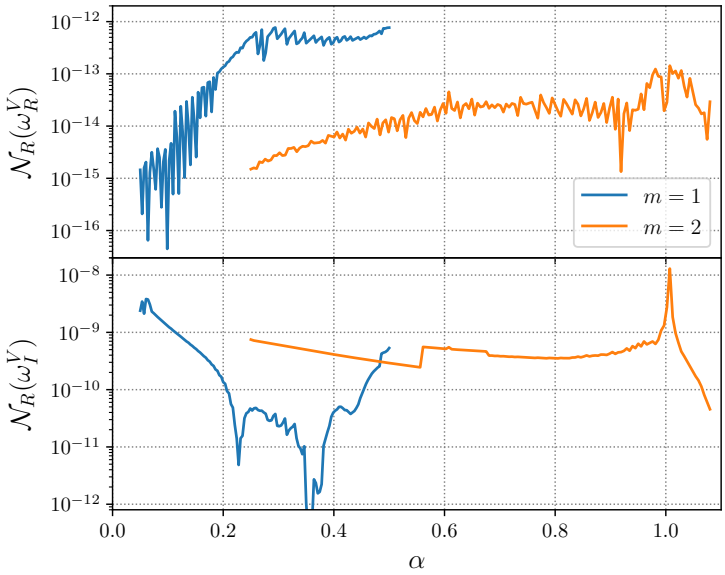

Figure E.2: The relative numerical error $\mathcal{N}_R$ of the real and imaginary parts of the frequency of the vector $m = 1$ and $m = 2$ superradiant states around a BH of spin $a_* = 0.985$.

as long as a sufficient number of terms is considered in the polar sector, the numerical uncertainties are dominated by the integration method used in the radial sector. We make use of the `BHPToolkit` to construct spherical and spheroidal harmonics [2]. In order to obtain estimates for the numerical uncertainty, we vary the step size of the radial numerical integration. In Figure E.2, we show upper bounds on the relative numerical uncertainty of the method described above to obtain the frequencies ω. As in the scalar case, the numerical uncertainty of the underlying numerical methods is below the interpolation error of `SuperRad` discussed in the next section.

E.3 Interpolation and Extrapolation Error of `SuperRad`

The uncertainties associated to the values of $\tau_I = 1/\omega_I$ and $f_{\rm GW} = \omega_R/\pi$ provided by `SuperRad` come from an interplay of interpolation errors, numerical errors, truncation errors of analytic expressions, and the theoretical assumptions made. Furthermore, due to the combination of methods involved, the overall uncertainty of `SuperRad` varies across the parameter space. In this appendix, we provide justifications for accuracy claims made in the main text, as well as establish upper bounds for uncertainties of the observables

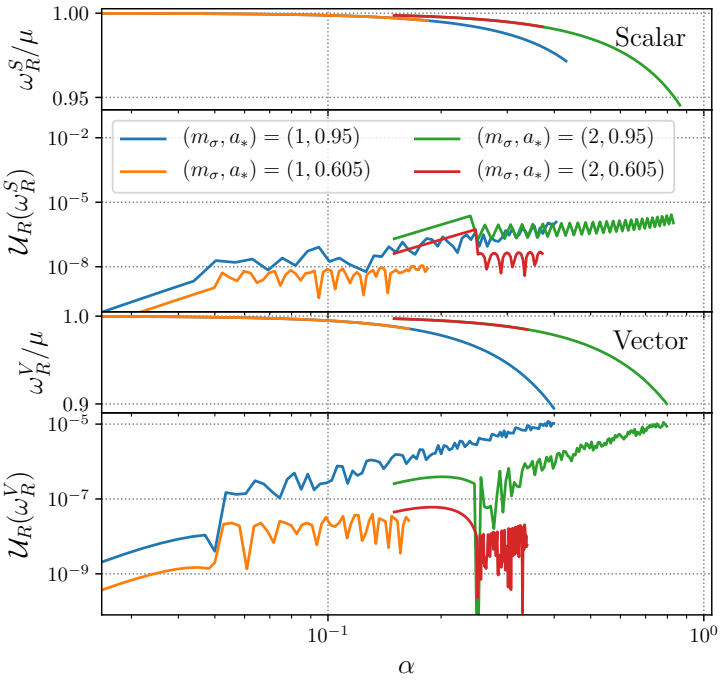

Figure E.3: We show a set of representative frequencies ω_R of a $m_\sigma = 1$ and 2 scalar *(top)* and vector *(bottom)* mode (with $\ell_S = m_S$ and $\hat{S} = -1$, respectively), assuming a BH spin of $a_* \in \{0.605, 0.95\}$, obtained by `SuperRad`. We also plot the relative interpolation/extrapolation error $\mathcal{U}_R$ of these predictions (see the main text for discussion).

contained in `SuperRad`.

As we show below, we find the interpolation and extrapolation error to be the dominant source of error for the waveform model, subdominant to the truncation error described in the previous section, and shown in Figure E.1 and Figure E.2. As described in the main text, and shown in Figure 6.2, in the relativistic regime labelled $\mathcal{D}_{\rm int}$, `SuperRad` uses linear interpolation functions to interpolate based on a grid of 320^2 data points. We quantify the interpolation error by directly computing the value of ω_R and ω_I at intermediate value to these data points using the methods outlined in the previous section, and compare them to the interpolated value. Similarly, we can directly compute the values of ω_R and ω_I in the non-relativistic regime $\mathcal{D}_{\rm fit}$, again using the accurate numerical methods from the previous section, and compare them to their extrapolated values obtained using the fits.

In Figure E.3 and Figure E.4, we show the relative error in interpolating or extrapolating ω_R and ω_I to a given point in `SuperRad`, compared to directly computing the value at that

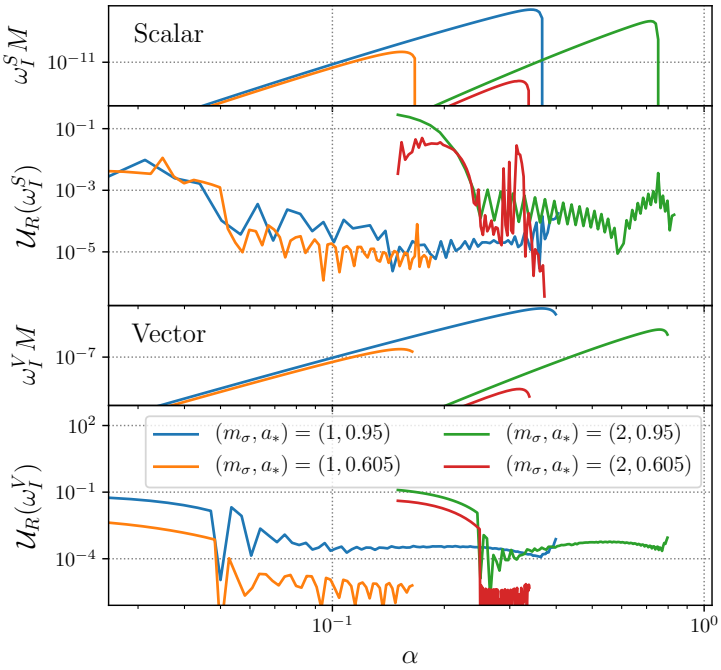

Figure E.4: We show a set of representative growth rates ω_I^σ of a $m_\sigma = 1, 2$ scalar *(top)* and vector *(bottom)* mode (with $\ell_S = m_S$ and $\hat{S} = -1$, respectively), assuming a BH spin of $a_* \in \{0.6, 0.95\}$, obtained by `SuperRad`. We also plot the relative interpolation/extrapolation error $\mathcal{U}_R$ of these predictions (see the main text for discussion).

point $\mathcal{U}_R(x) = |x - x_{\rm num.}|/x_{\rm num.}$. We show this for two fiducial spin values $a_* \in \{0.605, 0.95\}$ across the α-parameter space from a region in $\mathcal{D}_{\rm fit}$ to the entire $\mathcal{D}_{\rm int}$ at that spin. The uncertainty is relatively low in the relativistic regime $\mathcal{D}_{\rm int}$, spanning from $\alpha^{m_\sigma=1} = 0.05$ and $\alpha^{m_\sigma=2} = 0.25$ to maximal α. There, the relative uncertainty in the frequency ω_R does not exceed $\sim 10^{-5}$, while in the case of the growth rates ω_I, it is bounded by $\sim 10^{-2}$. In the extrapolated region $\mathcal{D}_{\rm fit}$, spanning from $\alpha^{m_\sigma=1} = 0.05$ and $\alpha^{m_\sigma=2} = 0.25$ towards small α, the uncertainty $\mathcal{U}_R(\omega_R)$ of the frequencies is well under control and decreases in the Newtonian limit. The growth rates, on the other hand, show larger uncertainties transitioning from $\mathcal{D}_{\rm int}$ towards smaller α. The fitting procedure, in this case, is more complex, which is reflected in the choices of p and q required for (6.14) (noted below) to be below or comparable to the difference between the purely analytic expressions and the numerical expressions obtained in parts of $\mathcal{D}_{\rm fit}$. The fit functions and the purely analytic estimates for ω_I have comparable accuracy for $\alpha \lesssim 0.05$ and $\alpha \lesssim 0.25$ for $m_\sigma = 1$ and

$m_\sigma = 2$, respectively. The uncertainties are, by construction, decreasing at sufficiently small α, while there remains an intermediate regime around $\alpha \approx 0.02$ for $m_\sigma = 1$ and $\alpha \approx 0.2$ for $m_\sigma = 2$, where the uncertainties first increase. This is a result of the lack of accurate analytical or numerical modeling in this regime. Lastly, since all numerical errors discussed in the previous appendices are below the uncertainties presented here, the latter can be understood as the overall uncertainties of the waveform model. Furthermore, comparing the uncertainties $\mathcal{U}_R$ presented here to the relative differences in Figure 6.3 and Figure 6.4, we see that the latter is always smaller or comparable to the former. We comment on the uncertainties in the GW emission in Appendix E.5. As can be seen in the temporal evolution of the GW frequency emitted by an $m_S = 1$ scalar cloud in Figure 6.1, the quantities (frequencies, timescales, frequency drifts etc.) exhibit a small discontinuity at the interface of $\mathcal{D}_{\rm fit}$ and $\mathcal{D}_{\rm int}$. This is important only, when the system is evolved adiabatically using (6.35), not when the saturation condition $\omega_R = m_\sigma \Omega_H$ is used to set the GW amplitude.

For completeness, we list the different domains $\mathcal{D}_{\rm int}$ used in `SuperRad` here. These domains are all bounded by the superradiance saturation condition $\omega_R = m_\sigma \Omega_H(a_*)$ at sufficiently large α, and by $a_* = 0.6$ and $a_* = 0.995$. At small α the regions $\mathcal{D}_{\rm int}$ are bounded by $\alpha_{m_\sigma=1} = 0.05$ and $\alpha_{m_\sigma=2} = 0.25$ for both the scalar and the vector clouds. The fit functions for ω_R in (6.10) contain the following terms: For $m_V = 1$ and 2 and $m_S = 1$ and 2, we set $q \in \{0, 1, \ldots, 3\}$ and $p \in \{6, 7, 8\}$. In all four cases, we added the term $\alpha^5 a_* (\sqrt{1 - a_*^2} - 1)$. The fit functions for ω_I in (6.14) contain the following terms: For $m_V = 1$, we set $p \in \{1, 2, \ldots, 10\}$, and $q \in \{0, 1\}$; for $m_V = 2$ we set $p \in \{5, 6, \ldots, 10\}$ and $q \in \{0, 1\}$; for $m_S = 1$ we set $p \in \{1, 2, 3\}$ and $q \in \{0, 1, \ldots, 3\}$; for $m_S = 2$ we alter the fit function slightly with $\hat{c}_{p,q} \to \delta_{q,1} \hat{c}_p$ and $\hat{b}_{p,q} \to \alpha^2 \hat{b}_{p,q}/a_*$ with $p \in \{12, \ldots, 22\}$ and $q \in \{0, 1, \ldots, 3\}$. These were fit against the numerical data in $\mathcal{D}_{\rm int}$ with $\alpha < \alpha_{\rm bound}$, where $\alpha_{\rm bound}^{m_\sigma=1} = 0.25$ and $\alpha_{\rm bound}^{m_\sigma=2} = 0.6$.

E.4 Frequency shift

In this appendix, we briefly discuss the leading-in-α contribution to the shift in frequency due to the self-gravity of the cloud $\Delta\omega_\sigma = \alpha^3 M_c F_\sigma / M^2$, where F_σ is defined in (6.21), as described in Sec. 6.4. For the scalar and vector boson clouds, these are given by

$$\begin{aligned} F_S &= \bar{F}[m_S], \\ F_V &= \bar{F}[m_V - 1], \end{aligned} \tag{E.15}$$

where

$$\bar{F}[b] = -\frac{2(b+1)\sqrt{\pi}\Gamma(2(b+1)) - \Gamma\left(2b+\frac{5}{2}\right)}{2(b+1)^3\sqrt{\pi}\Gamma(2(b+1))}. \tag{E.16}$$

In Table E.1, we present explicit values for $m_\sigma = 1, \ldots, 5$ for both the scalar and vector cases. The frequency shift monotonically decreases with increasing m_σ. The shift depends (to leading order in α) only on the ℓ_σ mode number of the considered field, i.e., the Bohr radius of these non-relativistic solutions, which determines F_σ, is dependent on the ℓ_σ mode number only.

E.5 Gravitational waves

In this appendix, we outline the frequency-domain methods used in the literature and this work to determine the GWs emitted from a superradiant cloud after the saturation of the instability, i.e., assuming $\omega_R = m_\sigma \Omega_H(a_*)$. In the context of the Teukolsky formalism for linear perturbations on a fixed Kerr spacetime $g_{\mu\nu}$, finding the GW power and strain reduces to finding the Weyl-Newman-Penrose scalar Ψ_4 at large distances. To that end, the field equations for linear metric perturbations on $g_{\mu\nu}$ are solved using a separation ansatz similar to the one used in the previous sections. The polar equation is the defining equation for spin-weighted spheroidal harmonics, while schematically the sourced radial Teukolsky equation takes the form [357]

$$\mathcal{D}^{a,M}_{\ell m\omega} R_{\ell m\omega}(r) = \hat{T}_{\ell m\omega}(r), \tag{E.17}$$

with sources $\hat{T}_{\ell m\omega}$. In this appendix, ℓ, m, and ω refer exclusively to modes characterizing the metric perturbations, not the states of the superradiant clouds. The second order radial

m_V	m_S	$M^2\Delta\omega_\sigma/(M_c\alpha^3)$
1	-	$-5/8$
2	1	$-93/512$
3	2	$-793/9216$
4	3	$-26333/524288$
5	4	$-43191/1310720$
6	5	$-1172755/50331648$

Table E.1: We list the first few leading-in-α contributions to the frequency shift $\Delta\omega_\sigma = \alpha^3 M_c F_\sigma / M^2$ for the oscillation frequency of scalar and vector clouds.

differential operator $\mathcal{D}^{a,M}_{\ell m\omega}$, for a Kerr spacetime of mass M and spin parameter a, is of Sturm-Liouville type and, hence, allows for the generic construction of a Green's function to solve the inhomogeneous problem ($\hat{T}_{\ell m\omega} \neq 0$) given the set of homogeneous solutions $R^H_{\ell m\omega}$ satisfying purely ingoing and purely outgoing boundary conditions at the horizon, $r = r_+$, and infinity, $r \to \infty$, respectively. At large distances r, the solution to the radial Teukolsky equation is

$$\begin{aligned} R_{\ell m\omega}(r \to \infty) &= \frac{r^3 e^{i\omega r_*}}{2i\omega B_{\ell m\omega}} \int_{r_+}^{\infty} dr' \frac{\hat{T}_{\ell m\omega} R^H_{\ell m\omega}}{\Delta^2} \\ &= Z^{\infty}_{\ell m} r^3 e^{i\omega r_*}. \end{aligned} \tag{E.18}$$

Here, r_* is the Tortoise coordinate of r, and we defined a set of variables $Z^{\infty}_{\ell m}$ containing information about the source (see, e.g., Ref. [338], for details). With this in hand, the GWs at infinity can be calculated as

$$\Psi_4 = \frac{1}{r} \sum_{\ell,m} \frac{Z^{\infty}_{\ell m}}{\sqrt{2\pi}} e^{i\omega(r_*-t)} {}_{-2}S_{\ell m}(\theta; c = a\omega) e^{im\varphi}. \tag{E.19}$$

Notice, the summation in (E.19) is over *spheroidal* ℓ, rather than *spherical* ℓ as done in Sec. 6.5.1. Here, we are using the normalization $\int d\cos\theta |{}_{-2}S_{\ell m}(\theta; c)|^2 = 1$. To recover the spherical harmonic GW modes $h^{\ell' m'}$, we rewrite the above, using

$$h = -\frac{2\Psi_4}{(2\omega_R)^2}, \tag{E.20}$$

leading to

$$r e^{i\omega t} h^{\ell' m'} = \sum_{\ell,m} \frac{-2 Z^{\infty}_{\ell m}}{\sqrt{2\pi}(2\omega_R)^2} C^{\ell' m'}_{\ell m} = \frac{-2\tilde{Z}^{\infty}_{\ell' m'}}{\sqrt{2\pi}(2\omega_R)^2}, \tag{E.21}$$

with

$$C^{\ell' m'}_{\ell m} = \int_{S^2} d\Omega {}_{-2}\bar{Y}_{\ell' m'}(\Omega) {}_{-2}S_{\ell m}(\theta; c = a\omega) e^{im\varphi}. \tag{E.22}$$

Note that when $c = 0$, $C^{\ell' m'}_{\ell m} = 2\pi \delta^{\ell'}_{\ell} \delta^{m'}_{m}$. The total emitted gravitational energy flux is

$$P_{\rm GW} = \sum_{\ell',m'} \frac{|\tilde{Z}^{\infty}_{\ell' m'}|^2}{8\pi^2 (2\omega_R)^2}. \tag{E.23}$$

Therefore, determining the GWs emitted depends on finding homogeneous solutions to the radial Teukolsky equation, as well as integrating these over the cloud sources $\hat{T}_{\ell m\omega}$. The three distinct approximations mentioned in the main text—flat, Schwarzschild, and Teukolsky—all emerge from (E.18) by dropping certain terms. In the flat approximation, the spin is neglected, $a = 0$, and the source equations are expanded to leading order in α, implying $M \to 0$. In this limit, both the homogeneous solutions and source functions can be constructed and integrated over analytically. In the Schwarzschild approximation, one also expands in α to leading order and assumes $a = 0$. However, one includes the gravitational potential terms present in the Schwarzschild Green's function, i.e., $M \neq 0$. For $\ell' = m' = 2$, the flat ansatz generally underestimates the emitted GW flux, while the Schwarzschild approximation overestimates the power. Solving the equation (E.17) numerically making no assumptions about α or a (referred to as the Teukolsky approximation in the main text) provides the most accurate predictions for $P_{\rm GW}$ and h, and is expected to give values intermediate to the flat and the Schwarzschild approximations. More details can be found in, for instance, Refs. [81, 50].

For $\ell' = m' > 2$, i.e., $m_\sigma > 1$, the GW energy flux has been computed analytically only in the flat approximation. In the scalar case, the total GW power emitted from a cloud with (n_S, m_S) and $\ell_S = m_S$, is given by [377]

$$P_{\rm GW} = C_{n_S m_S} \alpha^{Q_S} \frac{M_c^2}{M^2}, \tag{E.24}$$

where $Q_S = 4m_S + 10$ and

$$\begin{aligned} C_{n_S m_S} = &\frac{16^{m_S+1} m_S (2m_S - 1)}{n_S^{4m_S+8} (m_S + 1)\Gamma(m_S + 1)^4} \\ &\times \frac{\Gamma(2m_S - 1)^2 \Gamma(m_S + n_S + 1)^2}{\Gamma(4m_S + 3)\Gamma(n_S - m_S)^2}. \end{aligned} \tag{E.25}$$

In the vector case, for $m' > 1$, the GW power emitted from a $\hat{S} = -1$ superradiant state in the $\alpha \ll 1$ limit is [50]

$$P_{\rm GW} = K_{m_V} \alpha^{Q_V} \frac{M_c^2}{M^2}, \tag{E.26}$$

where $Q_V = 4m_V + 6$, $K_2 = 1/126, K_3 = 6 \times 10^{-6}, K_4 = 2 \times 10^{-9}$, and $K_5 = 4 \times 10^{-13}$.

The specifics of the methods we use to numerically solve (E.17) are discussed in detail in Ref. [338] (we make use of the `BHPToolkit` [2]). It involves constructing the sources $\hat{T}_{\ell m\omega}$ from the numerical superradiant solutions to (6.1), and integrating (E.18) numerically. In

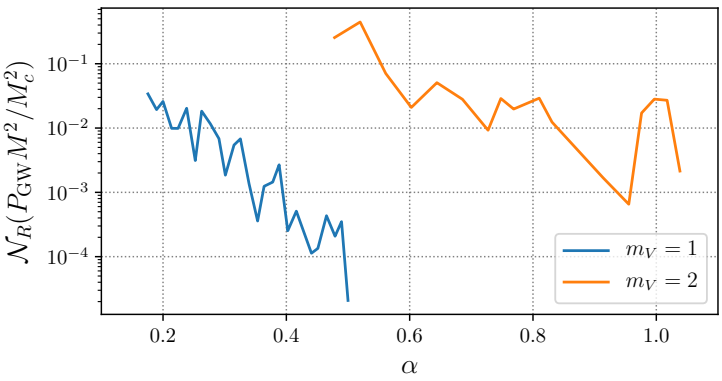

Figure E.5: The relative numerical error $\mathcal{N}_R$ of the total emitted GW energy flux $P_{\rm GW}$ from a vector cloud in the $m_V = 1$ and $m_V = 2$ superradiant states around a BH of spin $a = 0.985M$ in the relevant part of the parameter space.

Figure E.5, we present upper bounds on the numerical error of these methods across the entire parameter space, assuming a $m_V = 1$ and 2 vector cloud (analogous upper bounds are expected for scalar clouds). The bounds are obtained from varying the resolution of the underlying superradiant vector field solution together with the radial step size of the numerical integration of (E.18). The relative difference between estimates of $\tilde{P}_{\rm GW}$ with two different resolutions decreases with increasing resolution. The upper bounds shown in Figure E.5 are the relative difference between the default resolution used throughout, and half that resolution. As for the GW power calculation, the GW strain h is calculated from the solutions to (E.18), through (E.21). Since $h \sim \sqrt{P_{\rm GW}}$, the values for $\mathcal{N}_R(\tilde{P}_{\rm GW})$ can be interpreted as an estimate for the error $\mathcal{N}_R(h_{\times,+}M/M_c)$ for the amplitudes of the polarization waveform.

Lastly, the numerical data regimes $\tilde{D}_{\rm int}$ (defined in Sec. 6.5.2) is bounded at large α by the maximal α satisfying the superradiance saturation condition $\omega_R = m_\sigma \Omega_H$ at the corresponding spin a_*. From below, it is bounded by $\alpha_{\rm low}^{m_S=1} = 0.2$ and $\alpha_{\rm low}^{m_S=2} = 0.34$, for scalars and the two lowest azimuthal numbers, and $\alpha_{\rm low}^{m_V=1} = 0.17$ and $\alpha_{\rm low}^{m_V=2} = 0.45$, for vectors with the two lowest azimuthal numbers.